

**Detailed Electrochemical, Spectroscopic,
and Microscopic Study on the Influence
of Electrolyte Additives and Alumina
Coatings on the Aging of
 $\text{LiNi}_{0.4}\text{Mn}_{1.6}\text{O}_4$ based Cathodes**

Der Naturwissenschaftlichen Fakultät der
Friedrich-Alexander-Universität Erlangen-Nürnberg
zur
Erlangung des Doktorgrades Dr. rer. nat.

vorgelegt von
Stefanie A. Ostermeyer
aus Oettingen in Bayern

Als Dissertation genehmigt
von der Naturwissenschaftlichen Fakultät
der Friedrich-Alexander-Universität Erlangen-Nürnberg.

Tag der mündlichen Prüfung: 26.07.2016

Vorsitzender des Promotionsorgans: Prof. Dr. Jörn Wilms

Gutachter: Prof. Dr. Dirk M. Guldi

Prof. Dr.-Ing. Werner Schreiber

Die vorliegende Arbeit wurde in der Zeit von August 2012 bis Dezember 2015 in der VOLKSWAGEN VARTA Microbattery Forschungsgesellschaft mbH & Co. KG in Ellwangen, im Technologiezentrum in Isenbüttel der Volkswagen AG und am Department Chemie und Pharmazie am Lehrstuhl für Physikalische Chemie I der Friedrich-Alexander-Universität Erlangen-Nürnberg unter der Leitung von Prof. Dr. Dirk M. Guldi angefertigt.

Die Ergebnisse, Meinungen und Schlüsse dieser Dissertation sind nicht notwendigerweise die der Volkswagen AG.

Ich versichere hiermit eidesstattlich, dass ich die vorliegende Arbeit selbstständig und nur mit Hilfe der angegebenen Hilfsmittel angefertigt habe.

Stefanie Ostermeyer

*“Everything is theoretically impossible,
until it is done.”*

- Robert A. Heinlein -

*- Für meine Familie und Tobias -
Danke für alles*

Acknowledgement

In the first place, I would like to gratefully thank my advisor Prof. Dr. Dirk M. Guldi for his willingness to support my scientific work outside the Chair of Physical Chemistry I. I am very thankful for his continuous guidance, understanding, interest, and valuable advice.

Of course, I would like to acknowledge Prof. Dr.-Ing. Werner Schreiber and Dr. Konrad Holl for giving me the opportunity to accomplish the present PhD thesis at the VOLKSWAGEN VARTA Microbattery Forschungsgesellschaft mbH & Co. KG in Ellwangen. Additionally, I want to thank Prof. Dr.-Ing. Werner Schreiber for reviewing my PhD thesis.

I would like to express my sincere gratitude to Dr. Markus Pompetzki for his great supervision, patience, helpful advice, astute criticism, and continuous assistance during all stages of this work. Due to his constant support, I was able to gather detailed scientific background for the investigated systems and processes. Thank you also for taking time to review my PhD thesis. Furthermore, I enjoyed our motivating and inspiring conversations, not only about scientific issues.

Moreover, a huge thank you is addressed to all my colleagues from the VOLKSWAGEN VARTA Microbattery Forschungsgesellschaft mbH & Co. KG for their exceptional support and commitment. My special thanks are dedicated to the whole R&D group for assistance, sharing ideas, helping out in every aspect, and the outstanding team work. In that sense, thank you Stefanie Cadus, Dr. Sebastian Schebesta, Jürgen Möß, and Dr. Hartmut Bruglachner. I would also like to acknowledge all members of the open-plan office for the good discussions, and the very pleasant working atmosphere. Thanks also to Silke Scheler for introducing me to various techniques in the lab and Sandra Korella for assisting me with respect to formation and cycling procedures.

At the technology center Isenbüttel of the Volkswagen AG, I am grateful to all my colleagues for their effort, help, and good scientific exchange. Special thanks go to Dr. Frank Seyfried, Dr. Jörg Huslage, Dr. Wolfgang Zipprich, Dr. Linda Brinkhaus, Dr. Carla Cavalca de Araujo, Christoph Franke, Enrica Jochler, and Sylke Schilde.

Sincere thanks go to Clariant (now referred to as Johnson Matthey Battery Materials GmbH) for providing the cathode active material $\text{LiNi}_{0.4}\text{Mn}_{1.6}\text{O}_4$ as main component of the investigated cathodes. In this regard, it should be stressed that without their support and excellent cooperation none of the herein presented results could have been realized.

The following persons and various institutes or companies deserve great thanks of their high-quality processing of analytical and spectroscopic measurements. I wish to thank Dr. Meike Fleischhammer (ZSW), who carried out the XRD measurements. Dr. Ahmed S. A. Soliman (Volkswagen AG) and Daniel Burrow (Volkswagen AG) are acknowledged for providing me with the data of Raman spectroscopy and the SEM images, respectively. I want to thank Franziska Kröll (VARTA Microbattery GmbH), who conducted the ICP-OES measurements. Likewise, big thanks go to the group of Prof. Dr. Wolfram Jägermann, especially Natalia Schulz, (Institute of Materials science, Darmstadt University of Technology), for generating and discussing the XPS data.

Furthermore, I would like to thank all my friends for keeping me company, making my life colorful, regularly bringing smiles, and for your qualities in partying.

Of course, a giant thank you is dedicated to my parents, my sister, and my brother. I am grateful for your patience, support, trust, and love during education and life in general. Thank you for your help in all times.

I would like to most sincerely thank my partner Tobias. Thank you for your help, support, understanding, unrelenting encouragement, and most importantly your love. Thank you for making me more than I am.

Finally, I wish to thank God, the almighty, for his immense blessings and help provided to me throughout my life.

Kurzfassung

Derzeit ist die Reichweite von Fahrzeugen mit Verbrennungsmotoren nicht mit reinen Elektroantrieben realisierbar. Gegenwärtige Standardaktivmaterialien liefern hierfür zu geringe Energiedichten. Vor kurzem hat das Kathodenaktivmaterial Hochvoltspinell (z.B. $\text{LiNi}_{0,5}\text{Mn}_{1,5}\text{O}_4$) großes Interesse auf dem Gebiet der Lithium-Ionen-Batterietechnologie geweckt. Mit dessen Hilfe soll eine deutliche Steigerung der Energiedichten ermöglicht werden. Grund dafür ist die hohe theoretische mittlere Spannung von 4,7 V vs. Li des Materials bei einer moderaten theoretischen gravimetrischen Kapazität von 147 mAhg^{-1} . Allerdings weisen Hochvoltspinell-Vollzellen starke Kapazitätsverluste und eine sehr kurze Zyklenlebensdauer auf.^[1–6]

Das Hauptziel dieser Dissertation besteht darin, die elektrochemischen Eigenschaften von C// $\text{LiNi}_{0,4}\text{Mn}_{1,6}\text{O}_4$ Vollzellen zu verbessern. Dabei werden zwei verschiedene Strategien verfolgt: Elektrolytoptimierung durch die Zugabe von ausgewählten Additiven zu einer Standardelektrolytformulierung und Applikation von Al_2O_3 -Beschichtungen auf Elektroden mittels eines Rakelverfahrens. Ferner vermittelt diese Arbeit ein tieferes Verständnis über den Einfluss der angewendeten Elektrolytadditive und der Al_2O_3 -Schichten auf die Phasenzusammensetzung von $\text{LiNi}_{0,4}\text{Mn}_{1,6}\text{O}_4$ -Kompositkathoden, sowie auf das Ausschwemmungsverhalten der Übergangsmetalle, über die Struktur und die Zusammensetzung der SPI auf Hochvoltspinell-Elektroden und über die auftretenden Impedanzen in C// $\text{LiNi}_{0,4}\text{Mn}_{1,6}\text{O}_4$ Vollzellen.

Zunächst werden theoretischen Aspekte und Konzepte vorgestellt. Konkret wird die geschichtliche Entwicklung der Interkalations-Kathodenaktivmaterialien dargestellt, die wichtigsten Eigenschaften von Lithiumnickelmanganoxid-Spinellen beschrieben, Probleme und Aufgaben von Hochvoltspinell-Vollzellen aufgezeigt und die verwendeten Analysemethoden erläutert.

Dann wird die Ermittlung eines Referenzsystems und eine allgemeine elektrochemische Charakterisierung von C// $\text{LiNi}_{0,4}\text{Mn}_{1,6}\text{O}_4$ -Pouchzellen, die den Referenzelektrolyten (1 M LiPF_6 in EC/EMC/DMC (1/1/1, w/w/w)) enthalten, beschrieben. Anschließend sind CC/CV-Zyklisierungen und C-Ratentests von Hochvoltspinell-Vollzellen, die ausgewählte Elektrolytadditive und Al_2O_3 -Beschichtungen enthalten, aufgeführt. XRD-Analysen und Ramanspektroskopie wurden durchgeführt, um die Veränderung der Phasenzusammensetzungen von Kathoden nach Alterung von C// $\text{LiNi}_{0,4}\text{Mn}_{1,6}\text{O}_4$ Vollzellen mit unterschiedlichen Elektrolytadditiven und Al_2O_3 -Schichten auf den Elektroden zu untersuchen. Ramanspektroskopie wurde außerdem zur Bestimmung der Oxidationsstufen der Übergangsmetalle in den resultierenden Phasen verwendet. Mittels ICP-OES- und EDX-Messungen von Graphitanoden bei 0% SOC wurde das Ausschwemmungsverhalten der

Übergangsmetalle nach Zyklisierung von C//LiNi_{0,4}Mn_{1,6}O₄ Vollzellen mit unterschiedlichen Elektrolytadditiven und Al₂O₃-Beschichtungen studiert. XPS-Analysen von formierten und gezykelten C//LiNi_{0,4}Mn_{1,6}O₄-Pouchzellen wurden angewendet, um die Zusammensetzung und Entwicklung von Grenzschichten zwischen LiNi_{0,4}Mn_{1,6}O₄-Kathoden und unterschiedlichen Elektrolytformulierungen zu erforschen. Insbesondere wurde die Rolle der Elektrolytadditive im Zusammenhang mit dem Deckschichtaufbau untersucht. Elektrochemische Impedanzspektroskopie von formierten und gezykelten Hochvoltspinell-Zellen wurde ausgeführt, um ein tieferes Verständnis hinsichtlich der Wirkmechanismen der Elektrolytadditive und der Al₂O₃-Filme in der Vollzelle zu erlangen. Basierend auf den Ergebnissen aus diesen elektrochemischen, mikroskopischen und spektroskopischen Analysetechniken wurden CC/CV-Zyklisierungen mit Spinell-Vollzellen durchgeführt, die unterschiedliche Kombinationen der besten beiden Additive (0,5% TMP und 0,1% LiBOB) und Al₂O₃-beschichteter Kathoden enthielten. Abschließend wurde eine Zusammenfassung aller gewonnenen Ergebnisse erstellt.

Abstract

Currently, cars powered only by electricity cannot compete with drive systems comprising combustion engines in terms of driving range. The main limitation is based on the low energy densities of standard active materials for LIBs. Recently, the cathode active material high voltage spinel (e.g. $\text{LiNi}_{0.5}\text{Mn}_{1.5}\text{O}_4$) has triggered great interest in the field of the lithium ion battery technology. The latter is expected to enable a substantial enhancement of the cell energy densities owing to its high theoretical average voltage of 4.7 V vs. Li at a moderate theoretical gravimetric capacity of 147 mAhg^{-1} . Nevertheless, high voltage spinel full cells have been reported to show severe capacity losses and very restricted cycle lifes.^[1–6]

The main objective of this thesis is to improve the electrochemical performance of C// $\text{LiNi}_{0.4}\text{Mn}_{1.6}\text{O}_4$ full cells. Thereby, two different strategies are pursued: on one hand, electrolyte optimization by adding selected additives to a standard electrolyte formulation and on the other hand, application of Al_2O_3 coating layers on electrodes by a doctor blade process. Moreover, this thesis provides a better understanding regarding the influence of these electrolyte additives and the Al_2O_3 films on the phase composition and the transition metal dissolution behavior of $\text{LiNi}_{0.4}\text{Mn}_{1.6}\text{O}_4$ composite cathodes, the structure and the composition of the SPI on high voltage spinel electrode surfaces, and the impedance properties of C// $\text{LiNi}_{0.4}\text{Mn}_{1.6}\text{O}_4$ full cells.

At the beginning, the theoretical background needed to follow this thesis is provided. It includes the historical development of intercalation cathode active materials for rechargeable LIBs, important characteristics of lithium nickel manganese oxide spinels, problems and challenges of high voltage spinel full cells, and the description of the utilized methods of analysis.

Then, the establishment of a reference system and the general electrochemical characterization of C// $\text{LiNi}_{0.4}\text{Mn}_{1.6}\text{O}_4$ pouch cells containing the reference electrolyte (1 M LiPF_6 in EC/EMC/DMC (1/1/1, w/w/w)) is described. Subsequently, CC/CV-cycling experiments and rate capability tests of high voltage spinel full cells comprising selected electrolyte additives and Al_2O_3 coating layers are presented. XRD analyses and Raman spectroscopy were carried out to examine phase compositional changes of the cathode upon ageing C// $\text{LiNi}_{0.4}\text{Mn}_{1.6}\text{O}_4$ full cells containing different electrolyte additives and Al_2O_3 films on the electrodes. Raman spectroscopy is additionally used for determining the oxidation states of the transition metal ions within the resulting phases. By means of ICP-OES and EDX measurements transition metal dissolution studies are conducted with graphite anodes at 0% SOC after cycling C// $\text{LiNi}_{0.4}\text{Mn}_{1.6}\text{O}_4$ full cells including diverse electrolyte additives and Al_2O_3 coating layers. XPS analysis is applied to study the chemical nature and the development of the interfacial layers between $\text{LiNi}_{0.4}\text{Mn}_{1.6}\text{O}_4$ electrodes and the different electrolyte formulations after formatting and after cycling C// $\text{LiNi}_{0.4}\text{Mn}_{1.6}\text{O}_4$ pouch cells comprising selected electrolyte additives.

Especially, the role of each additive in the SPI structure is examined. Electrochemical impedance spectroscopy of formatted and cycled high voltage spinel full cells was accomplished to gather a deeper comprehension of the mechanism of each electrolyte additive and the Al_2O_3 coating layers regarding the entire full cell. Based on the results of the aforementioned electrochemical, microscopic, and spectroscopic analyses, CC/CV-cycling experiments were conducted with spinel full cells comprising different combinations of the two most beneficial additives (0.5% TMP and 0.1% LiBOB) and Al_2O_3 coated spinel cathodes. Finally, conclusions about all the obtained results are drawn.

List of abbreviations

Arabic abbreviations

A	ampere
Å	angstrom
A _E	electromagnetic field
A _{ex}	experimentally determined constant ($= 1.1 \cdot 10^{-9} \text{ V}^{-1}$)
A _s	area of the sample from which photoelectrons are detected
A _w	atomic weight
abbr.	abbreviation
AC	alternating current
Ag	silver
Ah	ampere-hour
aka	also known as
Al	aluminum
ALD	atomic layer deposition
approx.	approximately
As	arsenic
ASF	atomic sensitivity factor
at%	atomic percent
a.u.	arbitrary units
Au	gold
BET	Brunauer-Emmett-Teller
BEV	battery electric vehicle
BOL	begin of life
c	speed of light ($= 299,792,458 \frac{\text{m}}{\text{s}}$)
C	graphite
C _F	capacitor
C _L	coulomb
C _{specific}	specific capacity
3C	computer, communications and consumer electronics
ca.	circa
CAM	cathode active material
CC	constant current
Cd	cadmium
Ce	cerium
cf.	confer
CFSE	crystal field stabilization energy
cm	centimeter
CNLS	complex nonlinear least squares fitting
Co	cobalt
CPE	constant phase element

CPS	counts per second
CPSeV	counts per second electron volt
C-rate	current rate
Cr	chromium
Cu	copper
CV	constant voltage
CVS	chemical injection pump
d	layer thickness
d _a	distance between two atomic lattice planes
d _e	empirical constant ranging from 0 to 1
DAISY-BAT	DARmstädter Integriertes SYstem für BATterieforschung
DC	direct current
DEC	diethyl carbonate
Dq	differential of quanta
DMC	dimethyl carbonate
e	electron charge (= $1.60210 \cdot 10^{-19}$ C)
E	energy
E _B	binding energy
E _C	correlation energy
E _{el}	electric energy
E _F	Fermi energy
E _f (N - 1)	energy of the N-particle system in the final state
E _i (N)	energy of the N-particle system in the initial state
E _{kin}	kinetic energy
E _r	radiation energy
E _{relax}	relaxation energy
EC	ethylene carbonate
EDX	energy dispersive X-ray spectroscopy
e.g.	for example (exempli gratia)
EIS	electrochemical impedance spectroscopy
EMC	ethyl methyl carbonate
EOL	end of life
EREV	extended range electric vehicle
et al.	et alii or et aliae; and others
etc.	et cetera; and so on
EU	European union
EUCAR	European Council for Automotive Research and Development
eV	electron volt
EV	electric vehicle
f	frequency
f ₀	frequency of the laser
f _{max}	maximum frequency
f _{vib}	resonance frequency of a vibrating molecule

$f_{\text{X-ray}}$	X-ray flux in photons/(cm ² · s)
F	Faraday constant (= 96458 Cmol ⁻¹)
Fe	iron
FEC	fluoroethylene carbonate
F-EMC	methyl 2,2,2-trifluoroethyl carbonate
F-EPE	1,1,2,2-tetrafluoroethyl 2,2,3,3-tetrafluoropropylether
FTIR	Fourier transform infrared spectroscopy
FWHM	full width at half maximum
g	gram
Ga	gallium
GC	gas chromatography
GHz	gigahertz
GLN	glutaronitrile
h	hour
\hbar_P	reduced Planck constant (= $1.0545 \cdot 10^{-34}$ Js)
H_0	unperturbed Hamilton operator
\hbar_P	Planck constant (= $6.6256 \cdot 10^{-34}$ Js)
H_{PE}	perturbation operator
He	helium
HEV	hybrid electric vehicle
HF	hydrogen fluoride
HFIP	tris(1,1,1,3,3,3-hexafluoroisopropyl)phosphate
HMDS	hexamethyldisilazane
HOMO	highest occupied molecular orbital
hp	horsepower
HS	high spin
Hz	hertz
i	complex number ($i = \sqrt{-1}$)
I	current
I_0	amplitude of the AC current
I_A	intensity of a photoemission line for element A
I_{aS}	intensity of the anti-Stokes lines
I_B	integrated intensity of the bremspectrum
I_S	intensity of the Stokes lines
I_{Sub}^0	intensity of a photoemission line for the pure substrate
I_{Sub}^d	intensity of a photoemission line for the covered substrate
ICP-OES	inductively coupled plasma-optical emission spectroscopy
IR	infrared
j	total angular momentum quantum number
J	joule
k_B	Boltzmann constant (= $1.3806 \cdot 10^{-23}$ JK ⁻¹)
K	Kelvin
keV	kilo electron volt

kg	kilogram
kHz	kilohertz
l	azimuthal quantum number
L	liter
L ₁	inductor
La	lanthanum
LCO	lithium cobalt oxide
Li	lithium
LiAsF ₆	lithium hexafluoroarsenate
LIB	lithium ion battery
LiBF ₄	lithium tetrafluoroborate
LiBOB	lithium bis(oxalate)borate
LiClO ₄	lithium perchlorate
LiFAP	lithium tris(pentafluoroethyl)trifluorophosphate
LiFP ₆	lithium hexafluorophosphate
LMO	lithium manganese oxide spinel
LNO	lithium nickel oxide
LS	low spin
LiSO ₃ CF ₃	lithium trifluoromethanesulfonate
LiTFSi	lithium bis(trifluoromethanesulphonyl)imide
LTO	lithium titanate or lithium titanium oxide (Li ₄ Ti ₅ O ₁₂)
LUMO	lowest unoccupied molecular orbital
m	meter
m _e	electron mass (= 9.1091 · 10 ⁻³¹ kg)
m _q	magnetic quantum number
M	transition metal
M _m	molecular mass
mAh	milliampere-hour
mbar	millibar
Mg	magnesium
mHz	millihertz
MHz	megahertz
Min	minute
Mn	manganese
Mo	molybdenum
MOCVD	metalorganic chemical vapour deposition
mV	millivolt
mW	milliwatt
n	principal quantum number
n _λ	whole number of wavelengths
n _A	number of atoms of the element A per cm ³ of the sample
NaCMC	sodium carboxymethyl cellulose
NASICON	sodium super ionic conductor

Nb	niobium
NCM	lithium nickel cobalt manganese oxide
Nd	neodymium
Ne	neon
Ni	nickel
NiMH	nickel metal-hydride
nm	nanometer
NMC	lithium nickel manganese cobalt oxide
ns	nanoseconds
OCV	open circuit voltage
OSSE	octahedral site stabilization energy
p	momentum operator
Pb	lead
PC	propylene carbonate
PES	photoelectron spectroscopy
PLD	pulsed laser deposition
PHEV	plug-in hybrid electric vehicle
ppb	parts per billion ($= 10^{-9}$)
ppm	parts per million ($= 10^{-6}$)
Pr	praseodymium
Pt	platinum
PVDF	polyvinylidene fluoride
q	normal mode of the oscillating system
q ₀	vibrational amplitude
R	alkyl groups or hydrogen
R _{ct}	charge-transfer resistance
R _d	penetration depth
R _i	internal cell resistance
R _s	surface resistance
R _y	Rydberg constant ($= 1.097 \cdot 10^7 \text{ m}^{-1}$)
R _Ω	resistor
RE	reference electrode
ref.	reference
RF	radio frequency
rpm	revolutions per minute
Ru	ruthenium
s	spin quantum number
S	Siemens
S _c	screening constant
SA	succinic anhydride
SBR	Styrene-Butadiene Rubber
SEI	solid electrolyte interface
SEM	scanning electron microscopy or microscope

SEN	sebaconitrile
Si	silicon
S.G.	space group
SOC	state-of-charge
SPI	solid permeable interface
t	time
T	detection efficiency for electrons emitted from the sample
T _s	sample temperature
TEHP	tris(2-ethylhexyl) phosphate
TFPi	tris(2,2,2-trifluoroethyl)phosphite
Ti	titanium
TMP	trimethyl phosphate
TTSP	tris(trimethylsilyl) phosphate
U	AC voltage
U ₀	amplitude of the AC voltage
U _a	acceleration voltage
UHV	ultra-high vacuum
UPS	ultraviolet photoelectron spectroscopy
USA	United States of America
UV	ultraviolet
v	volume fraction
v _e	electron velocity
V	volt
V(r)	potential energy
vol%	volume percent
vs.	versus
w	mass fraction
W	watt
W ₁	Warburg
W _{i→f}	transition probability of a multi-particle system from an initial to a final state
Wh	watt-hour
WPPD	Whole Powder Pattern Decomposition
wt%	weight percent
x	number of electrons
XAFS	X-ray absorption fine structure
XANES	X-ray absorption near edge structure
XPS	X-ray photoelectron spectroscopy
X-ray	X-radiation
XRD	X-ray diffraction
y	efficiency in the photoelectric process for formation of photoelectrons of the normal photoelectron energy
Y	admittance

Z	impedance
Z_0	impedance of an ideal capacitance
Z_a	atomic number
Zr	zirconium
ZSW	Zentrum für Sonnenenergie- und Wasserstoffforschung Baden-Württemberg

Greek abbreviations

α	polarizability
α_0	polarizability at the equilibrium position
δ	optical skin depth
ΔE	energy difference
ΔE_d	energy resolution of the analyzer
ΔE_n	natural line width of the transition from the initial to the final state (lifetime effect)
ΔE_p	line width of the exciting radiation
$\Delta E(\text{FWHM})$	spectral line width
θ	angular efficiency factor for the instrumental arrangement based on the angle between the photon path and the detected electron
λ	wavelength
λ_e	mean free path
λ_{\min}	minimum wavelength
μ	magnetic permeability
μ_{ind}	induced electrical dipole
μg	microgram
μHz	microhertz
μL	microliter
μm	micrometer
ρ	mean density of the sample
σ	electronic conductivity
σ_A	photoelectric cross-section for the atomic orbital A in cm^2
Φ	phase angle
Φ_0	work function
Ψ_f	final state
Ψ_i	initial state
ω	angular frequency

Contents

Acknowledgement	VI
Kurzfassung	VIII
Abstract.....	X
List of abbreviations.....	XII
Contents.....	XIX
1. Introduction	1
2. Theoretical concepts	9
2.1 Historical development of intercalation cathode active materials for rechargeable lithium ion batteries.....	9
2.1.1 Layered lithium transition metal oxides	11
2.1.2 Polyanion-containing compounds	26
2.1.3 Spinel oxide cathodes.....	29
2.2 Lithium nickel manganese oxide spinels	38
2.2.1 The crystal structures of $\text{LiNi}_{0.5}\text{Mn}_{1.5}\text{O}_4$	39
2.2.2 Phase transitions upon cycling.....	42
2.2.3 Problems and challenges of high voltage spinel full cells.....	45
2.3 Methods of characterization	54
2.3.1 Cycling method: CC/CV-cycling.....	54
2.3.2 Three-electrode measurement.....	55
2.3.3 X-ray diffraction	59
2.3.4 Raman spectroscopy	65
2.3.5 Inductively coupled plasma-optical emission spectroscopy.....	73
2.3.6 Scanning electron microscopy and energy dispersive spectroscopy..	76
2.3.7 X-ray photoelectron spectroscopy.....	79
2.3.8 Electrochemical impedance spectroscopy	91
3. Motivation and objective.....	100
4. Experimental conditions	105
4.1 Chemicals and materials.....	105

4.2	Instruments	107
4.3	Sample preparation and measuring conditions.....	108
5.	Results and discussion	114
5.1	Compositional and morphological investigation of $\text{LiNi}_{0.4}\text{Mn}_{1.6}\text{O}_4$ as cathode active material.....	114
5.2	Electrochemical characterization of C// $\text{LiNi}_{0.4}\text{Mn}_{1.6}\text{O}_4$ full cells.....	116
5.2.1	<i>Determination of the reference system and general electrochemical response of $\text{LiNi}_{0.4}\text{Mn}_{1.6}\text{O}_4$ cathodes</i>	<i>116</i>
5.2.2	<i>Cycling stability studies.....</i>	<i>126</i>
5.2.3	<i>Rate capability tests.....</i>	<i>149</i>
5.3	Post-mortem analyses of the cathode active material – determination of different phase compositions	153
5.3.1	<i>X-ray diffraction.....</i>	<i>153</i>
5.3.2	<i>Raman spectroscopy.....</i>	<i>160</i>
5.4	Transition metal dissolution studies.....	175
5.5	Characterization of the solid permeable interface.....	186
5.6	Electrochemical impedance spectroscopy.....	230
5.7	Improvement of the cycling stability of C// $\text{LiNi}_{0.4}\text{Mn}_{1.6}\text{O}_4$ full cells.....	239
6.	Conclusion	242
7.	Appendix	250
7.1	X-ray diffraction.....	250
7.2	Raman spectroscopy.....	251
7.3	X-ray photoelectron spectroscopy	259
7.4	Electrochemical impedance spectroscopy.....	289
	References.....	XXI

1. Introduction

In recent decades, the demand for lithium ion batteries (LIBs) has grown considerably. During the years 2000 - 2015 a massive enhancement of worldwide LIBs sales has been registered.^[7] Currently, the LIB market is dominated by the 3C industry (computer, communications and consumer electronics).^[8] Mobile machines (e.g. industrial trucks, cleaning machines, construction machines, etc.), stationary storage systems (e.g. photovoltaic plants, uninterruptible power supply, autarkic power supply, etc.), and power tools play only a limited role. The automotive sector is also still in the early stages with respect to developing LIB driven cars.^[8] However, according to a forecast by the market research institute Roland Berger Strategy Consultants GmbH, automobiles will in the future increasingly be powered with LIBs.^[9] The main driving forces are environmental and political targets.

Due to the worldwide concern about the consequences of global warming and the depletion of fossil fuels, the trend towards energy saving, the reduction of greenhouse gas emissions, and the substitution of fossil fuels by other materials or technologies is evolving.^[10] In order to guarantee a sustainable, affordable, and environmentally friendly energy supply of the future, the Federal Government of Germany has defined ambitious goals.^[10,11] Alternative energy sources (e.g. renewables like wind and solar energies) are promoted for electricity production. For instance, Germany pursues the goal to cover 80% of its power supply with the help of renewables by 2050.^[10] Moreover, in 2050 the greenhouse gas emissions are supposed to be reduced by 80 - 95% compared with 1990.^[10] In compliance with the cars regulation of the European Union, all new passenger cars must not exceed the fleet-average CO₂ emission target of 95 g/km by 2020.^[12] Additionally, the Federal Government of Germany aims at having one million electric vehicles (EVs) on the roads by 2020 and Germany should transform into the lead market for electromobility.^[11] Thus, electrification of powertrains is a focus of automobile manufacturers leading, however, to new challenges to engineers and scientists. Nonetheless, the first electric motors for automobiles were already employed in the 19th century. In 1835, T. Davenport designed an engine for the first vehicle powered by electricity, an electric model train, and he was granted the first patent for an electric motor in 1837.^[13] Fourteen years later, C. G. Page built an electromagnetic engine for a battery driven electric locomotive, which achieved a speed of 19 miles an hour.^[14] However, it was the French physicist G. Planté, who laid the foundation for the development of EVs with the invention of the rechargeable lead-acid accumulator in 1859.^[15,16] Even today it is the most commonly used battery type and it dominates the field of starter batteries.^[15,17] The first EV in the world was assembled by G. Trouvé. He equipped a tricycle with a 0.1 hp DC motor powered by lead-acid batteries, which was shown at the Paris Exhibition in 1881.^[18] Nine years later, F. Porsche and L. Lohner presented the first hybrid electric vehicle, which combined an electric engine and a

2.5 hp Daimler gasoline engine to reach greater driving ranges.^[19] At that time, this concept was revolutionary and electric cars were on the rise, although automobiles comprising internal combustion engines were already available. At the beginning of the 20th century this changed, however, considerably and the market for electromobility was dying off as gasoline cars rapidly improved. The continuous development of internal combustion engines and the cheap oil price displaced the needs for electric vehicle technology and the electric drive became solely a niche product.^[20] It was not until the 1990s that electrically powered cars have again gained interest across the globe. Increased oil prices and the fact that significant progress has been made in the area of battery technology has promoted the electromobility market. Since then, the research in this field has continued to grow and lots of money has been invested in electromobility.^[21]

For the future, electric cars are regarded as a promising alternative to vehicles containing conventional combustion engines. Thereby, for the next decades, drive concepts could pass through an evolutionary process to finally lead to a pure electric vehicle (Figure 1).

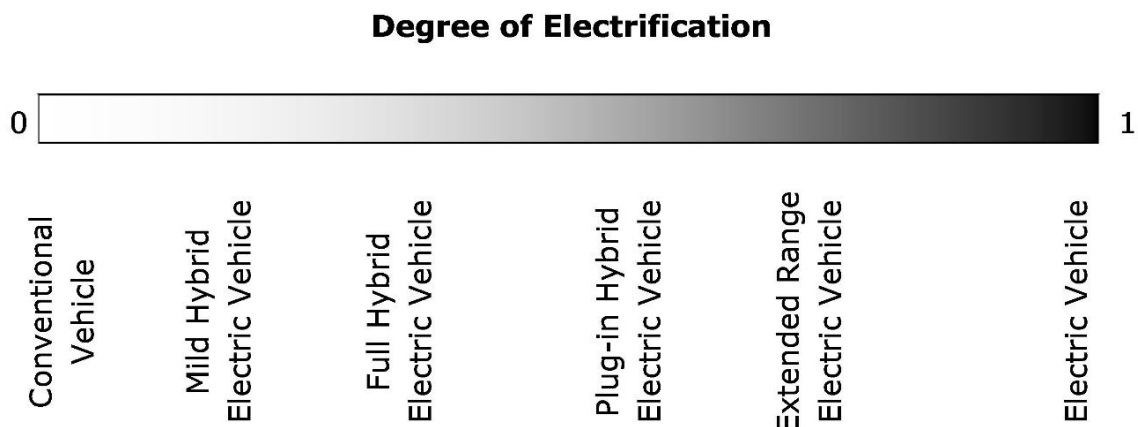


Figure 1 Degree of electrification of EVs. With modifications from^[22].

During the transition phase, internal combustion engines will be supported by a second, electrically based propulsion system. These vehicles are referred to as “hybrids,” or “hybrid electric vehicles” (HEVs). Depending on the degree of electrification and the combinations between the two systems, various levels of hybridization exist with different features. Micro hybrid electric vehicles only include an automatic start-stop system and are able to recover brake energy (recuperation). The powertrain comprises an internal combustion engine without electrical assistance.^[23,24]

In contrast, mild hybrid vehicles are equipped with an electric motor. Nonetheless, its torsional moment and its battery power are insufficient for pure electric driving. In this case, the electric machine just has a supportive character and works like an electric turbocharger.^[25]

Considering full hybrid electric vehicles, short distances or local city traffic is accomplishable by the electric engine alone. In practice, two types of design principles are distinguished: parallel and serial HEVs.^[26]

In a serial hybrid electric vehicle, there is no mechanical connection between the internal combustion engine and the electric one. Actually, the electric machine is exclusively responsible for the propulsion. The internal combustion engine only runs occasionally in an optimum operating range to produce electricity via a generator and, thus, to charge the battery during driving. Consequently, the internal combustion engine expands the driving range of the car. This is why HEV architectures are also named extended range electric vehicle (EREV).^[23,27]

The parallel hybrid is the most wide-spread technology. The internal combustion engine and the electric motor are coupled via a gear unit. Usually, the coupling occurs along the main axle. Hence, it is possible to drive in a mixed mode involving both propulsion systems or in a single mode.^[23,28]

A further development of the HEV concept is the Plug-in hybrid electric vehicle (PHEV). Here, the accumulator is not only charged by recuperation, but also externally by an electricity grid. Therefore, longer distances are accessible by pure electric driving.^[23,29]

Finally, battery electric vehicles (BEVs) include solely one energy storage device and one drive system without any additional internal combustion engine. This is the reason why these cars are also called “zero emission vehicles”. However, this is only true when the required electricity is generated by renewable energy sources. The actual propulsion occurs via the electric motor and the power of BEVs is provided by rechargeable battery packs. In order to compete with conventional cars comprising internal combustion engines, efficient batteries with high energy and power densities are needed.^[23] Subsequently, several aspects relevant for electromobility are elucidated.

Generally, battery cells for EVs are specified and evaluated according to the following five criteria: energy density, power density, lifetime, safety, and costs. On one hand, the gravimetric energy density or specific energy is defined by the energy content per mass of a battery cell (Whkg^{-1}). It determines the energy storage property of a cell and, hence, the electrical driving range. Due to the high demand on long driving ranges, the specific energy plays an important role regarding the competitiveness of BEVs vs. conventional cars. On the other hand, the volumetric energy density is given by the energy content per spatial volume (WhL^{-1}). Since the space in vehicles is limited, high volumetric energy densities are favored. Thereby, the so-called “inactive” materials like the separator, the electrolyte, the current collectors, and the cell housing have to be considered, too, as they have a significant impact on the overall cell weight and cell volume.^[15,30]

The specific power, which is expressed by the power divided by the mass of the battery cell (Wkg^{-1}), is crucial for the acceleration, the speed, and the quick charging capability of EVs. Typically, the limited rates of electron and ion transfer within the electrodes and at the electrode/electrolyte interfaces restrict the power of a battery cell. The surface, the porosity, and the wetting behavior of the electrodes have a major influence on the speed of the electrochemical reactions.^[30]

Batteries for automotive applications can be classified into BEV or high energy cells, PHEV cells, and HEV or high power cells. While PHEV cells should be a compromise between high energy and high power cells, high energy cells usually afford high storage capacities and low power densities, and high power cells deliver low energy densities and high power densities. The main difference of the two extreme types is the active material per electrode surface. High energy cells comprise thick electrodes with high contents of active materials to increase the storage capacities, whereas high power cells contain thin electrodes to enhance the reactions rates.^[30]

Furthermore, the service life of a battery cell should at least match the average lifetime of a new car, which is around ten to fifteen years. In practice, calendrical durability and driving cycles are represented by cycling battery cells at 1C until the capacity drops below 80% of the initial capacity. In order to simulate the seasonal temperature fluctuations, cycling and storage experiments are also performed under different temperatures (e.g. - 10 °C, + 23 °C, and + 45 °C). Operating at various C-rates helps to estimate the rate capability of cells.^[30]

Another very important aspect with respect to battery cells for automotive applications is safety. Since the battery cells store energy and contain highly flammable chemicals, they might generate explosive mixtures upon damage. Short circuits, overcharging, heat exposure, and collisions as in case of accidents are potential hazards. In the future, it is essential that commercialized battery cells or battery modules operate safely under various driving modes.^[31] To be able to compare the security of different battery cells with each other, the European Council for Automotive Research and Development (EUCAR) has determined a hazard level ranking, which is valid for all safety tests.^[32] It ranges from zero (no effect; most safe) to seven (explosion; most unsafe). Currently, most battery cells achieve a hazard level of four or less, but cell manufactures aim to make battery cells more secure and to achieve hazard levels of three or less.^[32]

For automobile manufacturers and prospective clients the costs of EVs in comparison to cars with internal combustion engines are a decisive factor and they will certainly influence the market acceptance of EVs. The cell chemistry, the production, and the battery system add up to the overall costs, whereby mass production and the development of more efficient manufacturing machines will lower the total costs in the future. Actually, costs between 200 and 600 €/kWh are predicted for 2020.^[33,34]

Aside from the electric motor, the battery has definitely a key function concerning the electric powertrain in EVs. Therefore, sequential improvements in battery technology have inter alia been necessary requirements for the expansion of the EV market. The first battery was invented by Alessandro Volta in 1800. He discovered that two metallic electrodes immersed in an electrolyte produce a continuous current. Its original voltaic pile comprised alternating discs of zinc and copper separated by a cardboard that had been soaked in saltwater.^[15]

In 1867, Leclanché developed a dry battery cell consisting of a carbon rod enclosed by manganese dioxide, which is dipped into a zinc cylinder containing an ammonium chloride paste. Although this cell is frequently referred to as carbon-zinc cell, it should be noted that the carbon does not contribute to the electrochemical reaction, but the active parts, which produce electricity, are zinc and manganese dioxide.^[35] The main disadvantage of this cell type is the participation of the electrolyte in the electrochemical reactions resulting in barely soluble intermediates (e.g. $\text{Zn}(\text{NH}_3)_2\text{Cl}_2$, $\text{ZnO} \cdot \text{Mn}_2\text{O}_3$, and $\text{ZnCl}_2 \cdot 4 \text{Zn}(\text{OH})_2$), which impede ionic diffusion processes. Moreover, chemical corrosion leads to the formation of hydrogen causing a rise of the internal cell pressure and the damage of the cell housing.^[36] The successor offers an improved performance and a longer service life as it comprises a zinc chloride solution instead of the ammonium chloride electrolyte.^[36] Today, one of the mostly used household batteries are alkaline ones. In comparison to the zinc chloride type, alkaline cells with a potassium hydroxide electrolyte solution, a zinc anode, and a manganese dioxide cathode have higher specific energies (150 Whkg^{-1}) and a longer shelf-life.^[37,38] Nevertheless, alkaline cells are usually not rechargeable and belong to the group of primary batteries.^[37]

In 1854, Sinsteden published first experimental results on lead-acid accumulators. Independent of this work, five years later, the French physicist Planté presented a technically more mature, rechargeable lead-acid battery. It consisted of two identical lead plates immersed in a diluted aqueous solution of sulfuric acid.^[15,39] In 1881, Fauré developed a system, in which the active materials are produced separately. He coated lead plates, and later lead grids, with a paste of red lead oxide, sulfuric acid, and water. Then, the electrodes were charged to form Pb and PbO_2 . At that time, the industrial manufacture of lead-acid batteries has started.^[15,39] For electromobility, lead-acid accumulators are not considered as they have only a limited specific energy of $25 - 40 \text{ Whkg}^{-1}$ and an insufficient cycle life of $400 - 800$ cycles.^[40,41]

In 1899, Jungner developed the first nickel-cadmium (NiCd) accumulator. Two years later, Edison invented the cheaper nickel-iron (NiFe) alternative. Both systems have a nickel oxyhydroxide cathode and a potassium hydroxide electrolyte solution. While the NiCd battery comprises a cadmium metal anode, the NiFe accumulator contains a metallic iron negative electrode.^[15] The NiFe concept is accompanied by several drawbacks such as low storage capacities of $50 - 55 \text{ Whkg}^{-1}$, safety issues due to the formation of hydrogen, high self-discharge, and loss of capacity at low ambient temperatures.^[41,42] The NiCd technology

affords good cycle life and is capable of accepting high charge and discharge rates, but also faces difficulties like a low energy density of approx. 50 Whkg^{-1} , environmental concerns because of the toxicity of cadmium, and energy losses owing to the so-called “memory effect”.^[41–43] This phenomenon describes the tendency of a battery to adjust its electrical behavior to a certain duty cycle, to which it has been repeatedly subjected. In other words, the accumulator can remember how much energy was drawn on previous discharges and it will not provide more capacity than was demanded before.^[43,44]

The next step towards higher energy densities was achieved with the commercialization of the rechargeable nickel metal-hydride (NiMH) battery around 1990.^[15] This battery consists of a nickel oxyhydroxide positive electrode, a KOH electrolyte, and an alloy anode in the form of AB_5 ($\text{A} = \text{La, Ce, Nd, and Pr}$ and $\text{B} = \text{Ni, Co, Mn, and Al}$).^[15,45] The metal alloy acts as a storage medium for hydrogen, which is the actual negative active material. This battery type has some advantages compared to earlier battery models such as a high specific energy of $60 - 80 \text{ Whkg}^{-1}$, a long cycle life, minimum environmental problems, a relative insensitivity to temperature (-30°C to $+45^\circ\text{C}$), and a rapid recharging capability. Nonetheless, NiMH accumulators also suffer from the “memory effect” and show a higher self-discharge rate than NiCd samples.^[46,47] NiMH batteries were mostly utilized in portable electronic devices (e.g. mobile phones, calculators, laptop computers, ...) and in toys.^[47] Although the NiMH technology was implemented in the first generation of HEVs, it has soon been substituted by lithium ion accumulators, which is primarily due to their higher energy densities and longer cycle lives.

The first commercial secondary lithium ion battery cells were produced by Exxon in the USA in 1970 with a lithium metal anode and a TiS_2 cathode.^[48] Metallic lithium is favored as material for the negative electrode because it is the lightest, solid element of the periodic system and, thus, has the highest volumetric (2100 mAhL^{-1}) and gravimetric (3860 mAhg^{-1}) capacity.^[15] Furthermore, the potential of this anode lies around 0.0 V vs. Li/Li^+ resulting in a maximum cell voltage.^[15] Nevertheless, 0.3% of lithium is lost in every cycling step, since it is not completely reprecipitated on the metallic surface. The most serious disadvantage is, however, the formation of dendrites, while reprecipitating during the discharge step. These lithium needles are a real safety problem as they can puncture the separator and, hence, cause a short circuit within the battery cell.^[15]

That is the reason why researchers looked for alternative anode materials. Intercalation materials came into the focus of research, because they are not prone to dendrite formation upon cycling. Since Sony revolutionized the battery market by introducing secondary LIBs with a carbon anode and a lithium cobalt oxide cathode in 1990, carbon-based anodes have been utilized in nearly all LIBs.^[49] Today, mainly synthetic and natural graphites are used as active materials for negative electrodes.^[15] Lithium ions intercalate into the graphite structure to form

LiC₆. Consequently, elementary, metallic lithium is no longer present in the battery cell and security risks are definitely reduced. Theoretically, each C₆ unit in a graphitic anode is able to reversibly store one lithium atom, which corresponds to a theoretical capacity of 372 mAhg⁻¹.^[15] Practically only ca. 0.9 lithium atoms are reversibly intercalated into the graphite anode. Approximately 10% of the lithium ions are consumed due to reactions with the electrolyte upon formatting the battery cell. Thereby, a so-called solid electrolyte interface (SEI) layer is established on the anode surface. This is an irreversible process, which is unavoidable. It protects the structure of the graphite electrode.^[15]

In order to further enhance the energy densities of LIBs, silicon seems to be a good choice as a future anode active material because it provides with 3578 mAhg⁻¹ a significantly higher theoretical specific capacity than carbon-based negative electrodes.^[50] Nevertheless, strong volume changes of Si throughout lithium insertion/extraction prevent the integration of this material in commercial cells. A possible way to minimize the influence of volume changes and to simultaneously increase the cell capacity involves the utilization of Si/C composites comprising only 5 - 20% silicon. Although these active materials are promising candidates to enhance the specific energy of LIBs, they need optimization prior to market maturity.^[51]

Apart from anode materials, the development of cathode materials has also been continuously pushed. Actually, the list of cathode active materials (CAMs) is very long and extensive. The three most prominent substance classes of intercalation materials are layered lithium transition metal oxides, polyanion-containing compounds, and spinel oxides. Among those the lithium transition metal oxides are of major relevance. LiCoO₂, LiNi_{0.80}Co_{0.15}Al_{0.05}O₂, and LiNi_{1/3}Mn_{1/3}Co_{1/3}O₂ are well-known representatives. A detailed review of the historical development of intercalation CAMs for rechargeable lithium ion batteries is given in chapter 2.1.

Currently, commercial LIBs for automotive applications reach specific energies between 150 and 200 Whkg⁻¹, volumetric energy densities of 250 - 530 WhL⁻¹, and specific powers up to 1500 Wkg⁻¹ in dependence of the utilized materials (e.g. cathode and anode active materials, separator, etc.).^[52] Figure 2 compares the specific energy and the specific power of different technologies in a Ragone plot.

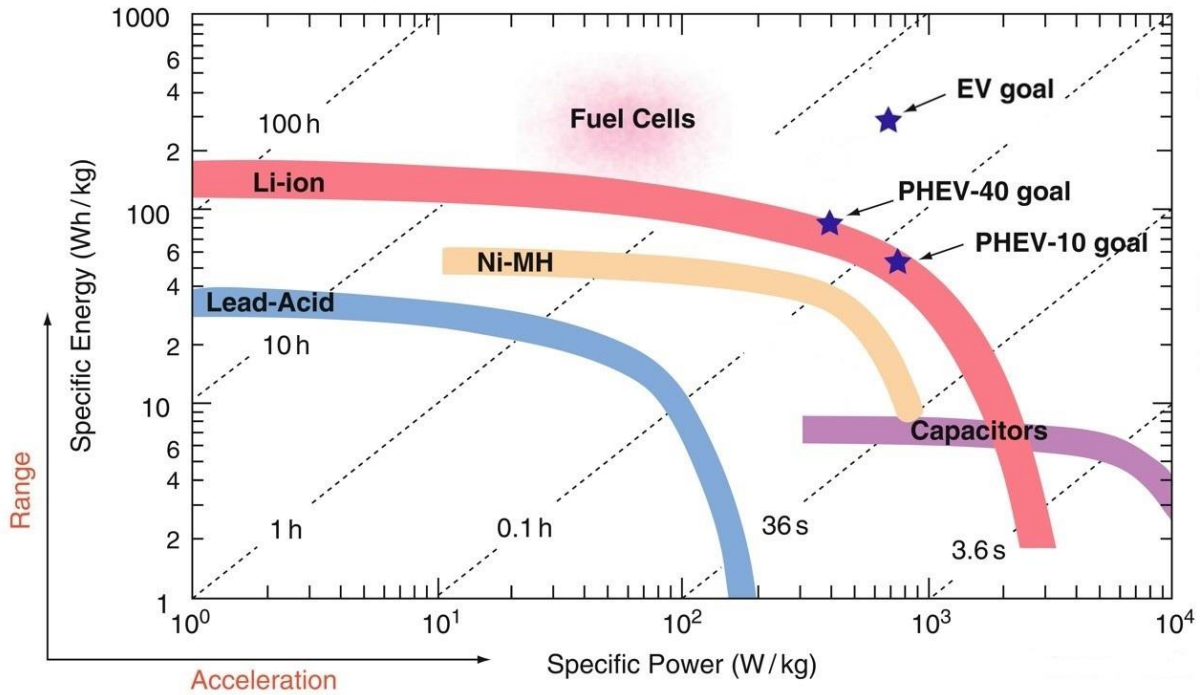


Figure 2 Ragone plot of diverse electrochemical devices. Goals for BEVs and PHEVs are also indicated. With modifications from^[53].

Full cells are considered as high energy systems and supercapacitors are regarded as high power technologies. LIBs possess intermediate power and energy features. There are also high energy cells or high power cells but up to now it is difficult to combine both – high energy and high power characteristics – in one LIB cell. While the current LIB concept is sufficient for PHEVs, substantial higher specific energies are needed for BEVs. The goal for the next five years is to achieve higher gravimetric energy densities between 250 and 300 Whkg⁻¹.^[54] Thereto, extensive research and development are essential.

A promising way to realize that goal is the application of nickel substituted manganese spinels (e.g. LiNi_{0.5}Mn_{1.5}O₄) as CAMs. They are also called high voltage spinels as they operate at a high theoretical average voltage of 4.7 V vs. Li.^[55] Together with their theoretical gravimetric capacity of 147 mAhg⁻¹ they are supposed to enable a substantial enhancement of cell energy densities. Nevertheless, the respective full cells have been reported to show severe capacity losses and very restricted cycle lifes.^[1–6] This thesis deals with the optimization of the electrochemical performance of high voltage spinel full cells to extend their high specific energy to long-term cycling periods.

2. Theoretical concepts

2.1 Historical development of intercalation cathode active materials for rechargeable lithium ion batteries

In 1978, Armand claimed insertion materials as the best solution for rechargeable and non-aqueous LIBs. Chalcogenides and sulfides were the first cathode materials of interest. R. Schöllhorn of Germany and J. Rouxel of France explored layered transition-metal sulfides and selenides as early as 1970.^[56] However, the breakthrough was reached by Exxon in the USA. It manufactured a LIB with metallic lithium as anode and TiS_2 as cathode, whose active material development was mainly driven by Whittingham and co-workers.^[48] On discharge at room temperature, Li^+ are inserted from the anode into the empty octahedral sites of the layered TiS_2 cathode and Ti^{4+} are reduced to Ti^{3+} . The mechanism is reversed in case of charging. The stable, hexagonal close-packed structure of TiS_2 , which is formed by a plane of titanium atoms between two sheets of sulfur atoms, provides quite good reversibility. No phase changes are observed upon charging/discharging. By means of excess lithium anodes, electrochemical ageing up to 1,000 cycles with a capacity loss less than 0.05% can be achieved.^[16,57,58] Consequently, a number of other layered sulfides and chalcogenides were studied during the 1970s and 1980s.^[58,59] For example, E-One Moli Energy Corporation in Canada produced commercial Li//MoS_2 coin cells.^[60] In order to overcome dendrite formation and, thus, severe safety problems, the metallic lithium was replaced by Li-Al alloys as anode materials. The combination of two intercalation substances as anode and cathode materials was proposed by Armand, Rao et al., and Murphy et al. in the 1970s.^[61]

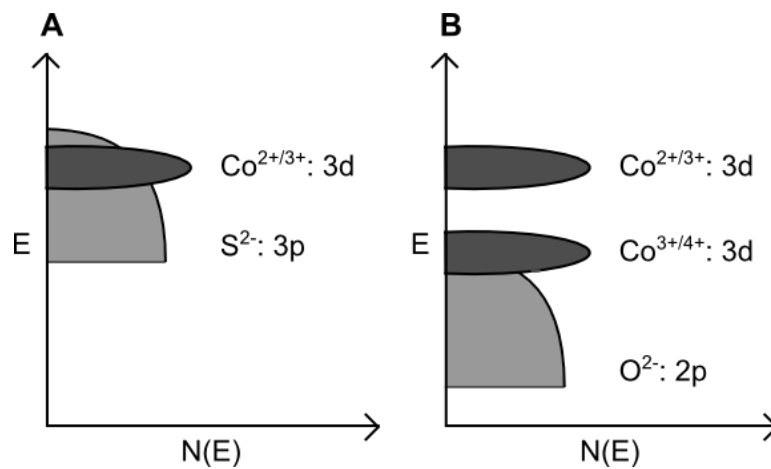
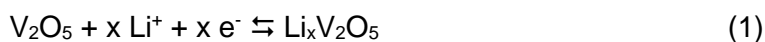


Figure 3 Relative energies of Co:3d bands and **A** the S^{2-} :3p band and **B** the O^{2-} :2p band. Adapted from^[16].

Nevertheless, batteries with chalcogenide and sulfide cathodes feature major limitations. Owing to their metallic character, they show low lithium ion conductivity or reaction speed.^[58] In addition, cells containing such cathodes deliver insufficient operating voltages (< 2.5 V). The higher-valent M^{n+} d band overlaps with the top of the nonmetallic p band. Hence, electrons are removed from the nonmetallic p band. In case of cobalt sulfide (Figure 3A), S_2^{2-} molecular ions are formed as a result of electron withdrawal from the S^{2-} :3p band. The high energy level of the nonmetallic p-bands in chalcogenides or sulfides prevents the generation of M^{n+} ions with higher oxidation states. Therefore, the cell voltage is constrained to < 2.5 V.^[16]

Due to these problems, scientists focused on other CAMs. Several metal oxides like MoO_3 ^[62], WO_3 ^[63], and chromium oxides^[64] were considered as reversible insertion electrodes. However, only Vanadium pentoxide, V_2O_5 has been explored for more than 30 years up to date.^[65] It is an interesting substance because of its low cost, abundance, facile synthesis, and high energy density. V_2O_5 has a layered structure with weak V-O bonds. It consists of puckering rows of VO_5 square pyramids along the c-axis of orthorhombic cells (Figure 4A). The general intercalation and deintercalation mechanism can be described as:



Nonetheless, V_2O_5 undergoes certain irreversible phase transitions during electrochemical cycling. The structural instability leads to pulverization of the cathode material and poor cycles. Rapid capacity loss, low electronic and ionic conductivity, and slow electrochemical kinetics makes the bulk form of V_2O_5 unsuitable for LIB applications. Nowadays, researchers concentrate on nanostructures of V_2O_5 , which overcome the disadvantages of the bulk material. Nanotubes, nanobelts, nanorods, nanowaxberries (Figure 4B), nanowires (Figure 4C), and nanoflowers are only some of the nanostructures, which are recognized to improve the structural and electrochemical properties of V_2O_5 , but with limiting success.^[58,66,67] In the 1970s, several layered oxides containing manganese, cobalt, chromium, and other metals were extensively investigated. Especially, Hagenmuller and Delmas promoted the study on these cathode candidates.^[68,69] Layered lithium transition metal compounds, however, did not play a major role at that time. This changed with the discovery of lithiating agents and convenient synthesis processes. To this end, the actual development of layered lithium transition metal oxides has started.^[58,69]

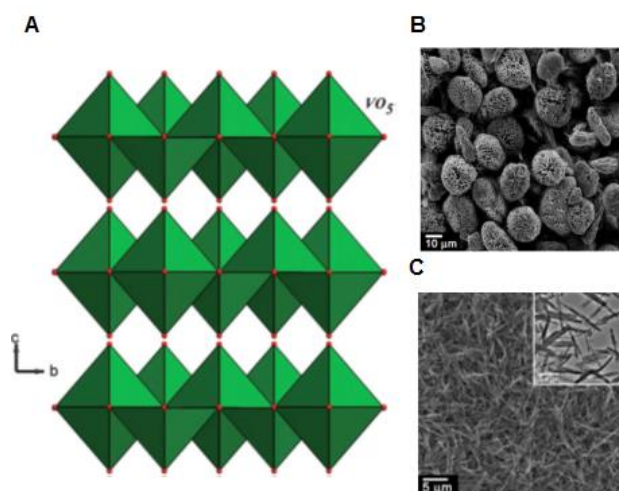


Figure 4 A Schematic structure of layered V_2O_5 .^[67] B SEM image of V_2O_5 nanowaxberries.^[66] C SEM image of V_2O_5 nanowires.^[66]

2.1.1 Layered lithium transition metal oxides

Goodenough and co-workers at the University of Oxford explored layered oxides $LiMO_2$ because the $O^{2-}:2p$ band is positioned at a lower energy level than the $S^{2-}:3p$ band (Figure 3).^[56] The ideal structure of $LiMO_2$ ($M = V, Cr, Co$, and Ni), which is isostructural with α - $NaFeO_2$, is illustrated in Figure 5.

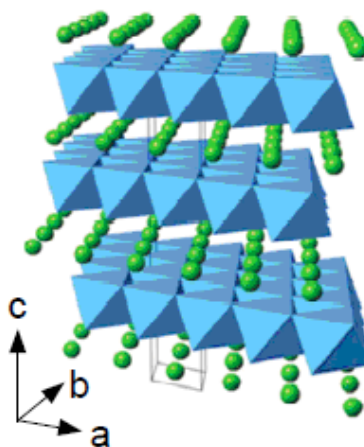


Figure 5 Schematic structure of the crystallographic form of $LiMO_2$ (blue: MO_6 octahedra, and green: lithium ions).^[70]

The M^{3+} and the Li^+ ions are located in alternating (111) layers of edge sharing octahedral interstitial sites forming cubic close-packed oxygen arrays with stack sequences of $-O-Li-O-M-O-$ along the c axis. According to the notation of Delmas and Hagenmüller, $LiMO_2$ is designated as “O3 layered structure”, indicating that the unit cell is composed of lithium ions coordinated to octahedral sites and three MO_2 sheets.^[69,71] This rhombohedral structure with lithium ions located in octahedral 3a, nickel ions in octahedral 3b, and oxygen ions in 6c sites

(S.G. R3m) provides two dimensional diffusion pathways for lithium ions between the MO_2 layers. Thereby, Li^+ ions move from one octahedral site plane to another via a tetrahedral site. Reversible Li^+ intercalation/deintercalation occurs without damaging the lattice structure. The good electronic properties of LiMO_2 materials are attributed to direct M-M interactions between the edge-sharing MO_6 octahedra.^[16]

The selection of suitable transition metals M for the CAM LiMO_2 is based on the following considerations. The energy difference between the d band of the redox pair $\text{M}^{3+/4+}$ and the top of the $\text{O}^{2-}2\text{p}$ band should be as small as possible in order to lower the Fermi energy E_F of the cathode and to increase the cell voltage. Nevertheless, the metal d band and the nonmetal p band should not overlap because Li removal would lead to the introduction of holes in the $\text{O}^{2-}2\text{p}$ band. In this case, peroxide ions O_2^{2-} would be generated and the loss of O_2 would be a consequence. Furthermore, the M^{3+} and M^{4+} ions should prefer strong octahedral sites to obtain structural stability.^[48] The octahedral site stabilization energies (OSSEs) of a few 3d transition metals are given in Table 1. The OSSEs are calculated by subtracting the crystal field stabilization energy (CFSE) of an octahedral coordination from a tetrahedral coordination.^[72]

Ion	Octahedral coordination		Tetrahedral coordination		OSSE
	Configuration	CFSE	Configuration	CFSE	
$\text{V}^{3+}: 3\text{d}^2$	$\text{t}_{2\text{g}}^2\text{e}_{\text{g}}^0$	-8 Dq	e^2t_2^0	-5.33 Dq	-2.67 Dq
$\text{Cr}^{3+}: 3\text{d}^3$	$\text{t}_{2\text{g}}^3\text{e}_{\text{g}}^0$	-12 Dq	e^2t_2^1 (HS)	-3.56 Dq	-8.44 Dq
$\text{Mn}^{3+}: 3\text{d}^4$	$\text{t}_{2\text{g}}^3\text{e}_{\text{g}}^1$ (HS)	-6 Dq	e^2t_2^2 (HS)	-1.78 Dq	-4.22 Dq
$\text{Fe}^{3+}: 3\text{d}^5$	$\text{t}_{2\text{g}}^3\text{e}_{\text{g}}^2$ (HS)	0 Dq	e^2t_2^3 (HS)	0.00 Dq	0.00 Dq
$\text{Co}^{3+}: 3\text{d}^6$	$\text{t}_{2\text{g}}^6\text{e}_{\text{g}}^0$ (LS)	-24 Dq	e^3t_2^3 (HS)	-2.67 Dq	-21.33 Dq
$\text{Ni}^{3+}: 3\text{d}^7$	$\text{t}_{2\text{g}}^6\text{e}_{\text{g}}^1$ (LS)	-18 Dq	e^4t_2^3 (HS)	-5.33 Dq	-12.67 Dq

Table 1 Crystal field stabilization energies (CFSEs) and octahedral site stabilization energies (OSSEs) of a few 3d transition metals. Adapted from^[72].

Based on these reflections, Goodenough concentrated on $\text{M} = \text{Cr}, \text{Co},$ and Ni . LiCrO_2 exhibits a disproportionation reaction ($3 \text{Cr}^{4+} \rightarrow 2 \text{Cr}^{3+} + \text{Cr}^{6+}$) upon lithium extraction, whereby Cr^{6+} ions occupy tetrahedral sites. Due to such irreversible structural changes, LiCrO_2 was already rejected at very early stage. First cell tests showed that LiCoO_2 (LCO) and LiNiO_2 (LNO) cathodes undergo reversible Li deintercalation at around 4.0 V vs. Li. Considering that the preparation of stoichiometric LNO was rather difficult, LCO emerged as the material of choice. But in 1980, no electrolytes appropriate for that potential range were available.^[48,56] It was not

until a decade later that Sony revolutionized the battery market by commercializing secondary LIBs with a carbon anode and a LCO cathode.^[49]

Lithium cobalt oxide (LiCoO₂)

Even today, LCO is the most commonly used standard material for the positive electrode in LIBs owing to its good electrochemical properties. Its specific capacity is about 145 mAhg⁻¹ and its average voltage amounts to 3.9 V.^[53] Moreover, LCO has a lithium diffusion coefficient of $5 \cdot 10^{-9} \text{ cm}^2\text{s}^{-1}$, which enables good lithium ion mobility and cycling at 4 - 10 mAcm⁻².^[58] The good electronic conductivity of Li_{1-x}CoO₂ (10^{-3} Scm^{-1}) is ascribed to direct Co-Co interactions with a partially filled t_{2g}^{6-x} band of the Co^{3+/4+} couple.^[73] As can be seen in Table 1, the highest OSSE is assigned to LCO, revealing that it affords the most stable structure comparing transition metals. Thus, LCO offers good cycle life. Thereby, the synthesis has a major impact on the material properties. In order to yield the O3 layered structure, the synthesis procedure must be accomplished at temperatures > 800 °C. At synthesis temperatures around 400 °C, Li⁺ and Co³⁺ ions are randomly distributed, forming a lithiated spinel-like phase ([Li₂]_{16c}[Co₂]_{16d}O₄, S.G. Fd3m) of poor electrochemical performance.^[16]

Although full extraction of Li⁺ from LCO predicts a theoretical specific capacity of 274 mAhg⁻¹, its real specific capacity is ca. 145 mAhg⁻¹. This is because reversible lithium intercalation and deintercalation in Li_{1-x}CoO₂ is only possible for $0 \leq x \leq 0.5$. Higher delithiated states initiate structural degeneration. The reason for the material instability is schematically depicted in Figure 6.

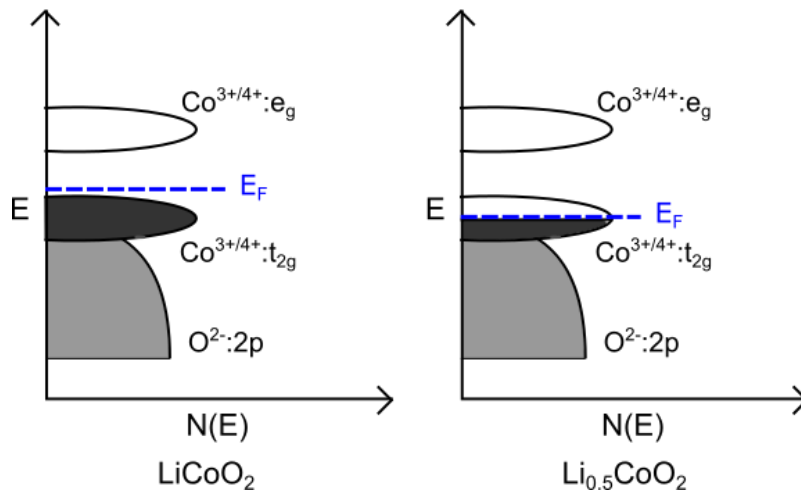
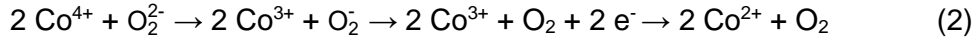


Figure 6 Change of the qualitative energy diagrams of Li_xCoO₂ depending on the lithium content. Adapted from^[70].

For the low-spin Co³⁺:3d⁶ configuration, the t_{2g} band is completely filled, while the e_g band is empty ($t_{2g}^6e_g^0$). In LCO, the t_{2g} band overlaps with the top of the O²⁻:2p band. When Li_{1-x}CoO₂ is

charged, Co^{3+} is oxidized to Co^{4+} by electron removal from the t_{2g} band. At potentials higher than 4.2 V, the topotactic delithiation mechanism exceeds $x \approx 0.5$, inducing a considerable reduction of electron density from the nonmetal p band. As a consequence, O_2 is eliminated according to the following reaction sequence:[48]



Oxygen removal from the lattice occurs over several cycles and not only during the first cycle on account of the hybridization of the $\text{Co}^{3+/4+}$:3d orbitals with the O^{2-} :p orbital.[16] Hence, this exothermic reaction presents a high safety risk and can cause a thermal runaway. Furthermore, the oxygen release is accompanied by particle breaking and contact losses. As a result, cobalt ions dissolve in the electrolyte, deposit on the graphite anode, and promote the electrochemical decomposition of the electrolyte (Figure 7). Slow reactions also take place with the electrolyte on the cathode. These features and the associated increase of the cell impedance tremendously diminish the cell cycle life.[53]

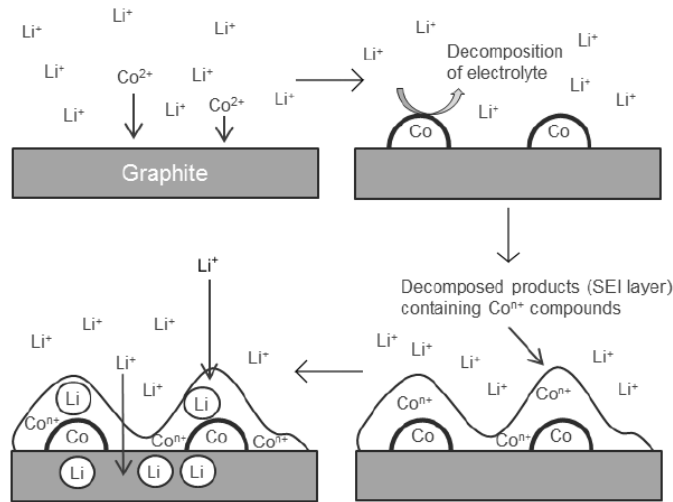


Figure 7 Drawing of the influence of Co dissolution on the electrolyte and the graphite anode. With modifications from[74].

As shown in the literature, surface modification by coating the particles with metal oxides such as ZrO_2 , Al_2O_3 , TiO_2 , SiO_2 , MgO , ZnO , AlPO_4 , and FePO_4 enables cycling of C//LCO cells up to 4.5 - 4.6 V and provides enhanced reversible capacities ($\approx 200 \text{ mAhg}^{-1}$).[16,75] More than 70% of the lithium ions are reversibly withdrawn from the LCO lattice and some of the coatings additionally suppress the side reaction of the CAM with the electrolyte.[16] Even though C//LCO batteries with higher energy densities are obtainable by using higher cut-off potentials, they are mainly used in small-format LIBs. Safety concerns, raised prices due to the limited availability of cobalt, and environmental issues caused by the toxicity of cobalt are some of the motives for scientists to search for alternatives.[76]

Lithium nickel oxide (LiNiO₂)

LiNiO₂ was first reported by Dyer et al. in 1954. Since Goodenough dealt with LNO as CAM for rechargeable LIBs in the 1980s, a number of studies on this topic followed.^[77] The driving forces for developing LNO were its lower cost, less toxicity, and potential for higher energy density in comparison to LCO.^[53] The structure of LiNiO₂ is based on α -NaFeO₂ analogous to LiCoO₂ and, thus, phase transformations during charging/discharging are similar in both cases. LNO delivers an operating voltage of around 4.0 V and up to 75% of the lithium ions are reversibly extracted from its lattice resulting in a specific capacity of ca. 200 mAhg⁻¹.^[57,78] The difference in capacity regarding LNO and LCO is explained by the energetic positions of their d orbitals (Figure 8).

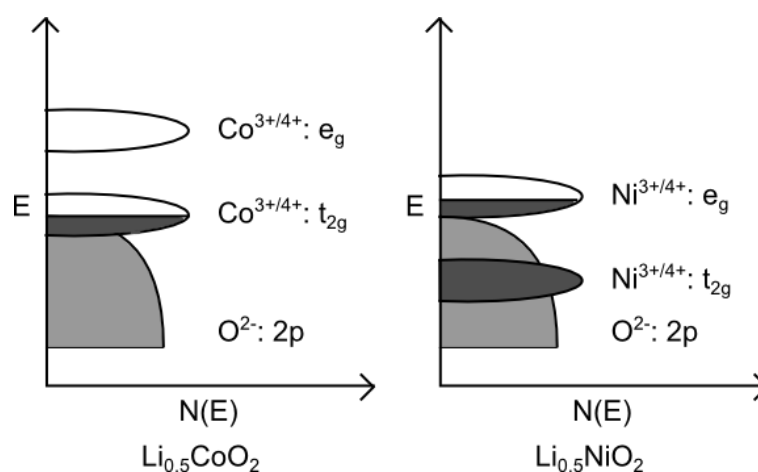


Figure 8 Qualitative energy diagrams of Li_{0.5}CoO₂ and Li_{0.5}NiO₂. Adapted from^[16].

As already pointed out, the specific capacity of LCO is related to the substantial overlap of the Co³⁺:t_{2g} band with the top of the O²⁻:2p band. The low-spin Ni³⁺ in Li_{1-x}NiO₂ has a 3d⁷ configuration (t_{2g}⁶e_g¹), whereby the e_g band only marginally touches the top of the O²⁻:2p band. Hence, stable lithium deintercalation typically proceeds until $x \approx 0.75$. For $x > 0.75$ oxygen is, however, released from LNO and structural corrosion sets in.^[49,72]

Despite the aforementioned advantages, LNO has not been established as CAM in LIBs because it suffers from a few drawbacks. On one hand, the preparation of well-ordered LNO is rather difficult. At high synthesis temperatures lithium partly evolves and some Ni³⁺ are reduced to Ni²⁺.^[79] By virtue of the comparable ionic charges and radii of Ni²⁺ and Li⁺ (0.69 Å vs. 0.76 Å), Ni²⁺ tend to migrate to the octahedral sites of the lithium plane. When the cation mixing throughout the synthesis of LNO is too high, an electrochemically inactive rock salt type phase (S.G. Fm3m) is generated in addition to the preferred O3 layered structure with a R-3m space group (Figure 9). Both crystal modifications coexist because they have very close lattice parameters impeding fractionation. Therefore, LNO is always contaminated with rock salt domains, which significantly reduce the electrochemical performance.^[57,80] As the actual

composition of LNO invariably comprises an excess of nickel, its chemistry is better described by $\text{Li}_{1-z}\text{Ni}_{1+z}\text{O}_2$ ($0 < z < 2$) or $[\text{Li}_{1-z}\text{Ni}_z^{2+}]_{3a}[\text{Ni}_z^{2+}\text{Ni}_{1-z}^{3+}]_{3b}\text{O}_2$.^[81] On the other hand, LNO has a lower OSSE than LCO (Table 1). Consequently, Ni^{3+} migrate from the octahedral sites of the nickel layer to the lithium 3a sites via the neighboring tetrahedral sites in charged LNO or under low heat (Figure 9). The disordering of the cations decreases the lithium diffusion coefficient and the power capability of the electrode.^[16,57]

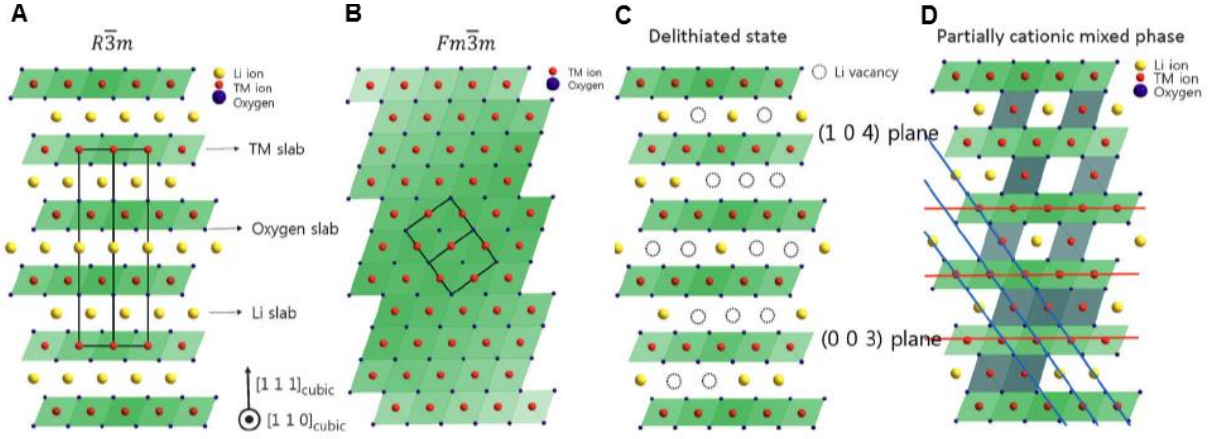
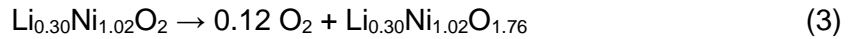


Figure 9 Illustration of the **A** hexagonal $R\bar{3}m$ structure, **B** rock salt type space group $Fm\bar{3}m$, **C** $R\bar{3}m$ lattice with Li vacancies in highly charged state, and **D** partially cation mixed phase with Ni ions in the Li sites (yellow: Li ions, red: nickel ions, dark blue: coordinated oxygen ions).^[80]

Other problems include the Jahn-Teller distortion related to the low-spin Ni^{3+} and irreversible phase transitions accompanied by substantial volume changes upon cycling.^[78] Finally, the extremely low thermal stability of $\text{Li}_{1-x}\text{NiO}_2$ results in oxygen losses in highly delithiated states:^[82]



The reason for the oxygen volatilization is referred to unstable Ni^{4+} , which are reduced to Ni^{3+} . Thereby, the $\alpha\text{-NaFeO}_2$ structure transforms into a pseudo-spinel phase and then into a highly disordered space group $R\bar{3}hm$. Oxygen release is a serious safety risk preventing the use of LNO in commercial LIBs.^[57]

Substituted lithium nickel oxides ($\text{LiNi}_{1-y}\text{Z}_y\text{O}_2$)

To eliminate the major shortcomings of LNO, Ni has been partially substituted by elements such as Co, Mg, Al, Fe, Ti, and Ga. In a few cases, sulfur and fluorine are used for replacing oxygen.^[72] The intention is to improve the structural stability, electrochemical capability, and thermal properties of LNO. Fe in $\text{LiNi}_{1-y}\text{Fe}_y\text{O}_2$, however, does not contribute to the stability of the layered lattice and reduces capacity with increasing y .^[58] Otherwise, redox inactive Al or

Mg enhance the thermal stabilization and suppresses cation disordering. Although, Al- or Mg-doped lithium nickel oxides exhibit a better electrochemical behavior than pure LNO, material collapses in highly charged states are still a problem.^[83,84]

Among all the examined dopants, most attention has been devoted to electrochemically active cobalt. Delmas et al.^[85,86–88] and Zhecheva et al.^[89] studied the structural details and physical features of $\text{LiNi}_{1-y}\text{Co}_y\text{O}_2$. Both groups observed that Co inhibits the migration of nickel into the lithium plane. Higher cobalt concentrations lead to more stable structures and higher cation ordering. In addition, Co impedes phase transitions associated with Li deintercalation resulting in less oxygen evolution compared to pure LNO. Co-substituted nickel oxides reveal a better thermal stability in the charged state. This is because of the Co-O bond being stronger than the Ni-O bond (binding energies: 1067 kJ/mol for CoO_2 and 1029 kJ/mol for NiO_2).^[72] Generally, the chemical composition of $\text{LiNi}_{1-y}\text{Co}_y\text{O}_2$ is a mixed crystal of LNO and LCO and alters with y (Figure 10).

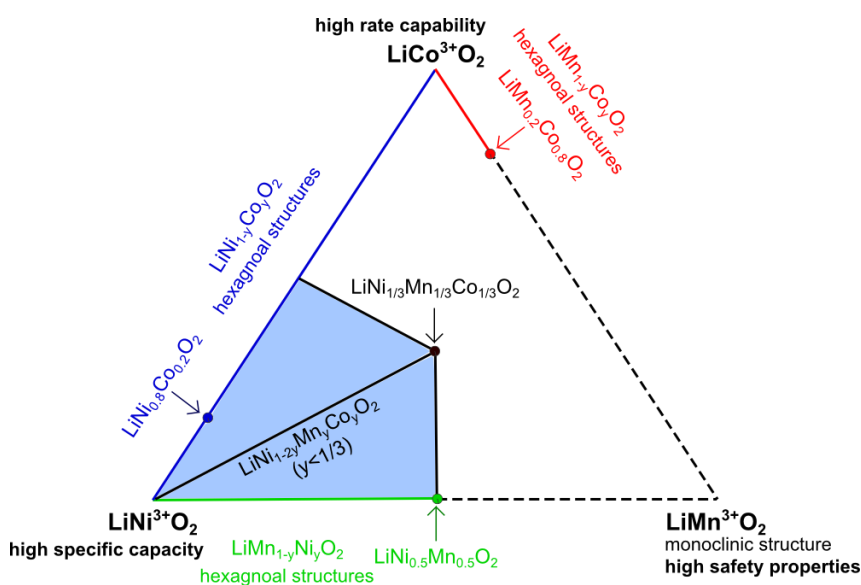


Figure 10 Compositional phase diagram of the lithium transition metal oxides LiCoO_2 , LiNiO_2 , and LiMnO_2 (blue line: $\text{LiNi}_{1-y}\text{Co}_y\text{O}_2$, red line: $\text{LiMn}_{1-y}\text{Co}_y\text{O}_2$, green line: $\text{LiMn}_{1-y}\text{Ni}_y\text{O}_2$ and bright blue region: Ni-rich NMCs). With modifications from^[78].

Increasing the cobalt content leads to an electrochemically more stable structure, whereas a greater amount of Ni enables higher capacities. Optimum $\text{LiNi}_{1-y}\text{Co}_y\text{O}_2$ ($y = 0.15 - 0.3$), share a reversible specific capacity around 180 mAhg^{-1} , which corresponds to the extraction of ca. 0.65 lithium ions from the cathode material.^[57] Thereby, Ni^{3+} are oxidized to Ni^{4+} prior to the oxidation of Co^{3+} to Co^{4+} .^[72] Regarding all the Co-doped lithium nickel oxides, $\text{LiNi}_{0.8}\text{Co}_{0.2}\text{O}_2$ exhibits the best charge-discharge behavior.^[90] It has been extensively investigated due to its low cost and high capacity.^[86–88,91]

While $\text{LiNi}_{1-y}\text{Co}_y\text{O}_2$ seems to be a promising cathode candidate, two problems remain unsolved. First, the migration of Ni^{3+} into the Li layer is still too high and causes capacity fading during cycling and, second, the generation of flammable gases during charging creates safety issues.^[78]

Al and Mg substitutions in $\text{LiNi}_{1-y}\text{Co}_y\text{O}_2$

Further developments of $\text{LiNi}_{1-y}\text{Co}_y\text{O}_2$ oxides aimed at partially substituting cobalt by magnesium or aluminum. Several authors discussed the impact of low concentrations of Mg and Al in $\text{LiNi}_{1-x-y}\text{Co}_x\text{Z}_y\text{O}_2$ ($\text{Z} = \text{Al}$ or Mg around 0.05 atoms/mol).^[84,92,93] Both substitutes prevent Ni migration to the Li sites and hexagonal phase conversions upon cycling. The significant stabilization of the delithiated form induces better thermal properties compared to $\text{LiNi}_{1-y}\text{Co}_y\text{O}_2$ and excellent cyclability with a high and constant capacity of ca. 170 - 180 mAhg^{-1} . Furthermore, thermal runaway upon overcharging is considerably reduced in $\text{LiNi}_{1-x-y}\text{Co}_x\text{Z}_y\text{O}_2$.^[72] The most commonly used composition is the nickel cobalt aluminum oxide $\text{LiNi}_{0.80}\text{Co}_{0.15}\text{Al}_{0.05}\text{O}_2$ or NCA. Its tremendous commercial success is also based on its relatively low cost. SAFT has produced cells containing this CAM, and achieved 1000 cycles at 80% depth of discharge. The energy density amounted to 120 - 130 Wh/kg .^[94] Lately, Panasonic has been constructing 18650 cylindrical cells with the chemical system C//NCA. The Tesla Model S comprises an 85 kWh battery pack including 7104 of such cells.^[95] According to the 2015 report,^[96] Tesla Motors intends to purchase 1.8 billion LIB cells from Panasonic in the period from 2014 to 2017. Moreover, Panasonic agreed on a partnership with Tesla Motors regarding a Gigafactory that is expected to deliver a cell output capacity of 35 GWh. Thereby, the production of C//NCA cells is not excluded.

Despite the enormous success of NCA, safety concerns remain due to the thermal instability and high specific capacity of this oxide.^[97] Additionally, it was published that NCA suffers from severe capacity fading at elevated temperatures (40 - 70 °C) owing to strong SEI growth and micro-cracking at grain boundaries.^[98]

Lithium manganese oxide (LiMnO_2)

Since manganese is an environmentally benign and relatively cheap raw material in comparison to cobalt or nickel, LiMnO_2 has received much attention as an economic and green alternative to LCO, LNO, etc.^[99,100] Likewise, it has been proven that manganese oxides are safer upon overcharging.^[78] Layered LiMnO_2 does not adopt the $\alpha\text{-NaFeO}_2$ lattice of LCO, but crystallizes in a monoclinically distorted structure (S.G. C2/m) due to the Jahn-Teller effect associated with the presence of low-spin Mn^{3+} .^[53] Monoclinic LiMnO_2 is characterized by good Li^+ conductivity and a rather smooth voltage profile.^[101] The preparation of layered LiMnO_2 involves an ion exchange reaction of Na^+ by Li^+ in NaMO_2 ($\text{M} = \text{Mn}$ and Fe).^[100,102] Higher

synthesis temperatures produce orthorhombic LiMnO_2 with Pnmm symmetry. In this structure, edge-sharing $[\text{LiO}_6]$ and $[\text{MnO}_6]$ octahedra are arranged in an alternating zigzag configuration.^[103] The monoclinic form is only metastable, whereas the orthorhombic form shows thermodynamic stability because of the stronger antiferromagnetic interactions between Mn^{3+} .^[104]

Although LiMnO_2 provides a very high specific capacity of $\approx 285 \text{ mAhg}^{-1}$ during the first charge process, the ensuing Li insertion does not restore the initial structure. Removal of more than 50% of Li^+ from the cathode material provokes manganese ions to penetrate into the vacant sites of the Li planes by traversing the neighboring tetrahedral sites on account of the low OSSE of Mn^{3+} (Table 1). The disproportion of Mn^{3+} into Mn^{2+} and Mn^{4+} supports this mechanism. As a result, poorly ordered crystal regions with a $\text{Li}[\text{Li}_x\text{Mn}_{2-x}]\text{O}_4$ spinel structure evolve and Mn^{2+} leach out in the electrolyte leading to a destabilized SEI (Figure 11).

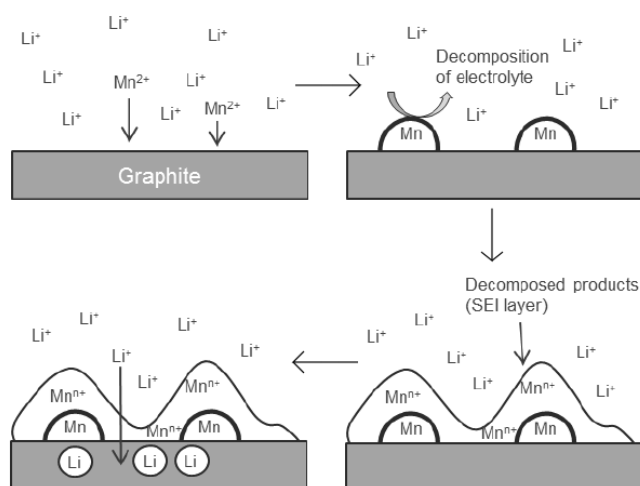


Figure 11 Drawing of the influence of Mn dissolution on the electrolyte and the graphite anode. With modifications from^[74].

Mn dissolution and irreversible phase conversions proceed throughout ageing and, thus, drastically depress the cycle life, the rate capability, and the capacity.^[105] Thereupon, Dahn et al. proposed an O2 layered Li_xMnO_2 (two MnO_2 sheets are contained in the unit cell), which does not convert into a spinel while cycling. The resulting electrode delivers a reversible capacity in the range of $150 - 180 \text{ mAhg}^{-1}$, but only at very low rates ($\approx \text{C}/40$). The insufficient rate capability exclude O2 layered Li_xMnO_2 from its use as CAM.^[106] Another very prominent manganese-containing CAM is the spinel LiMn_2O_4 . Its properties and electrochemical behavior are discussed later on.

Substituted lithium manganese oxides ($\text{LiMn}_{1-y}\text{Z}_y\text{O}_2$)

Further attempts to stabilize the layered LiMnO_2 have merged the direct ceramic syntheses with partial substitutions of Mn by Al^[107] and Cr^[108]. Besides suppressing layered to spinel phase transformations, low dopant concentrations, that is 3 - 5%, also stabilize the monoclinic over the orthorhombic structure. Consequently, improved cycle life and better capacity retention compared to pure LiMnO_2 have been achieved. Nevertheless, Al-doped oxides still undergo lattice changes upon cycling and yield defect spinel regions. In contrast, Cr substituents prevent spinel formation and enable capacities up to 160 - 190 mAhg⁻¹ at 55 °C with a rate of 30 mA/g. The high OSSE of Cr³⁺ prohibits conversion into spinel, but structural rearrangements still occur to generate a quasi-layered phase that has an negative impact on the cyclability.^[72]

Other approaches to realize stable layered lithium manganese oxides involve mixed crystals. For instance, $\text{LiMn}_{1-y}\text{Cr}_y\text{O}_2$ are mixed crystals of LiMnO_2 and LiCrO_2 . For $y \leq 0.7$, structures with space group C2/m are obtained. The monoclinic symmetry transforms into a hexagonal phase during the first charge. Thereby, Mn³⁺ are oxidized to Mn⁴⁺ prior to Cr³⁺ oxidation. $\text{LiMn}_{0.5}\text{Cr}_{0.5}\text{O}_2$ with an average voltage of ≈ 3.3 V can be operated in a voltage range of 2.5 - 4.4 V. The practical specific capacity amounts to 150 mAhg⁻¹. However, this CAM suffers from a serious capacity drop when cycled at high current rates. At compositions of $y \geq 0.75$ the R3m lattice is directly adopted, but rate capabilities are also poor.^[72]

Since it has been known that LCO is beneficial for electronic conductivity, structural stability, and performance properties, considerable interest has been aroused regarding mixed crystals of LiCoO_2 and LiMnO_2 . Unfortunately, LiCoO_2 and LiMnO_2 are not entirely miscible. Ohzuku et al. reported that a combination of both results in phase separation and concluded that they are not miscible at all.^[109] In contrast, Bruce et al.^[110] prepared $\text{LiMn}_{1-y}\text{Co}_y\text{O}_2$ with $y \leq 0.5$ and Stoyanova et al.^[111] proved that up to 80% of cobalt can be incorporated into the lithium manganese lattice. As a matter of fact, $y > 0.8$ is necessary to yield oxides having the space group R3m. Otherwise, the high manganese content induces a cubic or a tetragonal symmetry.^[111,112] Therefore, the line between LiCoO_2 and LiMnO_2 is illustrated as a black dotted line for cobalt concentrations below 80% in Figure 10.

$\text{LiMn}_{0.2}\text{Co}_{0.8}\text{O}_2$ with a $\alpha\text{-NaFeO}_2$ structure shows a low specific capacity of 134 mAhg⁻¹ at 1C, albeit Mn³⁺ and Co³⁺ are oxidized to Mn⁴⁺ and Co⁴⁺, respectively. Higher C-rates cause a notable decrease in capacity. Furthermore, Jahn-Teller Mn³⁺ engender local structural distortions and transformation to disordered spinel phases is not prohibited by Co substituents leading to inferior cycle life. Hence, the demand for $\text{LiMn}_{1-y}\text{Co}_y\text{O}_2$ cathodes ceased.^[78]

Instead LiNiO_2 – LiMnO_2 mixed crystals began to capture the attention of researchers. $\text{LiMn}_{1-y}\text{Ni}_y\text{O}_2$, which possess a R3m lattice within the range of $0.5 < y \leq 1$, were first investigated by Dahn et al. in 1992.^[113] A manganese to nickel ratio greater than one provokes

the formation of a spinel owing to the presence of Mn^{3+} . For example, $\text{LiNi}_{0.25}\text{Mn}_{0.75}\text{O}_2$ behaves similar to LiMnO_2 and develops a spinel rather than a layered phase upon ageing.^[58] In Figure 10, the green solid and the black dashed line between LiNiO_2 and LiMnO_2 indicate the hexagonal and the spinel symmetry, respectively. Spahr et al. stated the best electrochemical performance for $\text{LiNi}_{0.5}\text{Mn}_{0.5}\text{O}_2$, which contains Ni^{2+} and Mn^{4+} .^[114] Specific capacities of 150 - 200 mAhg^{-1} have been reported depending on the cutoff voltage and the current rate.^[72,76,114] The reversible oxidation of Ni^{2+} to Ni^{4+} enables such capacities, whereas Mn^{4+} is not oxidized further. Under mild cycling conditions reasonable capacity retention for at least 50 cycles are achievable.^[76,115,116] The strong OSSE of Mn^{4+} prevents manganese movement to the partially occupied 3a Li sites and, hence, no spinel emerges during charging/discharging.^[48] In addition, $\text{LiNi}_{0.5}\text{Mn}_{0.5}\text{O}_2$ offers a good thermal stability. Oxygen loss and material corrosion do not arise until a temperature of 300 °C is reached.^[117]

However, reliable synthesis of $\text{LiNi}_{0.5}\text{Mn}_{0.5}\text{O}_2$ is critical and 8 - 10% Ni ions are usually located in the lithium layers, blocking Li^+ diffusion. Consequently, the Li^+ diffusion coefficient (ca. $3 \cdot 10^{-10} \text{ cm}^2\text{s}^{-1}$) and the rate capability are significantly lower compared to LCO.^[58] Moreover, the poor electronic conductivity of $6.2 \cdot 10^{-5} \text{ Scm}^{-1}$ is ascribed to polaronic $\text{Ni}^{2+}/\text{Ni}^{3+}$. Recent studies reveal that surface coating and optimized calcination are suitable for enhancing the performance characteristics of $\text{LiNi}_{0.5}\text{Mn}_{0.5}\text{O}_2$.^[118] Besides, Dahn. et al. prepared $\text{LiNi}_{2/3}\text{Mn}_{1/3}\text{O}_2$ with a high reversible capacity of roughly 190 mAhg^{-1} at an end-of-charge-voltage of 4.6 V. Unfortunately, this CAM shows very limited cyclability at elevated temperatures and the thermal behavior is not sufficient for battery applications.^[119]

Lithium nickel manganese cobalt oxides ($\text{LiNi}_{1-y-z}\text{Mn}_y\text{Co}_z\text{O}_2$)

The next logical step towards a stabilized CAM with superior electrochemical features was the combination of the cost and safety advantages of manganese oxides with the structural benefits and the high energy density of cobalt and nickel oxides, respectively. $\text{LiNi}_{1-y-z}\text{Mn}_y\text{Co}_z\text{O}_2$ (NMCs, aka NCMs) were first explored by Liu et al. in 1999.^[91] Generally, NMCs have an O3 layered structure with R3m symmetry. Thereby, Co^{3+} , Ni^{2+} , and Mn^{4+} occupy the octahedral 3b sites, Li^+ are found on octahedral 3a sites, and oxygen ions are on 6c sites (Figure 5). In contrast, real lithium transition metal oxides exhibit cation mixing between nickel and lithium ions. About 2 - 10% of Ni ions are located in the Li plane of the NMC lattice, depending on the synthesis temperature and the Co concentration. The higher the Co content, the less pronounced is the cation disorder. A major drawback of the Ni occupation in the 3a sites is the deteriorated lithium diffusion and, hence, the diminished rate capability. Despite of this fact, 2 - 3% Ni on the Li sites helps to keep the structure organized at a high degree of deintercalation.^[58]

Regarding the charging process in lithium ion cells, mainly the oxidation of Ni^{2+} to Ni^{4+} compensates the Li^+ extraction from the electrode. The oxidation of Co^{3+} to Co^{4+} ensues in the later stages of the deintercalation and contributes only marginally to the overall capacity. Mn^{4+} remain inactive throughout the entire voltage range, which is typically between 2.5 and 4.2 V. The tetravalent state is important as it impedes manganese dissolution and the associated phase changes in comparison to Mn^{3+} . Likewise, manganese ions are essential to lower the prices of the CAMs and to realize a better thermal stability in NMCs relative to LCO, LNO, or NCA. Actually, NMCs begin to lose weight around 300 °C, which is similar to $\text{LiNi}_{0.5}\text{Mn}_{0.5}\text{O}_2$. The energy diagrams in Figure 12 demonstrate the overlap of the $\text{Co}^{3+/4+}t_{2g}$ band with the $\text{O}^{2-}2p$ band. While charging up to 4.2 V should not cause any problems, charging up to higher cutoff voltages of 4.5/4.6 V results in oxygen evolution and lattice rearrangements.^[58,70]

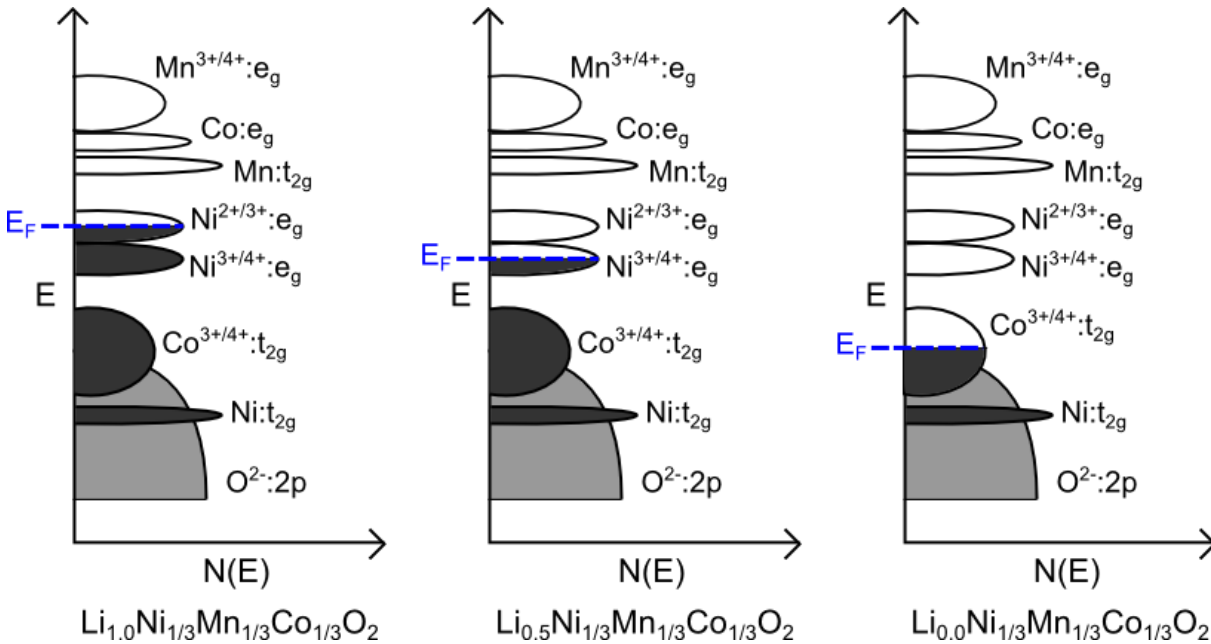


Figure 12 Qualitative energy diagrams of $\text{LiNi}_{1-y-z}\text{Mn}_y\text{Co}_z\text{O}_2$ for three different states of charge: **A** $x = 1$, **B** $x = 0.5$, and **C** $x = 0$. Adapted from^[70].

The most common and widespread composition is $\text{LiNi}_{1/3}\text{Mn}_{1/3}\text{Co}_{1/3}\text{O}_2$ or NMC-111 containing equal amounts of the transition metals (midpoint of the phase diagram triangle in Figure 10). Its lower cost, at least equal or better cyclability even at elevated temperatures, higher reversible capacity, and more favorable thermal stability compared to LCO render it an attractive and competitive CAM for consumer batteries.^[120,121] Practical specific capacities of 150 - 160 mAhg^{-1} have been reported for NMC-111 below 4.3 V.^[53,120,122] An increased cutoff voltage of 4.5 - 5.0 V provides higher capacities of ca. 200 - 220 mAhg^{-1} , but rapid capacity fading is evident.^[123,124] AlF_3 particle coating acts as an interfacial stabilizer on the surface of NMC-111 and enables effective cycling up to 4.5 V with proper rate capability.^[125]

Despite the mild thermal behavior of NMC-111, further studies have been conducted to decelerate its reactivity at high temperatures. For instance, partial substitution of aluminum for cobalt to yield $\text{LiNi}_{1/3}\text{Mn}_{1/3}\text{Co}_{1/3-y}\text{Al}_y\text{O}_2$ not only improved the security features of the delithiated materials, but also enhanced the electrochemical properties. Nonetheless, the degree of substitution must be kept rather low to maintain high specific capacities.^[126]

Since NMCs with increased energy densities and reduced costs are required for vehicular applications, Ni-rich transition metal oxides ($\text{LiNi}_z\text{Mn}_y\text{Co}_{1-y-z}\text{O}_2$, $0.1 \leq z \leq 0.5$) have moved into the focus of investigations. In Figure 10, these compounds are highlighted by a bright blue region. Usually, such CAMs have large reversible capacities ($\leq 200 \text{ mAhg}^{-1}$) and high operating voltages.^[80] Particularly, $\text{LiNi}_{1-2y}\text{Co}_y\text{Mn}_y\text{O}_2$ ($0 \leq y \leq \frac{1}{3}$) Ni-rich species with equal amounts of Co and Mn play an important role in research. They are depicted as a black line between NMC-111 and LNO in Figure 10. $\text{LiNi}_{0.8}\text{Mn}_{0.1}\text{Co}_{0.1}\text{O}_2$ (NMC-811), for example, delivers the highest specific capacity among the Ni-rich family ($\approx 180 \text{ mAhg}^{-1}$).^[127] Nevertheless, the large Ni content leads to restricted thermal stability and several non-stoichiometric phases due to migration of Ni ions to the Li sites analogous to the mechanism in LNO. The cation mixing seriously degrades lithium diffusion and lowers the rate performance. Additionally, NMC-811 includes Mn^{3+} ions, which produce spinel-like structural deteriorations and, thus, poor capacity retention upon cycling.^[78,80] Augmented Mn and Co concentrations decline the Ni/Li disorder as in the case of $\text{LiNi}_{0.6}\text{Mn}_{0.2}\text{Co}_{0.2}\text{O}_2$ (NMC-622). Moreover, the absence of Mn^{3+} affords better cyclability and thermal characteristics. The decreased amount of Ni impairs, however, the energy density.^[128] Regarding security aspects, Ni-rich $\text{LiNi}_{0.5}\text{Mn}_{0.3}\text{Co}_{0.2}\text{O}_2$ (NMC-532) is also an interesting CAM. But its specific capacity of 161 mAhg^{-1} gives only a small advantage in comparison to NMC-111.^[129] Al, Ti, and Mg dopants have been explored with respect to improve thermal and structural stability of Ni-rich NMCs.^[93,130]

Very recently, core-shell structured materials comprising a concentration-gradient outer layer have gained enormous scientific attention. Thereby, three approaches have been developed (Figure 13). One method is aimed at creating a pillar layered shell with rock salt domains around a Ni-rich core. By means of this procedure, Cho et al. prepared $\text{LiNi}_{0.62}\text{Co}_{0.11}\text{Mn}_{0.58}\text{O}_2$ with excellent thermodynamic and electrochemical stability up to 4.5 V at high temperatures.^[131] The other methods enclose the Ni-rich core by a thin manganese-rich spinel ($\text{Li}_{1+x}[\text{CoNi}_x\text{Mn}_{2-x}]_2\text{O}_4$) or a heat-resisting NMC shell. Superior behavior in thermal abuse tests compared to standard LNO and high capacities ($180 - 200 \text{ mAhg}^{-1}$) with satisfactory capacity retention at enhanced temperatures have been achieved.^[132] In spite of these promising experimental results, Ni-rich oxides still have many remaining challenges such as structural stability, surface side reactions, and safety issues.

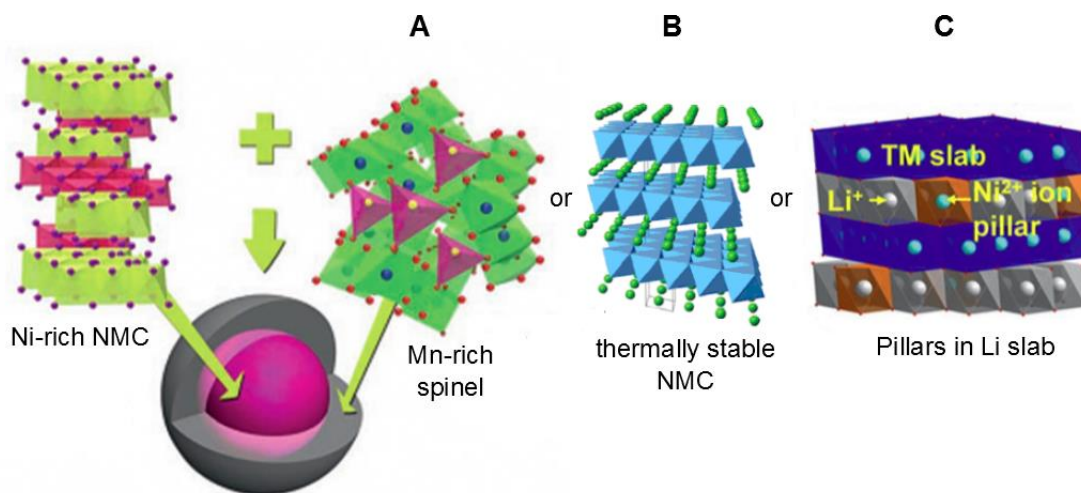


Figure 13 Schematic view of different concentration-gradient core-shell cathode materials. The Ni-rich core is enclosed by a **A** Mn-rich spinel, **B** thermally stable NMC, or **C** rock salt phase shell. Adapted from^[70,80].

Lithium-rich nickel manganese cobalt oxides

Another strategy to realize CAMs with high energy densities and good thermal features involves mixed crystals between Li_2MnO_3 and LiMO_2 ($M = \text{Cr, Ni, Co, Mn}_{0.5}\text{Ni}_{0.5}$, and $\text{Ni}_{1/3}\text{Mn}_{1/3}\text{Co}_{1/3}$). Li_2MnO_3 or $\text{Li}[\text{Li}_{1/3}\text{Mn}_{2/3}]\text{O}_4$ has a monoclinic structure with $C2/m$ symmetry where interslab octahedral sites are only occupied by Li^+ , while Li^+ and Mn^{4+} are located in the octahedral sites within the $[\text{Li}_{1/3}\text{Mn}_{2/3}]\text{O}_2$ slabs in a 1:2 ratio. Hence, one third of Mn is substituted by Li in the transition metal layer. The alternating Li and $[\text{Li}_{1/3}\text{Mn}_{2/3}]$ sheets are separated from each other by close-packed oxygen planes, which corresponds to an ABCABC stacking sequence.^[133] The thermodynamic stability of Li_2MnO_3 is based on the ordering of Li in the $[\text{Li}_{1/3}\text{Mn}_{2/3}]$ planes and on non-Jahn Teller distorted Mn^{4+} , whose strong OSSE prohibits Mn diffusion via the tetrahedral sites.^[72] Since Mn^{4+} cannot be further oxidized to an octahedrally coordinated state, Li_2MnO_3 was believed to be electrochemically inactive.^[72,134] Nonetheless, it has been combined with other transition metal oxides to generate strongly stabilized, cheap, and low-toxic CAMs.^[72] From 1997 till 1999, for example, Numata et al. synthesized $\text{Li}(\text{Li}_{x/3}\text{Mn}_{2x/3}\text{Co}_{1-x})\text{O}_2$ ($0 \leq x \leq 1$). But electrochemical performance tests, which were carried out up to 4.4 V revealed a decreasing capacity with an increasing manganese content.^[135] It was not until 1999, that Kalyani et al. discovered that Li_2MnO_3 is electrochemically activated on charging Li// Li_2MnO_3 cells to a cutoff voltage of 4.5 V.^[136] Numerous reports on Li-rich transition metal oxides, which can be denoted as $x \text{Li}_2\text{MnO}_3 \cdot (1-x) \text{LiMO}_2$ or $\text{Li}[\text{Li}_x\text{M}_{1-x}]\text{O}_2$ ($M = \text{Cr, Ni, Co, Mn}_{0.5}\text{Ni}_{0.5}$, and $\text{Ni}_{1/3}\text{Mn}_{1/3}\text{Co}_{1/3}$) have followed.^[97,115,137,138] Among the Li-rich compositions, $x \text{Li}_2\text{MnO}_3 \cdot (1-x) \text{LiNi}_{1/3}\text{Mn}_{1/3}\text{Co}_{1/3}\text{O}_2$ ($0 < x < 1$) are the most promising candidates. These so-called Li-rich NMCs were first published and developed by groups at Argonne National Laboratory in the US.^[139,140] Ideally, x should adopt values between 0.5 and 0.7.^[140,141] The structure of Li-rich NMCs is composed

of Li_2MnO_3 domains with C2/m symmetry, which are integrated in the hexagonal $\alpha\text{-NaFeO}_2$ lattice of $\text{LiNi}_{1/3}\text{Mn}_{1/3}\text{Co}_{1/3}\text{O}_2$ (S.G. R3m).^[142] In a cycling range of 2.0 - 4.4 V only the oxidations of Ni^{2+} and Co^{3+} to Ni^{3+} and Co^{4+} , respectively, contribute to the specific capacity of about 80 mAhg^{-1} . When Li-rich NMCs are charged above 4.5 V, Li_2MnO_3 is also involved in the intercalation/deintercalation process and anomalous high specific capacities greater 250 mAhg^{-1} are reached.^[16,53,143,144] The electrochemical activation of Li_2MnO_3 is based on two mechanisms. On one hand, Li^+ extraction from Li_2MnO_3 is accompanied by the simultaneous release of oxygen.^[138] On the other hand, protons, which are a result of electrolyte oxidation, displace Li^+ in the lattice.^[145] Both scenarios induce material corrosion. The loss of oxygen mainly occurs during the first cycle and Li_2MnO_3 partially decomposes. Some residual Li_2MnO_3 is further activated, but rapidly consumed in the following cycles. The resulting Li_xMO_y oxide is unstable upon cycling and undergoes continuous phase changes. Lithium and oxygen vacancies allow the migration of transition metal ions, especially Ni, to the Li layers. Consequently, defect tetragonal and cubic spinel structures develop, which drastically lower the rate capability and the average voltage (Figure 14).^[146]

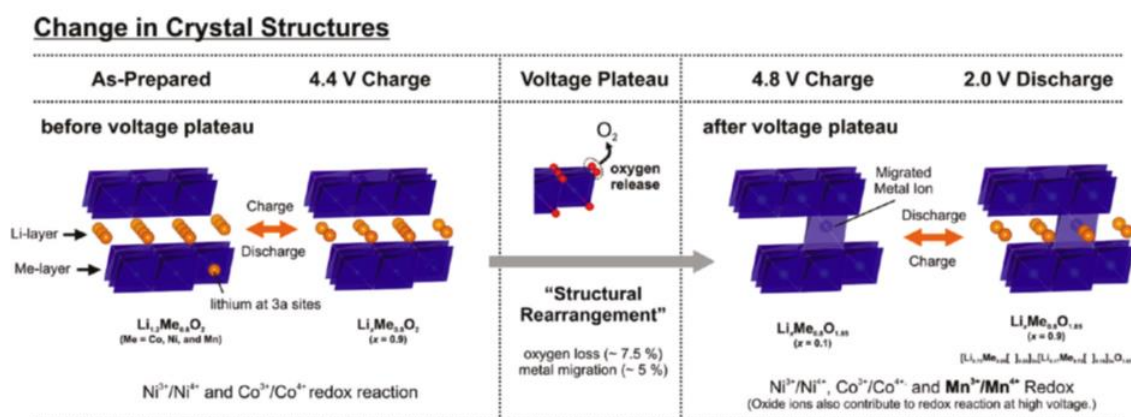


Figure 14 Illustration of the structural rearrangements in Li-rich NMC during cycling.^[147]

The structural rearrangements are irreversible because oxygen is lost due to the formation of Li_2O and side reactions with the electrolyte. Thereby, reaction products such as Li_2O_2 , LiO_2 , Li_2CO_3 , etc. are formed and the amount of mobile Li^+ for intercalation/deintercalation processes is constantly reduced.^[140,147] In summary, Li-rich NMCs feature the disadvantages of large irreversible capacity losses, poor rate performances, and short cycle life.^[148] The partial substitution of Mn by Ru considerably increased the coulomb efficiency of $\text{Li}_{1.2}\text{Mn}_{0.567}\text{Ni}_{0.166}\text{Co}_{0.067}\text{O}_2$.^[149] Besides, it has been shown that particle coatings such as Al_2O_3 , AlPO_4 , or AlF_3 significantly improve the capacity retention and the thermal stability of Li-rich NMCs.^[150] Nevertheless, further investigations and improvements are necessary to establish sufficient cyclability for commercialization.

2.1.2 Polyanion-containing compounds

Since layered lithium transition metal oxides tend to lose oxygen in their charged state owing to the low redox potential of $\text{Ni}^{3+/4+}$ and $\text{Co}^{3+/4+}$ couples, researchers have looked for alternative CAMs. Polyanion-containing compounds including NASICON-type (sodium super ionic conductor) crystal lattices $\text{Li}_x\text{M}_2(\text{XO}_4)_3$ ($\text{M} = \text{Ni, Co, Mn, Fe, Ti, or V}$; $\text{X} = \text{S, P, As, Mo, or W}$), olivine-type structures LiMX_xO_4 ($\text{M} = \text{Fe, Co, Mn, or Ni}$; $\text{X} = \text{P, Mo, W, or S}$), and tavorite-related substances $\text{LiMM}'_{1-\delta\delta}(\text{ZO}_4)\text{X}_{1-\alpha}\text{X}'_{\alpha}$ ($\text{M and/or M}' = \text{metal}$; $\text{Z} = \text{P or S}$; $\text{X and X}' = \text{O, OH, or a halogen}$) have attracted much attention.^[57] In the 1980s, Manthiram and Goodenough studied $\text{Fe}_2(\text{XO}_4)_3$ ($\text{X} = \text{S, Mo, or W}$) for the use as lithium insertion hosts.^[151] The $\text{Fe}^{2+/3+}$ redox couple offers good thermodynamic stability and combined with XO_4^{3-} rather than O^{2-} reasonable cell voltages are possible. The strength of the X-O bond determines the energetic position of the $\text{Fe}^{2+/3+}$ d orbital and, thus, the operating voltage of the material. $\text{Fe}_2(\text{SO}_4)_3$ has an average voltage of 3.6 V, which is 0.6 V higher than that for $\text{Fe}_2(\text{WO}_4)_3$ and $\text{Fe}_2(\text{MO}_4)_3$.^[16] Although they exhibit interesting electrochemical features in combination with a lithium anode, they failed in LIBs with a carbon anode because none of the electrodes provides lithium ions.

Metallophosphates with olivine structure (LiMPO_4)

Goodenough et al. thoroughly studied olivines with the general formula LiMPO_4 ($\text{M} = \text{Mn, Co, Ni, and Fe}$) in 1997.^[152] They were the first to recognize that LiFePO_4 (LFP) is a promising cathode candidate for LIBs.^[153] Since then numerous publications on LFP have appeared.^[154] This is due to the fact that LFP is environmentally benign, low-toxic, inexpensive, and the most safe available CAM.^[16] Its olivine-type structure consists of a hexagonal close-packed oxygen framework, whereby Li and Fe occupy half of the octahedral sites and P are located in one eighth of the tetrahedral sites (Figure 15). In the orthorhombic system (S.G. Pnma), FeO_6 octahedra share corners with each other and not edges. Therefore, lithium movement just takes place along the edge-sharing LiO_6 chains (b axis) affording one dimensional diffusion paths. The tetrahedral PO_4 groups separate the FeO_6 octahedra from each other by sharing one edge with a FeO_6 octahedron and two edges with a LiO_6 octahedron. The isolated FeO_6 octahedra notably hamper the electronic delocalization.^[70]

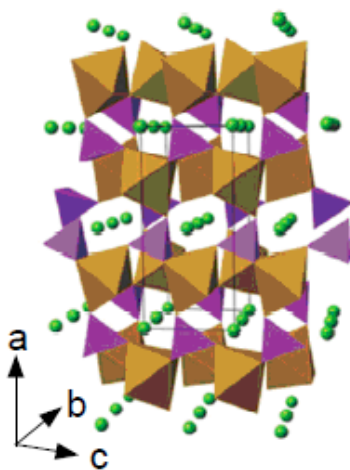


Figure 15 Schematic picture of the crystallographic structure of LiFePO_4 (brown: FeO_6 octahedra, purple: PO_4 tetrahedra, and green: lithium ions).^[70]

Initially, limited reversible capacities and rate capabilities were attributed to LFP. For example, Goodenough et al. reported a poor practical specific capacity of $< 120 \text{ mAhg}^{-1}$ for LFP even at low current densities.^[153] The theoretical capacity is ca. 170 mAhg^{-1} . Several approaches have been followed to overcome the intrinsically restricted electronic and ionic conductivity of LFP. Doping with supervalent cations such as Nb^{5+} , Zr^{4+} , Ti^{4+} , Mo^{6+} , and V^{5+} increased the electronic conductivity by two to eight orders of magnitude.^[155] Nonetheless, modeling infers that substitution of either Li or Fe is energetically unfavorable.^[156] In addition, Zr, Nb, and Cr dopants are found primarily in the Li sites and, hence, inhibit Li migration by blocking the diffusion channels.^[157]

Subsequent investigations revealed that minimizing the particle size and coating LFP with carbon or conductive polymers result in significant improvement of the electrochemical characteristics including capacities of around 160 mAhg^{-1} .^[158] Carbon coating has not only a positive effect on the electronic properties of LFP, but simultaneously reduces its size by impeding grain growth during sintering.^[159] Among all the various preparation methods, low-temperature microwave-assisted hydrothermal and solvothermal syntheses proved to be very reliable ways to produce LFP nanoparticles with excellent crystallinity.^[160] On account of the nanosized particles less anti-site defects, i.e. iron occupancy on the Li sites, occur. Consequently, the rate capability of LFP is enhanced.^[161] The diminution of the size to the nanometer scale effectively shortens the diffusion length of Li^+ . The electronic conductivity remains, however, low. Conductively coated LFP nanoparticles or LFP/carbon composites by contrast, offer superior electrochemical behavior.^[162] Remarkable capacity values of 165 and 61 mAhg^{-1} at the rate of 3 C and 65 C, respectively, have been achieved.^[163] Furthermore, LFP electrodes exhibit very long cycle life. The lithium extraction occurs via a two-phase process:



FePO_4 is practically isostructural with LiFePO_4 . In particular, only minimum displacements of the ordered olivine framework arise upon cycling.^[53] All of these benefits, especially the great advantage regarding safety, have led to the relatively fast commercialization of LFP. Its limited specific capacity and its low crystallographic density of 3.6 gcm^{-3} , which results in a small volumetric energy, restrict, nevertheless, the range of EVs comprising LIBs with LFP cathodes.^[164] Substituting Fe^{2+} by Mn^{2+} , Co^{2+} , or Ni^{2+} substantially improves the energy density of the corresponding cathodes owing to the higher redox potentials of the related CAMs. In spite of this, LiMnPO_4 , LiCoPO_4 , LiNiPO_4 , and the associated mixed crystals $\text{LiA}_{1-y}\text{B}_y\text{PO}_4$ ($\text{A} = \text{Fe}$, Mn , or Ni ; $\text{B} = \text{Mn}$ or Co) or $\text{LiMn}_{1/3}\text{Fe}_{1/3}\text{Co}_{1/3}\text{PO}_4$ still suffer from their poor intrinsic electronic and ionic conductivity. Reducing the particle size as well as coating with conductive polymers or carbon markedly increase the synthesis costs. Moreover, the doped compounds demonstrate lower thermal stability than LFP and unsatisfactory cyclability, which is due, among other things, to the fact that currently available electrolytes are not stable in the voltage window of Ni- and Co-containing species.^[16]

Other polyanionic compounds

Like LFP, favorite materials also profit from the strength of covalent phosphorous and oxygen bonds leading to good thermodynamic stability up to 175°C and excellent cycling features. Multidimensional Li^+ ion diffusion pathways (Figure 16A) provide high ionic conductivity and superb rate performance.^[76] For instance, LiVPO_4F still delivers 90% of its original capacity after 400 cycles at $\frac{\text{C}}{2}$ and the operating voltage is equal to 4.05 V. Nonetheless, it has only a specific discharge capacity of 140 mAhg^{-1} .^[165] The low energy density coupled with concerns about toxicity and environmental impact involving vanadium containing compositions has prevented the wide-spread application of favorite-type CAMs.

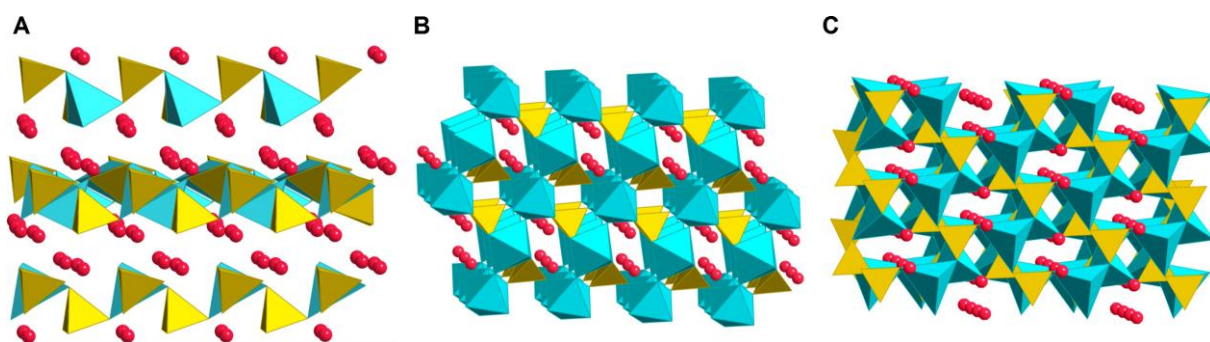


Figure 16 Crystal structures of **A** lithium intercalated silicates Li_2MSiO_4 (blue: transition metal ions, yellow: Si ions, and red: Li ions), **B** favorite LiMPO_4F (blue: transition metal ions, yellow: P ions, and red: Li ions), and **C** LiMBO_3 (blue: transition metal ions, yellow: B ions, and red: Li ions).^[76]

Recently, scientists directed their interest towards the family of silicates having the general Li_2MSiO_4 ($\text{M} = \text{Fe}, \text{Mn}, \text{and Co}$) composition because of the natural abundance of low-priced silicon and the theoretical capacity of 330 mAhg^{-1} , which corresponds to the extraction of two Li^+ ions per transition metal unit. The practical capacity, however, is typically limited to the deintercalation of one Li^+ ion at room temperature (166 mAhg^{-1}). Li_2MSiO_4 crystallizes in a Li_3PO_4 related structure, whereby all cations occupy tetrahedral sites (Figure 16B). The nature of the transition metal ions and the preparation methods determine the exact polymorphic phase.^[53,164] Nytén et al. were the first to characterize $\text{Li}_2\text{FeSiO}_4$ in 2005.^[166] Structural rearrangements upon the initial charge comprise lithium and iron site-mixing. Intriguingly, they have no negative impact on the cycle life and the Li diffusion ability. Hence, $\text{Li}_2\text{FeSiO}_4$ shows a stable specific capacity of around 140 mAhg^{-1} .^[164] In contrast, $\text{Li}_2\text{MnSiO}_4$ undergoes amorphization during cycling with severe capacity decay. Large irreversible capacity losses have been reported for $\text{Li}_2\text{CoSiO}_4$.^[164] Mixed metal compounds such as $\text{Li}_2\text{Mn}_x\text{Fe}_{1-x}\text{SiO}_4$ afford capacities of up to 250 mAhg^{-1} . Nevertheless, structural instability causes tremendous voltage fading over a range of ca. 4.5 - 1.0 V resulting in poor electrochemical behavior.^[53] Besides, all lithium metal silicates exhibit a characteristically minor electronic conductivity, which is even several orders of magnitude lower than that of LFP. In order to overcome this drawback, effective carbon coating and reducing the particle size are one of the primary challenges.^[167] One of the newest cathode intercalation materials are borates LiMBO_3 , which have a theoretical capacity of 220 mAhg^{-1} . The three-dimensional MBO_3 framework consists of MO_5 bipyramids and BO_3 trigonal planar shapes (Figure 16C). MO chains share edges along the $[-101]$ direction. Li atoms are located in two tetrahedral sites and the edge-shared chains of LiO_4 run parallel to the $[001]$ direction.^[76] An early publication by Legagneur and his group describes LiMBO_3 ($\text{M} = \text{Mn}, \text{Fe}, \text{and Co}$) with extremely low practical capacities, i.e. 9 mAhg^{-1} at $\frac{C}{250}$.^[168] It was not until 2010, that Yamada et al. recognized the actual potential of borates.^[169] They identified the moisture in air as the main reason for the inadequate electrochemical performance of LiMBO_3 . With proper handling of the cathodes more than 75% of the theoretical capacity was obtained at 2C. Nonetheless, in comparison to other CAMs, borates have many problems including poor cyclability. Thus, much work needs to be done to optimize synthesis approaches and operation conditions.

2.1.3 Spinel oxide cathodes

In 1981, Scrosati and Thackeray investigated the spinel magnetite Fe_3O_4 as CAM for LIBs because they looked for a cheaper and environmentally more friendly alternative for LCO.^[48] As Fe_3O_4 does not contain any lithium, it cannot be combined with a carbon anode in a battery cell. Instead, two years later, Thackeray and Goodenough proposed LiMn_2O_4 (LMO) as lithium insertion/extraction material.^[170]

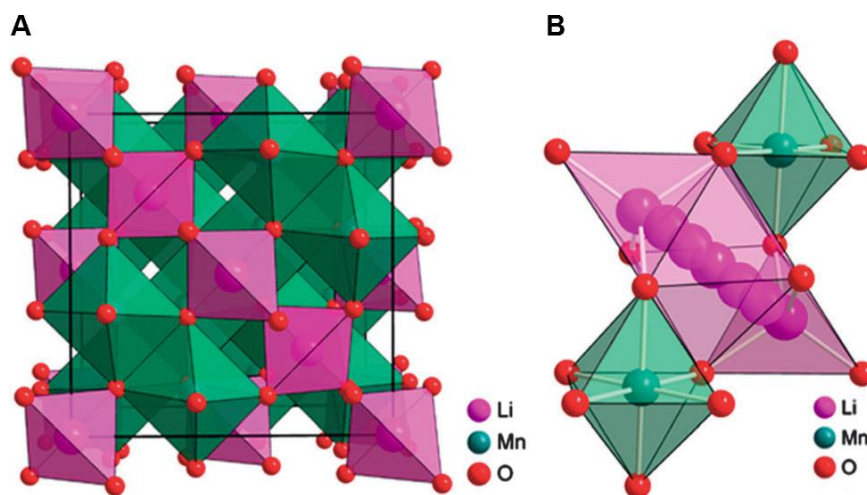


Figure 17 A Crystalline structure of LiMn_2O_4 and B its corresponding lithium diffusion pathways.^[171]

This oxide belongs to the AB_2O_4 spinel family, which is named after the original MgAl_2O_4 spinel. Commonly, the structure is composed of oxygen ions located on the 32e positions forming a cubic close-packed oxygen lattice, whereby $\frac{1}{8}$ of the tetrahedral (8a) and $\frac{1}{2}$ of the octahedral (16d) sites are filled by A and B cations, respectively (Figure 17A). The octahedral 16c sites remain unoccupied. Therefore, the cation distribution of the corresponding unit cell is given by $\{\text{A}\}_{8a}[\text{B}_2]_{16d}[\text{O}_4]_{32e}$.^[172] Regarding the three-dimensional framework of LMO with space group $\text{Fd}3\text{m}$ (O_h^7 factor group), edge-sharing MnO_6 octahedra permit good electronic conductivity via direct Mn-Mn interaction. During intercalation/deintercalation Li ions migrate from one 8a site to the adjacent empty 16c site and then to the next 8a site, i.e. along the transport paths 8a-16c-8a (Figure 17B). Reversibility is provided by the strong edge-shared $[\text{Mn}_2]\text{O}_4$ array that helps to maintain the spinel framework.^[16] The 3D network of interstitial sites allows fast uptake and release of Li^+ . Consequently, LiMn_2O_4 cathodes can be operated with quite high C-rates.^[171] In addition, LMO delivers a suitable electrode potential of ca. 4.1 V.^[70] The abundance of less toxic manganese in earth's crust guarantees long-term availability and low prices.^[173] Moreover, the chemical stability of LMO is considerably enhanced compared to LCO or LNO. The reason for this lies in the position of the d orbitals. Figure 18 depicts the band diagrams of $\text{Li}_{0.5}\text{Mn}_2\text{O}_4$, $\text{Li}_{0.5}\text{CoO}_2$, and $\text{Li}_{0.5}\text{NiO}_2$. Since LMO has an average oxidation state of 3.5, it consists to 50% of Mn^{4+} and Mn^{3+} ions. Only the latter ones are participating in the charging procedure. By virtue of the high-spin $\text{Mn}^{3+}:t_{2g}^3e_g^1$ configuration, electrons are only removed from the e_g orbital, which is located well above the top of the $\text{O}^{2-}:2p$ band.^[72] Hence, oxygen evolution from LMO is prohibited until 600°C is reached.^[174] In contrast, the $\text{Co}^{3+}:t_{2g}$ and the $\text{Ni}^{3+}:e_g$ orbitals of LCO and LNO, respectively, at least touch the top of the $\text{O}^{2-}:2p$ band leading to relatively early oxygen losses at discharged states or with rising temperature.^[72] Due to the positive properties, LMO was commercialized by NEC Moli Energy Corporation in 1996 and has attracted lots of attention in the field of secondary LIBs.^[175]

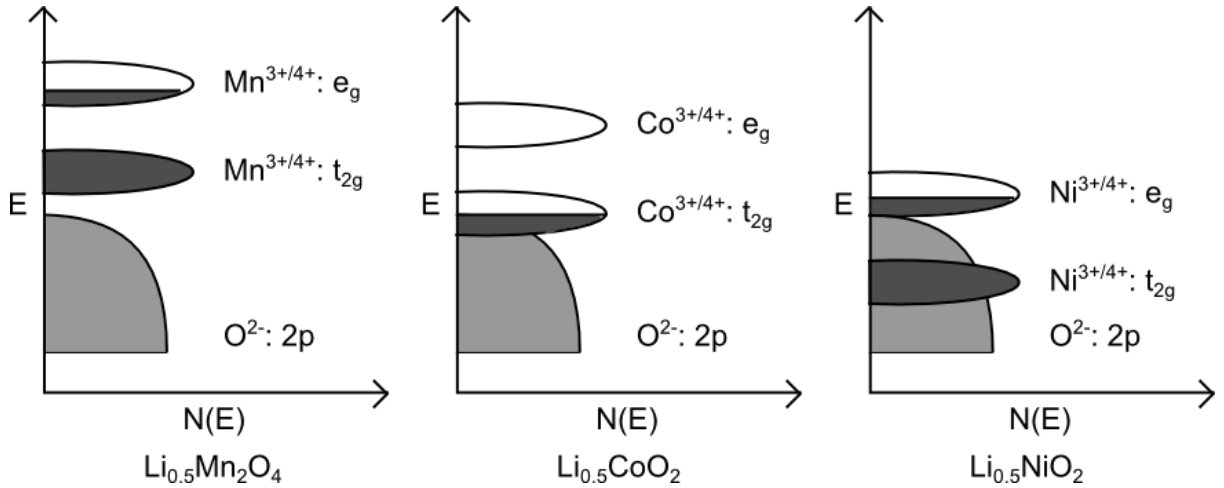
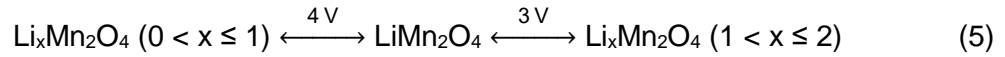


Figure 18 Qualitative energy diagrams of $\text{Li}_{0.5}\text{Mn}_2\text{O}_4$, $\text{Li}_{0.5}\text{CoO}_2$, and $\text{Li}_{0.5}\text{NiO}_2$. Adapted from^[72].

Two-phase electrochemical reactions can occur either at around 4 V through lithium extraction from the 8a tetrahedral sites of LMO or at ca. 3 V via additional lithium insertion into the vacant 16c sites according to the following mechanism:^[16]



Cycling $\text{Li}_x\text{Mn}_2\text{O}_4$ over the whole compositional range of $0 \leq x \leq 2$ would give a total capacity of 285 mAhg^{-1} . Nevertheless, LMO shows serious problems in the 3 V region. The incorporation of excess Li^+ causes electrostatic interactions between the ions on face-sharing 16c and 8a positions. As a result, Li^+ move from the tetrahedral to the adjacent 16c sites forming rock salt phases on the surface of the $\text{Li}_2\text{Mn}_2\text{O}_4$ particles.^[134] This displacement goes along with a Jahn-Teller distortion of the Mn^{3+}O_6 octahedra, which reduces the crystal symmetry from cubic to tetragonal. The transition is accompanied by a 6.5% increase in the unit cell volume and induces strain faults, particle cracking, and loss of electrical contact within the composite cathode. Thus, LMO exhibits quick capacity deterioration around 3 V.^[56,72]

The phenomenon of the cubic-to-tetragonal conversion can be explained by the ligand field theory (derived from the crystal field theory). Generally, the potential energy released during the complex formation between a positively charged metal center M^{m+} and n negatively charged or polarized ligands L ($\text{M}^{m+} + n \text{ L} \rightarrow \text{ML}_n^{m+}$) is based on the electrostatic attraction between M^{m+} and the n ligands as well as the electrostatic repulsion among the ligands themselves and between the atomic electron shell of M^{m+} and the ligands. The ligand field theory exclusively considers the electrostatic interaction between the d-electrons of transition metal complex centers (e.g. Mn^{3+}) and the surrounding anions such as O^{2-} . Thereby, it describes how the five d-orbitals ($d_{x^2-y^2}$, d_{z^2} , d_{xy} , d_{xz} , and d_{yz}) have to be distributed in order to attain a minimum repulsion with each other and with the electron pairs of M^{m+} . The d-orbitals of a ligand-free central metal ion are of equal energy (i.e. degenerate). If a spherically

symmetric field of negative charges is placed around the concerning transition metal center, these orbitals remain degenerate, but all of them are raised in energy. Otherwise, the introduction of the central ion in an octahedral arrangement of six ligands leads to the disappearance of the degeneracy and a splitting of the d-orbitals owing to the different repulsive forces between the bonding electron pairs and the d-electrons. The electrons of the orbitals $d_{x^2-y^2}$ and d_{z^2} with the highest electron density along the x-y- and the z-axis are more strongly repelled by the ligands. Thus, they are more energy-rich than the electrons of the d_{xy} -, d_{xz} -, and d_{yz} -orbitals, whose electron density lies further away from the ligands between the axes. For the O_h point group, the energetically lower orbitals belong to the t_{2g} irreducible representation, while the higher ones are e_g . In case of asymmetrically occupied octahedral complexes, a tetragonal distortion might be energetically favorable. Regarding, for example, the $t_{2g}^3 e_g^1$ configuration of high spin Mn^{3+} , stretching along the z-axis reduces the energy of the orbitals having a z component (d_{z^2} , d_{xz} , and d_{yz}). The associated decreased electrostatic repulsion by the ligands induces a stabilization of these orbitals. At the same time, the energy of the $d_{x^2-y^2}$ - and the d_{xy} -orbitals is raised to compensate the energy difference. However, Mn^{3+} reveal more electrons in the energetically lower orbitals than in the higher ones. Consequently, the square-planar complex is stabilized by this Jahn-Teller effect (Figure 19). In contrast, Mn^{4+} are Jahn-Teller inactive because they show a uniform electron distribution on the t_{2g} orbitals. An elongation or compression along the z-axis would not result in a stabilization.^[172]

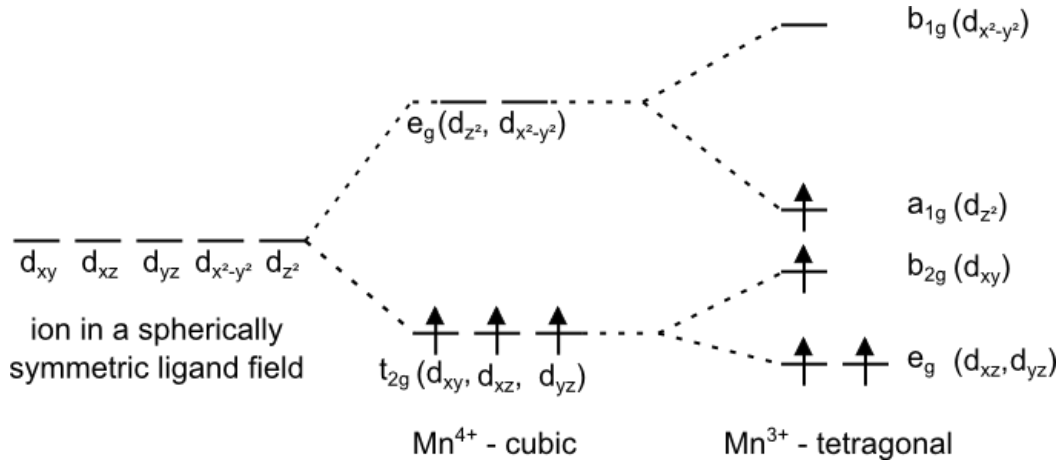
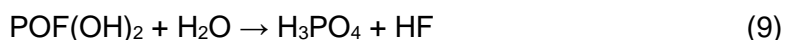
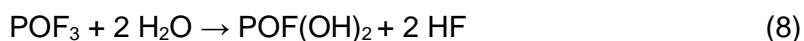
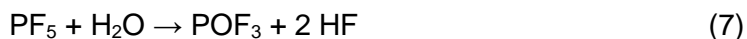


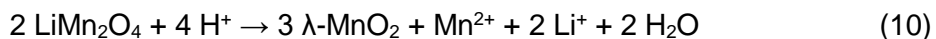
Figure 19 Illustration of the Jahn-Teller distortion in manganese oxides. With modifications from^[16].

Consequently, LMO is only used in the 4 V region. The enhanced voltage is due to the high activation energy required for Li^+ to move from one 8a site to another via the energetically unfavorable adjacent 16c octahedral site. For $0 < x \leq 1$, $Li_xMn_2O_4$ demonstrates a better cycling behavior, but the capacity is limited to 120 mAhg^{-1} , which corresponds to an extraction of ca. 0.8 Li^+ per formula. Unfortunately, the lithium manganese oxide spinel also displays capacity fading around 4 V and the deterioration is even more pronounced at elevated

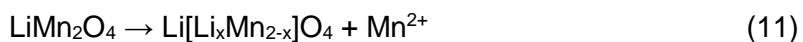
temperatures.^[72] There are several reasons for this. Loss of crystallinity, formation of oxygen-rich spinel, site exchange between Li and Mn, and development of micro-strain are sources for the capacity decay.^[176,177] In addition, at the end of discharge, the emergence of nonequilibrium conditions, i.e. the lithium insertion rate is higher than the diffusion rate from the surface to the bulk, causes a local decline of the average Mn oxidation state. The increased number of Jahn-Teller distorted Mn^{3+} leads to the production of tetragonal $\text{Li}_2\text{Mn}_2\text{O}_4$ at the particle surfaces.^[178] Furthermore, the delithiated electrodes irreversibly react with the organic electrolyte. Conductive carbon additives intensify the oxidation or decomposition.^[179,180] Finally, Mn dissolution in the electrolyte provokes, among other things, the loss of active material and, therefore, poor cyclability. Two different mechanisms are suggested for this process. Since trace amounts of H_2O are always found in LiPF_6 /organic electrolyte solutions, HF is generated according to the reactions below:^[181]



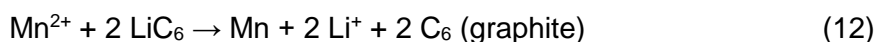
Mn^{3+} disproportionates into Mn^{2+} and Mn^{4+} at low potentials when ppm levels of acidic components are existent in the electrolyte. In 1981, Hunter experimentally proved the disproportion of LMO by stirring the powder in dilute sulfuric acid:^[182]



Mn^{2+} leach out in the electrolyte, whereas Mn^{4+} remain in the solid phase. It is confirmed that the vacant manganese sites are occupied by lithium ions. Hence, a defect lithium-rich spinel structure with strongly reduced capacity and cycle life is formed:^[53,183]



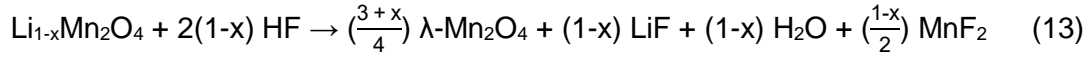
Besides, the divalent manganese ions migrate to the anode, are reduced, and precipitate as metallic Mn:^[4]



As a result, self-discharge of the lithiated graphite is promoted and severe electrolyte decomposition takes place, which engenders excessive SEI growth.^[183] By virtue of the presence of metallic Mn, the SEI becomes electronically conductive. Obviously, Li^+ are reduced before they can diffuse through the surface layer and deposit as metallic Li on the anode. Lithium plating is a well-known safety issue and the manifested lithium dendrites are

considered to lead to short circuits.^[184] The diminution of active lithium is reflected in a significant capacity drop.

In contrast to the disproportion of Mn^{3+} , Mn dissolution catalyzed by HF may also occur at higher states-of-charge (SOC). Thereby, HF reacts with LMO in the following manner:^[185]



Insoluble, isolating side reaction products like LiF, MnF_2 , and Mn_xO_y accumulate on the spinel electrode leading to an increase of the charge-transfer resistance. Thus, even a very small quantity of manganese in the electrolyte exerts a large negative influence on the cell performance. Figure 20 schematically illustrates the mentioned effects of Mn dissolution.

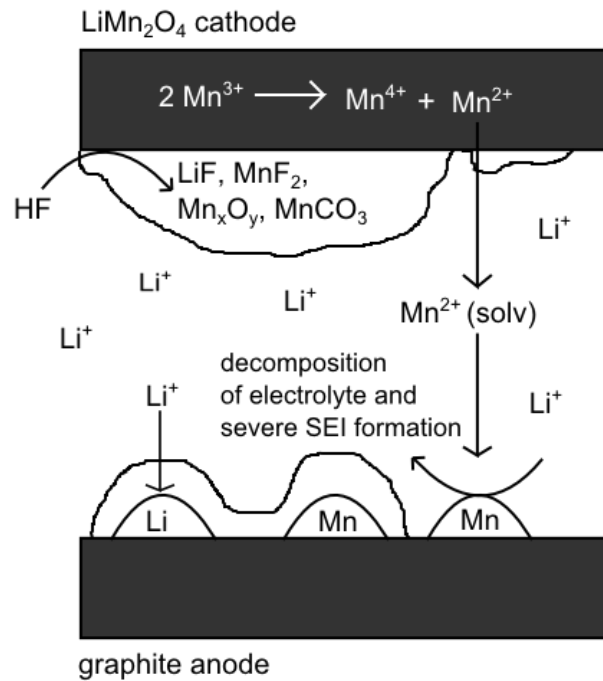


Figure 20 Dissolution of lithium manganese spinel and the related effects.

Numerous strategies have been pursued to improve the electrochemical characteristics of LMO. The preparation of the cation-deficient spinels $\text{Li}_{1-x}\text{Mn}_{2-2x}\text{O}_4$ has seemed to be very promising because of the enhanced Mn oxidation state. Nonetheless, they offer a diminished capacity in the 4 V region and it is hard to control the degree of non-stoichiometry during the synthesis.^[53] Another method to suppress the amount of Jahn-Teller active trivalent manganese in the spinel structure includes cation substitutions. First, lithium-rich modifications with the general formula $\text{Li}_{1+\delta}\text{Mn}_{2-\delta}\text{O}_4$ ($0 < \delta < 0.33$) have been examined. They cycle much better than LiMn_2O_4 , but the associated capacity is much lower.^[72] Later on, other transition metal cation dopants such as Mg^{2+} , Ni^{2+} , Zn^{2+} , Co^{3+} , Cr^{3+} , Cu^{2+} , and Fe^{3+} have been

investigated.^[180,186–192] Most of the doped spinels $\text{LiM}_x\text{Mn}_{2-x}\text{O}_4$ ($\text{M} = \text{Mg, Ni, Zn, Co, Cr, Fe, etc.}$ and $0 \leq x \leq 1$) exhibit a plateau near 4 V and an additional 5 V plateau. The former one correlates with the $\text{Mn}^{3+/4+}$ redox couple, while the latter one corresponds to the oxidation of the transition metal.^[16] Ni has emerged as an attractive substituent for Mn owing to the better cycling stability compared to the other candidates.^[189,193,194–196] Thereby, $\text{LiNi}_{0.5}\text{Mn}_{1.5}\text{O}_4$ is of particular interest on account of the smallest Mn^{3+} content.^[53,189] A detailed discussion on nickel doped spinels is given in the next chapter.

Further approaches to realize LMO with good capacity retention have shown varying degrees of success. They involve reduction of the surface area by tuning the particle morphology, partial substitution of O^{2-} ions by F^- ions, protective coatings of the spinel particles with oxides (e.g. LCO, ZrO_2 , SiO_2 , V_2O_5 , Al_2O_3 , and MgO), the use of new electrolyte additives that neutralize HF and absorb protons, applications of non-fluorinated conductive salts like lithium bis(oxalate)borate (LiBOB), and blending LMO powder with LNO, LCO, or lithium nickel cobalt oxide.^[16,53,67,177,197,198]

Lithium spinel oxide cathodes containing transition metals other than Mn have also been explored. LiNi_2O_4 and LiCo_2O_4 are two examples. Nevertheless, the majority of these materials features inferior electrochemical behavior. Therefore, they are not interesting as CAMs for industrial purposes.^[53]

Table 2 outlines the most important electrochemical properties of some CAMs and Figure 21 summarizes the historical development of intercalation cathode active materials for rechargeable LIBs.

2. Theoretical concepts

2.1 Historical development of intercalation cathode active materials for rechargeable LIBs

Cathode active material	Structure	Average Potential (V vs. Li)	Specific capacity (mAhg ⁻¹)	Specific energy (Whkg ⁻¹)
LiCoO ₂	layered	3.90	145	566
LiNiO ₂	layered	4.00	200	790
LiNi _{0.8} Co _{0.2} O ₂	layered	3.60	180	648
LiNi _{0.80} Co _{0.15} Al _{0.05} O ₂	layered	3.80	165	627
LiNi _{1/3} Mn _{1/3} Co _{1/3} O ₂	layered	3.80	155	589
LiNi _{0.6} Mn _{0.2} Co _{0.2} O ₂	layered	3.85	165	635
LiNi _{0.8} Mn _{0.1} Co _{0.1} O ₂	layered	3.90	180	702
Li-rich NMCs (e.g. Li _{1.2} Ni _{0.15} Mn _{0.55} Co _{0.1} O ₂)	layered	3.60	≥ 250	≥ 900
LiMn ₂ O ₄	spinel	4.10	120	492
LiMn _{1.5} Ni _{0.5} O ₄	spinel	4.70	135	635
LiFePO ₄	olivine	3.45	160	552
Li ₂ FeSiO ₄	tetrahedral	4.50	140	630
LiVPO ₄ F	tavorite	4.05	140	567

Table 2 Characteristics of several cathode active materials.^[16,53,55,57,70,76,78,129,144,199,200]

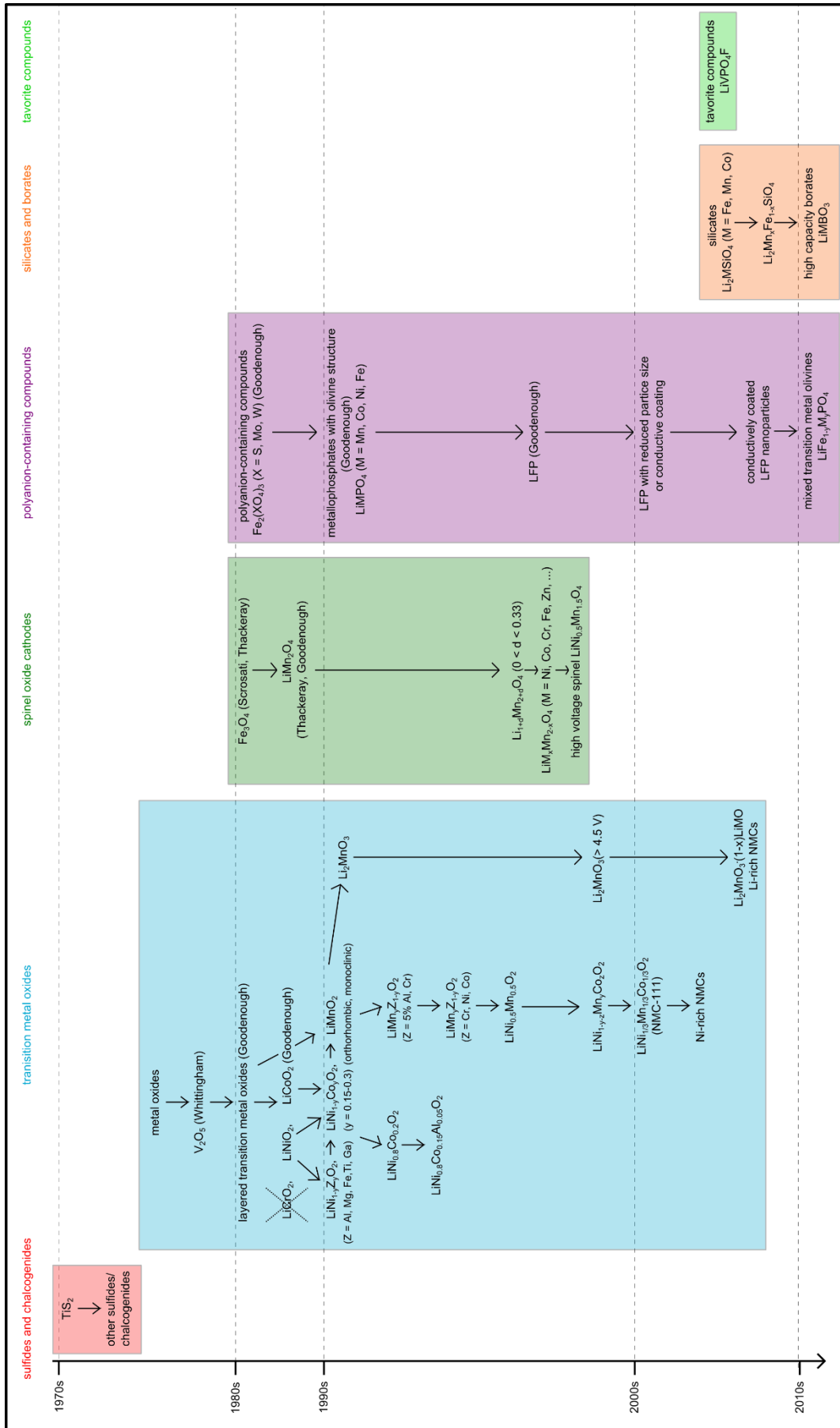


Figure 21 Overview of the historical development of intercalation cathode active materials for rechargeable lithium ion batteries.

2.2 Lithium nickel manganese oxide spinels

As mentioned in the previous chapter, several approaches have been pursued to improve the electrochemical features of LMO. One of the most popular and successful strategies are cation substitutions of manganese.^[180,186–192] Among them, nickel substituted manganese spinels ($\text{LiNi}_x\text{Mn}_{1-x}\text{O}_4$, $x \leq 0 \leq 0.5$) are of particular interest and have been studied by several groups.^[188,189,194,201,202] Generally, they can be written as $\text{LiNi}_x^{2+}\text{Mn}_{1-2x}^{3+}\text{Mn}_{1+x}^{4+}\text{O}_4$ with $x \leq 0 \leq 0.5$.^[203] The oxidation of Mn^{3+} to Mn^{4+} occurs at approx. 4.1 V, while the $\text{Ni}^{2+}/^{4+}$ redox couple is characterized by a long flat plateau below 4.8 V.^[55] The voltage plateaus can be explained by the crystal field theory. The 3d levels of the transition metals Mn and Ni split into e_g and t_{2g} orbitals, when they are octahedrally coordinated with oxygen. Considering the high-spin $\text{Mn}^{3+}:3d^4$ configuration, three electrons occupy the t_{2g} levels and one electron is in e_g . For Ni^{2+} , six electrons are located in the t_{2g} orbitals and two electrons are positioned in the e_g levels. The redox reactions $\text{Mn}^{3+} \rightarrow \text{Mn}^{4+}$ and $\text{Ni}^{2+} \rightarrow \text{Ni}^{4+}$ only involve the e_g bands. Thereby, the electron on the Mn e_g level has a binding energy of around 1.5 - 1.6 eV, corresponding to the 4.1 V plateau, whereas the electrons in the Ni e_g orbitals have a higher binding energy of about 2.1 eV. The increased energy needed to remove the electrons leads to the enhanced voltage plateau of up to ca. 4.7 V.^[55,188,203] Figure 22 demonstrates the evolution of the 3d electronic levels during charging $\text{LiNi}_x^{2+}\text{Mn}_{1-2x}^{3+}\text{Mn}_{1+x}^{4+}\text{O}_4$.

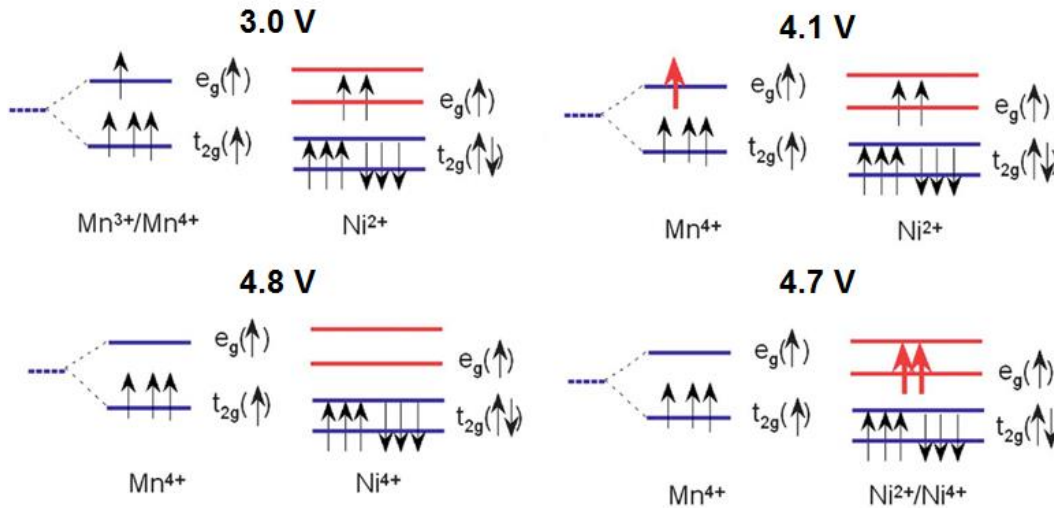


Figure 22 Schematic diagram of the 3d electronic orbitals of $\text{Mn}^{3+}/\text{Mn}^{4+}$ and Ni^{2+} in $\text{LiNi}_x^{2+}\text{Mn}_{1-2x}^{3+}\text{Mn}_{1+x}^{4+}\text{O}_4$ during the charge process. With modifications from^[55].

Since the lithium nickel manganese oxide spinel $\text{LiNi}_{0.5}\text{Mn}_{1.5}\text{O}_4$ has the smallest Mn^{3+} content of all $\text{LiNi}_x\text{Mn}_{1-x}\text{O}_4$ types, most researchers have focused on that substance as a very promising CAM.^[55,203–208] Mn^{3+} should be avoided within the spinel structure because they are prone to Jahn-Teller distortion and contribute to manganese dissolution (see chapter 2.1.3).^[70] Amine

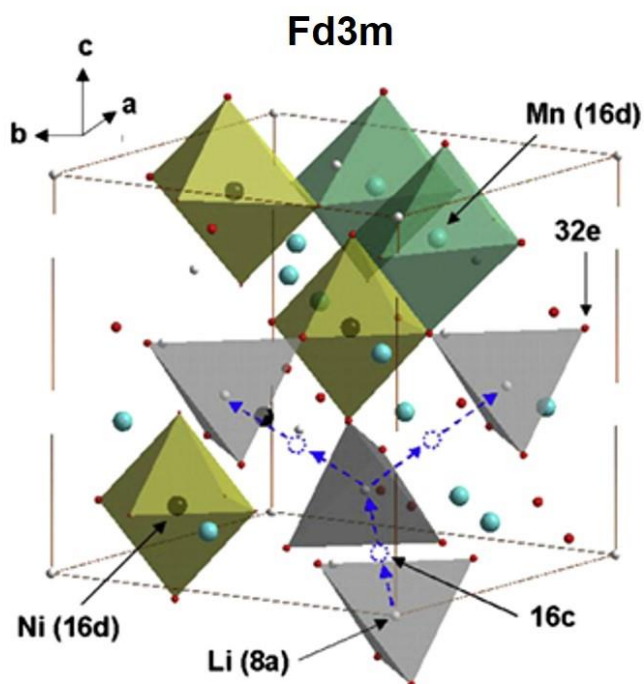
et al. and Dahn et al. were the first to discover that $\text{LiNi}_{0.5}\text{Mn}_{1.5}\text{O}_4$ can be used as 5 V class CAM for LIBs.^[187,189] $\text{LiNi}_{0.5}\text{Mn}_{1.5}\text{O}_4$ has a beneficial average potential of ca. 4.7 V vs. Li and a theoretical capacity of 147 mAhg^{-1} , which enable a high theoretical specific energy of 691 Whkg^{-1} .^[55] Higher nickel contents would only be advantageous with respect to an increase of the material's capacity. But simultaneously, the electronic conductivity would suffer on account of the complete absence of Mn^{3+} .^[209] More structural details are given below.

2.2.1 The crystal structures of $\text{LiNi}_{0.5}\text{Mn}_{1.5}\text{O}_4$

In dependence on the cation distribution, there are two possible crystallographic forms for the spinel $\text{LiNi}_{0.5}\text{Mn}_{1.5}\text{O}_4$: a face-centered, non-stoichiometric cation-disordered spinel (S.G. $\text{Fd}\bar{3}\text{m}$) and a primitive simple cubic crystal with a stoichiometric, cation-ordered network (S.G. $\text{P4}_3\bar{3}\text{2}$).^[205] Both structures are depicted in Figure 23.

Regarding the disordered phase (S.G. $\text{Fd}\bar{3}\text{m}$), Mn and Ni are randomly distributed in octahedral 16d sites, Li are located in tetrahedral 8a sites, and O, which are cubic close-packed, occupy the 32e positions.^[205] The vacant octahedral 16c sites enable good lithium ion conductivity through the formation of three-dimensional 8a-16c diffusion channels.^[207] In contrast, for the ordered phase (S.G. $\text{P4}_3\bar{3}\text{2}$) Ni and Mn are uniformly distributed in distinct 4b and 12d sites, respectively, resulting in a regular 3:1 ratio arrangement. Thereby, the vacant 16c sites are split into ordered 4a and 12d sites.^[207] O occupy the 24e and 8c Wyckoff positions, whereas Li are located in 8c sites. Since the lithium ion diffusion occurs via the 8c-4a and 8c-12d paths, the lithium migration is retarded by the occupied 4b and 12d positions.^[210]

A



B

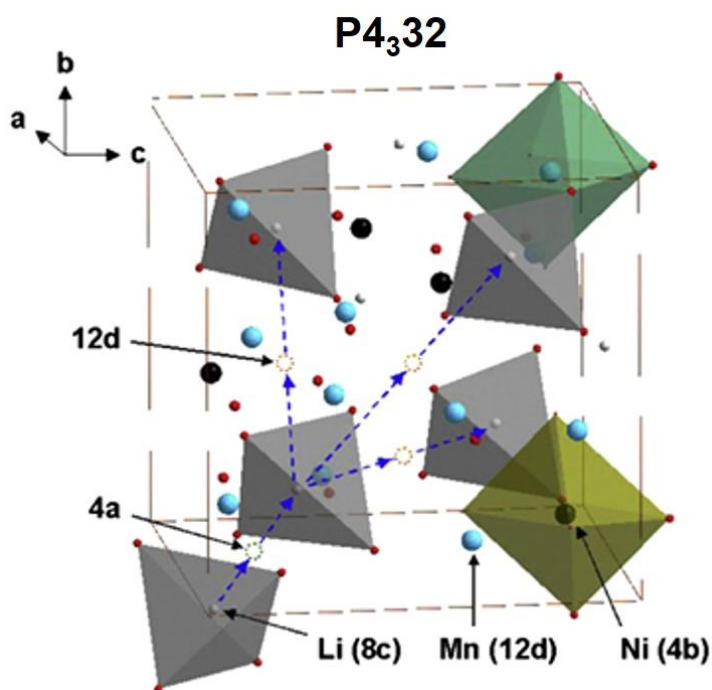


Figure 23 Schematic drawing of the two structures of $\text{LiNi}_{0.5}\text{Mn}_{1.5}\text{O}_4$ including the lithium ion diffusion paths. **A** face-centered spinel (S.G. $\text{Fd}3\text{m}$) and **B** primitive simple cubic (S.G. $\text{P}4_332$).^[207]

It is known that the synthetic routes and techniques define the properties of $\text{LiNi}_{0.5}\text{Mn}_{1.5}\text{O}_4$ (e.g. particle size and morphology) and decide which one of the two structures is produced. Actually, there are numerous synthetic methods for $\text{LiNi}_{0.5}\text{Mn}_{1.5}\text{O}_4$ like, for example, solid state reactions, molten salt syntheses, wet-chemical routes, spray techniques, and polymer-assisted methods.^[55,203,211,212,213,214] The synthesis of the disordered spinel structure under high calcination temperatures is typically accompanied by oxygen loss leading to the non-stoichiometric phase (S.G. $\text{Fd}\bar{3}\text{m}$).^[189,215,216] On account of the oxygen-deficiency within the spinel network, some Mn^{4+} are reduced to Mn^{3+} to afford charge neutrality.^[203] Furthermore, rock salt impurities, i.e. NiO and/or $\text{Li}_x\text{Ni}_{1-x}\text{O}$, are usually generated under such high temperature conditions (Figure 24).

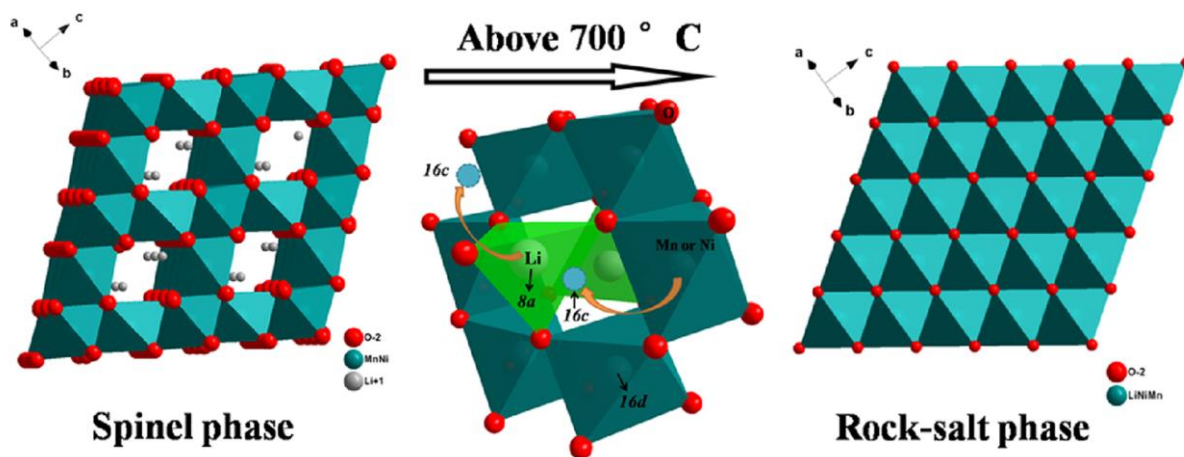


Figure 24 Schematic illustration of the transition from spinel to rock-salt phase above 700 °C. Ni and/or Mn ions migrate to interstitial octahedral 16c sites and displace the Li^+ ions from tetrahedral sites to octahedral sites.^[215]

These undesired side reaction products deteriorate the electrochemical features of the high voltage spinel material.^[189,217,218] To avoid rock salt impurities, but not Mn^{3+} associated with the disordered spinel fraction, slow cooling from the calcination temperature ($1\text{ }^\circ\text{Cmin}^{-1}$) is recommended.^[215] The ordered spinel phase (S.G. $\text{P4}_3\text{32}$) is obtained by annealing the sample at 700 °C in air or pure oxygen after the high temperature calcination. Then, ordering of Ni^{2+} and Mn^{4+} takes place and all oxygen vacancies are removed. The resulting powders do not contain any Mn^{3+} .^[205,215] Another approach concerns the direct synthesis under oxygen yielding the cubic spinel structure with the $\text{P4}_3\text{32}$ space group instead of $\text{Fd}\bar{3}\text{m}$.^[195,219]

The two spinel phases have different electrochemical characteristics. Considering the rate capability, the disordered structure is believed to be more beneficial than the ordered one.^[205,211,220,221] This is related to the higher ionic conductivity of the non-stoichiometric spinel given by the three-dimensional 8a-16c diffusion channels with low activation barriers for lithium ion migration. Li^+ movement within the stoichiometric spinel structures is impeded by the

stronger electrostatic repulsion from the transition metals, which occupy the 4b and 12d positions.^[195,205,220,222] Moreover, the disordered phase delivers a higher starting capacity than the ordered one due to the additional $\text{Mn}^{3+/4+}$ redox couple.^[204] Besides, a higher degree of ordering reduces the electronic conductivity of the spinel structure owing to the lack of Mn^{3+} . This is because the electron transfer is supported by electron hopping between Mn^{3+} and Mn^{4+} .^[123,222,223] Consequently, a low amount of Mn^{3+} within the structural network is favorable despite its tendency to disproportionate to Mn^{2+} and Mn^{4+} with the concomitant Jahn-Teller distortion. Although the oxygen vacancies in the non-stoichiometric spinel contribute to capacity fading, there is a consensus for the better cycling stability of non-stoichiometric high voltage spinel compared to the ordered phase.^[203,211,224] Therefore, the disordered structure is usually applied as CAM in LIBs.^[214,225] Nevertheless, the oxygen deficiencies and Mn^{3+} should be kept below a critical value in order that the negative effects remain minimal. Valuable analytical techniques to distinguish the two crystal structures are, for instance, X-ray diffraction (XRD), neutron diffraction, X-ray absorption fine structure (XAFS), X-ray absorption near edge structure (XANES), electron diffraction, Raman spectroscopy, and Fourier transform infrared spectroscopy (FTIR).^[195,203,224,226,227]

An effective method to control the crystallographic features and to stabilize the electrochemical performance of high voltage spinel electrodes is partial replacement of Ni and/or Mn in $\text{LiNi}_{0.5}\text{Mn}_{1.5}\text{O}_4$ by other metal cations.^[1,228] For example, the formation of rock salt impurities can be avoided by metal ion doping.^[1] In general, small amounts of elemental substitutions (e.g. Fe, Cr, Ru, Zr, Al, Co, Mg, Ga, and Cu) have been demonstrated to improve the cycling behavior of $\text{Li}/\text{LiNi}_{0.5}\text{Mn}_{1.5}\text{O}_4$ half cells.^[1,218,228–230,231]

2.2.2 Phase transitions upon cycling

The phase evolution of $\text{LiNi}_{0.5}\text{Mn}_{1.5}\text{O}_4$ throughout Li^+ intercalation/deintercalation has been studied by several research groups using both ex situ and in situ X-ray diffraction techniques.^[55,195,196,200,203,224,227,230,232–234,235] However, the reported results are partially conflicting and are strongly dependent on the examined sample. For example, Alcantara et al. found that $\text{Li}_1\text{Ni}_{0.5}\text{Mn}_{1.5}\text{O}_4$ exhibits a single cubic phase up to $\text{Li}_{0.5}\text{Ni}_{0.5}\text{Mn}_{1.5}\text{O}_4$. Further Li^+ extraction causes the XRD reflections to split and two cubic phases with different unit cell parameters are detectable from $\text{Li}_{0.45}\text{Ni}_{0.5}\text{Mn}_{1.5}\text{O}_4$ to $\text{Li}_0\text{Ni}_{0.5}\text{Mn}_{1.5}\text{O}_4$. Thereby, the second phase shows a contraction of the unit cell volume.^[196] Mukerjee and co-workers investigated the charge/discharge mechanism of Ni-doped spinels around 5 V by in situ X-ray diffraction. They demonstrated the coexistence of three phases in the upper voltage plateau (4.5 - 5.2 V) with minimal changes in the lattice parameters within each phase.^[227] Kim and his group compares the phase development of non-stoichiometric (S.G. $\text{Fd}3\text{m}$) and stoichiometric (S.G. $\text{P}4_332$) high voltage spinel cathodes ($\text{Li}_x\text{Ni}_{0.5}\text{Mn}_{1.5}\text{O}_4$) by XRD. The disordered structure undergoes a

one-step phase transition during Li^+ deintercalation from $x = 1 - 0.04$. Actually, the lattice constant of the first cubic phase decreases linearly upon Li^+ extraction until x equals approx. 0.25, whereas that of the second cubic phase remains nearly constant at ca. 8 Å. In contrast, the ordered structure reveals a two-step phase transition with three distinct cubic phases from $1 \leq x \leq 0.5$, $0.75 \leq x \leq 0.25$, and $0.25 \leq x \leq 0.04$ (Figure 25).^[195]

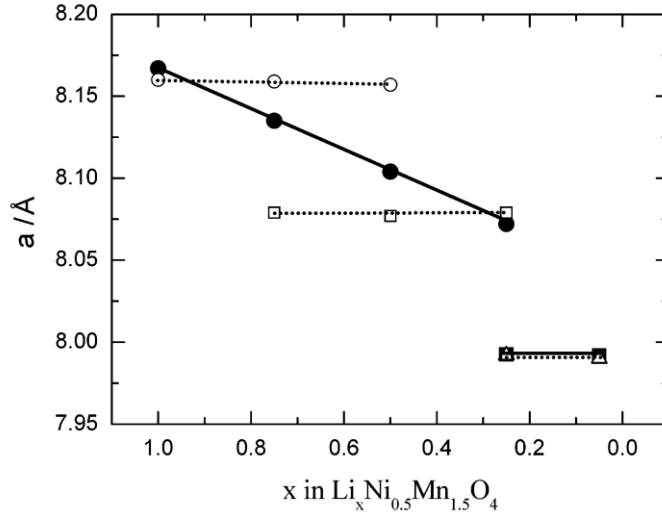


Figure 25 Variation in the lattice parameter a of non-stoichiometric (S.G. $\text{Fd}3\text{m}$, closed symbols) and stoichiometric (S.G. $\text{P}4_332$, open symbols) high voltage spinel electrodes ($\text{Li}_x\text{Ni}_{0.5}\text{Mn}_{1.5}\text{O}_4$) on charge.^[195]

Ozhuku et al. also studied the mechanism of Li^+ intercalation/deintercalation into/from ordered $\text{Li}_x\text{Ni}_{0.5}\text{Mn}_{1.5}\text{O}_4$ (S.G. $\text{P}4_332$). They observed two cubic/cubic two-phase reactions from $x = 1$ to $x = 0$. More precisely, $\text{Li}_0\text{Ni}_{0.5}\text{Mn}_{1.5}\text{O}_4$ (8.00 Å) is reduced to $\text{Li}_1\text{Ni}_{0.5}\text{Mn}_{1.5}\text{O}_4$ (8.17 Å) via $\text{Li}_{0.5}\text{Ni}_{0.5}\text{Mn}_{1.5}\text{O}_4$ (8.09 Å). In other words, the oxidation of Ni^{2+} to Ni^{3+} , and to Ni^{4+} induces the decrease of the lattice parameters from 8.17 to 8.00 Å.^[236] Idemoto and his group also identified three phases for $\text{Li}_x\text{Ni}_{0.5}\text{Mn}_{1.5}\text{O}_4$ (S.G. $\text{P}4_332$) in dependence of the valence state of nickel: Ni^{2+} ($a \approx 8.16$ Å) to Ni^{3+} ($a \approx 8.09$ Å) to Ni^{4+} ($a \approx 8.00$ Å).^[232] In contrast, a different phase evolution for the material with the $\text{P}4_332$ space group ($\text{Li}_x\text{Ni}_{0.5}\text{Mn}_{1.5}\text{O}_4$) was recognized by Wang and co-workers. The first cubic phase is stated as a solid solution phase from $1.0 \leq x \leq 0.2$ ($a \approx 8.17 - 8.16$ Å). A second cubic phase with a lattice constant of approx. 8.08 Å appears at around $x = 0.7$ through a biphasic transition. At $x = 0.5$ a third cubic phase starts growing while the other two phases are still present. They coexist till the end of charge (Figure 26B). For the $\text{Fd}3\text{m}$ high voltage spinel, three distinct steps are defined. The first cubic phase is assigned to a solid solution-type reaction with varying lattice parameters from $1 \leq x \leq 0.7$ (8.17 - 8.12 Å). From $x = 0.6$ a second phase develops with a refined lattice constant at ca. 8.08 Å and from $x = 0.4$ a third cubic phase becomes visible with a lattice parameter at around 8.00 Å (Figure 26A).^[224]

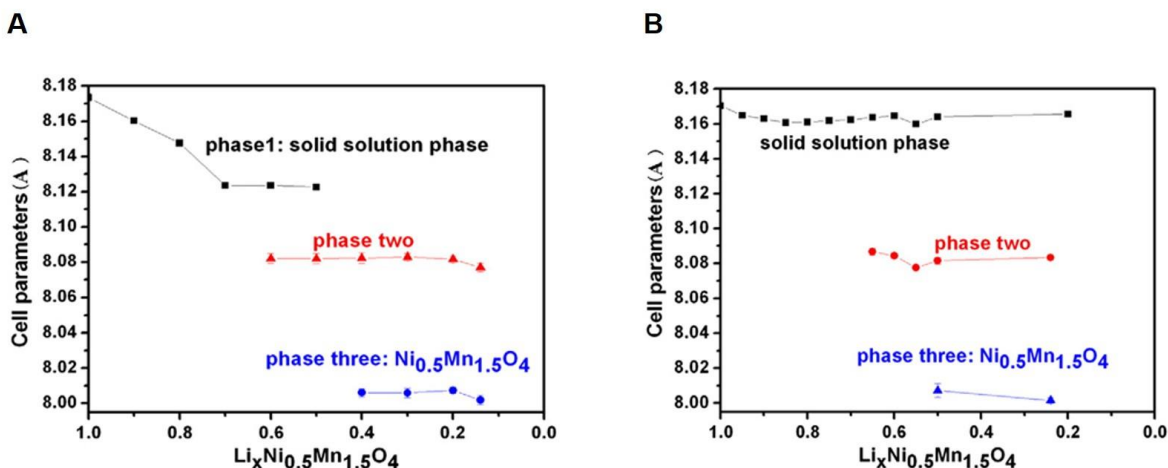


Figure 26 Evolution of the lattice constants of different phases during Li⁺ deintercalation. **A** Fd3m structure and **B** P4₃32 structure.^[224]

The group of Arai utilized XANES and XRD to investigate phase transition kinetics of LiNi_{0.5}Mn_{1.5}O₄. Nonetheless, the authors did not specify if their measurements were made with ordered or disordered high voltage spinel material. It is simply noted that the phase transitions proceed with the coexistence of Li₁Ni_{0.5}Mn_{1.5}O₄ and Li_{0.5}Ni_{0.5}Mn_{1.5}O₄ in the low potential plateau and that of Li_{0.5}Ni_{0.5}Mn_{1.5}O₄ and Li₀Ni_{0.5}Mn_{1.5}O₄ in the high potential region. The changes of the cubic phases are related to the oxidation state changes of the transition metals.^[233] Zhang et al. performed in situ XRD analysis on Li_xNi_{0.5}Mn_{1.5}O₄ with the P4₃32 space group. Two-step two-phase reactions between three cubic phases during lithium intercalation/deintercalation are registered. Interestingly the first cubic phase is present throughout the whole discharging process ($a \approx 8.17 - 8.15 \text{ \AA}$). The second cubic phase appears at $x \approx 0.85$ ($a \approx 8.09 \text{ \AA}$) and the third cubic phase evolves at $x \approx 0.4$ ($a \approx 8.00 \text{ \AA}$). All three phases coexist until $x = 0$.^[230] Another report deals with temperature controlled in situ XRD measurements for clarifying the reaction dynamics of thin LiNi_{0.5}Mn_{1.5}O₄ electrodes upon Li⁺ insertion/extraction at various temperatures. It is shown that the phase transitions of Li₁Ni_{0.5}Mn_{1.5}O₄ to Li₀Ni_{0.5}Mn_{1.5}O₄ occur in a stepwise manner via Li_{0.5}Ni_{0.5}Mn_{1.5}O₄ at room temperature and above. At lower temperatures, the complete delithiation to yield Li₀Ni_{0.5}Mn_{1.5}O₄ is restricted as the phase transition of Li_{0.5}Ni_{0.5}Mn_{1.5}O₄ to Li₀Ni_{0.5}Mn_{1.5}O₄ is rather slow and actually the rate determining step.^[234] Chen et al. also conducted in situ XRD studies of Li_xNi_{0.5}Mn_{1.5}O₄ cathodes (S.G. Fd3m) at room temperature. The formation of the second cubic phase Li_{0.5}Ni_{0.5}Mn_{1.5}O₄ ($a = 8.09 \text{ \AA}$) is already detected at $x > 0.71$ at the expense of the first cubic phase Li₁Ni_{0.5}Mn_{1.5}O₄ ($a = 8.17 \text{ \AA}$). The third cubic phase Li₀Ni_{0.5}Mn_{1.5}O₄ ($a = 8.00 \text{ \AA}$) appeared upon further Li⁺ removal, which rendered the coexistence of three cubic phases in the sample with an intermediate Li⁺ content of $0.25 < x \leq 0.71$. At $x \leq 0.25$, the spinel electrodes were solely composed of the second and third cubic phase. The dimensions of the lattice constants are supposed to be directly attributed to the transition metal oxidation states.^[200]

All in all, several publications report on investigating the phase transitions of $\text{LiNi}_{0.5}\text{Mn}_{1.5}\text{O}_4$ composite electrodes throughout Li^+ intercalation/deintercalation. Nevertheless, in dependence of the space group, the particle size, and the particle morphology different phase evolutions with only inaccurate and/or conflicting information on the transition metal valence states are observed.

2.2.3 Problems and challenges of high voltage spinel full cells

Although several researchers have put much effort on studying lithium nickel manganese oxide spinel materials, the breakthrough as CAM has not been achieved so far.^[1,55,57,203,229] One reason is certainly that many improvements attained, by for example, cation-doping, morphological particle control, surface modification, or electrolyte optimization have largely been realized in half cell configurations with a lithium metal anode but not in full cell setups comprising a graphite anode.^[1,203,214,229,237,238,239] For example, Figure 27 compares the cycling performance of half and full cells containing the doped high voltage spinel material $\text{LiNi}_{0.5-x}\text{Mn}_{1.5}\text{M}_x\text{O}_4$ ($\text{M} = \text{Co}, \text{Fe}, \text{Ga}, \text{and Cr}; x = 0 \text{ and } 0.08$). With the lithium metal anode all substituted samples exhibit a better cycling behavior than the undoped material ($x = 0$). In contrast, all doped samples still suffer severe capacity fading with the graphite anode.^[229]

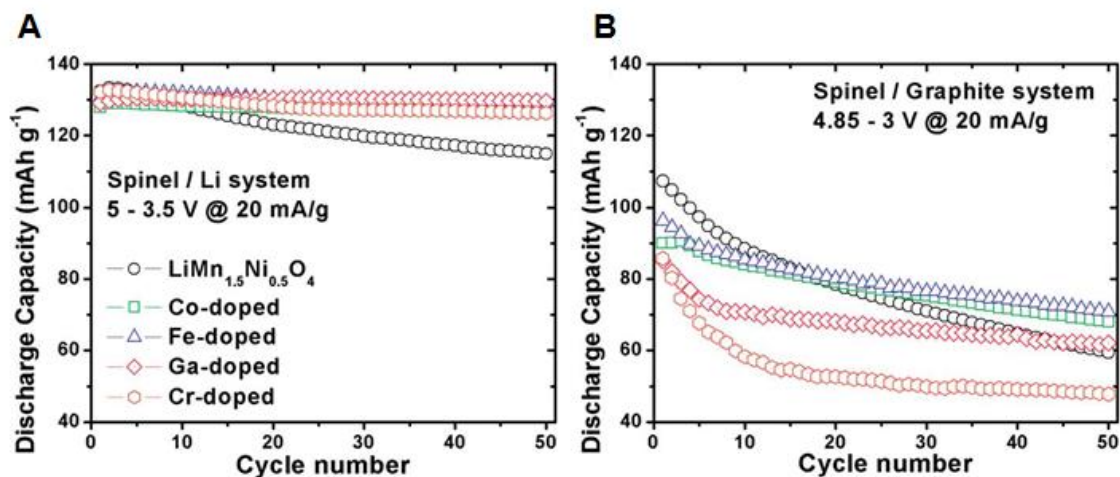


Figure 27 Cycle performance of $\text{LiNi}_{0.5-x}\text{Mn}_{1.5}\text{M}_x\text{O}_4$ ($\text{M} = \text{Co}, \text{Fe}, \text{Ga}, \text{and Cr}; x = 0 \text{ and } 0.08$) cathodes operated with different anodes: **A** with a lithium metal anode when cycled between 5.0 and 3.5 V and **B** with a graphite anode when cycled between 4.85 and 3.0 V.^[229]

The most important issues regarding the poor cyclability of C// $\text{LiNi}_{0.5}\text{Mn}_{1.5}\text{O}_4$ full cells hindering their commercialization are discussed in the following.

Electrolyte oxidation

Electrolyte solutions for rechargeable LIBs are primarily composed of lithium conducting salts (typically LiPF_6) dissolved in organic carbonates such as, for instance, ethylene carbonate (EC), dimethyl carbonate (DMC), diethyl carbonate (DEC), and ethyl methyl carbonate (EMC).^[240] It has been shown that the salt species have a minimal effect on the electrolyte stability, which is basically determined by the solvents.^[241,242] Carbonates are known to be reduced at ca. 1.0 V vs. Li and to be oxidized at ca. 4.7 V vs. Li.^[4,201,243–247] However, carbonate electrolyte mixtures have an oxidation potential of only approx. 4.5 V vs. a lithium nickel manganese oxide spinel composite electrode because the conductive carbon additive is believed to have a catalytic effect for electrolyte oxidation at high voltages.^[1,248,249,249–252]

In general, the electrochemically stable window of a liquid electrolyte is given by the energy separation E_g between its lowest unoccupied molecular orbital (LUMO) and its highest occupied molecular orbital (HOMO):^[201]

$$E_g = E_{\text{LUMO}} - E_{\text{HOMO}} \quad (14)$$

In a thermodynamically stable battery cell, the anode and cathode potentials μ_A and μ_C , respectively, are located within the window of the electrolyte, which constrains the open circuit voltage V_{OC} of a battery to

$$eV_{\text{OC}} = \mu_A - \mu_C \leq E_g \quad (15)$$

where e represents the electron charge.^[201] Otherwise, an anode with a bigger μ_A than the LUMO energy will reduce the electrolyte unless a passivation layer (SEI) establishes a barrier to prevent electron transfer from the anode to the electrolyte LUMO. Likewise, a cathode with a lower μ_C than the HOMO energy will oxidize the electrolyte unless the electron transfer from the electrolyte HOMO to the cathode is blocked by a protection layer (SPI).^[201] Thus, it is essential to either design high capacity electrodes matched to the HOMO and LUMO of the electrolyte or to formulate a non-aqueous electrolyte, which allows a large thermodynamically stable window in order to obtain high performance lithium ion cells. Another possibility implies the formation of stable passivating films on the electrodes. These protection layers should possess the following properties:^[16,201,253]

- the ability to rapidly self-heal when broken by the volume changes occurring throughout cycling a lithium ion cell
- high lithium ion conductivity permitting fast lithium ion transfer between the electrodes and the electrolyte

- high electronic resistance to avoid a thickening of the layers leading to high internal resistances and self-discharge, but without blocking the electron transfer between the active material particles and the current collectors
- low charge-transfer resistance
- uniform morphology and chemical composition for homogeneous current distribution
- good adhesion to the electrodes
- mechanical strength, flexibility, and integrity
- thermal stability
- insolubility in the electrolyte
- reasonable thickness

The combination of a graphite anode and a high voltage spinel cathode increases the cell voltage significantly as μ_c is noticeably lowered on account of the $\text{Ni}^{2+/4+}$ redox couple compared to standard CAMs (e.g. NMC-111). Figure 28 displays schematically the electronic density of states and Fermi energies for a $\text{Li}_x\text{Ni}_{0.5}\text{Mn}_{1.5}\text{O}_4$ electrode.

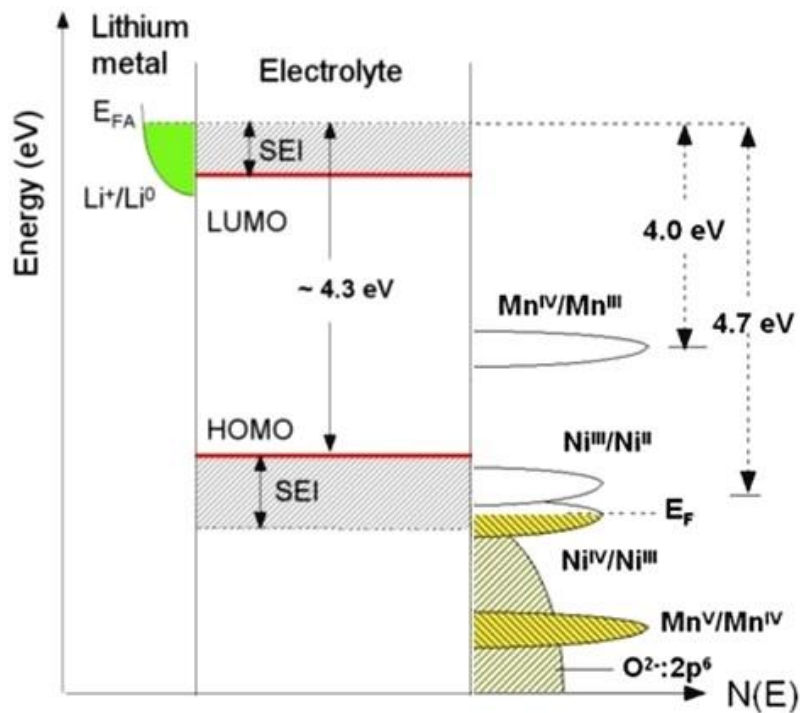


Figure 28 Schematic diagram depicting the electronic density of states and Fermi energies for a $\text{Li}_x\text{Ni}_{0.5}\text{Mn}_{1.5}\text{O}_4$ electrode. With modifications from^[70,203].

The energy of a redox couple is not only governed by its formal valence state, but it also depends on its position relative to the top of the anion p band. While Mn^{3+} can be easily oxidized to Mn^{4+} around the 4 V plateau, the Fermi energy E_F of the $\text{Ni}^{3+/4+}$ couple is pinned at

the top of the $O^{2-}:2p$ band determining the intrinsic voltage limit vs. Li for the cathode. Thereby, the empty states above E_F transform progressively from primarily d- to primarily p-symmetry upon oxidation. Hence, it is possible to access two formal valences on the active cation (Ni^{3+} and Ni^{4+}) without a voltage step on passing from one oxidation state to another. In contrast, the redox energy of the $Mn^{4+/5+}$ couple cannot be utilized as it lies well below the top of the $O^{2-}:2p$ band.^[201,203]

As can be seen, the Fermi energy E_F of the $Li_xNi_{0.5}Mn_{1.5}O_4$ electrode is positioned below the HOMO of a liquid carbonate electrolyte, which is about 4.3 V under the Fermi energy E_{FA} of a lithium metal anode. This is the reason why carbonate-based electrolytes are not stable throughout cycling C// $LiNi_{0.5}Mn_{1.5}O_4$ cells. Instead, the electrolyte components are oxidized above ca. 4.5 V and the corresponding reaction products deposit on the spinel electrode surface.^[1,55,203,245,246,248,251,252] The latter range from polyethylene carbonates, polyethylene oxides, lithium carbonates, lithium fluoride, to fluorophosphates. Therefore, reversible reactions within the cell are only obtained when a passivating, Li permeable layer is formed on the $LiNi_{0.5}Mn_{1.5}O_4$ electrode. This layer is called solid permeable interface (SPI). It prevents further electrolyte decomposition, which is accompanied by the self-discharge of the CAM to compensate for charge neutrality:^[4,206]



Although the oxidation of the alkyl carbonates results in the generation of a polymeric, Li conductive film, a strong performance degradation of high voltage spinel full cells is commonly reported.^[1–6,248,251] As a matter of fact, a carbonate-based SPI does not cover the composite cathode sufficiently to stop the undesired electrolyte corrosion and consumption of active Li^+ upon cycling.^[248,251] Up to now, several studies have been conducted to identify the mechanisms of electrolyte oxidation and the respective decomposition products.^[1,242,245,247,254–261] Aurbach et al. observed the generation of carbon dioxide, carbon monoxide, and carbonyl compounds such as chain organic carbonates, ketones, aldehydes, and formates by in situ FTIR measurements. Thereto, alkyl carbonate solutions of commonly used Li salts ($LiPF_6$, $LiAsF_6$, $LiClO_4$, $Li(NSO_2CF_3)_2$, etc.) were oxidized on metal electrodes including Au, Pt, and Al at onset potentials between 3.5 and 4 V vs. Li.^[242] Studies by Zhang and Ross revealed that the electrolyte formulation composed of 1 M $LiPF_6$ in EC/DMC develops CO_2 at the threshold voltage of 5 V vs. Li when using glassy carbon as the working electrode.^[254] Two other reports describe the formation of CO_2 and acetone on account of the decomposition of PC-based electrolytes at voltages higher than 4.0 V vs. Li.^[255,256] The gas generation causes bulging of pouch-type battery cells and is a serious performance and life issue. Recently, Leitner et al. speculated that excess amounts of CO_2 might be reduced at the anode to yield Li_2CO_3 , which consumes Li^+ ions and accelerates capacity decay.^[257,258]

Kanamura and his group investigated the electrochemical oxidation processes on Ni electrodes in propylene carbonate electrolytes by using cyclic voltammetry, X-ray photoelectron spectroscopy, and in situ Fourier transform infrared spectroscopy. According to their results, Ni cathodes, electrolyte salts, and solvents are oxidized at an anodic potential greater than 4.2 V vs. Li. This leads to the production of polycarbonates.^[259] Yang and co-workers examined the reaction of an electrolyte (1 M LiPF₆ in EC/DMC/DEC (1/1/1, w/w/w)) with the surface of LiNi_{0.5}Mn_{1.5}O₄ by storing LiNi_{0.5}Mn_{1.5}O₄/Li coin cells at high voltages (4.7 - 5.3 V vs. Li). By means of ex situ X-ray photoelectron spectroscopy (XPS) and IR spectroscopy, polyethylene carbonate was registered on the spinel electrode surface.^[245] Moreover, it was shown that the strong Lewis acid PF₅ catalyzes the ring-opening of EC, followed by its polymerization into polyethylene oxide and similar products.^[1,247,260,261] Kim et al. studied the electrolyte degradation after storing LiNi_{0.5}Mn_{1.5}O₄ cathodes in the electrolyte (1 M LiPF₆ in EC/DEC (1/1, v/v)) under different conditions: SOC, temperature, and storage time. The chemical composition of the aged electrolyte samples were determined by gas chromatography. Ethanol and diethyl ether were recognized as decomposition products, whereby the contents are strongly dependent on the test parameters. H₂O and CO₂ are also generated as undesired side-reaction products in lithium nickel manganese oxide spinel full cells.^[1,4] Besides, Edström et al. utilized synchrotron-based soft XPS to analyze the corrosion of the electrolyte 1 M LiPF₆ in EC/DEC (1/1, v/v) in the surface region of a conductive carbon electrode at high voltages up to 4.9 V. They identified the formation of hydrocarbons, ether species, LiF, and carbonates.^[250]

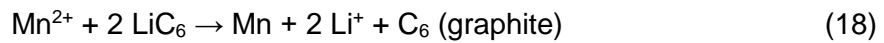
In order to stabilize the passivation layer on the LiNi_{0.5}Mn_{1.5}O₄ cathode surface many researchers have focused on adding electrolyte additives to the conventional electrolytes.^[5,262,262–279] Each novel electrolyte formulation suffers from some disadvantages. A real breakthrough has not been achieved so far. Another possibility involves the utilization of other electrolyte solvents, which have a greater oxidation stability than carbonates. Xu and Angell, for example, revealed that sulfone-based electrolytes exhibit a remarkable anodic stability of up to 5.8 V vs. Li.^[241,280] However, most sulfones are unable to generate a stable SEI on the graphite electrode, have high melting points, and high viscosities, which limit their implementation in lithium ion cells.^[1] Nitriles have also a higher oxidation stability than carbonates. Actually, electrolytes comprising up to 50 vol% dinitriles extend the anodic stability up to 6 V vs. Li.^[281] Nonetheless, dinitriles solvents have only a limited compatibility with metallic Li and lithiated graphite electrodes as lithium can reduce the nitrile group.^[282] Finally, attempts have been made to improve the oxidation stability of carbonates by replacing protons with fluorine, because then the HOMO of the electrolyte is lowered.^[263,283] But the LUMO of the electrolyte is lowered, too, which might be an issue for C//LiNi_{0.5}Mn_{1.5}O₄ full cells, when the fluorinated molecules are incapable of forming an effective SEI.^[283,284]

Transition metal dissolution

The inferior cyclability of high voltage spinel full cells is also ascribed to dissolution reactions of manganese and nickel into the electrolyte. Generally, two different mechanisms for transition metal dissolution are discussed. For instance, Mn^{3+} are known to disproportionate to Mn^{2+} and Mn^{4+} in the presence of trace amounts of acidic components as first observed by Hunter:^[4,182]



The resulting Mn^{2+} dissolve in the electrolyte, migrate to the anode, are reduced, and precipitate as metallic Mn:^[4]



As already described in chapter 2.1.3, the presence of metallic Mn on the graphite electrode provokes the self-discharge of the anode, causes the loss of active Li^+ , and induces massive SEI growth.^[183] Furthermore, the SEI becomes electronically conductive, which engenders Li plating.^[184] Although the Mn^{3+} content in $\text{LiNi}_{0.5}\text{Mn}_{1.5}\text{O}_4$ is much lower than in LMO, it still suffers from severe metal ion depletion. This is primarily due to the higher operating voltage, which supports the reaction of HF with the CAM:^[4,285,286]

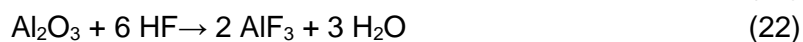


or



HF is generated in high voltage spinel full cells according to the equations 6 - 9 (see chapter 2.1.3). Thereby, the dissolution of Mn and Ni increases with SOC, temperature, and storage time of the full cells.^[1,4] The reaction products LiF , NiF_2 , and MnF_2 accumulate on the cathode surface, which enhances the cell impedance.^[4,287] Moreover, the loss of active material deteriorates the cycle life of the cells. Reactions 19 and 20 are closely related to the problem of electrolyte oxidation, since again the CAM is not protected sufficiently from the contact with electrolyte species. Consequently, surface coating of the lithium nickel manganese oxide spinel particles seems to be a promising way to prevent chemical interactions between the CAM and the electrolyte. Up to now, numerous different surface modifications of high voltage spinel particles including oxide coated layers (ZnO , SiO_2 , Bi_2O_3 , Al_2O_3 , ZrO_2 , LiCoO_2 , and LiAlO_2), noble metal layers (Zn , Au , and Ag), and phosphate layers (Li_3PO_4 , ZrP_2O_7 , FePO_4 , AlPO_4 , and LiFePO_4) have been applied. They have led to better cycling features and rate capability retention of the related cells.^[288,289,289–291] Nevertheless, excess coating should be avoided as it will lead to the loss of rate capability because of the low lithium-ion conductivity of the above mentioned materials.^[292] In addition, nano-sized oxide particles can act as HF

scavenger.^[293] For example, ZnO and Al₂O₃ coatings react with HF and reduce its active concentration in the electrolyte.^[292,294]



Besides, some electrolyte additives can also alleviate the HF concentration in the electrolyte by trapping HF, H₂O, or PF₅. Examples are lithium bis(oxalate)borate, tris(2,2,2-trifluoroethyl)phosphite, pyridine, 1-methyl-2-pyrrolidione, hexamethoxycyclotriphosphazene, hexamethylphosphoramide, tris(pentafluorophenyl)borane, dimethylacetamide, and hexamethyldisilazane.^[295,296,297–299] However, except for LiBOB, there are almost no systematic and comprehensive studies about the application of these additives in high voltage spinel full cells.^[295]

Additional challenges

It should be pointed out that not only the CAM and the electrolyte experience high voltages (> 4.8 V) upon cycling, but the separator, the binding agents, the conductive carbons, the current collectors, and the cell casing must also withstand these conditions. Only recently, researches have paid attention towards these supposedly passive and oxidative stable cell components.^[1,300,301]

Considering conductive carbons, carbon black additives are typically used for high voltage spinel full cells to establish electronically conductive pathways throughout the electrode.^[1] Graphitic powders are normally not applied for high voltage spinel electrodes because it is known that PF₆⁻ can intercalate into graphite at high voltages, which results in structural degradation of the electrode due to exfoliation.^[302] However, lately, it has been shown that carbon blacks, including the widely used Super P, also suffer from PF₆⁻ intercalation at voltages above 4.0 V vs. Li.^[1,249,303] Actually, Syzdek et al. suppose that all types of carbon blacks are electrochemically active towards LiPF₆ based organic carbonate electrolytes and that PF₆⁻ intercalation is not fully reversible. The associated morphological and structural changes of the carbon material lead to a gradual loss of power and charge capacity of the composite cathode.^[303] Furthermore, it has been demonstrated that conductive carbons catalyze the oxidation of carbonate-based electrolytes at the high voltages applied for lithium nickel manganese oxide spinel electrodes.^[1,248–251,304] For instance, Edström et al. confirmed the decomposition of 1 M LiPF₆ in EC/DEC (1/1, v/v) at the surface of carbon black particles at voltages of up to 4.9 V by synchrotron-based soft XPS.^[250] Demeaux and co-workers compared the oxidation of carbonate-based electrolyte solutions vs. different working electrodes including a bare Al current collector and electrodes composed of carbon black and PVDF by linear voltammetry. They verified that the carbon black containing electrodes exhibit

an earlier onset potential of electrolyte oxidation than the pure Al current collector.^[248] Similarly, Cabot published a patent, in which five carbon black powders with different degrees of graphitization and/or surface areas are investigated with respect to their activity towards electrolyte oxidation. Thereto, cyclic voltammograms of coin cells comprising a carbon black/PVDF electrode, a lithium anode, and 1 M LiPF₆ in EC/DMC/EMC (1/1/1, w/w/w) + 1% VC were recorded (Figure 29).

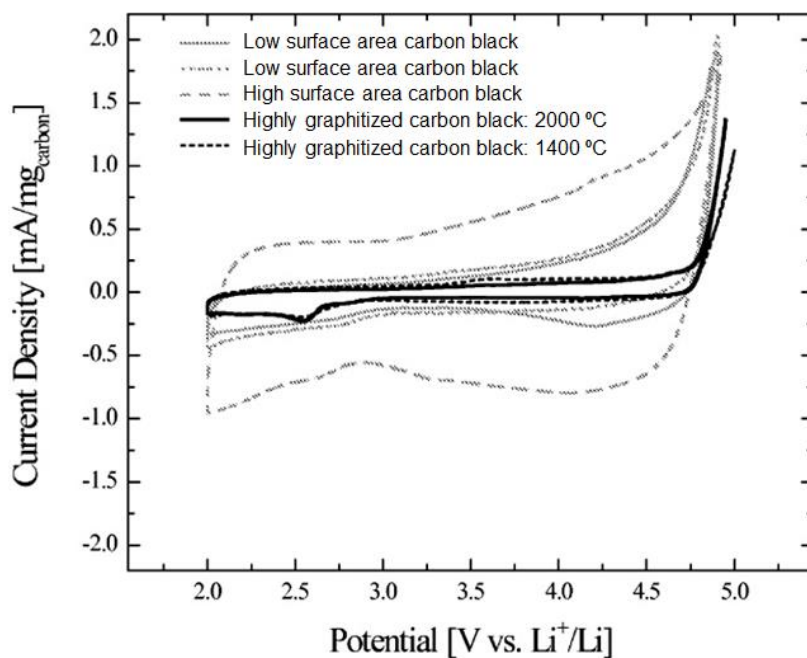


Figure 29 Cyclic voltammograms for carbon blacks with different degrees of graphitization and/or surface areas. With modifications from^[304].

As can be seen, large surface areas and many termination groups on the carbon surface lead to an onset of oxidation current at approx. 3.3 V. Importantly, the highly graphitized carbon materials reveal almost no oxidation currents up to ca. 4.7 V, which is due to electrolyte decomposition.^[304] Therefore, the reactivity of carbon black is believed to be primarily a result of large surface areas and possible functional groups (e.g. hydroxyl, carbonyl, and carboxyl) on the carbon surface.^[1,252,304]

Another important part of the composite cathode, the binder, is also affected by the high voltage within a lithium nickel manganese oxide spinel full cell. Nonetheless, only few researchers investigated this phenomenon.^[1,305,306] Fransson et al. observed large irreversible oxidation reactions involving the binder and the electrolyte salt LiPF₆.^[305] A publication by Yoon and his group reveals that the dominant failure mechanism of the 5 V LiNi_{0.5}Mn_{1.5}O₄ electrode at elevated temperature is the contact loss between the electrode and the current collector, between the LNMO particles, and between the LNMO and carbon particles. Delamination

implies that the binder is working improperly under extreme cycling conditions. As such, it contributes to the poor electrochemical performance of high voltage spinel full cells.^[1,306]

Moreover, the integrity and the anodic stability of the separator is essential and is a prerequisite for a good cyclability as well as a safe operation of lithium ion cells. Irrespective of this fact, only few reports are found regarding the oxidation stability of separators.^[1] Chen et al. investigated the electrochemical stability of five commercially available separators for lithium nickel manganese oxide spinel cathode materials. It was recognized that PE-based separators feature the highest oxidation stability. They suggested that surface reactions occurring among the active material, the separator, and the electrolyte at high voltages may lead to deposits on the surface of the separators. Such undesired accumulations impair the first-cycle efficiency, capacity, rate capability, and long-term cycling stability of high-voltage lithium ion cells.^[300] Moreover, some groups describe that the separators adopt a brown color after cycling at high voltages.^[1,260,300,307] This discoloration is attributed to transesterification in the separator and electrolyte decomposition products that appear on the surface of the separator.^[260,307] In order to achieve a good cycling behavior of high voltage spinel full cells, an oxidatively stable separator is necessary to avoid unfavorable side reactions, which may cause a decline in cyclability.

2.3 Methods of characterization

2.3.1 Cycling method: CC/CV-cycling

Cycling is an electrochemical technique applied to electrochemical cells to examine their long-term stability upon charging/discharging. Basically, a cell can be cycled with a constant current, during which the voltage change is recorded as a function of time (constant current cycling). When either the end-of-charge-voltage or the end-of-discharge-voltage is reached, the voltage might be kept constant until the current has decreased to a fixed target value (constant voltage cycling). Cycling procedures that involve charging/discharging steps at constant current (CC) mode and subsequently at constant voltage (CV) mode are also named CC/CV-cycling or galvanostatic/potentiostatic cycling.^[308]

The electric charge stored in a battery cell, i.e. the capacity, is given by:^[309]

$$Q = \int I(t)dt = I \cdot \Delta t \quad (23)$$

Q = electric charge stored in a battery cell

I = constant current

t = time

Considering battery cells, the capacity is usually expressed in terms of the specific weight or mass of the electroactive component. This specific capacity is typically referred to the CAM, which is the limiting factor for the maximum electric charges stored in a full cell.^[309] Furthermore, the specific discharge capacity is utilized rather than the specific charge capacity, because it represents the real usable energy (efficiency < 100%). Generally, the specific capacity is calculated according to the following equation:^[310,311]

$$C_{\text{specific}} = \frac{x \cdot F}{3600 \cdot M_m} \quad (24)$$

C_{specific} = specific capacity

x = number of electrons transferred per mole

F = Faraday constant (= 96458 Cmol⁻¹)

M_m = molecular mass of the electroactive species

The unities of the specific capacity are given by Ahkg⁻¹ or mAhg⁻¹. The desired velocity of a cycling procedure depends on the applied current. As such, the current needed to fully charge or discharge a battery cell during a given amount of time is called current rate or C-rate. For instance, for a battery cell with a nominal capacity of 1 Ah, a current of 0.1 A is defined as 0.1 C. In other words, the battery cell requires ten hours to be fully charged or discharged. High C-rates are beneficial with regard to high power densities. Concurrently, the specific energy is reduced rapidly owing to smaller capacities.^[311]

The data gained by CC/CV-cycling can also be utilized to calculate the differential capacity dQ/dU . By means of this method, voltage plateaus in the voltage-capacity diagram are typically transformed into peaks in the dQ/dU representation. Consequently, overlapping processes are more easily separated and identified. Nevertheless, the analysis is strongly correlated with the accuracy of the numerical differentiation of the raw data.^[312]

2.3.2 Three-electrode measurement

The insertion of a reference electrode (RE) into a lithium ion full cell consisting of a carbon-based anode and a cathode comprising a lithium intercalation active material (e.g. lithium transition metal oxides, metallophosphates, or spinel oxides) is required to determine the cell balancing. In fact, the balancing of a battery cell means the balancing of the involved electrodes. It is described by the ratio of their capacity densities [mAh/cm^2], which indicates the amount of charge stored per nominal area.^[309,313] Usually, cell balancing is expressed in terms of anode oversizing or undersizing. For instance, if the ratio of the capacity densities of anode vs. cathode equals to $2.2 \text{ mAh}/\text{cm}^2 : 2.0 \text{ mAh}/\text{cm}^2$, the anode oversizing corresponds to 10% at a given C-rate.

Basically, there are three major scenarios regarding cell balancing (Figure 30). Figure 30A depicts the case of anode undersizing. The main drawback of this setup is that the oversized cathode pushes the anode potential below 0 V vs. Li leading to lithium plating on the surface of the negative electrode.^[314–316] In other words, the anode is overintercalated and forced to accept more lithium ions than it may actually accommodate. Such a scenario results in the deposition of metallic lithium on the anode. The process is not completely reversible and, thus, cell capacity is lost.^[317,318,319] Moreover, Li plating is a well-known safety issue, as it might occur in the form of dendrite growth, which can cause an internal short circuit.^[320] Additionally, the cathode is insufficiently deintercalated and the respective active material is not entirely used.^[319] Consequently, specific energy is lost.

By contrast, in the case of extremely high anode oversizing, the cathode is overdeintercalated (Figure 30B). The high delithiation degree of the CAM might lead to a destabilization of its structure. Hence, a diminished cycling stability as well as a reduced safety of the lithium ion cells is likely to evolve.^[316,321] Besides, the higher potential of the positive electrode may provoke electrolyte degradation by oxidation reactions.^[321] Due to the fact that the active anode material is not totally involved in the lithium insertion/desertion processes, the specific energy of lithium ion cells with such an electrode combination is relatively low.^[309] Furthermore, very high anode oversizing should be avoided to keep the costs of LIBs low.

In fact, it is desirable to adjust the balancing of the positive and negative electrodes in such a way that nearly 100% of their active masses is used upon charging/discharging lithium ion cells to realize high specific energies. Simultaneously, cell features like the cycling behavior or the

safety properties should not be affected by incorrect cell balancing (i.e. anode undersizing or extremely high anode oversizing). This means that the anode potential should ideally adopt positive values just above 0 V vs. Li at the highest SOC of a lithium ion cell (Figure 30C).

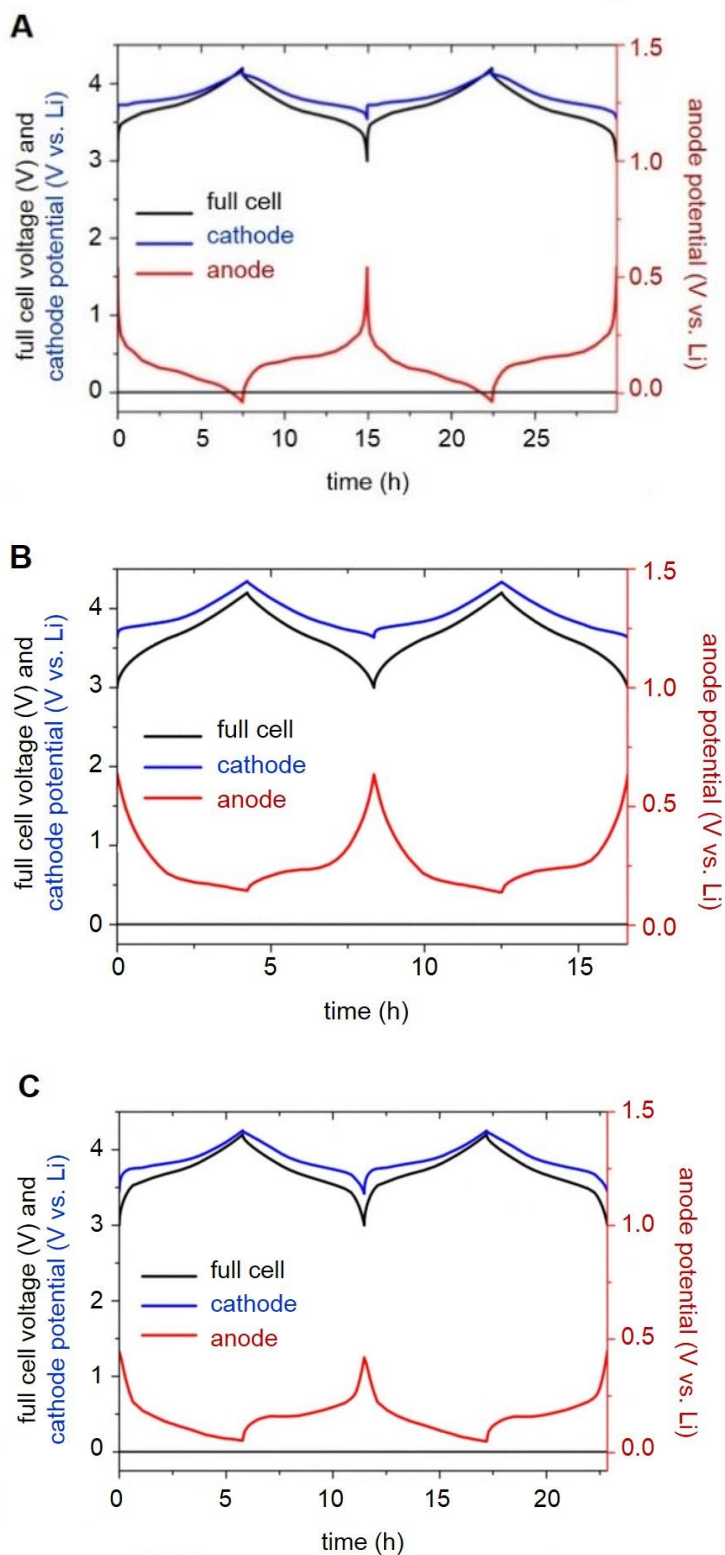


Figure 30 Representation of the three major scenarios regarding cell balancing: **A** anode undersizing, **B** extremely high anode oversizing, and **C** optimal cell balancing. With modifications from^[309].

A possible problem with two-electrode measurements is based on recording only the full cell voltage. It just gives the difference between the potentials of the anode and the cathode rather than absolute values. Therefore, no conclusion of the individual potentials of the single electrodes can be made. However, it is critical to derive the potential at each electrode to check the cell balancing and to dissect which one of the electrodes plays the most important part with respect to deterioration of cell characteristics.^[321,322] Furthermore, it is necessary to identify the changes of the electrode potentials under various cell operation conditions (e.g. long-term cycling, high and low C-rates, different temperatures, etc.) to develop stable and reliable lithium ion cells with high specific energies. Half cell measurements, i.e. the individual characterization of anode and cathode potentials against lithium metal, are inappropriate to estimate cell balancing, since interactions between anode and cathode are not considered.^[322] Only a three-electrode arrangement allows the correct adjustment of the electrodes within a battery cell.

The RE should meet several requirements. The reference potential must be stable over time in the cell environment under a variety of testing conditions.^[321,323–325] Actually, the potential of the RE is recommended to be high enough to avoid surface reactions like electrolyte reduction (≥ 0.8 V vs. Li) and it should be lower than 4.0 V vs. Li to prevent oxidative reactions with the electrolyte.^[321] Essentially, the RE must not participate in cell reactions, but just act as a non-infering spectator electrode.^[326] In addition, non-polarizability, reversibility, and reproducibility of the reference potential are important prerequisites of a RE.^[323–325]

The most common reference material is metallic lithium. Despite the fact that it is not ideal, because the lithium might be affected upon cell ageing (e.g. by the formation of a SEI), it is sufficiently reversible and non-polarizable.^[323,325,327] Moreover, the production of lithium-based REs is relatively simple and if the lithium is properly cleaned prior to the cell assembly, the RE potential is stable for several days.^[323,325,328] Other materials that have been utilized as materials for REs are LTO, LMO, LFP, alloys of lithium with metals such as tin, aluminum, bismuth, and antimony, Li_xRuO_2 , and transition metal polyanion compounds including pure or doped compositions of Li_xMPO_4 , $\text{Li}_x\text{M}_2\text{P}_2\text{O}_7$, $\text{Li}_x\text{MPO}_4\text{F}$, $\text{Li}_x\text{M}_2(\text{SO}_4)_3$, and $\text{Li}_x\text{M}_2(\text{PO}_4)_3$ ($\text{M} = \text{Ti}, \text{V}, \text{Cr}, \text{Fe}, \text{Mn}, \text{Ni}, \text{or Co}$).^[321,324] Among those materials LTO and LFP are the most prominent. Both undergo a two-phase reaction upon lithium insertion and provide a constant potential at 1.56 and 3.43 V vs. Li, respectively.^[321,323] Figure 31 shows a comparison of the current-potential curves of Li, Ag, and LTO reference electrodes. The non-polarizability of reference materials would be given by a vertical line in a current-potential diagram. As noted, silver metal is not a suitable choice for a RE because its equilibrium potential is not well defined. While not presented here, copper features the same problem as silver. As opposed to this, the observed potentials for Li and LTO are quite stable, which underlines their qualification as RE materials.^[329]

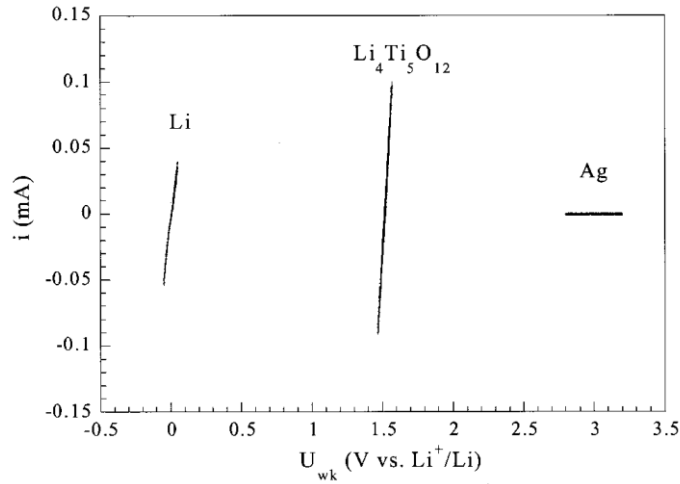


Figure 31 Current-potential curves at $v = 0.2 \text{ mVs}^{-1}$ for three different reference electrode materials: Li, LTO, and Ag.^[329]

Regarding the position and the design of a RE, the following aspects should be taken into account. The active material of a RE can be directly deposited or coated onto a metal current collector. Possible metal current collectors are copper, nickel, stainless steel, titanium, or any other material, which neither alloys nor corrodes under the operating potential window of the RE in the cell environment.^[321] To determine cell balancing, the RE is recommended to be placed adjacent to the negative electrode without contacting it. Indeed, the RE material should contact the separator positioned between the anode and the cathode.^[321] The inactive part of the RE may be wrapped or laminated in a porous, electronically insulating material (e.g. polyethylene or a ceramic paste), which is electrochemically inert to inhibit ionic conduct with the electrolyte. The tip of the RE, where the active material is placed, might be encapsulated by a porous polyolefin separator acting as an ionic bridge.^[321]

Although the utilization of a RE seems to be quite simple, several challenges should be considered. The introduction of a third electrode into a battery cell enhances the complexity of the cell design. Reengineering of the cell architecture is often necessary because an additional port in the cell housing is required. The extra feedthrough not only complicates the cell design, but also provides an additional safety risk due to an additional possible rupture and leakage site, which could cause the entire battery cell to fail.^[321] Furthermore, three-electrode cells containing a lithium RE have to be assembled in a glove box, making reproducibility and precise control of the alignment of the electrodes rather difficult.^[330]

In this thesis, a three-electrode cell is designed to monitor the individual potentials of a $\text{LiNi}_{0.4}\text{Mn}_{1.6}\text{O}_4$ cathode and a graphite anode upon CC/CV-cycling of the corresponding full cell. In this manner, it is possible to check if the cell balancing is correct or if an adjustment of the capacity densities is needed.

2.3.3 X-ray diffraction

The German physicist Wilhelm Conrad Röntgen discovered X-rays on 8 November 1895.^[331] X-rays are electromagnetic waves with wavelengths ranging from 10^{-12} to 10^{-8} m, which is on the same order of magnitude as atomic distances in condensed matter.^[332] Thus, nondestructive X-ray scattering techniques are especially qualified to investigate crystalline samples. In general, X-ray diffraction is applied for the identification of minerals, compounds and materials, the quantification of minerals, and the determination of crystal structures (unit-cell dimensions, symmetry, atom positions, energy densities, and grain sizes).^[333] Typically, X-radiation is produced in a vacuum-sealed tube containing two electrodes as shown in Figure 32.

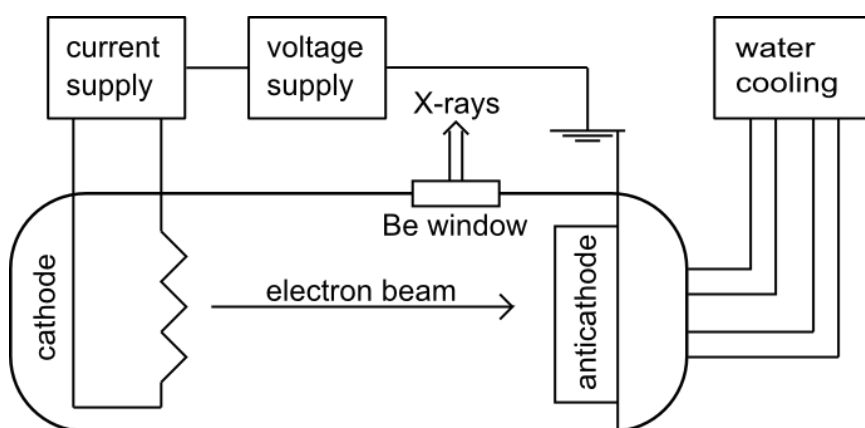


Figure 32 A schematic of the major components in a laboratory X-ray tube. Adapted from^[334].

The tungsten filament cathode is heated by a power supply and electrons are emitted from the metal. The released electrons are accelerated towards the water-cooled anticathode due to an electric field between the two electrodes established by a voltage source.^[334] More precisely, the acceleration voltage of the electron beam is in the range of 10 to 100 kV.^[335] High-speed electrons hit the metallic anticathode and collide with the atoms in the metal. Standard target materials are Cu, Mo, Co, W, Cr, Ni, and Fe. During the impact of the electrons with the anticathode, the kinetic energy of the electrons is mainly transformed into heat and less than 1% is converted into X-rays.^[336] Nonetheless, two types of X-rays are generated.

The continuous radiation or bremsstrahlung is a result of the deceleration of the high-velocity electrons in the electric field of the atomic nuclei. Since each electron loses its kinetic energy in a different way, the emitted highly energetic electromagnetic waves are a combination of X-rays with various wavelengths and continuous distribution. Therefore, this kind of X-radiation is also called white radiation and is characterized by a broad spectrum (Figure 33).

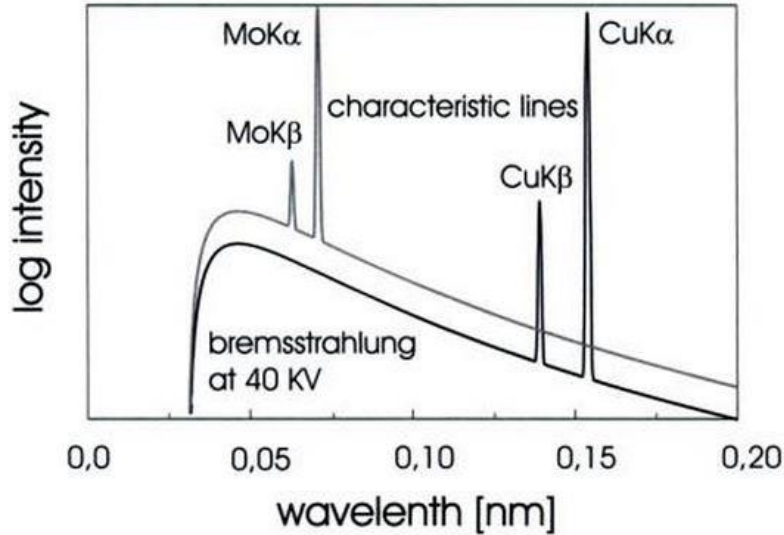


Figure 33 Schematic X-ray emission spectra of a copper and a molybdenum anticathode at 40 kV. Sharp characteristic lines on top of the smooth continuous bremsstrahlung spectrum represent the radiations. The K_{α} doublets (not resolved here) for Cu and Mo are shown at $\lambda_{\alpha_1} = 0.154056$ and $\lambda_{\alpha_2} = 0.154439$, and $\lambda_{\alpha_1} = 0.07093$ and $\lambda_{\alpha_2} = 0.071359$, respectively. Additionally, the K_{β} line for both targets, which is composed of several sublines, is illustrated with the center wavelength at $\lambda_{\beta} = 0.1396$ and 0.06323 , respectively.^[338]

The maximum energy or the shortest wavelength (threshold wavelength) of the bremsstrahlung is given by the entire loss of the kinetic energy of an accelerated electron during the slowing-down process.^[335] Duane and Hunt described this inverse photoelectric effect in 1915.^[334]

$$E_{el} = U_a \cdot e = E_{kin} = \frac{1}{2} \cdot m_e \cdot v_e^2 = E_r = h_P \cdot f_{max} = h_P \cdot \frac{c}{\lambda_{min}} \quad (25)$$

$$\lambda_{min} = \frac{h_P \cdot c}{U_a \cdot e} = \frac{1,2398}{U_a [kV]} [nm] \quad (26)$$

E_{el} = electric energy

U_a = acceleration voltage

e = electron charge ($= 1.60210 \cdot 10^{-19} C_L$)

E_{kin} = kinetic energy

m_e = electron mass ($= 9.1091 \cdot 10^{-31} kg$)

v_e = electron velocity

E_r = radiation energy

h_P = Planck constant ($= 6.6256 \cdot 10^{-34} Js$)

f_{max} = maximum frequency

c = speed of light ($= 299,792,458 \frac{m}{s}$)

λ_{min} = minimum wavelength

The shorter the wavelength, the higher is the penetrating power of the white radiation. According to the Duane-Hunt formula mentioned above, this threshold wavelength is strongly

linked to the acceleration voltage. An integration over the whole continuous spectrum proves the quadratic dependence of the total X-ray intensity on the acceleration voltage. This is in agreement with the fact, that a doubling of the voltage causes a doubling of the maximum kinetic energy of the electron beam and a doubling of the produced, accelerated, and slowed down electrons. Consequently, the area under the curve of the X-ray quanta is quadrupled. In case of doubling the current supply, only the amount of electrons is doubled and the maximum kinetic energy remains constant. In addition, the intensity of the bremspectrum strongly relates to the atomic number of the metallic target Z_a and can be estimated by equation 27.^[337]

$$I_B = A \cdot I \cdot U_a^2 \cdot Z_a \quad (27)$$

I_B = integrated intensity of the bremspectrum

A_{ex} = experimentally determined constant ($= 1.1 \cdot 10^{-9} \text{ V}^{-1}$)

I = current

U_a = acceleration voltage

Z_a = atomic number of the anticathode material

Another possibility of the high-speed electrons to interact with atoms in the anticathode is as follows. If the incoming electron has sufficient energy to eject an inner shell electron out of its place, ionization occurs and the atom is left in an excited state. This scenario is a discontinuous process and correlates with the atomic shell model. The kind of energy is denoted as an absorption edge. An electron from a higher shell fills the empty site of the inner shell and the atom regains its stable state. The whole process takes approx. 10 ns. The difference in binding energy between the involved electron energy levels is released as an X-ray photon of quantized wavelength.

$$\lambda = \frac{h_P \cdot c}{\Delta E} \quad (28)$$

λ = wavelength

h_P = Planck constant ($= 6.6256 \cdot 10^{-34} \text{ Js}$)

ΔE = energy difference between inner and outer shell electrons

c = speed of light ($= 299,792,458 \frac{\text{m}}{\text{s}}$)

This wavelength or frequency of the X-ray quantum only depends on the metallic target material and the corresponding atomic shells.^[337]

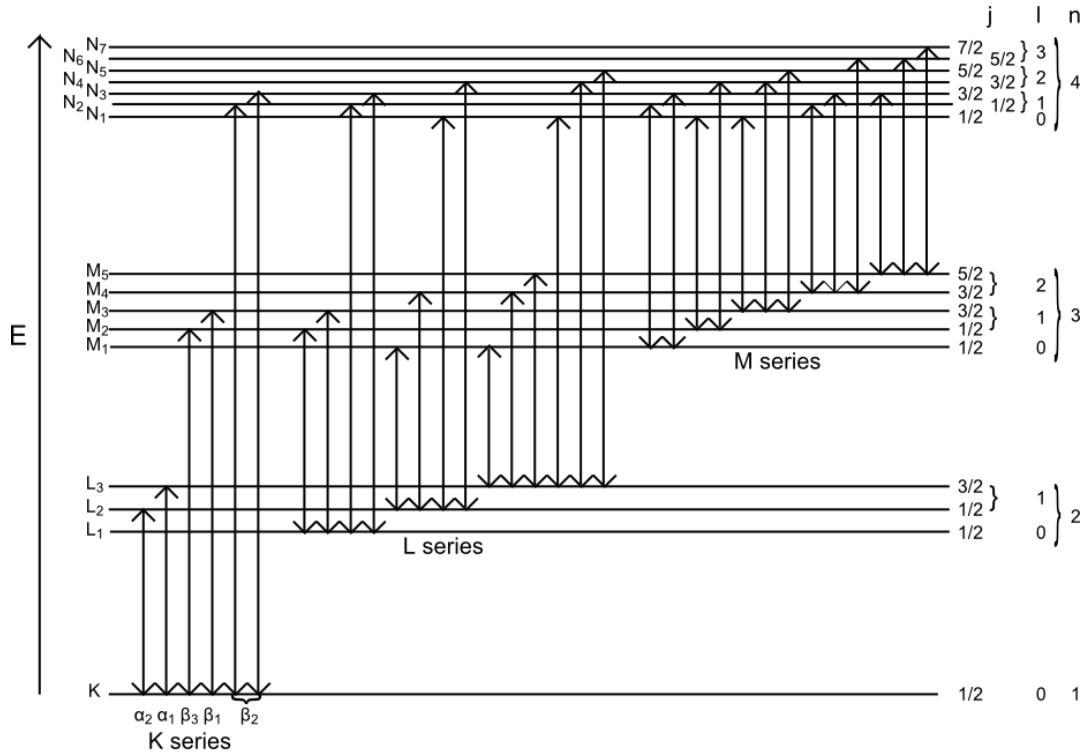


Figure 34 A section of an energy level diagram showing the allowed electron transitions of an atom involved in excitation and generation of X-rays. With modifications from^[335].

Analysis of the emitted radiation shows that the characteristic lines are assignable to given series with distinct fine structure. Figure 34 displays a section of the energy level diagram of an atom involved in the excitation and the generation of X-rays. The depicted scale, however, does not correspond to the actual energy differences between the electron shells. In fact, the energy difference between the K and L levels is ca. eight times larger as that between the L and M shells and about 40 times the size as that between the M and N levels.^[335] The presented electron transitions can be explained by specific selection rules. In general, the electron shells are named by the principal quantum number ($n = 1, 2, 3, 4, \dots, \infty$) or by a letter of the alphabet (K-, L-, M-, N-shell, etc.). In compliance with the Pauli Exclusion Principle, each shell can hold $2n^2$ electrons. Furthermore, each shell is comprised of one or more subshells (s, p, d, and f) that are determined by the azimuthal quantum number ($l = 0, 1, 2, 3, \dots, n-1$). This quantum number describes the form of the atomic orbitals. The spatial orientation of the atomic orbitals is given by the magnetic quantum number ($m_l = +l, \dots, +1, 0, -1, \dots, -l$). Additionally, electrons possess an intrinsic angular momentum or electron spin, which is defined as the spin quantum number ($s = \pm \frac{1}{2}$). The total angular momentum quantum number j is a combination of the azimuthal quantum number l and the spin quantum number s ($j = |l \pm s|$).^[172] Regarding electron transitions, the following selection rules are valid:^[335]

$$\begin{aligned}\Delta n &= \text{arbitrary} \\ \Delta l &= \pm 1 \\ \Delta j &= 0, \pm 1\end{aligned}\tag{29}$$

For X-ray diffraction analysis, the most significant radiations are those of the K series. The most intense characteristic line is the K_α doublet. Thereby, the electron transitions from L_3 ($2p_{3/2}$) to $K(1s)$ and from L_2 ($2p_{1/2}$) to $K(1s)$ correlate with the $K_{\alpha 1}$ and the $K_{\alpha 2}$ lines, respectively. The intensity ratio of the doublet is 2:1. The $K_{\beta 3,1}$ line has a much lower intensity and is a result of the electron transition from $M_{2,3}$ ($2p_{1/2, 3/2}$) to $K(1s)$.

In 1913, Moseley discovered the correlation between the frequency or energy of the characteristic radiation and the atomic number.

$$\frac{1}{\lambda} = \frac{f}{c} = R_y \cdot (Z_a - S_c)^2 \cdot \left(\frac{1}{n_1^2} - \frac{1}{n_2^2} \right)\tag{30}$$

$$E = h_P \cdot \frac{c}{\lambda} = h_P \cdot c \cdot R_y \cdot (Z_a - S_c)^2 \cdot \left(\frac{1}{n_1^2} - \frac{1}{n_2^2} \right)\tag{31}$$

λ = wavelength

f = frequency

c = speed of light ($= 299,792,458 \frac{m}{s}$)

R_y = Rydberg constant ($= 1.097 \cdot 10^7 m^{-1}$)

Z_a = atomic number

S_c = screening constant

n = principal quantum number

E = energy

h_P = Planck constant ($= 6.6256 \cdot 10^{-34} Js$)

The screening constant S_c accounts for the shielding of the nuclear charge by the inner electron shells. In case of the K_α line, S_c equals one and equation 30 turns into the following expression:^[335,339]

$$\frac{1}{\lambda} = \frac{f}{c} = \frac{3}{4} \cdot R_y \cdot (Z_a - 1)^2\tag{32}$$

Both types of the produced X-rays (continuous and characteristic radiation) leave the vacuum tube through a beryllium window and hit the sample. A goniometer allows sample rotation and tilt to select particular diffraction angles.^[340] By means of $(Z_a - 1)$ monochromatic filters such as Cu, Mo, Co, Fe, Cr, and Ag, the bremsstrahlung and the K_β radiation can be attenuated and the K_α lines are mostly diffracted from the set of atomic planes.^[334]

Bragg and Lawrence provided a geometric interpretation of the X-ray diffraction pattern. They regarded a crystal lattice as composed of sets of atomic planes, whereby all planes are assumed to be identical, parallel to each other, and equidistant from one another. When a

crystal is irradiated with monochromatic X-rays, a part of the beam is diffracted at the first plane, another part at the second plane and so on and on. Figure 35 demonstrates the diffraction of two X-rays at adjacent crystal planes.

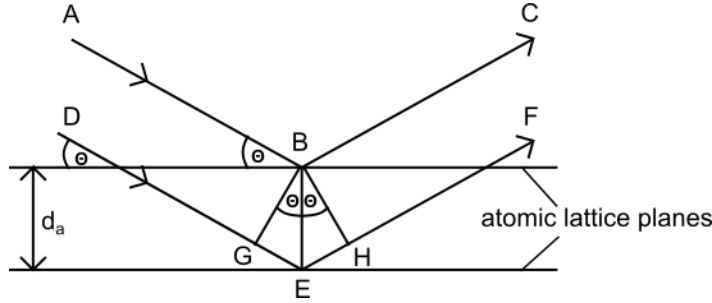


Figure 35 Derivation of Bragg's law for X-ray diffraction. With modifications from^[332].

The second beam DEF has to travel the additional distance $GE + EH$ as compared to the first beam ABC. Both beams are phase-shifted due to the difference in the path length. If the extra distance $GE + EH$ doesn't comply with a whole number n_λ of wavelengths λ , the diffracted waves are only weakly amplified (destructive interference). Conversely, if the difference in the path length equals an integral number n_λ of wavelengths λ , both beams interfere constructively.

$$GE + EH = n_\lambda \cdot \lambda \quad n_\lambda = 1, 2, 3 \dots \quad (33)$$

As can be seen from the geometric construction, the angles GBE and EBH are identical. They are denoted as glancing angle Θ . The length BE corresponds to the spacing d_a , which separates the two lattice planes. Consequently, the distances GE and EH can be calculated:

$$GE = EH = d_a \cdot \sin\Theta \quad \text{or} \quad GE + EH = 2 \cdot d_a \cdot \sin\Theta \quad (34)$$

By combining equations, 33 and 34 Bragg's law can be derived:

$$n_\lambda \cdot \lambda = 2 \cdot d_a \cdot \sin\Theta \quad n_\lambda = 1, 2, 3 \dots \quad (35)$$

The integer n_λ is known as the order of reflection. In summary, Bragg's law proves that constructive interference only occurs at very specific glancing angles Θ , which depend on the spacing d_a of the crystal and on the wavelength λ of the X-rays. The use of visible light is not possible, because the incident radiation has to adopt the wavelengths $n_\lambda \cdot \lambda \leq 2 \cdot d_a$. The Miller indices (hkl) designate the orientation of a plane or a set of planes parallel to one another with respect to the crystallographic system of coordinates in the reciprocal lattice.

Bragg's law is the fundamental equation in X-ray diffraction. A detailed analysis of all variables enables the interpretation of the different diffraction patterns.^[332] In this thesis, X-ray diffraction is used to reveal structural changes and phase transitions of the CAM high voltage spinel upon electrochemical cycling.

2.3.4 Raman spectroscopy

Raman scattering is a nondestructive vibrational technique, which provides structural information at the atomic scale on inorganic and organic compounds.^[341] It is based on the so-called Raman effect that was already predicted by A. Smekal in 1923, and in 1928 the scientist Sir C. V. Raman observed this phenomenon by means of filtered and focused sunlight.^[335] It relies on the interaction of light with matter (i.e. gas, solid, and liquid). Generally, a photon can be absorbed or scattered by a molecule. An absorption process requires that the energy of the incident photon is equal to the energy difference between two real electronic states and that the dipole moment of the molecule changes upon the transition (infrared absorption conditions).^[341] In contrast, photons, which are not absorbed will be elastically or inelastically scattered in all directions. This scattered light can be spectroscopically detected.^[341,342]

In case of elastic scattering, the energy of the incident photon corresponds to the one of the scattered photon. Thereby, the involved molecule is intermediately excited into a virtual state before relaxing into the final state, which is equivalent with the initial state. This process is commonly named Rayleigh scattering (Figure 36).^[341] The virtual state is not necessarily a true quantum state. Instead, the interaction between the oscillating electric field of the incident light and the molecule causes a very short-lived distortion of the electron cloud.^[342]

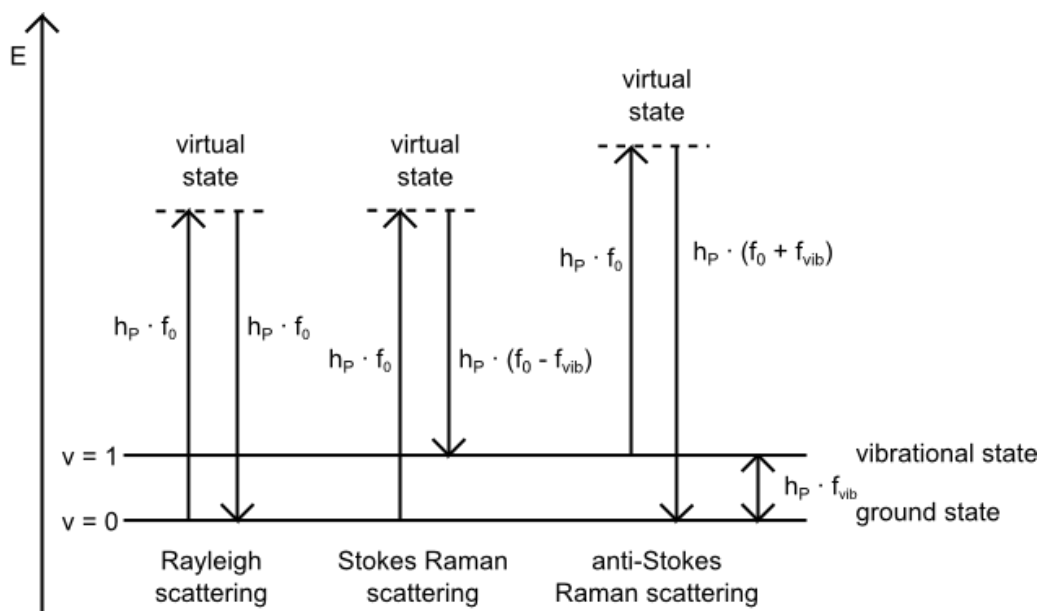


Figure 36 Energy level diagram for different Raman processes.

Besides, the electron cloud of the molecule can be perturbed by molecular vibrations and for a very small fraction of light (approx. 1 in 10^7 photons) a vibrational motion occurs.^[341,342] The interaction of optical and molecular oscillations leads to the transfer of a quantum of vibrational energy between the incident photon and the molecule. The remaining energy is scattered

inelastically. Therefore, the energies of the incident and scattered photons are no longer equal.^[341] Considering inelastic scattering, two different possibilities are distinguished:

- **Stokes Raman scattering:** A part of the energy of the incoming photon is transferred to the molecule, which relaxes into an energetically excited vibrational state. Consequently, the scattered photon is lower in energy than the incident photon by an amount equal to the vibrational energy $h_P \cdot f_{\text{vib}}$.^[341,342]
- **anti-Stokes Raman scattering:** When the incident photon interacts with a molecule which is already in a vibrationally excited state, the photon may gain energy from the molecule. Hence, the scattered photon has a higher frequency ($f_0 + f_{\text{vib}}$) after the relaxation of the molecule into the ground state.^[341,342]

In another scenario, known as resonance Raman spectroscopy, the energy of the incident photon equals the energy of an electronic transition. In this case, the molecule is not excited into a virtual state, but a real molecular state. Thus, the respective Raman bands are much more intense than those described before (by as much as a factor of 10^6).^[341] Nevertheless, the main disadvantage of resonance Raman spectroscopy is enhanced fluorescence and degradation of the sample due to the high energy of the incoming laser light.^[341]

For the classical interpretation of the Raman effect the wave theory of light is used. The incident optical electromagnetic field A_E is calculated by equation 36:^[342]

$$A_E = A_0 \cdot \cos(2 \cdot \pi \cdot f_0 \cdot t) \quad (36)$$

A_E = electromagnetic field

A_0 = amplitude

f_0 = frequency of the laser

t = time

Vibrational Raman scattering is based on the fact that the oscillating electric field of the incoming light induces a change in the polarizability α of the molecule. The polarizability is a measure for its ease to distort the electron cloud around a molecule.^[341] The induced electrical dipole μ_{ind} is given by equation 37:^[335]

$$\mu_{\text{ind}} = \alpha \cdot A_E \quad (37)$$

μ_{ind} = induced electrical dipole

α = polarizability

A_E = electromagnetic field

When equations 36 and 37 are combined, the electrical dipole is expressed as:

$$\mu_{\text{ind}} = \alpha \cdot A_0 \cdot \cos(2 \cdot \pi \cdot f_0 \cdot t) \quad (38)$$

If the irradiated molecule is vibrating with a frequency f_{vib} the normal mode q is reformulated as:^[343]

$$q = q_0 \cdot \cos(2 \cdot \pi \cdot f_{\text{vib}} \cdot t) \quad (39)$$

q = normal mode of the oscillating system

q_0 = vibrational amplitude

f_{vib} = resonance frequency of a vibrating molecule

t = time

For small vibrational amplitudes, the polarizability α is a linear function of q .^[343]

$$\alpha = \alpha_0 + \left(\frac{\delta\alpha}{\delta q}\right)_0 \cdot q + \dots \quad (40)$$

α = polarizability

α_0 = polarizability at the equilibrium position

$\left(\frac{\delta\alpha}{\delta q}\right)_0$ = rate of change of α with respect to the change in q
evaluated at the equilibrium position

Combining equations 38, 39, and 40, we obtain:

$$\begin{aligned} \mu_{\text{ind}} &= \alpha \cdot A_0 \cdot \cos(2 \cdot \pi \cdot f_0 \cdot t) \\ &= \alpha_0 \cdot A_0 \cdot \cos(2 \cdot \pi \cdot f_0 \cdot t) + \left(\frac{\delta\alpha}{\delta q}\right)_0 \cdot q \cdot A_0 \cdot \cos(2 \cdot \pi \cdot f_0 \cdot t) \\ &= \alpha_0 \cdot A_0 \cdot \cos(2 \cdot \pi \cdot f_0 \cdot t) + \left(\frac{\delta\alpha}{\delta q}\right)_0 \cdot q_0 \cdot A_0 \cdot \cos(2 \cdot \pi \cdot f_0 \cdot t) \cdot \cos(2 \cdot \pi \cdot f_{\text{vib}} \cdot t) \end{aligned} \quad (41)$$

Then, using the trigonometric formula for the product of two cosine functions, the induced electrical dipole is equivalent to:

$$\begin{aligned} \mu_{\text{ind}} &= \alpha_0 \cdot A_0 \cdot \cos(2 \cdot \pi \cdot f_0 \cdot t) && \text{(Rayleigh)} \\ &+ \frac{1}{2} \cdot \left(\frac{\delta\alpha}{\delta q}\right)_0 \cdot q_0 \cdot A_0 \cdot \cos[2 \cdot \pi \cdot (f_0 - f_{\text{vib}}) \cdot t] && \text{(Stokes Raman scattering)} \\ &+ \frac{1}{2} \cdot \left(\frac{\delta\alpha}{\delta q}\right)_0 \cdot q_0 \cdot A_0 \cdot \cos[2 \cdot \pi \cdot (f_0 + f_{\text{vib}}) \cdot t] && \text{(anti-Stokes Raman scattering)} \end{aligned} \quad (42)$$

The first term of equation 42 corresponds to the Rayleigh scattering as it is not affected by molecular vibrations. The second and the third terms refer to inelastic scattering. More precisely, the second term relates to the red-shifted Stokes Raman scattering, while the third term denotes the blue-shifted anti-Stokes Raman scattering. If $\left(\frac{\delta\alpha}{\delta q}\right)_0$ is zero, the vibration is

not Raman-active. In other words, to be Raman-active, the rate of change of polarizability with the vibration must not be zero.^[343]

Although the anti-Stokes and Stokes Raman lines are symmetrically positioned relative to the Rayleigh line, the former ones are usually much weaker than the latter ones. The physical reason for the difference in intensity between Stokes and anti-Stokes bands is linked to the electron population of the respective initial states. At room temperature, the occupation of the vibrationally excited states of a molecule is significantly more improbable than the occupation of the ground state. Actually, if the system is at thermal equilibrium, the ratio of the Stokes and anti-Stokes intensity is governed by the sample temperature in accordance with the Boltzmann distribution:^[344]

$$\frac{I_S}{I_{aS}} = \frac{(f_0 - f_{vib})^4}{(f_0 + f_{vib})^4} \cdot e^{\frac{h_P \cdot f_{vib}}{k_B \cdot T_s}} \quad (43)$$

I_S = intensity of the Stokes lines

I_{aS} = intensity of the anti-Stokes lines

f_0 = frequency of the laser

f_{vib} = resonance frequency of a vibrating molecule

h_P = Planck constant (= $6.6256 \cdot 10^{-34}$ Js)

k_B = Boltzmann constant (= $1.3806 \cdot 10^{-23}$ JK⁻¹)

T_s = sample temperature

Quantum mechanical considerations only allow discrete atomic displacements for a given molecule. These normal modes refer to molecular vibrations, where each atom of a molecule moves with the same frequency.^[341] A molecule with N atoms possesses 3N degrees of freedom representing its translational, rotational, and vibrational motions. While a linear molecule with N atoms has 3N - 5 normal modes of vibration, a nonlinear molecule has 3N - 6 normal modes of vibration.^[335] There are several types of motion, which contribute to the vibrational modes and can lead to a rather complex vibrational behavior. In the following, some examples of molecular vibrations are illustrated.

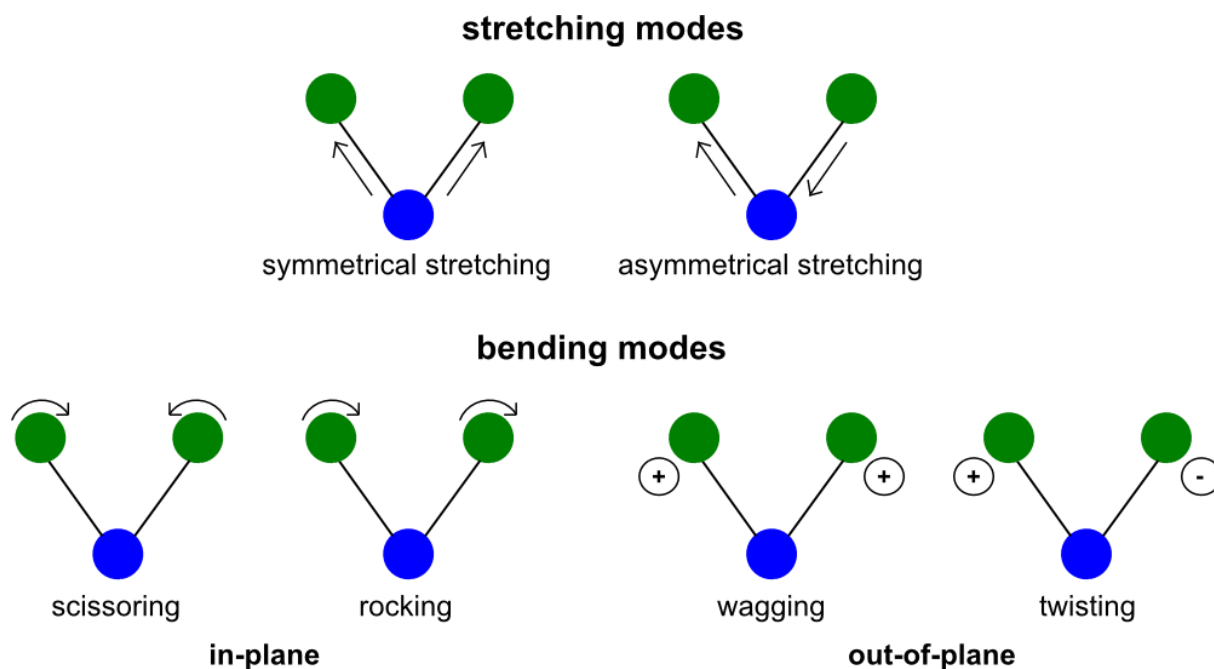


Figure 37 Examples of molecular vibrations.

The two stretching modes, namely symmetrical stretching and asymmetrical stretching, describe changes of bonds in the same or in opposite directions, respectively. The other vibrational motions belong to the group of bending modes involving changes of bond angles. They are also named deformation modes. Bending vibrations require lower energies and appear at lower frequencies than stretching modes. There are two types: in-plane and out-of-plane bending. Regarding the former the atoms remain in the same plane as the nodal plane of the system as in the case of scissoring or rocking vibrations. In the scissoring deformation mode two atoms swing in concert towards opposite directions and in the rocking deformation mode two atoms move simultaneously to the same side and then to the other side. Concerning out-of-plane bending modes, the atoms move in and out of the nodal plane (e.g. wagging and twisting deformation). While in the wagging mode two atoms swing up and down out of the nodal plane in unison, in the twisting mode one atom moves up and the other moves down relative to the nodal plane.^[345]

In general, molecules or crystals can be classified according to symmetry elements or operations that leave at least one common point unchanged. In group theory, the point group representation uniquely defines a molecule by a set of symmetry operations, such as rotations (C_n), reflections (σ_h , σ_v , and σ_d), inversion (i), and improper rotations ($S_n = C_n\sigma_h$). The complete information of all symmetry transformations in a point group is provided by character tables. They include the number and degeneracy of normal modes and enable to determine whether a vibrational motion is IR-active, Raman-active or both.^[341,346]

Actually, Raman spectroscopy is known as the method of choice for the characterization of various carbons from three to zero dimensions such as 3D graphite, 2D graphene, 1D carbon

nanotubes, and 0D fullerenes.^[347] It offers vibrational and crystallographic information, as well as knowledge about physical properties related to electron and phonon interactions.^[347] Consequently, Raman spectroscopy is also a prominent technique for investigating carbon-based anode materials used in LIBs. By means of the resonance Raman effect, involving optically allowed electronic transitions (optical absorption or emission), very intense Raman signals can be observed providing precise structural information.^[341,347] The axial resolution of opaque materials depends on the optical skin depth δ of the laser beam, which is given by equation 44:^[341]

$$\delta = \left(\frac{2 \cdot \lambda}{\mu \cdot \sigma} \right)^{\frac{1}{2}} \quad (44)$$

δ = optical skin depth
 λ = laser wavelength
 μ = magnetic permeability
 σ = electronic conductivity

Therefore, a high electronic conductivity of the examined sample leads to a low optical skin depth.

Moreover, Raman spectroscopy is well suited for the analysis and characterization of the local structure of CAMs like transition metal oxides utilized in LIBs. For instance, with this vibrational technique structural phases can be identified, although several environments are present as in case of composite electrodes. Besides, the wavenumbers and relative intensities of the Raman bands give information about the crystal symmetry, coordination geometry, and metal oxidation states.^[341] Thus, it is possible to differentiate various kinds of metal oxides, whose atomic arrangements are close to one another, to distinguish between different metal oxides having the same elementary analysis (e.g. MnO_2 , Mn_3O_4 , Mn_2O_3 , etc.), or to recognize compounds with the same stoichiometry but different crystalline structures (e.g. cubic or hexagonal LiCoO_2).^[341]

When a conventional Raman spectrometer is coupled to an optical microscope, the technique is called Raman microscopy. This nondestructive analysis has usually a spatial resolution of less than 1 μm . The latter is determined by the selected laser wavelength and the numerical aperture of the microscope objective.^[341] Raman microscopy allows the investigation of heterogeneous mixtures such as LIB electrodes, which are composed of one or two active materials, a binder, and conductive additives because the lateral resolution at the electrode surface corresponds to a typical particle size of a few micrometers.^[341] Local structural information and the chemical composition of each component can therefore be provided individually.

In this thesis, Raman spectroscopy is applied to reveal the phase compositions of the differently treated $\text{LiNi}_{0.4}\text{Mn}_{1.6}\text{O}_4$ electrodes and to determine the oxidation states of the nickel and manganese ions. The fundamentals for these examinations are given by the interpretation of the vibrational motions of LMO. White et al. conducted a complete factor group analysis of the vibrational spectrum of an ideal spinel structure of the general formula AB_2O_4 .^[348] Since the spinel structure belongs to space group $\text{Fd}3\text{m}$ or factor group O_h^7 , its normal modes of vibration are classified according to the irreducible representations of O_h^7 point group. In Table 3, the normal modes of the spinel structure are categorized.

Symmetry species	Total modes	Acoustic modes	Translatory modes	Rotary modes	Internal modes	Selection rules
A_{1g}	1	0	0	0	1 (A_1)	Raman-active
A_{2g}	0	0	0	0	0	-
E_g	1	0	0	0	1 (E)	Raman-active
T_{1g}	1	0	0	1	0	Inactive
T_{2g}	3	0	1	0	2 (T_2)	Raman-active
A_{1u}	0	0	0	0	0	-
A_{2u}	2	0	1	0	1 (A_1)	Inactive
E_u	2	0	1	0	1 (E)	Inactive
T_{1u}	5	1	2	0	2 (T_2)	IR-active, not Raman-active
T_{2u}	2	0	1	1	0	Inactive

Table 3 Classification of the normal modes of the spinel structure with the general formula AB_2O_4 .^[348]

The vibrational modes of a crystal are determinable analogous to those in a free molecule. Thereby, N is the number of atoms in a unit cell, which has $3N$ degrees of freedom. Three of them represent pure translations and appear as the acoustic modes involved in the propagation of sound waves through the crystal.^[348] However, free rotational movements do not occur in a crystal as the unit cell has a fixed orientation within the crystal. The remaining $3N - 3$ normal modes of vibration are distributed between internal (intramolecular) modes, translatory modes (lattice vibrations of the molecule), and rotary modes. The latter describe rotations of the molecule within the crystal that would become free rotations in the limit of zero

interaction of groups within the structure.^[348] Thus, the number of total modes of the various symmetry species in a crystal are expressed as:^[349]

$$\begin{aligned}\Gamma_{\text{total}} &= \Gamma_{\text{acoustic}} + \Gamma_{\text{vibrational}} \\ &= \Gamma_{\text{acoustic}} + \Gamma_{\text{translatory}} + \Gamma_{\text{rotary}} + \Gamma_{\text{internal}} \\ &= A_{1g} + E_g + T_{1g} + 3T_{2g} + 2A_{2u} + 2E_u + 5T_{1u} + 2T_{2u}\end{aligned}\quad (45)$$

Consequently, the irreducible representation for the vibrational modes of a perfect spinel structure is equivalent to:^[349,350]

$$\Gamma_{\text{vibrational}} = \Gamma_{\text{total}} - \Gamma_{\text{acoustic}} = A_{1g} + E_g + T_{1g} + 3T_{2g} + 2A_{2u} + 2E_u + 4T_{1u} + 2T_{2u} \quad (46)$$

The symmetrical stretching mode A_{1g} (ν_s), the symmetrical deformation mode E_g (δ_s), and the three symmetrical bending modes T_{2g} (δ_s) are Raman-active, whereas the remaining four asymmetrical bending or stretching modes T_{1u} are IR-active:^[349,350]

$$\Gamma_{\text{Raman}} = A_{1g} + E_g + 3T_{2g} \quad (47)$$

$$\Gamma_{\text{IR}} = 4T_{1u} \quad (48)$$

The other modes are inactive. It has to be noted that this analysis is only valid for an ideal spinel structure lacking defects or dopants. Figure 38 depicts the Raman-active vibrational modes of the spinel structure LiMn_2O_4 .

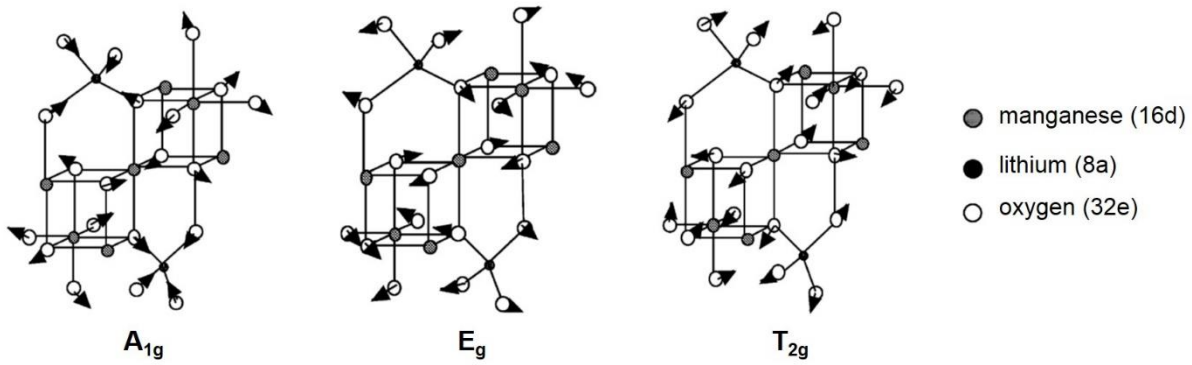


Figure 38 Raman-active vibrational modes of the spinel structure LiMn_2O_4 . With modifications from^[350].

2.3.5 Inductively coupled plasma-optical emission spectroscopy

Inductively coupled plasma-optical emission spectroscopy (ICP-OES) is one of the most effective methods for qualitative and quantitative multi-element analysis via optical spectroscopy. Modern instruments are capable of determining approx. 70 different elements. The detection limit is typically in the $\mu\text{g/L}$ range (ppb) allowing the detection of trace elements.^[351,352] Commonly, ICP-OES is used for bulk analysis of liquid samples or solids dissolved in liquids to identify elements and quantify their concentrations. The main advantages of this technique are its speed, wide linear dynamic range, low detection limits, and relatively small interference effects.^[352,353] The key component of an ICP-OES instrument is the ICP torch (Figure 39).

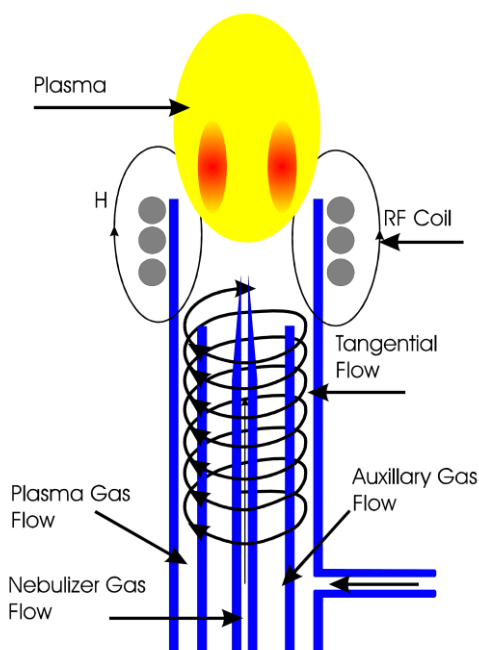


Figure 39 Schematic illustration of an ICP torch.^[353]

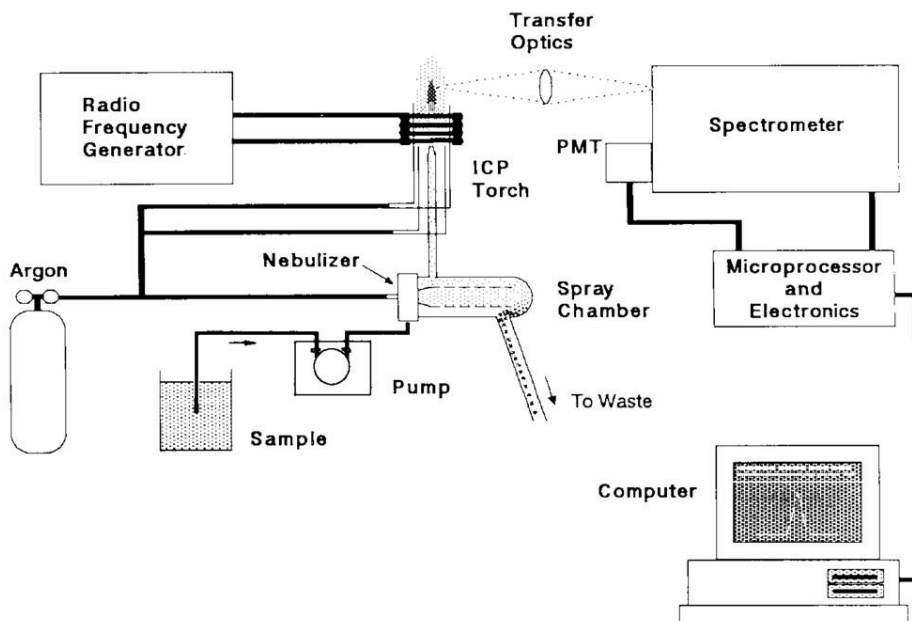
Usually, the torch consists of three concentric quartz tubes and the top end of the torch is surrounded by a water-cooled copper coil, called load coil, which is connected to a radio frequency (RF) generator. Application of RF power (ca. 700 - 1500 W) to the load coil results in an alternating current that oscillates inside the coil at a rate corresponding to the frequency of the generator (27 or 40 MHz).^[351] As a consequence, RF electric and magnetic fields are established in the area around the top of the torch. Routinely, argon gas is directed through the torch and is ignited by a tesla coil to cause electrons to be stripped from argon. These electrons are caught up within the oscillating magnetic fields and are accelerated by them. The procedure of adding energy to electrons by the use of a coil in this manner is referred to as inductive coupling.^[351] The produced high-energy electrons further collide with other argon

atoms generating more argon ions. A chain reaction of collisional ionization is initiated and continues until argon is broken down into a plasma consisting of argon atoms, electrons, and argon ions. It is also known as inductively coupled plasma (ICP) discharge.^[351] Since RF energy is constantly transferred to the load coil, the plasma is sustained within the torch. Normally, the plasma appears very intense, brilliant white, and teardrop-shaped. The plasma temperature in the analytical zone is extremely high ranging from 5,000 to 8,000 K.^[351,353]

Figure 40 displays the general setup and major components of an ICP-OES instrument, as well as the most important steps involved in the examination of a sample. Principally, an ICP-OES instrument is composed of a sample introduction system, an ICP torch with nebulizer, a RF generator, and an optical measurement system.^[352] Although all three states of matter (gas, solid, and liquid) have been successfully injected into an ICP, most samples start as liquids. These are nebulized into an aerosol, a very fine mist of sample droplets with a diameter of 1 - 10 μm .^[351,353] Next, this aerosol is transported into the center of the ICP by an argon flow. The high temperature plasma removes the solvent from the aerosol creating microscopic salt particles (**desolvation**), which are decomposed into a gas of individual molecules (**vaporization**), and, which are further dissociated into atoms (**atomization**).^[351] These atoms are then excited and/or ionized on account of collisions with energetic electrons. Subsequently, the energy is released in the form of characteristic wavelengths. The emitted light is polychromatic. Therefore, it must be separated into individual wavelengths in order that the emission from each species can be identified without any interferences. Consequently, monochromators or polychromators are placed in front of a photosensitive detector such as a photo-multiplier tube or a charge-injection device. The detected radiation is turned into electronic signals, which are converted into concentration information for the analyst.^[351]

In this work, ICP-OES measurements of graphite anodes at 0% SOC are conducted after cycling C//LiNi_{0.4}Mn_{1.6}O₄ pouch cells to clarify whether and to what extent the dissolution of nickel and manganese, and the subsequent deposition of the metals on the counter electrode take place upon cycling.

A



B

1. Sample preparation: some samples require special preparation including treatment with acids, heating and microwave digestion.

2. Nebulization: liquid converted to aerosol.

3. Desolvation/Vaporization: water is driven off, and remaining solid and liquid portions are converted to gases

4. Atomization: gas phase bonds are broken, and only atoms are present. Plasma temperature and inert chemical environment are important at this stage.

5. Excitation/Emission: atoms gain energy from collisions and emit light of a characteristic wavelength.

6. Separation/Detection: a grating disperses light that is quantitatively measured.

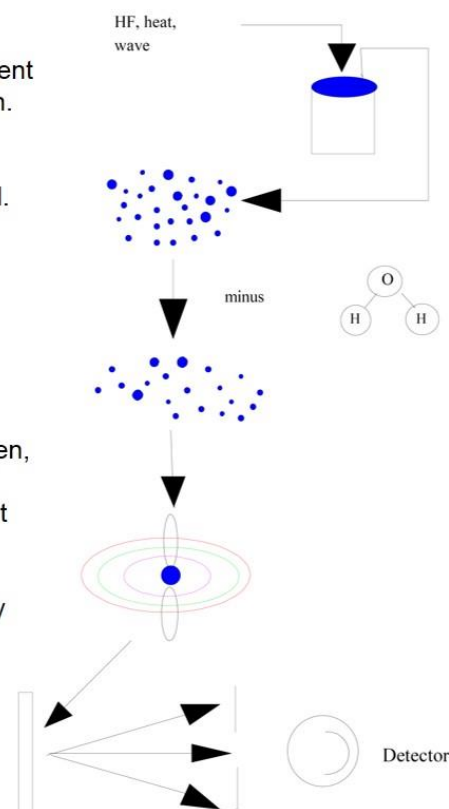


Figure 40 A Major components and layout of a typical ICP-OES instrument.^[351] B Presentation of the steps involved in ICP-OES sample analysis.^[353]

2.3.6 Scanning electron microscopy and energy dispersive spectroscopy

The history of the scanning electron microscope (SEM) began with an apparatus built by Zworykin, Hiller, and Snyder in 1942.^[354] Its resolution was, however, only 1 μm , which is less than that of a light microscope (0.1 μm).^[355] Several technological advancements increased the resolution up to 0.05 μm and in the early 1960s the first commercial instrument appeared. Since then the design of SEMs has been constantly evolved and improved.^[355,356]

Today, the maximum instrumental resolution of SEMs is in the order of 1 - 5 nm.^[357] Generally, a SEM permits the observation and characterization of organic and inorganic materials by delivering high resolution topographical images of sample surfaces in a variety of different contrast modes.^[357,358] Thereto, a finely focused electron beam is scanned in a raster across the surface of a specimen. The interaction of the incident electron beam with the sample causes the emission of electrons and photons including secondary electrons, backscattered electrons, Auger electrons, characteristic X-rays, and other photons of various energies. These signals are used to analyze the specimen in terms of surface topography, crystallography, or composition.^[357]

The basic layout of a conventional SEM comprises an electron gun, tow condenser lenses, an objective lens, an electron detection system, and a set of deflectors. All components are operated in a vacuum atmosphere.^[356] Figure 41 displays a schematic drawing of a typical SEM.

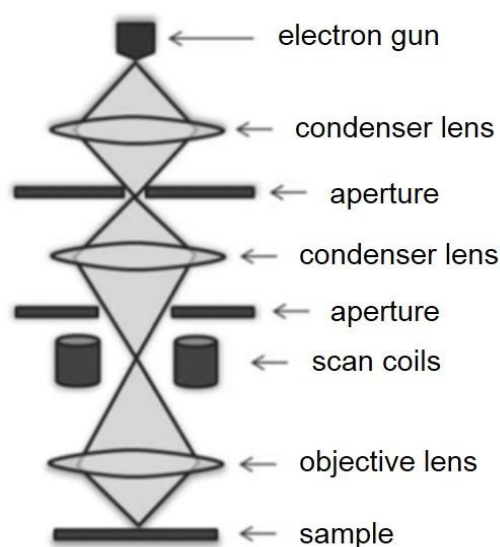


Figure 41 Schematic drawing of the basic layout of a typical SEM. With modifications from^[359].

The electron gun produces electrons and accelerates them to an energy in the range of 0.1 - 30 keV.^[357] The electron source can be a thermionic emitter such as a hot tungsten or

lanthanum hexaboride filament, a Schottky type electron source, or a field emission type electron gun.^[360] The three-stage electron lens system is applied to demagnify the electron beam to a small spot of approx. 1 - 10 nm in diameter from an original crossover diameter more than a thousand times larger located inside the electron gun.^[356,360] In most SEMs, the electron beam is directed from the objective lens into the sample chamber, where it interacts with the specimen. A deflection system, consisting of two pairs of magnetic coils in front of the objective lens, moves the electron-probe in a raster-like mode across the sample and synchronously works with a computer display monitor.^[356] Thereby, the magnification of the sample is defined by the ratio of the linear size of the viewing screen to the linear size of the raster on the sample. A magnification of the observed sample section can simply be achieved by a reduction of the scan coil current, while keeping the image size on the display monitor constant.^[356]

The highly energetic focused electron beam interacts elastically and inelastically with the specimen. The volume, in which these interactions take place, is called interaction volume. Figure 42 gives an overview of this process.

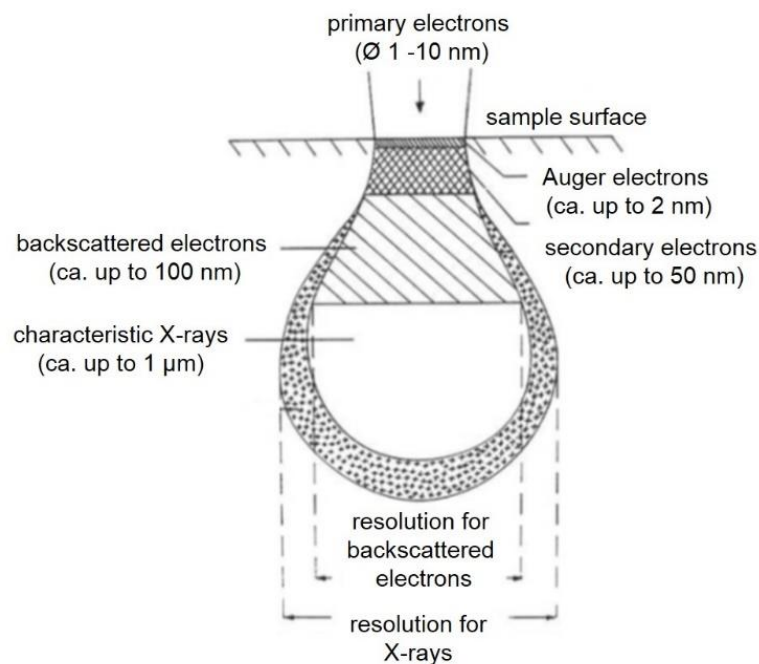


Figure 42 Interaction volume and emitted signals. With modifications from^[359].

The penetration of the primary electrons into the sample causes the scattering of electrons from a variety of different depths. The diverse signals are collected by electron detectors. Secondary electrons with a main energy range from 0.5 to 5 eV are created by inelastic collisions and escape from close to the specimen surface. As opposed to this, backscattered electrons with an energy from 50 eV up to the primary beam energy are generated by multiple elastic collisions and are emitted from deeper sample levels. These two signals are the most

prominent regarding the formation of a SEM image.^[356] Auger electrons evolve from inner atomic shells after ionization processes as an alternative to characteristic X-ray emission. Their energies show up as distinctive peaks in the energy spectrum and provide material contrast information.^[356]

The final signal yield and image resolution is strongly influenced by the way the incident electron beam is scattered inside the specimen. Actually, the penetration depth R_d of the primary electrons depends on the atomic number Z_a , the mean density of the sample at the point of impact ρ , and the energy of the primary electron beam, which is directly proportional to the applied acceleration voltage U_a . The subsequent approximate formula for estimating R_d has been given by Kanaya and Okayama in 1972:^[356]

$$R_d = \frac{0.0276 \cdot A_w \cdot U_a^{1.67}}{Z_a^{0.889} \cdot \rho} [\mu\text{m}] \quad (49)$$

R_d = penetration depth of the primary electrons

A_w = atomic weight

U_a = acceleration voltage

Z_a = atomic number

ρ = mean density of the sample at the point of impact

During a SEM experiment, characteristic X-rays are also emitted from the sample on account of the electron bombardment. These X-rays can be utilized for both qualitative elemental identification and quantitative elemental information from regions of the specimen up to circa one cubic micrometer in depth under normal operating conditions.^[357] The corresponding technique is known as energy dispersive X-ray spectroscopy (EDX). EDX is usually a standard attachment to most conventional SEMs. Nonetheless, this method has some notable limitations. On one hand, X-rays are generated deep within a comparatively large interaction volume. The acceleration voltage of the incident electron beam has to be typically between 10 to 30 keV to overcome the work function of the elements with high atomic number. This results in a rather low lateral resolution with ranges between 1 - 5 μm . On the other hand, EDX has a lower sensitivity for lighter elements such as, for example, He or Li. In fact, the technique is restricted to elements with an atomic number of four and larger.^[356]

Within this thesis, SEM is used to characterize the morphology of $\text{LiNi}_{0.4}\text{Mn}_{1.6}\text{O}_4$ electrodes and EDX is applied to reveal Mn and Ni elemental distributions on the surface of graphite anodes after cycling C// $\text{LiNi}_{0.4}\text{Mn}_{1.6}\text{O}_4$ pouch cells at 45 °C.

2.3.7 X-ray photoelectron spectroscopy

Photoelectron spectroscopy (PES) is one of the most important techniques for the investigation of chemical compositions, chemical bonds, and electronic structures of interfaces and surfaces.^[361] Information is gained by photoionization of atoms or molecules and by energy dispersive analysis of the emitted photoelectrons. In dependence of the applied excitation energy, two methods are distinguished. On one hand, for ultraviolet photoelectron spectroscopy (UPS) vacuum ultraviolet radiation of gas-discharge lamps (e.g. helium source; $hf = 10 - 40$ eV) is utilized to excite the electrons in the valence levels.^[362] On the other hand, in the case of X-ray photoelectron spectroscopy (XPS) monochromatic soft X-rays (e.g. Al K_{α} ; $hf = 100 - 10,000$ eV) are used to excite inner shell electrons.^[362] Originally, a high-resolution XPS analyzer was developed by Siegbahn and his research group at the University of Uppsala in Sweden in the 1960s.^[361,363] The method is also known as electron spectroscopy for chemical analysis (ESCA).^[363] Subsequently, the principal fundamentals of XPS are described and elucidated.

The physical principle and fundamental functionality of XPS

Generally, electrons in atoms have defined binding energies, which can approximately be determined by equation 50 (Bohr's atomic model):^[364]

$$E_B \approx - \frac{Z_a^2}{n^2} \cdot 13.6 \text{ eV} \quad (50)$$

E_B = binding energy

Z_a = atomic number

n = principal quantum number

Consequently, the binding energy of electrons is a function of the quantum number n and the atomic number Z_a and, thus, it is characteristic for elements. While valence electrons provide information about chemical bonds, inner shell electrons deliver information on the chemical composition of materials. Therefore, the binding energy distribution of core electrons serves as a chemical fingerprint for the identification of single atoms. This fact is the foundation for all XPS investigations.^[365]

The physical principle of PES is based on the photoelectric effect, which was first introduced by Einstein in 1905.^[335] Accordingly, the absorption of a photon by an atom leads to its ionization via the emission of an electron when the energy of the incident photon is greater than the work function of the examined sample Φ_0 and the electron binding energy E_B . In other words, an electron with a binding energy E_B in an occupied initial state (core level in case of XPS) is excited into a vacuum final state by a photon with the following energy:^[361]

$$E = h_P \cdot f > E_B + \Phi_0 \quad (51)$$

E = energy of a photon

h_P = Planck constant ($= 6.6256 \cdot 10^{-34}$ Js)

f = frequency

E_B = binding energy of an electron

Φ_0 = work function of the examined sample

The physical principle of the photoemission process is sketched in Figure 43.

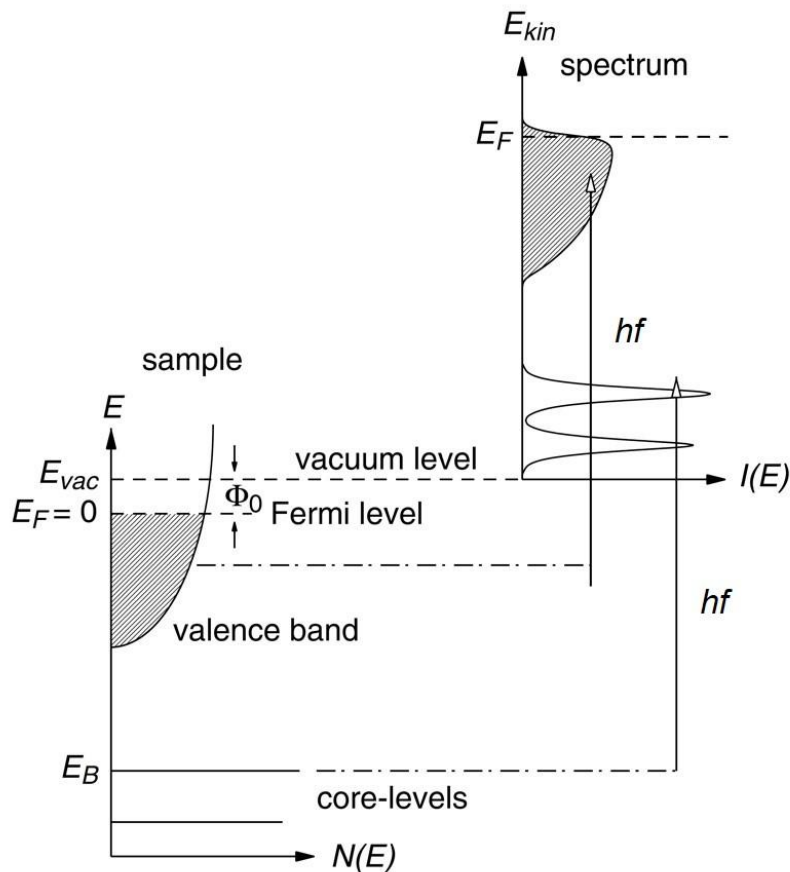


Figure 43 Schematic image of the photoemission process in the single-particle picture.^[361]

The photoelectron spectrum, namely the distribution of the emitted photoelectrons over the kinetic energy $I(E_{kin})$, is detected by an electron energy analyzer. In a first order approach it is an image of the occupied density of electronic states $N(E_B)$ in the examined material.^[361]

Figure 44 displays the typical functionality of a photoemission spectrometer.

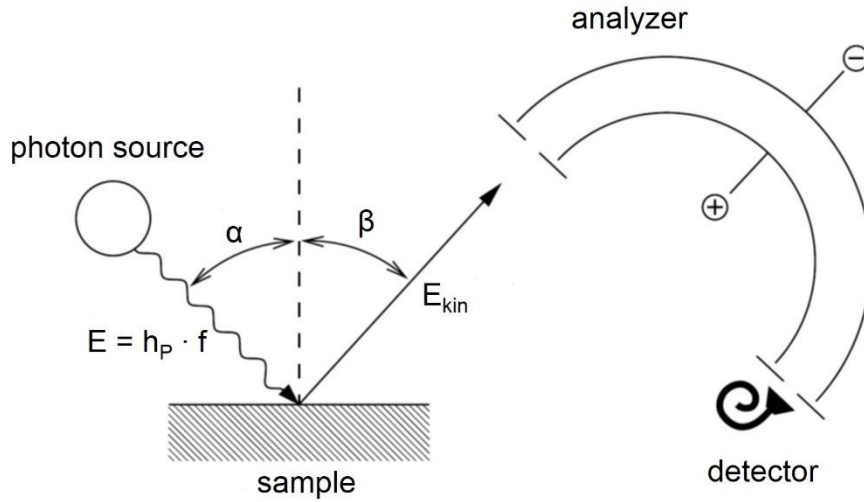


Figure 44 Fundamental functionality of a modern photoemission spectrometer. Monochromatic photons with the energy $h_P \cdot f$ are produced by a light source (e.g. Al K_α X-ray anode) and hit the sample surface under an angle α with respect to the normal surface. The kinetic energy E_{kin} of the photoelectrons can be analyzed by an electrostatic analyzer. The whole setup is evacuated to ultra-high vacuum (UHV, typically $p \leq 10^{-10}$ mbar). With modifications from^[361].

The energy balance of a photoionization process can also be expressed by the subsequent equations according to Koopman's theorem:^[366]

$$E_i(N) + h_P \cdot f - \Phi_0 = E_f(N - 1) + E_{kin} \quad (52)$$

$$E_{kin} = h_P \cdot f - \Phi_0 - (E_f(N - 1) - E_i(N)) \text{ with } E_B = E_f(N - 1) - E_i(N) \quad (53)$$

$$E_B = h_P \cdot f - \Phi_0 - E_{kin} \quad (54)$$

$E_i(N)$ = energy of the N-particle system (atom) in the initial state

$E_f(N - 1)$ = energy of the N-particle system (atom) in the final state

E_{kin} = kinetic energy of the emitted electrons

E_B = binding energy of the electrons

$h_P \cdot f$ = energy of the photons

Φ_0 = work function of the examined sample

The N-particle picture represents electrons in a solid. Koopman believed that N - 1 remaining electrons in a solid are not influenced by the formation of a hole on account of a photoexcitation process. This is why this assumption is called frozen orbital approximation.^[367] However, in practice, the whole multi-particle system is affected by the irradiation with X-rays and the photohole changes the potential of the remaining N - 1 electrons. Actually, they relax into lower energy states. Moreover, Koopman's theorem must be corrected owing to different correlation energies in the initial and the final states.^[361,367] Hence, in order to avoid an overestimation of the binding energy equation 54 must be adjusted as follows:

$$E_B = h_P \cdot f - \Phi_0 - E_{kin} - E_{relax} - E_C \quad (55)$$

E_B = binding energy of the electrons

E_{relax} = relaxation energy

E_C = correlation energy

$h_P \cdot f$ = energy of the photons

Φ_0 = work function of the examined sample

The most general theoretical interpretation of photoemission spectra is based on Fermi's golden rule. This approach describes the transition probability of a multi-particle system from an initial to a final state due to photoexcitation:^[368]

$$W_{i \rightarrow f} = \frac{2\pi}{\hbar_P} \cdot |\langle \Psi_f | H_{PE} | \Psi_i \rangle|^2 \cdot \delta \cdot (E_f(N-1) - E_i(N) - h_P \cdot f) \quad (56)$$

$W_{i \rightarrow f}$ = transition probability of a multi-particle system from an initial to a final state

\hbar_P = reduced Planck constant (= $1.0545 \cdot 10^{-34}$ Js)

Ψ_f = final state

Ψ_i = initial state

H_{PE} = perturbation operator

$E_i(N)$ = energy of the N-particle system (atom) in the initial state

$E_f(N-1)$ = energy of the N-particle system (atom) in the final state

$h_P \cdot f$ = energy of the photons

The probability $W_{i \rightarrow f}$ for the generation of a photoelectron also signifies the intensity of a photoemission line, that is, the amount of generated photoelectrons. The perturbation operator H_{PE} denotes the interaction of an electron in the N-particle system with the electromagnetic field A_E . Thereby, the momentum operator $p = -i \cdot \hbar_P \cdot \nabla$ transforms into $p \rightarrow p + \frac{e}{c} \cdot A$:^[361]

$$\begin{aligned}
 H &= \frac{1}{2 \cdot m_e} \cdot \left[p + \frac{e}{c} \cdot A_E \right]^2 + e \cdot V(r) \\
 &= \frac{p^2}{2 \cdot m_e} + \frac{e}{2 \cdot c \cdot m_e} \cdot (A_E \cdot p + p \cdot A_E) + \frac{e^2}{2 \cdot c^2 \cdot m_e} \cdot A_E^2 + e \cdot V(r) \\
 &= H_0 + H_{PE}
 \end{aligned} \tag{57}$$

$$H_{PE} = \frac{e}{2 \cdot c \cdot m_e} \cdot (A_E \cdot p + p \cdot A_E) + \frac{e^2}{2 \cdot c^2 \cdot m_e} \cdot A_E^2 \tag{58}$$

m_e = electron mass (= $9.1091 \cdot 10^{-31}$ kg)

p = momentum operator

e = electron charge (= $1.60210 \cdot 10^{-19}$ C_L)

c = speed of light (= $299,792,458 \frac{m}{s}$)

A_E = electromagnetic field

$V(r)$ = potential energy

H_0 = unperturbed Hamilton operator

H_{PE} = perturbation operator

Equation 58 can be simplified when specific surface effects are neglected (e.g. $\nabla \cdot A_E = 0$ in case of translational invariance of a solid):^[361,369]

$$H_{PE} = \frac{e}{c \cdot m_e} \cdot A_E \cdot p \tag{59}$$

H_{PE} = perturbation operator

e = electron charge (= $1.60210 \cdot 10^{-19}$ C)

c = speed of light (= $299,792,458 \frac{m}{s}$)

m_e = electron mass (= $9.1091 \cdot 10^{-31}$ kg)

A_E = electromagnetic field

p = momentum operator

This approximation is an appropriate basis for the quantum mechanical consideration of most photoemission investigations. More detailed information about the theory of photoemission processes can, for example, be found in reference [370].

Depth of information

The high surface sensitivity is one of the most important properties of XPS. The key to this is not the penetration depth of the X-rays, which is in the micrometer range, but the mean free path λ_e of the photoelectrons, which depends on the kinetic energy of the emitted electrons. Experimental values of the mean free path of various materials are depicted in Figure 45.^[365]

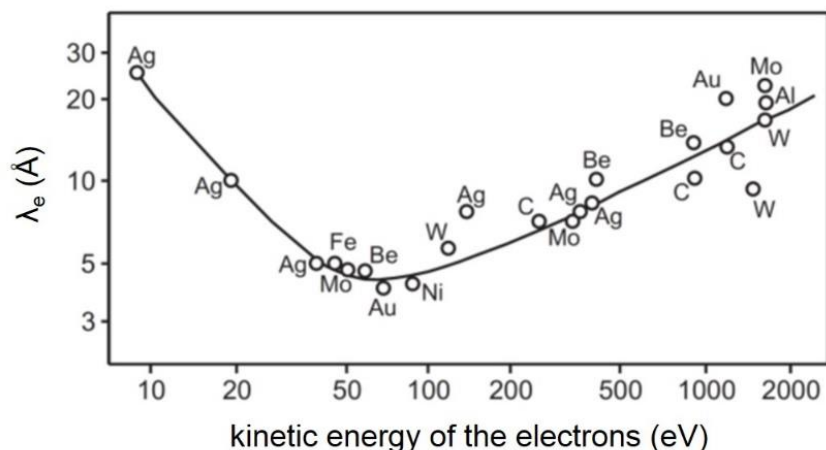


Figure 45 Plot of the mean free path λ_e vs. the kinetic energy of the electrons for diverse materials.^[365]

The curve is the result of an empirically determined formula for metals. As such, the mean free path has a minimum around $\lambda_e \approx 5 \text{ Å}$ at a kinetic energy of $E_{\text{kin}} \approx 50 \text{ eV}$.^[365] For kinetic energies up to 2,000 eV (as possible in case of XPS), the mean free path increases up to $\lambda_e \approx 10 - 20 \text{ Å}$ according to $\lambda_e \sim \sqrt{E_{\text{kin}}}$.^[365] Therefore, the mean free path varies only slightly between different materials and its limiting range is responsible for the surface sensitivity of XPS.

Quantitative analysis

Usually, a XPS spectrum is obtained at a particular photon energy by recording the number of photoelectrons as a function of kinetic energy. By means of equation 55 the binding energy can be calculated. Most of the time, the intensity of photoelectron lines is plotted vs. the binding energy. The distinct lines in a XPS spectrum reflect the core levels of the material. Typically, XPS spectra are quantified in terms of peak intensities and peak positions. The peak positions indicate the elemental and chemical composition, whereas the peak intensities reveal the relative concentrations of the different components.^[371] Actually, the peak intensity is represented by the area of the photoemission line and depends on diverse parameters as expressed by equation 60:^[363]

$$I_A = n_A \cdot f_{X\text{-ray}} \cdot \sigma_A \cdot \theta \cdot y \cdot \lambda_e \cdot A_s \cdot T \quad (60)$$

I_A = intensity of a photoemission line for element A

n_A = number of atoms of the element A per cm^3 of the sample

$f_{X\text{-ray}}$ = X-ray flux in photons/ $(\text{cm}^2 \cdot \text{s})$

σ_A = photoelectric cross-section for the atomic orbital A in cm^2

θ = angular efficiency factor for the instrumental arrangement based on the angle between the photon path and the detected electron

y = efficiency in the photoelectric process for formation of photoelectrons of the normal photoelectron energy

λ_e = mean free path of the photoelectrons in the sample

A_s = area of the sample, from which photoelectrons are detected

T = detection efficiency for electrons emitted from the sample

Consequently, the number of atoms of the element A of the sample is given by:^[363]

$$n_A = \frac{I_A}{f_{X\text{-ray}} \cdot \sigma_A \cdot \theta \cdot y \cdot \lambda_e \cdot A_s \cdot T} \quad (61)$$

The denominator in equation 61 is defined as the atomic sensitivity factor (ASF). For the investigation of a homogeneous sample consisting of elements A and B, the following relation can be derived:^[365]

$$\frac{n_A}{n_B} = \frac{I_A \cdot \text{ASF}_B}{I_B \cdot \text{ASF}_A} \quad (62)$$

The reproducibility of quantitative XPS analyses lies between 5 and 15%. In favorable cases, an element sensitivity of 0.1 - 1 at% is achievable.^[365] Generally, for any spectrometer, it is possible to define multiple sets of ASF values for all elements in dependence of the X-ray source and the angles relative to the analyzer.^[363]

Determination of layer thicknesses with XPS

The thickness of sufficiently thin surface layers (e.g. oxide films) might be determined with the help of XPS. Thereto, the correlation between the intensity of a photoemission line, the mean free path, and the angle of the analysis instrument is decisive (cf. equation 60). The procedure elucidated below refers only to homogeneously thick layers. Figure 46 demonstrates the geometric relationships, which are relevant for the determination of layer thicknesses.^[365]

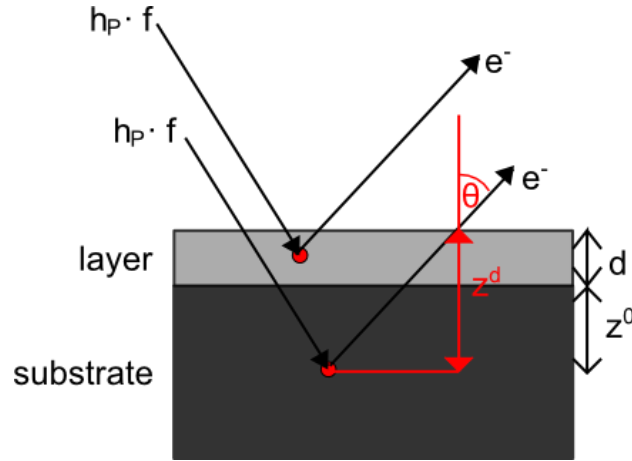


Figure 46 Simplified schematic of the geometric relationships, which are relevant for the determination of layer thicknesses.

The film thickness is represented by d , z^d signifies the emission depth of the detected photoelectrons with $z^d = z^0 + d$, and θ denotes the angle between the normal of the sample surface and the photoelectron emission direction. For the determination of the layer thickness, the ratio of the intensities of the photoemission lines of the pure substrate I_{Sub}^0 and the covered substrate I_{Sub}^d is utilized. Regarding a covered sample, the photoelectrons must additionally pass through the film with thickness d to get to the analyzer. Thereby, the number of photoelectrons decreases exponentially. When both measurements are conducted under the same conditions and provided that the distribution of element A is equal in both cases, the equation 63 is valid:^[365,372]

$$\frac{I_{\text{Sub}}^d}{I_{\text{Sub}}^0} = \exp \left(-\frac{d}{\lambda_e \cdot \cos(\theta)} \right) \quad (63)$$

I_{Sub}^0 = intensity of a photoemission line for the pure substrate

I_{Sub}^d = intensity of a photoemission line for the covered substrate

d = layer thickness

λ_e = mean free path of the photoelectrons in the sample

θ = angle between the normal of the sample surface and the electron emission direction

Thus, the thickness of the layer is calculable when λ_e and θ are known for the investigated system:

$$d = -\lambda_e \cdot \cos(\theta) \cdot \ln \frac{I_{\text{Sub}}^d}{I_{\text{Sub}}^0} \quad (64)$$

Strictly speaking equations 63 and 64 are only valid for dense and homogeneous surface films with $\theta \geq 1$.^[373]

Chemical shift

The exact binding energy of an electron does not only depend on the ionized orbital, but also on the oxidation state and the chemical environment of the examined element. Changes of these factors lead to shifts of the energetic positions of the photoemission lines in the XPS spectra. These shifts are called “chemical shifts”. Elements in higher valence states have higher binding energies owing to their higher effective nuclear charges. Hence, one of the strengths of XPS is the possibility to distinguish between different oxidation states and chemical environments. Nevertheless, the distinction of minor chemical shifts is limited by the spectral line width $\Delta E(\text{FWHM})$, which is influenced by the following variables:^[365,374]

$$\Delta E(\text{FWHM}) = \sqrt{(\Delta E_n^2 + \Delta E_p^2 + \Delta E_d^2)} \quad (65)$$

$\Delta E(\text{FWHM})$ = spectral line width

ΔE_n = natural line width of the transition from the initial to the final state (lifetime effect)

ΔE_p = line width of the exciting radiation

ΔE_d = energy resolution of the analyzer

Most commonly, the line width of the radiation source (monochromator) has the biggest impact on $\Delta E(\text{FWHM})$.^[374]

Additional spectral features in a photoemission spectrum

Generally, the ejection of an inner shell electron from an atom generates an electronically excited state with a core hole in the shell. Then, the energetically excited ion can relax via two different routes (Figure 47):

- **X-ray fluorescence:** the core hole is filled by an electron from an outer shell with simultaneous emission of a photon. Thereby, the energy of the photon equals to the energy difference of the two core levels involved in the process.^[363,375]
- **Auger process:** the core hole is filled by an electron from an outer shell, and a second electron is simultaneously emitted, carrying off the excess energy. As a consequence, the remaining ion is in a doubly ionized state. The nomenclature of Auger emissions is the same as for X-ray processes (see chapter 2.3.3). In contrast to the kinetic energy of XPS photoelectrons, the kinetic energy of Auger electrons is independent on the exciting radiation. Therefore, a change of the radiation source causes a change of the photoemission line positions. The positions of the Auger emission lines remain, however, unmodified.^[363,375]

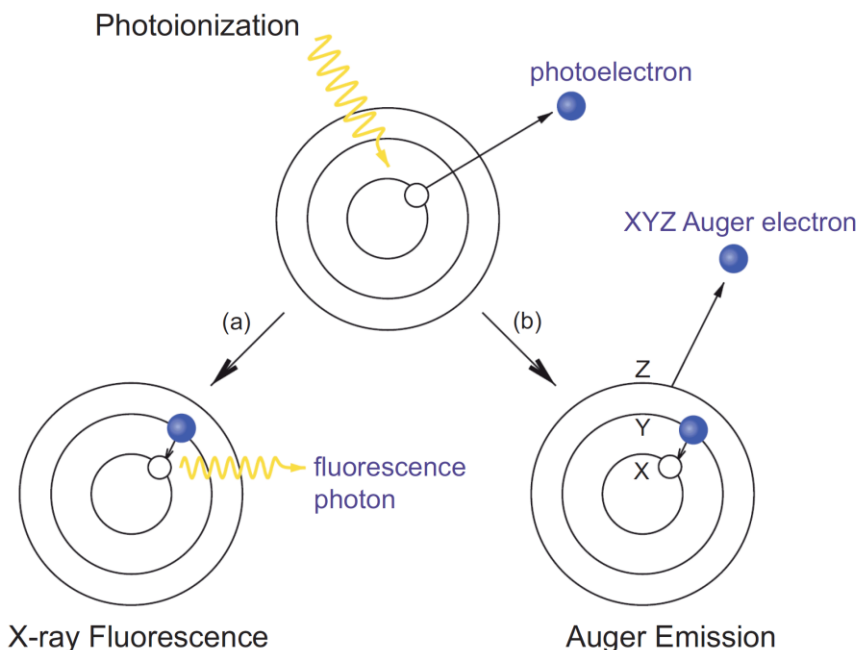


Figure 47 Schematic of X-ray fluorescence and the Auger processes following a photoionization event.^[375]

X-ray fluorescence and the Auger electron emission are competitive processes. The latter occurs roughly 10^{-14} s after the photoemission. For a binding energy range below 1.5 keV and for elements with a low atomic number the non-radiative decay dominates.^[363,375]

Another phenomenon in XPS spectra is the splitting of photoemission lines into **multiplets**. The p, d, and f levels split into doublets upon ionization (Figure 48).

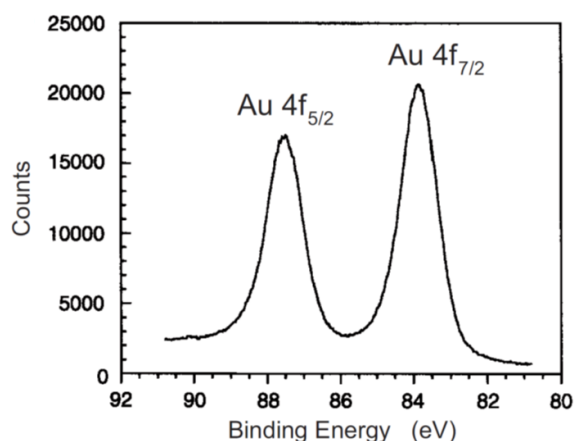


Figure 48 The splitting of the 4f-photoemission line of gold into a doublet arises from the spin-orbit coupling.^[375]

The effect is a result of spin-orbit coupling between unpaired electrons. While the inner subshells of an atom are completely filled in the initial state, in the final state after the photoemission one electron has been removed and an unpaired spin is left in a core level.^[365]

The movement of an electron around the nucleus is connected with the azimuthal quantum number l . Furthermore, the electron has an electron spin, which is defined as the spin quantum number $s = \pm \frac{1}{2}$. As already mentioned in chapter 2.3.3, the total angular momentum quantum number j is a combination of the azimuthal quantum number l and the spin quantum number s ($j = |l \pm s|$).^[172] Thus, for a s-electron with $l = 0$, the total angular momentum quantum number j equals to $\frac{1}{2}$, independently of the direction of the electron spin. Accordingly, the corresponding s-photoemission line is not split. In contrast, for a p-electron with $l = 1$ and $s = \frac{1}{2}$, j can adopt the values $j^+ = l + \frac{1}{2} = \frac{3}{2}$ or $j^- = l - \frac{1}{2} = \frac{1}{2}$. Consequently, the p-photoemission line is split into a doublet. Unpaired electrons in the d and f shells behave similarly.^[335] The intensity ratio of the spin-orbit components is given by the ratio of the respective multiplicities: $2j^+ + 1 : 2j^- + 1$.^[375] Table 4 summarizes the spin-orbit parameters of XPS lines.

Subshell	l	s	$j = l \pm s $	Ratio of the degeneracies ($2j + 1$)
s	0	$\frac{1}{2}$	$\frac{1}{2}$	-
p	1	$\frac{1}{2}$	$\frac{1}{2}, \frac{3}{2}$	1 : 2
d	2	$\frac{1}{2}$	$\frac{3}{2}, \frac{5}{2}$	2 : 3
f	3	$\frac{1}{2}$	$\frac{5}{2}, \frac{7}{2}$	3 : 4

Table 4 Spin-orbit splitting parameters of XPS lines.

The simultaneous excitation of several electrons in an atom may also cause so-called **shake-up and shake-off satellite lines**. In both processes, electronically excited final states are created upon the emission of an electron. Here, the emitted photoelectron transfers a defined part of its energy to a remaining electron. In the case of shake-up and shake-off transitions this electron is additionally promoted from an occupied energy level into a bound unoccupied state below the vacuum level or into an unoccupied state in the continuum above the vacuum level, respectively (Figure 49). The first scenario involves an ionization and excitation process, whereas the second one leads to a doubly ionized atom.^[365,375]

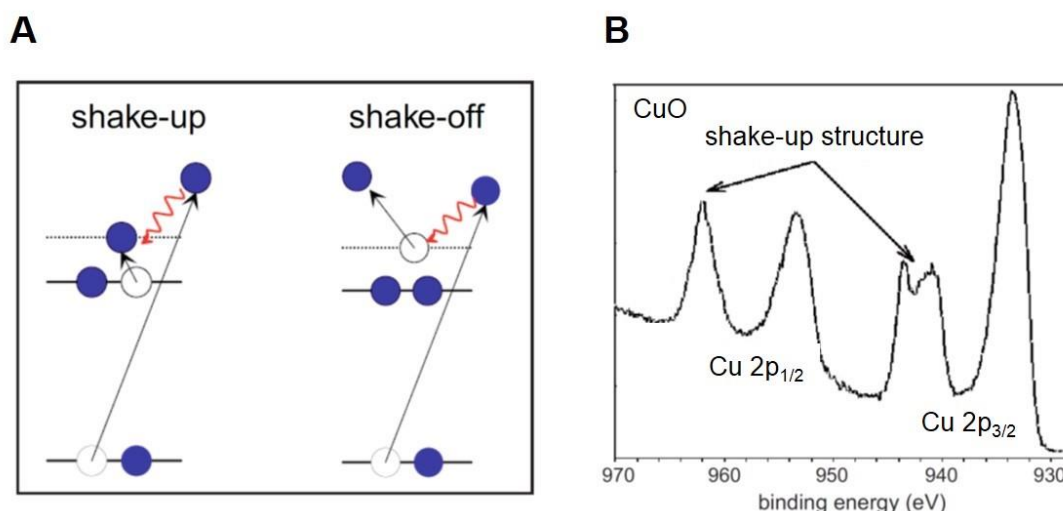


Figure 49 **A** Illustration of shake-up and shake-off transitions. **B** Shake-up structure in a Cu2p spectrum of copper(II) oxide (CuO).^[375]

Aside from shake-up and shake-off satellites, **plasmon loss satellites** can appear in XPS spectra. They arise from the excitation of quantized collective oscillations of the free electron gas density with respect to the positively charged ion cores. Plasmon satellites are found at higher binding energies relative to the corresponding photoemission line by amounts of $n(\hbar\omega_p) + m(\hbar\omega_s)$, where n and m are integers and $\hbar\omega_p$ and $\hbar\omega_s$ are the energies of a bulk and a surface plasmon, respectively (Figure 50).^[375]

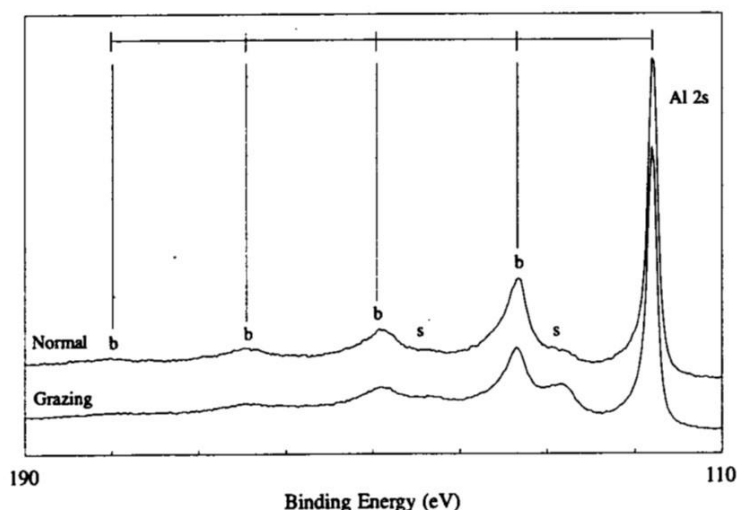


Figure 50 Surface (s) and bulk (b) plasmon lines associated with the Al2s at normal and at grazing take-off angles.^[363]

Moreover, electrons suffer from **inelastic scattering processes**, while moving towards the analyzer resulting in a gradual increase of the background in XPS spectra. This renders background subtraction necessary for XPS interpretation. There are numerous background correction possibilities available. For most analyses the basic linear, Shirley, and universal

cross-section Tougaard functions are the tools of choice. Actually, none of the background types offer a completely correct subtraction method. Hence, the selection of one background model over another is rather based on the choice of the least wrong than the most right. Detailed information on this subject is provided in the literature.^[376]

The major part of a XPS spectrum recorded with a routinely used Al K α X-ray tube consists of K $\alpha_{1,2}$ transitions. Nonetheless, there are also some minor X-ray contributions at higher photon energies such as, for instance, K β . This radiation produces additional photoelectrons, which lead to extra lines in the XPS spectrum at lower binding energies. These lines are named ***X-ray satellites***.^[363,365]

Finally, further artifacts are so-called ***X-ray ghost lines***. They might originate from Mg impurities in the Al anode or vice versa, the Cu or Ag anode based structure, oxidation of the anode, or the generation of X-ray photons in the thin Al foil of the X-ray window. The most intense spectral peaks create additional emissions in the XPS spectra. Although such minor lines can be puzzling, they appear only rarely with non-monochromatic X-ray sources and are not possible with monochromatic radiation.^[363,365]

In this thesis, XPS spectroscopy is utilized to study the chemical nature and the development of the interfacial layers between the LiNi_{0.4}Mn_{1.6}O₄ electrodes and the different electrolyte formulations (see chapter 5.5).

2.3.8 Electrochemical impedance spectroscopy

In the 1880s, the establishment of electrochemical impedance spectroscopy (EIS) was initiated by O. Heaviside, who introduced impedance into electrical engineering.^[253,377] A. E. Kennelly and C. P. Steinmetz extended his extraordinary work rather soon by vector diagrams and complex representation.^[377] Nowadays, EIS has become a very appropriate method in materials research and development. The respective results can often be correlated with many complex materials variables: from mass transport, rates of chemical reactions, corrosion, and dielectric properties, to defects, microstructure, and compositional influences on the conductance of solids.^[378] EIS is suitable for the investigation of ageing phenomena and degradation effects in fuel cells and rechargeable batteries.^[253,377] The following properties make this technique a powerful diagnostic tool:^[253,379]

- it is a linear technique, where the results are readily interpreted in terms of linear systems theory
- multiple parameters are determined by a single measurement
- it is a nondestructive method

- if the measurements are over an infinite frequency range (theoretically), the impedance contains all of the information that are obtained from the examined system by linear electrical response methods
- it has a high experimental efficiency (i.e. the amount of information transferred to the observer compared to the amount produced by the experiment)
- the validity of the generated data is controlled by integral transform techniques (e.g. the Kramers-Kronig transforms), which are independent of the involved physical and chemical processes

During an impedance measurement, a sinusoidal AC voltage U with an angular frequency ω and a defined small amplitude U_0 is applied. Thereby, the voltage signal is equivalent to:^[380]

$$U = U_0 \cdot \sin(\omega \cdot t) \quad (66)$$

U = AC voltage as a function of time

U_0 = amplitude of the AC voltage

$\omega = 2 \cdot \pi \cdot f$ = angular frequency

t = time

Regarding the analysis of a linear or pseudolinear system, the response to the sinusoidal AC voltage input U is an induced sinusoidal AC current I with the same angular frequency ω , but shifted by the phase angle Φ :^[380]

$$I = I_0 \cdot \sin(\omega \cdot t + \Phi) \quad (67)$$

I = AC current as a function of time

I_0 = amplitude of the AC current

$\omega = 2 \cdot \pi \cdot f$ = angular frequency

t = time

Φ = phase angle

By the utilization of the subsequent Euler's relationship

$$e^{(i \cdot \Phi)} = \cos(\Phi) + i \cdot \sin(\Phi) \text{ with the complex number } i = \sqrt{-1} \quad (68)$$

it is possible to express the AC voltage and the AC current as complex functions:^[380]

$$U = U_0 \cdot e^{(i \cdot \omega \cdot t)} \quad (69)$$

$$I = I_0 \cdot e^{[i \cdot (\omega \cdot t + \Phi)]} \quad (70)$$

Accordingly, Figure 51 demonstrates that the sinusoidal curves U and I can also be pictured by vectors with the lengths U_0 and I_0 , rotating around the origin of the vector diagram with the angular frequency ω .

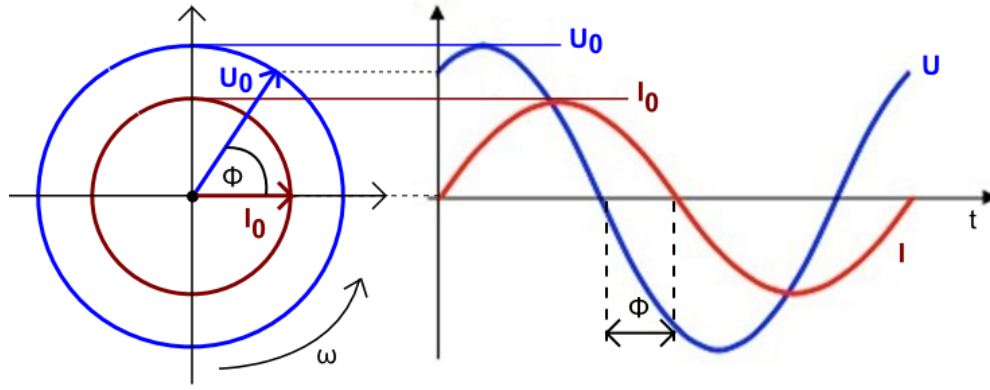


Figure 51 Vector diagram and sinusoidal curves of the input potential U and the current response I in dependence of time. With modifications from^[381].

Analogous to Ohm's law the AC resistance or impedance Z of the system is defined as the ratio of input voltage U and measured output current I :^[380]

$$Z = \frac{U}{I} = \frac{U_0 \cdot e^{(i \cdot \omega \cdot t)}}{I_0 \cdot e^{[i \cdot (\omega \cdot t + \Phi)]}} = \frac{U_0}{I_0} \cdot e^{(-i \cdot \Phi)} = |Z| \cdot e^{(-i \cdot \Phi)} \quad (71)$$

Thus, the impedance Z is a complex number that can be split into a real and an imaginary part:^[380]

$$\begin{aligned} Z &= |Z| \cdot e^{(-i \cdot \Phi)} \\ &= |Z| \cdot [\cos(\Phi) - i \cdot \sin(\Phi)] \\ &= |Z| \cdot \cos(\Phi) - i \cdot |Z| \cdot \sin(\Phi) \\ &= Z' - i \cdot Z'' \\ &= \text{real part} - \text{imaginary part} \end{aligned} \quad (72)$$

The reciprocal value of the impedance Z is the admittance Y ^[382]

$$Y = \frac{1}{Z} = \frac{I}{U} = \frac{I_0 \cdot e^{[i \cdot (\omega \cdot t + \Phi)]}}{U_0 \cdot e^{(i \cdot \omega \cdot t)}} = \frac{I_0}{U_0} \cdot e^{(i \cdot \Phi)} = \frac{1}{|Z|} \cdot e^{(i \cdot \Phi)} \quad (73)$$

and the phase angle Φ at a particular angular frequency ω is given by:^[380]

$$\tan(\Phi) = \frac{Z''}{Z'} \quad \text{or} \quad \Phi = \arctan\left(\frac{Z''}{Z'}\right) \quad (74)$$

The phase angle Φ and the impedance Z depend on the angular frequency ω of the utilized voltage U . Modern impedance measurement equipment enables the automatic application of the voltage input with variable frequencies, while the output impedance (current) responses

are collected as the frequency is scanned from very high (MHz - GHz) values, where timescale of the signal is in micro- and nanoseconds, to very low frequencies (μHz) with timescales of the order of hours.^[380] Consequently, it is possible to determine the full set of parameters when the measurement is carried out over a large number of frequencies.

The above described procedure for recording EIS data is named potentiostatic mode because a sinusoidal AC voltage perturbation is superimposed on a fixed DC voltage, applied to the investigated system, and the respective sinusoidal current response is logged.^[383] This measurement mode is recommended for most impedance experiments due to its extreme wide dynamic range and uncomplicated perturbation amplitude control.^[384] However, in the case of battery cells the potentiostatic procedure is likely to lead to systematic measurement errors since their equilibrium voltage is variable with respect to their SOC or may change upon the process control. Moreover, EIS measurements of battery cells are accomplishable under various test parameters such as temperature variations causing a significant drift of the potential. This would result in a dramatic drift of the DC voltage if the potentiostatic mode is utilized. As a fixed DC current is more often representative of the stationary state of a battery cell than a fixed voltage, a controlled DC current is better suited for EIS experiments with battery cells.^[383,385] Therefore, the galvanostatic mode is preferred for EIS measurements with electrochemical cells. This operation mode is conducted at a fixed DC current, which is superimposed by a sinusoidal current perturbation. The resulting sinusoidal potential response is recorded to determine the impedance.^[383] In the pseudo-galvanostatic mode, the DC current and the AC voltage amplitude are set. Similarly to the considerations for the true galvanostatic mode, DC current control is recommended for investigations of drifting systems. The given AC voltage amplitude ensures that the resulting voltage amplitude response values do neither become unwantedly small, nor unacceptably high in relation to the nonlinear properties. More precisely, the voltage amplitude is nearly equal for all frequencies.^[383,385,386]

The results obtained from an EIS measurement are usually depicted in a so-called Nyquist plot or complex-plane impedance plot, where the imaginary impedance part $-Z''$ (y-axis) is plotted vs. the real impedance part Z' (x-axis).^[387] Exemplarily, Figure 52 displays an arbitrary Nyquist plot.

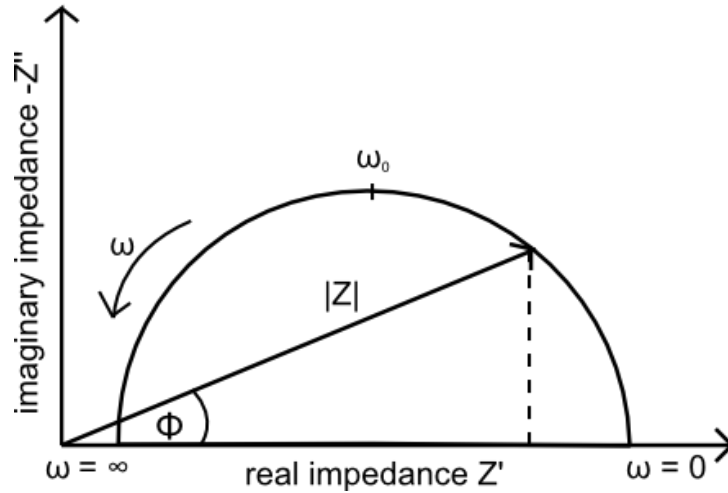


Figure 52 Representation of the Data of an EIS measurement in a Nyquist plot. With modifications from^[388].

Commonly, the complex conjugated form of Z is represented in this plot. Hence, the algebraic sign of Z'' is negative. Besides, it should be noted that each point on the Nyquist plot marks the impedance at one specific frequency, which increases from the right to the left. Nevertheless, it is not visible what frequency was used to record the data points. By means of this diagram the impedance is illustrated as a vector of length $|Z|$ and the phase angle Φ is positioned between this vector and the x-axis.^[388]

The analysis and interpretation of EIS measurements is typically accomplished with the help of equivalent electrical circuit models. Most of the circuit elements are standard electrical components like the resistor R_Ω , the capacitor C_F , and the inductor L_1 . In addition, there are elements, which are specifically defined for electrochemical processes. By the combination of these electrical components, a network of parallel or series connections is realized, and the individual electrochemical resistances are simulated. Table 5 lists the most common circuit elements, their circuit symbol, their impedance, and the corresponding Nyquist plot.


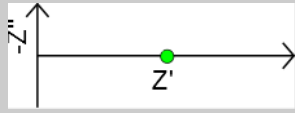

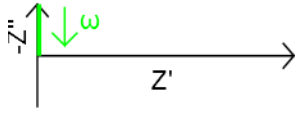
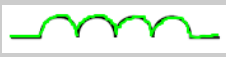
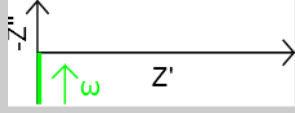

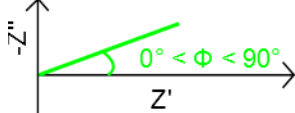

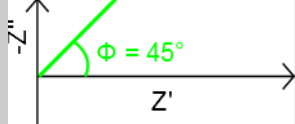

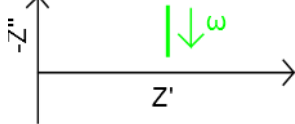

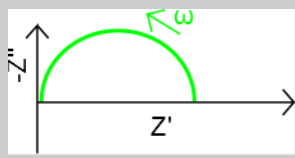
Circuit element	Circuit symbol	Impedance	Nyquist plot
Resistance R_Ω		$Z = R_\Omega$	
Capacitor C_F		$Z = \frac{1}{i \cdot \omega \cdot C_F}$	
Inductor L_1		$Z = i \cdot \omega \cdot L_1$	
Constant phase element (CPE)		$Z = Z_0 \cdot \frac{1}{(i \cdot \omega)^{d_e}}$	
Warburg W_1		$Z = Z_0 \cdot \frac{1}{(i \cdot \omega)^{0.5}}$	
Series connection RC element		$Z = Z_1 + Z_2$	
Parallel connection RC element		$Z = \left(\frac{1}{Z_1} + \frac{1}{Z_2} \right)^{-1}$	

Table 5 Most common circuit elements, their circuit symbol, their impedance, and the corresponding Nyquist plot. With modifications from^[389].

As can be seen, the resistance R_Ω is independent of frequency and has no imaginary part. According to Ohm's law, the current through a resistor is always in phase with the voltage ($\Phi = 0^\circ$).^[390] Regarding the capacitor, its impedance is a function of frequency and has only an imaginary part. Actually, a capacitor's impedance declines with increasing frequency. The current through a capacitor is phase shifted by -90° with respect to the voltage.^[390] In contrast, the impedance of an inductor raises with frequency and the respective current is phase shifted by 90° relating to the voltage. But like capacitors, inductors have only an imaginary impedance component.^[390] Considering the impedance formula of the constant phase element (CPE),

Z_0 is the impedance of an ideal capacitor and d_e is an empirical constant, ranging from 0 to 1. Interestingly, CPE behaves as a pure capacitor when $d_e = 1$, whereas it behaves as a pure resistor when $d_e = 0$. Moreover, the CPE becomes equivalent to the so-called Warburg element W_1 when $d_e = 0.5$. A Warburg impedance is featured by identical real and imaginary contributions, resulting in a phase angle of 45° .^[390]

As already mentioned, EIS is a valuable technique for the interpretation of fundamental electrochemical and electronic processes.^[378] Although, this method seems to be simple in principle, there are some noteworthy difficulties. An important complication of EIS analysis is based on the fact that the equivalent circuit elements represent ideal lumped-constant properties. An electrochemical cell is, however, not a perfect system, which renders an equivalent circuit that consists only of ideal electrical circuit components inadequate to describe the electrical response. This is why in practice distributed impedance elements such as CPEs are additionally used to simulate the experimental EIS data. These components significantly improve the fitting for a cell with distributed properties.^[378] Another major disadvantage of EIS is associated with the possible ambiguities in interpretation. There is a very large amount of possibilities for the composition of the equivalent circuit simulating the measured EIS data. Actually, an equivalent circuit including three or more circuit elements can often be rearranged in various ways and still yields exactly the same results.^[378] Thereto, Figure 53 shows a flow diagram suggesting a general characterization procedure for EIS studies involving material-electrode systems like battery cells.

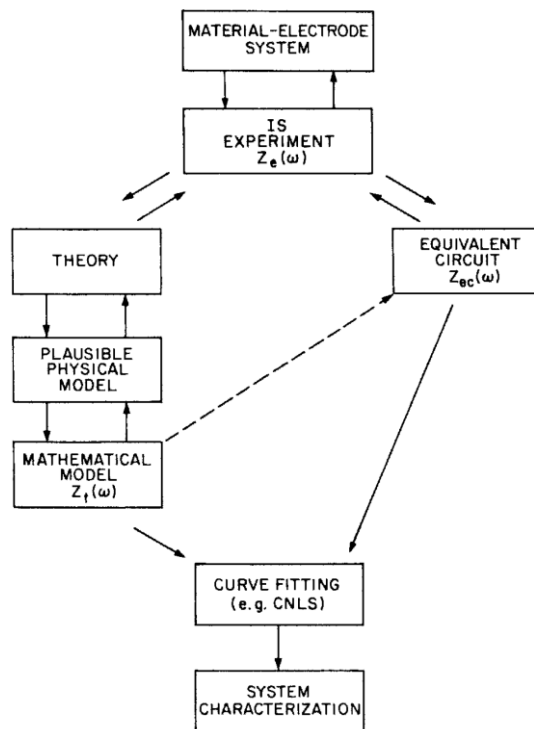


Figure 53 Flow diagram for the EIS measurement and characterization of a material-electrode system.^[378]

This means that some basic rules should be obeyed, while analyzing EIS spectra:^[378]

- utilization of the knowledge of the physical and chemical processes involved
- comparison of the equivalent circuits with the predictions of a physical model, which might yield simpler expressions for the elements of one of the circuits than for the others
- usage of the criterion of simplicity: given equally good fits, the circuit with the smallest number of elements is recommended
- implementation of several EIS measurements under different conditions (e.g. temperature variation or changes regarding the electrodes): the circuit in which the changes of the fitting parameters are least, and/or closest to the theoretical expectations should be preferred

Then, the impedance analysis of battery cells enables the creation of a working kinetic model of a whole cell, the evaluation of the effect of the cell components on material power capability, and even a comparison between different chemistries.^[378] Figure 54 displays the kinetic steps that occur in most LIBs and the corresponding impedance spectrum of intercalation materials, originally proposed by Barsoukov et al.^[378,391]

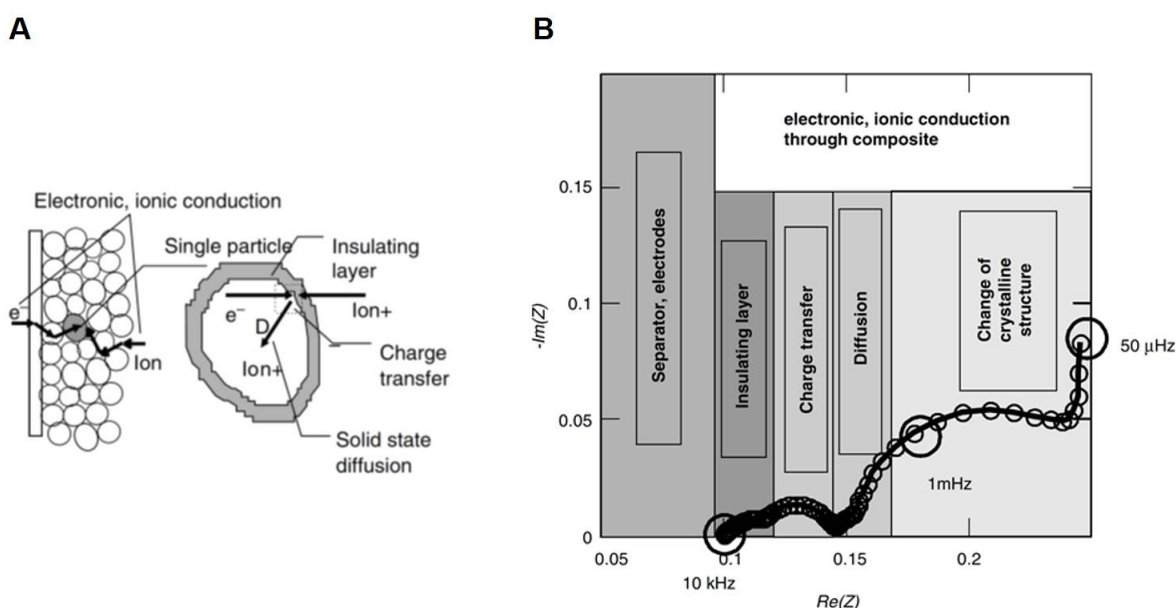


Figure 54 **A** Kinetic steps common in most LIBs. **B** Corresponding impedance spectrum of intercalation materials.^[378]

The processes are:^[253,378]

- ionic conduction through the electrolyte into the cavities between electrode particles and electronic conduction through the conductive part of the active layer
- lithium ion migration through the surface insulating layer of the active material denoting the resistance of the surface film (high frequency semi-circle in a Nyquist plot)
- electrochemical reactions at the electrolyte-film and at the film-particle interfaces signifying charge-transfer resistances, including electron transfer resistance on the electronic/ionic conduction boundary (middle to high frequency semi-circle in a Nyquist plot)
- lithium ion diffusion into the bulk of the active material particles via solid-state diffusion characterizing the Warburg impedance that appears in the low-frequency region of the Nyquist plot

Other processes, like for example, the change of the crystalline structure, are likely to become limiting at frequencies below 1 mHz.^[378] Conduction through the electrolyte, the porous separator, and the wires of the experimental setup are not depicted in Figure 54. They all dominate the high frequency features of an impedance spectrum above 10 kHz. At even higher frequencies, the inductance of the wires and electrode winding is noticeable.^[378]

In this work, EIS of formatted and cycled C//LiNi_{0.4}Mn_{1.6}O₄ pouch cells is accomplished to get a deeper comprehension of the mechanism of each electrolyte additive and the Al₂O₃ coating layers regarding the entire full cell.

3. Motivation and objective

As already mentioned in the introduction, LIBs for automotive applications are generally characterized according to the following five criteria: energy density, power density, lifetime, safety, and costs. The main advantage of high voltage spinel full cells in comparison to conventional NMC-111 full cells is their enhanced specific energy due to their high average potential of ca. 4.7 V vs. Li, which could lead to greater driving ranges for EVs.^[55] However, the main drawback of lithium nickel manganese oxide spinel full cells is their limited cycle life, which means a rapid decline of energy density with increasing cycle number. Figure 55 depicts the 1C cycling performances of a C//LiNi_{0.4}Mn_{1.6}O₄ and a C//NMC-111 full cell at room temperature. For the spinel cell a voltage window of 3.3 - 4.8 V was applied and the NMC cell was cycled between 3.0 and 4.2 V. The distinction in the voltage regions of the two cells is ascribed to the different activity of the redox couples of the CAMs. NMC-111 belongs to the group of layered lithium transition metal oxides and, therefore, offers other electrochemical features than the spinel material LiNi_{0.4}Mn_{1.6}O₄. Nonetheless, both performances are compared because NMC-111 is already used as a commercial CAM in LIBs in combination with a graphite anode and, thus, is a good indicator for the quality of the C//LiNi_{0.4}Mn_{1.6}O₄ cell.

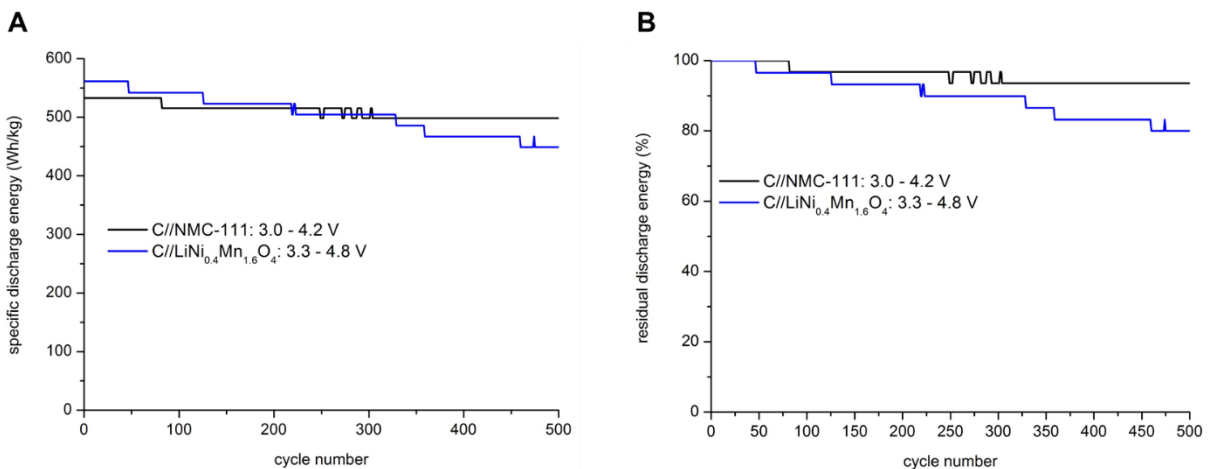


Figure 55 **A** Specific discharge energy vs. cycle number plots and **B** residual discharge energy vs. cycle number plots of a C//LiNi_{0.4}Mn_{1.6}O₄ and a C//NMC-111 full cell at room temperature at 1C. The spinel cell is cycled between 3.3 and 4.8 V and the NMC-111 cell is cycled between 3.0 and 4.2 V.

As can be seen, the cathode of the C//LiNi_{0.4}Mn_{1.6}O₄ full cell provides an initial specific energy of ca. 561 Wh/kg, whereas the cathode of the C//NMC-111 full cell delivers only 533 Wh/kg at the beginning of the cycling experiment. Nonetheless, the high voltage spinel cell exhibits a faster capacity fading than the NMC-111 cell. The residual discharge energy of the former cell is found to be 80% after 500 cycles. Hence, the actual energy density is only available in the first few cycles. This cycling behavior is insufficient with regard to automotive applications.

Therefore, the overall aim of this work is to stabilize the cycle life of high voltage spinel full cells in order that their high specific energy is accessible over a long-term cycling period.

As described in chapter 2.2 the two major issues concerning lithium nickel manganese oxide spinel full cells are transition metal dissolution and electrolyte oxidation. Figure 56 illustrates the possible degradation reactions occurring while cycling these cells. The base electrolyte (usually carbonate components) is oxidized at the surface of the charged cathode, whereupon a non-controlled, porous film is established. Due to the permeable structure of this SPI the electrolyte remains in contact with the composite cathode throughout cycling, which results in massive electrolyte decomposition and a thick SPI layer. Furthermore, HF can attack the spinel particles leading to Mn and Ni dissolution. The transition metals migrate through the electrolyte and accumulate on the anode surface causing severe SEI formation, depletion of active Li^+ , and lithium plating. Besides, HF might also cause the breakdown of the SEI by reacting with film components such as Li_2CO_3 . All these mechanisms contribute to the deterioration of high voltage spinel full cells.

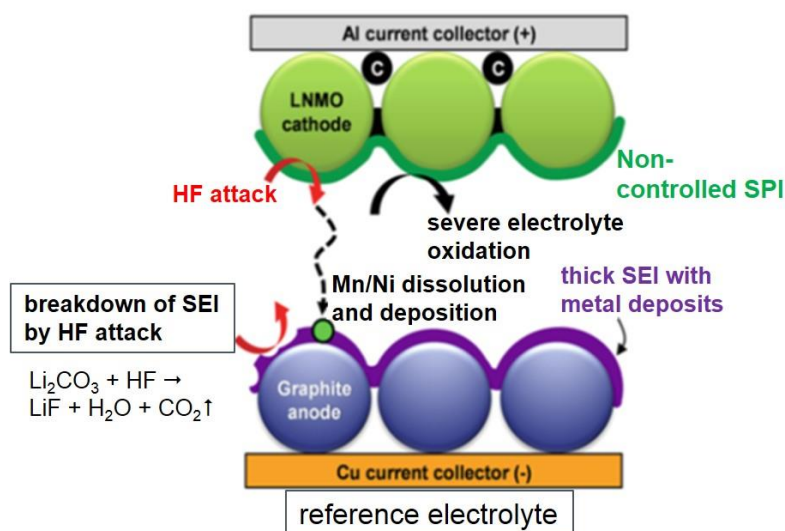


Figure 56 Schematic illustration of possible degradation mechanisms occurring upon cycling high voltage spinel full cells. With modifications from^[270].

Within this thesis the subsequent two strategies are pursued to alleviate the above named ageing phenomena and to improve the cycling stability of $\text{C}/\text{LiNi}_{0.4}\text{Mn}_{1.6}\text{O}_4$ full cells:

- electrolyte optimization by adding selected additives in certain concentrations to a standard electrolyte formulation
- application of Al_2O_3 coating layers on the electrodes (anode, cathode, and both) by a doctor blade process

The utilization of selected electrolyte additives in C//LiNi_{0.4}Mn_{1.6}O₄ cells is based on two ideas. On one hand, the additives are supposed to participate in the SPI generation to create a stable, covering, and preferably non-porous layer on the cathode surface. Then further electrolyte oxidation can be diminished since the direct contact between the composite cathode and the electrolyte components is suppressed. Hence, the additive-derived SPI remains rather thin and less Li⁺ are consumed. Likewise, a dense SPI should prohibit the interaction between HF and the CAM particles. In this manner, transition metal dissolution can be reduced. On the other hand, the additives can scavenge HF, PF₅, and/or H₂O from the electrolyte and, thereby, also weaken the Mn and Ni depletion. Figure 57 summarizes the possible functions of electrolyte additives in high voltage spinel full cells.

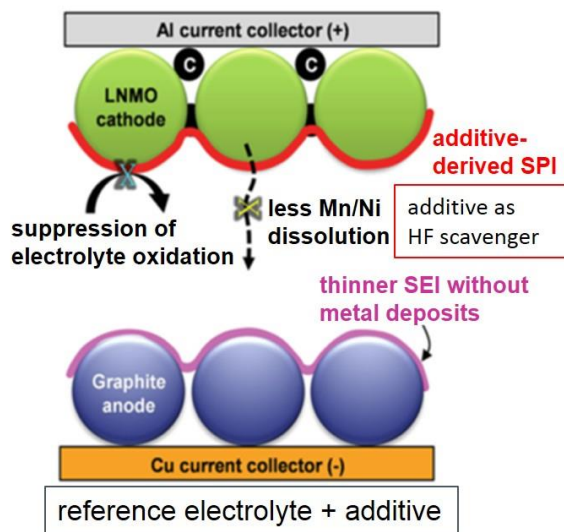


Figure 57 Schematic illustration of the possible functions of electrolyte additives in high voltage spinel full cells. With modifications from^[270].

The other approach, which involves the application of an aqueous Al₂O₃ slurry on a graphite anode, on a LiNi_{0.4}Mn_{1.6}O₄ cathode, or on both electrodes by a doctor blade process, aims at scavenging HF from the electrolyte solution (Figure 58).

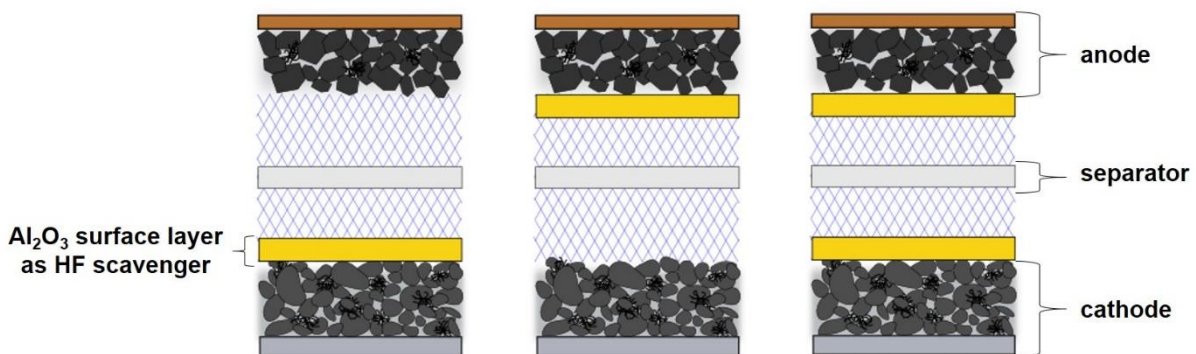


Figure 58 Schematic picture of the application locations of the Al₂O₃ layers within C//LiNi_{0.4}Mn_{1.6}O₄ full cells.

Thus, transition metal dissolution should be inhibited within the cell and less metallic Mn and Ni is expected to be found on the anode. Moreover, degradation of the CAM and excessive SEI production is intended to be avoided.

Initially, a reference system is established and a general electrochemical characterization of C//LiNi_{0.4}Mn_{1.6}O₄ pouch cells comprising the base electrolyte (1 M LiPF₆ in EC/EMC/DMC (1/1/1, w/w/w)) is accomplished in order to be able to examine and assess the ageing phenomena of LiNi_{0.4}Mn_{1.6}O₄ electrodes. For instance, the ideal voltage range of high voltage spinel full cells has to be verified and identified. The goal is to achieve the greatest possible energy density over cycle life. Besides, three-electrode measurements are essential to guarantee that the cell is balanced correctly. This means prevention of lithium plating on the anode and inhibition of an overdeintercalation/destabilization of the CAM. Both failure mechanisms must be excluded prior to further investigations.

When the reference system is determined, 1C CC/CV-cycling experiments are conducted at 45 °C with C//LiNi_{0.4}Mn_{1.6}O₄ pouch cells containing selected electrolyte additives or Al₂O₃ coating layers on the electrodes. The high temperature is chosen to accelerate the degradation processes within the cells and, hence, to observe the impact of the additives and the ceramic films on the cell performance earlier. Furthermore, rate capability tests are carried out with the electrolyte- and Al₂O₃-modified cells before (BOL) and after (EOL) the cycling stability tests at 45 °C. The purpose is to study the influence of the additives and the ceramic layers on the charge-transfer processes at the electrode surfaces under various current loads at different states of health.

XRD analyses of fresh and cycled spinel electrodes reveal structural changes and phase transitions upon cycling high voltage spinel full cells in dependence of the applied electrolyte additives. To complement the structural investigations, Raman spectra of completely discharged cathodes are recorded after formatting C//LiNi_{0.4}Mn_{1.6}O₄ full cells at 23 °C and after cycling these cells for 250 cycles at 45 °C without and with the utilized electrolyte additives and the Al₂O₃-coated electrodes. Moreover, Raman scattering is an appropriate method to determine the oxidation states of the transition metals within different structural phases.

The depletion of Mn and Ni ions from the composite cathodes is verified by ICP-OES and EDX measurements of the respective graphite anodes at 0% SOC after cycling the spinel pouch cells at 45 °C for 250 cycles. Thereby, the effect of the electrolyte additives and the ceramic films on the transition metal dissolution behavior is of particular interest.

XPS studies of formatted and cycled LiNi_{0.4}Mn_{1.6}O₄ electrodes are conducted to principally examine the chemical nature and the development of the interfacial layers between the cathodes and the diverse electrolyte formulations. The participation of each additive in the SPI structure is investigated and correlated with the electrochemical characteristics of high voltage spinel full cells.

Electrochemical impedance spectroscopy of formatted and cycled C//LiNi_{0.4}Mn_{1.6}O₄ pouch cells is carried out to get a deeper comprehension of the mechanisms of the electrolyte additives and the Al₂O₃ coating layers regarding the entire full cells. Then not only the cathode part of the lithium ion cell is taken into account, but the influence of the anode side is also considered. Finally, the cycling performance of C//LiNi_{0.4}Mn_{1.6}O₄ pouch cells is further improved by applying the results obtained from the electrochemical, microscopic, and spectroscopic analyses.

4. Experimental conditions

4.1 Chemicals and materials

Electrode materials

The cathode active material powder ($\text{LiMn}_{1.6}\text{Ni}_{0.4}\text{O}_4$) was provided by Clariant (now referred to as Johnson Matthey Battery Materials GmbH). Carbon black C-ENERGY™ SUPER C65 (Brunauer-Emmett-Teller (BET) surface area = $62 \text{ m}^2\text{g}^{-1}$, ash content = 0.01 wt%) was purchased from Timcal. Polyvinylidene fluoride (PVDF) binder Kynar™ ADX-161 was purchased from Arkema. N-ethyl-pyrrolidon (NEP) was supplied by BASF. Aluminum foil A1N30H18 (15 μm thickness) was purchased from Nippon Foil Mfg. Co., Ltd. The graphite anode was provided by VOLKSWAGEN VARTA Microbattery Forschungsgesellschaft mbH & Co. KG.

Electrolyte chemicals

The reference electrolyte solution 1 M LiPF_6 in EC/EMC/DMC (1/1/1, w/w/w) was purchased from BASF with an initial water content of < 7 ppm and an initial HF content of < 20 ppm. The following additives were utilized for the development of new electrolyte formulations without further purification:

Additive abbr.	Additive name	Supplier
FEC	fluoroethylene carbonate	Novolyte Technologies, Inc. (now referred to as BASF)
HFiP	tris(1,1,1,3,3,3-hexafluoroisopropyl) phosphate	Suzhou Fluolyte Co., LTD.
HMDS	hexamethyldisilazane	Sigma-Aldrich Co. LLC.
LiBOB	lithium bis(oxalato)borate	Chemetall GmbH
LiTFSI	lithium bis(trifluoromethanesulfonyl)imide	3M
SA	succinic anhydride	Sigma-Aldrich Co. LLC.
SEN	sebaconitrile	Merck KGaA
TEHP	tris(2-ethylhexyl) phosphate	Merck KGaA
TFPi	tris(2,2,2-trifluoroethyl) phosphite	Sigma-Aldrich Co. LLC.
TMP	trimethyl phosphate	Sigma-Aldrich Co. LLC.
TTSP	tris(trimethylsilyl) phosphate	TCI Deutschland GmbH

Table 6 Utilized additives and corresponding suppliers.

Separator

The separator VS1220A1 was purchased from Teijin Limited. Its thickness and its porosity were 20 μm and 48%, respectively.

Other cell materials

Chromated aluminum current collectors were purchased from Laminazione Sottile S.p.A and nickel current collectors were purchased from AMETEK, Inc. Polyethylene lamination pads were supplied by Showa Denko Europe GmbH. The adhesive tape polyimide anti-acid, anti-alkali was purchased from Shenzhen Meixin Electronics Co., Ltd. The pouch foil was provided by Showa Denko Europe GmbH. Lithium metal with a thickness of 140 μm for the RE was provided by Chemetall GmbH.

4.2 Instruments

- **CC/CV-cycling and differential capacity:** potentiostat-galvanostat unloading installation MCCD from VARTA Microbattery GmbH; potentiostat-galvanostat multifunction SERIES 4000 Automated Test System from Maccor, Inc.
- **Three-electrode measurement:** multifunction SERIES 4000 Automated Test System from Maccor, Inc.
- **X-ray diffraction spectroscopy:** X-ray diffractometer theta/theta D5000 from Siemens with a Bragg-Brentano copper tube (40 kV and 40 mA) and a secondary graphite-monochromator
- **Raman spectroscopy:** FT-Raman microscope LabRAM ARAMIS from Horiba Jobin Yvon GmbH with a liquid N₂-cooled detector; excitation wavelength 632 nm (He-Ne-laser with 17 mW)
- **Inductively coupled plasma-optical emission spectroscopy:** 720-ES ICP optical emission spectrometer from Varian Inc.
- **Scanning electron microscopy:** scanning electron microscope Phenom ProX from Phenom-World equipped with an energy dispersive X-ray spectrometer; field-emission scanning electron microscope Vega TS 5136 XM from TESCAN equipped with an energy dispersive X-ray analysis unit AZ-TecEnergy Standard from Oxford Instruments
- **X-ray photoelectron spectroscopy:** X-ray photoelectron spectroscope PHI Model 5000 from Physical Electronics, Inc. included in the DAISY-BAT (DArmstädter Integriertes SYstem für BATterieforschung)
- **Electrochemical impedance spectroscopy:** potentiostat-galvanostat ZENNIUM with a frequency response analyzer (FRA) unit with a frequency range up to 4 MHz at ± 2.5 A and at a compliance voltage of ± 14 V from ZAHNER-elektrik GmbH & Co. KG
- **Glove box:** MB-200B modular glovebox workstation with vacuum oven (250 °C) from MBRAUN; H₂O < 1 ppm; O₂ < 1 ppm
- **Rheometer:** Kinexus pro+ from Malvern Instruments Ltd.
- **Calender:** type EW 160 · 200 from Bühler & Co. GmbH

4.3 Sample preparation and measuring conditions

Cathode preparation

Cathodes were prepared by coating an aluminum foil with a slurry composed of 94 wt% $\text{LiNi}_{0.4}\text{Mn}_{1.6}\text{O}_4$, 3 wt% SUPER C65, and 2 wt% KynarTM ADX-161. First, the binder was dissolved in NEP. Then, carbon black was added to this binder solution, while stirring the suspension with a dissolver at 400 rpm. After stirring for 45 min at 1,800 rpm, the active material was added and the whole suspension was stirred for 2 h at 1,400 rpm. Next, the paste was casted onto the aluminum foil with a doctor blade and the cathodes were dried for 0.5 h at 120 °C. Finally, the cathodes were calendered yielding a film thickness of ca. 70 μm and an electrode density of ca. 2.9 gcm^{-3} .

Cell assembly of two-electrode pouch cells

$\text{LiNi}_{0.4}\text{Mn}_{1.6}\text{O}_4$ cathodes and graphite anodes of 3.1 cm x 5.0 cm and 3.25 cm x 5.15 cm, respectively, were punched and dried at 150 °C for 15 h and 130 °C for 5 h under vacuum, respectively. Chromated aluminum and nickel current collectors were welded to the cathode and anode, respectively, and the welding points were masked with polyimide adhesive tape. Separators of 3.6 cm x 5.4 cm were cut by a laser. The electrodes and the separator were stacked (anode - separator - cathode) and put into a pouch. Pouches containing the electrodes and the separator were dried at 95 °C for 15 h under vacuum and inserted into a glove box. 400 μL electrolyte was filled into the pouches before the cells were sealed. The final size of a pouch cell was: 0.5 mm thickness, 35 mm width, and 62 mm length.

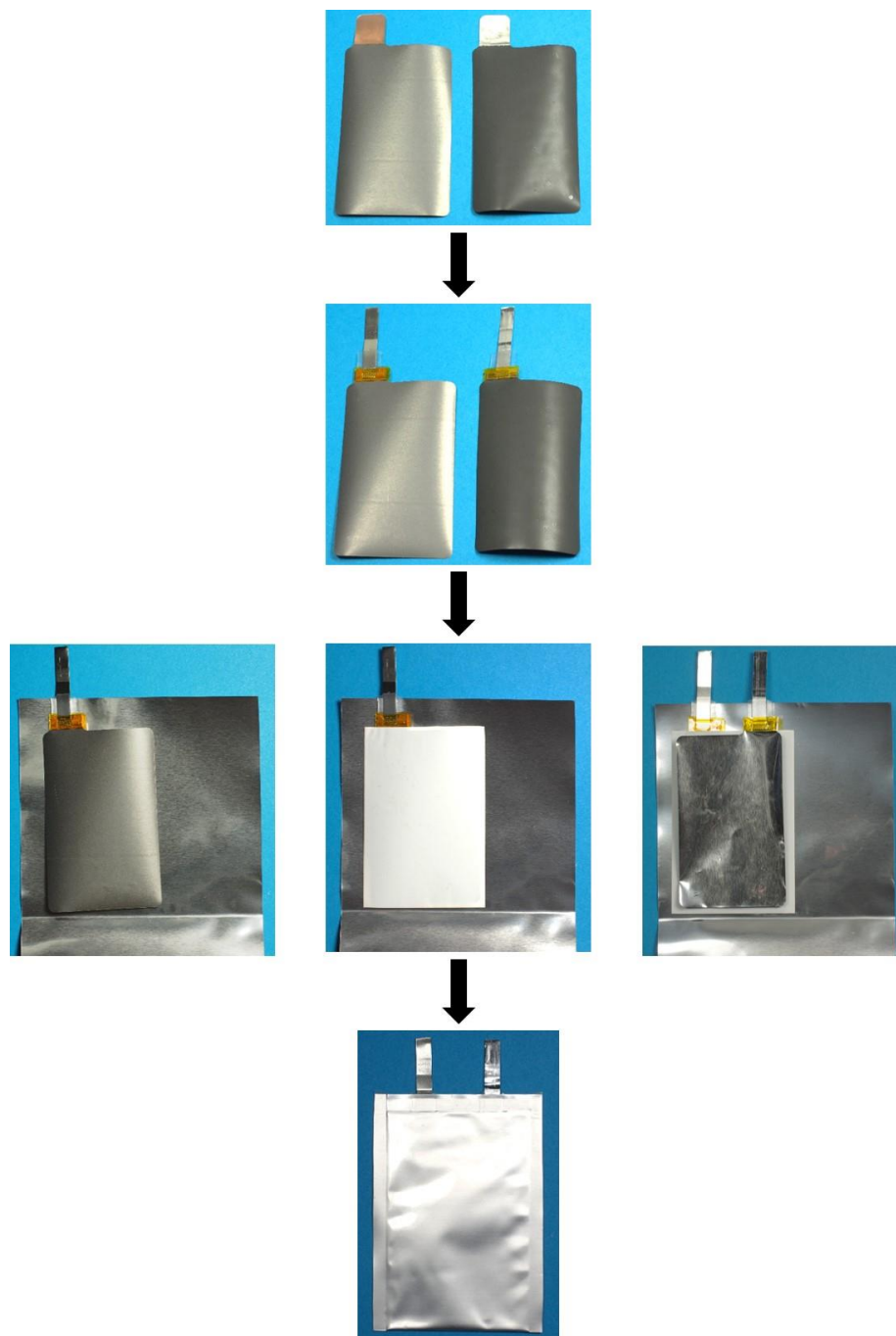


Figure 59 Cell assembly of a two-electrode pouch cell.

Cell assembly of three-electrode pouch cells

Generally, the three-electrode pouch cells were assembled similarly to the two-electrode pouch cells. However, in addition, a RE was built and inserted into the full cell. Thereto, a nickel current collector of 50 mm x 4 mm size and 70 μm thickness was laminated by polypropylene except for the tip. Then, the collector and some separator sheets of 10 mm x 10 mm were dried at 95 $^{\circ}\text{C}$ for 15 h under vacuum. The subsequent RE preparation was made in a glove box. Around the bare tip of the current collector a lithium sheet of 7 mm x 7 mm was folded, which was further encapsulated by a separator sheet. The separator was fixed with a polyimide

adhesive tape. This RE was placed immediately adjacent to the negative electrode in the pouch cell without direct contact. In fact, the RE was in direct contact with the separator positioned between the anode and the cathode.

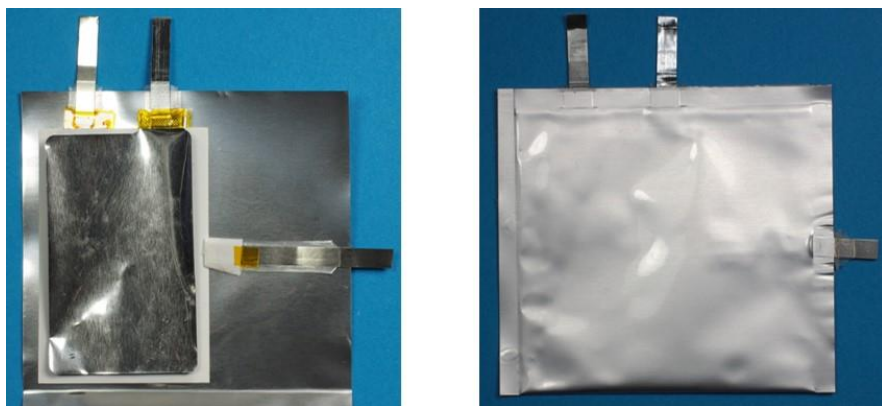


Figure 60 Three-electrode arrangement.

CC/CV-cycling

Electrochemical characterization was performed both with two-electrode and three-electrode pouch cells. Regarding the latter, a separate auxiliary voltage input was used for monitoring the potential of the positive electrode, which was cycled versus the negative electrode. The potential of the anode referred to Li metal was then obtained by subtracting the total voltage of the full cell from the potential of the cathode.

Generally, all pouch cells were formatted in a voltage window of 3.3 - 4.8 V at 0.1C at 23 °C for two cycles, followed by three 1C cycles between 3.3 and 4.8 V at 23 °C. After this formation procedure the cells were cycled with a constant current in the voltage range from 3.3 to 4.8 V at 1C at 45 °C. Thereby, a constant voltage step was applied at the cutoff-voltages of 3.3 and 4.8 V. Indeed, the end-of-discharge-voltage and the end-of-charge-voltage were kept constant until the current decreased to 0.05C. The current for 1C could be determined by the product of the theoretical specific capacity and the absolute mass of the CAM. Variations in the cycling parameters are directly mentioned in the text. The differential capacity dQ/dU was directly determined by the program software MIMSciEnt.

X-ray diffraction

XRD diffraction of fully discharged $\text{LiNi}_{0.4}\text{Mn}_{1.6}\text{O}_4$ cathodes (0% SOC) was accomplished after 250 cycles at 45 °C to investigate changes of the spinel structure during cycling C// $\text{LiNi}_{0.4}\text{Mn}_{1.6}\text{O}_4$ pouch cells without and with various electrolyte additives. The cycled cells were disassembled in a discharged state within a glove box and the cathodes were washed with dimethyl carbonate as well as dried over night at room temperature under argon atmosphere.

The XRD patterns were collected in reflection mode in an angular range between 10 and 120 ° in step scan mode (step size 0.03 °, counting time 12 s/step). The divergence aperture was 0.5 °. Scattered beam slit and detector slit were 1 and 0.2 mm, respectively. XRD analysis was done by the method “Whole Powder Pattern Decomposition (WPPD)” after Pawley.^[392] The XRD measurements were carried out by the Zentrum für Sonnenenergie- und Wasserstoffforschung Baden-Württemberg (ZSW).

Raman spectroscopy

Raman spectroscopy was conducted with fully discharged $\text{LiNi}_{0.4}\text{Mn}_{1.6}\text{O}_4$ cathodes (0% SOC) after full cell formation at 23 °C and after 250 cycles at 45 °C without and with the utilized electrolyte additives and the Al_2O_3 coating layers. The formatted and cycled cells were disassembled in a discharged state within a glove box and the cathodes were washed with dimethyl carbonate as well as dried over night at room temperature under argon atmosphere. An He-Ne-laser with an excitation wavelength of 632 nm and a power of 17 mW was applied to the sample surface. The diameter of the laser beam at the sample was 0.9 μm . The measurements were taken with a neutral density filter (1% permeability) and a confocal microscope with a 100 μm aperture giving a lateral resolution of 0.4 μm . The hole and slit were adjusted to 150 and 112 μm , respectively. The Raman spectroscopic measurements were carried out by Volkswagen AG. The obtained Raman spectra were fitted with OriginPro 8 to a Lorentz function.

Inductively coupled plasma-optical emission spectroscopy

ICP-OES measurements of graphite anodes at 0% SOC were conducted after cycling C// $\text{LiNi}_{0.4}\text{Mn}_{1.6}\text{O}_4$ pouch cells at 45 °C for 250 cycles in the voltage window of 3.3 - 4.8 V. The cycled cells were disassembled in a discharged state within a glove box and the anodes were washed with dimethyl carbonate as well as dried over night at room temperature under argon atmosphere. The anode paste/powder was scrapped off the copper current collector. 1 g of this anode powder was dissolved in 10 mL concentrated hydrochloric acid in order to perform the analyses.

Scanning electron microscopy and energy dispersive spectroscopy

SEM micrographs of the $\text{LiNi}_{0.4}\text{Mn}_{1.6}\text{O}_4$ raw substance and the calendered $\text{LiNi}_{0.4}\text{Mn}_{1.6}\text{O}_4$ cathodes were utilized to investigate particle and electrode morphology, respectively. The sample preparation includes either spreading a small portion of the CAM powder onto a conductive carbon tape on a SEM pin stub, which is later mounted on a specimen holder or directly mounting the cathode on a sample holder. After introducing the sample into the

chamber, evacuation took place and images were taken. The acceleration voltage and spot size were varied for different experiments and are given in the bar below each image. EDX of graphite anodes was accomplished to verify the results obtained by ICP-OES. Sample preparation was the same as in case of $\text{LiNi}_{0.4}\text{Mn}_{1.6}\text{O}_4$ cathodes.

X-ray photoelectron spectroscopy

XPS analyses were applied to principally study the chemical nature and the development of the interfacial layers between the $\text{LiNi}_{0.4}\text{Mn}_{1.6}\text{O}_4$ electrodes and the different electrolyte formulations after formatting C// $\text{LiNi}_{0.4}\text{Mn}_{1.6}\text{O}_4$ pouch cells containing various electrolyte additives at 23 °C and after cycling these cells for 250 cycles at 45 °C. The formatted and cycled cells were disassembled in a discharged state within a glove box and the cathodes were washed with dimethyl carbonate as well as dried over night at room temperature under vacuum. Then, the cathodes were transferred into the ultra-high vacuum (UHV) chamber for the XPS experiments without any contact to air or moisture by using a transfer chamber. The base pressure in the UHV chamber was about 10^{-10} mbar. For the XPS measurements a focused monochromatic Al K_{α} radiation ($hf = 1,486.6$ eV) was utilized. The diameter of the X-ray illuminated area was 200 μm . The XPS spectra were collected at a pass energy of 23.5 eV. The spectrometer was calibrated using the photoemission line Ag $3d_{5/2}$ with a binding energy of 368.3 eV. All XPS measurements were carried out by the Darmstadt University of Technology. The complete measurements setup is shown in Figure 61.

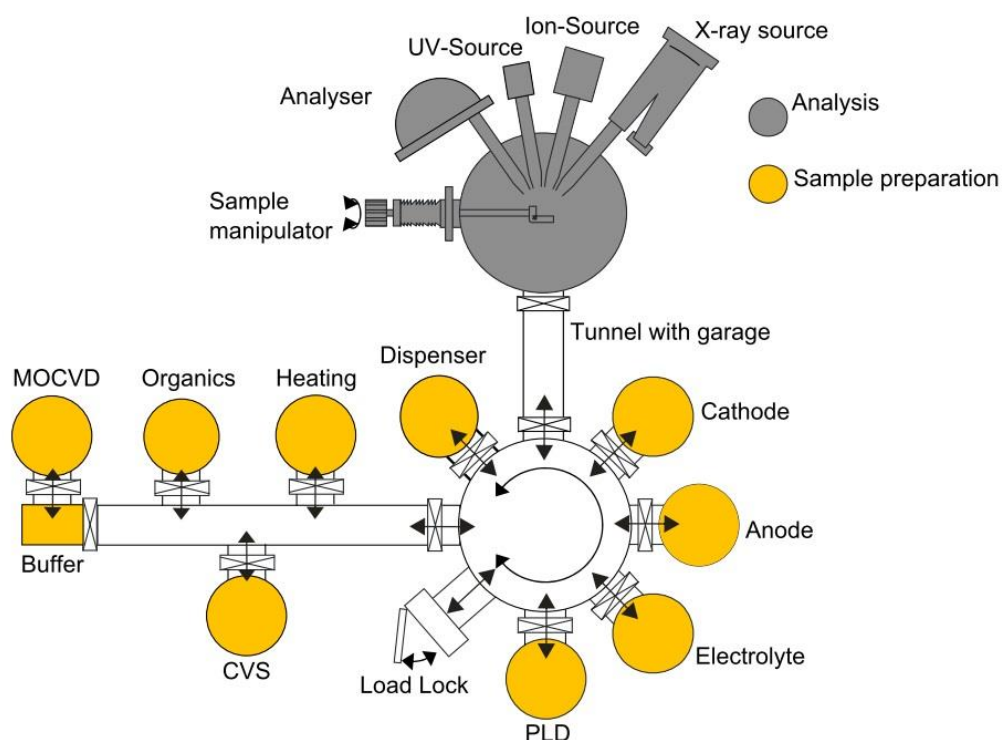


Figure 61 DArmstädter Integriertes SYstem für BATterieforschung (DAISY-BAT).^[393]

The background under the XPS spectra was subtracted using the Shirley-type function. The photoelectron peak positions and areas were obtained by a weighed least-square fitting of model curves (70% Gaussian, 30% Lorentzian) to the experimental data. The peak fitting procedure was performed with CasaXPS software.

Electrochemical impedance spectroscopy

EIS measurements were operated with formatted and cycled C//LiNi_{0.4}Mn_{1.6}O₄ pouch cells using the pseudo-galvanostatic mode. The examinations were carried out at 23 °C using an AC 10 mV voltage amplitude and a 1 μ A DC current. The frequency range ranged from 1 MHz to 50 mHz. All EIS measurements were carried out at 80% SOC of the cells. Nyquist diagrams were fit with ZView.

5. Results and discussion

5.1 Compositional and morphological investigation of $\text{LiNi}_{0.4}\text{Mn}_{1.6}\text{O}_4$ as cathode active material

The lithium nickel manganese oxide spinel powder was analyzed by ICP-OES. The elemental composition of the material is $\text{LiMn}_{1.59}\text{Ni}_{0.38}\text{O}_4$, which is in good agreement with the theoretically expected stoichiometry $\text{LiMn}_{1.6}\text{Ni}_{0.4}\text{O}_4$.

SEM micrographs of the starting material and the related particle size distribution are depicted in Figure 62. As can be seen, the sample is composed of granules with well-defined crystalline octahedral particles. Consequently, a rather broad spread of particle sizes is observed. The primary particles have diameters of 0.2 - 2.0 μm . In contrast, the granules strongly differ in size and are in the range of 2 - 50 μm . Thereby, most of them adopt diameters between 5 and 25 μm .

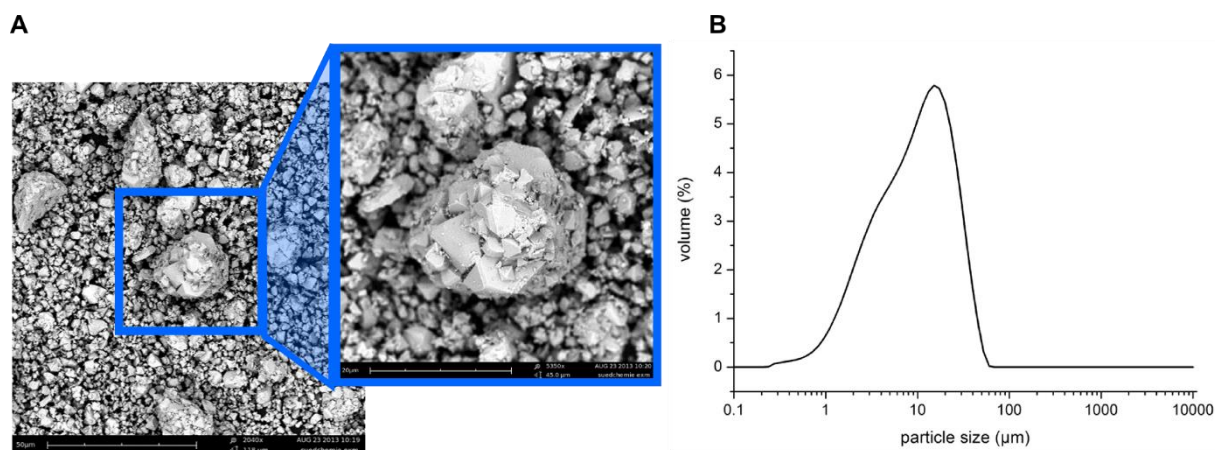


Figure 62 A SEM images of $\text{LiNi}_{0.4}\text{Mn}_{1.6}\text{O}_4$ powder particles with 2,000- and 5,000-times amplification. B Particle size distribution of the $\text{LiNi}_{0.4}\text{Mn}_{1.6}\text{O}_4$ powder.

SEM images of calendered $\text{LiNi}_{0.4}\text{Mn}_{1.6}\text{O}_4$ electrodes are shown in Figure 63. They reveal a homogenous embedding of the spinel particles in the carbon-binder matrix. Due to the octahedral shape, small size, and low crystalline density (4.2 g cm^{-3})^[394] of the particles, the porosity of the cathode film is lower compared to electrode films with spherical NMC-111 particles. The overall porosity of the cathode film, calculated from the raw densities, is around 30% and offers sufficient wettability of the spinel electrodes. The cathode film has a thickness of ca. 70 μm after calendering and the electrode density amounts to 2.9 g cm^{-3} . The cross-sections of the cathodes demonstrate that the spinel particles are, to some extent, pressed into the aluminum foil, affording good electronic conductivity.

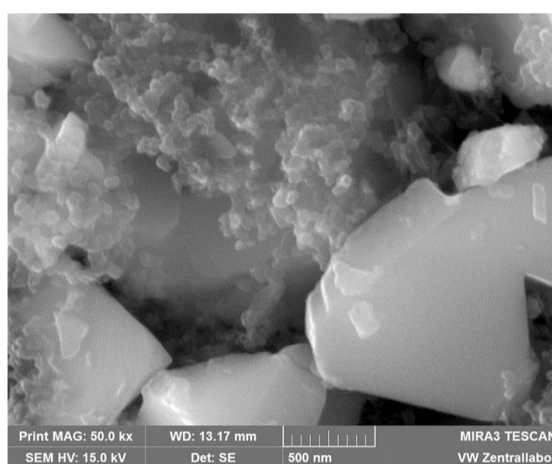
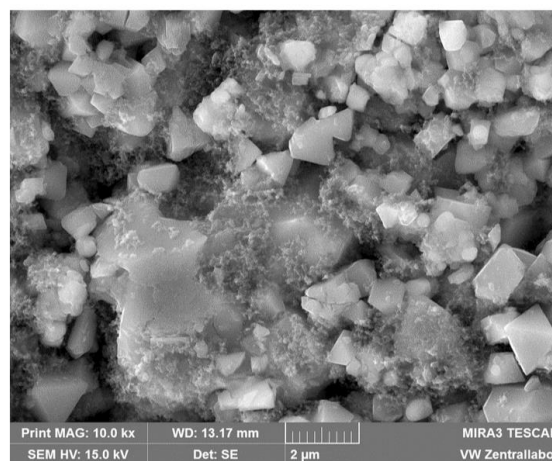
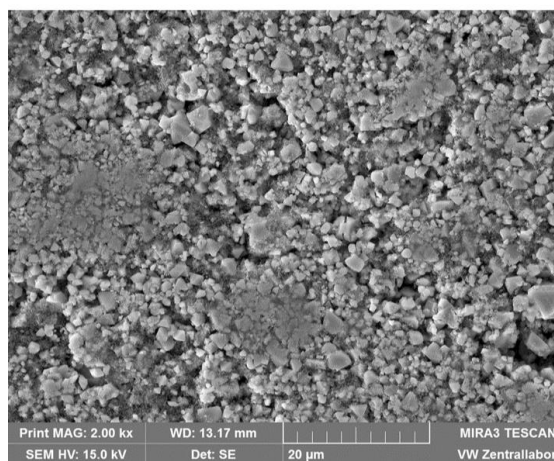
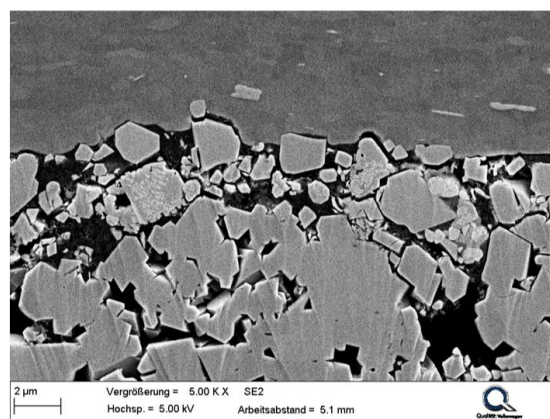
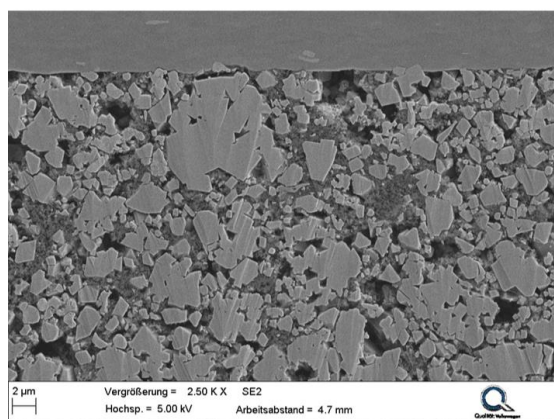
5.1 Compositional and morphological investigation of $\text{LiNi}_{0.4}\text{Mn}_{1.6}\text{O}_4$ as cathode active material**A****B**

Figure 63 SEM images of a $\text{LiNi}_{0.4}\text{Mn}_{1.6}\text{O}_4$ composite electrode. **A** View of the electrode surface with 2,000-, 10,000- and 50,000-times amplification. **B** Cross-sections of the electrode with 2,500- and 5,000-times amplification.

5.2 Electrochemical characterization of C//LiNi_{0.4}Mn_{1.6}O₄ full cells

5.2.1 Determination of the reference system and general electrochemical response of LiNi_{0.4}Mn_{1.6}O₄ cathodes

In order to investigate and evaluate ageing phenomena of LiNi_{0.4}Mn_{1.6}O₄ cathodes, a reference system has to be established. In this work the electrodes, the separator, the electrolyte, and the cell assembly outlined in chapter 4 are set as references. Subsequently, a general electrochemical characterization of the spinel cathode is accomplished and the most suitable operating voltage range for C//LiNi_{0.4}Mn_{1.6}O₆ full cells is determined.

Differential capacity plot

Figure 64 displays the calculated differential capacity dQ/dU profile of a C//LiNi_{0.4}Mn_{1.6}O₆ full cell at room temperature. The cell was cycled two times in a region of 3.3 - 4.8 V prior to the actual measurement between 2.0 and 4.9 V at a current density of 1C. The voltage window is extended to ensure that the entire electrochemical activity of the spinel is covered.

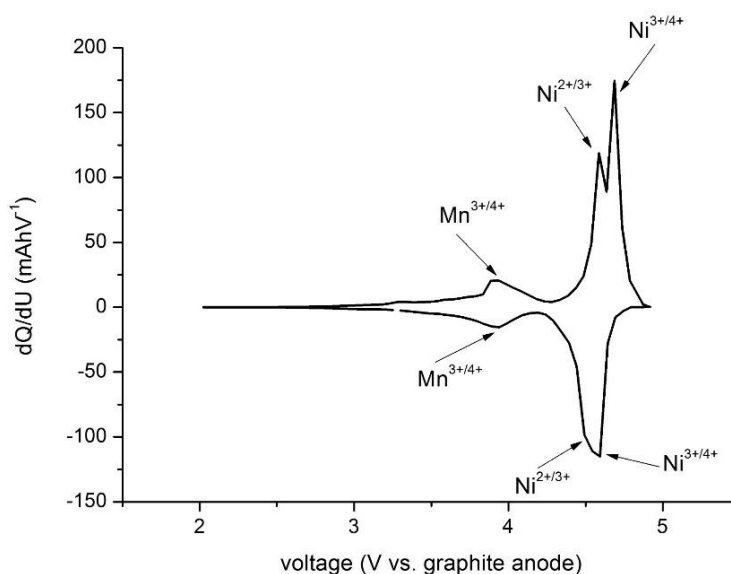


Figure 64 Calculated differential capacity dQ/dU profile of a C//LiNi_{0.4}Mn_{1.6}O₆ full cell at room temperature between 2.0 and 4.9 V at 1C.

As expected, three distinctive peaks are identified. Removal of Li from the tetrahedral sites of the spinel framework initially probes the oxidation of $\text{Mn}^{3+} \rightarrow \text{Mn}^{4+}$ around 3.9 V vs graphite. Further Li deintercalation leads to the oxidation of $\text{Ni}^{2+} \rightarrow \text{Ni}^{3+}$ and $\text{Ni}^{3+} \rightarrow \text{Ni}^{4+}$. The corresponding anodic peaks are found at 4.6 and 4.7 V vs. graphite, respectively. During discharging all oxidized species are reduced to their original oxidation state. The reaction of the $\text{Mn}^{3+/4+}$ redox couple is still detected at 3.9 V vs. graphite, whereas the two cathodic nickel

peaks are shifted towards lower voltages of 4.5 and 4.6 V vs. graphite and are not as well resolved as the associated anodic peaks. This behavior is related to polarization effects and is more pronounced at high C-rates. It has been pointed out that the Ni^{2+/3+} and Ni^{3+/4+} redox energies are strongly influenced by the adjacent ionic environment.^[395] For example, ordered LiNi_{0.5}Mn_{1.5}O₄ spinels exhibit a larger displacement in the voltage of the oxidation and reduction reactions than disordered spinels induced by a diminished electronic and ionic conductivity due to the considerably decreased Mn³⁺ concentration.^[396] Overall, the disordered LiNi_{0.4}Mn_{1.6}O₄ spinel shows good reversibility upon intercalation/deintercalation. Since the more exact chemical formula of this spinel is expressed by LiNi_{0.4}²⁺Mn_{0.2}³⁺Mn_{1.4}⁴⁺O₄, it can be concluded that only about 20% of the capacity arises from the oxidation of Mn³⁺ to Mn⁴⁺ and the remaining 80% can be ascribed to the Ni^{2+/4+} redox couple. According to the literature, the charge/discharge process of LiNi_{0.5}Mn_{1.5}O₄ occurs via two reversible phase transitions between three cubic phases related to the lithium content and the different oxidation states of the transition metals.^[230,233,234,397] The group of Baddour-Hadjean described two cubic/cubic phase mechanisms for Li_yNi_{0.4}Mn_{1.6}O₄ from y = 1 to y = 0.^[349] However, the reported results are partially conflicting as they depend on the examined sample (see chapter 2.2.2).

CC/CV-cycling

Next, CC/CV-cycling experiments were conducted with C//LiNi_{0.4}Mn_{1.6}O₆ full cells at room temperature (Figure 65). Various voltage ranges were applied at a charge-discharge rate of 1C to verify the one enabling the best cycle life and specific capacity.

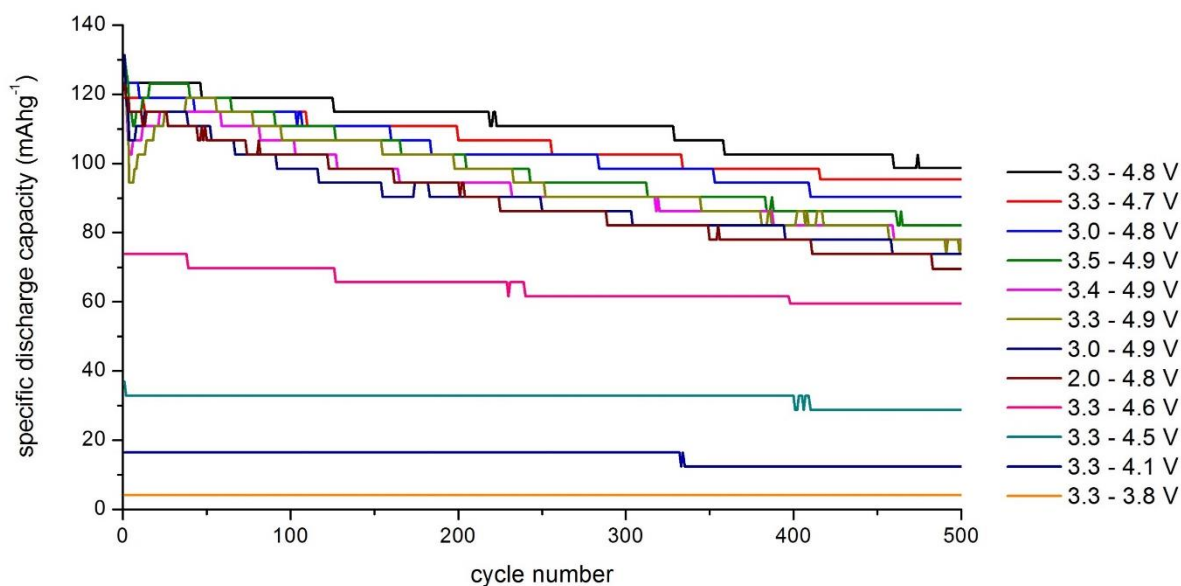


Figure 65 Specific discharge capacity vs. cycle number plots of C//LiNi_{0.4}Mn_{1.6}O₆ full cells at 1C and at room temperature in dependence of the voltage ranges.

Low end-of-charge-voltages down to 3.8 V were also studied to demonstrate the beginning of the contribution of the Mn^{3+/4+} and Ni^{2+/4+} couples to the capacity of the cell chemistry. Merely a negligible specific discharge capacity of ca. 4.1 mAhg⁻¹ is noticed for the cell cycled in the voltage window from 3.3 to 3.8 V because the CAM is not electrochemically triggered in this section. Nevertheless, a minimal capacity is observed owing to the commencing oxidation of Mn³⁺ and the existence of a minor amount of movable lithium ions in the electrolyte. Slightly larger specific capacities of 16.4 and 36.9 mAhg⁻¹ are determined for the cutoff voltages of 4.1 and 4.5 V, respectively. This is due to the reaction of Mn³⁺ to Mn⁴⁺, which is progressively actuated. As illustrated in Figure 64, the Ni^{2+/3+} redox chemistry is not active until 4.6 V are reached. That explains the higher capacity of 73.8 mAhg⁻¹ for the region of 3.3 - 4.6 V. Further raising the end-of-charge-voltage to 4.7, 4.8, and 4.9 V results in full activation of the CAM including the Ni^{3+/4+} redox couple and enhanced specific capacities of 118.9, 123.3, and 131.1 mAhg⁻¹ are registered, respectively. Regarding the cells examined between 3.3 V and the stated diverse charge cutoff voltages, more serious capacity fading is perceived with elevated end-of-charge-voltages. This might be due to several factors such as intensified electrolyte, binder, and carbon black decomposition and strengthened transition metal dissolution. Moreover, the small-sized primary particles of LiNi_{0.4}Mn_{1.6}O₄ offer a high surface area, which increases the probability for undesirable side reactions with the electrolyte.

In Figure 65, a few cells reveal a sudden decay and then a growth of the specific capacity in the first cycles after formation. On one hand, it is possible that the porous cathode is not completely wetted at the beginning of the electrochemical experiment. While cycling the electrolyte penetrates into the pores of CAM and, therefore, additional capacity is available. On the other hand, the repeated steps of lithium insertion and extraction cause changes of the LiNi_{0.4}Mn_{1.6}O₄ structure. More precisely, an increase of the pore volumes takes place and, as a consequence, the electrolyte diffuses deeper into the structure of the CAM. Thus, more matter is involved in the redox reactions leading to supplementary capacity.

Apart from the discharge cutoff voltage of 3.3 V, also lower and higher end-of-discharge-voltages in combination with 4.8 and 4.9 V charge cutoff voltages are tested. This is done to validate the most appropriate cycling range for C//LiNi_{0.4}Mn_{1.6}O₄ full cells and to analyze to what extent the cell capacity is really influenced by the redox chemistries. Altogether, the cycling stability deteriorates from 3.3 - 4.8 to 3.3 - 4.7, 3.0 - 4.8, 3.5 - 4.9, 3.4 - 4.9, 3.3 - 4.9, 3.0 - 4.9, and 2.0 - 4.8 V. Although the cells examined up to 4.9 V show a higher specific capacity in the first cycle of the CC/CV experiment than the ones with reduced end-of-charge-voltages, they suffer from a stronger capacity decay. The selected cutoff discharge voltages have no impact on the initial capacity confirming that the Mn^{3+/4+} couple is primarily active above 3.5 V vs. graphite anode. But the end-of-discharge-voltages significantly

affect the cell life, which declines from 3.5 to 2.0 V. The reason for this relates to the anode side of the cell. A more detailed elucidation is given later on.

Obviously, the cell operated in a voltage window of 3.3 - 4.8 V delivers the best performance of all measured cells. It still provides a specific discharge capacity of 98.6 mAhg⁻¹ after 500 cycles, i.e. a capacity retention of 80%. This is quite impressive. Most reports show severe capacity losses for full cells containing a graphite anode and a high voltage spinel electrode even at room temperature, at low current densities, or comprising electrodes with low active material loadings or little specific capacity densities.^[1-6] Most likely, the carbonate-based standard electrolyte formulation has already formed a stable passivation layer on the cathode surface and, thus, electrolyte oxidation is possibly suppressed. Chapter 5.5 will give detailed information on this subject.

Specific energy and voltage profile

Nonetheless, the cycling behavior is not the only aspect with respect to the selection of a convenient voltage region. The specific energy of the CAM, which is the product of the specific discharge capacity multiplied by the average voltage, has to be considered, too. In this context, just the cells tested with charge cutoff voltages of 4.8 and 4.9 V are evaluated more carefully. Table 7 summarizes the main electrochemical properties of C//LiNi_{0.4}Mn_{1.6}O₄ full cells investigated under the different voltage applications. Figure 66 depicts the associated discharge profiles of the first cycle after formation at 1C and room temperature and the related specific energies. All cells feature a long, flat plateau present at ca. 4.6 - 4.5 V characterizing the reduction of Ni⁴⁺ → Ni²⁺ and a plateau at 4.0 - 3.8 V originating from the Mn^{3+/4+} activity in agreement with Figure 64.

It is demonstrated that the full cells cycled between 3.5 and 4.9 V offer the highest specific energy in the first cycle (600 Whkg⁻¹) and those measured in the range of 2.0 - 4.8 V exhibit the lowest gravimetric energy density (559 Whkg⁻¹). Notably, the energy difference between the 4.8 and 4.9 end-of-charge-voltages is about 40 Whkg⁻¹, which is principally due to the gap in the discharge capacities as the average voltages are very similar to each other. Nevertheless, the remarkable specific energies of the cells with the 4.9 V cutoff voltage are merely valid for the first few cycles because of the fast capacity decay while cycling (Figure 65). In the ensuing cycles, their capacity and their gravimetric energy density drop to the same level and even below the values of the cells with an end-of-charge-voltage of 4.8 V. In sum, the specific energy decreases for all cells during cycling but the degeneration is more critical for the cells with the 4.9 V cutoff voltage. Hence, the 3.3 - 4.8 V window provides the highest amount of gravimetric energy density over cycle life.

Specific energy (Whkg ⁻¹)	Specific discharge capacity (1 st cycle) (mAhg ⁻¹)	Average voltage (V)	Voltage range (V)	Residual capacity after 500 cycles (%)
600.0	131.4	4.57	3.5 - 4.9	62.4
598.9	131.3	4.56	3.4 - 4.9	59.4
598.5	131.1	4.56	3.3 - 4.9	59.4
596.6	131.4	4.54	3.0 - 4.9	56.2
561.4	123.3	4.55	3.3 - 4.8	80.0
559.6	123.3	4.54	3.0 - 4.8	73.2
559.1	123.0	4.54	2.0 - 4.8	56.5

Table 7 Electrochemical data of C//LiNi_{0.4}Mn_{1.6}O₄ full cells cycled for 500 cycles within different voltage windows at 1C and at room temperature.

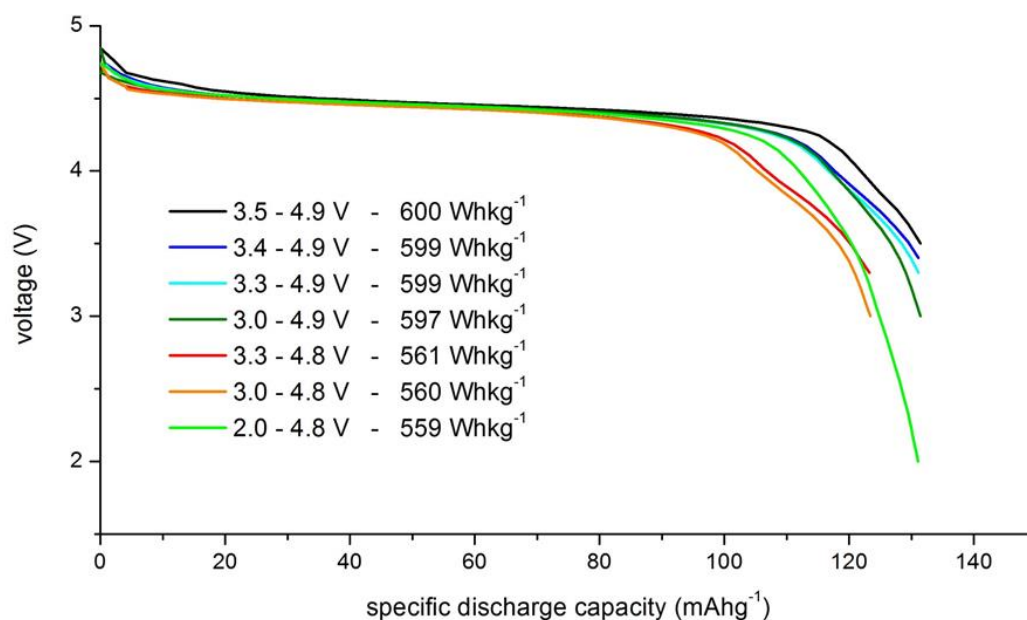


Figure 66 Voltage profiles of the first cycle of C//LiNi_{0.4}Mn_{1.6}O₄ full cells operated within various voltage ranges at 1C and at room temperature and related specific energies.

The potential of the negative electrode does not fall below the 0 V potential line throughout the whole experiment. Instead, it lies always at ca. 0.07 - 0.08 V vs. Li pertaining to the fully charged states of the cell. Deposition of metallic lithium on the anode is known to occur when the anode potential adopts negative values.^[314–316] Therefore, it can be assumed that, at least in the first few cycles, no lithium plating occurs due to a suitable ratio of anode and cathode capacities.

Likewise, balancing seems to be acceptable in terms of achieving a potential difference as large as possible between the Li//C and Li//LiNi_{0.4}Mn_{1.6}O₄ half cell potentials attaining a preferably high specific energy. The small anode potential or slight anode oversizing of approx. 4% at 0.1C allows the activation of nearly 100% of the active masses of both electrodes. As a result, high specific capacities are realized. The cathode potential is detected at ca. 0.07 - 0.08 V above the full cell voltage in the highest states of charge. Thus, for a 4.9 V charge cutoff voltage the potential of the positive electrode reaches almost 5.0 V during charging. This leads to more severe corrosion or decomposition of the electrolyte, binder, carbon black, and CAM compared to the end-of-charge-voltage of 4.8 V. Consequently, the cells charged up to 4.9 V display a faster capacity fading than those operated up to 4.8 V.

Influence of the discharge cutoff voltages on the cell performance

Furthermore, the examined voltage ranges reveal a dissimilar behavior of the potentials of the positive and negative electrodes while discharging (Table 8).

Voltage range (V)	Cathode potential at 0% SOC (Li//LiNi _{0.4} Mn _{1.6} O ₄) (V vs. Li)	Anode potential at 0% SOC (Li//C) (V vs. Li)
3.5 - 4.9	3.83 - 3.85	0.33 - 0.35
3.4 - 4.9	3.75 - 3.77	0.35 - 0.37
3.3 - 4.9	3.78 - 3.81	0.48 - 0.51
3.0 - 4.9	3.55 - 3.58	0.55 - 0.58
3.3 - 4.8	3.75 - 3.76	0.45 - 0.46
3.0 - 4.8	3.53 - 3.56	0.53 - 0.56
2.0 - 4.8	3.96 - 4.02	1.96 - 2.02

Table 8 Examined voltage ranges and associated cathode (Li//LiNi_{0.4}Mn_{1.6}O₄) and anode (Li//C) potentials in the completely discharged states of a C//LiNi_{0.4}Mn_{1.6}O₄ full cell.

Thereby, it is recognized that particularly the anode potentials strongly depend on the discharge cutoff voltages. Regarding the same charge cutoff voltage, the following connection is established. The lower the end-of-discharge-voltage, the higher is the associated Li//C potential in the completely discharged states of the cell. This circumstance relates to the fact that the cycling performance declines with decreasing discharge cutoff voltage (Figure 65). The 2.0 - 4.8 V region is a special case and is discussed later on. The position of the cathode potential, which ranges from 3.53 to 3.85 V vs. Li in the lowest states of charge (excluding 2.0 - 4.8 V), has no detrimental effect on the cell. The location of the anode potential influences, however, the stability of the SEI and, hence, the electrochemical characteristics of the full cell. Commonly, SEI formation starts below 1.3 V vs. Li in the presence of alkyl carbonates and the layer becomes thicker when the potential is further lowered.^[398,399] During delithiation of the graphite anode, the Li//C potential is raised again. Now, partial dissolution of the SEI takes place. Thus, upon cycling SEI formation and dissolution are in a dynamic equilibrium.^[72] The higher the potential of the negative electrode is situated above the 0 V potential in the discharged state of the full cell, the more unstable is the SEI and the more serious is the weakening of this surface layer. Accordingly, throughout cycling lithium is consumed more rapidly due to permanent SEI reconstitution and thick layers are built up. Therefore, faster capacity deterioration is determined for the cells operated with diminished end-of-discharge-voltages.

The voltage region 2.0 - 4.8 V – a special case

The 2.0 - 4.8 V window unveils a different behavior for the potential of the positive electrode upon discharging compared to the other examined voltage regions. When the full cell reaches a voltage of ca. 2.7 - 2.8 V, the Li//LiNi_{0.4}Mn_{1.6}O₄ potential stops shrinking at around 3.5 - 3.6 V vs. Li and augments up to \approx 4.0 V vs. Li until the full cell is totally discharged to 2.0 V. This implies that the cathode begins to release Li⁺ at about 3.5 - 3.6 V vs. Li or in other words is already charged again, whereas the full cell is still discharged. Simultaneously the Li//C potential increases up to ca. 2.0 V vs. Li. This indicates that the entire deintercalation of Li⁺ is accompanied by complete SEI dissolution and degradation of the graphite anode. The anode can only provide Li⁺, which have been inserted in the cycles before or that have been used to generate the SEI layer. No additional lithium is available to further discharge the cathode below 3.5 V vs. Li. This would only be feasible in the case of a lithium anode instead of graphite as demonstrated in the past.^[400] Consequently, the lithium metal reference electrode is not contributing to the reaction in the full cell confirming the good quality of the three-electrode setup. The LiNi_{0.4}Mn_{1.6}O₄ electrode already starts to extract Li⁺ prior to the overall discharge of the full cell in order to compensate the high Li//C potential that primarily originates from the corrosion of the anode. The disintegration of the negative electrode is even

more intensified in the second cycle between 2.0 and 4.8 V. The deformed or divergent curves of the ensuing cycles (3.3 - 4.9 V) prove the damage of the anode.

Interim conclusion

For the following investigations of C//LiNi_{0.4}Mn_{1.6}O₄ full cells the 3.3 - 4.8 V region is utilized. This voltage window affords the best cycle life and, hence, delivers the largest sum of specific energy over cycling of all studied ranges, despite the comparably lower original specific discharge capacity. Moreover, it has been shown that, at least in the first few cycles, the 3.3 - 4.8 V cell is well balanced with respect to the prevention of lithium plating and considering the attainment of a rather high gravimetric energy density. The increase of the anode potential in the discharged state of the full cell is tolerable and does not cause an irreversible cell damage.

Long-term three-electrode cycling experiment

Finally, a long-term cycling experiment was performed with a three-electrode C//LiNi_{0.4}Mn_{1.6}O₄ pouch cell between 3.3 and 4.8 V at room temperature. Here, the objective is to ensure that improper cell balancing is indeed not the reason for capacity fading. Initially, ten cycles were recorded including the data of the reference electrode. Owing to the lack of three-electrode measurement channels, just the cycling data of the full cell were recorded. Nevertheless, the two-electrode cycling was paused after 50, 250, and 500 cycles to monitor the development of the individual potentials of anode and cathode. The cycling performance of the corresponding cell is illustrated in Figure 68.

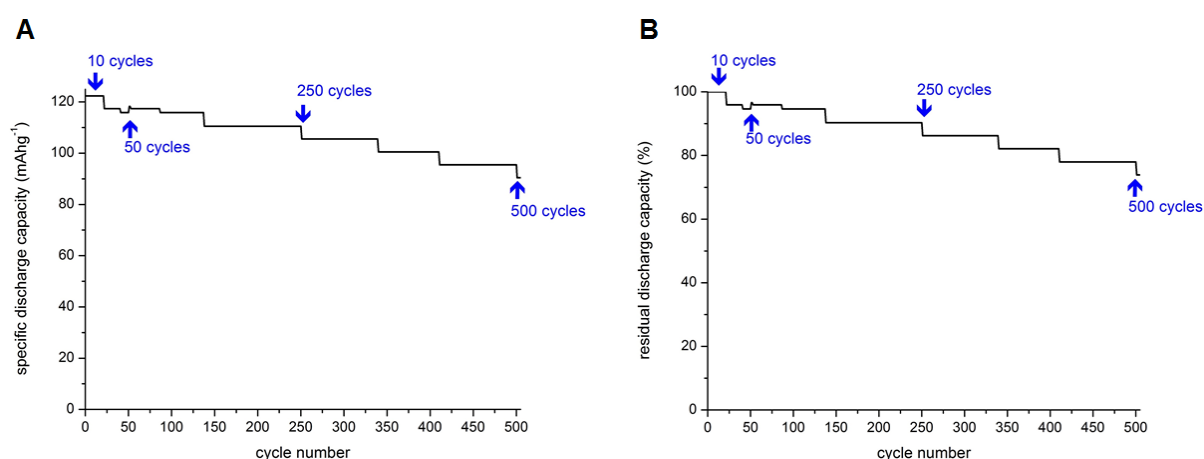


Figure 68 **A** Specific discharge capacity vs. cycle number plot and **B** residual discharge capacity vs. cycle number plot of a C//LiNi_{0.4}Mn_{1.6}O₄ three-electrode pouch cell cycled between 3.3 and 4.8 V at 1C at room temperature. The arrows indicate the interruption of the two-electrode cycling and the beginning of the three-electrode measurement, which was conducted for five cycles in each case.

The arrows indicate the interruption of the two-electrode cycling and the beginning of the three-electrode measurement, which was conducted for five cycles in each case. The specific starting capacity amounts to 122.3 mAhg⁻¹, which is virtually the same as that reported for the 3.3 - 4.8 V region. The capacity decay proceeds, however, more rapidly than in the two-electrode assembly. After 500 cycles, the capacity retention is only 74% compared to 80% in the two-electrode setup. The cycling interruptions and pauses are presumably responsible for the poorer electrochemical features of the three-electrode pouch cell.

Figure 69 depicts the full cell voltage (green line), the anode (black line), and the cathode (red line) potentials of the first ten cycles and after 50, 250, and 500 cycles for five cycles. Throughout the whole experiment the anode potential adopts positive values. Thus, no lithium precipitation on the anode surface arises. As a matter of fact, no lithium plating is observed on the surface of the negative electrode after opening the cell in the glovebox.

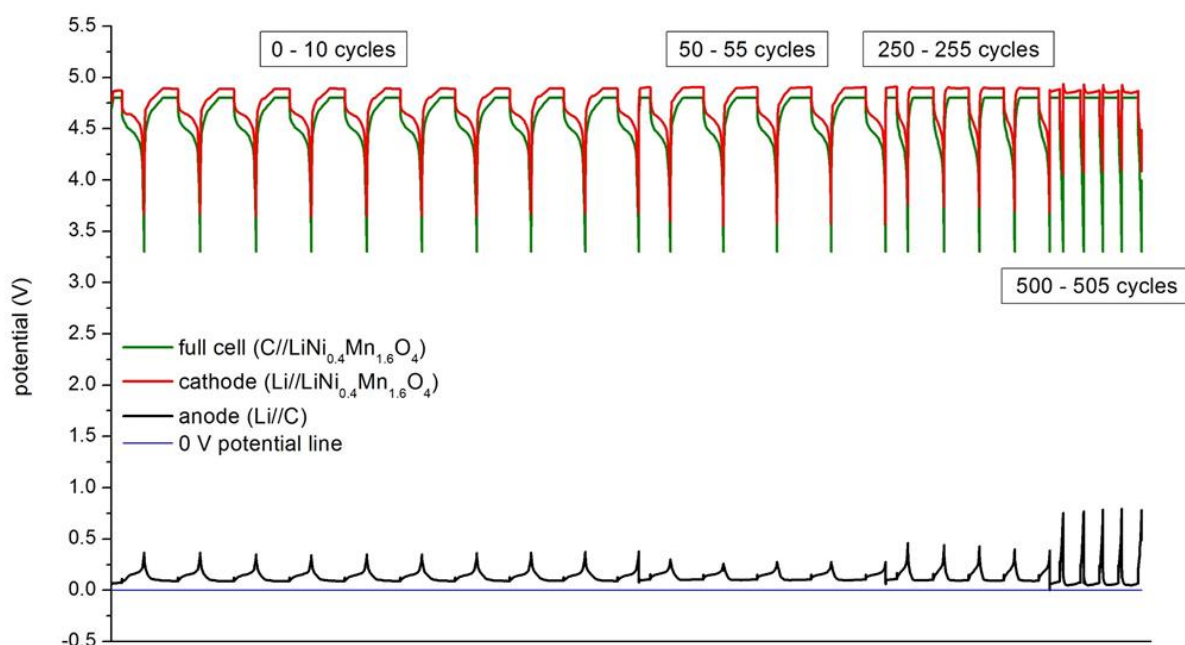


Figure 69 Voltage profile of a three-electrode C//LiNi_{0.4}Mn_{1.6}O₄ pouch cell operated within the 3.3 - 4.8 V region and the corresponding measured cathode potential (Li//LiNi_{0.4}Mn_{1.6}O₄) and the calculated anode (Li//C) potential measured at room temperature at 1C. The first ten cycles and five cycles after 50, 250, and 500 cycles are depicted.

Consequently, the electrodes are also balanced correctly with respect to long-term cycling. In the highest states of charge, the anode potential is registered at 0.07 - 0.08 V vs. Li regarding the cycles from 0 to 255. For the last five cycles, it declines slightly to 0.05 - 0.06 V. Analogously, the cathode potential is positioned at 4.87 - 4.88 V vs. Li for a minimum of 255 cycles before it decreases to 4.85 - 4.86 V vs. Li after 500 cycles. Evidently, ageing mechanisms take place that lead to the potential drops. The degeneration of the spinel cell is even more noticeable considering the enhancement of the anode and cathode potentials in

the lowest states of charge during cycling. The potentials of the negative and positive electrodes rise from ca. 0.30 up to ca. 0.79 V and from 3.60 to 4.09 V, respectively. Besides, the time required for one charge/discharge cycle becomes shorter and shorter with increasing cycle number. All these phenomena occur due to electrochemical consumption of active lithium during CC/CV-cycling by, for example, massive surface layer formation.

If lithium is lost, the CAM is not entirely restored upon discharging. Consequently, the respective cathode potential is higher in the completely discharged state of the full cell. The anode potential follows to compensate the lithium deficit and the 3.3 V cutoff voltage of the full cell is still reached.

During the subsequent charge process less lithium is deintercalated and the associated potential is lowered below 4.87 - 4.88 V vs. Li. Hence, the anode receives only a reduced amount of lithium ions. But the potential of the negative electrode drops and secures the 4.8 V end-of-charge voltage of the full cell. Probably, some of the pores of the carbon anode are clogged by the components of a thick SEI. This scenario has already been described in the literature.^[318,401] Therefore, the negative electrode takes up only a limited number of Li⁺ before plating takes place.

Conclusion

Altogether, the marginal anode oversizing of ca. 4% at 0.1C is sufficient to prevent deposition of metallic lithium throughout cycling. In addition, the accurate balancing of the electrodes enables high specific capacities due to the almost complete involvement of both active materials in the electrochemical processes. Thus, the capacity decay of the C//LiNi_{0.4}Mn_{1.6}O₄ pouch cell is not the result of incorrect balancing. Instead, serious loss of active lithium is suggested to be the main source of the cycling behavior. The reasons for this will be discussed later in this thesis.

5.2.2 Cycling stability studies

In general, the cycle life and the specific energy are important parameters, which determine the suitability of lithium ion accumulators for certain applications. The automotive industry demands highly energetic LIBs to realize long-range electric cars and the battery service life should at least match the average life expectancy of a new car. The latter is around ten to fifteen years. CC/CV-cycling is a prominent method to estimate the longevity and specific energy of lithium ion batteries or cells and to examine the influence of diverse experimental conditions. Hereafter, the impact of different temperatures, electrolyte additives, and Al₂O₃ coating layers on the cycling behavior of C//LiNi_{0.4}Mn_{1.6}O₄ full cells is investigated and evaluated.

Temperature dependence

First of all, full cells containing a graphite anode and a LiNi_{0.4}Mn_{1.6}O₄ cathode were cycled between 3.3 and 4.8 V at 1C, whereby three different temperatures were applied (Figure 70). The cells exhibit specific starting capacities of 123.3, 123.7, and 95.2 mAhg⁻¹ at 23, 35, and 45 °C, respectively, and the residual discharge capacities are found to be 90%, 76%, and 61%, respectively. As expected the capacity decay proceeds faster at higher temperatures, because the ageing processes are accelerated according to Arrhenius. At 45 °C, an immediate capacity loss during the initial cycle is observed. Therefore, intensified ageing mechanisms must occur such as for instance the formation of thicker SEI on the graphite surface. Some layer components are not stable at elevated temperatures and they readily decompose to create a porous SEI with partly bare graphite surfaces. As a consequence, additional SEI formation evolves.^[402] Concurrently, a thicker SPI on the cathode surface might develop. Electrolyte oxidation and film growth on the positive electrode are recognized processes in high voltage spinel cells.^[1,4,229] Both scenarios, extra SEI as well as supplementary SPI formation, result in irreversible consumption of electrochemically active Li⁺.

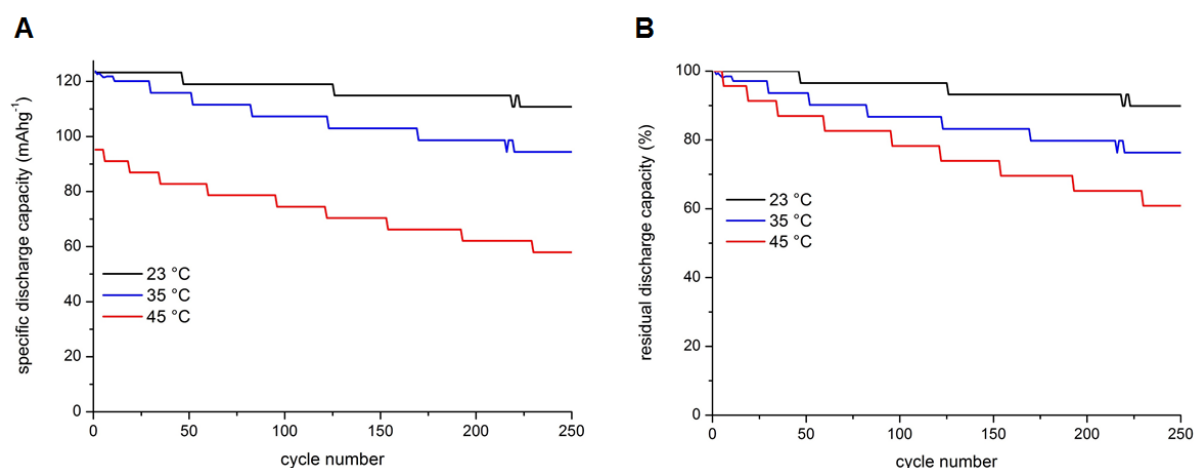


Figure 70 **A** Specific discharge capacity vs. cycle number plots and **B** residual discharge capacity vs. cycle number plots of C//LiNi_{0.4}Mn_{1.6}O₄ cells cycled between 3.3 and 4.8 V at 1C as a function of the temperature.

Afterwards, it attempts to improve the cycle life of C//LiNi_{0.4}Mn_{1.6}O₄ cells by selected electrolyte additives and Al₂O₃ coating layers on the electrodes. The cycling stability studies are all conducted with a current rate of 1C at 45 °C in order to accelerate the degradation of the full cell and, thus, to track the effect of the electrolyte additives or the ceramic layers. Furthermore, good high temperature performance is a prerequisite for applying high voltage spinel LIBs in EVs, HEVs, or PHEVs.

Electrolyte optimization

Many researchers have focused on developing novel electrolytes and electrolyte additives to extend the cycling performance of high voltage spinel electrodes operated at high potentials.^[5,262,262–267] Nonetheless, each novel electrolyte formulation features some disadvantages.

As outlined in chapter 3, in this work the utilization of selected electrolyte additives in C//LiNi_{0.4}Mn_{1.6}O₄ cells is based on two ideas. On one hand, the additives are supposed to form a more stable SPI on the cathode surface than the reference electrolyte (1 M LiPF₆ in EC/EMC/DMC (1/1/1, w/w/w)) without any additives. If the layer is dense enough and covers the full surface of the spinel electrode, it prohibits further electrolyte oxidation because the direct contact between the composite cathode and the electrolyte components no longer exists. Hence, the additive stabilized SPI remains rather thin and less Li⁺ are depleted. Likewise, the SPI should prevent the interaction between HF and the LiNi_{0.4}Mn_{1.6}O₄ particles. Therefore, transition metal dissolution can be suppressed. On the other hand, the additives might already trap PF₅ from the conducting salt, H₂O, and/or HF from the electrolyte and alleviate Mn and Ni dissolution.

Herein, additives belonging to the groups of anhydrides, borates, fluorinated carbonates, imides, nitriles, phosphates, phosphites, and silicon-containing compounds are investigated. In the literature additives or cosolvents from similar or same substance classes have been reported to improve the electrochemical properties of high voltage materials.^[268–277] Adding substances such as sulfones and biphenyls to the base electrolyte have also been shown to enhance the electrochemical behavior of high voltage spinel cells.^[5,266,278,279] Nevertheless, they are not considered due to the following reasons. Sulfone-based electrolytes suffer from very high viscosities with low conductivities. Low sulfone concentrations in carbonate-based electrolytes also diminish the conductivity owing to incomplete dissociation.^[266] The utilization of biphenyls as additives or cosolvents is critical as they decrease the ionic conductivity, too. The formed polymer layer on top of the cathode is frequently too thick to enable fast lithium diffusion.^[5]

Table 9 provides an overview of all examined electrolyte additives. The additives are listed alphabetically. Originally, 0.5% of each additive was added to the reference electrolyte. Then, higher and lower concentrations were tested to determine the ideal concentration of each additive.

Additive abbr.	Additive name	0.1%	0.5%	1%	1.5%	2%	2.5%	5%	10%
FEC	fluoroethylene carbonate	✓	✓				✓	✓	✓
HFiP	tris(1,1,1,3,3,3-hexafluoroisopropyl) phosphate	✓	✓	✓					
HMDS	hexamethyldisilazane	✓	✓		✓	✓			
LiBOB	lithium bis(oxalato)borate	✓	✓	✓	✓				
LiTFSI	lithium bis(trifluoromethanesulfonyl) imide		✓	✓	✓				
SA	succinic anhydride		✓				✓	✓	✓
SEN	sebaconitrile		✓	✓		✓			
TEHP	tris(2-ethylhexyl) phosphate	✓	✓		✓				
TFPi	tris(2,2,2-trifluoroethyl) phosphite	✓	✓	✓					
TMP	trimethyl phosphate	✓	✓	✓	✓				
TTSP	tris(trimethylsilyl) phosphate	✓	✓		1.7%				

Table 9 Overview of all examined electrolyte additives. The associated concentrations are given in weight percent.

Fluoroethylene carbonate

Generally, fluorinated cyclic and linear carbonates are interesting candidates for LIB electrolytes as they possess more desirable physical properties like, for example, lower melting point, increased oxidation stability, and less flammability as compared to the non-fluorine substituted carbonates.^[263,403] Among all explored fluorinated carbonate additives or cosolvents, fluoroethylene carbonate (FEC) is the most prominent (Figure 71). Its capability to form a stable SEI on graphitic anodes has been thoroughly studied.^[404,405] In addition, FEC has been found to improve the cycle performance of silicon anodes.^[406]

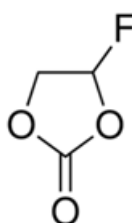


Figure 71 Chemical structure of fluoroethylene carbonate.

As opposed to this, the impact of FEC on the electrochemical characteristics of cathodes has been much less investigated.^[405,407] Recently, FEC has been tested as additive or cosolvent in

high voltage spinel cells. S. Passerini et al. demonstrated the beneficial effect of adding both 1.6 wt% FEC and 2 wt% SA to the base electrolyte (1 M LiPF₆ or 1 M LiFAP in EC/DMC (1/1, w/w)) on charge retention over cycling and on self-discharge of C//LiNi_{0.4}Mn_{1.6}O₄ Swagelok™-type cells.^[408] K. Amine and his group examined a new electrolyte composed of 1 M LiPF₆ in FEC/F-EMC/F-EPE (3/5/2, v/v/v) in C//LiNi_{0.5}Mn_{1.5}O₄ coin cells. The electrolyte improved the voltage stability and the cycling behavior of the cell at room temperature and at 55 °C compared to an electrolyte of 1.2 M LiPF₆ in EC/EMC (3/7, w/w) due to fewer solid decomposition products on anode and cathode.^[6] In another report by H.-C. Shin and co-workers, the addition of 1 wt% FEC to 1.5 M LiPF₆ in EC/DEC (1/1, v/v) reduces the ageing mechanisms of half cells comprising LiNi_{0.5}Mn_{1.5}O₄ at 55 °C. A protective surface film with fluoride-containing components and free fluoride ions is proposed to prevent LiF accumulation on the cathode and, hence, extends the cell life.^[409] Moreover, Si//LiNi_{0.5}Mn_{1.5}O₄ cells including the electrolyte formulation 1 M LiPF₆ in FEC/DMC (1/4, w/w) showed an excellent cycling stability.^[271]

In this thesis, a comparative study of the carbonate-based reference electrolyte and the related FEC-added electrolyte solutions was accomplished. Figure 72 displays the cycle life of C//LiNi_{0.4}Mn_{1.6}O₄ pouch cells without and with diverse contents of FEC.

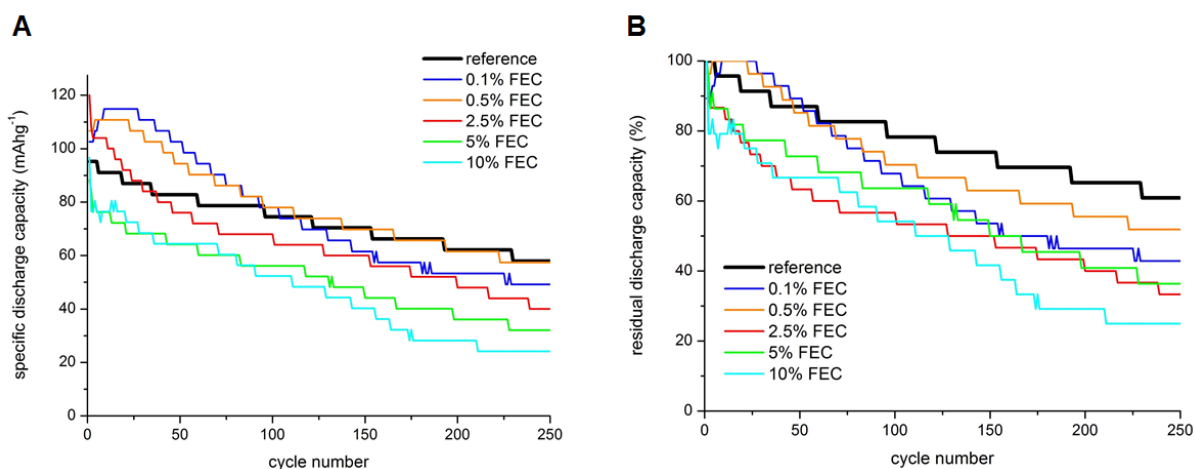


Figure 72 **A** Specific discharge capacity vs. cycle number plots and **B** residual discharge capacity vs. cycle number plots of C//LiNi_{0.4}Mn_{1.6}O₄ cells cycled between 3.3 and 4.8 V at 1C at 45 °C in 1 M LiPF₆ EC/EMC/DMC (1/1/1, w/w/w) without and with 0.1, 0.5, 2.5, 5, and 10% FEC.

The reference cell is depicted as a black line. Its initial capacity is 95.2 mAhg⁻¹, which diminishes to 58.0 mAhg⁻¹ (61% residual discharge capacity) after 250 cycles. As can be seen, adding concentrations of 5 and 10% FEC to the base electrolyte leads to an overall deterioration of the cycling features. The formation of very thick surface films on the electrodes, which is accompanied by a severe loss of active lithium ions, is the reason for this rapid capacity decay. In contrast, the specific starting capacity of the spinel cell is significantly improved by 0.1%, 0.5%, and 2.5% FEC. It amounts to 114.9, 110.8, and 120.0 mAhg⁻¹,

respectively. Nonetheless, all FEC-containing electrolytes exhibit a faster electrochemical degeneration than the reference one. Still, the cell with 0.5% FEC delivers the highest gravimetric energy density regarding the whole cycle life. Its specific discharge capacity after cycling equals to 57.4 mAhg⁻¹, which is almost as high as in the reference and corresponds to 52% capacity retention. But, owing to the greater initial capacity, higher total specific energy is achievable. This additive concentration is recommended for C//LiNi_{0.4}Mn_{1.6}O₄ cells as it offers the largest advantages over the base electrolyte of all FEC quantities. Higher and lower amounts of FEC result in deterioration of the ageing phenomena.

The investigations of the mechanisms of FEC are outlined in chapter 5.3 and following. Thereto, the cell with 2.5% FEC was selected, since it revealed the best cycling behavior at the starting point of the analyses.

Hexamethyldisilazane

Hexamethyldisilazane (HMDS) is an organosilicon compound having the molecular formula C₆H₁₉NSi₂ (Figure 73). Typically, it is used for the preparation of organic and inorganic trimethylsilyl derivatives or as laboratory reagent.^[410]

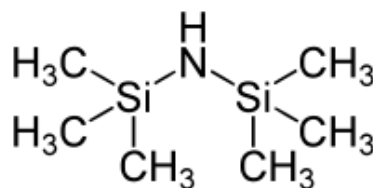


Figure 73 Chemical structure of hexamethyldisilazane.

In 2001, H. Yamane et al. discovered that HMDS significantly suppresses Mn dissolution of Li_{1.01}Mn_{1.99}O₄ cathodes after high temperature storage at 80 °C owing to the removal of H₂O and the neutralization of HF.^[198] Furthermore, J.-S. Liu and his group confirmed the positive effect of HMDS on the cycle performance of LiMn₂O₄ electrodes.^[411] As far as we are aware, there is, however, no detailed study on the electrochemical and physical properties of lithium electrolytes containing the additive HMDS for lithium nickel manganese oxides spinels as CAMs.

In this work, HMDS is investigated, for the first time, as additive for lithium ion cells including a graphite anode and a high voltage spinel cathode. Figure 74 represents the capacity retention of C//LiNi_{0.4}Mn_{1.6}O₄ cells cycled between 3.3 and 4.8 V at 45 °C without and with 0.1%, 0.5%, 1.5%, and 2% HMDS. The addition of 2% of the organic silicon substance to the base electrolyte (light blue line) engenders a drastic reduction of the initial cell capacity. Therefore, merely a specific discharge capacity of 49.8 mAhg⁻¹ is realized after 250 cycles. The high amount of HMDS may initiate an immediate, excessive production of surface layers on the

electrodes, which is responsible for the low specific starting capacity. All other additive concentrations lead to a higher specific starting capacity than the reference electrolyte (black line) and at least the same or even higher specific discharge capacities are achieved at the end of cycling. The cells with 0.1% (dark blue line) and 0.5% HMDS (red line) start at 115.8 and 122.6 mAhg⁻¹, respectively, but quickly lose capacity upon charging and discharging to 57.9 and 57.6 mAhg⁻¹, respectively. Nevertheless, they afford more specific energy over cycle life than the reference. The best CC/CV-cycling stability is attained by utilizing 1.5% HMDS (green line). Although capacity fading still exists, there is a considerable improvement as compared to the baseline. 60% residual discharge capacity (61.5 mAhg⁻¹) is obtained after 250 cycles. For the post-mortem analyses, the cell with 0.5% HMDS was chosen as it offers the greatest sum of specific energy over cycling.

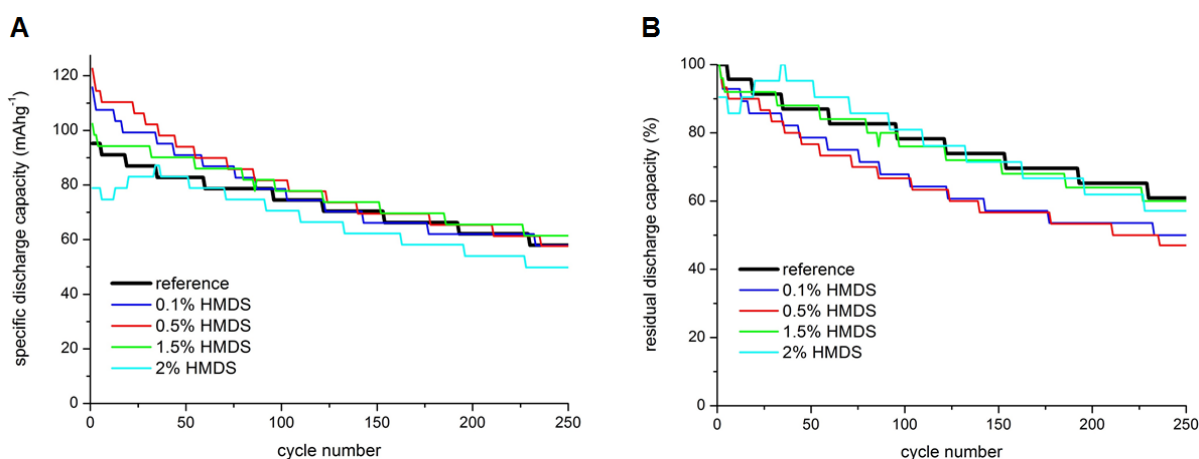


Figure 74 **A** Specific discharge capacity vs. cycle number plots and **B** residual discharge capacity vs. cycle number plots of C//LiNi_{0.4}Mn_{1.6}O₄ cells cycled between 3.3 and 4.8 V at 1C at 45 °C in 1 M LiPF₆ EC/EMC/DMC (1/1/1, w/w/w) without and with 0.1, 0.5, 1.5, and 2% HMDS.

Lithium bis(oxalato)borate

Among various additives for lithium nickel manganese oxide spinels, lithium bis(oxalato)borate or LiBOB (Figure 75) is one of the most promising candidates.

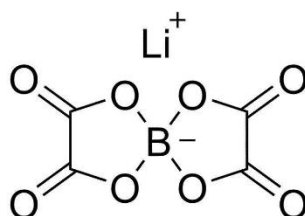


Figure 75 Chemical structure of Lithium bis(oxalato)borate.

It has been recognized as a bifunctional electrolyte component, which is able to form stable surface films on high voltage spinel cathodes and graphitic anodes and it is known to inhibit

Mn dissolution.^[272] The incorporation of LiBOB into carbonate-based electrolyte formulations has been reported to substantially enhance the electrochemical features of Li//LiNi_{0.5}Mn_{1.5}O₄ and graphite//LiNi_{0.5}Mn_{1.5}O₄ cells.^[247,269,272,307]

Within this study, several quantities of LiBOB were tested for C//LiNi_{0.4}Mn_{1.6}O₄ pouch cells via CC/CV-cycling experiments at 45 °C in order to determine the optimum additive concentration (Figure 76).

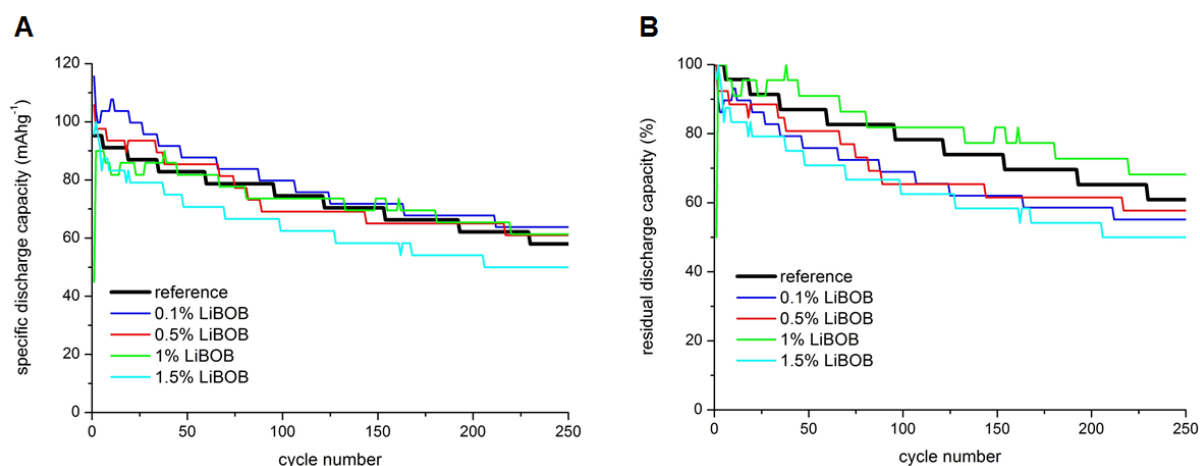


Figure 76 **A** Specific discharge capacity vs. cycle number plots and **B** residual discharge capacity vs. cycle number plots of C//LiNi_{0.4}Mn_{1.6}O₄ cells cycled between 3.3 and 4.8 V at 1C at 45 °C in 1 M LiPF₆ EC/EMC/DMC (1/1/1, w/w/w) without and with 0.1, 0.5, 1, and 1.5% LiBOB.

The addition of 1.5% LiBOB to the reference electrolyte (bright blue line) has a negative impact on the cycle life. The specific discharge capacity after cycling merely equals to 49.9 mAhg⁻¹. Severe SEI and/or SPI generation is presumably the reason for the fast capacity fading. In contrast, all cells with lower additive concentrations exhibit better performances than the reference with respect to the specific discharge capacity after 250 cycles. The residual discharge curve of 1% LiBOB (green line) shows the most favorable behavior of all curves. It reaches 61.3 mAhg⁻¹ at the end of the cycling, corresponding to 68% of its original capacity. Nonetheless, the highest specific energy over all cycles is observed for the cell comprising 0.1% LiBOB (dark blue line) since it has a starting capacity of 115.7 mAhg⁻¹, which only drops to 63.8 mAhg⁻¹ after 250 cycles. The 0.5% LiBOB cell (red line) also improves the final specific discharge capacity, which equals to 61.0 mAhg⁻¹, and enhances the gravimetric energy density of the C//LiNi_{0.4}Mn_{1.6}O₄ cell compared to the base electrolyte, although it is not as high as that of the cell with 0.1% LiBOB.

To clarify the influence of LiBOB on the characteristics of C//LiNi_{0.4}Mn_{1.6}O₄ cells, microscopic and spectroscopic examinations were undertaken with 0.5% LiBOB cells, as they had demonstrated the best cycling properties at the starting point of the analyses.

Lithium bis(trifluoromethanesulfonyl)imide

Generally, electrolytes with lithium bis(trifluoromethanesulfonyl)imide or LiTFSI (Figure 77) are somewhat less conductive than LiPF₆ electrolytes. But, the former salt has a higher thermal stability, is not prone to hydrolysis owing to very stable C-F bonds, has a higher degree of ionic dissociation, and is well soluble in non-aqueous electrolytes.^[398,412] The main drawback of LiTFSI in aprotic solvent-based electrolytes is, however, its tendency to corrode Al current collectors. This has prevented the wide-spread application of LiTFSI rather than LiPF₆.^[413–415] In contrast, LiTFSI does not cause any corrosion of the Al current collector in ionic liquids^[416], nor do highly concentrated LiTFSI electrolytes.^[417]

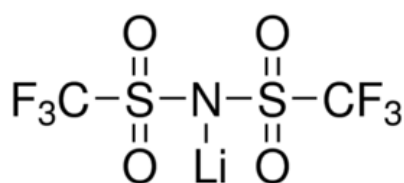


Figure 77 Chemical structure of Lithium bis(trifluoromethanesulfonyl)imide.

In this thesis LiTFSI is utilized, for the first time, as an electrolyte additive in a carbonate-containing electrolyte formulation for the CAM high voltage spinel. But, as illustrated in Figure 78, all additive concentrations result in capacities, which fade more quickly than those of the reference electrolyte (black line).

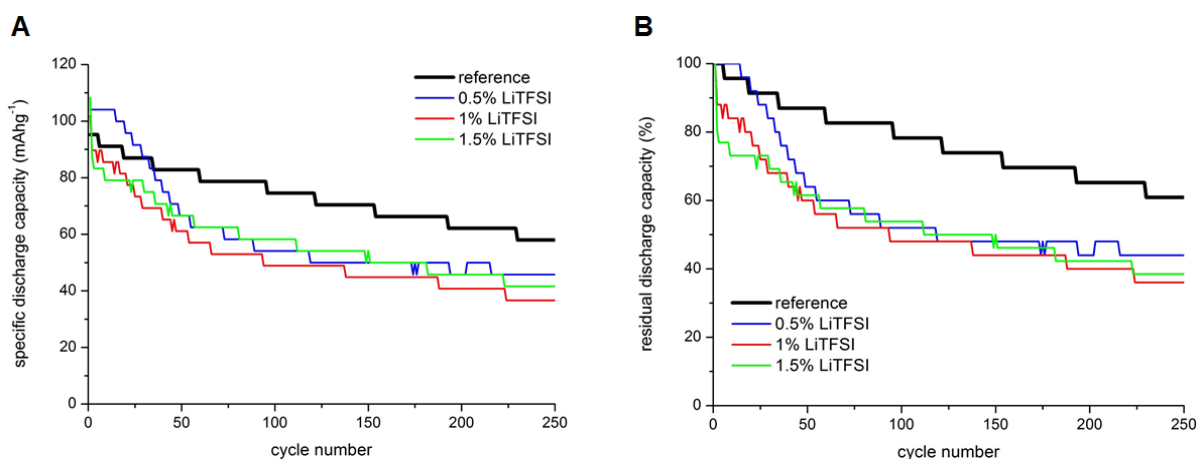


Figure 78 **A** Specific discharge capacity vs. cycle number plots and **B** residual discharge capacity vs. cycle number plots of C//LiNi_{0.4}Mn_{1.6}O₄ cells cycled between 3.3 and 4.8 V at 1C at 45 °C in 1 M LiPF₆ EC/EMC/DMC (1/1/1, w/w/w) without and with 0.5, 1, and 1.5% LiTFSI.

The worst result is registered for the cell with 1% LiTFSI (red line). It shows just 36.7 mAhg⁻¹ or 36% of its initial capacity after cycling. Applying 0.5% LiTFSI (blue line) helps to keep the initial specific discharge capacity at 104.1 mAhg⁻¹ for 14 cycles before it starts to decrease

down to 45.8 mAhg⁻¹, whereas 1.5% LiTFSI (green line) leads again to a lower specific discharge capacity of 41.6 mAhg⁻¹ after 250 cycles.

Gassing is identified as the primary reason for the poor cyclability of the cells containing LiTFSI. These cells have not only become very thick while cycling but they even have burst towards the end of the CC/CV-cycling experiment. This is due to the pressure of formed gases such as, for instance, CO₂ or H₂. Consequently, LiTFSI promotes the decomposition of the base electrolyte and is unstable at high voltages up to 4.8 V. Winter et al. have revealed that various electrolyte degradation processes, including TFSI-anion decomposition, occur prior to the actual corrosion of the Al current collector in rechargeable LIBs with 1 M LiTFSI in EC/DEC (3/7, w/w).^[418] Nevertheless, no corrosion of the Al current collector is detected in the C//LiNi_{0.4}Mn_{1.6}O₄ cells comprising LiTFSI after cycling. A passivation reaction involving LiPF₆ prohibits its deterioration.^[61,419] In spite of the fact that electrolyte oxidation and gassing are predominantly responsible for the rapid capacity decay, post-mortem analyses of the high voltage spinel cell with 1.5% LiTFSI were carried out. However, not all characterization methods could be applied because of cell damage.

Succinic anhydride

Lately, researchers have focused on anhydrides as additives to improve the features of non-aqueous electrolytes for lithium nickel manganese oxide electrodes. Glutaric anhydride, for example, has been recognized to alter the composition of the LiNi_{0.4}Mn_{1.6}O₄ cathode/electrolyte interphase by promoting stable fluorophosphates and lowering the relative amount of resistive LiF. Thereby, capacity fading upon cycling and self-discharge mechanisms are suppressed through a thicker but more ionically conductive SPI, which behaves like a polymer electrolyte interface.^[420] Besides, succinic anhydride or SA (Figure 79) has been added to a solution of 1 M LiPF₆ in EC/DMC (1/1 v/v) to reduce the self-discharge of Li//LiNi_{0.4}Mn_{1.6}O₄ SwagelokTM-type cells.^[273] An enhanced coulombic efficiency and a decreased capacity loss per cycle is noticed with the incorporation of SA. S. Passerini and his group have explored the electrochemical behavior of C//LiNi_{0.4}Mn_{1.6}O₄ full cells with 1.6 wt% FEC and 2 wt% SA added to the base electrolyte (1 M LiPF₆ or 1 M LiFAP in EC/DMC (1/1, w/w)).^[408] The combination of both additives increases the capacity retention over cycling and diminishes the self-discharge of the lithium nickel manganese oxide cells.

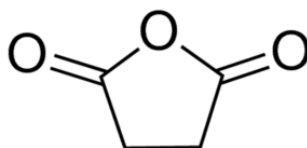


Figure 79 Chemical structure of succinic anhydride.

Hereafter, four SA concentrations were investigated to check whether the above stated positive results are applicable to C//LiNi_{0.4}Mn_{1.6}O₄ pouch cells. Unexpectedly, all SA-containing cells display an enormous degradation of the cycling performance compared to the reference (Figure 80). The cells with 0.5% (dark blue line), 2.5% (red line), 5% (green line), and 10% SA (bright blue line) start at specific discharge capacities of 88.6, 95.6, 87.5, and 109.4 mAhg⁻¹, respectively. The associated final residual discharge capacity values correspond to only 25%, 32%, 20%, and 4%, respectively. Contrary to what is reported in the literature, high as well as low amounts of SA cause a drastic capacity decline throughout cycling. In the following, spectroscopic and microscopic studies were conducted with the 2.5% SA cell to determine the origin of the poor cyclability.

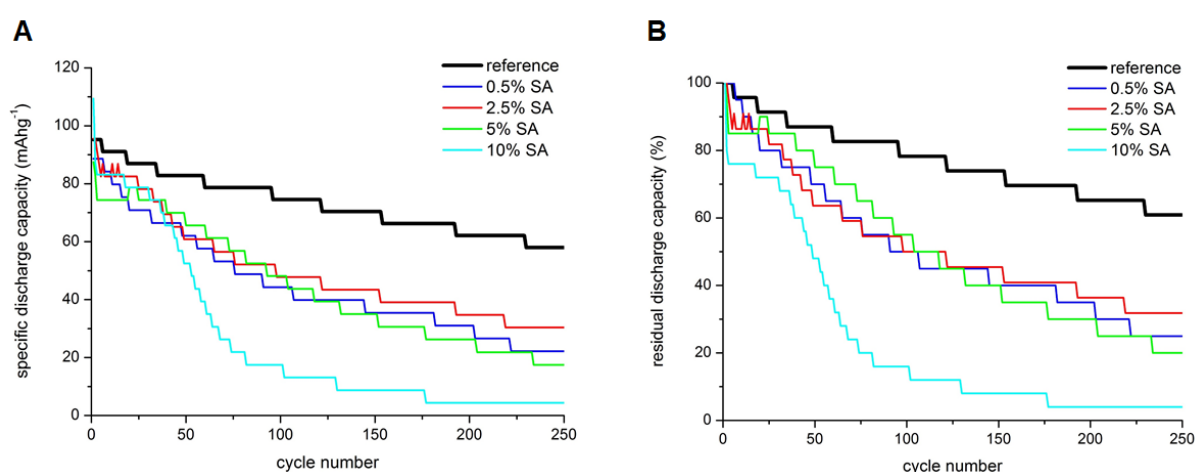


Figure 80 **A** Specific discharge capacity vs. cycle number plots and **B** residual discharge capacity vs. cycle number plots of C//LiNi_{0.4}Mn_{1.6}O₄ cells cycled between 3.3 and 4.8 V at 1C at 45 °C in 1 M LiPF₆ EC/EMC/DMC (1/1/1, w/w/w) without and with 0.5, 2.5, 5, and 10% SA.

Sebaconitrile

Commonly, nitrile solvent-based electrolytes are known to meet a variety of requirements such as improved low temperature performance and enhanced thermal and electrochemical stability at high temperature and voltage (up to 6 V vs. Li).^[277,421] Glutaronitrile (GLN), for instance, has been evaluated by Y. Abu-Lebdeh and I. Davidson as co-solvent in electrolyte mixtures to realize the formulation 1 M LiTFSI in GLN/EC (1/1, v/v) for C//LCO cells. It showed moderately good discharge capacities and low capacity fade up to 100 cycles.^[422] The same authors have also tested the effect of 1 M LiTFSI or 1 M LiTFSI/0.1 M LiBOB in ADN/EC electrolytes (1/1, v/v) on C//LCO lithium ion cells.^[281] Discharge capacities of 108 mAhg⁻¹ with very good capacity retention were obtained. TIAX LLC has developed a butyronitrile-based electrolyte.^[277] With the addition of at least 10 vol% butyronitrile to 1 M LiPF₆ in EC/EMC (3/7, w/w) or EC/DMC/EMC (1/1/1, w/w/w) excellent high voltage and high temperature cycling stabilities of C//LiNi_{0.5}Mn_{1.5}O₅ cells have been demonstrated. Sebaconitrile or SEN (Figure 81)

has already been studied as additive in 1 M LiPF₆ or 1 M LiBF₄ dissolved in EC/DMC (1/1 w/w) for Li//LiCoO₂ or Li//LiCoPO₄ cells.^[423] Although SEN provides better stability at higher potentials, the cycling of LiCoPO₄, which is conducted up to 6 V vs Li⁺/Li, shows low reversibility and efficiency of insertion/deinsertion processes due to the oxidative decomposition of the electrolyte. Several nitriles have been cited in patents as possible cosolvents or additives for capacitors or batteries by Samsung and Ube Industries.^[424]

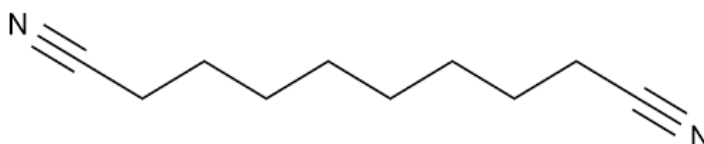


Figure 81 Chemical structure of sebaconitrile.

Nonetheless, to the best of our knowledge, there is no detailed investigation of SEN added to carbonate-based electrolytes for high voltage spinel cathodes. In this work, SEN is selected as additive of all commercially available aliphatic dinitriles because it exhibits a faster formation of a cathodic protective layer than dinitriles with shorter alkane chains.^[425] The cycling behavior of C//LiNi_{0.4}Mn_{1.6}O₄ pouch cells comprising the reference electrolyte 1 M LiPF₆ in EC/EMC/DMC (1/1/1, w/w/w) without (black line) and with 0.5% (blue line), 1% (red line), and 2% SEN (green line) is depicted in Figure 82.

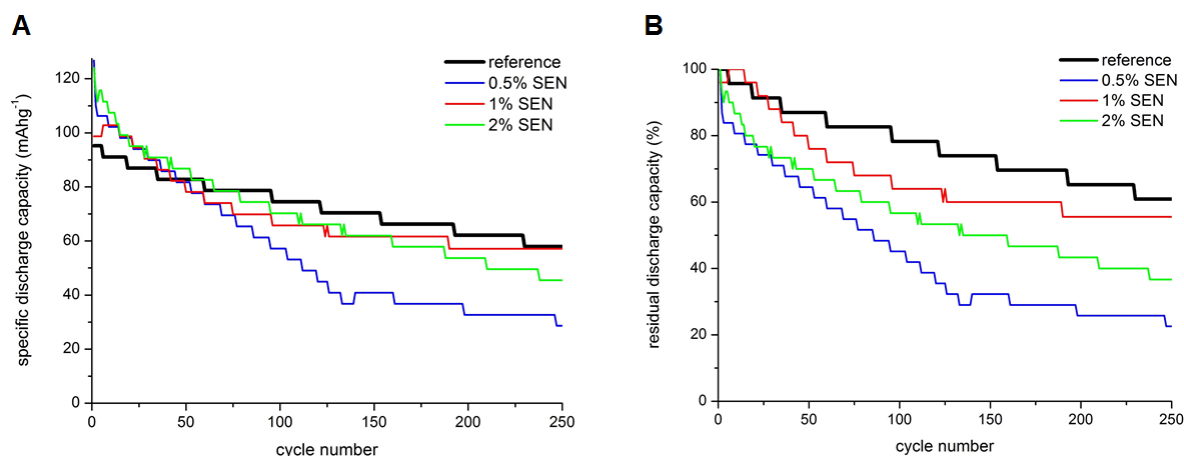


Figure 82 **A** Specific discharge capacity vs. cycle number plots and **B** residual discharge capacity vs. cycle number plots of C//LiNi_{0.4}Mn_{1.6}O₄ cells cycled between 3.3 and 4.8 V at 1C at 45 °C in 1 M LiPF₆ EC/EMC/DMC (1/1/1, w/w/w) without and with 0.5, 1, and 2% SEN.

All additive concentrations enable a higher specific starting capacity than the base electrolyte (black line). But at the same time, the presence of SEN exacerbates the capacity degeneration. Employing 1% SEN gives the best result of all three different amounts. The related cell delivers an initial specific discharge capacity of 98.7 mAhg⁻¹ and maintains 57.1 mAhg⁻¹ after cycling

(56% residual discharge capacity). Hence, further examinations are accomplished with the C//LiNi_{0.4}Mn_{1.6}O₄ pouch cell including 1% SEN.

Tris-(1,1,1,3,3,3-hexafluoroisopropyl) phosphate

Tris-(1,1,1,3,3,3-hexafluoroisopropyl) phosphate or HFiP (Figure 83) was first employed as an additive in an electrolyte composed of 1.0 M LiPF₆ in EC/EMC (3/7, w/w/w) for Li//LiNi_{0.5}Mn_{1.5}O₄ coin cells by A. v. Cresce and K. Xu in 2011.^[264] They identified the highly fluorinated phosphate ester structure as stabilizer of carbonate-based electrolytes on 5 V class cathode surfaces. Besides, they proved that HFiP forms a protective interfacial chemistry on the LiNi_{0.5}Mn_{1.5}O₄ cathode, and on account of this, enhances the electrochemical properties of the spinel cell. One year later, they patented the application of HFiP in non-aqueous electrolytes for C//LiNi_{0.5}Mn_{1.5}O₄ cells.^[274] Another year later, Du Pont patented the handling of HFiP in carbonate-containing electrolytes for C//Li_xNi_yM_zMn_{2-y-z}O_{4-d} cells ($x = 0.03 - 1.0$, $y = 0.3 - 0.6$, $z = 0.01 - 0.18$, $d = 0 - 0.3$, and M = one or more of Cr, Fe, Co, Li, Al, Ga, Nb, Mo, Ti, Zr, Mg, Zn, V, and Cu).^[275]

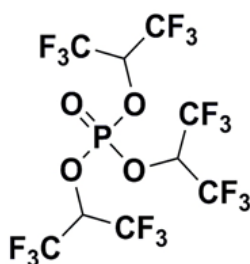


Figure 83 Chemical structure of tris-(1,1,1,3,3,3-hexafluoroisopropyl) phosphate.

Herein, the influence of HFiP on the cycling characteristics of C//LiNi_{0.4}Mn_{1.6}O₄ pouch cells at 45 °C was evaluated. Figure 84 illustrates the cycle life of the reference cell (black line) and of the cells with 0.1% (blue line), 0.5% (red line), and 1% HFiP (green line). Each additive concentration induces an increase of the initial specific discharge capacity of the spinel cells. When using 0.1% HFiP, LiNi_{0.4}Mn_{1.6}O₄ provides 101.7 mAhg⁻¹ but maintains only 44.8 mAhg⁻¹ after 250 cycles (44% residual discharge capacity). With the addition of 0.5% HFiP, the spinel full cell exhibits a specific starting capacity of 99.2 mAhg⁻¹ and still yields 57.9 mAhg⁻¹ after cycling, which is virtually the same as that of the reference cell. Consequently, a bit more of specific energy is gained over cycle life with 0.5% HFiP compared to the base electrolyte. A further augmentation of the additive concentration up to 1% causes, however, again a decline in the final specific discharge capacity to 53.9 mAhg⁻¹. This is contrary to the results of A. v. Cresce and K. Xu, who reported a stabilized electrochemical behavior of Li//LiNi_{0.5}Mn_{1.5}O₄ cells, when 1% HFiP is added to a carbonate-based electrolyte.^[264] The benefits and drawbacks of HFiP were analyzed by several microscopic and spectroscopic methods.

Detailed information is given in the following chapters. All examinations were carried out with 0.5% HFiP cells, as they show the most marked improvement with respect to the generation of specific energy.

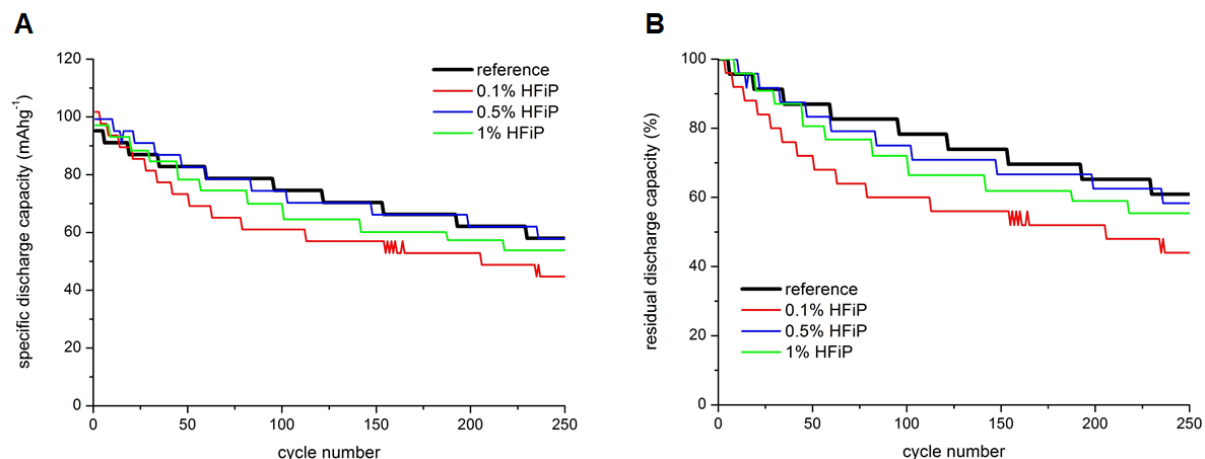


Figure 84 **A** Specific discharge capacity vs. cycle number plots and **B** residual discharge capacity vs. cycle number plots of C//LiNi_{0.4}Mn_{1.6}O₄ cells cycled between 3.3 and 4.8 V at 1C at 45 °C in 1 M LiPF₆ EC/EMC/DMC (1/1/1, w/w/w) without and with 0.1, 0.5, and 1% HFiP.

Tris(2-ethylhexyl) phosphate

The chemical structure of tris(2-ethylhexyl) phosphate (TEHP) is represented in Figure 85. Like HFiP, the application of TEHP as additive or cosolvent for non-aqueous electrolytes in C//LiNi_{0.5}Mn_{1.5}O₄ cells has been patented by A. v. Cresce and K. Xu owing to its advantageous impact on the interfacial chemistries formed at high potentials.^[274] Besides, du Pont claimed the utilization of TEHP in carbonate-based electrolytes for C//Li_xNi_yM_zMn_{2-y-z}O_{4-d} cells ($x = 0.03 - 1.0$, $y = 0.3 - 0.6$, $z = 0.01 - 0.18$, $d = 0 - 0.3$, and M = one or more of Cr, Fe, Co, Li, Al, Ga, Nb, Mo, Ti, Zr, Mg, Zn, V, and Cu).^[275] No other publications on TEHP with lithium nickel manganese oxide spinel cathodes are known.

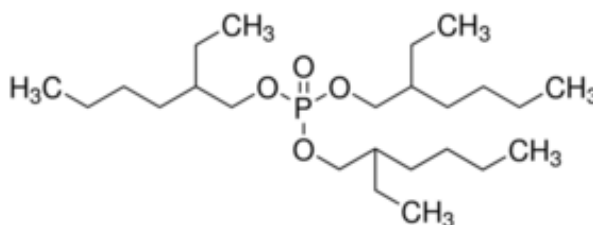


Figure 85 Chemical structure of tris(2-ethylhexyl) phosphate.

Herein, C//LiNi_{0.4}Mn_{1.6}O₄ pouch cells with diverse quantities of TEHP are characterized. Figure 86 illustrates the cycle life of the reference (black line) and the TEHP-containing cells at 45 °C between 3.3 and 4.8 V.

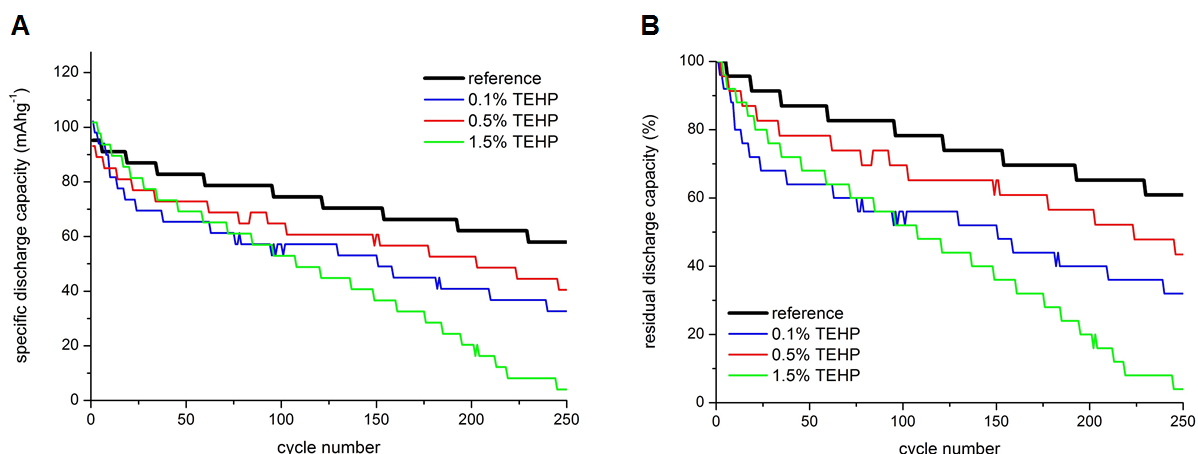


Figure 86 **A** Specific discharge capacity vs. cycle number plots and **B** residual discharge capacity vs. cycle number plots of C//LiNi_{0.4}Mn_{1.6}O₄ cells cycled between 3.3 and 4.8 V at 1C at 45 °C in 1 M LiPF₆ EC/EMC/DMC (1/1/1, w/w/w) without and with 0.1, 0.5, and 1.5% TEHP.

The cells with 0.1% (blue line), 0.5% (red line), and 1% TEHP (green line) afford specific starting capacities of 102.2, 93.1, and 101.8 mAhg⁻¹, respectively, and the associated capacity retention amounts to 32%, 43%, and 4%, respectively. Therefore, TEHP is not supportive in terms of stabilizing the cycling properties of the cell chemistry C//LiNi_{0.4}Mn_{1.6}O₄. Instead, the additive aggravates the capacity decay. Post-mortem analyses of the 0.5% TEHP cell were done to find the major source of this deterioration.

Tris(2,2,2-trifluoroethyl) phosphite

The fluorinated alkyl phosphite tris(2,2,2-trifluoroethyl) phosphite or TFPi (Figure 87) was first reported as a thermal stabilizer for electrolytes comprising LiPF₆ of Li ion cells.^[297,298,398] Then, in 2012, A. v. Cresce and K. Xu tested TFPi as additive or cosolvent for non-aqueous electrolytes in C//LiNi_{0.5}Mn_{1.5}O₄ cells. They recognized the contribution of phosphite to the generation of a protective SPI layer. One year later, du Pont patented the utilization of TFPi in carbonate-based electrolytes for C//Li_xNi_yM_zMn_{2-y-z}O_{4-d} cells ($x = 0.03 - 1.0$, $y = 0.3 - 0.6$, $z = 0.01 - 0.18$, $d = 0 - 0.3$, and M = one or more of Cr, Fe, Co, Li, Al, Ga, Nb, Mo, Ti, Zr, Mg, Zn, V, and Cu).^[275]

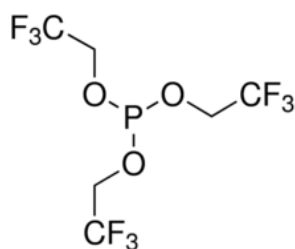


Figure 87 Chemical structure of tris(2,2,2-trifluoroethyl)phosphite.

In this study, three different amounts of TFPi were added to the base electrolyte 1 M LiPF₆ in EC/EMC/DMC (1/1/1, w/w/w) in order to conclude the ideal concentration of TFPi for C//LiNi_{0.4}Mn_{1.6}O₄ cells. Thereto, 1C CC/CV-cycling experiments were conducted at 45 °C in the voltage region of 3.3 - 4.8 V (Figure 88). 0.1%, 0.5%, and 1.5% TFPi lead to a distinct improvement of the initial specific discharge capacity of 110.0, 115.4, and 111.0 mAhg⁻¹, respectively, compared to the reference with a specific starting capacity of 95.2 mAhg⁻¹. The cell with 0.1% TFPi exhibits, however, only a residual discharge capacity of 48% (53.0 mAhg⁻¹). 52% capacity retention (57.6 mAhg⁻¹) is achieved with 1.5% TFPi. The most beneficial effect is realized with the 0.5% TFPi cell, which still reveals 63.7 mAhg⁻¹ after cycling. This additive concentration is even superior to the reference considering the specific energy gained over cycle life. Thus, the cell containing 0.5% TFPi was used for the spectroscopic and microscopic investigations of the mechanisms of the additive.

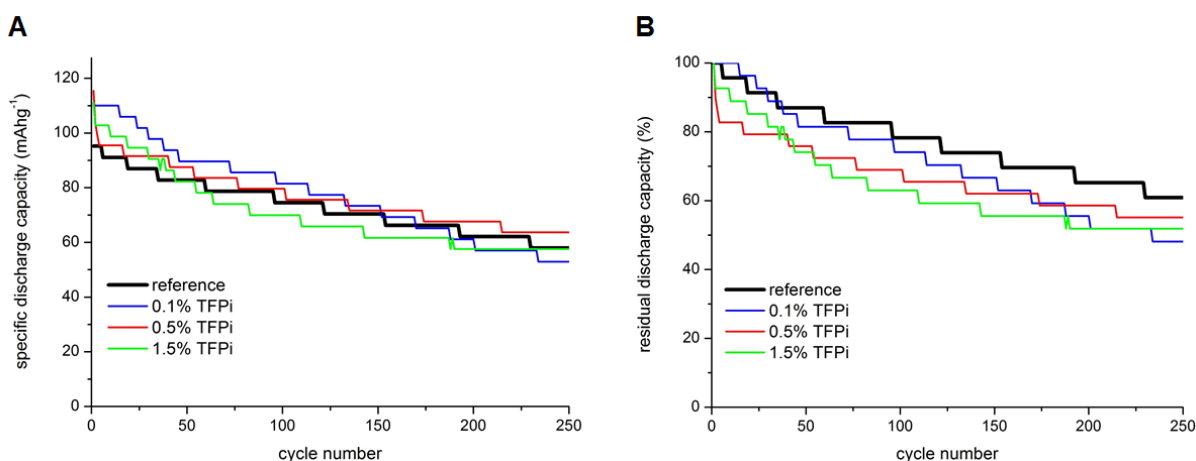


Figure 88 **A** Specific discharge capacity vs. cycle number plots and **B** residual discharge capacity vs. cycle number plots of C//LiNi_{0.4}Mn_{1.6}O₄ cells cycled between 3.3 and 4.8 V at 1C at 45 °C in 1 M LiPF₆ EC/EMC/DMC (1/1/1, w/w/w) without and with 0.1, 0.5, and 1.5% TFPi.

Trimethyl phosphate

Alkylphosphates are primarily known as flame retardant agents.^[205,398] Wang and colleagues were the first to propose trimethyl phosphate (TMP, see Figure 89) as a flame retardant additive or cosolvent in a mixed carbonate-based electrolyte solution.^[426]

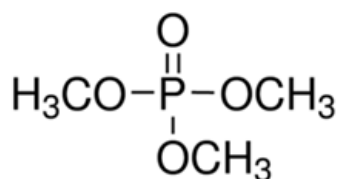


Figure 89 Chemical structure of trimethyl phosphate.

Typically, more than 20 vol% of TMP and less than 20 vol% DEC are necessary to alleviate the flammability of ternary systems such as 1 M LiPF₆ in EC/PC/TMP and 1 M LiPF₆ in EC/DEC/TMP.^[205,427] The high quantity of TMP helps to reduce the thermal decomposition of the conducting salt LiPF₆ by trapping organic radicals (e.g. H·) and the performance of common lithiated transition metal oxides like LCO or LMO is enhanced by TMP-containing electrolytes.^[398,426] Nevertheless, large amounts of TMP are not compatible with graphitic anodes. The additive hinders the formation of a compact SEI.^[205,398] Moreover, Wang and co-workers from Japan Aerospace Exploration Agency stated in 2006: “The poor reduction stability of the TMP solvent has led some authors to conclude that the goal of a TMP-based nonflammable electrolyte is impractical for lithium-ion cells.”^[428]

In contrast, TMP has been patented as additive or cosolvent for non-aqueous electrolytes in C//LiNi_{0.5}Mn_{1.5}O₄ cells by A. v. Cresce and K. Xu owing to its influence on the cathode surface layer.^[274] Furthermore, du Pont claimed the utilization of TMP in carbonate-based electrolytes for C//Li_xNi_yM_zMn_{2-y-z}O_{4-d} cells ($x = 0.03 - 1.0$, $y = 0.3 - 0.6$, $z = 0.01 - 0.18$, $d = 0 - 0.3$, and M = one or more of Cr, Fe, Co, Li, Al, Ga, Nb, Mo, Ti, Zr, Mg, Zn, V, and Cu).^[275] Recently, Utsugi et al. have demonstrated that the cycle performance of LTO//LiNi_{0.5}Mn_{1.5}O₄ coin cells is increased by the electrolyte formulation 1 M LiPF₆ in TMP.^[268] They corroborated that a polymer film derived from decomposition of TMP was formed on the cathode particles diminishing further electrolyte oxidation.

In this thesis, the impact of TMP on the electrochemical features of C//LiNi_{0.4}Mn_{1.6}O₄ pouch cells is explored. Figure 90 displays the cycling behavior of C//LiNi_{0.4}Mn_{1.6}O₄ full cells without and with various quantities of TMP.

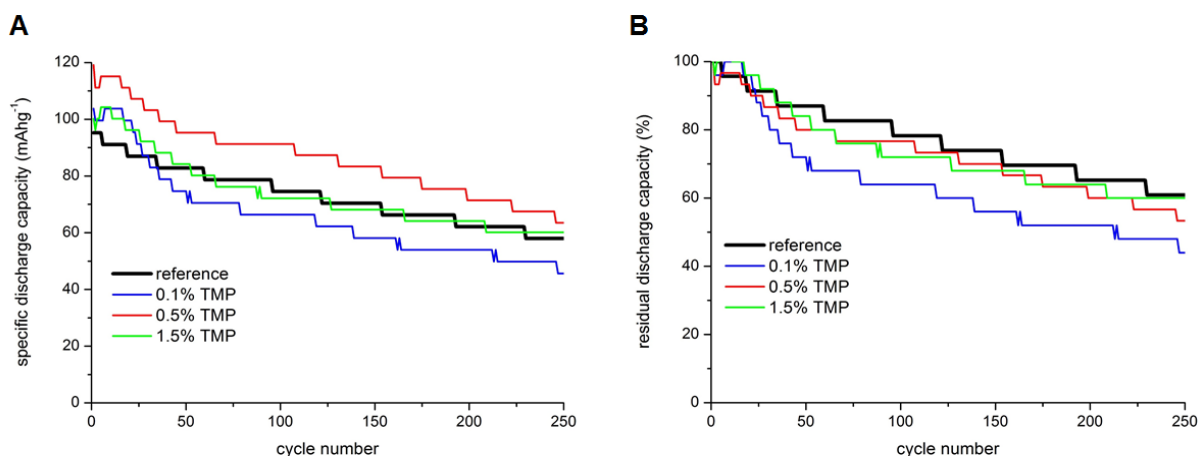


Figure 90 **A** Specific discharge capacity vs. cycle number plots and **B** residual discharge capacity vs. cycle number plots of C//LiNi_{0.4}Mn_{1.6}O₄ cells cycled between 3.3 and 4.8 V at 1C at 45 °C in 1 M LiPF₆ EC/EMC/DMC (1/1/1, w/w/w) without and with 0.1, 0.5, and 1.5% TMP.

All three additive concentrations result in higher initial specific discharge capacities than the base electrolyte (black line). Especially, the cell with 0.5% TMP (red line) provides an elevated

specific discharge capacity of 119.1 mAhg⁻¹. 0.1% TMP (blue line) causes a rapid capacity decline and merely 44% of the original capacity is attained after 250 cycles. 1.5% (green line) and 0.5% TMP improve the final specific discharge capacity to 60.1 and 63.5 mAhg⁻¹, respectively. The electrolyte with 0.5% TMP delivers the most specific energy regarding the whole cycle life and, hence, this additive concentration is recommended for C//LiNi_{0.4}Mn_{1.6}O₄ full cells. The modes of action of TMP are analyzed by microscopic and spectroscopic methods in the following chapters.

Tris(trimethylsilyl) phosphate

N.-S. Choi and his group have pointed out that tris(trimethylsilyl) phosphite is a promising additive for 5 V-class LiNi_{0.5}Mn_{1.5}O₄ cathode materials because it suppresses the decomposition of LiPF₆ by hydrolysis, effectively eliminates HF promoting Mn and Ni dissolution, and is involved in the generation of a protective layer on the cathode surface. As a consequence, excellent cycling stability of high voltage spinel full cells has been reported.^[270] Likewise, the patent by Bhat et al. shows enhanced cyclability of C//LiNi_{0.5}Mn_{1.5}O₅ cells when carbonate-based electrolytes include tris(trimethylsilyl) phosphate or TTSP (Figure 91).^[276] Besides, Li W. and co-workers have found that incorporation of TTSP in carbonate-containing electrolytes for Li//LiNi_{0.5}Mn_{1.5}O₄ half cells leads to good capacity retention. They identified TTSP as a film-forming agent, which inhibits the oxidation of electrolyte and the dissolution of manganese during cycling.^[429]

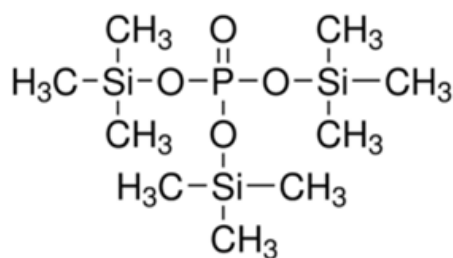


Figure 91 Chemical structure of tris(trimethylsilyl) phosphate.

In this work, organophosphorus TTSP is investigated as additive for the base electrolyte 1 M LiPF₆ in EC/EMC/DMC (1/1/1, w/w/w) in order to improve the electrochemical properties of LiNi_{0.4}Mn_{1.6}O₄ electrodes. Figure 92 depicts the specific discharge capacity vs. cycle number obtained upon CC/CV-cycling between 3.3 and 4.8 V at 45 °C for C//LiNi_{0.4}Mn_{1.6}O₄ pouch cells without (black line) and with several amounts of TTSP.

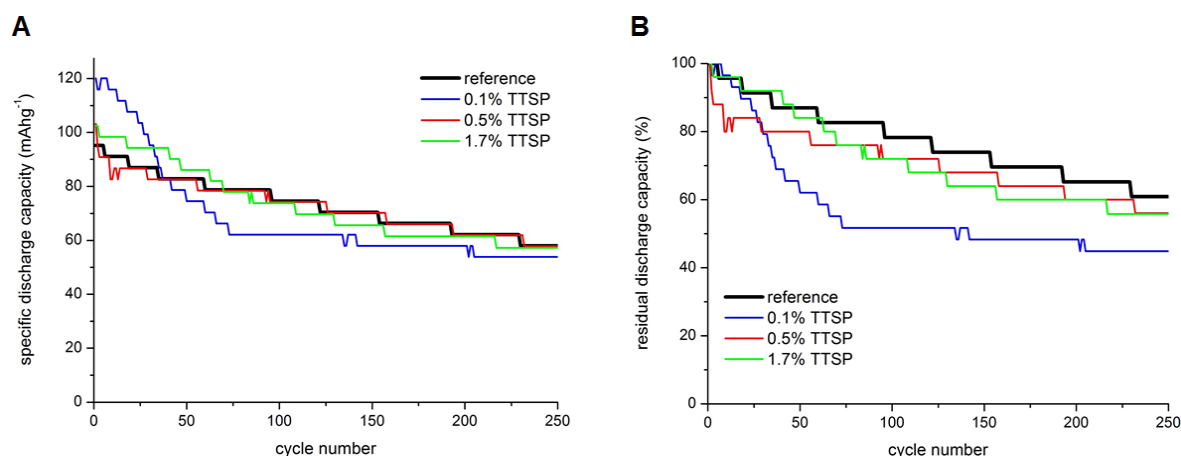


Figure 92 **A** Specific discharge capacity vs. cycle number plots and **B** residual discharge capacity vs. cycle number plots of C//LiNi_{0.4}Mn_{1.6}O₄ cells cycled between 3.3 and 4.8 V at 1C at 45 °C in 1 M LiPF₆ EC/EMC/DMC (1/1/1, w/w/w) without and with 0.1, 0.5, and 1.7% TTSP.

The cells comprising 0.1% (blue line), 0.5% (red line), and 1.7% TTSP (green line) reveal specific starting capacities of 120.1, 103.2, and 102.5 mAhg⁻¹, respectively, and the corresponding residual discharge capacities equal to 45%, 56%, and 56%, respectively. Thus, the good results described within literature could not be confirmed. The cell with 0.1% TTSP exhibits a drastic capacity deterioration, whereas the cell with 0.5% TTSP has almost no influence on the performance of C//LiNi_{0.4}Mn_{1.6}O₄ cells. The 1.7% TTSP cell offers a higher starting capacity but a little lower end capacity as the reference after cycling. For analyses, the last mentioned additive concentration is selected to examine the functional mechanism of TTSP on LiNi_{0.4}Mn_{1.6}O₄ cathodes.

Conclusion

HMDS, LiTFSI, and SEN were studied, for the first time, as electrolyte additives for the CAM lithium nickel manganese oxide spinel. However, only HMDS improves the electrochemical characteristics of C//LiNi_{0.4}Mn_{1.6}O₄ pouch cells. Figure 93 summarizes the CC/CV-cycling behavior of the high voltage spinel full cells with the reference electrolyte and with the best additive concentrations. The additives are ordered according to their decreasing beneficial effect. Hereby, the ones named above the reference enable a higher specific energy over cycle life than the base electrolyte. As can be seen, the cell containing 0.5% TMP displays by far the most advantageous cyclability, while 2.5% SA causes the most severe capacity fading.

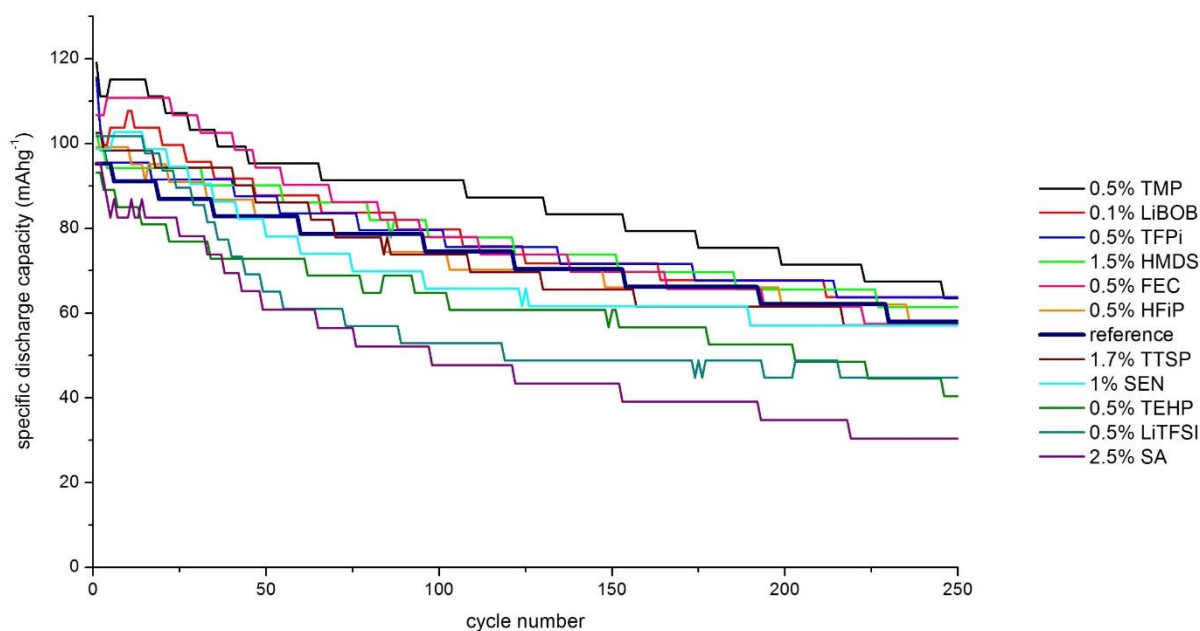


Figure 93 Specific discharge capacity vs. cycle number plots of C//LiNi_{0.4}Mn_{1.6}O₆ full cells cycled between 3.3 and 4.8 V at 1C at 45 °C in 1 M LiPF₆ EC/EMC/DMC (1/1/1, w/w/w) without and with various electrolyte additives.

Finally, Table 10 represents the C//LiNi_{0.4}Mn_{1.6}O₆ full cells with the additive concentrations that were investigated by microscopic and spectroscopic methods. Again, the substances are ordered according to their decreasing beneficial effect, whereby the ones named above the reference enable a higher specific energy over cycle life than the base electrolyte. For each additive, the concentration that revealed the best cycling behavior at the starting point of the analyses has been selected.

Ranking of the cycling stability	Additive	Influence on the cycling stability
1	0.5% TMP	+
2	0.5% TFPI	+
3	0.5% LiBOB	+
4	0.5% HMDS	+
5	0.5% HFiP	+
6	reference	0
7	1.7% TTSP	-
8	1% SEN	-
9	2.5% FEC	-
10	0.5% TEHP	-
11	1.5% LiTFSI	-
12	2.5% SA	-

Table 10 Overview of the additive concentrations that were investigated by microscopic and spectroscopic methods.

Optimization with Al₂O₃ coating layers

Another strategy to enhance the electrochemical properties of high voltage spinel electrodes is surface coating of the particles or of the prefabricated electrodes. Herein, an aqueous Al₂O₃ slurry is coated on graphite anodes and on LiNi_{0.4}Mn_{1.6}O₄ cathodes by doctor blading. The resulting thicknesses of the ceramic films were about 4 - 5 µm. Figure 94 shows cross-sections of a calendered LiNi_{0.4}Mn_{1.6}O₄ electrode with an Al₂O₃ layer on top of it prior to the cell tests. The images clearly reveal the small-sized, quite uniformly deposited Al₂O₃ particles on the outer surface of the cathode. The grainy and porous nanostructured ceramic layer provides sufficient pathways for electron and lithium ion transfer and, hence, ensures good reversibility of the charge/discharge processes. As outlined in chapter 3, Al₂O₃ should prevent Mn and Ni dissolution into the electrolyte by scavenging HF and is supposed to alleviate the deposition of Mn²⁺ and Ni²⁺ on the graphite surface, which implies avoiding excessive SEI formation and inhibiting damage to the SEI layer.

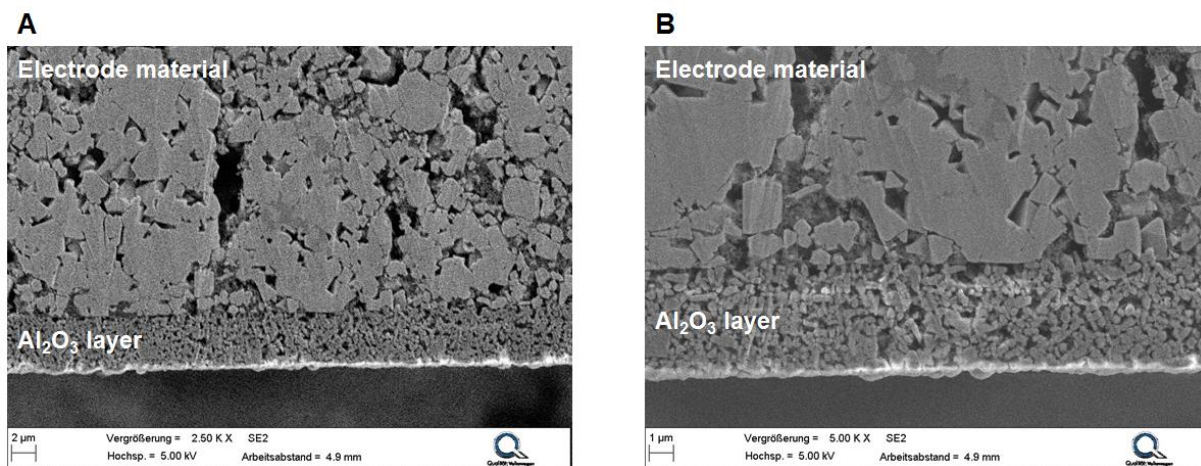


Figure 94 Cross-sections of a LiNi_{0.4}Mn_{1.6}O₄ composite electrode with **A** 2,500- and **B** 5,000-times amplification.

The positive impact of coating Al₂O₃ onto the surface of high voltage spinel particles on their electrochemical performance has already been verified.^[290,291,430–432] Usually, two mechanisms are proposed. On one hand, the ceramic layer traps HF from the electrolyte and, thus, prohibits transition metal dissolution. On the other hand, Al₂O₃ coating acts as a physical protection layer. It blocks direct contact between the non-aqueous electrolyte and the CAM. As a consequence, less side reactions involving electrolyte decomposition occur. It is important to note that complete coverage is the key for the latter functionality.^[1,292]

Lately, the process of atomic layer deposition (ALD) has been established to coat ultrathin Al₂O₃ surface coatings on lithium nickel manganese oxide cathodes. For example, P. Lu and his group have prepared Al₂O₃-modified LiNi_{0.5}Mn_{1.5}O₄ thin-film electrodes by pulsed laser deposition. They have found increased cycling stability and rate capability of the associated half cells. Notably, 20 nm thick Al₂O₃-modified samples showed the best results. The ceramic layer not only minimizes harmful side reactions between the spinel material and the electrolyte, but also guarantees rapid diffusion and migration of lithium ions in the course of intercalation/deintercalation.^[433] L. Hu et al. describe enhanced cycling characteristics for Li//LiNi_{0.5}Mn_{1.5}O₄ coin cells, when the cathode surface is coated with ultrathin ALD-Al₂O₃ layers (< 1 nm). It has been confirmed that the ceramic coating reduces electrolyte oxidation on high voltage LIB cathodes.^[434] Similarly, C. Zhou and co-workers have demonstrated excellent capacity retention for ALD-Al₂O₃-modified LiNi_{0.5}Mn_{1.5}O₄ electrodes in half cells. The extremely thin ceramic layer mitigates undesirable side reactions during cycling and maintains the electronic and ionic conductivity of the spinel cathode.^[435] Moreover, P. Lu et al. have investigated thin atomic layer deposited Al₂O₃ surface coatings (< 5 nm) on graphite and LiNi_{0.5}Mn_{1.5}O₄ electrodes by galvanostatic cycling experiments of the corresponding full cells. It has been recognized that although Al₂O₃ layers on the positive electrode suppress Mn dissolution, the Al₂O₃ coating on the negative electrode is even more advantageous. Here,

additionally Mn deposition on the graphite anode is prevented. Consistently, the ceramic layer on the graphite electrode leads to better cell lives than coating on the spinel cathode.^[436]

In this study, the electrochemical performance of pouch cells containing Al₂O₃-coated graphite anodes and LiNi_{0.4}Mn_{1.6}O₄ cathodes is evaluated and compared to the reference cell comprising bare electrodes. Figure 95 illustrates the 1C cycling properties of the C//LiNi_{0.4}Mn_{1.6}O₄ full cells without (black line) and with a ceramic layer on the cathode (blue line), on the anode (red line), and on both electrodes (green line) in the voltage window of 3.3 - 4.8 V at 45 °C.

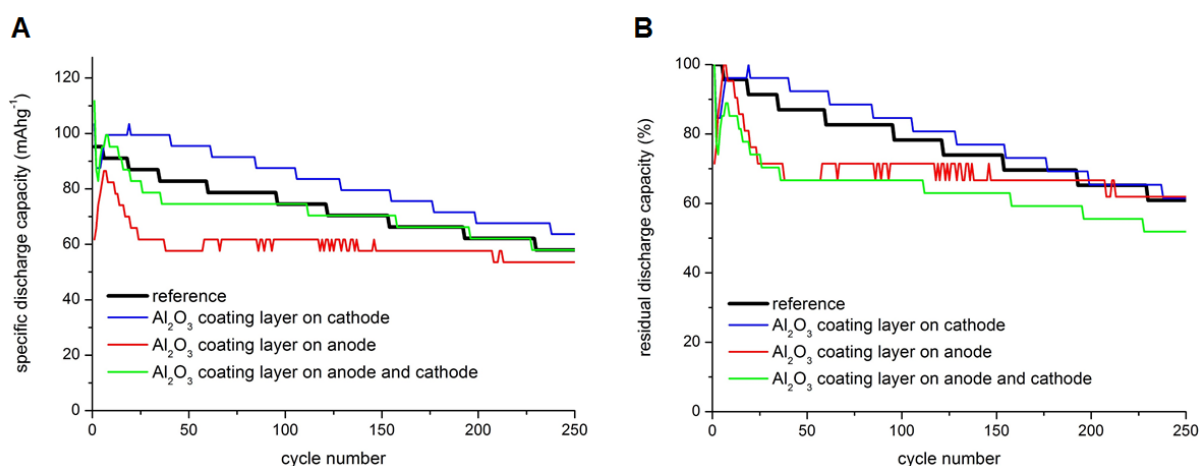


Figure 95 **A** Specific discharge capacity vs. cycle number plots and **B** residual discharge capacity vs. cycle number plots of C//LiNi_{0.4}Mn_{1.6}O₄ cells cycled between 3.3 and 4.8 V at 1C at 45 °C in 1 M LiPF₆ EC/EMC/DMC (1/1/1, w/w/w) without and with a ceramic layer on the spinel cathode, on the graphite anode, and on both electrodes.

The reference exhibits an initial specific discharge capacity of 95.2 mAhg⁻¹, which diminishes to 58.0 mAhg⁻¹ after 250 cycles. Interestingly, the Al₂O₃ coating on both electrodes causes a rapid capacity decay at the beginning of cycling. Afterwards, the cell life is stabilized. This phenomenon is also observed for the cell with the Al₂O₃-coated anode. Therefore, it is believed that the ceramic layer on the graphite electrode hampers SEI formation. It results in a rather thick surface layer that is not fully developed or stabilized until ca. 25 cycles after starting the cycling experiment. The initial fast capacity decline reflects the additional consumption of active lithium ions due to the severe SEI generation. While the cell with the Al₂O₃-modified anode offers only 53.5 mAhg⁻¹ or 62% of its original capacity after cycling, the cell with both coated electrodes features a final capacity of 58.0 mAhg⁻¹ (52% residual discharge capacity). The better performance of the latter cell is ascribed to the positive influence of Al₂O₃. Regarding the full cell with the ceramic layer deposited on the spinel electrode, a high specific starting capacity of 103.4 mAhg⁻¹ is achieved and superior cyclability with 62% capacity retention (63.7 mAhg⁻¹) over 250 cycles is attained. Al₂O₃ coating also impedes surface layer formation on the cathode. Nonetheless, in this case, the suppression of direct contact between the

electrode materials and the electrolyte is favorable to circumvent harmful side reactions upon cycling.

Conclusion

As far as we are aware, there is no report so far involving detailed investigations of the combined use of Al₂O₃-modified LiNi_{0.4}Mn_{1.6}O₄ cathodes and Al₂O₃-modified graphite anodes (4 - 5 μ m layer thickness). The cycling stability examinations above demonstrate that the cell with Al₂O₃ coating on the spinel cathode produces the most specific energy, which is markedly greater as the gravimetric energy gained by the reference. Microscopic and spectroscopic post-mortem analyses of the full cell including both Al₂O₃-modified electrodes will give more information on the impact of the ceramic layer on the electrochemical features of high voltage spinel full cells in the following chapters.

5.2.3 Rate capability tests

Apart from CC/CV-cycling experiments, rate capability tests were conducted with C//LiNi_{0.4}Mn_{1.6}O₄ to examine the suitability of the electrolyte additives and the Al₂O₃ films for facilitating charge-transfer processes at the electrode surfaces. Thereto, the correlating full cells were cycled for four cycles between 3.3 and 4.8 V at room temperature under subsequently varied C-rates. The applied charge/discharge rates were increased from 1C to 5C, then reduced to 0.1C, and finally enhanced again to 1C. Owing to this order, it is possible to tell if the particular cell is irreversibly damaged by the high C-rate of 5C or if it recovers after cycling with lower C-rates. The rate capability studies were accomplished at BOL and EOL to verify the charging capability of these cells after 250 cycles.

Electrolyte optimization

A comparison of the rate capability between C//LiNi_{0.4}Mn_{1.6}O₄ cells without and with various different electrolyte additives before cycling is depicted in Figure 96A. For the reference cell, specific discharge capacities of 116.8, 37.3, 118.2, and 112.8 mAhg⁻¹ are detected for the C-rates of 1, 5, 0.1, and 1C, respectively. The strong capacity decay at 5C reveals that the lithium diffusion processes upon intercalation/deintercalation are too slow to realize a satisfactory capacity at the high C-rate. In other words, the time for completely charging/discharging the cathode or the anode is insufficient and the actual potential of the CAM cannot be used. Nevertheless, at the second 1C cycle approx. 97% of the original capacity is retained in LiNi_{0.4}Mn_{1.6}O₄. This represents good structural integrity and leaves no structural damage after high current cycling. The 0.1C discharge capacity is slightly higher than the 1C value. Here, more time is available for the lithium ions to migrate from the cathode

to the anode and vice versa. Considering the additive-containing full cells at BOL, an overall similar behavior is noted. The cells comprising 0.5% TMP, 0.5% HFiP, 1.7% TTSP, 1% SEN, 2.5% FEC, and 2.5% SA afford higher specific discharge capacities compared to the base electrolyte for all C-rates. Hence, these additives enable faster diffusion kinetics at BOL. On the contrary, 0.5% TFPi, 0.5% TEHP, and 1.5% LiTFSI lead to higher 1C and 0.1C capacities, but to significantly lower 5C capacities than the baseline. Cells with 0.5% LiBOB, and 0.5% HMDS unveil nearly the same specific discharge capacity values as the reference cell.

The rate capability tests of the same cells after the CC/CV-cycling experiments are displayed in Figure 96B. At EOL, the cell cycled in the base electrolyte provides much lower capacities than before. 32.4, 2.4, 44.5, and 32.9 mAhg⁻¹ are registered at 1, 5, 0.1, and 1C, respectively. Consequently, lots of lithium is consumed. Side reactions and massive surface layer formation on the electrodes are responsible. Thus, the spinel structure is not completely retained. It shows a lithium deficit. Obviously, the 0.5% TMP cell, which delivers 7.2 mAhg⁻¹ at 5C and up to 52.0 mAhg⁻¹ at 1C is the best performing one with respect to the rate capability of C//LiNi_{0.4}Mn_{1.6}O₄ cells. Therefore, the TMP-derived SEI/SPI facilitates charge-transfer processes at the electrodes. 0.5% LiBOB and 0.5% HMDS also engender higher specific discharge capacities than the reference electrolyte. The introduction of 1.7% TTSP and 0.5% TEHP into the base electrolyte exacerbates the rate capability of the spinel full cells. This is because the former additives develop low-impedance protective layers on the anode/cathode surfaces, whereas the latter hamper faster kinetics of the electrodes. Cells containing 0.5% TFPi and 0.5% HFiP exhibit capacities similar to the reference. Results concerning other additives are not presented, since their capacity values were zero for all C-rates. This proves the negative effect of these substances on the cycling properties and the rate capability of C//LiNi_{0.4}Mn_{1.6}O₄ cells.

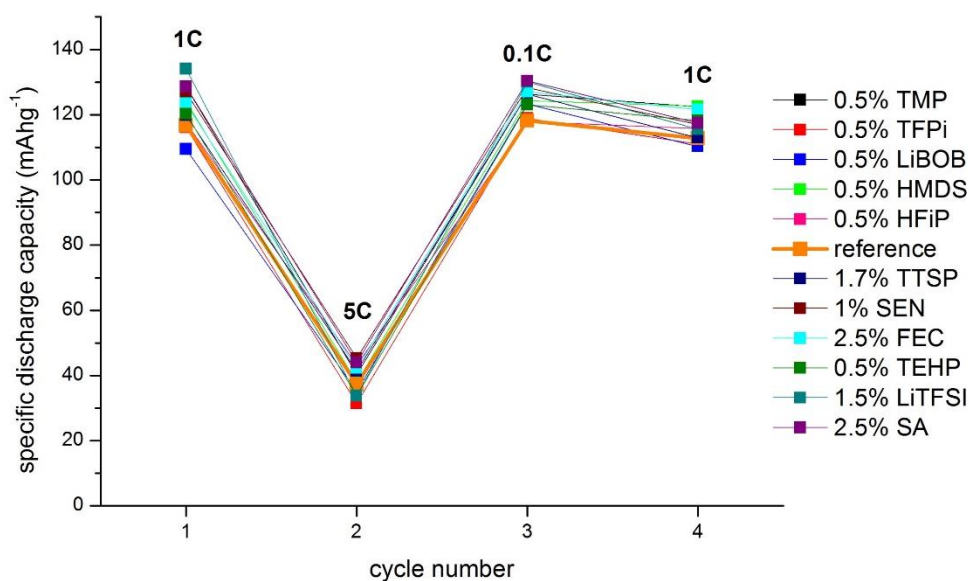
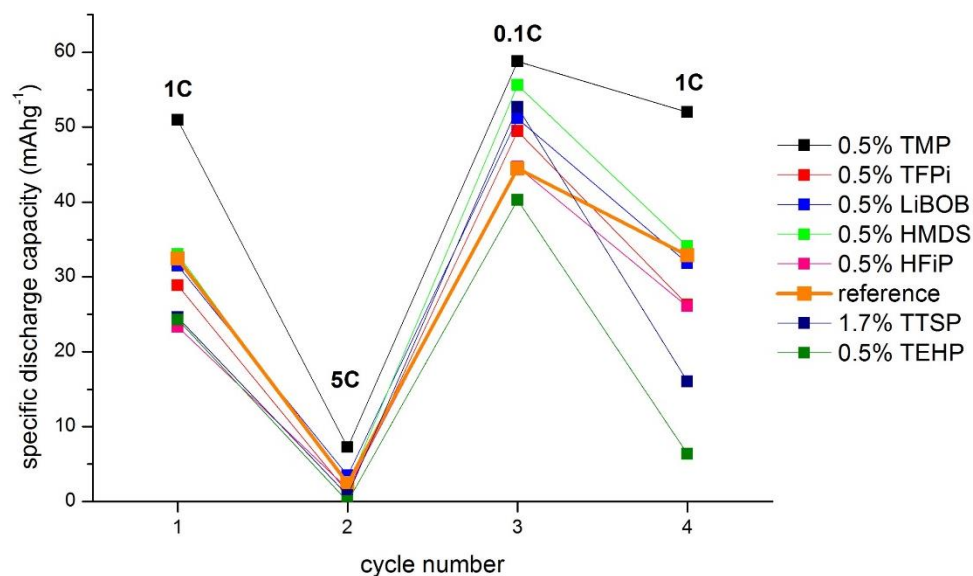
A**B**

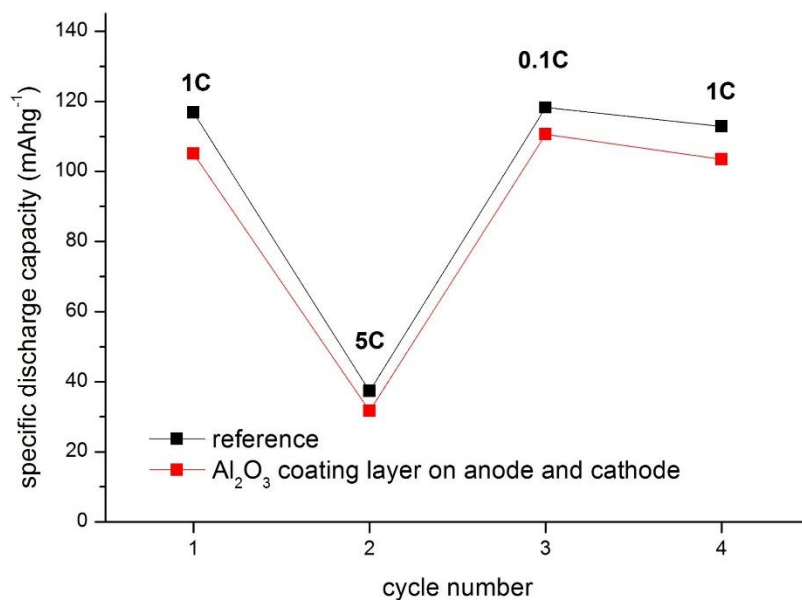
Figure 96 Rate capability tests of C//LiNi_{0.4}Mn_{1.6}O₄ pouch cells without and with various electrolyte additives cycled between 3.3 and 4.8 V at room temperature at different C-rates **A** before and **B** after the CC/CV-cycling experiments at 45 °C.

Optimization with Al₂O₃ coating layers

The rate capability of the cells with bare and Al₂O₃-coated graphite and spinel electrodes before and after the cycling stability studies is illustrated in Figure 97. At BOL, the Al₂O₃-modified sample reveals lower specific discharge capacities for all measured C-rates than the reference. At EOL, compared with pristine electrodes, the modified sample offers appreciably higher capacities in the whole C-rate cycling. In fact, the 1, 5, 0.1, and 1C capacities equal to 37.6, 7.7, 52.5, and 37.7 mAhg⁻¹, respectively. Therefore, Al₂O₃ helps to

lower resistances at the electrode surfaces with increasing cycle number and plays an important role in improving the electrochemical characteristics of C//LiNi_{0.4}Mn_{1.6}O₄ cells.

A



B

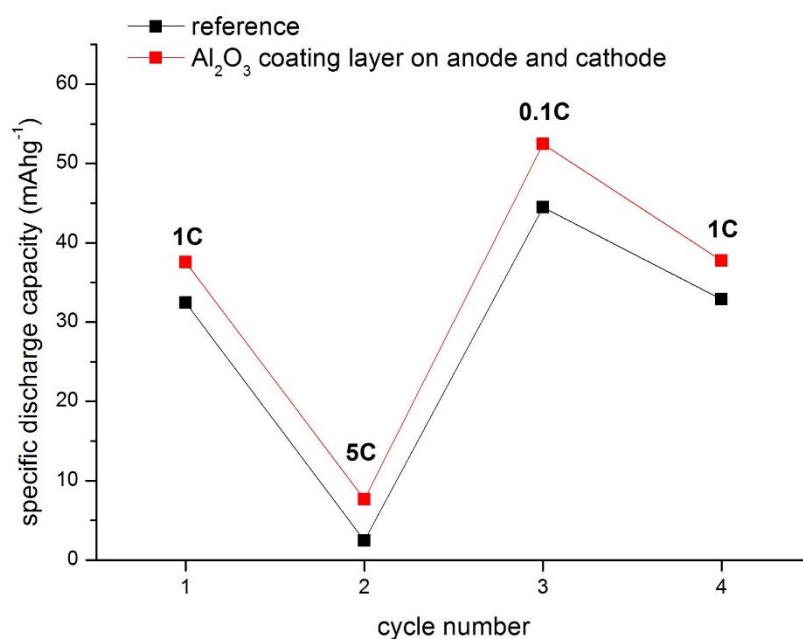


Figure 97 Rate capability tests of C//LiNi_{0.4}Mn_{1.6}O₄ pouch cells with bare and Al₂O₃-coated electrodes cycled between 3.3 and 4.8 V at room temperature at different C-rates **A** before and **B** after the CC/CV-cycling experiments at 45 °C.

5.3 Post-mortem analyses of the cathode active material – determination of different phase compositions

5.3.1 X-ray diffraction

As outlined in chapter 2.2.2, numerous publications refer to two topotactic two-phase reactions of $\text{LiNi}_{0.5}\text{Mn}_{1.5}\text{O}_4$ involving three cubic phases throughout charging/discharging. All of them depend on the lithium content and the transition metal oxidation states, whereby the reports are partially conflicting.^[195,200,206,224,230,233] In this work, non-destructive ex situ XRD spectroscopy of fully discharged $\text{LiNi}_{0.4}\text{Mn}_{1.6}\text{O}_4$ cathodes (0% SOC) was performed after 250 cycles at 45 °C to investigate changes of the spinel structure during cycling C// $\text{LiNi}_{0.4}\text{Mn}_{1.6}\text{O}_4$ pouch cells without and with various electrolyte additives. All reflections and the corresponding 2θ -values are listed in Table 12 and all refined results are summarized in Table 13. The cell comprising 1.5% LiTFSI was not analyzed by XRD because of cell damage due to massive gassing while cycling.

Figure 98A represents the XRD pattern for a fresh $\text{LiNi}_{0.4}\text{Mn}_{1.6}\text{O}_4$ cathode, which exhibits a phase-pure cubic spinel structure lacking impurities such as NiO or $\text{Li}_x\text{Ni}_{1-x}\text{O}$. The sharp reflections from the (111), (220), (311), (222), (400), (331), (511), (440), (531), (442), (533), (622), (444), (551), (731), (800), and (733) planes are characteristic for $\text{LiNi}_{0.4}\text{Mn}_{1.6}\text{O}_4$ (JCPDS#80-2162, see chapter 7). They indicate that the original material is highly crystalline. Performing Rietveld refinement gives the following cation distribution for $\text{LiNi}_{0.4}\text{Mn}_{1.6}\text{O}_4$ (S.G. Fd3m). Li ions occupy the tetrahedral 8a sites, Ni and Mn ions are randomly distributed in octahedral 16d sites, and O ions are located in 32e sites (Table 11). The associated lattice parameter and the cell volume equal to $a = 8.18 \text{ \AA}$ and $V = 547 \text{ \AA}^3$, respectively. Subsequently, this structure is denoted as the first cubic phase of $\text{LiNi}_{0.4}\text{Mn}_{1.6}\text{O}_4$.

Atom	Wyckoff position	X	Y	Z	occupancy
Li	8a	1/8	1/8	1/8	1
Ni	16d	1/2	1/2	1/2	0.2
Mn	16d	1/2	1/2	1/2	0.8
O	32e	0.263	0.263	0.263	1

Table 11 Structural parameters obtained from Rietveld refinement of a fresh $\text{LiNi}_{0.4}\text{Mn}_{1.6}\text{O}_4$ cathode based on space group Fd3m.

5.3 Post-mortem analyses of the CAM – determination of different phase compositions

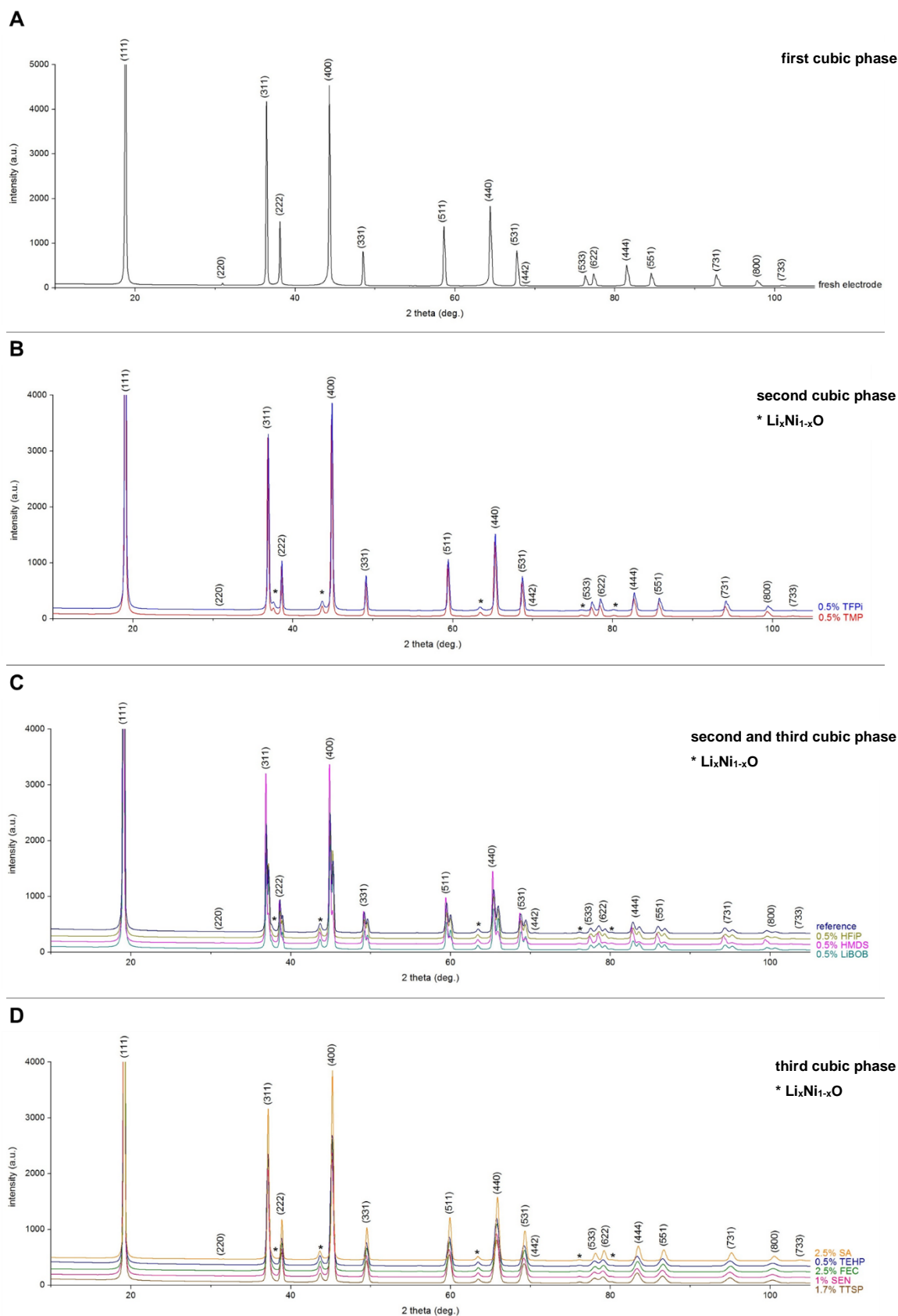


Figure 98 X-ray diffraction spectra of fresh and cycled $\text{LiNi}_{0.4}\text{Mn}_{1.6}\text{O}_4$ cathodes (1C; 45 °C; 0% SOC) of cells without and with various electrolyte additives. The spinel material reveals three cubic phases in dependence of the lithium content as well as the transition metal oxidation states: **A** first cubic phase, **B** second cubic phase, **C** second and third cubic phase, and **D** third cubic phase.

Figure 98B - D displays the XRD patterns of the spinel electrodes after cycling at 45 °C in the additive-free reference electrolyte and with diverse electrolyte additives. Interestingly, different XRD patterns are observed after 250 cycles. All cycled cathodes reveal decreased and slightly broadened intensities compared to the fresh one. The weakened spinel diffractions are attributed to thick layers of electrolyte decomposition products on top of the cathode. It is assumed that each additive provokes the formation of another composition of SPI, which might protect the electrode from structural corrosion upon cycling. More detailed information on the SPI layer is discussed in chapter 5.5. The broadening of the reflection is directly related to the loss of crystallinity, which is initiated by increased defects of the cycled $\text{LiNi}_{0.4}\text{Mn}_{1.6}\text{O}_4$ like for example voids introduced by transition metal dissolution.

The diffraction intensity of the (220) plane near $2\theta \approx 31^\circ$ diminishes for the cycled spinel material in contrast to the fresh one. Generally, this reflection originates from cations occupying the 8a tetrahedral sites. As already stated, in the fresh $\text{LiNi}_{0.4}\text{Mn}_{1.6}\text{O}_4$ cathode only Li ions are located in the 8a sites. On one hand, the decline of the (220) diffraction is assigned to the development of a thick SPI, which attenuates all reflection intensities. On the other hand, it implies the loss of active Li ions during cycling. This is confirmed by cycling stability studies in the previous chapter. Additionally, the extremely low diffraction intensity precludes the occupation of 8a tetrahedral sites by transition metal ions (Mn and/or Ni), since in this case the (220) reflection would be stronger than for the fresh electrode due to the better diffraction ability of Ni and Mn cations compared to Li ions.^[5,223,437]

The XRD spectra of the cycled $\text{LiNi}_{0.4}\text{Mn}_{1.6}\text{O}_4$ cathodes show five additional reflections at $2\theta = 37.6^\circ, 43.7^\circ, 63.4^\circ, 76.1^\circ$, and 80.1° as marked by asterisks in Figure 98B - D. They are ascribed to the presence of $\text{Li}_x\text{Ni}_{1-x}\text{O}$ impurities ($x < 1$), which are produced throughout the electrochemical process (NiO, JCPDS#04-0835, see chapter 7).^[189,253,438] Unfortunately, it is impossible to determine the exact amount of the generated $\text{Li}_x\text{Ni}_{1-x}\text{O}$ for each sample, because the respective reflections are rather small and are partially overlapped with the diffractions of the spinel material. Nevertheless, structural deterioration of the CAM takes place and is, among other things, responsible for capacity fading in CC/CV-cycling experiments.

5. Results and discussion

5.3 Post-mortem analyses of the CAM – determination of different phase compositions

hkl	Fresh electr. 2 Θ (°)	0.5% TMP 2 Θ (°)	0.5% TFPi 2 Θ (°)	0.5% LiBOB 2 Θ (°)	0.5% HMDS 2 Θ (°)	0.5% HFIP 2 Θ (°)	Ref. 2 Θ (°)	1.7% TTSP 2 Θ (°)	1% SEN 2 Θ (°)	2.5% FEC 2 Θ (°)	0.5% TEHP 2 Θ (°)	2.5% SA 2 Θ (°)
111	18.8	19.0	19.1	19.1 19.2	19.1 19.2	19.1 19.2	19.1 19.2	19.1 19.2	19.2	19.2	19.2	19.2
220	30.9	31.3	31.3	31.4 31.6	31.4 31.6	31.4 31.6	31.4 31.6	31.4 31.6	31.5	31.5	31.5	31.5
311	36.4	36.9	36.9	37.0 37.2	36.9 37.2	36.9 37.2	36.9 37.2	37.0 37.2	37.2	37.2	37.2	37.2
Li _x Ni _{1-x} O	-	37.6	37.6	37.6	37.6	37.6	37.6	37.6	37.6	37.6	37.6	37.6
222	38.1	38.6	38.6	38.7 39.0	38.6 38.9	38.6 38.9	38.7 38.9	38.7 38.9	38.9	38.9	38.9	38.9
Li _x Ni _{1-x} O	-	43.7	43.7	43.7	43.7	43.7	43.7	43.7	43.7	43.7	43.7	43.7
400	44.3	44.9	44.9	45.0 45.3	44.9 45.2	44.9 45.2	44.9 45.3	45.0 45.3	45.2	45.2	45.2	45.2
331	48.5	49.1	49.2	49.2 49.6	49.1 49.6	49.2 49.6	49.2 49.6	49.2 49.6	49.5	49.5	49.5	49.5
511	58.6	59.4	59.4	59.5 60.0	59.4 60.0	59.5 60.0	59.5 60.0	59.5 60.0	59.9	59.9	59.9	59.9
Li _x Ni _{1-x} O	-	63.4	63.4	63.4	63.4	63.4	63.4	63.4	63.4	63.4	63.4	63.4
440	64.4	65.3	65.3	65.4 65.9	65.3 65.9	65.4 65.9	65.4 65.9	65.4 65.9	65.8	65.8	65.8	65.9
531	67.8	68.7	68.7	68.8 69.4	68.7 69.3	68.8 69.3	68.8 69.4	68.8 69.4	69.3	69.3	69.3	69.4
442	68.8	69.7	69.8	69.8 70.6	69.8 70.6	69.8 70.6	69.8 70.6	69.8 70.6	70.5	70.6	70.5	70.5
Li _x Ni _{1-x} O	-	76.1	76.1	76.1	76.1	76.1	76.1	76.1	76.1	76.1	76.1	76.1
533	76.3	77.4	77.4	77.5 78.0	77.4 78.0	77.5 78.1	77.4 78.0	77.4 78.0	78.0	78.1	78.0	78.1
622	77.4	78.5	78.5	78.6 79.2	78.5 79.1	78.6 79.2	78.6 79.2	78.6 79.2	79.1	79.1	79.1	79.2
Li _x Ni _{1-x} O	-	80.1	80.1	80.1	80.1	80.1	80.1	80.1	80.1	80.1	80.1	80.1
444	81.5	82.7	82.7	82.8 83.5	82.7 83.4	82.8 83.5	82.8 83.5	82.8 83.5	83.4	83.4	83.4	83.5
551	84.6	85.8	85.8	85.7 86.7	85.8 86.7	85.9 86.7	85.9 86.7	85.9 86.7	86.6	86.6	86.6	86.7
731	92.7	94.2	94.2	94.3 95.1	94.2 95.0	94.3 95.0	94.3 95.1	94.3 95.1	95.0	95.1	95.0	95.1
800	97.8	99.4	99.4	99.5 100.6	99.4 100.5	99.5 100.6	99.5 100.6	99.5 100.6	100.5	100.6	100.5	100.5
733	100.9	102.7	102.7	102.8 103.8	102.7 103.8	102.8 103.8	102.8 103.9	102.8 103.9	103.8	103.9	103.8	103.8

Table 12 XRD reflections and corresponding 2 Θ -values of fresh and cycled LiNi_{0.4}Mn_{1.6}O₄ cathodes (1C; 45 °C; 0% SOC) of cells without and with various electrolyte additives.

	Fresh electr.	0.5% TMP	0.5% TFPi	0.5% LiBOB	0.5% HMDS	0.5% HFiP	Ref.	1.7% TTSP	1% SEN	2.5% FEC	0.5% TEHP	2.5% SA
a (Å)	8.18	8.09	8.08	8.07 8.02	8.08 8.02	8.07 8.01	8.07 8.01	8.03	8.03	8.03	8.03	8.02
V (Å ³)	547	529	528	526 516	528 516	526 514	526 514	518	518	518	518	516
R_{wp} (%)	15.4	17.0	19.9	14.5 14.5	15.1 15.1	16.8 16.8	14.8 14.8	16.9	16.8	15.8	16.0	13.8
R_{Bragg} (%)	1.76	2.52	3.97	1.92 1.70	1.90 1.16	1.35 1.16	1.35 1.16	2.74	2.56	2.11	2.34	1.06

Table 13 Refinement results for fresh and cycled $\text{LiNi}_{0.4}\text{Mn}_{1.6}\text{O}_4$ cathodes (1C; 45 °C; 0% SOC) of cells without and with various electrolyte additives based on space group Fd3m.

More importantly, the reflections of the spinel electrodes shift to higher 2Θ angles after 250 cycles at 45 °C. These diffraction shifts correspond to two newly formed, distinct cubic phases of the same space group as the initial phase but with different refined lattice constants of 8.07 - 8.09 Å (second cubic phase) and 8.01 - 8.03 Å (third cubic phase). Thus, the cell parameters decrease by $\approx 1\%$ and $\approx 2\%$ compared to the first cubic phase (8.18 Å). The estimated values of the cubic lattice constants for the three phases are in good agreement with the literature.^[195,200,232,233,236,349,439] Thereby, it has to be noted that typically phase transitions are correlated with charge and discharge processes rather than cycling. Moreover, only Baddour-Hadjean et al. have examined the structural changes of the high voltage spinel material with the composition $\text{LiNi}_{0.4}\text{Mn}_{1.6}\text{O}_4$, while the others refer to the composition $\text{LiNi}_{0.5}\text{Mn}_{1.5}\text{O}_4$.^[349]

Regarding the cycled $\text{LiNi}_{0.4}\text{Mn}_{1.6}\text{O}_4$ cathodes, 0.5% TMP and 0.5% TFPi lead to the generation of the second cubic phase, whereas 1.7% TTSP, 1% SEN, 2.5% FEC, 0.5% TEHP, and 2.5% SA result in the formation of the third cubic phase. The reference cell and the cells containing 0.5% HFiP, 0.5% HMDS, and 0.5% LiBOB exhibit both, the second and the third cubic phase of $\text{LiNi}_{0.4}\text{Mn}_{1.6}\text{O}_4$ after 250 cycles at 45 °C. Figure 99 gives an overview of the lattice constants of the fresh and the cycled $\text{LiNi}_{0.4}\text{Mn}_{1.6}\text{O}_4$ cathodes in dependence of the applied electrolyte additive. The smaller lattice dimensions of the second and third cubic phases and the associated reflection shifts towards higher 2Θ angles are directly connected to a reduced lithium content as well as higher transition metal oxidation states in the spinel lattice.

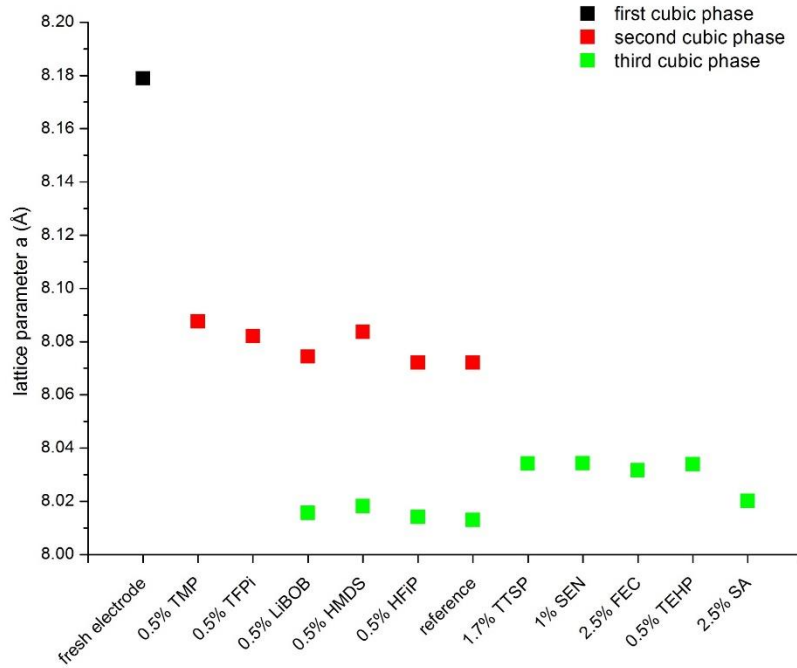


Figure 99 Overview of the lattice constants of the fresh and the cycled $\text{LiNi}_{0.4}\text{Mn}_{1.6}\text{O}_4$ cathodes (1C; 45 °C; 0% SOC) in dependence of the applied electrolyte additive.

While, the fresh cathode has no lithium deficiency, the cycled electrodes have lost different amounts of active lithium due to side reactions with the electrolyte, HF or trace amounts of H_2O . As outlined in chapter 5.2, the base electrolyte and the diverse electrolyte additives have variable effects on the cycling stability of C// $\text{LiNi}_{0.4}\text{Mn}_{1.6}\text{O}_4$ pouch cells. Hence, they change the residual quantity of lithium in the positive electrodes. Calculating the lithium content x in the completely discharged $\text{Li}_x\text{Ni}_{0.4}\text{Mn}_{1.6}\text{O}_4$ cathodes from the specific discharge capacities obtained after cycling, gives the following correlations:

first cubic phase: $x = 1$

second cubic phase: $0.432 \leq x \leq 0.433$

second and third cubic phase: $0.392 \leq x \leq 0.415$

third cubic phase: $0.207 \leq x \leq 0.390$

Consequently, the longer the cell is aged and the lower the amount of lithium is in the spinel cathode, the more pronounced is the phase transition within the $\text{LiNi}_{0.4}\text{Mn}_{1.6}\text{O}_4$ material. The second cubic phase represents only slightly aged spinel electrodes, whereas the third cubic phase signifies severely aged $\text{LiNi}_{0.4}\text{Mn}_{1.6}\text{O}_4$ cathodes. To the best of our knowledge, this is the first time that ageing degrees of $\text{LiNi}_{0.4}\text{Mn}_{1.6}\text{O}_4$ electrodes have been identified by means of their phase composition.

With declining lithium content, the transition metal valence states increase on account of charge compensation. Initially, Mn^{3+} ($r \approx 0.65 \text{ Å}$) is oxidized to Mn^{4+} ($r \approx 0.53 \text{ Å}$) and then Ni^{2+} ($r \approx 0.69 \text{ Å}$) to Ni^{3+} ($r \approx 0.56 \text{ Å}$) and to Ni^{4+} ($r \approx 0.48 \text{ Å}$).^[232,440] Therefore, the diminution of the

lattice parameters is concordant to the diminishing ionic radii of the transition metal ions and the corresponding shortened Mn-O and Ni-O bond lengths. Actually, the Mn³⁺-O bond length of ≈ 2.01 Å reduces to 1.89 Å for the Mn⁴⁺-O bond length, while the Ni²⁺-O, Ni³⁺-O, and Ni⁴⁺-O bond lengths equal to ≈ 2.06 , ≈ 1.97 , and ≈ 1.88 Å, respectively.^[441] Based on the previously calculated intercalation stages of the cycled spinel electrodes, the subsequent oxidation states are expected:

first cubic phase: Ni²⁺, Mn^{3+/4+}

second cubic phase: Ni^{2+/3+}, Mn⁴⁺

third cubic phase: Ni^{3+/4+}, Mn⁴⁺

However, the real valance states of each transition metal in LiNi_{0.4}Mn_{1.6}O₄ are determined by Raman spectroscopy, which is elucidated in the next chapter.

Conclusion

The cycled LiNi_{0.4}Mn_{1.6}O₄ cathodes reveal considerable changes in their XRD patterns compared to the fresh electrode. A thick SPI layer and presumably transition metal dissolution cause the shrinkage and the broadening of the reflection intensities, respectively. Moreover, the formation of Li_xNi_{1-x}O impurities contributes to the structural deterioration of the CAM upon cycling. The ageing of the spinel electrodes is strongly influenced, to a varying extent, by the reference electrolyte and the diverse electrolyte additives. This leads to different phase compositions of the cycled LiNi_{0.4}Mn_{1.6}O₄ cathodes. Herein it is shown, for the first time, that ageing of LiNi_{0.4}Mn_{1.6}O₄ electrodes is derived from their phase composition at 0% SOC. An electrolyte additive is only effective when just the second cubic phase is observed for the cycled and completely discharged spinel electrode. In this work, 0.5% TMP and 0.5% TFPi have the most beneficial impact on the electrochemical characteristics of C//LiNi_{0.4}Mn_{1.6}O₄ cells. The corresponding cycled cathodes exhibit solely the second cubic phase at 0% SOC. 0.5% LiBOB, 0.5% HMDS, and 0.5% HFiP deliver both cubic phases and 1.7% TTSP, 1% SEN, 2.5% FEC, 0.5% TEHP, and 2.5% SA provide the third cubic phase of LiNi_{0.4}Mn_{1.6}O₄ after 250 cycles at 45 °C. Hereby, the latter additives weaken the cycling behavior of the spinel full cells. Cycled C//LiNi_{0.4}Mn_{1.6}O₄ pouch cells with Al₂O₃-modified electrodes were not investigated by X-ray diffraction owing to the thickness of the ceramic layer.

5.3.2 Raman spectroscopy

The structural properties of fully discharged $\text{LiNi}_{0.4}\text{Mn}_{1.6}\text{O}_4$ cathodes (0% SOC) were also studied by Raman spectroscopy after formation at 23 °C and after 250 cycles at 45 °C without and with the utilized electrolyte additives and the Al_2O_3 coating layers. Raman scattering is capable of probing the vibration modes of cations and the coordinated oxygen ions in transition metal oxides. It is very sensitive to local variations of the crystal symmetry. When cells are formatted or cycled, lithium is removed from the spinel lattice due to side reactions with the electrolyte, HF, or trace amounts of H_2O . Accordingly, the transition metals are oxidized and the environment of the oxygen atoms is changed resulting in an alteration of the Raman signals.

Literature references

There are merely three authors, which report on Raman spectra of $\text{LiNi}_{0.4}\text{Mn}_{1.6}\text{O}_4$ cathodes.^[194,349,440] Park et al. and Wei et al., however, have simply shown the spectra of fully intercalated $\text{LiNi}_{0.4}\text{Mn}_{1.6}\text{O}_4$ electrodes without discussing the vibrational modes regarding band shifts, symmetry elements (A_{1g} , T_{2g} , and E_g), and the attribution of the Raman signals to the corresponding transition metal cation oxygen bonds and their valence states ($\text{Li}^+\text{-O}$, $\text{Ni}^{2+}\text{-O}$, $\text{Mn}^{3+}\text{-O}$, ...).^[194,440] On the contrary, Baddour-Hadjean and co-workers have extensively studied Raman scattering of $\text{LiNi}_{0.4}\text{Mn}_{1.6}\text{O}_4$ cathodes including the assignment of the Raman bands to the respective symmetry species and to the transition metal cation oxygen bonds (Table 14).^[349] This group has also proven the existence of three cubic phases for $\text{LiNi}_{0.4}\text{Mn}_{1.6}\text{O}_4$ by Raman spectroscopy. Nevertheless, they confined their investigations to the observation of structural changes upon charging and discharging processes. Hence, the spectra have been recorded at different SOC. No examination of cycled spinel electrodes has been carried out.

Considering $\text{LiNi}_{0.5}\text{Mn}_{1.5}\text{O}_4$ cathode more Raman data are available for both crystal structures (Fd3m and $P4_332$).^[200,223,349,442–448] But, in none of these publications spinel electrodes are characterized after cycling. Instead, most of the time, only the modification of the vibrational modes of LMO with the introduction of Ni^{2+} ions in the spinel lattice is described or the Raman spectra are simply used to present the differences between the Fd3m and $P4_332$ space groups. Thereby, Raman responses often are insufficiently discussed. Usually, just the A_{1g} band is interpreted and an increase of the vibrational modes for the $P4_332$ symmetry is noticed compared to the Fd3m symmetry. Sometimes, the attribution of the Raman signals to the symmetry species is not consistent but contradictory as seen in the Tables 14 and 15. They give an overview of high voltage spinel Raman frequencies and the associated symmetries, according to various literature references.

Baddour-Hadjean ^[349]		Uchida ^[442]		Massot ^[443]			Kostecki ^[200]		Mauger ^[444]		
Raman ω (cm ⁻¹)	Symmetry species	Raman ω (cm ⁻¹)	Symmetry species	Raman ω (cm ⁻¹): P4 ₁ 32	Raman ω (cm ⁻¹): Fd3m	Symmetry species	Raman ω (cm ⁻¹)	Symmetry species	Raman ω (cm ⁻¹): P4 ₁ 32	Raman ω (cm ⁻¹): Fd3m	Symmetry species
163	T _{2g} ¹	-	-	202	-	-	-	-	202	-	-
220	T _{2g} ¹	-	-	240	-	-	-	-	240	-	-
-	-	-	-	335	340	-	-	-	327	335	-
-	-	-	-	387	-	-	-	-	378	-	-
407	E _g	407	-	407	398	-	404	E _g	407	395	-
487	T _{2g} ²	-	-	-	-	-	-	-	-	-	-
500	T _{2g} ²	500	-	495	498	-	496	T _{2g} ²	495	496	-
513	T _{2g} ²	-	-	540	-	-	-	-	-	-	-
-	-	-	-	583	-	T _{2g} ³	-	-	-	582	T _{2g} ³
593	A _{1g}	-	-	595	602	T _{2g} ³	593	T _{2g} ³	595	605	T _{2g} ³
613	A _{1g}	615	A _{1g}	611	-	T _{2g} ³	612	T _{2g} ³	611	-	-
640	A _{1g}	-	-	638	638	A _{1g}	635	A _{1g}	638	636	A _{1g}
653	T _{2g} ³	-	-	-	665	-	-	-	-	-	-

Table 14 Raman frequencies and their respective attributions according to literature references.

Crisci ^[445]		Sun ^[446]		Zhao ^[447]			Kim ^[448]		Cho ^[223]		
Raman ω (cm ⁻¹)	Symmetry species	Raman ω (cm ⁻¹)	Symmetry species	Raman ω (cm ⁻¹): P4 ₁ 32	Raman ω (cm ⁻¹): Fd3m	Symmetry species	Raman ω (cm ⁻¹)	Symmetry species	Raman ω (cm ⁻¹): P4 ₁ 32	Raman ω (cm ⁻¹): Fd3m	Symmetry species
-	-	-	-	-	-	-	-	-	119	120	-
-	-	-	-	170	169	-	-	-	152	152	-
-	-	-	-	228	-	-	-	-	213	-	-
-	-	-	-	249	-	-	-	-	284	-	-
-	-	-	-	337	-	-	-	-	364	-	-
411	T _{2g} ¹	400	-	416	415	-	400	T _{2g} ¹	396	394	-
498	T _{2g} ²	488	-	-	-	-	-	-	-	-	-
505	T _{2g} ²	-	-	510	510	-	492	T _{2g} ²	488	489	-
-	-	-	-	-	-	-	-	-	515	-	-
-	-	-	-	-	-	-	-	-	-	589	T _{2g} ³
580 - 620	T _{2g} ³	602	T _{2g} ³	604	-	T _{2g} ³	-	-	584	596	T _{2g} ³
642	A _{1g}	633	A _{1g}	621	610	T _{2g} ³	590	T _{2g} ³	602	602	T _{2g} ³
-	-	-	-	649	649	A _{1g}	633	A _{1g}	630	628	A _{1g}
-	-	-	-	-	-	-	-	-	-	-	-

Table 15 Raman frequencies and their respective attributions according to literature references.

In this thesis, the vibrational technique is adopted to further confirm the phase compositions of the differently treated positive electrodes and to determine the oxidation states of the nickel and manganese ions.

As described in chapter 2.3.4, the vibrational modes of the manganese spinel LMO with space group $Fd3m$ (O_h^7) are:^[350]

$$\Gamma_{\text{vibrational}} = A_{1g} + E_g + T_{1g} + 3T_{2g} + 2A_{2u} + 2E_u + 4T_{1u} + 2T_{2u} \quad (75)$$

where the symmetrical stretching mode A_{1g} (ν_s), the symmetrical deformation mode E_g (δ_s), and the three symmetrical bending modes T_{2g} (δ_s) are Raman-active. The remaining four asymmetrical bending or stretching modes T_{1u} are only IR-active. Any of the remaining modes are inactive. Hence, for an ideal spinel structure lacking defects or dopants the following five vibrational Raman modes are expected:

$$\Gamma_{\text{Raman}} = A_{1g} + E_g + 3T_{2g} \quad (76)$$

Reference cathode

Formatted reference $\text{LiNi}_{0.4}\text{Mn}_{1.6}\text{O}_4$ cathode

Figure 100 demonstrates the Raman spectra of $\text{LiNi}_{0.4}\text{Mn}_{1.6}\text{O}_4$ reference cathodes after formation at 23 °C and after cycling in the voltage window of 3.3 - 4.8 V at 45 °C. They feature normalized y-axes concerning the strongest Raman band. Three phase compositions are visible. Formatting the reference C// $\text{LiNi}_{0.4}\text{Mn}_{1.6}\text{O}_4$ cell without any electrolyte additives or Al_2O_3 coating layers leads to the first cubic phase exhibiting 10 sharp vibrational modes (Figure 100A). The sharpness of the Raman bands indicates well separated Ni and Mn sites with integer valence state distribution (Ni^{2+} , Mn^{3+} , and Mn^{4+}).^[445] Thereby, the oxidation states of the transition metals M are identified on the basis of their distinct band positions as the frequencies of the M-O vibrations depend on the corresponding bond strengths and lengths. Higher valence states of the transition metal cations relate to stronger and shorter M-O bonds and, in consequence, to higher binding energies and associated wavenumbers.

By virtue of the unequal occupancy of Mn^{3+} and Mn^{4+} in $\text{LiNi}_{0.4}\text{Mn}_{1.6}\text{O}_4$, the electron hopping rate between manganese cations and, thus, the electrical conductivity is lower than for unsubstituted LiMn_2O_4 . Here, Mn^{3+} and Mn^{4+} have an equal 16d site occupancy of 0.5. This cannot be fully compensated by the nickel cations. In case of Raman spectroscopy, however, a diminished electrical conductivity is advantageous because of a greater optical skin depth of the incident laser beam providing a higher scattering intensity.^[194]

The observation of broad, but split Raman bands representing a larger number of Raman signals compared to those predicted for undoped LMO is mainly attributed to the introduction

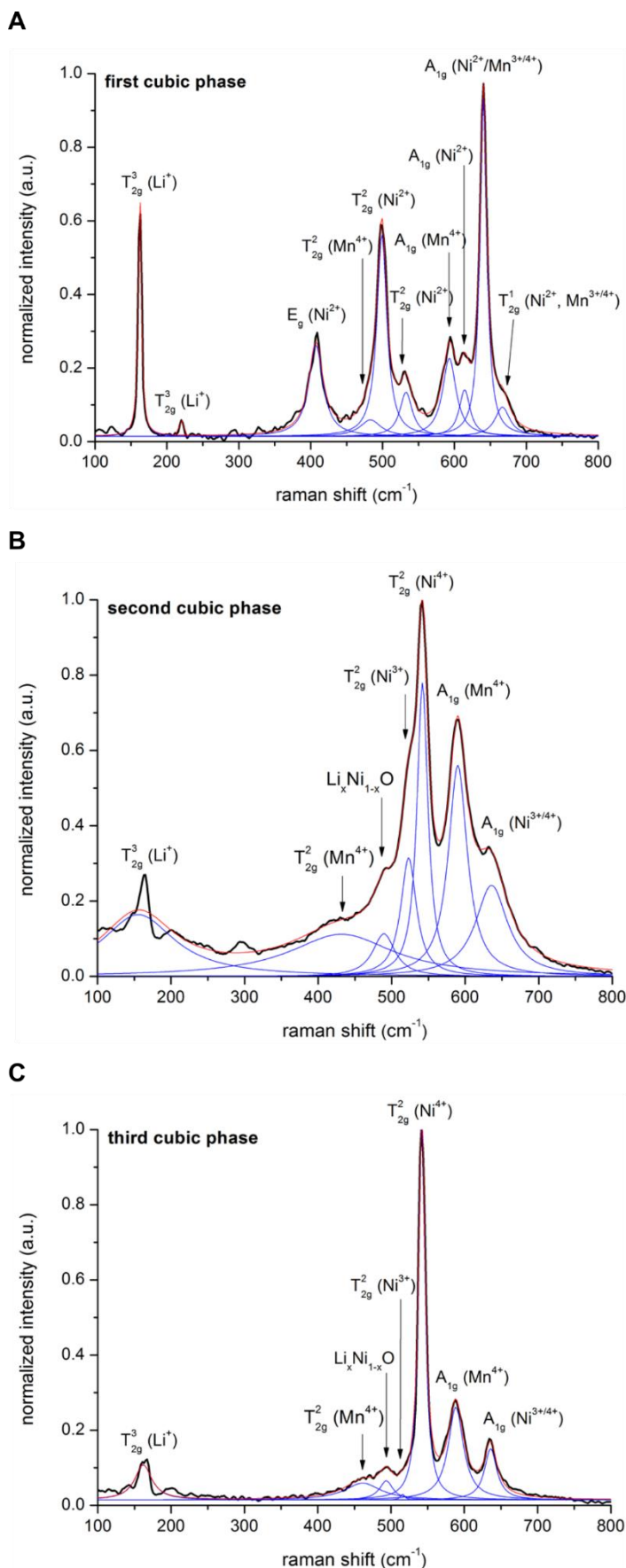


Figure 100 Raman spectra of completely discharged reference $\text{LiNi}_{0.4}\text{Mn}_{1.6}\text{O}_4$ cathodes after formation at 23 °C (**A** first cubic phase) and after cycling in the voltage window of 3.3 - 4.8 V at 45 °C (**B** second and **C** third cubic phase).

of nickel and to the simultaneous existence of Mn^{3+} and Mn^{4+} ions. The latter provoke stretching vibrations of both locally distorted MnO_6^{9-} and isotropic MnO_6^{8-} octahedra.^[350] The local Jahn-Teller related lattice distortions of Mn^{3+} featuring larger ionic radii than Mn^{4+} cations cause a loss of translation invariance. In fact, a breakdown of the Raman selection rules is supposed and, thus, more vibrational modes than projected are registered in $\text{LiNi}_{0.4}\text{Mn}_{1.6}\text{O}_4$.^[449]

A common feature of high voltage spinel Raman spectra is the strong A_{1g} band between 550 and 650 cm^{-1} and a group of bands between 100 and 550 cm^{-1} of weaker intensity. The intense A_{1g} signal is generally viewed as the stretching of the 16d site cation oxygen bonds.^[450] The splitting of this vibrational mode is ascribed to the stretching of the $\text{Mn}^{4+}\text{-O}$, $\text{Ni}^{2+}\text{-O}$, and a mixture of the $\text{Ni}^{2+}\text{-}$ and $\text{Mn}^{3+/4+}\text{-O}$ bonds at ≈ 592 , 615, and 640 cm^{-1} , respectively. Consequently, the Mn^{3+} to Mn^{4+} ratio or the average manganese oxidation state is reflected by the A_{1g} Raman response.

The weak shoulder at $\approx 666 \text{ cm}^{-1}$ has T_{2g} symmetry and also originates from bending vibrations of the 16d site cation oxygen bonds ($\text{Ni}^{2+}\text{-}$ and $\text{Mn}^{3+/4+}\text{-O}$ bonds). The second Raman-active band of T_{2g} symmetry is rather broad and composed of one $\text{Mn}^{4+}\text{-}$ and two $\text{Ni}^{2+}\text{-O}$ bending modes at approx. 475, 500, and 525 cm^{-1} , respectively. At ca. 407 cm^{-1} , a phonon line corresponding to the E_g symmetrical deformation mode is detected. It is assigned to the vibration of $\text{Ni}^{2+}\text{-O}$ bonds.

The lowest energy T_{2g}^3 phonons at around 163 and 220 cm^{-1} are predominantly derived from a vibration of the Li sublattice. As such they are the $\text{Li}^+\text{-O}$ stretching motion, which is a part of the tetrahedral cation movements of LiO_4 .^[341] Tarte has proposed that the tetrahedral vibration of LiO_4 appear in the low wavenumber region, because the low charge of monovalent Li^+ ions counteracts the effect of the shortness of the $\text{Li}^+\text{-O}$ distances and reduces the frequency.^[451] Notably, for LiMn_2O_4 the $\text{Li}^+\text{-O}$ vibrational mode is usually located between 365 - 382 cm^{-1} .^[341,350,449] Nonetheless, Baddour-Hadjean et al. have also examined $\text{LiNi}_{0.4}\text{Mn}_{1.6}\text{O}_4$ cathodes by Raman spectroscopy and they registered the T_{2g}^3 symmetry in the low frequency region at 163 and 220 cm^{-1} , too.^[349]

After formation, the spinel lattice of the reference $\text{LiNi}_{0.4}\text{Mn}_{1.6}\text{O}_4$ cathode is largely intercalated again by Li^+ and the electrode shows good reversibility throughout the formation process. The oxidation states of the transition metal cations are found to be Ni^{2+} and $\text{Mn}^{3+/4+}$. Table 16 summarizes the Raman signals of the formatted $\text{LiNi}_{0.4}\text{Mn}_{1.6}\text{O}_4$ reference cathode, which represents the first cubic phase.

Symmetry species	Assignment	Raman ω (cm ⁻¹)
T_{2g}^3	δ_s (Li ⁺ -O)	163 (s), 220 (w)
E_g	δ_s (Ni ²⁺ -O)	407 (m)
T_{2g}^2	δ_s (Mn ⁴⁺ -O)	475 (w)
T_{2g}^2	δ_s (Ni ²⁺ -O)	500 (s), 525 (w)
A_{1g}	ν_s (Mn ⁴⁺ -O)	592 (w)
A_{1g}	ν_s (Ni ²⁺ -O)	615 (w)
A_{1g}	ν_s (Ni ²⁺ -O, Mn ^{3+/4+} -O)	640 (vs)
T_{2g}^1	δ_s (Ni ²⁺ -O, Mn ^{3+/4+} -O)	666 (sh)

Table 16 Position, intensity, symmetry, and assignments of the Raman-active modes of the formatted reference LiNi_{0.4}Mn_{1.6}O₄ cathode (0% SOC) representing the first cubic phase (w = weak, m = medium, s = strong, vs = very strong, sh = shoulder).

Cycled reference LiNi_{0.4}Mn_{1.6}O₄ cathode

The Raman spectra of the cycled LiNi_{0.4}Mn_{1.6}O₄ reference electrode recorded at several positions are substantially different. They disclose the presence of two phases in the sample. In agreement with the crystallographic data, two phases correspond to the second and the third cubic phase of LiNi_{0.4}Mn_{1.6}O₄ (Figures 100B and 100C). For both phases the intensity of the low frequency mode T_{2g}^3 (Li⁺) at ≈ 163 cm⁻¹ is significantly reduced and the Raman band at 220 cm⁻¹ disappeared completely. This is due to the fact that electrochemically active lithium ions are consumed upon cycling and, therefore, the spinel lattice is not entirely reintercalated at 0% SOC. If the cathode is fully delithiated, the T_{2g}^3 symmetry reflects the vibrations of oxygen ions only.^[350] Besides, the E_g (Ni²⁺) phonon line at approx. 407 cm⁻¹ is invisible.

Considering the medium frequency range, the T_{2g}^2 (Mn⁴⁺) signal positioned at ca. 475 cm⁻¹ for the first cubic phase is slightly shifted to a lower frequency domain for the second and the third cubic phases. While the Raman band is rather broad with respect to the second cubic phase (ca. 300 - 600 cm⁻¹), a narrower one is observed for the third cubic phase at around 470 cm⁻¹. The differences in the T_{2g}^2 (Mn⁴⁺) modes regarding the three phases are in direct connection with the development of the nickel cation valence states and their weak or dominant Raman signals.

Actually, the two Ni²⁺-O bending modes of the first cubic phase are replaced by Ni³⁺-O and Ni⁴⁺-O Raman bands at approx. 530 and 542 cm⁻¹, respectively, for the second and the third

cubic phase. All of these nickel oxygen bonds have the T_{2g}^2 symmetry. The shifts of the symmetric bending vibration of NiO_6 to higher frequency regions is related to the shortness of the Ni-O bond lengths on account of the enhanced oxidation state of the nickel ions. Obviously, for the third cubic phase the T_{2g}^2 (Ni^{3+}) Raman signal is clearly diminished compared to the second cubic phase and the T_{2g}^2 (Ni^{4+}) phonon line is much sharper and more prominent. As a result, the amount of Ni^{3+} is noticeably lower and the Ni^{4+} content is much higher in the third cubic phase than in the second one. In other words, the intense high frequency Raman response T_{2g}^2 (Ni^{4+}) corroborates that in the third cubic phase a large percentage of Ni^{3+} is oxidized to Ni^{4+} . Consequently, some parts of the reference electrode have lost more lithium upon cycling (third cubic phase) than other parts (second cubic phase).

Remarkably, at $\approx 500\text{ cm}^{-1}$ an additional Raman mode is found for both phases after cycling. It is typically viewed as the vibration of NiO .^[440,444] Hence, the formation of $Li_xNi_{1-x}O$ impurities throughout cycling is confirmed by Raman spectroscopy. The existence of $Li_xNi_{1-x}O$ proves that structural deterioration of CAM takes place causing accelerated capacity fading of the C// $LiNi_{0.4}Mn_{1.6}O_4$ cell.

Concerning the A_{1g} signal, its intensity declines continuously from the first to the second and to the third cubic phase owing to the pronounced increase of the Ni^{4+} -O Raman band. Moreover, A_{1g} phonons are only composed of the Mn^{4+} -O and the $Ni^{3+/4+}$ -O stretching modes located at ca. 590 and 649 cm^{-1} , respectively. No vibrations of Ni^{2+} -O and Mn^{3+} -O bonds are detected anymore, since the Ni^{2+} and Mn^{3+} ions are oxidized to $Ni^{3+/4+}$ and Mn^{4+} ions, respectively, for the cycled $LiNi_{0.4}Mn_{1.6}O_4$ cathode. Further, the Raman response T_{2g}^1 (Ni^{2+} , $Mn^{3+/4+}$) disappeared for both phases.

Table 17 illustrates the evolution of the transition metal oxidation states of the formatted and the cycled $LiNi_{0.4}Mn_{1.6}O_4$ reference cathodes by means of the changes in the position of the Raman-active bands. The phase composition of $LiNi_{0.4}Mn_{1.6}O_4$ is strongly dependent on the lithium content and the transition metal valence states.

Symmetry species	Assignment	First cubic phase Raman ω (cm ⁻¹)	Second cubic phase Raman ω (cm ⁻¹)	Third cubic phase Raman ω (cm ⁻¹)
T_{2g}^3	δ_s (Li ⁺ -O)	163 (s), 220 (w)	163 (m)	163 (w)
E_g	δ_s (Ni ²⁺ -O)	407 (m)	-	-
T_{2g}^2	δ_s (Mn ⁴⁺ -O)	475 (w)	300 - 600	470 (w)
T_{2g}^2	δ_s (Ni ²⁺ -O)	500 (s), 525 (w)		
	δ_s (Ni ²⁺ -O) Li _x Ni _{1-x} O	-	500 (w)	500 (w)
T_{2g}^2	δ_s (Ni ³⁺ -O)	-	530 (m)	530 (vw)
T_{2g}^2	δ_s (Ni ⁴⁺ -O)	-	542 (vs)	542 (vs)
A_{1g}	ν_s (Mn ⁴⁺ -O)	592 (w)	590 (s)	590 (m)
A_{1g}	ν_s (Ni ²⁺ -O)	615 (w)	-	-
A_{1g}	ν_s (Ni ²⁺ -O, Mn ^{3+/4+} -O)	640 (vs)	-	-
A_{1g}	ν_s (Ni ^{3+/4+} -O)	-	640 (m)	640 (m)
T_{2g}^1	δ_s (Ni ²⁺ -O, Mn ^{3+/4+} -O)	666 (sh)	-	-

Table 17 Position, intensity, symmetry, and assignments of the Raman-active modes of the formatted and the cycled reference LiNi_{0.4}Mn_{1.6}O₄ cathodes (0% SOC). The transition metal oxidation states determine the phase composition of LiNi_{0.4}Mn_{1.6}O₄ (vw = very weak, w = weak, m = medium, s = strong, vs = very strong, sh = shoulder).

Conclusion

In conclusion, the formatted LiNi_{0.4}Mn_{1.6}O₄ reference cathode leads to the first cubic phase, which is characterized by Ni²⁺ and Mn^{3+/4+} ions. In contrast, the cycled reference spinel electrode involves the second and the third cubic phase with Li_xNi_{1-x}O impurities. The associated transition metal oxidation states are Mn⁴⁺, Ni³⁺, and Ni⁴⁺. Hereby, the third cubic phase features only a very small amount of Ni³⁺. Thus, in accordance with the XRD data the phase composition of the LiNi_{0.4}Mn_{1.6}O₄ electrode relates to the ageing degree of the spinel electrode. The first cubic phase denotes the most intact and the third cubic phase marks the most impaired cathode.

Formatted $\text{LiNi}_{0.4}\text{Mn}_{1.6}\text{O}_4$ cathodes**Electrolyte optimization (formatted cells)**

After formatting C// $\text{LiNi}_{0.4}\text{Mn}_{1.6}\text{O}_4$ pouch cells containing electrolytes with the diverse electrolyte additives selected in chapter 5.2, Raman spectroscopy of the corresponding totally discharged cathodes (0% SOC) was conducted to verify if the additives have already a significant effect on the structural properties of CAM in the first few cycles. Figure 101A depicts the Raman spectra of the formatted spinel electrodes, which are ordered according to the decreasing effect of the electrolyte additive regarding the cycle life. The individual deconvoluted spectra are shown in chapter 7 (appendix). For comparative purposes, the vibrational modes of the reference are displayed, too. Independently of the electrolyte additive, all cathodes exhibit solely the first cubic phase of $\text{LiNi}_{0.4}\text{Mn}_{1.6}\text{O}_4$ with the characteristic A_{1g} , E_g , and T_{2g} symmetries that are elucidated above. The oxidation states of the transition metals Ni and Mn equal to 2^+ and $3^{+}/4^+$, respectively. Therefore, each cathode is adequately intercalated again by lithium ions after the last formation step and the spinel framework is maintained. The amount of consumed lithium ions has been determined by cycling the spinel cell in the voltage window of 3.3 - 4.8 V at 0.1C for one cycle at the end of the formation. The lithium content in the $\text{LiNi}_{0.4}\text{Mn}_{1.6}\text{O}_4$ cathodes has been calculated from the specific discharge capacities at 0% SOC. With the exception of the 0.5% TEHP and 0.5% HMDS samples, the irreversible loss of lithium ions amounts to approx. 15% after formation. The 0.5% TEHP and 0.5% HMDS additives enhance the lithium consumption to ca. 20%, which is presumably due to reinforced surface layer generation during the formation cycles. This higher lithium deficiency is also visible in the Raman spectra by a diminished intensity of the T_{2g}^3 (Li^+) phonon line.

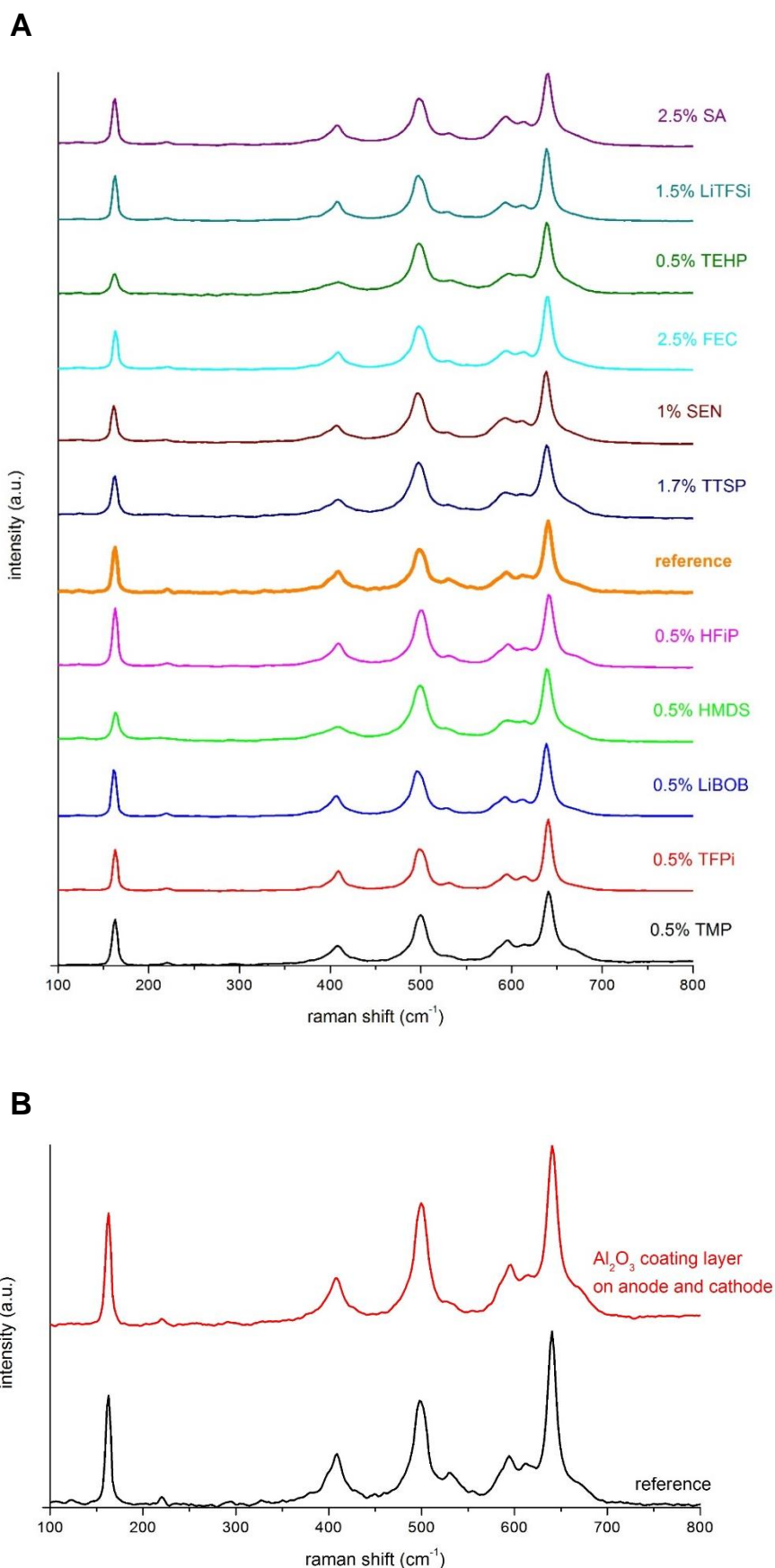


Figure 101 Raman spectra of formatted $\text{LiNi}_{0.4}\text{Mn}_{1.6}\text{O}_4$ cathodes (23 °C; 0% SOC) **A** without and with various electrolyte additives and **B** with Al_2O_3 -modified electrodes resulting in the first cubic phase.

Optimization with Al₂O₃ coating layers (formatted cells)

Likewise, Al₂O₃-coated spinel cathodes were analyzed by Raman spectroscopy after formatting C//LiNi_{0.4}Mn_{1.6}O₄ pouch cells comprising Al₂O₃-modified electrodes (Figure 101B). Once more, the first cubic phase with the transition metal valence states of Ni²⁺ and Mn^{3+/4+} is obtained. Hence, the Al₂O₃ coating does not contribute to an enhancement of the lithium loss during formation. More precisely, approx. 15% of active lithium ions are consumed, which corresponds to the same quantity as in the case of the reference. Accordingly, the T_{2g}³ (Li⁺) Raman bands of both spectra have a similar intensity. Despite the 4 - 5 μm thick Al₂O₃ layer, enough lithium ions are reintercalated into the cathode at the end of the formation to establish the first cubic phase again.

With the help of all of these Raman data and the computed lithium contents *x* in the formatted Li_{*x*}Ni_{0.4}Mn_{1.6}O₄ cathodes (0% SOC) the composition of the first cubic phase is estimated:

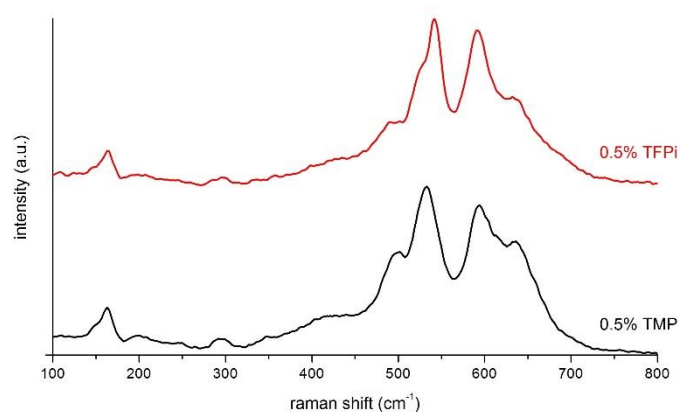
first cubic phase: Li_{1.0 - 0.78}Ni_{0.4}²⁺Mn_{1.6}^{3+/4+}O₄

Consequently, the expected oxidation states of the transition metals for the first cubic phase, as stated earlier, are confirmed.

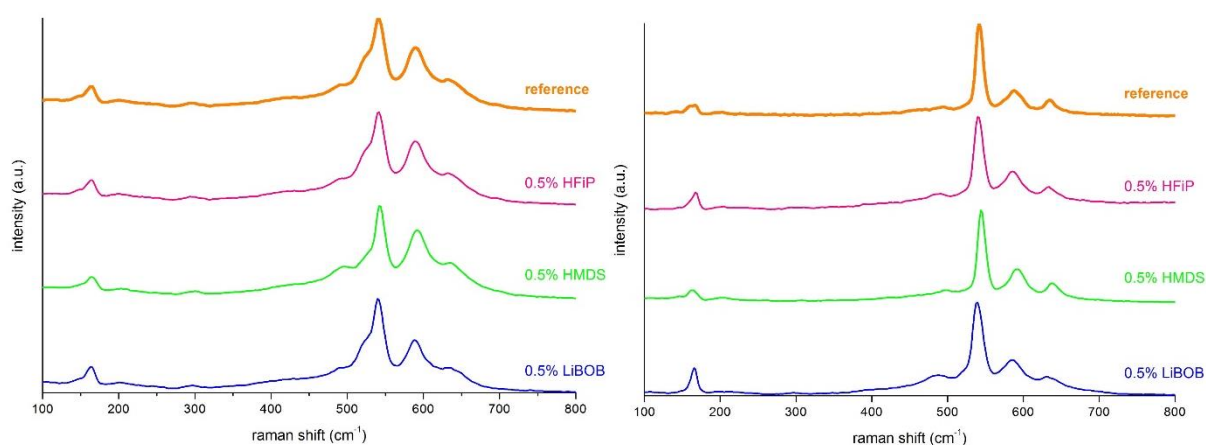
Cycled LiNi_{0.4}Mn_{1.6}O₄ cathodes**Electrolyte optimization (cycled cells)**

The Raman spectra of LiNi_{0.4}Mn_{1.6}O₄ cathodes cycled for 250 cycles at 45 °C with and without various electrolyte additives are illustrated in Figure 102. The individual deconvoluted spectra are shown in chapter 7 (appendix). In compliance with the crystallographic records, 0.5% TMP and 0.5% TFPi lead to the generation of the second cubic phase (Figure 102A), whereas 1.7% TTSP, 1% SEN, 2.5% FEC, 0.5% TEHP, 1.5% LiTFSI, and 2.5% SA produce the third cubic phase (Figure 102C). Other additives such as 0.5% LiBOB, 0.5% HMDS, and 0.5% HFIP and the base electrolyte cause the formation of both cubic phases (Figure 102B). Therefore, it is confirmed that the effect of the electrolyte additive on the cycling stability of the full cell is reflected by the phase composition of the LiNi_{0.4}Mn_{1.6}O₄ cathode.

As mentioned before, the second and the third cubic phase reveal the existence of unfavorable Li_{*x*}Ni_{1-*x*}O impurities and both phases are characterized by a well-developed T_{2g}² (Ni⁴⁺) Raman band. This is considerably more pronounced for the third cubic phase. It implies higher Ni⁴⁺, but less Ni³⁺ and Li⁺ contents for the third cubic phase compared to the second cubic phase, although only minor differences between the intensities of the T_{2g}³ (Li⁺) signals of both phases are visible.

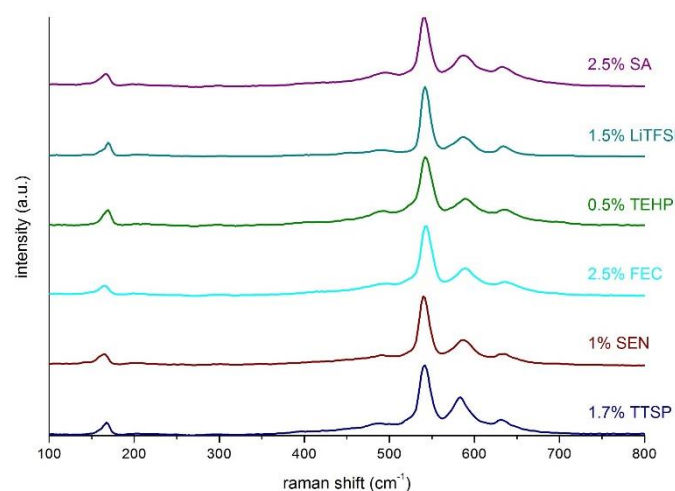
A

second cubic phase

B

second cubic phase

third cubic phase

C

third cubic phase

Figure 102 Raman spectra of cycled $\text{LiNi}_{0.4}\text{Mn}_{1.6}\text{O}_4$ cathodes (1C; 45 °C; 0% SOC) **A** with 0.5% TMP and 0.5% TFPI (second cubic phase), **B** with 0.5% LiBOB, 0.5% HMDS, 0.5% HFIP, and the reference electrolyte (second and third cubic phase), and **C** with 1.7% TTSP, 1% SEN, 2.5% FEC, 0.5% TEHP, 1.5% LiTFSi, and 2.5% SA (third cubic phase).

Optimization with Al₂O₃ coating layers (cycled cells)

Similarly, Raman spectroscopy of Al₂O₃-coated LiNi_{0.4}Mn_{1.6}O₄ cathodes was accomplished after cycling C//LiNi_{0.4}Mn_{1.6}O₄ pouch cells with Al₂O₃-modified electrodes at 45 °C in the voltage range of 3.3 - 4.8 V (Figure 103). Interestingly, both cubic phases are observed for the cycled cathode as in the case of the reference. This is in agreement with the results of the CC/CV-cycling experiments. Here, the base electrolyte and the Al₂O₃ coating on both electrodes result in about the same discharge capacity after 250 cycles.

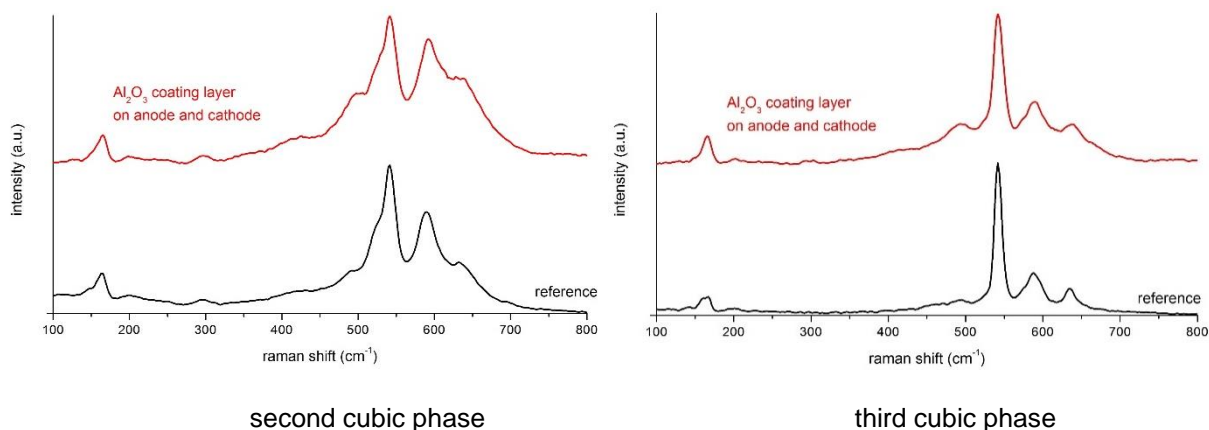


Figure 103 Raman spectra of cycled LiNi_{0.4}Mn_{1.6}O₄ cathodes (1C; 45 °C; 0% SOC) with and without Al₂O₃-modified electrodes (second and third cubic phase).

Calculating the lithium content x in the completely discharged Li _{x} Ni_{0.4}Mn_{1.6}O₄ cathodes (electrolyte and Al₂O₃-optimized full cells) from the specific discharge capacities achieved after cycling, gives the following phase compositions:

second cubic phase: Li_{0.433 - 0.432}Ni_{0.4 - x} ^{3+/4+}Mn_{1.6 - y} ⁴⁺O₄

third cubic phase: Li_{0.390 - 0.207}Ni_{0.4 - x} ^{3+/4+}Mn_{1.6 - y} ⁴⁺O₄, but with only a minor Ni³⁺ content

The transition metal valence states of the second cubic phase are higher than expected and the oxidation of Ni³⁺ to Ni⁴⁺ is already strongly progressed. Therefore, severe transition metal dissolution must have occurred throughout cycling. The variables x and y describe the unknown amounts of nickel and manganese lost upon the CC/CV experiment. ICP-OES and EDX measurements were conducted to examine this phenomenon and are outlined in the next chapter.

Conclusion

In summary, the phase compositions found by XRD spectroscopy could be confirmed by the Raman scattering technique. In addition, the Al_2O_3 -coated spinel electrodes after cycling C// $\text{LiNi}_{0.4}\text{Mn}_{1.6}\text{O}_4$ pouch cells with Al_2O_3 -modified electrodes at 45 °C are composed of the second and the third cubic phases. Generally, for the first time, three cubic phases with the characteristic A_{1g} , E_g , and T_{2g} symmetries of $\text{LiNi}_{0.4}\text{Mn}_{1.6}\text{O}_4$ cathodes (0% SOC) were determined by Raman spectroscopy after formatting and cycling the corresponding spinel full cells. Furthermore, the lithium contents and the oxidation states of the transition metal cations were identified for the particular cubic phases:

first cubic phase: $\text{Li}_{1.0-0.78}\text{Ni}_{0.4}^{2+}\text{Mn}_{1.6}^{3+/4+}\text{O}_4$

second cubic phase: $\text{Li}_{0.433-0.432}\text{Ni}_{0.4-x}^{3+/4+}\text{Mn}_{1.6-y}^{4+}\text{O}_4$

third cubic phase: $\text{Li}_{0.390-0.207}\text{Ni}_{0.4-x}^{3+/4+}\text{Mn}_{1.6-y}^{4+}\text{O}_4$, but with only a minor Ni^{3+} content

Thus, ageing of the spinel electrode is given by its phase composition at 0% SOC and is corroborated Raman and XRD spectroscopy. While the first cubic phase represents the most intact, the third cubic phase signifies the most harmed cathode. Nonetheless, the detected valence states for the cycled completely discharged cathodes do not coincide with the expected ones. Consequently, nickel and manganese ions have probably been washed out of CAM during cycling. In the subsequent chapter, this circumstance is verified by ICP-OES and EDX measurements.

5.4 Transition metal dissolution studies

As described in the chapters 2.1.3 and 2.2.3, one of the major failure mechanisms of LMO and high voltage spinel cathodes in full cells is transition metal dissolution into the electrolyte with a negative effect on both electrodes.^[1,3,4,295] On one hand, the cathode suffers from the loss of active material and, in addition, undesired reaction products such as LiF, MnF₂, NiF₂, and polymerized organic species are formed. They are known to accumulate on the surface of the spinel electrode.^[4,287] On the other hand, metal deposition on the graphite anode causes lithium plating and catalyzed electrolyte decomposition, which is accompanied by a destabilization and an excessive growth of the SEI.^[3,74,452] As a consequence, substantial consumption of lithium ions is reflected by a significant capacity decay of the associated full cells throughout cycling.^[4]

The origin of the transition metal dissolution is mainly ascribed to the existence of trace amounts of acidic components in the electrolyte. This results in the formation of HF in LiPF₆/organic electrolyte solutions, where ppm levels of H₂O are present (see equations 6 - 9 in chapter 2.1.3).^[181] HF not only catalyzes the disproportion of Mn³⁺ to Mn²⁺ and Mn⁴⁺, but also reacts with the CAM at high potentials according to the equations 19 - 20 (chapter 2.2.3). In the literature, several approaches to prohibit transition metal dissolution concerning manganese spinels are proposed including the application of various surface layer coatings on the active material particles or on the electrodes and the utilization of diverse electrolyte additives with, however, limited success.^[247,270,289,429,432,453] Both strategies aim at scavenging HF or establishing a physical protection layer between the spinel cathode and the electrolyte to suppress chemical side reactions.

In this work, ICP-OES and EDX measurements of graphite anodes at 0% SOC are conducted after cycling C//LiNi_{0.4}Mn_{1.6}O₄ pouch cells at 45°C for 250 cycles in the voltage window of 3.3 - 4.8 V. This is done to clarify whether and to what extent the dissolution of nickel and manganese, and the subsequent deposition of the metals on the counter electrode take place upon cycling. Moreover, the influence of the selected electrolyte additives and the Al₂O₃-modified electrodes on the transition metal dissolution behavior of the C//LiNi_{0.4}Mn_{1.6}O₄ full cells is investigated.

The reference cell

Figure 104A displays the experimentally obtained nickel and manganese concentrations migrated from the spinel to the graphite electrode, while cycling the reference C//LiNi_{0.4}Mn_{1.6}O₄ pouch cell at 45 °C. In order to achieve a better understanding of the impact of the transition metal dissolution, the related total amounts of nickel and manganese on the anode are calculated (Figure 104B). Actually, 1.27% and 0.27% of Mn and Ni ions are dissolved from the LiNi_{0.4}Mn_{1.6}O₄ composite cathode. This corresponds to 1,886 and 106 µg Mn and Ni, respectively, on the graphite anode. It should be considered that the actual sum of the dissolved transition metal ions is even higher as typically more than twice as much Ni and Mn are registered in the electrolyte solution.^[4,33] Nonetheless, it is noted that the concentration of dissolved Mn is 4.76 times as large as that of Ni in the spinel electrode. This value is clearly higher than the stoichiometric ratio of Mn/Ni in the LiNi_{0.4}Mn_{1.6}O₄ material, demonstrating a stronger tendency of Mn to be washed out the CAM as compared to Ni. In terms of the calculated overall amounts of the transition metals, the pronounced dissolution of Mn ions becomes even more apparent.

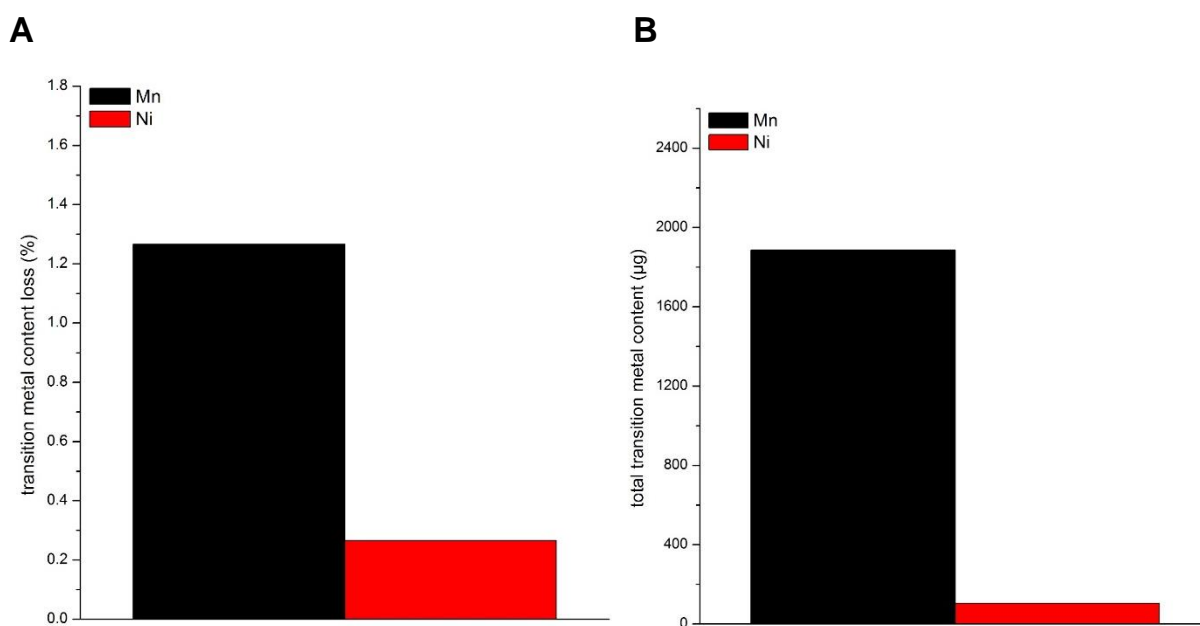


Figure 104 **A** Nickel and manganese concentrations migrated from the spinel to the graphite electrode while cycling the reference C//LiNi_{0.4}Mn_{1.6}O₄ pouch cell at 45 °C for 250 cycles. **B** Calculated related total amounts of nickel and manganese found on the anode.

The EDX elemental mapping analysis of the cycled anode is shown in Figure 105. The Mn and Ni elemental distributions in the sample are rather uniform and indicate a homogenous arrangement of Mn and Ni on the graphite electrode. Furthermore, the intensified densities for the Mn mapping compared to Ni confirm the ICP-OES data and the fact that Mn dissolves

more easily than Ni. The associated SEM picture unveils the EDX recording position of the graphite anode, which is partly covered by SEI components.

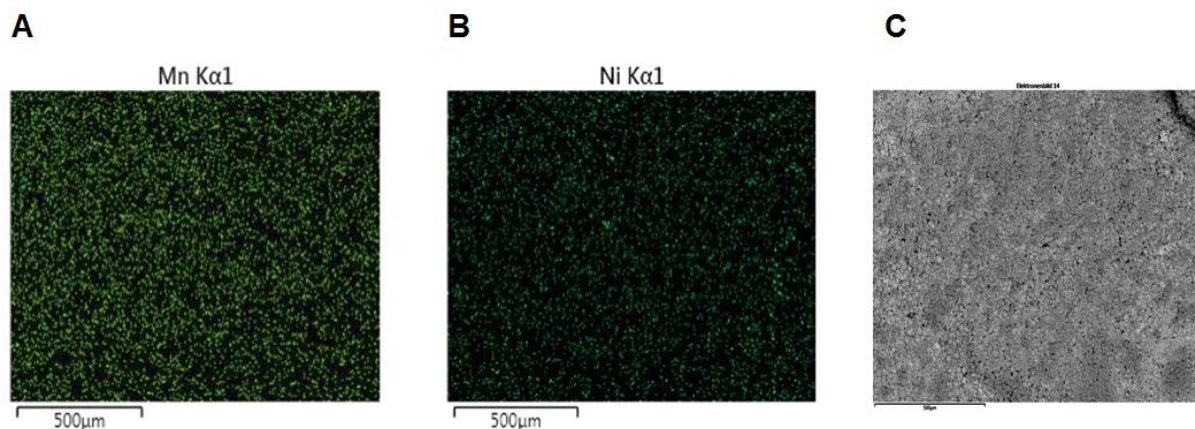
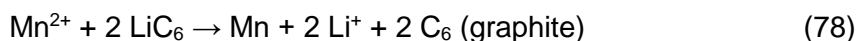
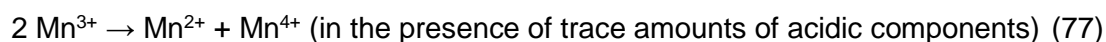


Figure 105 EDX area mappings of a graphite anode at 0% SOC (**A** Mn and **B** Ni elemental distributions) after cycling a C//LiNi_{0.4}Mn_{1.6}O₄ pouch cell at 45 °C for 250 cycles and the corresponding SEM picture (**C**).

Based on the equations 17 - 20 in chapter 2.2.3, the following reactions are suggested for the transition metal dissolution mechanism in C//LiNi_{0.4}Mn_{1.6}O₄ pouch cells:

Disproportion of Mn³⁺[4]

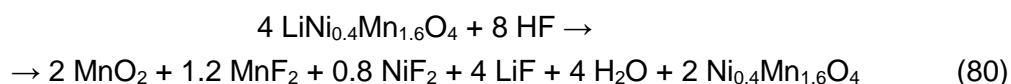


As already mentioned in the previous sections, Mn²⁺ leaches out into the electrolyte and is reduced on the surface of the counter electrode. Thus, self-discharge of the lithiated graphite is initiated, active Li⁺ ions are depleted, and electrolyte decomposition takes place leading to the formation of very thick SEI layers.^[183] In addition, lithium plating might occur on account of the presence of metallic Mn.^[184] But, Mn³⁺ is only a minority in the active material LiNi_{0.4}Mn_{1.6}O₄ (at most 20%). Therefore, the subsequent reactions are supposed to be primarily responsible for the transition metal dissolution.

Decomposition of LiNi_{0.4}Mn_{1.6}O₄ by HF^[4,285,286]



or



These decompositions of $\text{LiNi}_{0.4}\text{Mn}_{1.6}\text{O}_4$ by HF contribute, inter alia, to the diminution of the cycle life. In contrast to reaction 80, no generation of MnO_2 is observed on the cathode surface by XRD spectroscopy. Hence, reaction 79 seems to be more feasible. The insoluble reaction products LiF , MnF_2 , and NiF_2 might accumulate on the spinel electrode resulting in an increase of the charge-transfer resistance. XPS and EIS studies outlined in chapters 5.5 and 5.6 will give more information on the surface composition of the cathode and the respective resistances.

Since the acidic component HF is the main initiator of the transition metal dissolution, replacing LiPF_6 by other conducting salts appears to be a promising approach to circumvent this problem. Nevertheless, most of the other conducting salts have some considerable limitations hindering their wide-spread applications in lithium ion full cells.^[253,398,454] Usually, electrolytes comprising lithium tetrafluoroborate (LiBF_4) have a substantially lower conductivity relative to those containing LiPF_6 .^[455] The main drawback of LITFSI and lithium trifluoromethanesulfonate (LiSO_3CF_3) in aprotic solvent-based electrolytes is their tendency to strongly corrode the Al current collector, in addition to a reduced ionic conductivity.^[413,414,456] Lithium perchlorate (LiClO_4) and lithium hexafluoroarsenate (LiAsF_6) were both widely used for electrolyte research in the 1970s and 1980s. But, nowadays their utilization is largely precluded due their explosive and highly toxic potential.^[398,457] The significantly decreased conductivity of electrolytes containing LiBOB or lithium difluoro(oxalato)borate (LiODFB) rather than LiPF_6 is the major impediment to their use as conducting salts in commercial LIBs.^[458]

Another strategy to overcome the difficulties of non-aqueous electrolytes is the application of ionic liquids, which are solely composed of ionic species without any organic molecules. Their main benefits are reduced flammability, diminished volatility, high thermal stability, and a relatively good ionic conductivity.^[398,459] However, the electrochemical performance of lithium ion battery cells including ionic liquids is rather poor especially when compared to conventional organic electrolytes.^[398] The primary reason for this is the enhanced viscosity of ionic liquids, which is 1 - 3 orders of magnitude higher than those of conventional solvents.^[460] Moreover, ionic liquids exhibit a poor wettability of the electrodes and the separator as well as a restricted reductive stability.^[461]

On account of these issues, ionic liquids and conducting salts other than LiPF_6 were not investigated within this work. Instead, various electrolyte additives and Al_2O_3 -coated electrodes were analyzed by ICP-OES and EDX measurements with respect to their effect on the transition metal dissolution characteristics of $\text{C}/\text{LiNi}_{0.4}\text{Mn}_{1.6}\text{O}_4$ pouch cells.

Electrolyte optimization

The anodes of C//LiNi_{0.4}Mn_{1.6}O₄ full cells were examined by ICP-OES at 0% SOC after 250 cycles at 45 °C. Figure 106A depicts the experimentally determined transition metal content losses from the spinel electrode and Figure 106B illustrates the calculated total amount of Ni and Mn on the graphite electrode. For comparison, the results of the reference cell are also shown. The additives are ordered according to their decreasing effects, whereby those placed on the left side of the reference enable a greater specific energy over cycle life than the base electrolyte.

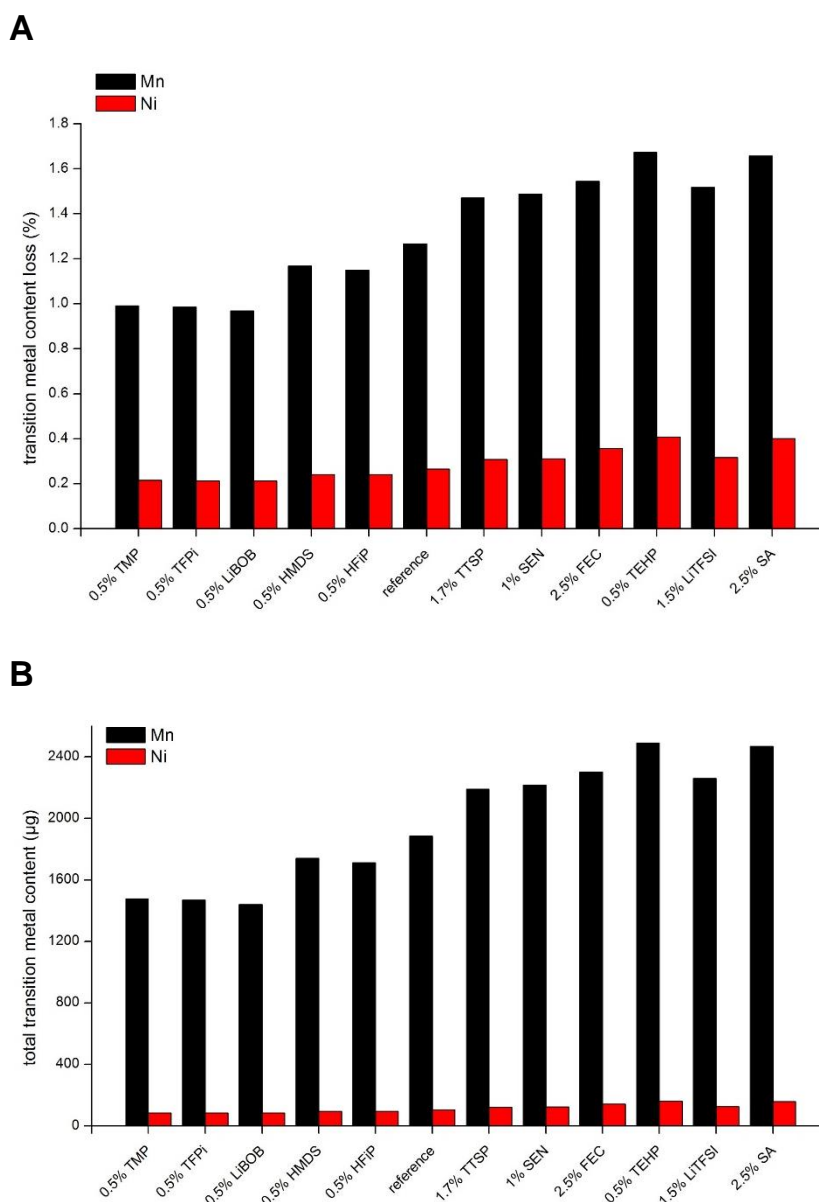


Figure 106 **A** Nickel and manganese concentrations migrated from the spinel to the graphite electrode while cycling C//LiNi_{0.4}Mn_{1.6}O₄ pouch cells containing various electrolyte additives at 45 °C for 250 cycles. **B** Calculated related total amounts of nickel and manganese found on the anode.

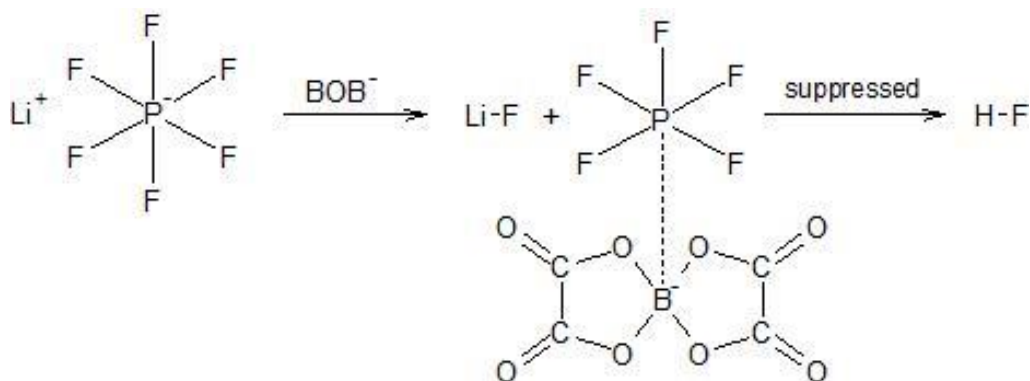
Generally, it can be seen that for all samples Mn dissolution is more prominent than Ni dissolution. More precisely, the concentration of the washed-out Mn is about 4.5 - 4.8 times higher than that of Ni. Therefore, the additives have virtually no influence on the relative ratios of dissolved Mn and Ni. Or in other words, both transition metal contents change similarly in dependence of the respective electrolyte additive, which changes the HF concentration in the full cells.

Remarkably, the ICP-OES data largely correlate with the results of the CC/CV-cycling experiments (see chapter 5.2.2). All those additives that have improved the cycle life of C//LiNi_{0.4}Mn_{1.6}O₄ full cells, reveal a reduced transition metal dissolution compared to the reference. A poorer cycling performance is connected with an enhanced amount of Mn and Ni deposited on the negative electrode. Hence, the metal ion diminution of the cathode is in direct connection with the electrochemical characteristics of the C//LiNi_{0.4}Mn_{1.6}O₄ pouch cell. The increase of the transition metal dissolution is attributed to the formation of porous and/or very thick SPI layers on the cathode surfaces as the water content in the cells comprising various electrolyte additives remained constantly low. A highly porous SPI with bare spinel electrode surfaces cannot completely prevent the direct contact between the electrolyte components and the active material. Consequently, HF attack proceeds and more Mn and Ni leach out into the electrolyte. The longer the SPI is unstable, the more serious is the depletion of Mn and Ni. The properties of the different cathode surface layers are analyzed by XPS, as outlined in the next chapter.

0.5% TEHP and 2.5% SA lead to the most severe transition metal dissolution with 2,492 and 2,469 µg Mn and 162 and 159 µg Ni, respectively, accumulated on the graphite electrode. This is in agreement with the fast capacity fading of the associated full cells. The stronger ageing of the 2.5% SA cell is probably caused by more detrimental SPI features. Although the cycling behavior of the full cell with 1.5% LiTFSI is inferior to the one with 0.5% TEHP, less Mn and Ni are detected on the anode. This is most likely related to the fact that the 1.5% LiTFSI full cell is damaged by massive gassing throughout the cycling experiment.

Regarding the electrolyte additives, reducing the transition metal dissolution, two scenarios are suggested: elimination of HF, H₂O, or PF₅ and/or establishment of a physical protection layer by a thin and stable SPI. Here, just the first mechanism is considered as the subsequent chapter will provide more detailed information on the function of the SPI.

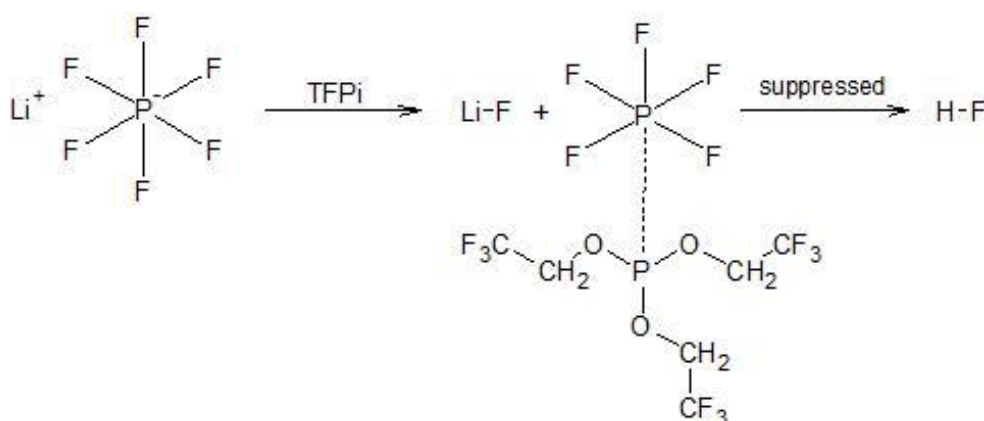
0.5% LiBOB minimizes the precipitation of Mn and Ni to 1,442 and 85 µg or to 0.97% and 0.21%, respectively, which are the lowest values for all examined additives. As elucidated by Kim et al. LiBOB is able to sequester PF₅, a strong Lewis acid, that initiates the formation of HF pursuant to the equations 6 - 9 in chapter 2.1.3.^[247] Scheme 1 demonstrates the possible mechanism of LiBOB in C//LiNi_{0.4}Mn_{1.6}O₄ full cells containing LiPF₆/organic electrolyte solutions.



Scheme 1 Proposed interaction of LiBOB with LiPF₆ resulting in suppressed HF generation.

Whether LiBOB also takes part in the structure of the cathode SPI as proposed by Choi and by Lucht is discussed later on.^[272,307]

Besides, 0.5% TMP and 0.5% TFPI also weaken the transition metal dissolution. Actually, only 1,477 and 1,468 µg Mn and 86 and 84 µg Ni, respectively, are registered on the graphite electrode after 250 cycles. While TMP is known to lower the metal deposits exclusively by stabilizing the SPI,^[274,275] TFPI is believed to trap PF₅ according to the following mechanism:^[253,295]

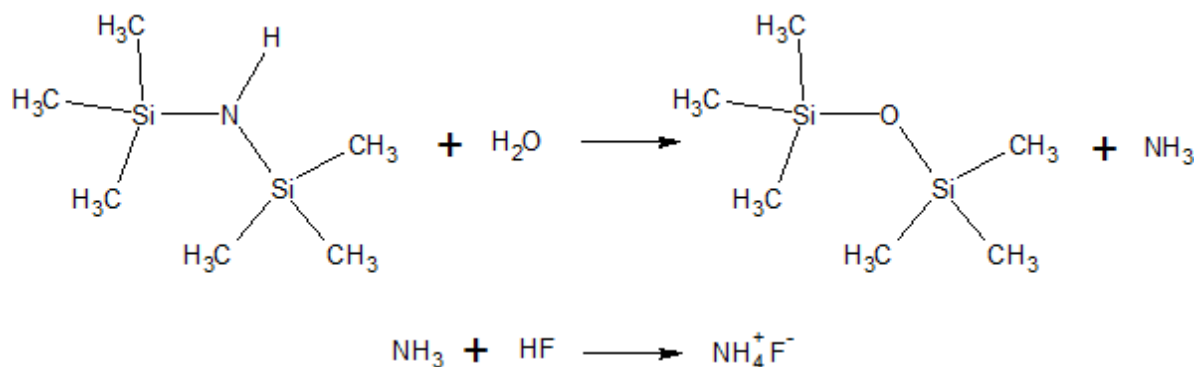


Scheme 2 Proposed interaction of TFPI with LiPF₆ resulting in suppressed HF generation.

Thus, the production of HF and the loss of active material are alleviated and the cycle life of C//LiNi_{0.4}Mn_{1.6}O₄ full cells is significantly extended as confirmed by the cycling stability studies in chapter 5.2.

Furthermore, it is observed that the Mn and Ni concentrations leached out from the composite cathode drop to 1.15 and 0.24% for the cell cycled with 0.5% HFiP. The lower identified contents of the transition metals on the anode denote that the film on the LiNi_{0.4}Mn_{1.6}O₄ electrode formed by HFiP is protective and suppresses Mn and Ni depletion. No evidence for removal of HF, H₂O, or PF₅ is given by HFiP.

As opposed to this, the organosilicon compound HMDS is suggested to eliminate water and HF impurities by the following reactions and, therefore, to improve the cell performance:^[295,454]



Scheme 3 Proposed interaction of HMDS with H₂O leading to suppressed HF generation.

In fact, the Ni and Mn amounts found on the graphite electrode equal to 1,740 and 96 µg, respectively, for the 0.5% HMDS cell. These values are lower as compared to the reference, but slightly higher than those for the 0.5% HFiP sample. Differences in the SPI compositions and properties are possibly responsible for this trend. If and to what extent HMDS is involved in building up a surface film on the cathode, is investigated by XPS as described in chapter 5.5.

The results obtained by ICP-OES measurements were reviewed and confirmed by EDX spectroscopy, which was also conducted with the cycled anodes at 0% SOC. Exemplarily, Figures 107 and 108 represent the Mn and Ni elemental distributions in the negative electrodes of the 0.5% TMP and the 0.5% TEHP cells, that is, those with the lowest and the highest transition metal dissolution, respectively.

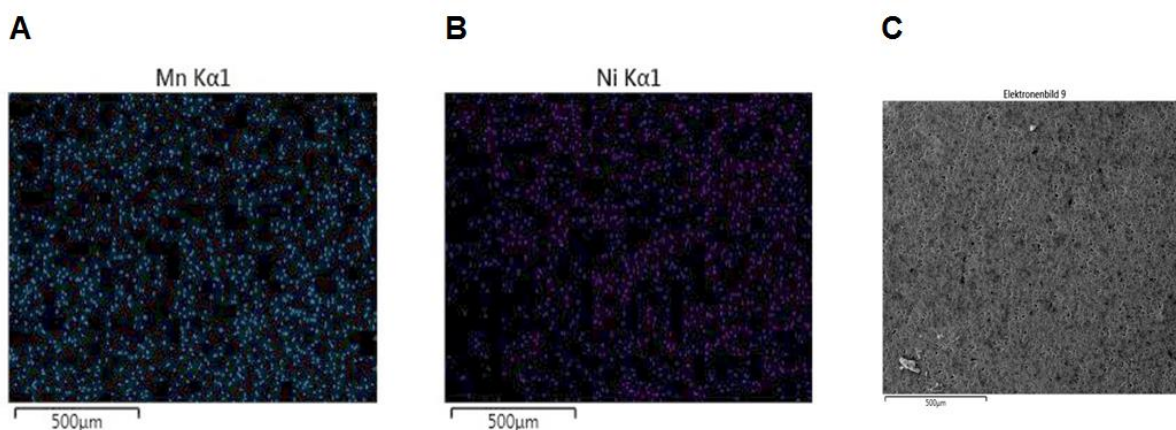


Figure 107 EDX area mappings of a graphite anode at 0% SOC (**A** Mn and **B** Ni elemental distributions) after cycling a C//LiNi_{0.4}Mn_{1.6}O₄ pouch cell with 0.5% TMP at 45 °C for 250 cycles and the corresponding SEM picture (**C**).

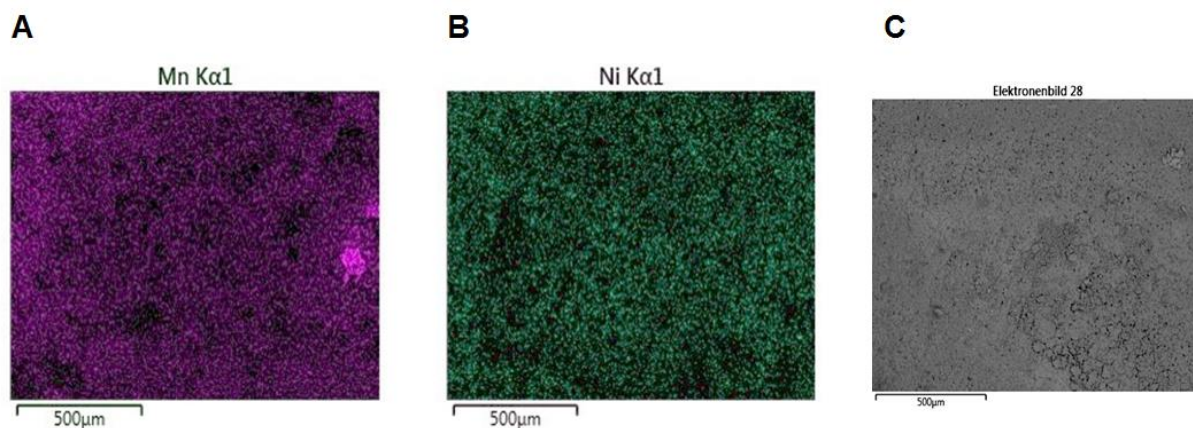


Figure 108 EDX area mappings of a graphite anode at 0% SOC (**A** Mn and **B** Ni elemental distributions) after cycling a C//LiNi_{0.4}Mn_{1.6}O₄ pouch cell with 0.5% TEHP at 45 °C for 250 cycles and the corresponding SEM picture (**C**).

As can be seen, for the 0.5% TMP graphite electrode Mn and Ni particles are more uniformly or homogeneously arranged than for the 0.5% TEHP sample. In the latter, regions with varying intensities are observed. Especially, the Mn mapping reveals a highly concentrated accumulation of Mn particles. This is probably due to the increasingly contaminated graphite surface upon cycling, which then offers more and less favorable locations for the metal ions to deposit. Besides, the overall metal ion dissolution is more pronounced for the pouch cell containing 0.5% TEHP. As already shown by ICP-OES, it also exceeds the transition metal depletion of the reference (cf. Figure 106). The associated SEM pictures unveil the EDX recording positions of the graphite anodes, which are partly covered by SEI components

Optimization with Al₂O₃ coating layers

Additionally, transition metal dissolution studies have been accomplished with C//LiNi_{0.4}Mn_{1.6}O₄ pouch cells including bare and Al₂O₃-modified electrodes. After 250 cycles at 45 °C and between 3.3 and 4.8 V, the full cells were disassembled at 0% SOC and the anodes were analyzed by ICP-OES. Actually, the anodes of spinel full cells with ceramic layers on the cathode, on the anode, and on both electrodes are examined. Figure 109A displays the experimentally obtained transition metal content losses from the cathodes and Figure 109B illustrates the calculated total amount of Ni and Mn precipitated on the graphite electrode. For comparison, the results of the reference cell are also presented.

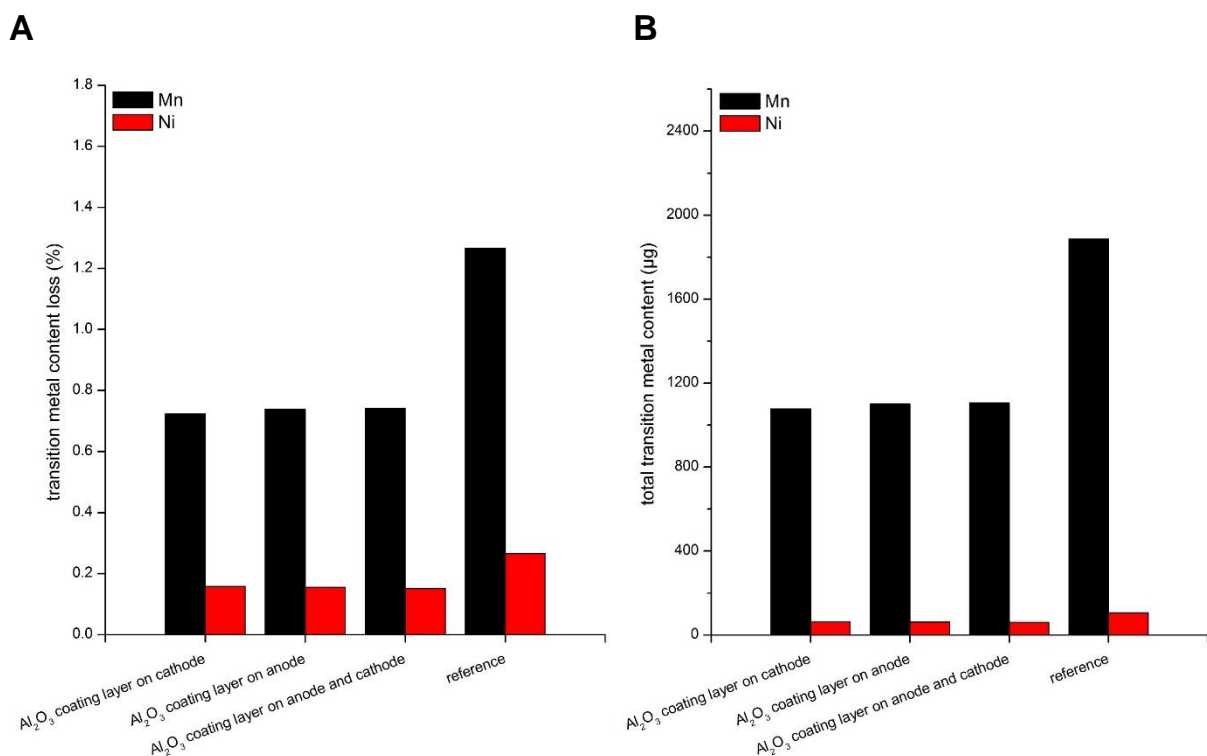


Figure 109 **A** Nickel and manganese concentrations migrated from the spinel to the graphite electrode while cycling C//LiNi_{0.4}Mn_{1.6}O₄ pouch cells without and with a ceramic layer on the spinel cathode, on the graphite anode, and on both electrodes at 45 °C for 250 cycles. **B** Calculated related total amounts of nickel and manganese found on the anode.

Interestingly, all three full cells comprising Al₂O₃-modified electrodes effectively suppress metal ion depletion from the composite spinel electrodes regardless of the application location and the number of the Al₂O₃ coating layers. Only around 1,100 and 61 µg Mn and Ni, respectively, have been accumulated on the anodes after 250 cycles. That corresponds to approx. 0.74% and 0.15% Mn and Ni, respectively, which are leached out from the cathodes. Consequently, the modification of the electrodes with Al₂O₃ surface layers is more beneficial with respect to the reduction of transition metal dissolution than any electrolyte additive. Commonly, Al₂O₃ is supposed to react with HF in the electrolyte:^[292]



In the presence of the HF scavenger Al₂O₃, a part of the acidic component is removed and the electrolyte is neutralized. To this end, the corrosion of the cathode and the transition metal dissolution decline. The cycling behavior in the first few cycles of the C//LiNi_{0.4}Mn_{1.6}O₄ pouch cells comprising differently located Al₂O₃-modified electrodes is, therefore, attributed to a hampered SEI formation in terms of graphite anodes modified with ceramic layers. EDX measurements of anodes cycled in C//LiNi_{0.4}Mn_{1.6}O₄ pouch cells with Al₂O₃ coating layers on both electrodes are in accordance with the ICP-OES data and corroborate the low Mn and Ni deposits (Figure 110).

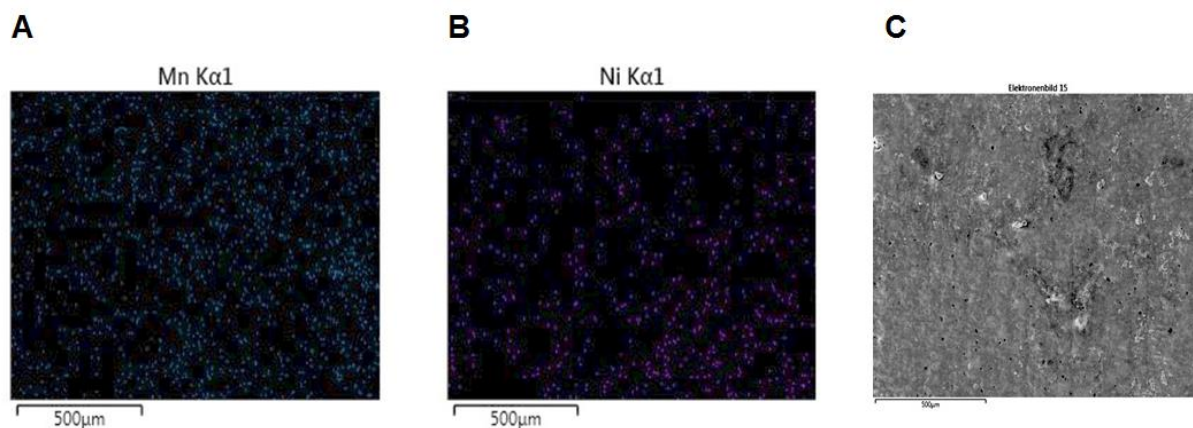


Figure 110 EDX area mappings of a graphite anode at 0% SOC (**A** Mn and **B** Ni elemental distributions) after cycling a C//LiNi_{0.4}Mn_{1.6}O₄ pouch cell with Al₂O₃ coating layers on both electrodes at 45°C for 250 cycles and the corresponding SEM picture (**C**).

Conclusion

In summary, it has been recognized by ICP-OES and EDX analyses that transition metal dissolution is indeed a major issue for C//LiNi_{0.4}Mn_{1.6}O₄ pouch cells. Thereby, Mn is more easily washed out the spinel active material than Ni. The metal ion depletion is primarily caused by HF in the electrolyte. Of all electrolyte additives, 0.5% LiBOB has the most beneficial impact on transition metal dissolution, whereas 0.5% TEHP leads to the highest metal contents on the anode. The positive influence of additives is related to the elimination of HF, H₂O, or PF₅ and/or the establishment of a physical protection layer by a rather thin and stable SPI. An increase of metal ion diminution in the cathodes is presumably based on thick and porous SPI layers. Moreover, Al₂O₃ has been proven to be an effective HF scavenger alleviating transition metal dissolution. All in all, there is a direct connection between the degree of metal ion depletion and the cycling stability of the C//LiNi_{0.4}Mn_{1.6}O₄ pouch cells. In this work, only the Mn and Ni contents on the graphite electrode are considered. However, the actual sum of the dissolved transition metal ions is even higher as in general more than twice as much Ni and Mn are registered in the electrolyte solution.^[4,33] Thus, the oxidation states of the three cubic phases determined in the previous chapter can be justified. In the subsequent chapter, the results of the XPS investigations are discussed.

5.5 Characterization of the solid permeable interface

Generally, it is accepted that LiPF_6 /non-aqueous electrolyte solutions are oxidized on the cathode side of high voltage spinel cells as the $\text{Ni}^{2+/4+}$ redox couple is activated at ca. ≥ 4.7 V vs. Li. This is clearly below the HOMO of common liquid carbonate-based electrolytes as already mentioned in chapter 2.2.3.^[229,243,253] Inside the composite cathode, the conductive carbon is believed to have a catalytic effect on the electrolyte oxidation at high voltages so that the carbonate electrolyte mixtures are already oxidized at approx. 4.5 V.^[1,248,249,249–252] If the decomposed products adhere to the cathode surface further side reactions are suppressed, film formation is reduced, and cycling behavior of the corresponding cells is stabilized. Nevertheless, the development of a SPI layer is always accompanied by degradation of the cell performance due to an increased electrode resistance and lithium ion consumption. This leads to capacity losses.^[243,307,462,463] Therefore, a dense, and preferably thin SPI film with high lithium ion conductivity is desirable to maintain ion transport upon charging/discharging. Concurrently, its electronic conductivity must be kept as low as possible. The thickness and the composition of the SPI strongly influence the electrochemical features of lithium ion cells and depend on various parameters. For example, temperature, storage time, cycle number, SOC, potential, cathode structure, and electrolyte formulation.^[464–466] While the interfacial layer on the anode side, the SEI, has been thoroughly studied, there is much less known about the SPI on the cathode surface. This is mainly because traditional CAMs such as NMCs or LCO are typically operated up to only 4.2 V. Under these conditions standard organic electrolytes are considered oxidatively stable.^[243,464]

Edström and Eriksson et al. conducted XPS depth profile analyses of manganese spinel electrodes stored or cycled at 60 °C. They found a SPI with a stacked structure on the cathode surface, whereby organic polymers and polycarbonates are positioned underneath Li-rich layers indicating that the inner region is close to the cathode and P-O species like $\text{Li}_x\text{PO}_y\text{F}_z$ mark the outer region near the electrolyte.^[465,466] This is in contrast to the composition of the SEI, where the inorganic phase is located at the anode side and the organic layers are placed on top.^[398] Recently, several researchers have focused on investigating the interfacial layers between high voltage spinel cathodes and the electrolytes.^[2,4,239,239,244,245,250,268,270–272,287,307,408,429,462,467,468] Nonetheless, most examinations just concentrate on half cells comprising lithium anodes, which compensate lithium losses during cycling in contrast to graphite anodes and, consequently, enable longer cycle lives.^[239,244,245,248–250,272,285,307,429,467–469] Although many of the SPI components are known, the mechanism of SPI formation, the structure, the thickness, and the function of the SPI are poorly understood.^[465,466,470] Additionally, the involvement of numerous electrolyte additives in the generation of the surface layer is unclear.^[243]

In this thesis, XPS analysis is applied to study the chemical nature and the development of the interfacial layers between the $\text{LiNi}_{0.4}\text{Mn}_{1.6}\text{O}_4$ electrodes and the different electrolyte formulations after formatting C// $\text{LiNi}_{0.4}\text{Mn}_{1.6}\text{O}_4$ pouch cells containing various electrolyte additives at 23 °C and after cycling these cells for 250 cycles at 45 °C. Especially, the role of each additive in the SPI structure is examined. Thereto, the full cells were disassembled at 0% SOC in a glove box purged with argon gas and the cathode was transferred to the X-ray photoelectron spectrometer without any contact to air or moisture. In the following, the XPS results are presented and the thickness of the SPI is partly corroborated by SEM images. XPS data are summarized in the appendix (chapter 7). Precise knowledge of the chemical system and good reference values are essential to develop a suitable model for the nature of the species based on the deconvoluted high resolution spectra. The quantitative evaluation of the XPS data is critical and problematic owing to the sample roughnesses and non-uniform film thicknesses of the SPI layers.^[471] Hence, herein only qualitative interpretation of the XPS records is accomplished. Since all measurements were performed under the same conditions a direct comparison of all the batches is feasible and valuable for the elucidation of the SPI properties. The binding energies and the relative area under the peaks provide the relevant information.

The reference cell

Figures 111 and 112 display the XPS spectra of $\text{LiNi}_{0.4}\text{Mn}_{1.6}\text{O}_4$ electrodes in the Mn2p, Ni2p, C1s, O1s, F1s, and P2p regions after formation at 23 °C and after cycling at 45 °C. The concentrations of Mn and Ni have decreased after 250 cycles, whereas the concentrations of C, O, F, and P have increased. Thus, SPI is evidently generated throughout cycling and covers the bulk material with organic/inorganic components.

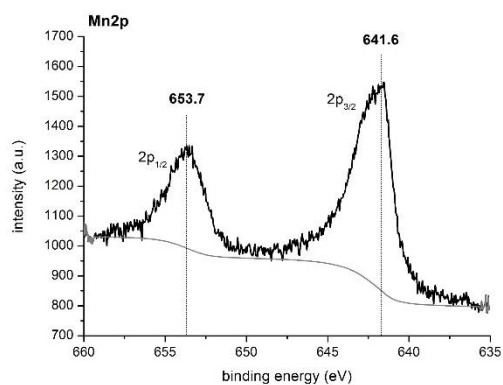
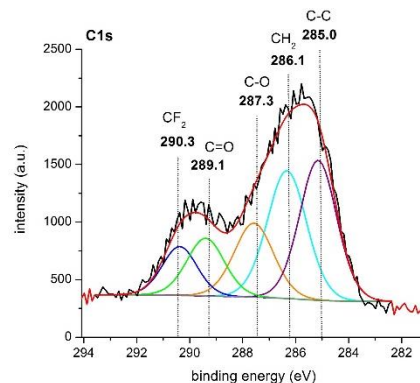
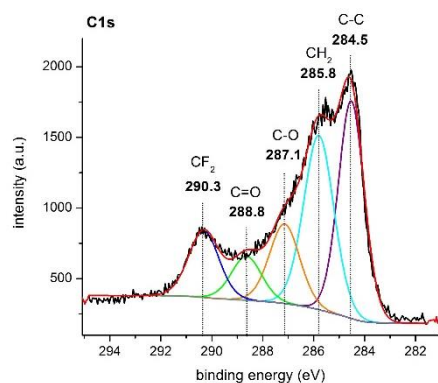
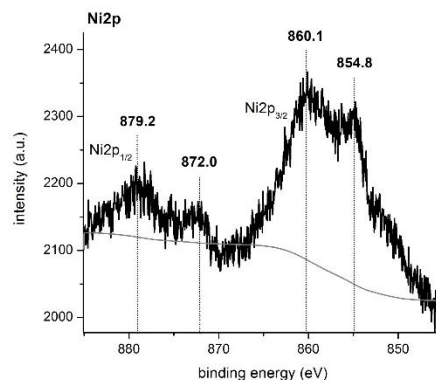
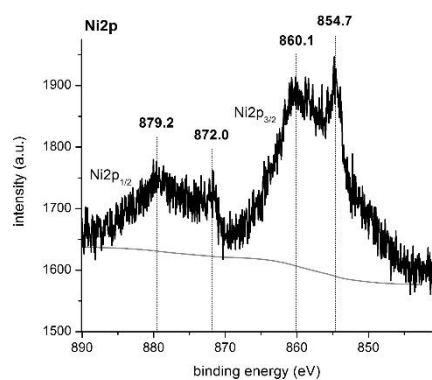
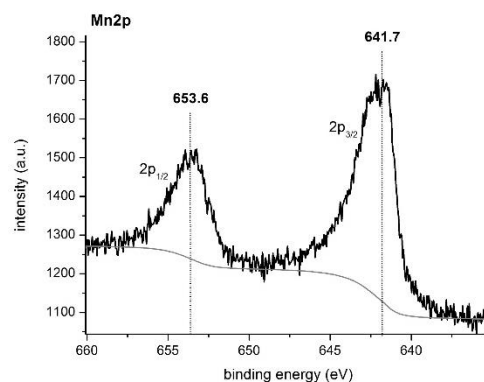
A**B**

Figure 111 XPS spectra of $\text{LiNi}_{0.4}\text{Mn}_{1.6}\text{O}_4$ electrodes at 0% SOC after **A** formatting C// $\text{LiNi}_{0.4}\text{Mn}_{1.6}\text{O}_4$ pouch cells containing the base electrolyte at 23 °C and after **B** cycling these cells for 250 cycles at 45 °C.

5.5 Characterization of the solid permeable interface

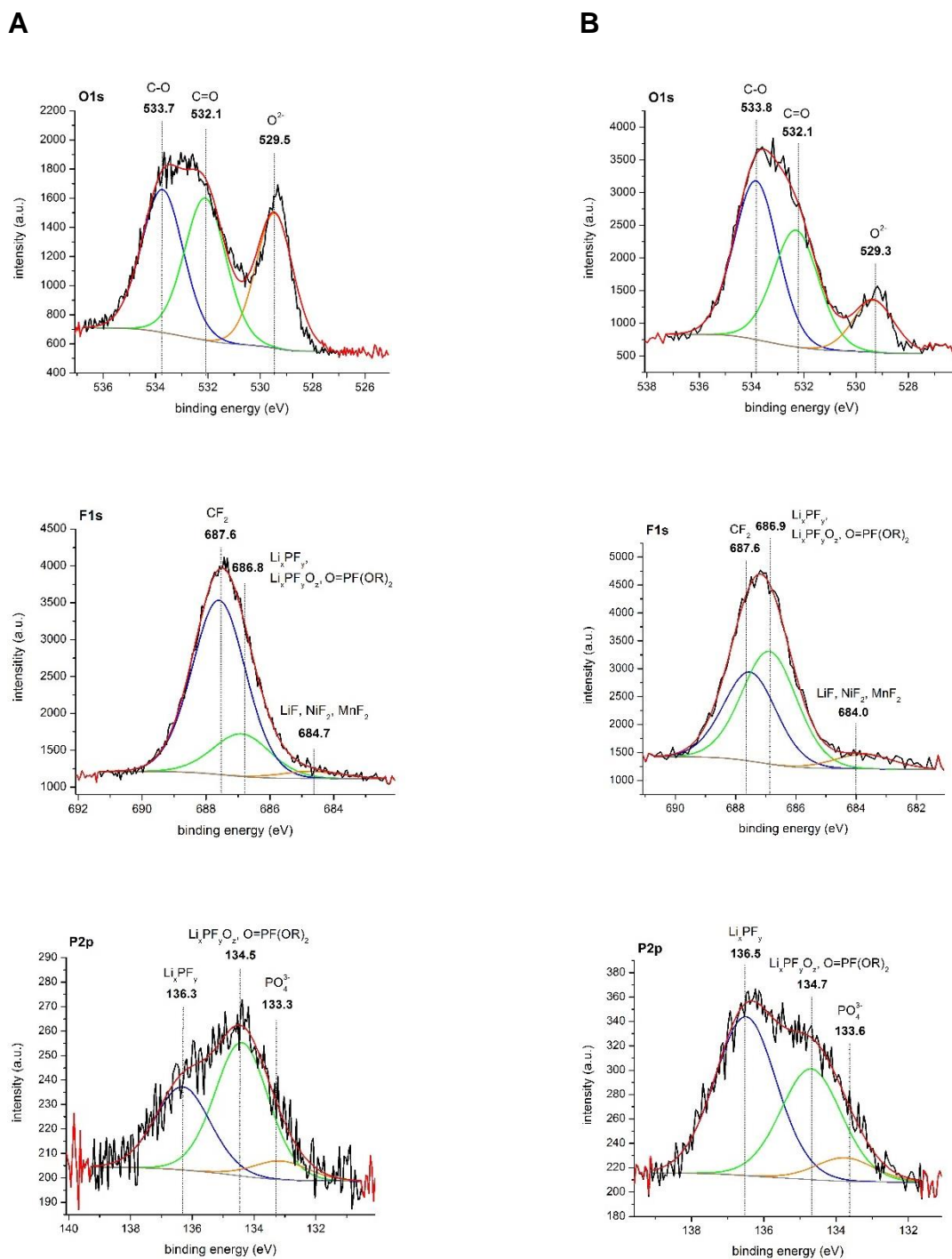


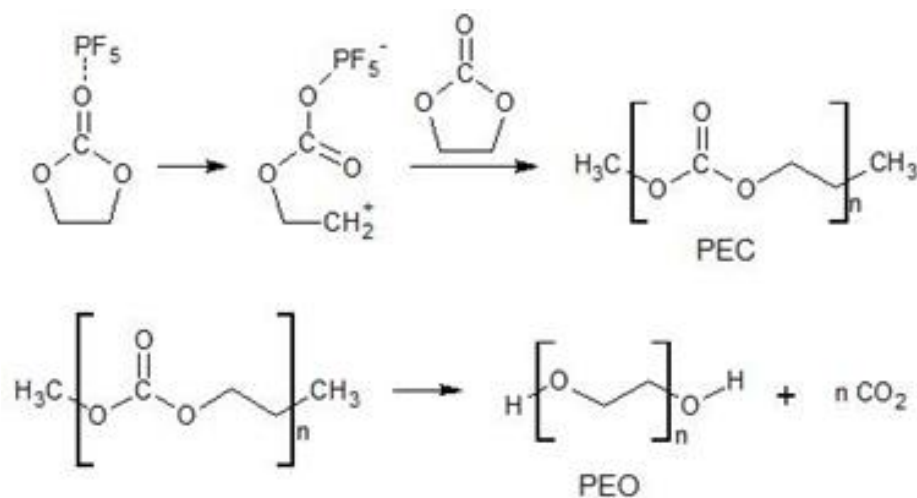
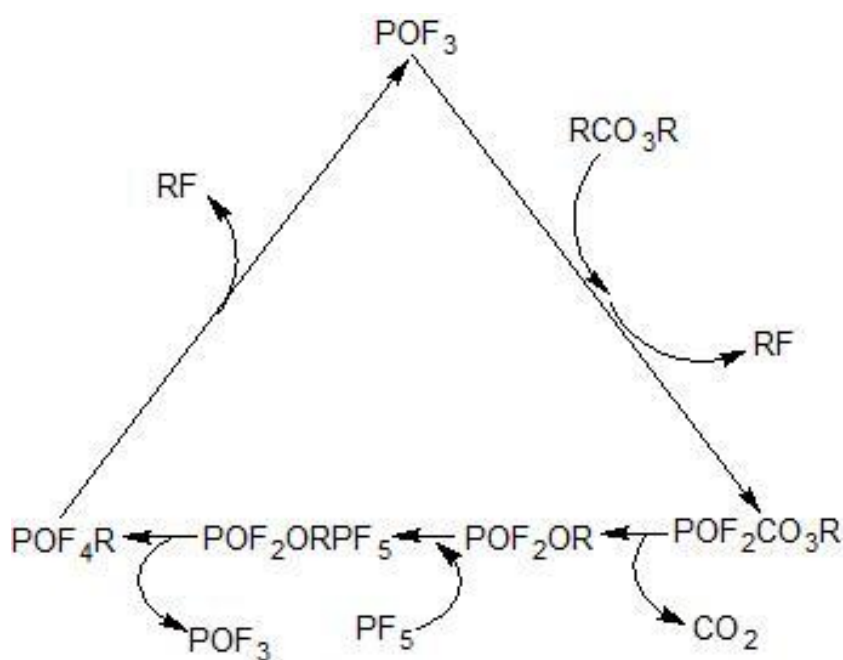
Figure 112 XPS spectra of LiNi_{0.4}Mn_{1.6}O₄ electrodes at 0% SOC after **A** formatting C//LiNi_{0.4}Mn_{1.6}O₄ pouch cells containing the base electrolyte at 23 °C and after **B** cycling these cells for 250 cycles at 45 °C.

Mn2p: Regarding the Mn2p spectra, the Mn2p_{3/2} signal is observed at a binding energy of 641.6 and 641.7 eV after formation and after cycling, respectively. The spin-orbit splitting is the energy separation between the Mn2p_{3/2} and Mn2p_{1/2} levels and amounts to approx. 12 eV. These results are very similar to the reported data for Mn2p_{3/2} and Mn2p_{1/2} in spinels.^[448,472,473] Because of the binding position of Mn2p_{3/2} it is assumed that Mn adopts primarily the tetravalent oxidation state, which is in agreement with the Raman data. According to the literature, lower valence states are usually detected at lower binding energies.^[363,448,472] Moreover, the shapes of the Mn2p_{1/2} and Mn2p_{3/2} peaks indicate mainly Mn⁴⁺ states and the satellite of Mn2p_{3/2} is superimposed by the Mn2p_{1/2} band, which is just the case for Mn³⁺ and Mn⁴⁺.^[213] In spite of this, it is quite difficult to obtain the exact distribution of trivalent and tetravalent oxidation states from XPS based solely on the Mn2p spectrum.^[474,475] It is, however feasible to conclude that Mn⁴⁺ is more dominant than Mn³⁺ for the formatted sample and it has already been shown by Raman spectroscopy that the cycled spinel cathode includes only Mn⁴⁺. Other Mn species like for example MnF₂ or Mn_xO_y, which might be a part of the SPI are not observable in the Mn2p spectrum due to the broadness of the Mn2p_{3/2} and Mn2p_{1/2} signals.^[363,476]

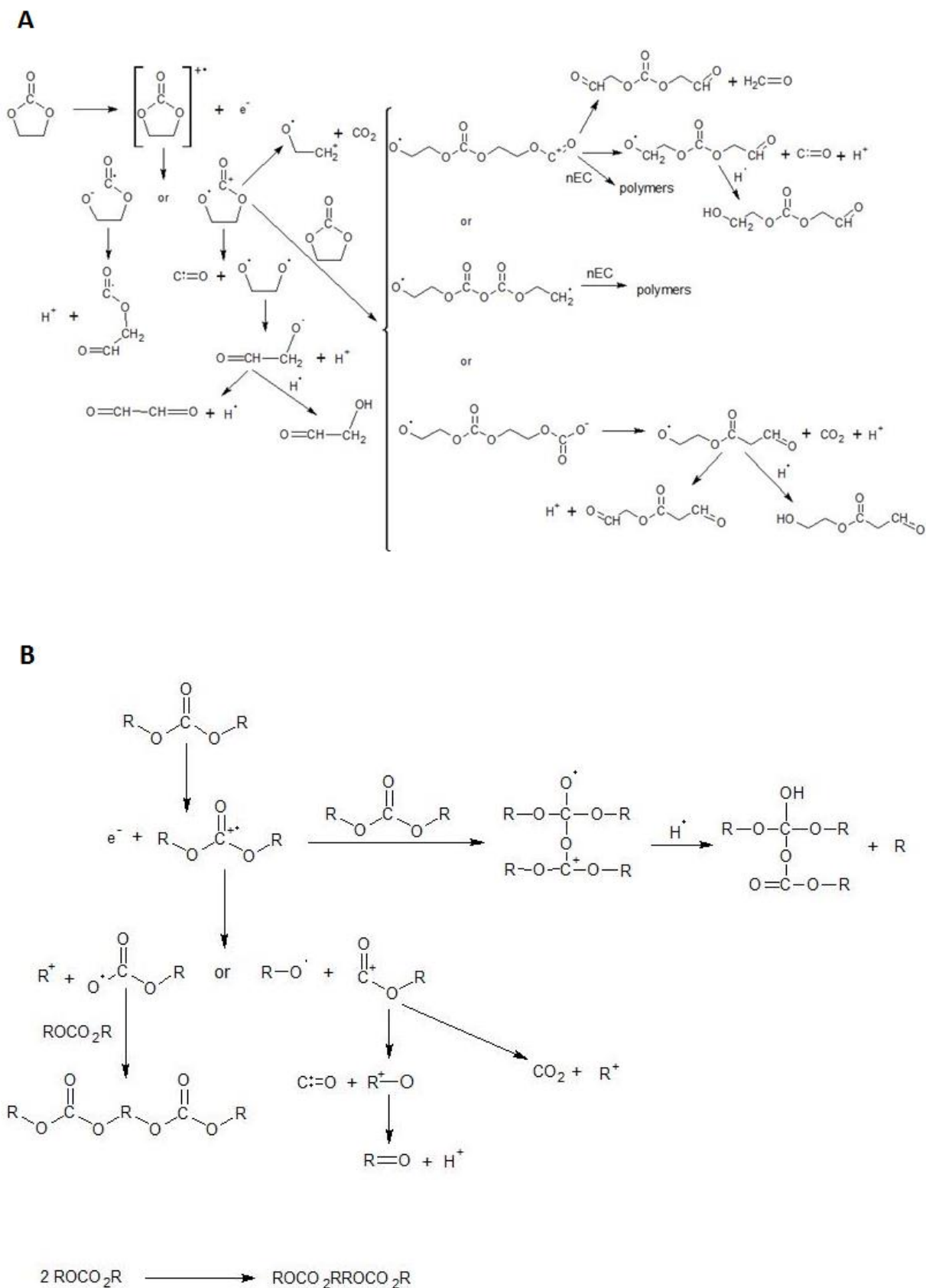
Ni2p: For the formatted LiNi_{0.4}Mn_{1.6}O₄ electrodes, the XPS spectrum of Ni reveals a major asymmetric peak at 854.7 eV and a smaller signal at 872.0 eV due to Ni2p_{3/2} and Ni2p_{1/2}, respectively. The additional emissions visible at around 860.1 and 879.2 eV are rather broad and are attributed to the existence of satellites, which are superimposed by F(KL₁L_{2,3}) and F(KL₁L₁) Auger transitions originating from fluoride containing components such as LiF.^[363,474] Consequently, the determination of the Ni oxidation states is very problematic. The binding energy of Ni2p_{3/2} is, however, close to that reported for NiO (854.8 eV).^[477,478] Therefore, it is supposed that Ni²⁺ are stabilized in the spinel structure after formation. Raman spectroscopy has corroborated the same valence state for Ni in the formatted spinel cathodes. Interestingly, the Ni2p spectrum of the cycled sample reveals identical binding positions for Ni2p_{3/2} and Ni2p_{1/2} at 854.8 and 872.0 eV, respectively and the extra signals are also observable. This would mean that the dominant oxidation state of Ni is still divalent after 250 cycles, which is in contrast to the Raman results unveiling Ni³⁺ and Ni⁴⁺. The reason for the registration of Ni²⁺ can presumably be ascribed to the development of Li_xNi_{1-x}O impurities as found by XRD and Raman analyses. Ni³⁺ and Ni⁴⁺ present in the cycled LiNi_{0.4}Mn_{1.6}O₄ electrodes cannot be verified by XPS because of the broad signals of the satellites and the F(KL₁L_{2,3}) and F(KL₁L₁) Auger transitions. Higher valent Ni states would be positioned in these regions and are most likely superimposed by the satellites and Auger peaks. This is also why it is impossible to recognize if there are Ni compounds (e.g. NiF₂) included in the SPI film.

C1s: The C1s spectrum of the formatted cathode has a prominent band at 284.5 eV from the conductive carbon within the electrode. Besides, two characteristic PVDF features are seen at 285.8 and 290.3 eV due to CH₂, and CF₂, respectively. The much stronger intensity of the CH₂ peak alludes to the existence of electrolyte decomposition products as, for instance, ethers (H₂C=CH₂) and other hydrocarbon chains. Since the constitutive elements of the cathode are clearly detected, it can be concluded that after formation only a thin surface layer is formed. C-O and C=O groups are located at 287.1 and 288.8 eV, respectively, in a ratio of approx. 2:1 as expected for polyethylene carbonate (PEC, Scheme 4). Generally, the C-O peak indicates decomposed species such as alkoxides and carbonates (e.g. RCH₂OLi, PEC, ROCO₂Li, Li₂CO₃, ROLi, ROH, and ROR), while the C=O peak solely refers to carbonyl components (mainly carbonates, e.g. PEC, ROCO₂Li and Li₂CO₃).^[363,479,480] R in the chemical formulas represents alkyl groups or hydrogen. All of these are a result of the oxidation of the electrolyte and the appearance of the C-O or C=O bands in the C1s spectrum of the reference demonstrate that electrolyte decomposition takes place during formation. The oxidation of the carbonates at the surface of LiNi_{0.4}Mn_{1.6}O₄ is commonly described to occur at around 4.7 V vs. Li.^[4,201,243–247] Thereby, it has to be considered that the single carbonate solvents have some differences in the electrochemical stability. Actually, cyclic carbonates are slightly more stable than linear ones. Examples are: EC ≈ PC (≥ 4.7 V) > DMC ≈ EMC (≥ 4.5 V).^[249,251] Here, the oxidation potentials are measured vs. a high voltage spinel composite electrode. Binary and tertiary electrolyte mixtures exhibit nearly the same oxidation potential vs. the composite cathode (≥ 4.5 V).^[249,251] Schemes 4 and 5 depict a variety of possible oxidative reaction pathways of EC, DMC, and EMC, the main components of the base electrolyte.

Scheme 4A shows the decomposition reaction of EC initiated by the strong Lewis acid PF₅, which catalyzes the ring-opening polymerization of EC to yield PEC or polyethylene oxides (PEO).^[1,247,260,261] Under standard conditions (voltages up to 4.2 V and ambient temperature) the reactions are endothermic.^[481] Nonetheless, since the reference C//LiNi_{0.4}Mn_{1.6}O₄ full cell was cycled up to 4.8 V at 45 °C, enough activation energy could be provided to trigger the polymerization of EC. The 2:1 ratio of the C-O and C=O peaks suggests the generation of PEC after formatting the reference cell. The driving force is the evolution of CO₂. A minor swelling of the spinel cell was observed after cycling confirming the development of gases such as CO₂. This gas can further be reduced to formate, oxalate, carbonate, and CO.^[260] Here, just the reaction of PF₅ with EC is demonstrated. But, actually the oxidation of other carbonates like for example EMC can also be catalyzed by PF₅.^[482]

A**B**

Scheme 4 **A** Lewis-acid-catalyzed ring-opening polymerization of EC. Adapted from^[245,247,260]. **B** Autocatalytic decomposition of LiPF_6 -based carbonate electrolytes (R = alkyl groups). Adapted from^[295].



Scheme 5 Possible reactions of **A** EC and **B** linear carbonates (R = alkyl groups) under oxidative conditions. Adapted from^[242].

The origin of the autocatalytic decomposition of LiPF_6 -based carbonate electrolytes (Scheme 4B) is trace impurities of water producing HF according to the equations 6 - 9 in chapter 2.1.3.^[181] The resulting POF_3 is the starting point of the reaction cycle and catalyzes the corrosion of carbonates (e.g. EC, DMC, and EMC).^[295] Until now, many research groups have investigated the autocatalytic decomposition cycle in dependence of various organic carbonates used as electrolyte solvents.^[483] Carbon dioxide (CO_2), ethylene ($\text{H}_2\text{C}=\text{CH}_2$), fluorophosphoric acid ($\text{O}=\text{PF}(\text{OH})_2$), difluorophosphoric acid ($\text{O}=\text{PF}_2(\text{OH})$), dialkyl fluorophosphates ($\text{O}=\text{PF}(\text{OR})_2$), alkyl difluorophosphates ($\text{O}=\text{PF}_2(\text{OR})$), alkyl fluorides (RF), and PEC were identified as main degradation products. At least, carbonates and alkyl groups are also generated upon the formation of $\text{C//LiNi}_{0.4}\text{Mn}_{1.6}\text{O}$ pouch cells as can be seen in the C1s spectrum.

Scheme 5 displays alternative reactions of EC and linear carbonates under oxidative conditions without the catalytic effect of LiPF_6 .^[242] Obviously, the oxidation of carbonates is multifold and leads to new carbonyl compounds, which include open chain organic carbonates, ketones, aldehydes, and formates. Small fragmented molecules are supposed to dimerize or oligomerize to larger ones. These long chain polycarbonates are believed to accumulate on the cathode surface during the operation of Li ion cells.^[242] The herein conducted XPS studies cannot completely differ between the decomposed products. But, it can be verified to what extent the oxidation of the electrolyte took place and the principal chemical nature of the SPI is determined.

The C1s spectrum of the cycled positive electrode reveals an enhanced CH_2 signal at 286.1 eV and significantly increased C-O and C=O signals at 287.3 and 289.1 eV, respectively, in comparison to the formatted cell. The CF_2 (290.3 eV) and C-C (285.0 eV) peaks exhibit lower percentage peak areas. Thus, a thick SPI has been formed throughout cycling. Especially, the C=O peak has become more pronounced after 250 cycles unveiling the intensified generation of compounds with carbonyl groups.

O1s: The O1s spectrum of the formatted cathode has a sharp feature around 529.5 eV originating from the $\text{LiNi}_{0.4}\text{Mn}_{1.6}\text{O}_4$ oxygen, and two bands from the surface film at 533.7 and at 532.1 eV. The former refers to carbonate, phosphate (e.g. $\text{PO}(\text{OR})_3$), and fluorophosphate (e.g. $\text{O}=\text{PF}(\text{OR})_2$, $\text{Li}_x\text{PF}_y\text{O}_z$), while the latter denotes carbonyl and alkoxy species.^[363,479,480] In agreement with the C1s region, the O^{2-} band is clearly visible at 529.5 eV signifying the existence of a rather thin SPI. After 250 cycles, the lattice oxygen (529.3 eV) is strongly reduced, whereas the C-O (533.8 eV) and C=O (532.1 eV) peaks have grown considerably indicating excessive SPI formation including carbonates. The much higher signal intensity of C-O as compared to C=O is related to an enhanced contribution of PEC, phosphates, and fluorophosphates to the surface layer. The development of a $\text{Li}_x\text{Ni}_{1-x}\text{O}$ impurity cannot be proven by the O1s section as the signal is superimposed by the O^{2-} band.

F1s: After formatting C//LiNi_{0.4}Mn_{1.6}O₄ pouch cells, the F1s spectrum of the cathode is composed of CF₂ (687.6 eV) from the PVDF binder, a mixture of Li_xPF_y, Li_xPF_yO_z, and O=PFOR (686.8 eV), and LiF (684.7 eV) as a result of LiPF₆ corrosion. If NiF₂ and MnF₂ are also present on the electrode surface is hard to tell as the respective signals overlap with the LiF peak.^[363,474,477] Li_xPF_yO_z and O=PFOR represent fluorophosphates. In case of the reference cell, the amount of O=PFOR is proposed to be rather low. Decomposition products of LiPF₆ are the main source of the LiF and Li_xPF_yO_z/O=PFOR signals and tend to easily precipitate on the LiNi_{0.4}Mn_{1.6}O₄ surface.^[430,484,485] Moreover, LiPF₆ itself participates in the SPI and adds up to the cell resistance.^[238,486] For the cycled spinel electrode the bands of LiF (684.0 eV) and Li_xPF_y/Li_xPF_yO_z (686.9 eV) are much stronger, while the peak area of the CF₂ signal (687.6 eV) is smaller than after formation. Consequently, an increase of the SPI thickness has occurred upon cycling.

P2p: The P2p region of the formatted cathode has a quite broad shape involving phosphate species (e.g. PO₄³⁻, OP(OR)₃) at 133.3 eV, fluorophosphates Li_xPF_yO_z/O=PFOR at 134.5 eV, and Li_xPF_y residues at 136.3 eV. Degradation products such as Li_xPF_y and Li_xPF_yO_z/O=PFOR, were found to grow with cycling. Hence, it is suggested that some components of the surface film are not stable upon cycling at 45 °C between 3.3 and 4.8 V and decompose to create a porous SPI that only partially passivates the electrode particles. As a matter of fact, fresh electrolyte is constantly transported to the exposed sections of the cathode surface and the degradation reactions continue to form organic and inorganic species. Nevertheless, the incomplete SPI is sufficient to stabilize the cycling behavior of C//LiNi_{0.4}Mn_{1.6}O₄ pouch cells in order that still 95.2 mAhg⁻¹ (61% residual capacity) have been achieved after 250 cycles at 45 °C at 1C between 3.3 and 4.8 V (Figure 70, chapter 5.2.2).

Conclusion

The surfaces of the reference LiNi_{0.4}Mn_{1.6}O₄ cathodes were analyzed by XPS after formation at 23 °C and after 250 cycles at 45 °C. It is shown that the base electrolyte is not stable under these conditions. The generation of a film consisting of organics and inorganics on the spinel electrode surface is documented. After formatting C//LiNi_{0.4}Mn_{1.6}O₄ pouch cells, a thin SPI has already formed and becomes substantially thicker during cycling. Carbonyl species (mainly carbonates, e.g. PEC), alkyl groups, alkoxides, hydroxides, phosphates, fluorophosphates, and residues of the conducting salt LiPF₆ are components of this surface layer as confirmed by the C1s, O1s, F1s, and P2p spectra. Since the SPI keeps growing upon cycling, it is concluded that some layer components are not stable under the oxidative cycling conditions and decompose to form a porous surface film. Then, the cathode particles are only partially passivated by the film and the reference electrolyte is continuously oxidized at the bare positions of the electrode. Besides, the Mn2p spectrum reveals the dominance of Mn⁴⁺ vs.

Mn³⁺ for the formatted sample, and the cycled one solely contains Mn⁴⁺ as proven by Raman spectroscopy. The interpretation of the Ni2p region is much more critical because of the appearance of additional emissions like satellites, which are superimposed by F(KL₁L_{2,3}) and F(KL₁L₁) Auger transitions. Therefore, in this case, trivalent and tetravalent Ni ions cannot be determined by XPS. In spite of this, the development of Li_xNi_{1-x}O impurities and Ni²⁺ could be identified in the cycled and the formatted spinel electrode, respectively.

Electrolyte optimization

Hereafter, the influence of various electrolyte additives on the structure of the SPI is investigated by XPS. The additives are ordered according to their decreasing beneficial effect on the CC/CV cycle life of C//LiNi_{0.4}Mn_{1.6}O₄ full cells (see chapter 5.2.2). The cell comprising 1.5% LiTFSI was not analyzed by XRD, because of the cell damage that has been triggered by massive gassing during cycling. The Mn2p and Ni2p regions are not discussed in detail anymore as no major differences are detected relative to the references. The spectra are displayed in the appendix (chapter7).

Trimethyl phosphate

After formatting and cycling C//LiNi_{0.4}Mn_{1.6}O₄ pouch cells comprising 0.5% TMP, XPS measurements of the respective cathodes were carried out to examine the nature of the film generated on the electrode particles (Figure 113). Only Utsugi et al. have studied the polymer layer derived from the decomposition of TMP on the surface of a high voltage spinel cathode by XPS.^[268] Nonetheless, in contrast to this work, Utsugi concentrated on the cycle performance of LTO//LiNi_{0.5}Mn_{1.5}O₄ coin cells and merely elucidated the C1s and P2p regions.

C1s: Regarding the C1s spectrum of the spinel electrode formatted with 0.5% TMP, a high similarity to the corresponding reference spectrum is visible. However, the overall peak area of the C-C signal at 284.5 eV is slightly lower. The PVDF characteristics CH₂ and CF₂ appear at 285.7 and 290.3 eV, respectively, whereby the latter is more pronounced for the 0.5% TMP sample than for the reference indicating a higher number of alkyl fluorides. Both the C-O and C=O bands are significantly stronger compared to the electrode formatted without any additive. This suggests that more carbonates and alkoxides accumulate on the surface of the cathode. Hence, after formation more electrolyte degradation products are observed for the 0.5% TMP cell than for the reference but the SPI is still rather thin. The C1s region of the LiNi_{0.4}Mn_{1.6}O₄ electrode cycled with 0.5% TMP looks notably different in comparison to the formatted one. Surprisingly, the peak areas of the C-O and C=O bands at 287.1 and 288.9 eV, respectively, have not increased after 250 cycles. This implies that no additional carbonates and alkoxides precipitated on the cathode surface. The signal of the conductive carbon (284.7 eV) is marginally diminished owing to an enhancement of the CH₂ band (285.9 eV).

5. Results and discussion

5.5 Characterization of the solid permeable interface

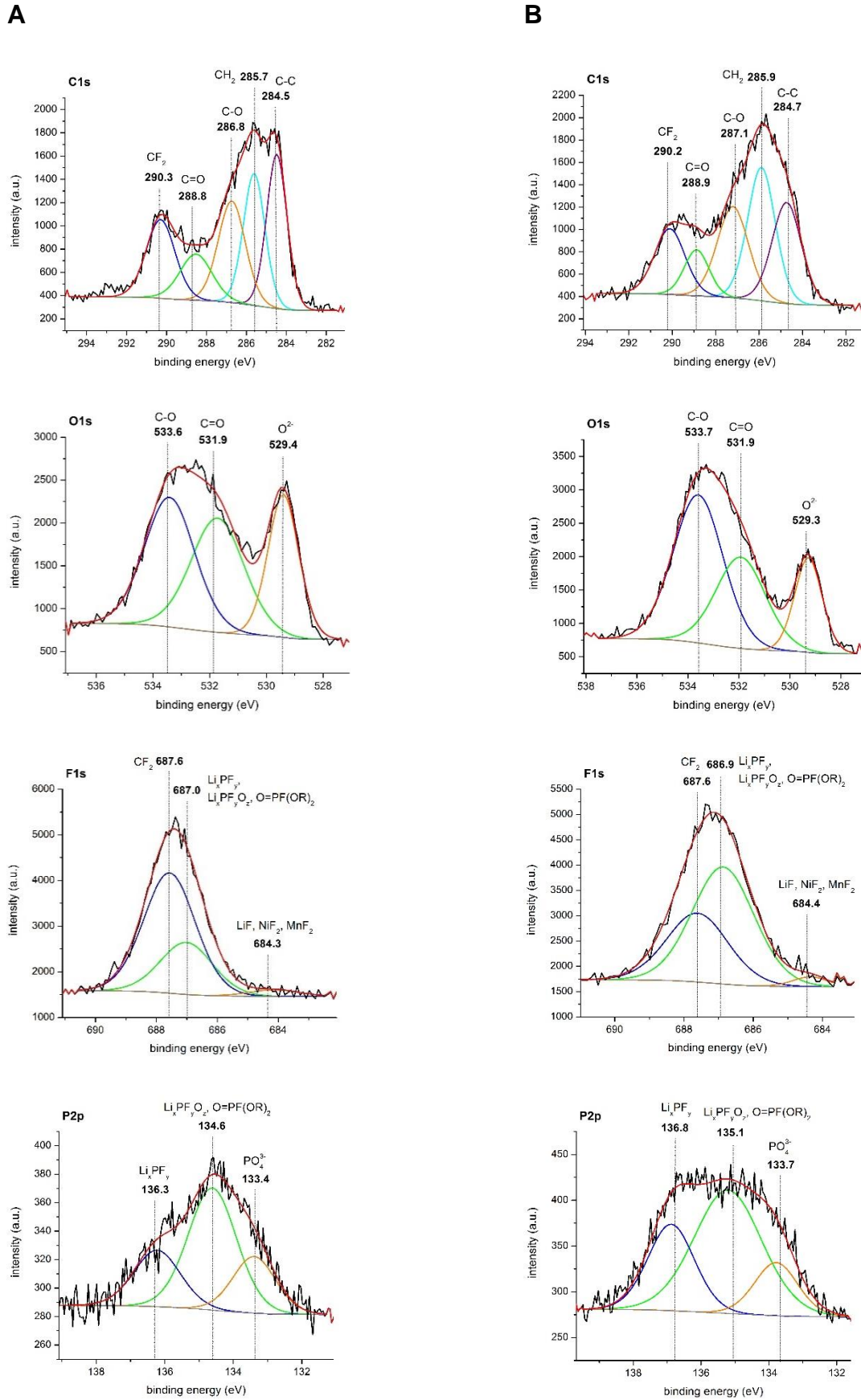


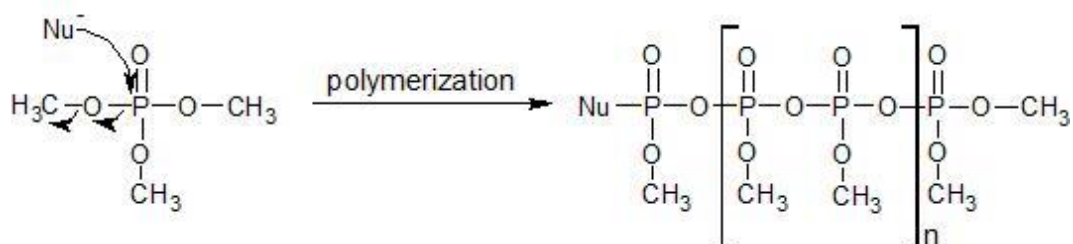
Figure 113 XPS spectra of LiNi_{0.4}Mn_{1.6}O₄ electrodes at 0% SOC after **A** formatting C//LiNi_{0.4}Mn_{1.6}O₄ pouch cells with 0.5% TMP at 23 °C and after **B** cycling these cells for 250 cycles at 45 °C.

O1s: Analysis of the O1s regions of the spinel electrodes after formatting and cycling C//LiNi_{0.4}Mn_{1.6}O₄ pouch cells with 0.5% TMP confirm the results obtained from the C1s spectra. The formatted 0.5% TMP sample unveils larger peak areas for the C-O and C=O bands at 533.6 and 531.9 eV, respectively, than for the reference pointing to higher amounts of carbonates and alkoxides deposited on the cathode surface. Concurrently, the signal detected at 529.4 eV attributed to O²⁻ from the LiNi_{0.4}Mn_{1.6}O₄ lattice, has a smaller percentage peak area than the one in the reference spectrum. Considering the O1s spectrum of the spinel electrode cycled with 0.5% TMP, the O²⁻ band (529.3 eV) is further reduced because of the substantial growth of the C-O signal (533.7 eV). As opposed to this, the C=O peak area remains virtually unchanged. Consequently, the development of carbonates and alkoxides is impaired after formation. This is the reason why the O²⁻ peak area is still larger than for the reference. Nevertheless, phosphate, fluorophosphate, and Li_xPF_yO_z species might be the origin of the distinct C-O band after 250 cycles.

F1s: The area of the CF₂ signal at 687.6 eV in the F1s spectrum of the formatted 0.5% TMP sample is a little larger compared to the reference, although the peak area assigned to Li_xPF_y/Li_xPF_yO_z/O=PFOR components (687.0 eV) is markedly larger. This underpins the fact that alkyl fluorides are present in the SPI. Furthermore, the strong and broad band at 687.0 eV denotes the participation of TMP in the structure of the surface film. The existence of metal fluorides (LiF, NiF₂, or MnF₂) is given by the band at 684.3 eV, which is slightly more intense relative to the reference. Cycling C//LiNi_{0.4}Mn_{1.6}O₄ full cells leads to a strong increase of the Li_xPF_y/Li_xPF_yO_z/O=PFOR species (686.9 eV) in the SPI and on account of this the CF₂ (687.6 eV) and the LiF/NiF₂/MnF₂ peaks (684.4 eV) reduce in intensity. It is assumed that TMP is mainly responsible for the accumulation of Li_xPF_y/Li_xPF_yO_z/O=PFOR.

P2p: Examination of the P2p spectrum of the cathode formatted with 0.5% TMP reveals three characteristic signals at 133.4, 134.6, and 136.3 eV, which are ascribed to phosphates, fluorophosphates, and conducting salt residues, respectively. PO₄³⁻ and Li_xPF_yO_z/O=PFOR reveal greater peak areas than same in the reference spectrum. Li_xPF_y is slightly weaker. This proves that LiPF₆ residues and decomposition products are not the only source for fluorophosphates. For the cycled spinel electrode all three components in the structure of the surface layer are even more evident. Thereby, PO₄³⁻ and Li_xPF_yO_z/O=PFOR dominate. Thus, TMP definitely participates in the SPI formation.

In summary, the addition of 0.5% TMP to the base electrolyte causes a reduction of Li_xPF_y and carbonates in the structure of the cathode surface film and enhances the contributions of phosphates and fluorophosphates compared to reference cells without any additives. Utsugi and co-workers proposed the following film formation mechanism:



Scheme 6 Film formation mechanism of TMP on a $\text{LiNi}_{0.4}\text{Mn}_{1.6}\text{O}_4$ cathode. Adapted from^[268].

Nucleophiles such as fluoride ions (F^-) or alkoxide ions (CH_3O^-) attack the phosphorus atom of TMP. The resulting fragment reacts with another TMP and a chain reaction proceeds successively to generate a polymer surface layer on the spinel electrode.^[268] This film is even visible in the SEM images as documented in Figure 114.

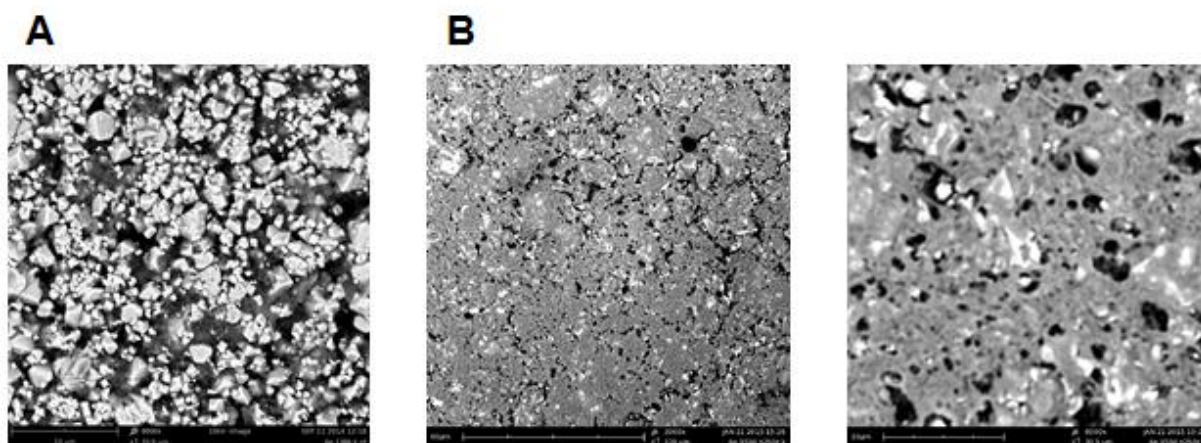


Figure 114 **A** SEM image of the surface of a $\text{LiNi}_{0.4}\text{Mn}_{1.6}\text{O}_4$ composite electrode after 0 cycles with 8,000-times amplification. **B** SEM images of the surface of a $\text{LiNi}_{0.4}\text{Mn}_{1.6}\text{O}_4$ composite electrode after 250 cycles at 45 °C in the base electrolyte containing 0.5% TMP with 2,000- (middle) and 8,000-times amplification (right).

Fractures in the surface film might be due to the preparation process of the electrode for the SEM analysis. Nonetheless, the TMP-derived SPI is proposed to be a porous layer network as the amount of phosphates and fluorophosphates increases during cycling. Generally, the TMP-based surface layer influences the cycling behavior of $\text{C}/\text{LiNi}_{0.4}\text{Mn}_{1.6}\text{O}_4$ pouch cells containing 0.5% TMP. As a matter of fact, a phosphate-containing SPI with only low proportions of the conducting salt has a beneficial effect on the electrochemical performance of $\text{C}/\text{LiNi}_{0.4}\text{Mn}_{1.6}\text{O}_4$ full cells, whereas SPIs consisting primarily of carbonates have a negative influence on the cycling properties. Very low concentrations of TMP (e.g. 0.1%) cannot, however, stabilize the surface film on the spinel electrode and after a few promising cycles capacity fading sets in (see chapter 5.2.2 Figure 90). Higher concentrations of TMP such as 1.5% lead to the generation of thick and/or resistive layers, which result in accelerated cell ageing for the cells of this thesis.

Tris(2,2,2-trifluoroethyl) phosphite

C1s: Figure 115 illustrates the XPS patterns of $\text{LiNi}_{0.4}\text{Mn}_{1.6}\text{O}_4$ electrodes from the formatted and the cycled full cells comprising 0.5% TFPi. After the formation of $\text{C}/\text{LiNi}_{0.4}\text{Mn}_{1.6}\text{O}_4$ cells the C1s regions of the reference and the 0.5% TFPi sample are very similar. The major differences are that the peak area of the CH_2 band at 285.9 eV is somewhat smaller and that the signal of the conductive carbon at 284.6 eV is stronger than in the reference spectrum. This implies the generation of a thinner SPI throughout the formation, which changes significantly upon cycling. Then, the C-C band (284.7 eV) is substantially lowered as in the case of 0.5% TMP cells. This is because of the production of a relatively thick surface film. The peak areas of all four signals including the CH_2 (285.9 eV), the C-O (287.2 eV), the C=O (289.0 eV), and the CF_2 bands (290.2 eV) are substantially increased after 250 cycles. Therefore, hydrocarbon chains, alkoxides, carbonates, and alkyl fluorides are likely to be part of the SPI. Nevertheless, fewer carbonyl groups are involved in the SPI in comparison to the reference. The enhancement of the CF_2 peak is attributed to the CF_3 groups in TFPi and strongly suggests that TFPi plays an important role in the surface layer formation.

O1s: In agreement with the C1s pattern, the O1s region of the cathode formatted with 0.5% TFPi is virtually identical to the reference spectrum. Hereby, the O^{2-} signal at 529.5 eV is more prominent confirming the generation of a rather thin SPI. The C-O and C=O bands at 533.7 and 532.0 eV, respectively, exhibit nearly the same low peak areas signifying the existence of carbonates, alkoxides, phosphates, and fluorophosphates in the SPI structure. After 250 cycles, the intensity of the O^{2-} signal (529.4 eV) is drastically reduced and simultaneously, the peak areas of the C-O and C=O bands are noticeably enlarged. This implies severe SPI production. The higher intensity of the C-O signal versus C=O one is connected to the enhanced formation of carbonates, phosphates, and fluorophosphates.

F1s: The F1s spectrum of the formatted 0.5% TFPi sample unveils a greater sum of $\text{Li}_x\text{PF}_y\text{O}_z/\text{Li}_x\text{PF}_y/\text{O}=\text{PFOR}$ (686.9 eV) and CF_2 -containing components (687.7 eV) than in the reference underlining the involvement of TFPi in the SPI structure. Besides, the signal for LiF, NiF_2 , and/or MnF_2 present at 684.2 eV has about the same peak area as in the reference chart. After 250 cycles, this signal is declined. Although the cycled cathode provides larger amounts of $\text{Li}_x\text{PF}_y\text{O}_z$, $\text{O}=\text{PFOR}$, and Li_xPF_y (687.0 eV) than the formatted cathode, the respective peak area is considerably reduced in comparison to the reference. The P2p spectrum gives more detailed information.

5. Results and discussion

5.5 Characterization of the solid permeable interface

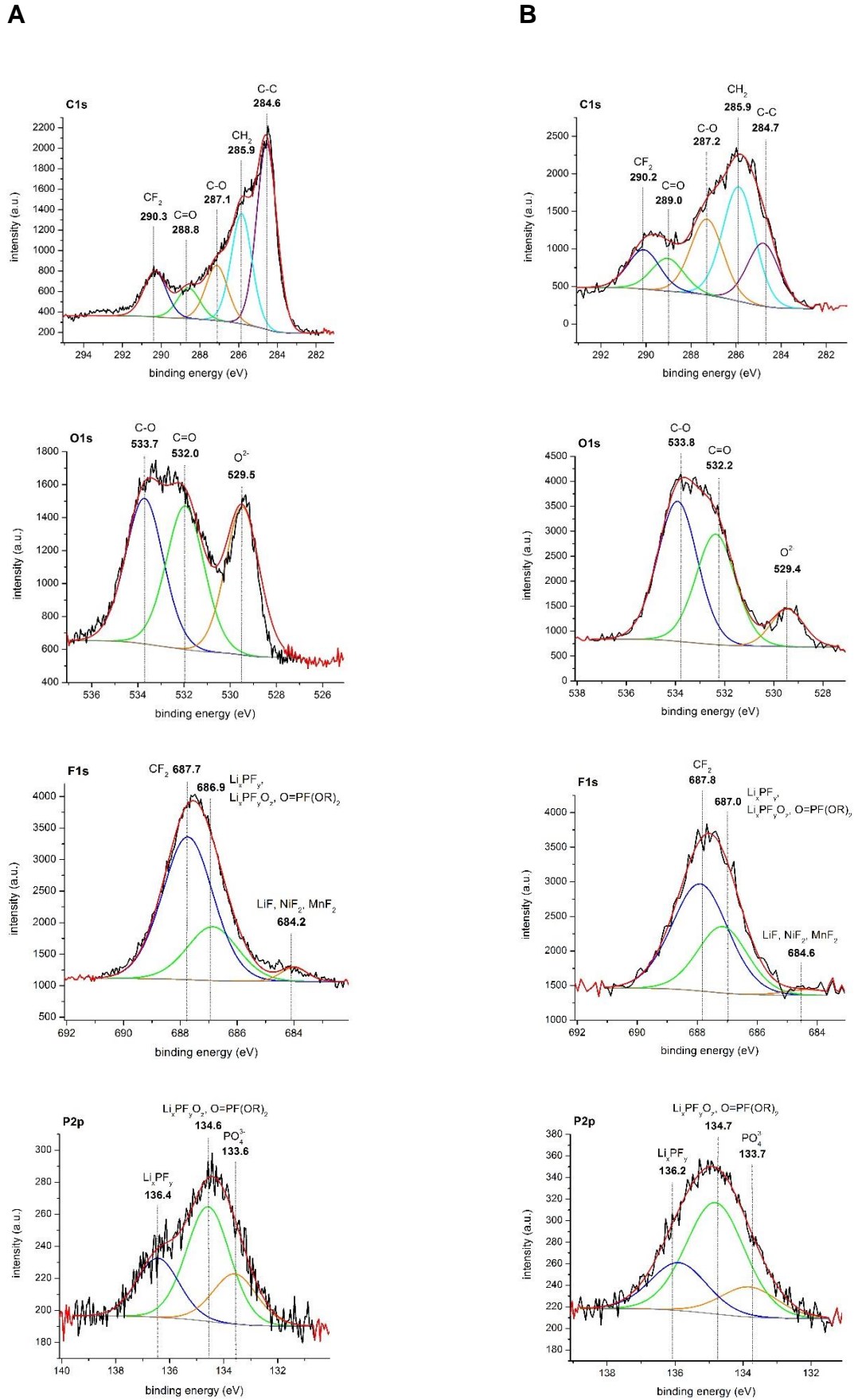
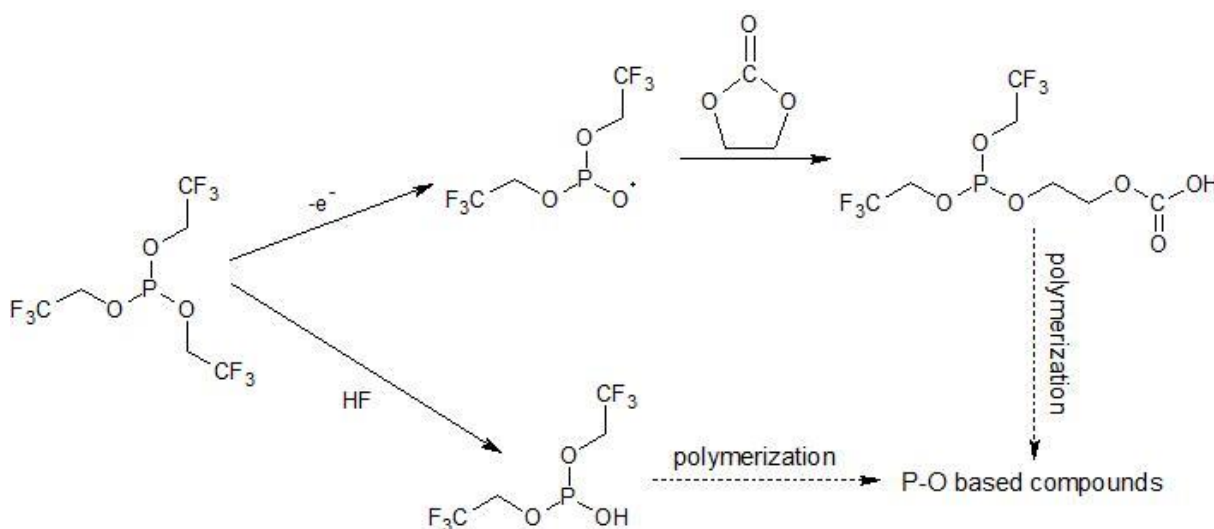


Figure 115 XPS spectra of LiNi_{0.4}Mn_{1.6}O₄ electrodes at 0% SOC after **A** formatting C//LiNi_{0.4}Mn_{1.6}O₄ pouch cells with 0.5% TFPI at 23 °C and after **B** cycling these cells for 250 cycles at 45 °C.

P2p: Formatting C//LiNi_{0.4}Mn_{1.6}O₄ pouch cells comprising 0.5% TFPi leads to the development of a significant amount of phosphates (133.6 eV) on the surface of the cathode as shown in Figure 115. Hence, TFPi is certainly integrated in the SPI. Relative high intensities of Li_xPF_yO_z/O=PFOR (134.6 eV) and Li_xPF_y (136.4 eV) coincide with this fact. Proportions of phosphates (133.7 eV) and fluorophosphates (134.7 eV) grow during cycling, whereas the peak area of the conducting salt residues (136.2 eV) hardly increases. This observation corroborates the participation of TFPi in the cathode surface film and explains the relatively low peak area of the mixed Li_xPF_yO_z/Li_xPF_y signal in the F1s spectrum.

All in all, the base electrolyte with 0.5% TFPi leads to a similar structure of the SPI as the one with 0.5% TMP. However, the surface layer of the phosphite contains a slightly higher content of carbonyl groups than that of the 0.5% TMP sample. This is probably the reason for the poorer cycling performance of the 0.5% TFPi cell in comparison to the 0.5% TMP cell. Nevertheless, the cycling stability of the C//LiNi_{0.4}Mn_{1.6}O₄ cell including 0.5% TFPi is still quite good and better than that of the reference (see chapter 5.2.2). High quantities of phosphates and fluorophosphates in the SPI are believed to be responsible for this trend. Aside from LiPF₆, TFPi is suggested to release these species. To the best of our knowledge there is no report on analyzing TFPi-based surface layers formed on high voltage spinel electrodes by XPS. The mechanism displayed in Scheme 7, which is proposed for the polymerization of TFPi, is in accordance with the results on tris(trimethylsilyl) phosphite as presented in the literature^[270]. Phosphite can react with HF in the electrolyte solution. As a consequence, P-OH groups are formed. Furthermore, polymers based on the P-O lattice are released and accumulate on the cathode surface. In this way, HF is also scavenged by TFPi. Under oxidative conditions, TFPi also generates radicals, which can further react with other electrolyte components (e.g. EC) to produce long chain molecules that contribute to the SPI formation.



Scheme 7 Schematic representation of two possible reaction mechanisms for the electrochemical decomposition of TFPi. Adapted from^[270].

A SEM picture of the surface film generated by the reference electrolyte comprising 0.5% TFPi is depicted in Figure 116.

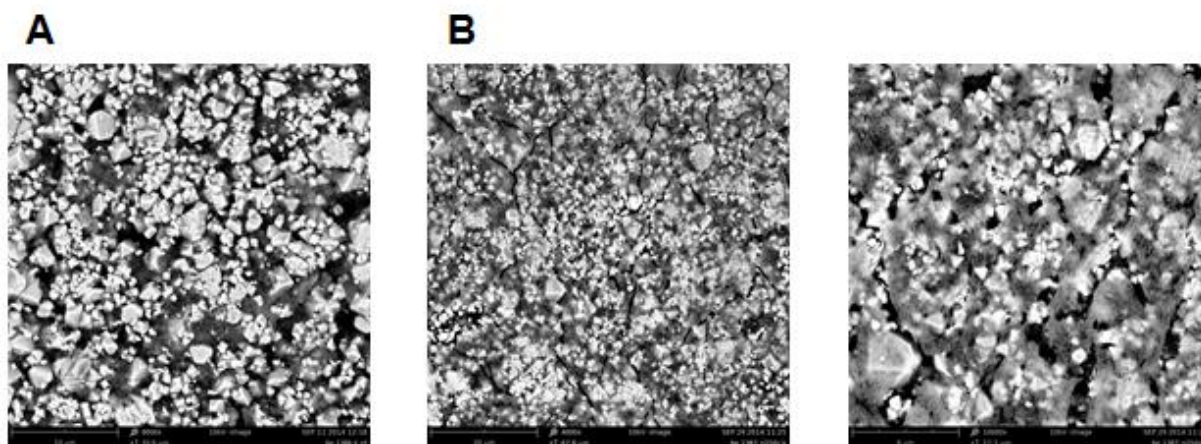


Figure 116 **A** SEM image of the surface of a $\text{LiNi}_{0.4}\text{Mn}_{1.6}\text{O}_4$ composite electrode after 0 cycles with 8,000-times amplification. **B** SEM images of the surface of a $\text{LiNi}_{0.4}\text{Mn}_{1.6}\text{O}_4$ composite electrode after 250 cycles at 45 °C in the base electrolyte containing 0.5% TFPi with 4,000- (middle) and 10,000-times amplification (right).

The SPI looks considerably different from those created by the 0.5% TMP cell. This is presumably due to the different functional groups of the two additives (CF_3 vs. CH_3). Since the SPI continuously develops during cycling, electrolyte can still interact with the cathode and the resulting film is porous. Nonetheless, the SPI properties indubitably help to improve the cycling characteristics of $\text{C//LiNi}_{0.4}\text{Mn}_{1.6}\text{O}_4$ full cells. The concentration of 0.5% TFPi seems to be the best compromise as 0.1% TFPi only stabilizes the surface film in the first few cycles and 1.5% TFPi creates thick and/or resistive layers (see chapter 5.2.2, Figure 88).

Lithium bis(oxalato)borate

LiBOB is known to effectively suppress electrolyte oxidation by the production of a stable SPI on high voltage spinel cathode surfaces.^[247,272,307,467] Herein, XPS measurements of a $\text{LiNi}_{0.4}\text{Mn}_{1.6}\text{O}_4$ cathode cycled with 0.5% LiBOB at 45 °C between 3.3 and 4.8 V are accomplished to identify the decomposed elements on the electrode and to either verify or dispute the literature results. Figure 117 gathers the corresponding XPS regions.

5.5 Characterization of the solid permeable interface

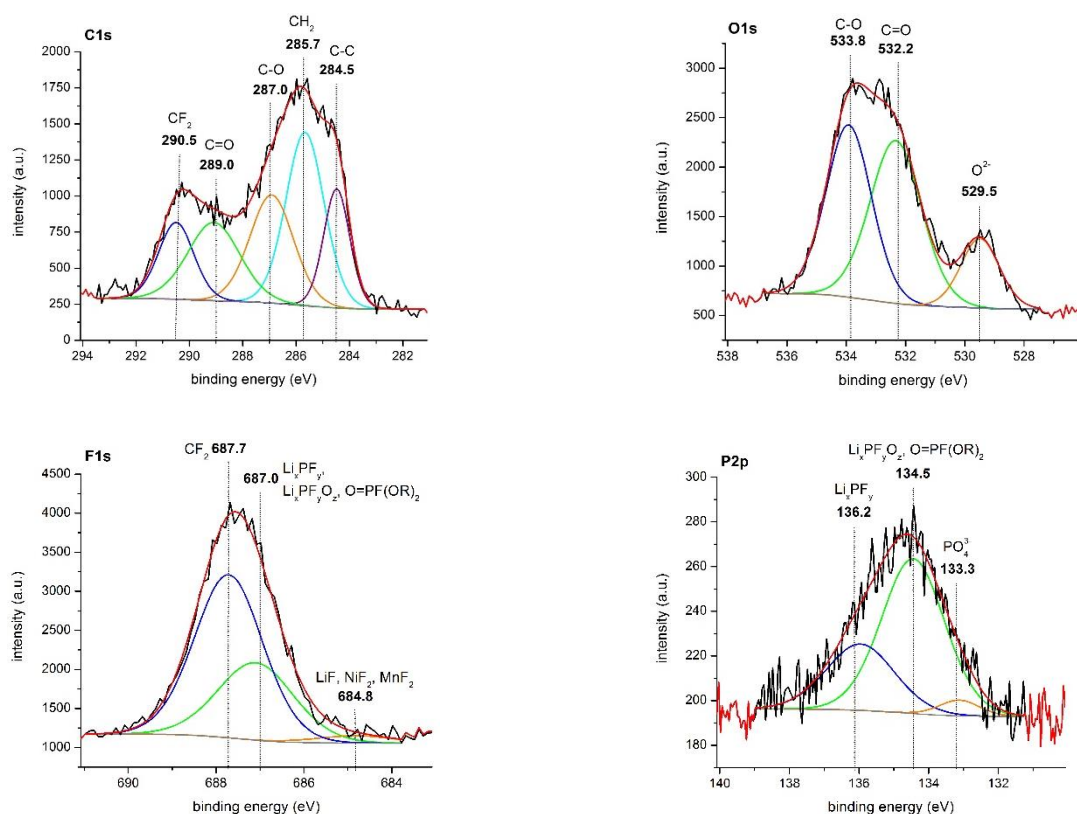


Figure 117 XPS spectra of LiNi_{0.4}Mn_{1.6}O₄ electrodes at 0% SOC after cycling C//LiNi_{0.4}Mn_{1.6}O₄ pouch cells with 0.5% LiBOB for 250 cycles at 45 °C between 3.3 and 4.8 V.

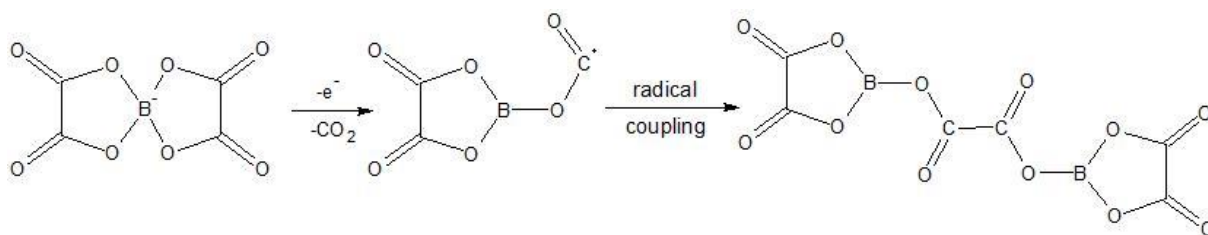
C1s: The C1s spectrum reveals five types of carbons. The peak area from the carbon of the spinel cathode (C-C; 284.5 eV) is considerably lower than in the reference and the 0.5% TFPi sample indicating serious SPI formation. The bands of carbon bonded to hydrogen (CH₂; 285.7 eV) and fluorine (CF₂; 290.5 eV) have about the same peak areas as in the reference. This is consistent with the fact that LiBOB does not introduce many C-H and no C-F bonds in the SPI. In contrast to this, the signals of the carbon singly bonded to oxygen (C-O; 287.0 eV) and of the carbon of the carbonyl groups (C=O; 289.0 eV) are much more intense as those in the reference and the 0.5% TFPi cell. Thus, LiBOB is clearly part of the surface layer formed on the cathode.

O1s: The metal oxide signal at 529.5 eV in the O1s pattern is very low owing to the strong presence of C=O components (532.2 eV) in the SPI. Nevertheless, the carbonyl band has a similar peak area as that of the reference and is even smaller than that of the 0.5% TFPi batch. This is probably a result of low concentrations of alkoxides within the surface film structure. The peak area of the C-O band is also reduced compared to the reference denoting that phosphates and fluorophosphates do not play an important role in SPI production. Nevertheless, both the C-O as well as the C=O signals are obviously greater in percentage than in the reference spectrum signifying the involvement of LiBOB in the surface layer.

F1s: Analysis of the F1s spectrum offers additional information. The PVDF band at 687.7 eV remains distinct after 250 cycles because the $\text{Li}_x\text{PF}_y/\text{Li}_x\text{PF}_y\text{O}_z/\text{O}=\text{PFOR}$ and the $\text{LiF}/\text{NiF}_2/\text{MnF}_2$ peaks have not grown much. Consequently, the development of phosphates, fluorophosphates, conducting salt residues, and metal fluorides is inhibited by the LiBOB-based SPI.

P2p: Supplementary to the F1s data, the P2p spectrum of the cycled spinel electrode is investigated by XPS. It is composed of PO_4^{3-} (133.3 eV), $\text{Li}_x\text{PF}_y\text{O}_z/\text{O}=\text{PFOR}$ (134.5 eV), and Li_xPF_y (136.2 eV). In comparison to the base electrolyte, noticeably less phosphates, fluorophosphates, or salt deposits are registered with 0.5% LiBOB. This is in compliance with the F1s region and confirms that the LiBOB-containing SPI alleviates the decomposition of LiPF_6 .

In short, 0.5% LiBOB is included in the SPI generation of $\text{C}/\text{LiNi}_{0.4}\text{Mn}_{1.6}\text{O}_4$ pouch cells as the surface layer comprises high contents of carbonyl species and the corrosion of the conducting salt is effectively suppressed in agreement with literature. Scheme 8 illustrates the formation of a surface film with LiBOB molecules according to Lucht, Choi, and Cui et al.^[269,272,307]



Scheme 8 Film formation mechanism of LiBOB on a $\text{LiNi}_{0.4}\text{Mn}_{1.6}\text{O}_4$ cathode.^[269,272,307]

Under oxidative conditions, as given upon cycling the system $\text{C}/\text{LiNi}_{0.4}\text{Mn}_{1.6}\text{O}_4$ at 45 °C in the voltage range of 3.3 and 4.8 V, LiBOB creates borate radicals, which subsequently cross-link and produce polymers leading to a passivating layer.^[269,272] The SPI seems to be rather thin, but very stable since electrolyte oxidation is declined in comparison to the reference. Ion-dipole interactions between electron-deficient boron in the SPI and electron-rich anions such as PF_6^- may prevent electrolyte degradation.^[299,307,487] This explains why the cycling stability of a high voltage spinel full cell containing 0.5% LiBOB is better than that of a cell without any additives (see chapter 5.2.2). However, the capacity fading is faster than that of the 0.5% TFPi cell. Decreasing the concentration of 0.5% LiBOB to 0.1% LiBOB improves the cycling performance of the respective full cell and is even superior to that with 0.5% TFPi (see chapter 5.2). A thinner SPI with the same properties as that of the 0.5% LiBOB sample is likely to be responsible for this behavior. If the film becomes too thick, the amount of carbonates is too enormous and counteracts the electron deficiency of boron. Consequently, less Lewis acid-base adducts are likely to be formed.

Hexamethyldisilazane

As previously mentioned in chapter 5.2.2, HMDS is studied, for the first time, as additive for lithium ion cells including a graphite anode and a high voltage spinel cathode. After formation C//LiNi_{0.4}Mn_{1.6}O₄ full cells at 23 °C and after cycling these cells at 45 °C XPS measurements of the corresponding cathodes were conducted to check whether organosilicons take part in the SPI production (Figure 118).

C1s: After formation, the C1s spectrum of the spinel electrode shows substantially stronger CH₂ (285.7 eV), C-O (287.0 eV), and C=O bands (289.1 eV) than seen in the reference. It suggests an excessive SPI generation incorporating hydrocarbon chains, alkoxides, and carbonates. Especially the C-O peak is slightly more intense, because it probably overlaps with carbon bond to nitrogen (C-N). Therefore, HMDS provokes fast electrolyte corrosion and a thickening of the surface layer. Accordingly, the peak area of the conductive carbon at 284.5 eV is reduced, while the CF₂ peak area (290.4 eV) is very similar to that in the reference. Surprisingly, cycling C//LiNi_{0.4}Mn_{1.6}O₄ pouch cells comprising 0.5% HMDS does not lead to a further increase of the SPI thickness as derived from XPS. Instead a decline of mainly alkyl groups, but also alkoxides and carbonates in the SPI are detected as the peak areas of the CH₂ (285.7 eV), C-O (286.9 eV), and C=O bands (288.8 eV) are reduced. They actually adopt values, which are nearly analogous to those of the formatted standard electrode. The remaining two bands, that is, the C-C (284.5 eV) and the CF₂ bands (290.2 eV) exhibit greater peak areas than before as the composite cathode is again stronger visible. Hence, after 250 cycles parts of the organic SPI have dissolved in the electrolyte implying that the HMDS-based surface film is not stable throughout cycling.

O1s: Examinations of the O1s region of the cathode formatted with 0.5% HMDS confirm the above observations. The C-O and C=O bands at 533.6 and 531.9 eV, respectively, are considerably larger than those of the reference. Aside from carbonates and alkoxides, phosphates and fluorophosphates are responsible for the SPI thickness. Simultaneously, the sharp feature around 529.5 eV originating from the LiNi_{0.4}Mn_{1.6}O₄ oxygen has a relatively lower percentage peak area, when compared to the reference spectrum. Cycling C//LiNi_{0.4}Mn_{1.6}O₄ pouch cells causes a diminution of the C-O (533.5 eV) and C=O signals (531.4 eV) and concomitantly, an enhancement of the O²⁻ band (529.3 eV). Thus, some of the organics of the SPI are depleted. Thereby, the peak area of the C-O band is noticeably less reduced than the C=O one alluding to the stability of phosphate-containing species in the SPI.

5. Results and discussion
5.5 Characterization of the solid permeable interface

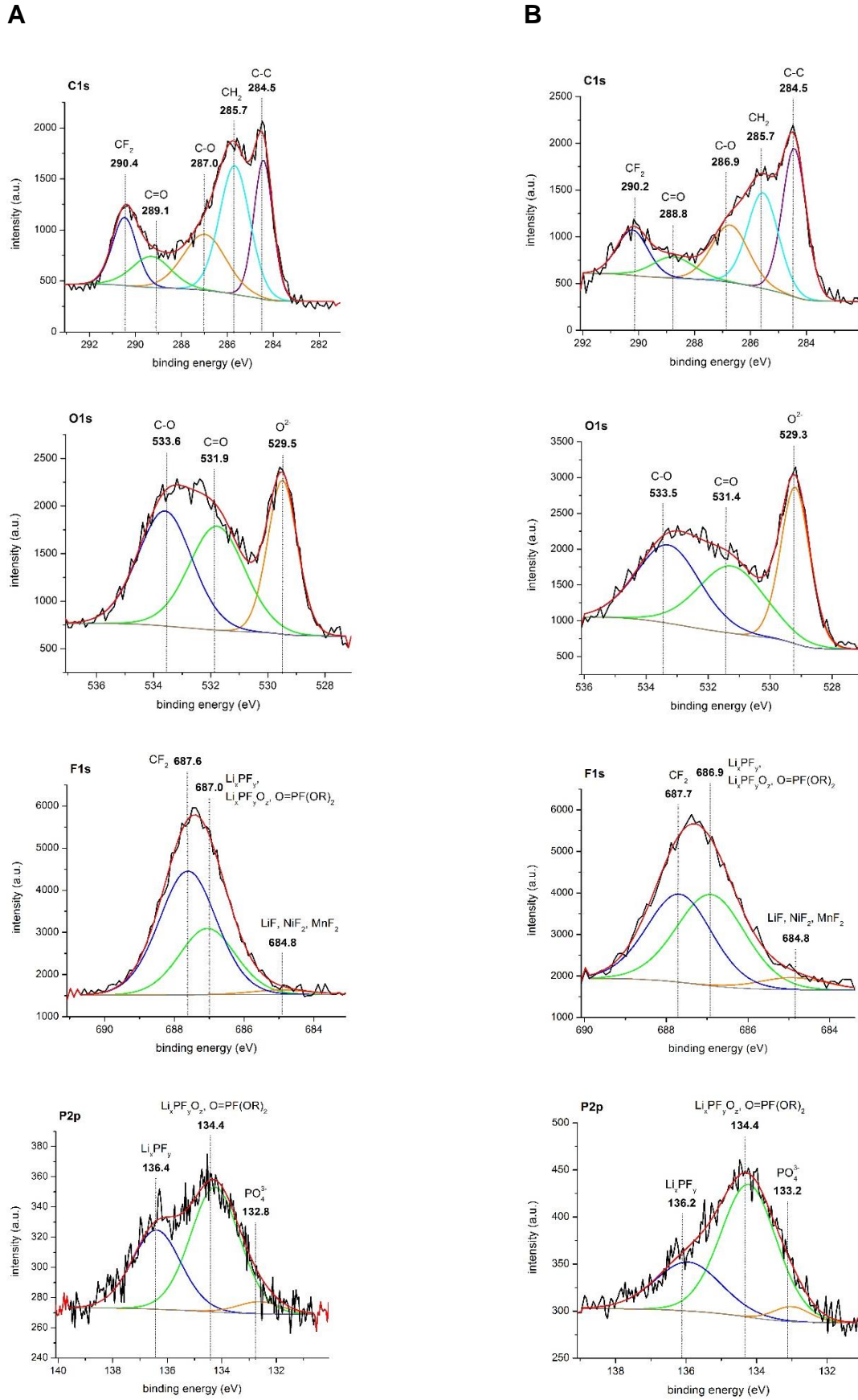


Figure 118 XPS spectra of LiNi_{0.4}Mn_{1.6}O₄ electrodes at 0% SOC after **A** formatting C//LiNi_{0.4}Mn_{1.6}O₄ pouch cells with 0.5% HMDS at 23 °C and after **B** cycling these cells for 250 cycles at 45 °C.

F1s: Regarding the F1s pattern of the formatted 0.5% HMDS electrode, three prominent signals are found at 687.6, 687.0, and 684.8 eV, which relate to PVDF and alkyl fluorides, $\text{Li}_x\text{PF}_y/\text{Li}_x\text{PF}_y\text{O}_z/\text{O}=\text{PFOR}$, and $\text{LiF}/\text{NiF}_2/\text{MnF}_2$, respectively. In this case, the intensity of the $\text{Li}_x\text{PF}_y/\text{Li}_x\text{PF}_y\text{O}_z/\text{O}=\text{PFOR}$ band is solely the result of the decomposition of the conducting salt and is much stronger than that of the reference. Consequently, the structure and thickness of the surface film is also based on LiPF_6 corrosion products. In contrast to the organic phase of the SPI, the inorganic phase is stable upon cycling, since the peak areas of the $\text{Li}_x\text{PF}_y/\text{Li}_x\text{PF}_y\text{O}_z/\text{O}=\text{PFOR}$ (686.9 eV) and $\text{LiF}/\text{NiF}_2/\text{MnF}_2$ signals (684.8 eV) have increased, whereas that of the CF_2 band (687.7 eV) has declined after 250 cycles.

P2p: The P2p spectrum complements the F1s data. Much higher quantities of Li_xPF_y (136.4 eV) and $\text{Li}_x\text{PF}_y\text{O}_z/\text{O}=\text{PFOR}$ (134.4 eV) are seen for the formatted 0.5% HMDS sample relative to the reference, while the signal for the phosphate (132.8 eV) has approx. the same intensity as that in the reference. All three components add up to the SPI. After 250 cycles, mainly the $\text{Li}_x\text{PF}_y\text{O}_z/\text{O}=\text{PFOR}$ species have grown underlining the stability of fluorophosphates.

In conclusion, 0.5% HMDS induces the generation of a much thicker SPI in comparison to the reference during formatting C// $\text{LiNi}_{0.4}\text{Mn}_{1.6}\text{O}_4$ pouch cells. Alkoxides, alkyl groups, carbonates, phosphates, fluorophosphates, and metal fluorides are recognized to be involved in the network of the surface layer. Nonetheless, after 250 cycles some of the organics of the SPI are dissolved in the electrolyte and only the inorganics such as PO_4^{3-} , $\text{Li}_x\text{PF}_y\text{O}_z$, $\text{O}=\text{PFOR}$, LiF , NiF_2 , and MnF_2 increase with cycle number. HMDS is presumably not suitable for stabilizing surface films on the spinel cathode. That might be due to its tendency to react with water, which is always present in trace amounts in the cell as described in chapter 5.4 (Scheme 3). Despite of this, the addition of 0.5% HMDS to the base electrolyte helps to achieve better CC/CV-cycling results (see chapter 5.2.2). On one hand, HMDS reduces Mn and Ni dissolution by scavenging HF and H_2O as outlined in chapter 5.4. On the other hand, the SPI produced during formation is protective in the beginning of the cycling tests and only loses its passivating effect after a few cycles. Adding 1.5% HMDS to the base electrolyte leads to an even thicker layer after formation, which is in agreement with the lower starting capacity of this full cell compared to that comprising 0.5% HMDS (see chapter 5.2.2). The thicker film is stable for longer cycling times and, therefore, enables a better residual capacity. Nevertheless, the cycling stability cannot keep up with losses in gravimetric energy density. For the C// $\text{LiNi}_{0.4}\text{Mn}_{1.6}\text{O}_4$ pouch cell including 2% HMDS this scenario is intensified and the specific energy gained over 250 cycles is much lower than that of the reference.

Tris-(1,1,1,3,3,3-hexafluoroisopropyl) phosphate

HFiP has already been utilized as stabilizer in carbonate-based electrolytes on 5 V class cathode surfaces by A. v. Cresce, K. Xu and Du Pont.^[264,274,275] It is supposed to induce protective interfacial chemistry on $\text{LiNi}_{0.5}\text{Mn}_{1.5}\text{O}_4$ cathodes, and on account of this, to enhance the electrochemical properties of spinel cells. As shown in chapter 5.2.2, 0.5% HFiP exhibits a better cycling behavior relative to the reference. However, this is the first time that XPS investigations of formatted and cycled $\text{LiNi}_{0.4}\text{Mn}_{1.6}\text{O}_4$ electrodes are conducted. The respective spectra are displayed in Figure 119.

C1s: The C1s region of the cathode formatted with 0.5% HFiP unveils five characteristic bands at 284.5, 285.7, 286.9, 288.8, and 290.3 eV, which are correlated with C-C, CH_2 , C-O, C=O, and CF_2 , respectively. The peak area of the CH_2 signal is very similar to that of the reference, whereas the C-O and C=O bands are marginally stronger. This indicates that higher quantities of electrolyte degradation products such as carbonates and alkoxides are present on the spinel electrode surface compared to the reference. Moreover, the peak area of the CF_2 band is greater than that of the standard suggesting that the CF_3 groups of HFiP participate in the SPI generation. Consequently, the signal of the conductive carbon is smaller compared to the reference. Cycling C// $\text{LiNi}_{0.4}\text{Mn}_{1.6}\text{O}_4$ pouch cells with 0.5% HFiP delivers slightly augmented CH_2 (285.7 eV), C-O (287.0 eV), and C=O bands (288.8 eV). These have almost the same peak area as those of the reference after 250 cycles. Hence, electrolyte corrosion proceeds upon cycling, but it is not as severe as prior to the formation step. The peak area of the CF_2 signal has also grown with increasing cycle number signifying the involvement of HFiP in the SPI structure. The diminished signal of the conductive carbon is located at 284.6 eV.

O1s: The O1s spectrum obtained after formatting C// $\text{LiNi}_{0.4}\text{Mn}_{1.6}\text{O}_4$ full cells comprising 0.5% HFiP exhibits clearly enhanced C-O and C=O bands at 533.6 and 531.9 eV, respectively, compared to the reference. This is due to the formation of a thicker SPI with carbonyl, alkoxy, phosphate, and fluorophosphate components. As a result, the relative peak area of the O^{2-} band is lower in comparison to the O1s spectrum of the cell including the base electrolyte. After 250 cycles, the signal of the lattice oxygen (529.3 eV) is reduced and the peak areas of the C-O (533.6 eV) and C=O bands (532.0 eV) are further extended. Nonetheless, the amount of carbonyl groups and alkoxides in the surface film have only slightly risen. The much stronger intensity of the C-O peak compared to that of C=O suggests the existence of carbonates (e.g. PEC), phosphates, and fluorophosphates.

5. Results and discussion

5.5 Characterization of the solid permeable interface

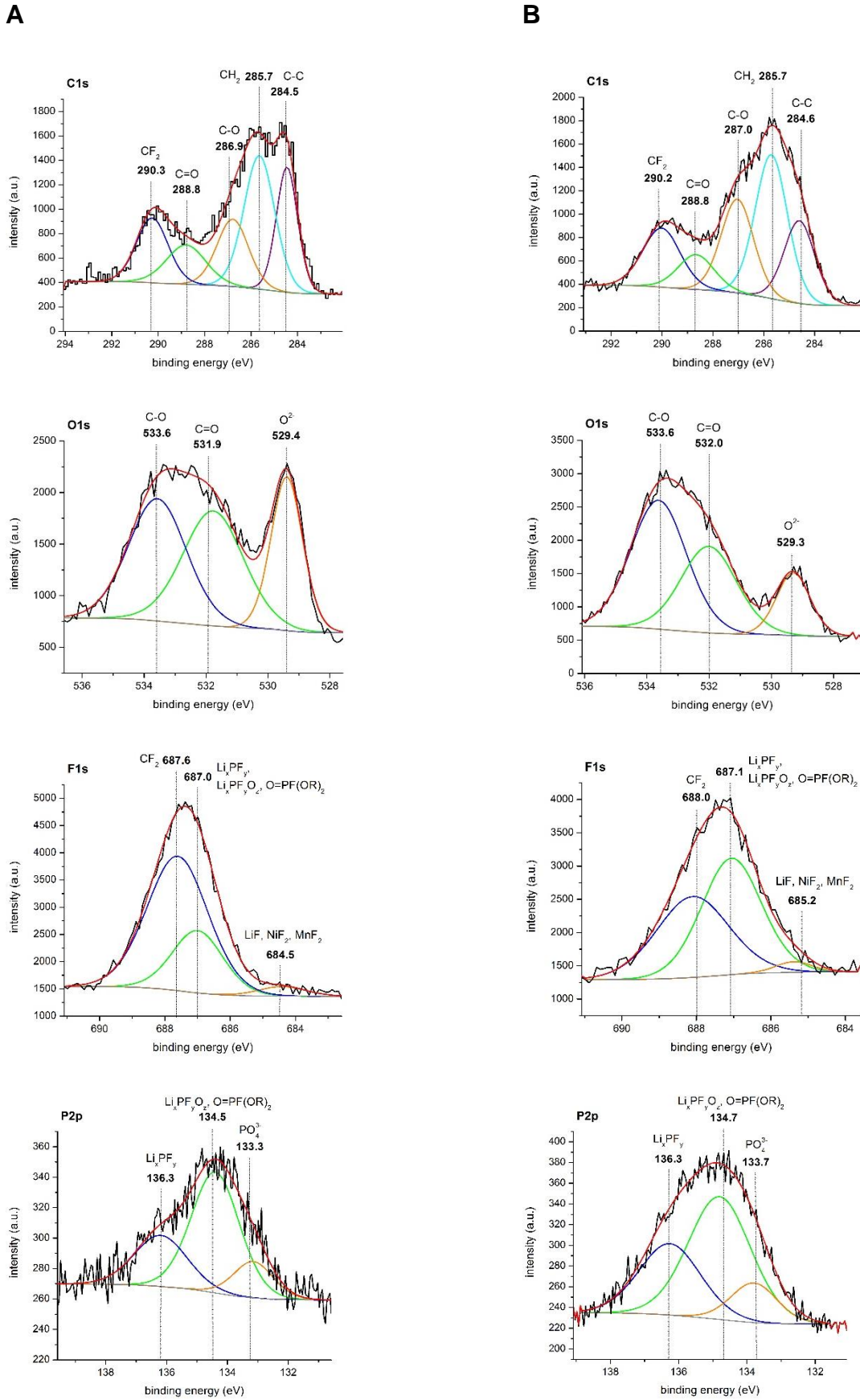
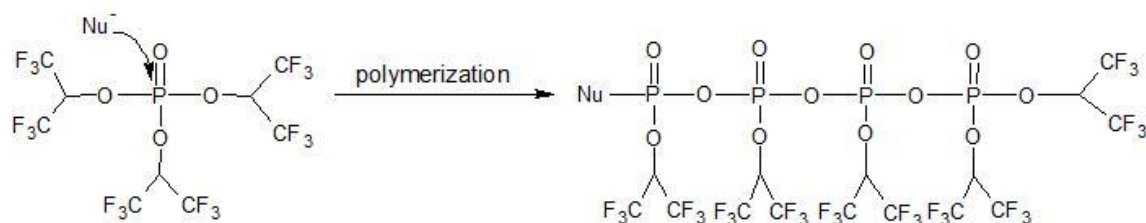


Figure 119 XPS spectra of LiNi_{0.4}Mn_{1.6}O₄ electrodes at 0% SOC after **A** formatting C//LiNi_{0.4}Mn_{1.6}O₄ pouch cells with 0.5% HFIP at 23 °C and after **B** cycling these cells for 250 cycles at 45 °C.

F1s: Considering the F1s pattern of the formatted 0.5% HFiP sample, a prominent feature is detected at 687.6 eV representing CF_2 groups of the PVDF binder and CF_3 groups of HFiP integrated in the surface film. Furthermore, higher quantities of Li_xPF_y , $\text{Li}_x\text{PF}_y\text{O}_z$, O=PFOR (687.0 eV), LiF , NiF_2 , and/or MnF_2 (684.5 eV) are found on the surface of the spinel cathode than for the reference. Thus, formatting C// $\text{LiNi}_{0.4}\text{Mn}_{1.6}\text{O}_4$ full cells containing 0.5% HFiP leads to a thicker surface film in comparison to the reference. As opposed to this, cycling these cells induces solely the enhancement of the $\text{Li}_x\text{PF}_y/\text{Li}_x\text{PF}_y\text{O}_z/\text{O=PFOR}$ band (687.1 eV), whereby it is still lower than that of the reference after 250 cycles. Hence, electrolyte and salt degradation is inhibited by the addition of 0.5% HFiP to the base electrolyte. Although the peak area of the CF_2 band in the C1s region has increased after cycling, it (688.0 eV) has declined in the F1s spectrum. This is due to the strong contribution of the $\text{Li}_x\text{PF}_y/\text{Li}_x\text{PF}_y\text{O}_z/\text{O=PFOR}$ signal. As a consequence, the peak area of the $\text{LiF}/\text{NiF}_2/\text{MnF}_2$ band (685.2 eV) also appears after the formation step.

P2p: The P2p spectrum of the spinel electrode formatted with 0.5% HFiP shows higher contents of phosphates (133.3 eV) and fluorophosphates (134.5 eV) than the reference, while the amount of conducting salt residues (136.3 eV) in the SPI is similar to that of the reference. HFiP is proposed to be the source for PO_4^{3-} and $\text{Li}_x\text{PF}_y\text{O}_z/\text{O=PFOR}$. After 250 cycles, the peak areas of all three species are intensified. Indeed, higher PO_4^{3-} and $\text{Li}_x\text{PF}_y\text{O}_z/\text{O=PFOR}$ originating from HFiP are registered than for the reference. Nevertheless, the values of their peak areas are lower compared to the 0.5% TFPi cell. Concurrently, less Li_xPF_y are included in the surface layer than for the standard film but more than in the case of the 0.5% TFPi-derived SPI. Since the cycling behavior of the 0.5% HFiP cell is better than that of the reference and worse than that of the 0.5% TFPi cell, it is concluded that phosphates and fluorophosphates stabilize surface films, whereas the conducting salts are not beneficial with respect to layer formation.

Summarizing this section, it should be noted that HFiP provokes the production of a thicker film on the cathode surface than the base electrolyte during formation. Carbonates, alkoxides, phosphates, fluorophosphates, and conducting salt residues are incorporated in the SPI. In addition, HFiP itself is also integrated into the layer. It is further demonstrated that the film is rather stable throughout cycling as the amount of electrolyte decomposition products is only slightly enhanced on the $\text{LiNi}_{0.4}\text{Mn}_{1.6}\text{O}_4$ electrode surface after 250 cycles. Finally, it is thinner as that of the reference. Interestingly, phosphates and fluorophosphates, which mainly arise from HFiP, help to passivate the cathode surface and are responsible for the better electrochemical performance of C// $\text{LiNi}_{0.4}\text{Mn}_{1.6}\text{O}_4$ pouch cells comprising 0.5% HFiP versus spinel full cells without any additives. Scheme 9 depicts a possible mechanism for the polymerization of HFiP.



Scheme 9 Polymerization mechanism of HFiP while cycling C//LiNi_{0.4}Mn_{1.6}O₄ full cells.

The film formation proceeds analogously to the one elucidated above for TMP. Likewise, the SPI is made visible by SEM imaging (Figure 120).

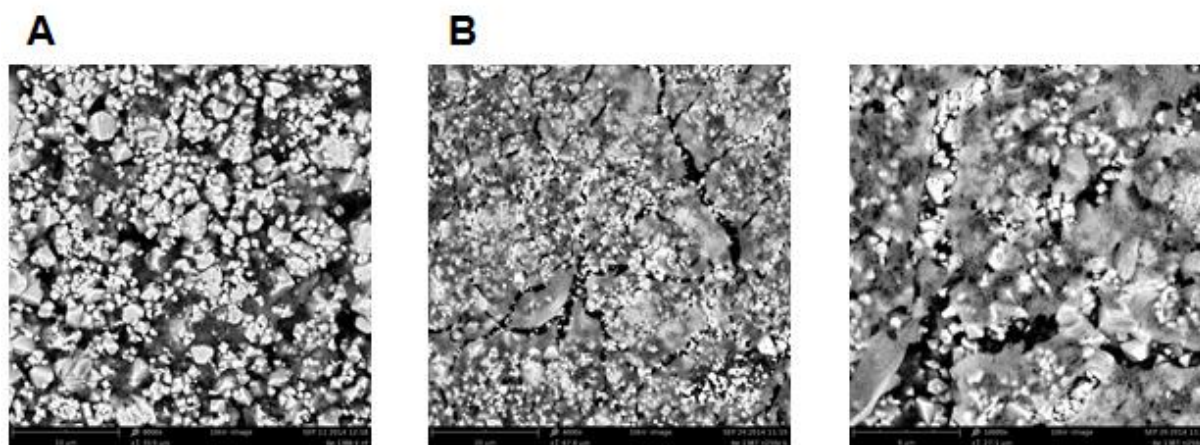


Figure 120 **A** SEM image of the surface of a LiNi_{0.4}Mn_{1.6}O₄ composite electrode after 0 cycles with 8,000-times amplification. **B** SEM images of the surface of a LiNi_{0.4}Mn_{1.6}O₄ composite electrode after 250 cycles at 45 °C in the base electrolyte containing 0.5% HFiP with 4,000- (middle) and 10,000-times amplification (right).

The established surface film looks very similar to that generated by 0.5% TFPi. The identical functional groups of both additives (CF_3) are probably the reason for this similarity. As outlined in chapter 5.2.2, only 0.5% HFiP has an advantageous effect on the cycling features of C//LiNi_{0.4}Mn_{1.6}O₄ pouch cells. Higher and lower quantities of HFiP cause a rapid capacity decay. The concentration of 0.1% is too low to form a stable layer and the addition of 1% is too high resulting in thick or resistive films.

Tris(trimethylsilyl) phosphate

Li W. and co-workers have found that the introduction of TTSP in carbonate-containing electrolytes for Li//LiNi_{0.5}Mn_{1.5}O₄ coin cells leads to good capacity retention. They have shown by means of XPS that TTSP generates a stable surface film on LiNi_{0.5}Mn_{1.5}O₄ cathode surfaces, which inhibits the oxidation of the electrolyte and improves the cycling characteristics of Li//LiNi_{0.5}Mn_{1.5}O₄ half cells.^[429] In this thesis, the benefits of TTSP with respect to the CC/CV-cycling behavior of C//LiNi_{0.4}Mn_{1.6}O₄ pouch cells could not be verified (see chapter 5.2.2, Figure 92). XPS analyses of LiNi_{0.4}Mn_{1.6}O₄ electrodes from formatted and cycled full cells including 1.7% TTSP are carried out to understand the different surface chemistry of the cathode with standard and TTSP-based electrolytes (Figures 121 and 122).

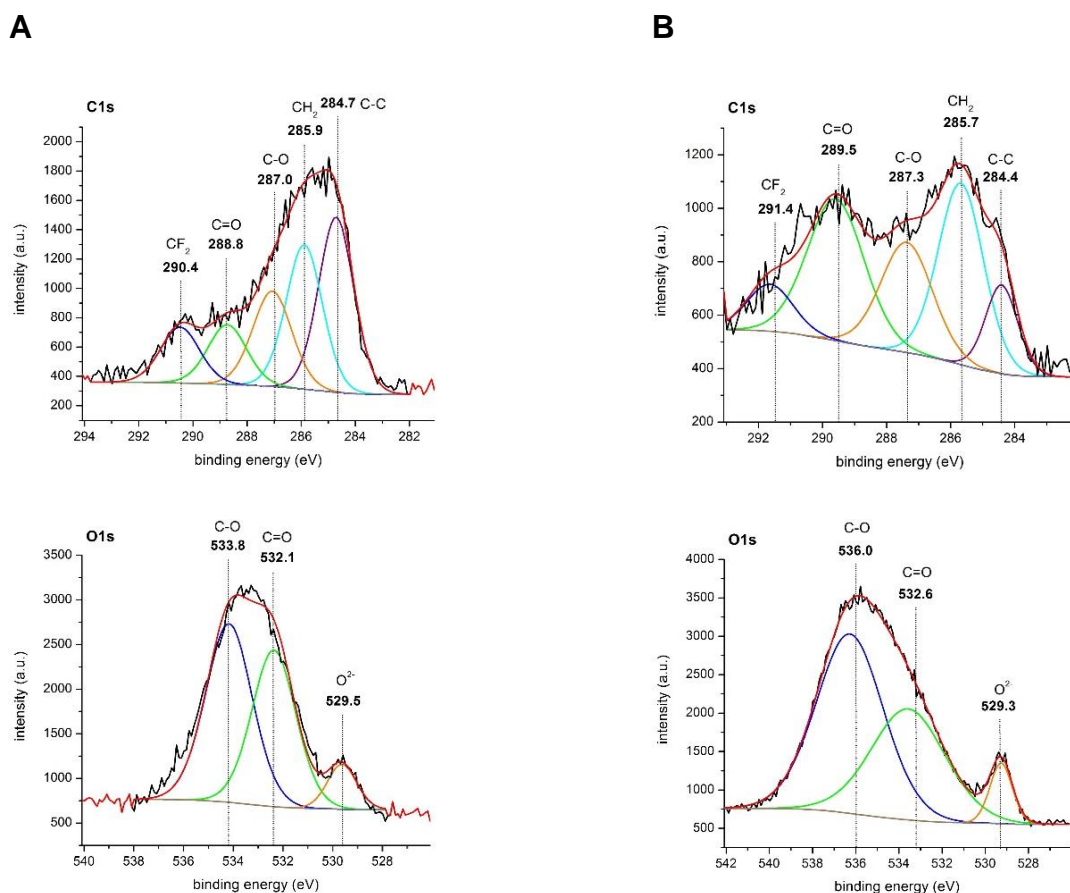


Figure 121 XPS spectra of LiNi_{0.4}Mn_{1.6}O₄ electrodes at 0% SOC after **A** formatting C//LiNi_{0.4}Mn_{1.6}O₄ pouch cells with 1.7% TTSP at 23 °C and after **B** cycling these cells for 250 cycles at 45 °C.

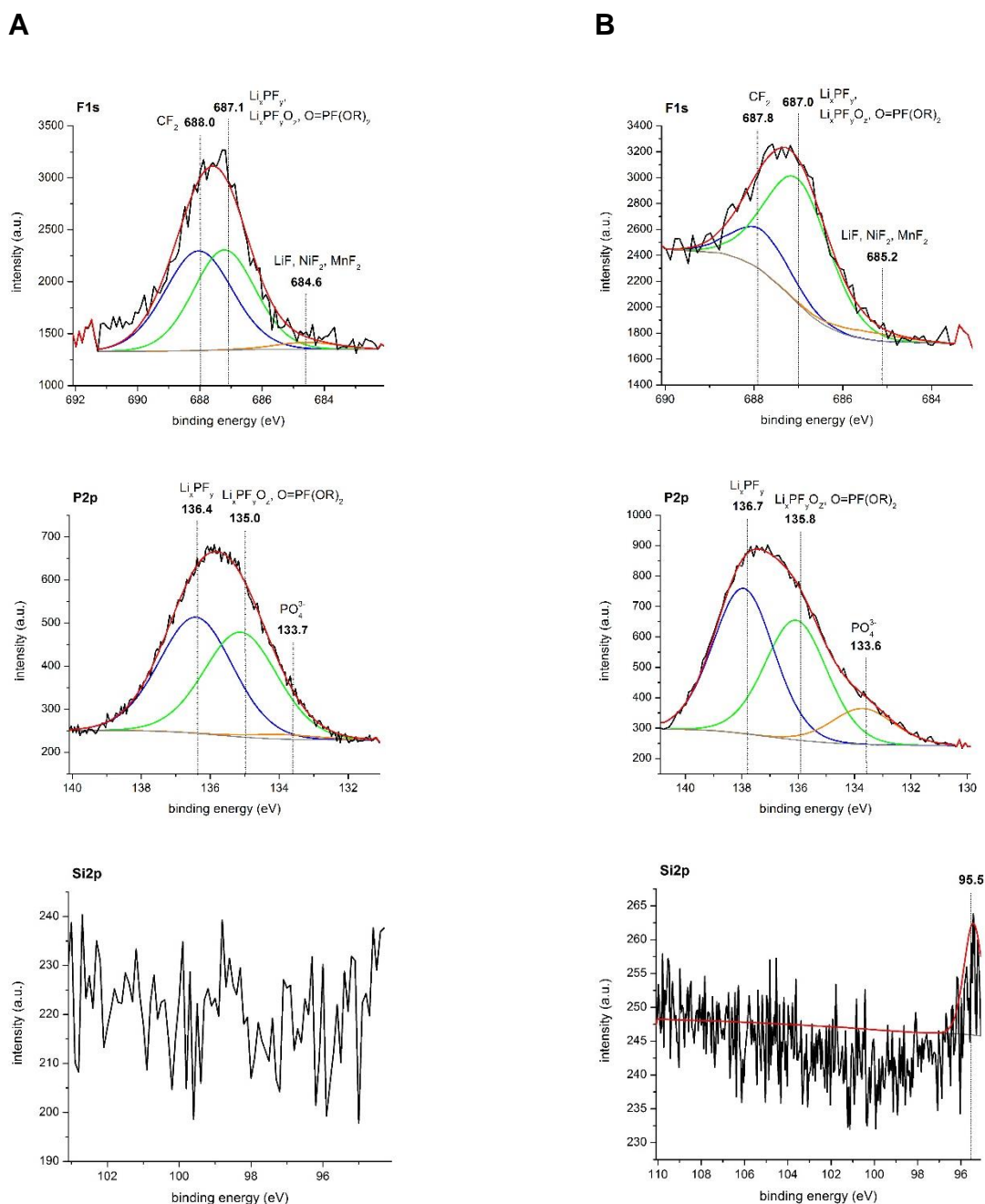


Figure 122 XPS spectra of $\text{LiNi}_{0.4}\text{Mn}_{1.6}\text{O}_4$ electrodes at 0% SOC after **A** formatting C// $\text{LiNi}_{0.4}\text{Mn}_{1.6}\text{O}_4$ pouch cells with 1.7% TTSP at 23 °C and after **B** cycling these cells for 250 cycles at 45 °C.

C1s: In contrast to the reference, the C1s spectrum of the spinel electrode formatted with 1.7% TTSP reveals greater C-O (287.0 eV) and C=O signals (288.8 eV) and a smaller CH_2 band (285.9 eV) indicating higher quantities of alkoxy and carbonyl groups and lower quantities of CH_2 in the SPI network. The peak areas of the conductive carbon (284.7 eV) and of CF_2 (290.4 eV) are approx. the same relative to those of the cell formatted with the base electrolyte. The ratio of the peak intensities changes drastically upon cycling. The C-C (284.4 eV) and CF_2 signals (291.4 eV) are remarkably reduced, whereas the relative peak areas of CH_2 (285.7 eV), C-O (287.3 eV), and especially C=O (289.5 eV) increase enormously. Consequently, the surface film has grown extensively with carbonyl compounds playing the

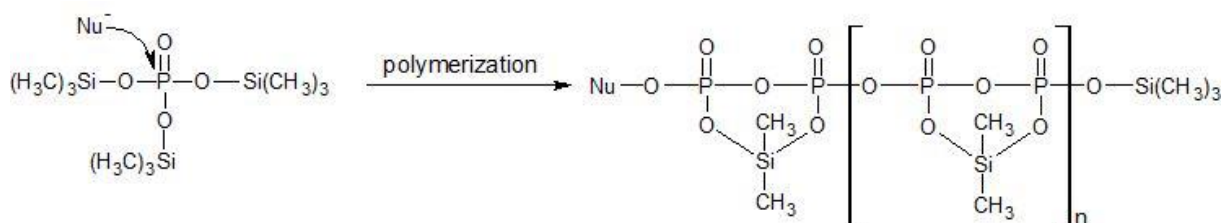
most important role. Thus, TTSP does not inhibit electrolyte corrosion, but somehow accelerates the oxidation. Although the relative peak areas of CH₂, C-O, and C=O have strongly augmented after 250 cycles, the actual area values have only slightly increased or have even reduced. This unexpected behavior relates to the other SPI species and is elucidated later.

O1s: After formatting C//LiNi_{0.4}Mn_{1.6}O₄ full cells, the O1s pattern exhibits already substantially enhanced C-O and C=O bands at 533.8 and 532.1 eV, respectively, which are clearly more intense than those of the reference after 250 cycles. Accordingly, the electrode is covered by a very thick SPI and the oxygen signal of LiNi_{0.4}Mn_{1.6}O₄ is extremely low. In agreement with the C1s spectrum, many carbonyl compounds and alkoxides are incorporated in the SPI. In addition, lots of phosphates and fluorophosphates are integrated in the surface layer to explain the large peak areas. After 250 cycles, the phenomenon is even stronger. Tremendously larger C-O (536.0 eV) and C=O peak areas (532.6 eV) are registered and the O²⁻ band (529.3 eV) is further reduced. Carbonates and alkoxides are certainly produced throughout the cycling but the exceptionally great peak area of the C-O signal is a result of the participation of phosphates and fluorophosphates in the surface film formed. The slight shift of the C-O signal to higher binding energies underlines this assumption.

F1s: The F1s region of the cathode formatted with 1.7% TTSP unveils a distinct Li_xPF_y/Li_xPF_yO_z/O=PFOR peak at 687.1 eV, which is more prominent than any of the F1s spectra discussed so far after formation. Concurrently, the CF₂ (688.0 eV) and LiF/NiF₂/MnF₂ bands (684.6 eV) are considerably diminished. Therefore, the contribution of TTSP to the SPI production is given. Cycling C//LiNi_{0.4}Mn_{1.6}O₄ pouch cells induces such a strong enhancement of the Li_xPF_y/Li_xPF_yO_z/O=PFOR signal (687.0 eV) that the PVDF (CF₂) and the LiF/NiF₂/MnF₂ peaks are superimposed by its intensity. Hence, the decomposition and polymerization of TTSP proceeds with increasing cycle number.

P2p: While the peak area of the PO₄³⁻ band at 133.7 eV is greater than that of the reference in the P2p spectrum after formatting C//LiNi_{0.4}Mn_{1.6}O₄ pouch cells, it is still smaller than that generated by the other phosphate-containing additives after formation. Nonetheless, a very large amount of fluorophosphates (135.0 eV) and salt residues (136.4 eV) participates in the SPI. This underpins the fact that TTSP but also high concentrations of the LiPF₆ conducting salt are involved in the surface film structure. After 250 cycles, the phosphate band at 133.6 eV is enormously enhanced and the peak area is greater than that of all other phosphate-based additives. Moreover, Li_xPF_y (136.7 eV) and Li_xPF_yO_z/O=PFOR (135.8 eV) have drastically increased. Apparently, TTSP takes part in the surface layer network and leads to the production of a very thick layer.

Si2p: The best evidence for the contribution of TTSP to the SPI generation is given by the Si2p spectra in Figure 122. While after formation the amount of TTSP integrated in the surface film of the $\text{LiNi}_{0.4}\text{Mn}_{1.6}\text{O}_4$ cathode is too low to be detected in the Si2p region, after 250 cycles a band is clearly noticed at 95.5 eV, which signifies the existence of silicon in the SPI.^[363] A possible polymerization mechanism of TTSP is given in Scheme 10:



Scheme 10 Possible film formation mechanism of TTSP while cycling C// $\text{LiNi}_{0.4}\text{Mn}_{1.6}\text{O}_4$ full cells. With modifications from^[239].

The reaction proceeds similar to the one for TMP. In this case, however, Si takes also part in the mechanism and creates a strong polymeric network. The thick surface layer is visible in SEM images (Figure 123).

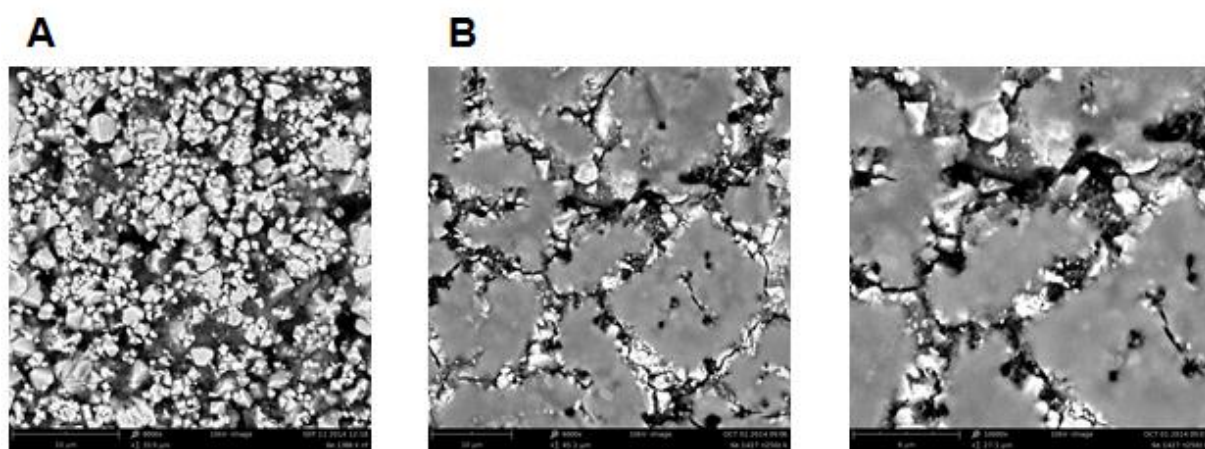


Figure 123 **A** SEM image of the surface of a $\text{LiNi}_{0.4}\text{Mn}_{1.6}\text{O}_4$ composite electrode after 0 cycles with 8,000-times amplification. **B** SEM images of the surface of a $\text{LiNi}_{0.4}\text{Mn}_{1.6}\text{O}_4$ composite electrode after 250 cycles at 45 °C in the base electrolyte containing 1.7% TTSP with 6,000- (middle) and 10,000-times amplification (right).

The TTSP-derived SPI looks different from those depicted so far. The incorporation of Si might be the reason. The fractures in the layer are very likely due to the preparation of the spinel electrode for the SEM measurements. Nevertheless, the films must be porous, since throughout cycling massive SPI generation is observed. In addition, Si might catalyze the electrolyte degradation.

As aforementioned, the actual peak areas of the carbonyl and alkoxy groups have only slightly increased or have even reduced upon cycling, whereas the relative peak areas have

substantially increased. This phenomenon relates to circumstances that tremendous quantities of phosphates and fluorophosphates are present on top of the carbonyl and alkoxy species. In other words, the organics of the SPI are covered by inorganics. This is in compliance with the results of Edström and Eriksson et al., who conducted XPS depth profile analyses of manganese spinel electrodes stored or cycled at 60 °C.^[465,466] In spite of the extremely thick SPI produced by 1.7% TTSP, the cycling behavior of the respective full cell is still moderate (see chapter 5.2.2, Figure 92). Lower concentrations like, for instance, 0.1% and 0.5% TTSP presumably establish thinner layers. But, 0.1% TTSP is insufficient to stabilize the SPI effectively and 0.5% TTSP just reveals similar cycling features as the reference.

Sebaconitrile

To the best of our knowledge there is no detailed investigation of SEN added to carbonate-based electrolytes for high voltage spinel electrodes. In this section, XPS spectra of cathodes from formatted and cycled C//LiNi_{0.4}Mn_{1.6}O₄ pouch cells comprising 1% SEN are examined (Figures 124 and 125) to study the influence of this additive on the surface chemistry of the electrodes.

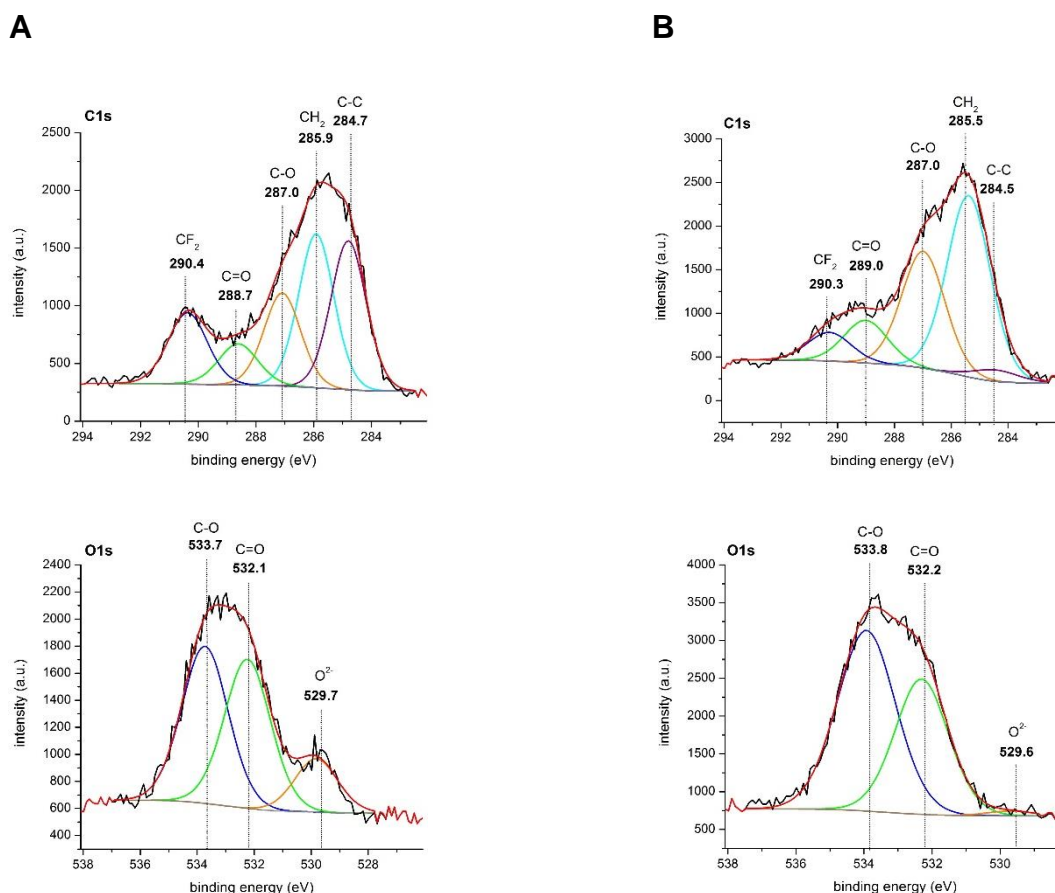


Figure 124 XPS spectra of LiNi_{0.4}Mn_{1.6}O₄ electrodes at 0% SOC after **A** formatting C//LiNi_{0.4}Mn_{1.6}O₄ pouch cells with 1% SEN at 23 °C and after **B** cycling these cells for 250 cycles at 45 °C.

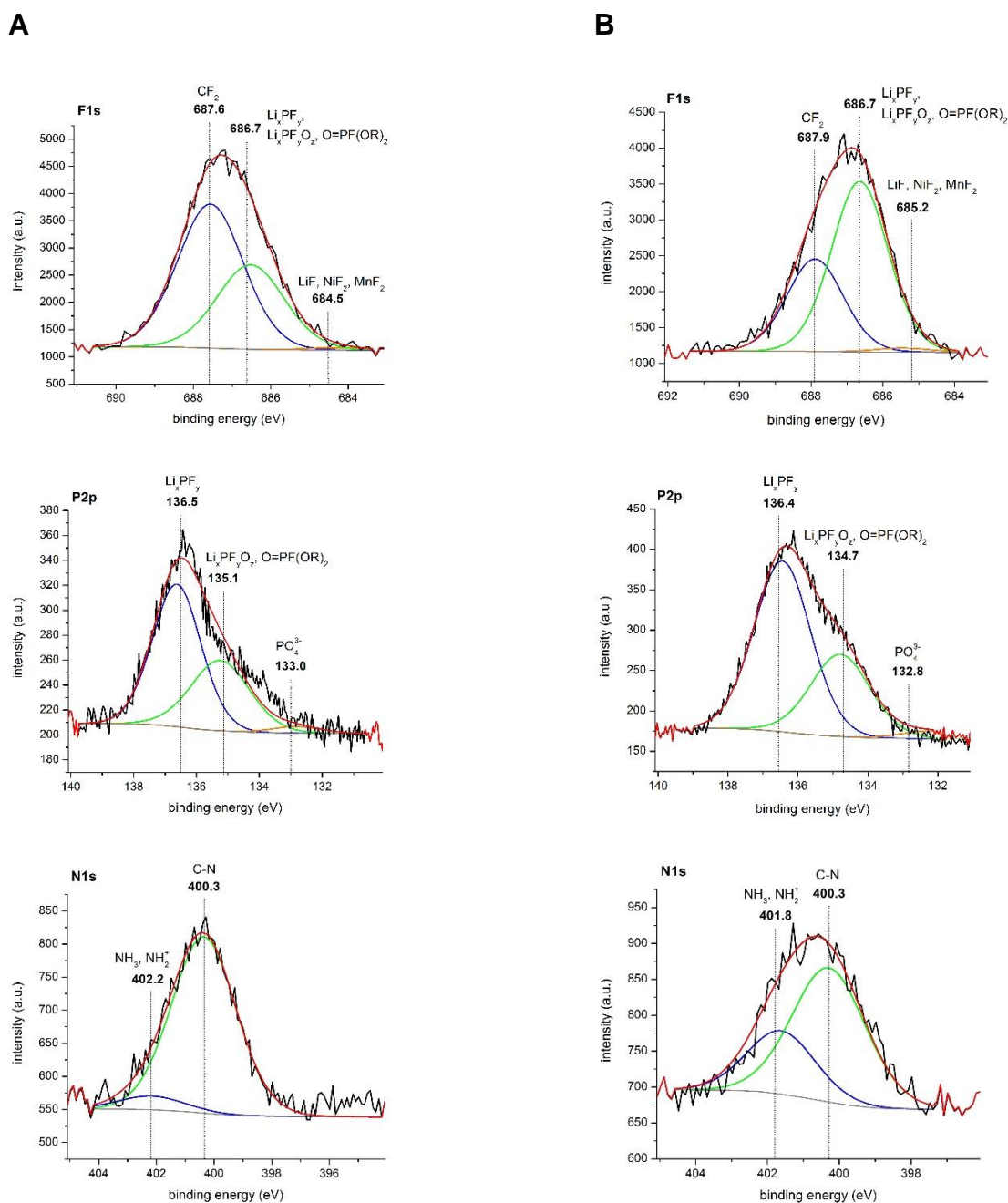


Figure 125 XPS spectra of LiNi_{0.4}Mn_{1.6}O₄ electrodes at 0% SOC after **A** formatting C//LiNi_{0.4}Mn_{1.6}O₄ pouch cells with 1% SEN at 23 °C and after **B** cycling these cells for 250 cycles at 45 °C.

C1s: The formatted cathode shows five characteristic bands corresponding to the active material (conductive carbon at 284.7 eV), the PVDF binder (CF₂ and CH₂ at 290.4 and 285.9 eV, respectively), and organic contaminants (C=O and C-O at 288.7 and 287.0 eV, respectively). In comparison to the standard electrolyte, more carbonates and alkoxides are found in the surface layer. After 250 cycles, the spinel electrode is significantly covered by decomposition products as the C-C band at 284.5 eV is hardly visible. Furthermore, the peak area of the CF₂ band (290.3 eV) is diminished. In contrast, the intensities of C=O (289.0 eV), C-O (287.0 eV), and CH₂ (285.5 eV) are substantially increased. The ratio of the C-O vs. C=O peak areas is nearly 2:1 suggesting that carbonates are mainly involved in the surface

layer. SEN has probably reacted in an acid-catalyzed hydrolysis, which results in carbonates from the original nitrile.^[488] The strongly amplified CH₂ band confirms the participation of SEN in the SPI layer network. Since the C-N signal overlaps with the C-O one no additional bands are detected.^[363,423]

O1s: The O1s spectrum of the cathode formatted with 1% SEN provides an already strongly reduced signal of the LiNi_{0.4}Mn_{1.6}O₄ oxygen (529.7 eV). In addition, greatly enhanced C-O and C=O bands are registered at 533.7 and 532.1 eV, respectively. Thus, lots of carbonyl and alkoxy groups contribute to the surface film. In agreement with the C1s spectrum, the amount of these compounds has enormously grown upon cycling. The O²⁻ peak at 529.6 eV is nearly vanished due to the thick organic phase.

F1s: After formatting C//LiNi_{0.4}Mn_{1.6}O₄ pouch cells with 1% SEN the F1s spectrum of the spinel electrode exhibits an intense Li_xPF_y/Li_xPF_yO_z/O=PFOR band (686.7 eV). As no extra phosphate source except for the conducting salt LiPF₆ is available, salt degradation must be responsible. Besides, little quantities of LiF, NiF₂, and/or MnF₂ are noticed at 684.5 eV. The PVDF component CF₂ (687.6 eV) is lowered relative to the reference. After 250 cycles, the peak area of the Li_xPF_y/Li_xPF_yO_z/O=PFOR band (686.7 eV) dominates the spectrum. Consequently, the SEN-based SPI does not prevent the corrosion of LiPF₆. The amount of LiF, NiF₂, and/or MnF₂ (685.2 eV) has also slightly increased. The weak CF₂ band is identified at 687.9 eV.

P2p: The P2p spectra corroborate the conclusions drawn from the F1s patterns. While the phosphate signal (133.0 eV) is rather small after formation, the Li_xPF_yO_z/O=PFOR band (135.1 eV) and especially the Li_xPF_y peak (136.5 eV) are more pronounced in comparison to the reference. The intensities of all three species have grown throughout cycling. Thereby, the value of the Li_xPF_y peak area has considerably intensified demonstrating contributions from the conducting salt in the SPI network.

N1s: Finally, the N1s regions of the spinel electrodes formatted and cycled with 1% SEN underpin the involvement of nitrile in the SPI structure. After formation, two nitrogen peaks at 402.2 and 400.3 eV are present, corresponding to NH₂⁺ and/or NH₃ and C-N bonds, respectively. Interestingly, after 250 cycles, the intensity of NH₂⁺ and/or NH₃ groups have increased, whereas that of the C-N species have slightly decreased. This also indicates that SEN has partially been hydrolyzed to carboxylic acids and ammonium.

In conclusion, 1% SEN has established a layer on the spinel electrode surface upon cycling C//LiNi_{0.4}Mn_{1.6}O₄ pouch cells at 45 °C between 3.3 and 4.8 V. This SPI contains obviously more alkyl bonds, carbonyl groups, and salt residues than the reference. The two latter are expected to impair the origin of the faster capacity fading of the full cells comprising 1% SEN in comparison to the cells without any additive. 0.5% SEN even induces more rapid cell ageing as the surface film on the cathode is unstable upon cycling (see chapter 5.2.2, Figure 82). The

addition of 2% SEN to the base electrolyte leads to an enhanced production of carbonyl compounds and the corrosion of LiPF_6 . As a consequence, a faster capacity decay is observed (see chapter 5.2.2).

Fluoroethylene carbonate

C1s: Figure 126 displays the XPS regions of spinel electrodes after formatting and cycling C// $\text{LiNi}_{0.4}\text{Mn}_{1.6}\text{O}_4$ pouch cells including 2.5% FEC. Regarding the C1s spectrum of the formatted cathode it is recognized that the peak areas of the CF_2 (290.3 eV), C=O (288.7 eV), and C-O signals (286.9 eV) are larger than those observed in the reference reflecting higher quantities of carbonyl, alkoxy, and CF_2 species in the SPI. As a result, the C-C band at 284.6 eV is slightly diminished compared to the reference. The peak areas of the CH_2 signals are very similar to each other. After 250 cycles, the intensity of the conductive carbon band (284.6 eV) has further disappeared because the amount of carbonyl (mainly carbonates), alkoxy, and CF_2 groups in the surface layer has increased. Hence, as an additive FEC changes the composition of the SPI in comparison to the base electrolyte and takes part in the layer network.

O1s: The O1s patterns of the formatted and cycled cathodes confirm the C1s data. The O^{2-} signal of the active material is progressively reduced with increasing cycle number since carbonates and alkoxides continue to precipitate on the electrode surface. This also supports the assumption that FEC contributes to the surface film structure, but it does not inhibit electrolyte oxidation.

F1s: Analysis of the F1s spectrum of the spinel electrode formatted with 2.5% FEC leads to three signals at 687.6, 687.0, and 684.8 eV, which are ascribed to CF_2 , $\text{Li}_x\text{PF}_y/\text{Li}_x\text{PF}_y\text{O}_z/\text{O}=\text{PFOR}$, and $\text{LiF}/\text{NiF}_2/\text{MnF}_2$, respectively. All three peaks are slightly more distinctive as those in the reference spectrum. The greater sum of CF_2 species relates to the participation of FEC in the SPI, whereas the higher intensities of the other species are mainly attributed to a reinforced decomposition of the conducting salt LiPF_6 . Cycling C// $\text{LiNi}_{0.4}\text{Mn}_{1.6}\text{O}_4$ full cells causes a substantial enhancement of all compounds implying ongoing electrolyte corrosion. Nonetheless, less salt degradation products are found than on the surface of the reference and the cycled 1% SEN sample.

5. Results and discussion

5.5 Characterization of the solid permeable interface

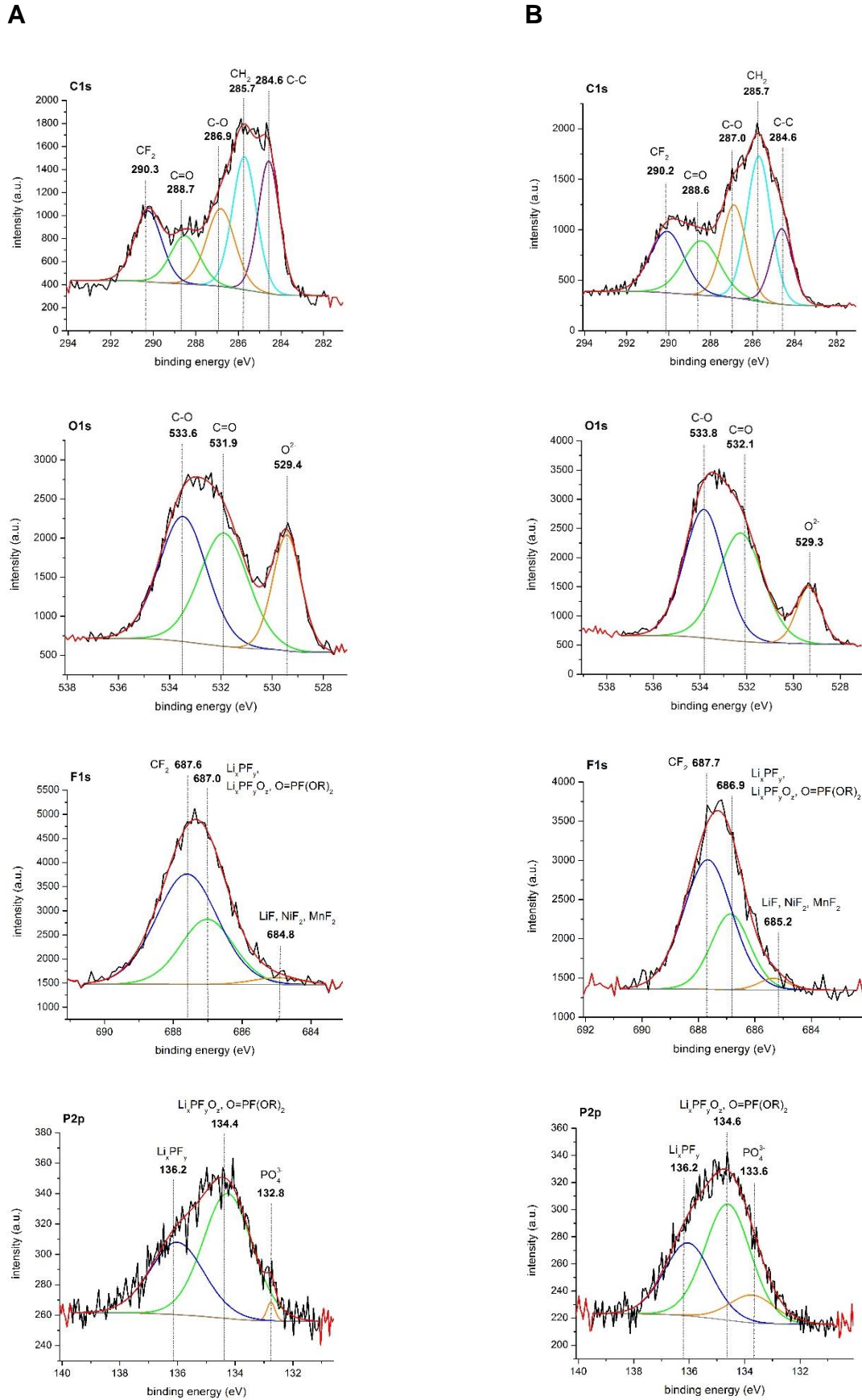


Figure 126 XPS spectra of LiNi_{0.4}Mn_{1.6}O₄ electrodes at 0% SOC after **A** formatting C//LiNi_{0.4}Mn_{1.6}O₄ pouch cells with 2.5% FEC at 23 °C and after **B** cycling these cells for 250 cycles at 45 °C.

P2p: After formation the influence of the phosphate species (132.8 eV) on the SPI is rather small. Accordingly, more Li_xPF_y (136.2 eV) and $\text{Li}_x\text{PF}_y\text{O}_z/\text{O}=\text{PFOR}$ (134.3 eV) are registered on the surface of the cathode particles than for the reference. The CC/CV-cycling experiment provokes the generation of additional PO_4^{3-} (133.6 eV) and fluorophosphates (134.6 eV), while no additional salt residues (136.2 eV) are noticed. All in all, the amount of phosphates is about the same as in case of the reference but less fluorophosphates and salt degradation products are observed.

Interestingly, the combination of relatively low quantities of phosphates and fluorophosphates in the surface layer and large accumulations of carbonyl species worsens the cycling performance relative to the reference and that of the 1% SEN cell (see chapter 5.2.2). Reducing the FEC concentration to 0.5% is an improvement with respect to the cycling characteristics of the spinel full cells because the carbonyl groups in the surface film are diminished. 0.1% FEC is, however, too low to provide sufficient SPI stability and higher additive concentrations just exacerbate the phenomena observed for the 1.5% FEC sample.

Tris(2-ethylhexyl) phosphate

Although TEHP has been claimed as film-forming agent for non-aqueous electrolytes in C// $\text{LiNi}_{0.5}\text{Mn}_{1.5}\text{O}_4$ cells by A. v. Cresce and du Pont, there are no publications on XPS measurements regarding high voltage spinel cells comprising TEHP.^[274,275] Herein, XPS investigations on spinel electrodes are carried out after formatting C// $\text{LiNi}_{0.4}\text{Mn}_{1.6}\text{O}_4$ pouch cells with 0.5% TEHP at 23 °C and after cycling these cells for 250 cycles at 45 °C in the voltage range from 3.3 to 4.8 V (Figure 127).

C1s: The C1s spectrum obtained after formation exhibits a weaker conductive carbon band (284.5 eV) than the reference owing to a greater contributions from carbonyl, alkoxy, and alkyl groups. The CF_2 signal (290.4 eV), which is primarily assigned to the PVDF binder, has approx. the same peak area as that of the reference. After 250 cycles, the C-C (284.6 eV) and the CF_2 peaks (290.4 eV) are extensively reduced on account of a substantial enhancement of the alkyl (285.7 eV), the carbonyl, and alkoxy bonds in the SPI network. Especially, the growth of the alkyl groups is a clear indication that TEHP is involved in the film generation.

O1s: The O1s region of the cathode formatted with 0.5% TEHP reveals larger C-O (533.6 eV) and C=O bands (531.9 eV) and a smaller O^{2-} signal (529.5 eV) than the reference, which is in compliance with the C1s information. Remarkably, the cycled electrode shows an immense increase of the C-O (533.7 eV) and C=O signals (532.2 eV) signifying high quantities of carbonates and alkoxides, but also phosphates and fluorophosphates in the SPI. As a result, the signal of the lattice oxygen at 529.4 eV is quite low.

5. Results and discussion

5.5 Characterization of the solid permeable interface

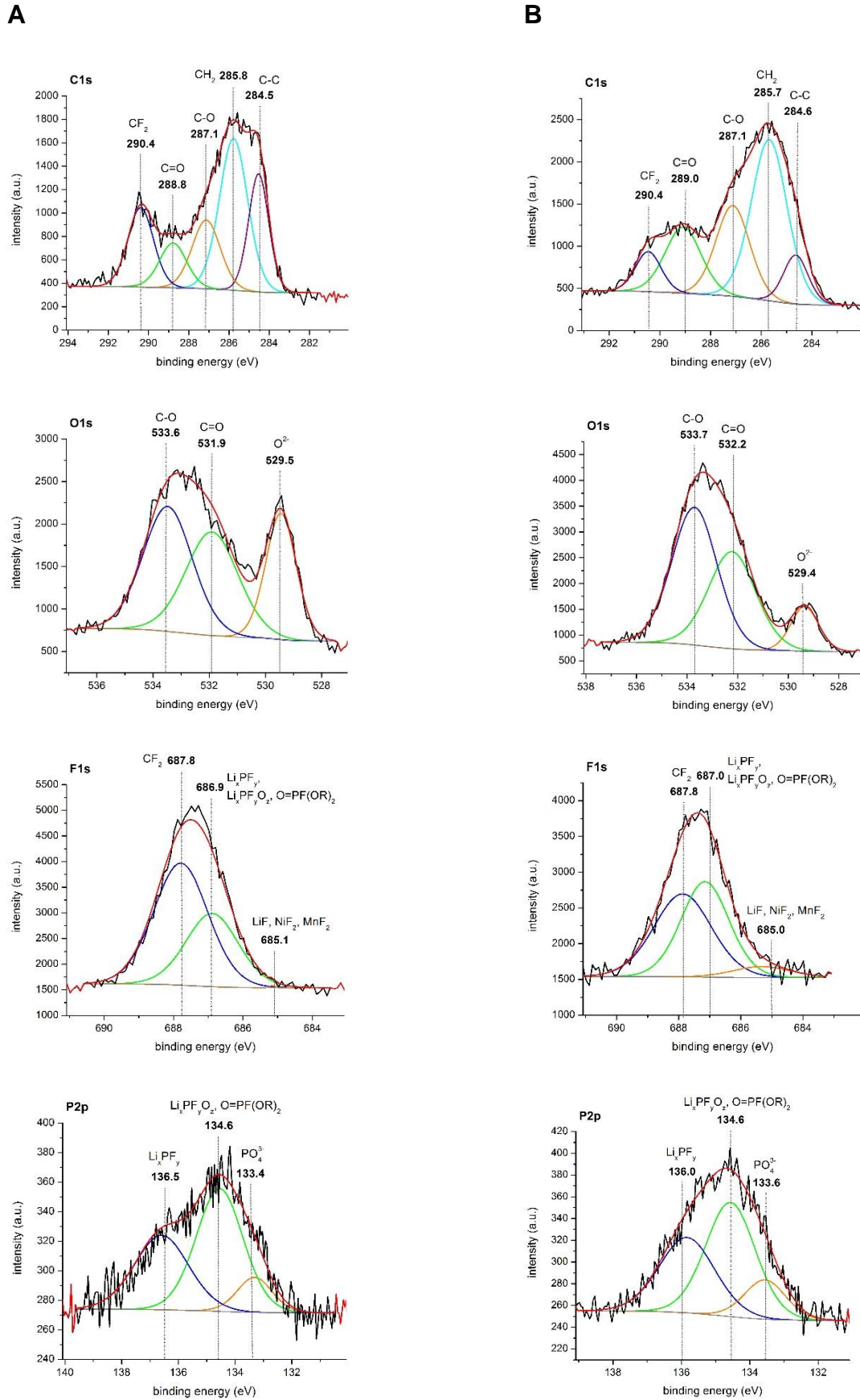
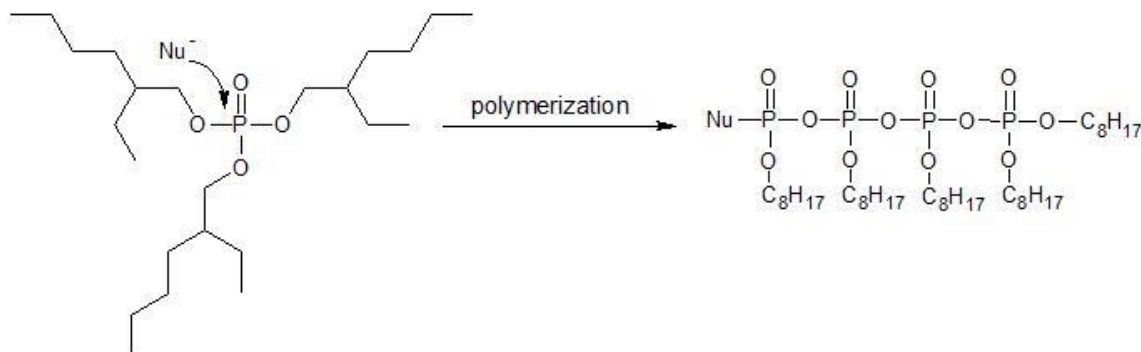


Figure 127 XPS spectra of LiNi_{0.4}Mn_{1.6}O₄ electrodes at 0% SOC after **A** formatting C//LiNi_{0.4}Mn_{1.6}O₄ pouch cells with 0.5% TEHP at 23 °C and after **B** cycling these cells for 250 cycles at 45 °C.

F1s: Examining the F1s region of the cathode after formatting C//LiNi_{0.4}Mn_{1.6}O₄ pouch cells results in three features at 687.8, 686.9, and 685.1 eV corresponding to CF₂, Li_xPF_y/Li_xPF_yO_z/O=PFOR, and LiF/NiF₂/MnF₂ species, respectively. Although the PVDF peak (CF₂) is still very dominant, the Li_xPF_y/Li_xPF_yO_z/O=PFOR peak is intensified compared to the reference. The amount of metal fluorides is, however, very low. The latter changes considerably upon cycling. The peak area of the LiF/NiF₂/MnF₂ band (685.0 eV) has increased after 250 cycles and, additionally, more salt residues and fluorophosphates (687.0 eV) are present on the surface of the electrode. Consequently, the CF₂ signal at 687.8 eV is weaker than before.

P2p: The P2p spectra of the cycled and formatted cathode essentially coincide with the F1s data. Nonetheless, the impact of TEHP on the SPI becomes more evident as the PO₄³⁻ band, which is already stronger than in the reference spectrum after formation, grows with increasing cycle number. Moreover, it is recognized that Li_xPF_yO_z/O=PFOR outweigh Li_xPF_y. This corroborates the participation of THEP in the layer network, too.

In summary, it is demonstrated that TEHP is included in the SPI structure because very high quantities of alkyl, carbonyl, alkoxy, and phosphate groups are detected on the spinel electrode surface after 250 cycles. Scheme 11 illustrates a possible film formation mechanism according to the one that has been elucidated above for TMP.



Scheme 11 Possible film formation mechanism for TEHP.

It has to be noted that the large hydrocarbon chains are likely to be connected with each other. In spite of the polymerization of TEHP, the additive has no passivating function, since electrolyte degradation is not prevented but reinforced. A rather thick and dense SPI has developed as can be seen in Figure 128. Especially, the large accumulation of organic components is proposed to influence the cycling properties of the C//LiNi_{0.4}Mn_{1.6}O₄ full cells. Thus, higher additive concentrations fail to improve the electrochemical behavior of the cells. Unexpectedly, 0.1% TEHP accelerates the cell ageing. This is presumably due to the fact that lower TEHP concentrations not only reduce the amount of organics but also the sum of phosphates and fluorophosphates in the SPI.

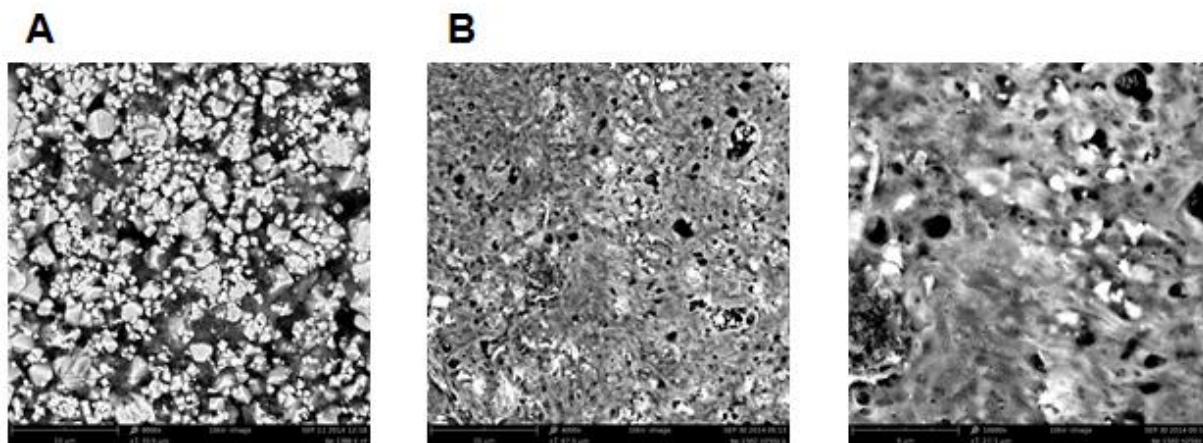


Figure 128 **A** SEM image of the surface of a $\text{LiNi}_{0.4}\text{Mn}_{1.6}\text{O}_4$ composite electrode after 0 cycles with 8,000-times amplification. **B** SEM images of the surface of a $\text{LiNi}_{0.4}\text{Mn}_{1.6}\text{O}_4$ composite electrode after 250 cycles at 45 °C in the base electrolyte containing 0.5% TEHP with 4,000- (middle) and 10,000-times amplification (right).

Succinic anhydride

As outlined in chapter 5.2.2, SA has already been used as electrolyte additive for high voltage spinel cells.^[408] Thereby, Passerini and co-workers have used XPS measurements to study modified cathode surfaces of cycled $\text{Li}/\text{LiNi}_{0.4}\text{Mn}_{1.6}\text{O}_4$ SwagelokTM-type cells comprising 4 and 8 wt% SA. They recognized the formation of a thinner and more stable SPI compared to the base electrolyte.^[273] In this thesis, XPS analysis is the method of choice to investigate the surface of spinel electrodes after cycling $\text{C}/\text{LiNi}_{0.4}\text{Mn}_{1.6}\text{O}_4$ pouch cells containing 2.5% SA at 45 °C between 3.3 and 4.8 V to determine the origin of their poor cyclability. The respective spectra are depicted in Figure 129.

C1s: The C1s region unveils very intense C-O (287.0 eV) and C=O bonds (289.2 eV), which are attributed to decomposed species such as alkoxides and carbonates. Indeed, the peak area of the C=O signal is remarkably large and definitely more pronounced than that of the reference. Hence, SA seems to be incorporated in the SPI. Furthermore, the peak area of the CH_2 band at 285.7 eV is slightly enhanced compared to that of the reference. In contrast, lower C-C (284.5 eV) and CF_2 signals (290.4 eV) are found on the cathode surface owing the strong accumulation of the organics.

O1s: In agreement with the aforementioned results, the O1s spectrum also exhibits distinctive C-O and C=O bands at 533.7 and 532.1 eV, respectively. The former corresponds to the presence of carbonyl species, whereas the latter denotes carbonyl compounds and alkoxides. Thereby, mainly carbonates are involved in the surface film. This implies the participation of SA in the SPI. Nevertheless, it has to be noted that P-O compounds like for instance $\text{PO}(\text{OR})_3$ and $\text{O}=\text{PF}(\text{OR})_2$ may also contribute to the band at 533.7 eV. More information on the integration of phosphates and fluorophosphates on the SPI is derived from the F1s and P2p spectra.

5.5 Characterization of the solid permeable interface

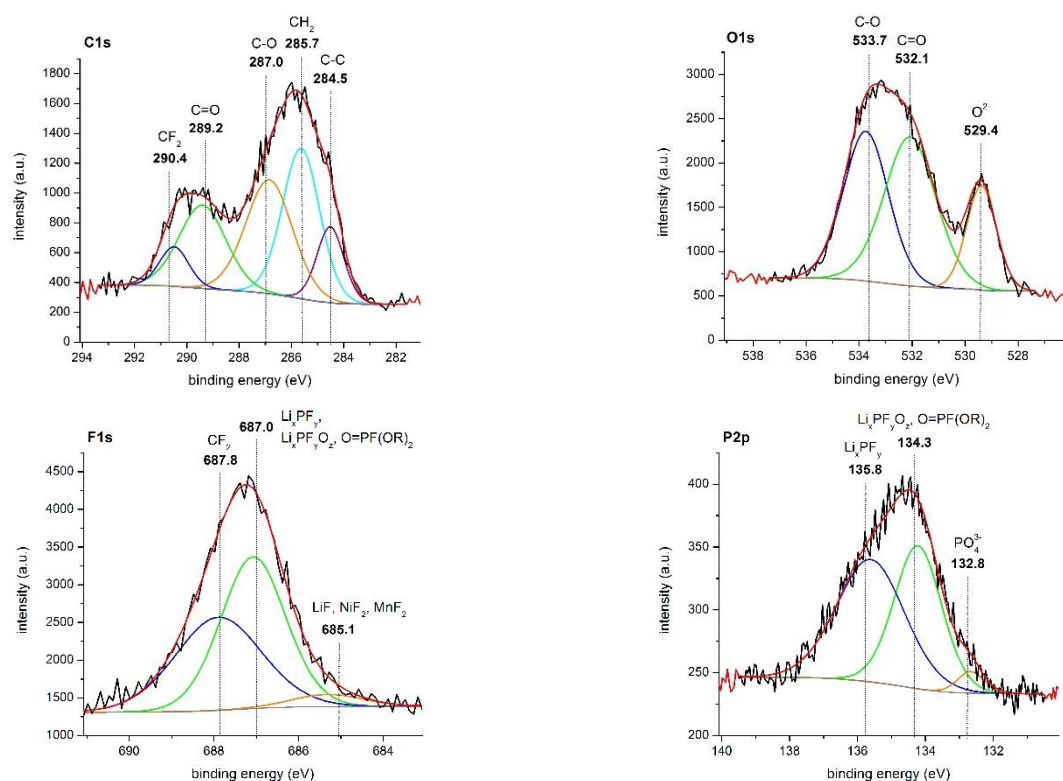


Figure 129 XPS spectra of LiNi_{0.4}Mn_{1.6}O₄ electrodes at 0% SOC after cycling C//LiNi_{0.4}Mn_{1.6}O₄ pouch cells with 2.5% SA for 250 cycles at 45 °C between 3.3 and 4.8 V.

F1s: Actually, the amount of salt residues and fluorophosphates (687.0 eV) in the SPI is only slightly greater compared to the reference. In addition, less metal fluorides (685.1 eV) are present in the surface layer as noticed in the F1s spectrum.

P2p: The P2p spectrum verifies these observations. Thereby, it is interesting to see that more Li_xPF_y (135.8 eV) than Li_xPF_yO_z/O=PFOR (134.3 eV) are produced on the spinel electrode particles. Phosphates (132.8 eV) only play a minor role in the structure of the surface film.

All in all, the analyzed surface layer is modified by the addition of 2.5% SA to the base electrolyte. The SPI is primarily characterized by large amounts of carbonyl groups involved in the film network with no major precipitations of phosphates on the cathode surface. It is assumed that these organics are the main reason for the fast capacity fading of C//LiNi_{0.4}Mn_{1.6}O₄ full cells comprising 2.5% SA. As a consequence, higher SA concentrations lead to a more severe cycling behavior (see chapter 5.2.2, Figure 80). The addition of 0.5% SA also causes poor cyclability as the number of carbonates incorporated in the layer is probably still too high. Thus, the results of Passerini et al. could not be confirmed. Instead, SA is found to induce more rapid cell ageing. It is possible that the different cell design, that is, Swagelok™-type cells vs. pouch cells, lead to the different cycling and XPS results.

Conclusion

In conclusion almost none of the applied additives could prevent a thickening of the SPI upon cycling C//LiNi_{0.4}Mn_{1.6}O₄ pouch cells at 45 °C in the voltage window of 3.3 and 4.8 V. In nearly all cases the SPI has become bigger with increasing cycle number. This implies that some layer components are not stable at elevated temperatures and readily decompose to create relatively porous surface films. Hence, fresh electrolyte can constantly be transported to exposed sections of the cathode surface resulting in continuous degradation reactions.

An exception is the addition of 0.5% HMDS to the standard electrolyte. Although the HMDS-based SPI is rather thick after formatting C//LiNi_{0.4}Mn_{1.6}O₄ pouch cells, it is not stable upon cycling and becomes much thinner than that of the reference. The tendency of HMDS to react with water, which is always present in trace amounts in the cell, is believed to be the origin for the unstable surface layer. Nevertheless, a better CC/CV-cycling behavior is achieved with 0.5% HMDS than with the base electrolyte (see chapter 5.2.2). On one hand, HMDS reduces Mn and Ni dissolution by scavenging HF and H₂O as outlined in chapter 5.4. On the other hand, the SPI produced during formation is protective in the beginning of the cycling tests and only loses its passivating effect after a few cycles.

Table 18 provides a ranking of the SPI thicknesses concerning all applied electrolyte additives in relation to the reference. The additives are ordered according to their decreasing benefits, whereby those listed above the reference enable a higher specific energy over cycle life than the base electrolyte. While 0.5% HMDS produces the thinnest SPI of all additives, 1.7% TTSP generates by far the thickest film of all additives. As can be seen, the thicknesses of the surface layers on the cathode are not directly correlated to the cycling performance of the respective full cells. Instead, it is supposed that the composition of the SPI is more relevant and has a stronger impact on the electrochemical features of the pouch cells. The influence of the SEI on the anode surface is not discussed in this section.

Table 18 summarizes the XPS results and gives an overview on the diverse SPI compositions in dependence of the electrolyte additives. The reference cell serves as a benchmark with equally sized circles. Greater circles signify higher quantities of the respective components within the SPI structure in comparison to the reference, whereas smaller circles denote lower amounts.

Each additive modifies the structure of the SPI layer in another way and different film compositions are detected. Generally, it is recognized that phosphates and fluorophosphates included in the SPI improve the cycling performance of spinel full cells, whereas too many carbonyl and alkoxy groups have a negative effect on the cycling stability. Likewise, salt residues accelerate the capacity decay of the cells. Therefore, most phosphate-based additives are beneficial with regard to the electrochemical characteristics of C//LiNi_{0.4}Mn_{1.6}O₄ pouch cells. Actually, 0.5% TMP and 0.5% TFPi provide the two best cycling results of all

additives. Nevertheless, long hydrocarbon side chains should be avoided (cf. 1.7% TTSP or 0.5% TEHP). Moreover, 2.5% SA, 0.5% TEHP, 2.5% FEC, 1% SEN, and 1.7% TTSP produce high quantities of carbonates on the spinel electrode leading to a poor cyclability. An exception is the addition of 0.5% LiBOB to the standard electrolyte. This additive also generates lots of carbonates on the cathode surface but the cells still offer a very good cycling behavior. This is related to the electron-deficient boron atoms, which interact with electron-rich anions (e.g. PF_6^-), and, which stabilize the SPI. Another special case is 0.5% HMDS, which is elucidated above.

By means of analyzing the TTSP-derived SPI more precise information on the film composition could be gathered. It is found that the organics of the layer are located at the cathode side underneath the inorganics, which are positioned towards the electrolyte side. This coincides with the results reported by Edström and Eriksson et al., who conducted XPS depth profile analyses of manganese spinel electrodes stored or cycled at 60 °C. ^[465,466]

Finally, it should be noted that in this thesis TFPI-, HMDS-, SEN-, and TEHP-derived surface layers on high voltage spinel cathodes have been analyzed for the first time. Cycled C//LiNi_{0.4}Mn_{1.6}O₄ pouch cells with Al₂O₃-modified electrodes were not investigated by XPS owing to measuring problems involving the thickness of the ceramic layer. In the next chapter, EIS measurements will reveal the effect of the various additives and the Al₂O₃-modified electrodes on the impedance of formatted and cycled C//LiNi_{0.4}Mn_{1.6}O₄ full cells. Then, the influence of the SEI is also considered.

	CH ₂ , PVDF, alkyl groups	C=O carbonyl components (mainly carbonates)	C-O alkoxides	CF ₂ , PVDF alkyl fluorides	Li _x PF _y salt residues	Li _x PF _y O _z O=PFOR fluorophosphates	PO ₄ ³⁻ phosphates	LiF, NiF ₂ , MnF ₂ metal fluorides	Si silicon	NH ²⁺ /NH ₃ , C-N amines, nitriles	Ranking of the SPI thicknesses
0.5% TMP	●	●	●	●	●	●	●	●			0
0.5% TFPi	●	●	●	●	●	●	●	●			0
0.5% LiBOB	●	●	●	●	●	●	●	●			-
0.5% HMDS	●	●	●	●	●	●	●	●		●	---
0.5% HFiP	●	●	●	●	●	●	●	●			-
ref.	●	●	●	●	●	●	●	●			0
1.7% TTSP	●	●	●	●	●	●	●	●	●		+++
1% SEN	●	●	●	●	●	●	●	●		●	+
2.5% FEC	●	●	●	●	●	●	●	●			-
0.5% TEHP	●	●	●	●	●	●	●	●			+
2.5% SA	●	●	●	●	●	●	●	●			+

Table 18 Overview on the diverse SPI compositions in dependence of the electrolyte additives and ranking of the SPI thicknesses.

5.6 Electrochemical impedance spectroscopy

Next, we focused on electrochemical impedance spectroscopy of formatted and cycled C//LiNi_{0.4}Mn_{1.6}O₄ pouch cells to get a deeper comprehension of the mechanism of each electrolyte additive and the Al₂O₃ coating layers regarding the entire full cell. Now not only the cathode part of the lithium ion cell is taken into account, but the anode is also considered. Generally, EIS is helpful to differentiate the contribution of Li ion migration through the surface films, charge-transfer through the electrode-electrolyte interface, and the solid-state diffusion of Li ions in the active materials.^[489] As an example, Figure 130 illustrates the Nyquist plot of the reference C//LiNi_{0.4}Mn_{1.6}O₄ pouch cell after formation. It can be clearly divided into five impedance contributions.

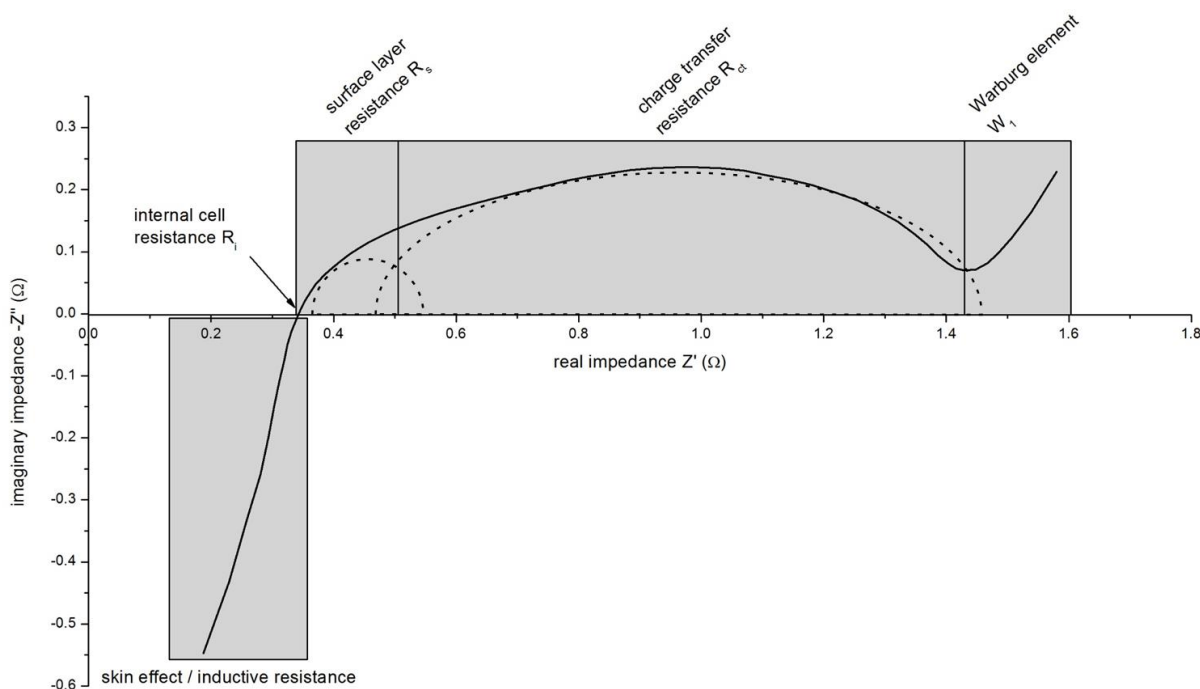


Figure 130 An example of a Nyquist plot of a C//LiNi_{0.4}Mn_{1.6}O₄ pouch cell.

The skin effect is based on the inductive resistance of a conductor and adopts negative $-Z''$ values as can be seen in the diagram above. The alternating polarity of the current flow changes the magnetic field around the electrical conductor and the resulting currents are directed opposite to the alternating current source. Thereby, the changing magnetic field provokes a stronger counter-voltage within the conductor than on its surface. More precisely, the generated counter-voltage is largest in the centerline of the conductor and, thus, the current flow shifts to the surface. The effective cross-section of the conductor is reduced and the inductivity is enhanced. The higher the frequency, the more pronounced becomes the skin

effect and at very high frequencies only a very small area of the conductor surface, the skin, is electrically conductive.^[490]

The intercept of the semi-circle in the high frequency region with the x-axis (real impedance) is attributed to the internal resistance R_i of the cell, which is caused by all the ohmic resistances existent in the cell. These are, for instance, the resistances of the electrolyte, the separator, the current collectors, and the cell body. In addition, R_i is dependent on the distance of the electrodes to each other and the electrode areas.^[431,491]

The diameter of the semi-circle in the high frequency region represents the lithium ion migration through the surface layers on the electrodes (surface resistance R_s). It overlaps with a depressed semi-circle in the medium frequency region, whose diameter corresponds to the charge-transfer resistance R_{ct} at the electrolyte-film and at the film-particle interfaces. The slope at low frequencies is assigned to the lithium ion diffusion in the bulk electrodes and is called Warburg impedance.^[269,484,491,492]

Typically, impedance spectra are analyzed and interpreted by modelling electrical equivalent circuits describing physical processes as outlined in chapter 2.3.8. In case of the Nyquist plots of formatted and cycled C//LiNi_{0.4}Mn_{1.6}O₄ pouch cells attained by EIS measurements, the subsequent equivalent circuit is utilized for fitting the experimental data.

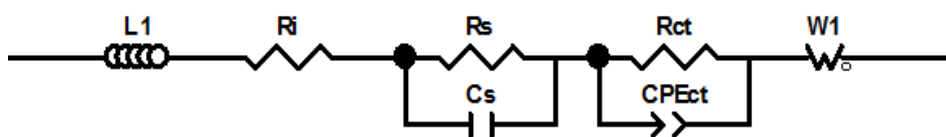


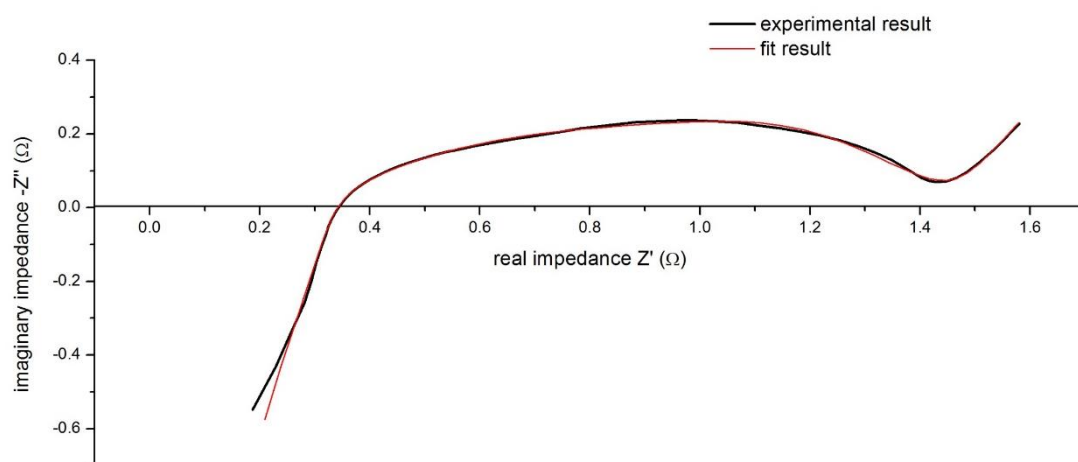
Figure 131 Equivalent circuit used to fit the electrochemical impedance spectra.

L_1 and R_i denote the inductive resistance and the internal cell resistance, respectively. The formation of the surface layer, which is characterized by a lower ionic conductivity compared to the liquid electrolyte, is given by the resistor R_s and a capacitor C_s placed in parallel. R_s signifies the migration of lithium ions inside the surface film and C_s represents the polarization of the film. The charge-transfer resistance R_{ct} is coupled to a constant phase element CPE_{ct} , which reflects the charge-transfer through an electrochemical double layer at the interface of two phases with different potentials (e.g. electrolyte-film and film-particle interfaces). The constant phase element is selected instead of a capacitor because of the roughness and inhomogeneity of the composite electrodes as demonstrated by a depressed semicircle in Figure 130. W_1 is the Warburg impedance related to the solid state diffusion of lithium ions inside the high voltage spinel particles.^[491,493]

The reference cell

Figure 132 illustrates the Nyquist diagrams obtained after formatting C//LiNi_{0.4}Mn_{1.6}O₄ pouch cells comprising the base electrolyte at 23 °C and after cycling these cells at 45 °C for 250 cycles.

A



B

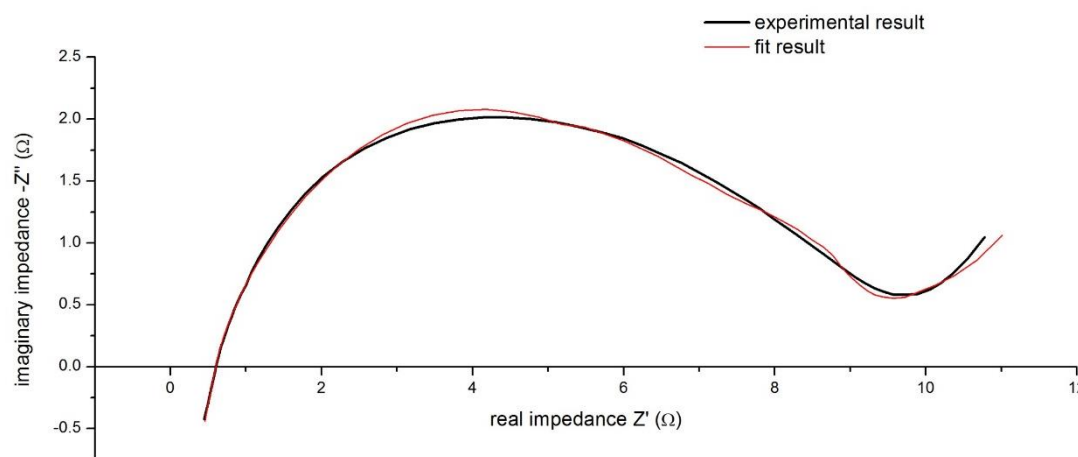


Figure 132 Nyquist plots of C//LiNi_{0.4}Mn_{1.6}O₄ cells at 80% SOC after **A** formatting C//LiNi_{0.4}Mn_{1.6}O₄ pouch cells containing the base electrolyte at 23 °C and after **B** cycling these cells for 250 cycles at 45 °C.

After formation, R_i , R_s , and R_{ct} equal to 0.4, 0.3, and 1.2 Ω , respectively, and after 250 cycles all resistances have substantially increased to 0.7, 0.5, and 7.9 Ω , respectively. One explanation for the elevated resistance R_i is the degradation of the conducting salt LiPF₆. A lower amount of LiPF₆ relates to lower ionic conductivity of the cell. Furthermore, the internal resistance is indirectly a result of the surface layer formation. Lithium ions are consumed by electrolyte oxidation/reduction and are no longer available as charge carriers. Consequently,

the ionic conductivity of the electrolyte is diminished and the resistance is enhanced. The generation of a SPI has already been proven by XPS analyses and SEI formation is a permanent feature while operating lithium ion cells. The increase of the surface resistance is in agreement with these observations. Generally, a higher charge-transfer resistance can be ascribed to new grain boundaries owing to structural changes and/or to impeded lithium ion pathways as in case of a forming surface film. Here, the latter aspect is proposed to be responsible for the augmentation of R_{ct} . Thereby, the compositions of the surface films determine the thicknesses of the electrochemical double layers at the electrolyte-film and film-particle interfaces, and therefore the strength of R_{ct} .

Electrolyte optimization

Figure 133 shows the values acquired from the equivalent circuit fitting of the internal resistance R_i , the surface resistance R_s , and the charge-transfer resistance R_{ct} for formatted and cycled C//LiNi_{0.4}Mn_{1.6}O₄ pouch cells with and without various electrolyte additives. For comparison, the diagram displaying the R_{ct} values after 250 cycles additionally contains the specific discharge capacity values after cycling C//LiNi_{0.4}Mn_{1.6}O₄ cells. All corresponding Nyquist plots and EIS data are depicted in the appendix (chapter 7). The cell containing 1.5% LiTFSI was only analyzed after formation because of the cell damage that has been triggered by massive gassing while cycling.

After formatting C//LiNi_{0.4}Mn_{1.6}O₄ full cells, R_i , R_s , and R_{ct} of the most cells adopt nearly the same values as those of the reference within the limits of accuracy of the measurements. Hence, similar thicknesses of the SEI/SPI with comparable charge-transfer properties are assumed. What is most interesting are the higher resistances R_i and R_s caused by 1% SEN and 2.5% SA compared to the reference indicating more surface film generation on either one or both electrodes. It has been demonstrated by XPS analyses that 1% SEN indeed leads to a noticeably thicker SPI than the standard electrolyte after formation. In contrast, the 1.5% LiTFSI cell displays lower R_i and R_s values in comparison to the reference reflecting thinner surface layers. It is supposed that LiTFSI is responsible for excessive gas production inside the cell partially inhibiting the accumulation of decomposed species on the electrodes. Regarding the charge-transfer resistance R_{ct} of the formatted spinel full cells, 2.5% SA provokes the highest resistance among all additives. This is probably due to a large amount of carbonates, which are already integrated in the surface films. This is also why 0.5% LiBOB contributes to a slightly higher R_{ct} value than the reference. The other additives induce approx. identical charge-transfer resistances without any major differences.

5. Results and discussion
5.6 Electrochemical impedance spectroscopy

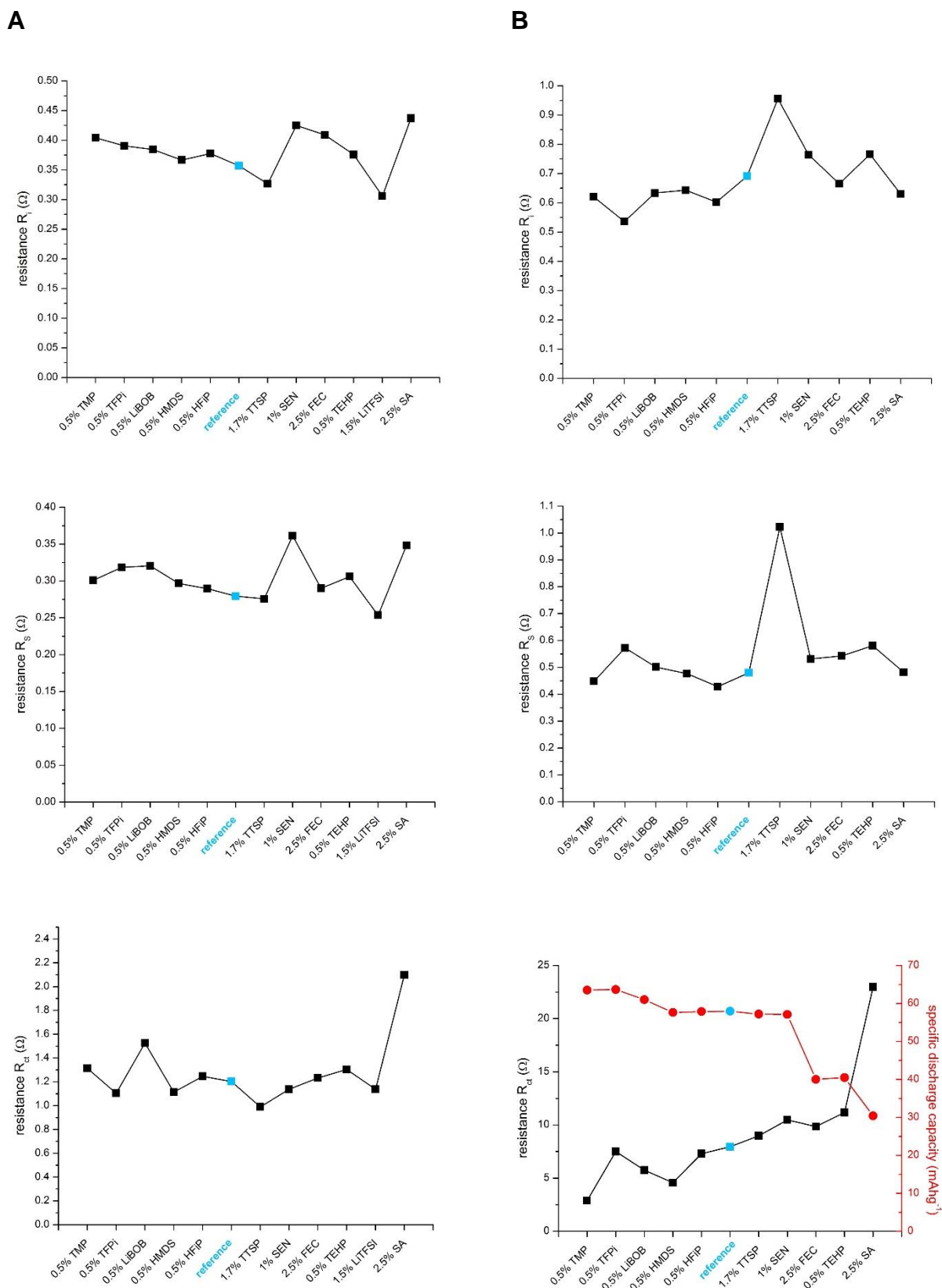


Figure 133 Fitted values R_i , R_s , and R_{ct} of electrochemical impedance measurements of C//LiNi_{0.4}Mn_{1.6}O₄ pouch cells with and without various electrolyte additives **A** after formation at 23 °C and **B** after 250 cycles at 45 °C between 3.3 and 4.8 V. The diagram displaying the R_{ct} values after 250 cycles additionally contains the specific discharge capacity values after cycling C//LiNi_{0.4}Mn_{1.6}O₄ cells for comparison reasons.

Considering the cycled C//LiNi_{0.4}Mn_{1.6}O₄ pouch cells, R_i , R_s , and R_{ct} of all cells have markedly increased. Nevertheless, the additives, which have improved the cycling behavior of the spinel full cells (0.5% TMP, 0.5% TFPi, 0.5% LiBOB, 0.5% HMDS, and 0.5% HFiP) lead to lower or at least similar resistances than the cell with the base electrolyte. For instance, the cell including 0.5% TMP exhibits diminished internal and surface resistances compared to the reference suggesting slightly thinner surface layers formed on the electrodes. XPS investigations have revealed that the SPI has about the same thickness as that of the reference. As a consequence, TMP is not supposed to support surface film formation on the anode and the corresponding SEI must be thinner compared to the reference. Moreover, the addition of 0.5% TMP to the standard electrolyte results in the lowest charge-transfer resistance. The reason for this are most likely the very high quantities of phosphates and fluorophosphates in the SPI. Concurrently, less carbonyl and hydroxyl groups have been detected in the SPI by XPS compared to the reference. Besides, the additive clearly hampers transition metal dissolution and precipitation on the anode surface as outlined in chapter 5.4. Interestingly, for the 0.5% TFPi cell, R_i and R_s behave differently as R_i is smaller and R_s is larger compared to the reference. The lower internal resistance is presumably a result of the smaller salt residues in the SPI as found by XPS and is not related to thin surface layers. Actually, the thickness of the SPI created by 0.5% TFPi is very similar to that of the reference (see chapter 5.5). Therefore, the marginally higher surface resistance R_s compared to the reference is probably due to a thicker SEI on the anode surface. This might be also the reason for the greater charge-transfer resistance of the cell comprising 0.5% TFPi in comparison to the 0.5% TMP cell. Likewise, the TFPi-derived SPI contains a slightly higher content of carbonyl groups than that of the 0.5% TMP sample (see chapter 5.5).

R_i and R_s of the cells including 0.5% LiBOB, 0.5% HMDS, and 0.5% HFiP are comparable to each other and to the reference. All three additives, but especially 0.5% LiBOB and 0.5% HMDS, are supposed to contribute to the SEI on the anode surface as their SPI thicknesses are detected to be thinner as that of the reference (see chapter 5.5). Regarding these three additives, 0.5% HMDS leads to the lowest charge-transfer resistance, which is most likely due to the extremely thin SPI with very low carbonyl groups. 0.5% HFiP has a higher R_{ct} because of the greater accumulation of carbonyl compounds on the cathode surface. In spite of the many carbonyl groups within the SPI, 0.5% LiBOB leads to a relatively low R_{ct} . It is an exception, as boron in the SPI layer network can counteract the negative inductive effect of the carbonyl groups. More information is given later on.

In contrast, the additives, which have accelerated the capacity decay of C//LiNi_{0.4}Mn_{1.6}O₄ pouch cells (1.7% TTSP, 1% SEN, 2.5% FEC, 0.5% TEHP, and 2.5% SA), cause higher or nearly identical resistances than the base electrolyte. Enhanced R_i and R_s are attributed to a greater sum of decomposition products on the anode and/or cathode surface. Since for the

2.5% FEC cell a thinner SPI is registered than for the reference (see chapter 5.5), the higher R_s is ascribed to a rather thick SEI. The other additives lead to thicker surface films on the cathode as demonstrated in chapter 5.5. Nonetheless their participation in the SEI layer network on the anode is not excluded.

1.7% TTSP generates an extremely thick SPI and/or SEI. In this case, the layer on the cathode surface is the origin of the high internal and surface resistances as proven by XPS. In spite of this, the respective charge-transfer resistance is rather low. It is believed that the large amounts of phosphates and fluorophosphates, which are also incorporated in this SPI, weaken the negative influence of the carbonates and, thus, reduce the charge-transfer resistance within the cell. In contrast, 2.5% SA does not induce more film formation than 1.7% TTSP, but the resulting R_{ct} is exceptionally high after 250 cycles. High quantities of carbonate species are thought to be the source of the extensively increased resistance R_{ct} , whereby only low amounts of phosphates are present in the SPI. Furthermore, nickel and manganese particles that accumulate on the anode surface upon cycling also add to the charge-transfer resistance (see chapter 5.4).

In general, the surface film on the cathode has a strong impact on the cycling behavior of the full cells. Thereby, surface films primarily consisting of phosphates and fluorophosphates are considered more stable in the oxidative environment given in the spinel full cells as those based on carbonyl compounds (mainly carbonates). The latter are more reactive towards PF_5 or POF_3 and might be further decomposed to CO_2 and alkyl fluorides. Moreover, the negative inductive effect of oxygen atoms is much more pronounced in carbonates than in phosphates because of the nature of their chemical bonds. While in carbonates only electrons from the second shell are involved in the chemical bonds, phosphor in phosphates provides electrons from the third shell for the bonding with oxygen. Consequently, carbonates are much stronger molecular dipoles than phosphates, provoke stronger polarizations, establish much thicker electrochemical double layers at the electrolyte-film and film-particle interfaces, and are the main reason for enhanced charge-transfer resistances of C//LiNi_{0.4}Mn_{1.6}O₄ pouch cells. The carbonate-based additive LiBOB is an exception due to the presence of electron-deficient boron within the structure. These may form Lewis acid-base adducts with electron-rich anions such as PF_6^- . All the data obtained by EIS measurements are in good agreement with the results gained by rate capability tests (see chapter 5.2.3).

Optimization with Al₂O₃ coating layers

Subsequently, changes in the resistances of bare and Al₂O₃-coated electrodes are investigated by EIS after formatting and cycling C//LiNi_{0.4}Mn_{1.6}O₄ pouch cells as visible in Figure 134. The corresponding Nyquist plots and EIS statistics are illustrated in the appendix (chapter 7). For comparison, the diagram displaying the R_{ct} values after 250 cycles additionally contains the specific discharge capacity values after cycling C//LiNi_{0.4}Mn_{1.6}O₄ cells.

After formation, R_i , R_s , and R_{ct} are higher than those for the reference owing to the thick coating layers, which may cause unwanted side effects such as suppressed ionic conductivity and greater Li ion diffusion barriers. In other words, Li ion migration is impeded by the insulating Al₂O₃ films. As expected, the resistances of both samples have substantially increased after 250 cycles at 45 °C in the voltage window of 3.3 and 4.8 V. But surprisingly, the Al₂O₃-modified electrodes lead to lower resistances in comparison to the bare electrodes. Actually, R_i , R_s , and R_{ct} equal to 0.7, 0.5, and 7.9 Ω , respectively, for the reference and 0.6, 0.4, and 7.7 Ω , respectively for the cell comprising the Al₂O₃-coated anode and cathode. Therefore, Al₂O₃ coating layers restrain undesired side reactions during cycling (e.g. electrolyte decomposition), inhibit the generation of resistive layers, and suppress the development of impedances. Besides, the protective effects of Al₂O₃ films do not hinder lithium ion transfer as R_{ct} is even smaller compared to the reference. Again, the EIS data correlate well with the results of the rate capability tests (see chapter 5.2.3).

5. Results and discussion
5.6 Electrochemical impedance spectroscopy

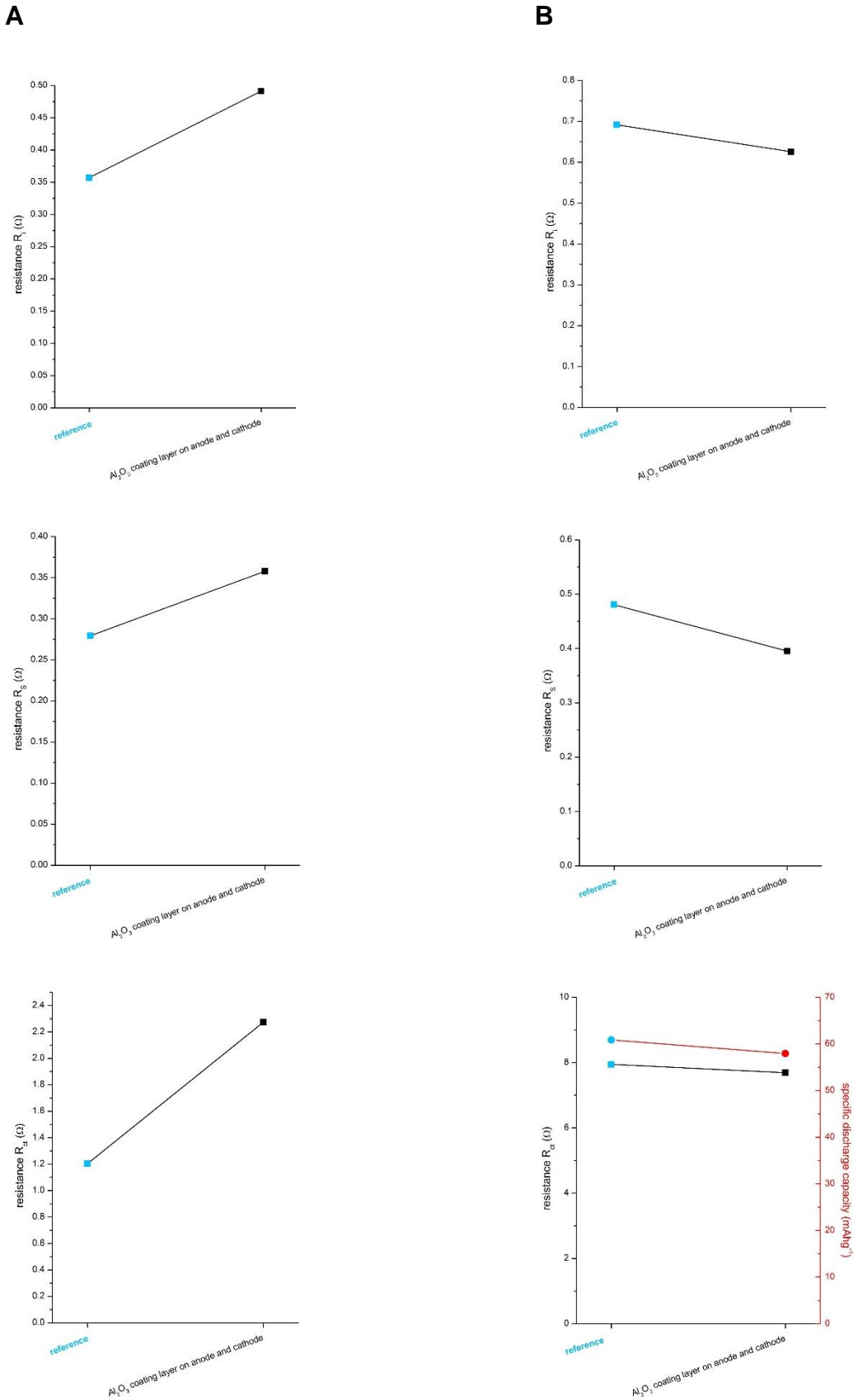


Figure 134 Fitted values R_i , R_s , and R_{ct} of electrochemical impedance measurements of C//LiNi_{0.4}Mn_{1.6}O₄ pouch cells without and with a ceramic layer on both electrodes **A** after formation at 23 °C and **B** after 250 cycles at 45 °C between 3.3 and 4.8 V. The diagram displaying the R_{ct} values after 250 cycles additionally contains the specific discharge capacity values after cycling C//LiNi_{0.4}Mn_{1.6}O₄ cells for comparison reasons.

5.7 Improvement of the cycling stability of C//LiNi_{0.4}Mn_{1.6}O₄ full cells

Finally, attempts have been made to improve the cycling characteristics of C//LiNi_{0.4}Mn_{1.6}O₄ pouch cells, based on the findings of the previous experiments. Thereto, 1C CC/CV-cycling experiments were conducted with spinel full cells comprising various modifications at 45 °C in the voltage region of 3.3 - 4.8 V (Figure 135 - 137). For comparison purposes the cycle life of the reference (thick black line), the 0.5% TMP cell (dark blue line), and the cell containing an Al₂O₃-coated cathode (green line) are depicted, too, in each diagram.

First of all, a cell with an Al₂O₃-coated cathode and 0.5% TMP added to the standard electrolyte was cycled. Hereby, 63.7 mAhg⁻¹ is measured at the end of cycling, corresponding to 70% of its original capacity (Figure 135, red line). The idea was to gather the beneficial aspects of both components in one cell and to realize a more stable cycling behavior compared to the cells tested before. It has been shown that 0.5% TMP weakens the transition metal dissolution and establishes a quite favorable SPI with high concentrations of phosphates on the surface of the cathode, while Al₂O₃-modified spinel electrodes have been proven to suppress the development of high impedances and to be an effective HF scavenger. In fact, the corresponding cell displays slightly better cycling features than the ones containing only 0.5% TMP or only the Al₂O₃-coated cathode.

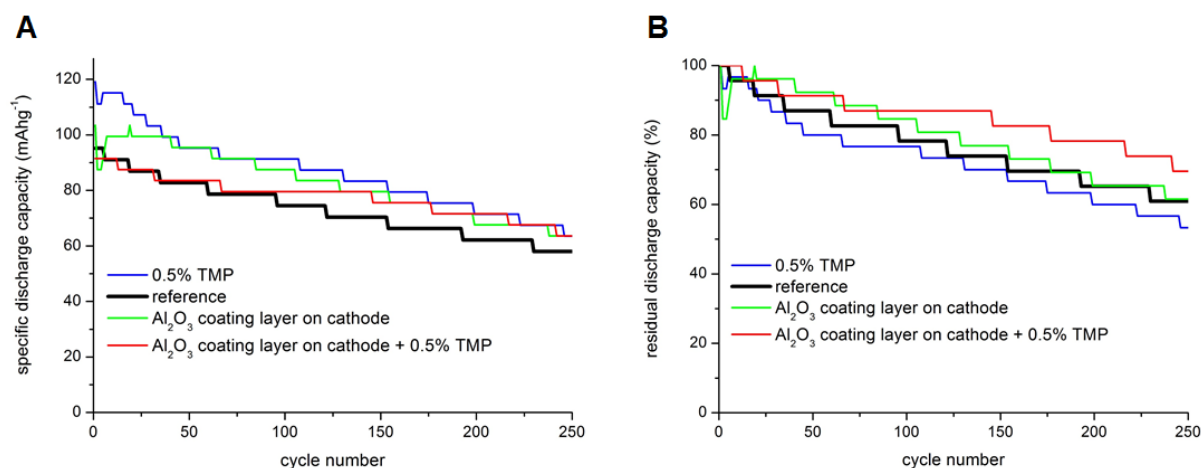


Figure 135 **A** Specific discharge capacity vs. cycle number plots and **B** residual discharge capacity vs. cycle number plots of C//LiNi_{0.4}Mn_{1.6}O₄ cells with various modifications cycled between 3.3 and 4.8 V at 1C at 45 °C. Here, especially, the cell containing 0.5% TMP and an Al₂O₃ layer on the cathode is considered (red line).

In another attempt, 0.5% TMP and 0.1% LiBOB were added to the base electrolyte to combine the advantages of phosphate- and borate-based surface films, that is, their protective and low-impedance properties, in a single full cell. Moreover, both additives were found to reduce

Mn and Ni depletion from the composite spinel electrode. The respective cell reveals a significantly decelerated capacity fading compared to the reference, since 67% of the starting capacity (95.5 mAhg⁻¹) are retained after 250 cycles (Figure 136, bright blue line). Nonetheless, the large capacity drop at the beginning of the cycling, which is presumably due to the generation of a TMP- and LiBOB-derived surface layer, prevents an even better cycle life.

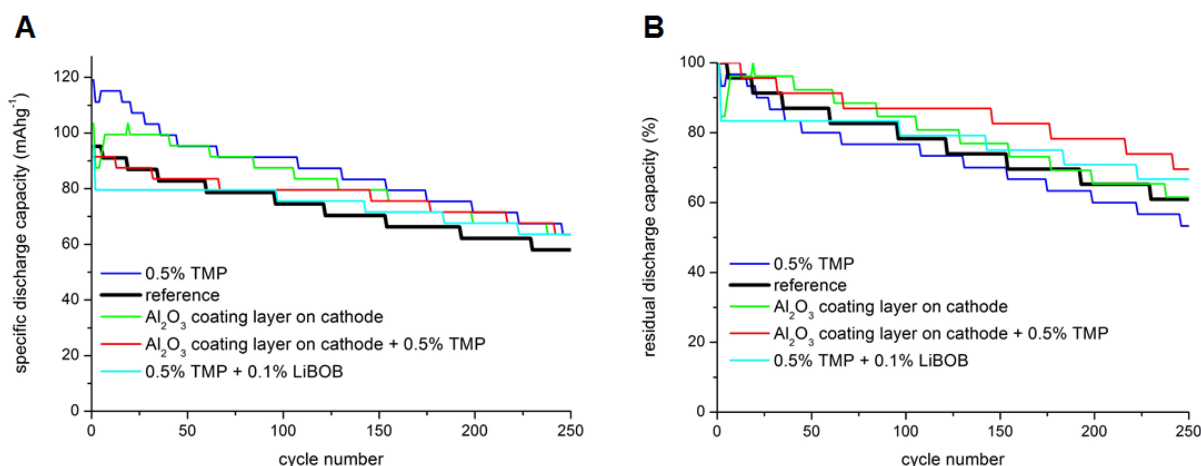


Figure 136 **A** Specific discharge capacity vs. cycle number plots and **B** residual discharge capacity vs. cycle number plots of C//LiNi_{0.4}Mn_{1.6}O₄ cells with various modifications cycled between 3.3 and 4.8 V at 1C at 45 °C. Here, especially, the cell containing 0.5% TMP and 0.1% LiBOB is considered (bright blue line).

Next, the electrolyte including 0.5% TMP and 0.1% LiBOB was combined with an Al₂O₃-modified spinel electrode in one full cell because the coating layer has been demonstrated to effectively prevent transition metal dissolution and to inhibit the production of resistive and thick surface films. Actually, for the relevant cell still 71.6 mAhg⁻¹ is measured after 250 cycles, which corresponds to 72% residual capacity (Figure 137, orange line). These values are the best among all cycled cells confirming the positive influence of all three modifications relative to the reference. Consequently, it has been shown, for the first time, that the cycling performance of C//LiNi_{0.4}Mn_{1.6}O₄ pouch cells is considerably improved by the combination of adding 0.5% TMP and 0.1% LiBOB to the base electrolyte and coating the spinel electrode with an Al₂O₃-based ceramic layer.

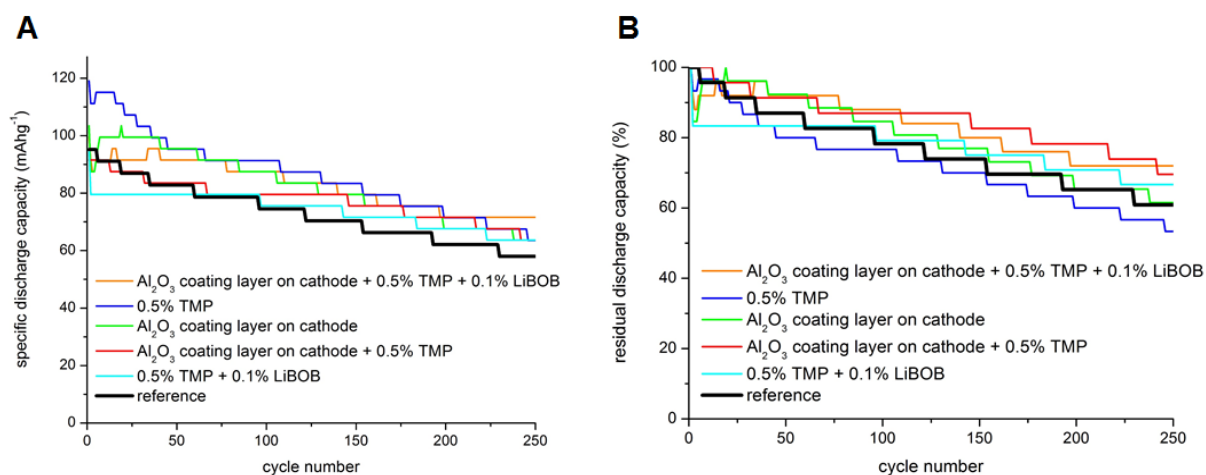
5.7 Improvement of the cycling stability of C//LiNi_{0.4}Mn_{1.6}O₄ full cells

Figure 137 **A** Specific discharge capacity vs. cycle number plots and **B** residual discharge capacity vs. cycle number plots of C//LiNi_{0.4}Mn_{1.6}O₄ cells with various modifications cycled between 3.3 and 4.8 V at 1C at 45 °C. Here, especially, the cell containing 0.5% TMP, 0.1% LiBOB, and an Al₂O₃-modified spinel electrode is considered (orange line).

6. Conclusion

Currently, cars powered only by electricity cannot compete with drive systems comprising combustion engines in terms of driving range. This main limitation is based on the low energy densities of standard active materials for LIBs. Recently, the cathode active material high voltage spinel (e.g. $\text{LiNi}_{0.5}\text{Mn}_{1.5}\text{O}_4$) has triggered great interest in the field of the lithium ion battery technology. The latter is expected to enable a substantial enhancement of the cell energy densities owing to its high theoretical average voltage of 4.7 V vs. Li at a moderate theoretical gravimetric capacity of 147 mAhg^{-1} . Nevertheless, high voltage spinel full cells have been reported to show severe capacity losses and very restricted cycle lifes.^[1–6]

Herein, two different approaches to improve the electrochemical performance of C// $\text{LiNi}_{0.4}\text{Mn}_{1.6}\text{O}_4$ pouch cells are addressed: on one hand, electrolyte optimization by adding selected additives in distinct concentrations to a standard electrolyte formulation and on the other hand, application of Al_2O_3 coating layers on the electrodes by a doctor blade process. Moreover, this thesis offers a better understanding regarding the influence of these electrolyte additives and the Al_2O_3 films on a number of aspects. For example, the phase composition and the transition metal dissolution behavior of $\text{LiNi}_{0.4}\text{Mn}_{1.6}\text{O}_4$ composite cathodes, the structure and composition of the SPI on high voltage spinel electrode surfaces, and the impedance properties of C// $\text{LiNi}_{0.4}\text{Mn}_{1.6}\text{O}_4$ full cells.

First of all, a **reference system** was established and a general **electrochemical characterization** of C// $\text{LiNi}_{0.4}\text{Mn}_{1.6}\text{O}_4$ pouch cells containing the reference electrolyte (1 M LiPF_6 in EC/EMC/DMC (1/1/1, w/w/w)) was conducted to investigate and evaluate ageing phenomena of $\text{LiNi}_{0.4}\text{Mn}_{1.6}\text{O}_4$ electrodes. The spinel full cells comprising the base electrolyte were cycled in diverse voltage windows at 1C at room temperature to verify the one enabling the best cycling characteristics and specific capacity. To this end, the range of 3.3 - 4.8 V was determined as the most advantageous cycling condition in terms of gravimetric energy density as a function of cycle life. As a matter of fact, a specific discharge capacity of 98.6 mAhg^{-1} after 500 cycles, i.e. a capacity retention of 80% was detected, which is already a quite good result. For automotive applications higher cycling stabilities are, however, a must. Three-electrode measurements were additionally carried out to ensure that improper cell balancing is not the reason for capacity fading. A marginal anode oversizing of approx. 4% at 0.1C was recognized to be sufficient to prevent lithium plating on the anode and still to guarantee a relatively high specific energy throughout cycling. It was confirmed that the capacity decay of C// $\text{LiNi}_{0.4}\text{Mn}_{1.6}\text{O}_4$ pouch cells is not caused by erroneous balancing. Instead, serious loss of active lithium is suggested to be one of the main sources of the unsatisfactory cycling performance.

Subsequently, assays were performed to improve the cycle life of C//LiNi_{0.4}Mn_{1.6}O₄ cells by selected electrolyte additives with certain concentrations and Al₂O₃ coating layers on the electrodes. Thereto **CC/CV-cycling experiments** were conducted with a current rate of 1C between 3.3 and 4.8 V at an elevated temperature of 45 °C to accelerate the degradation of the full cells and, thus, to track the effect of the electrolyte additives or the ceramic layers on the cell properties.

Among all probed compounds HMDS, LiTFSI, and SEN were studied, for the first time, as electrolyte additives for the CAM lithium nickel manganese oxide spinel. However, only HMDS improves the electrochemical features of C//LiNi_{0.4}Mn_{1.6}O₄ pouch cells. Cells comprising 0.5% TMP displayed by far the most beneficial cyclability. Likewise, the addition of 0.1% LiBOB, 0.5% TFPi, 1.5% HMDS, 0.5% FEC, or 0.5% HFiP to the base electrolyte led to enhanced specific capacities after 250 cycles compared to a reference. In contrast, cells including 1.7% TTSP, 1% SEN, 0.5% TEHP, and 0.5% LiTFSI exhibited a poorer cycling behavior than a reference, while the cell with 2.5% SA revealed the most severe capacity deterioration. For microscopic and spectroscopic examinations the following additive concentrations were chosen because they provided the best cycling performance at the starting point of the analyses: 0.5% TMP, 0.5% TFPi, 0.5% LiBOB, 0.5% HMDS, 0.5% HFiP, 1.7% TTSP, 1% SEN, 2.5% FEC, 0.5% TEHP, 1.5% LiTFSi, and 2.5% SA.

Concerning the ceramic layers, three different possibilities were considered. Coating the aqueous Al₂O₃ slurry on the graphite anode, on the LiNi_{0.4}Mn_{1.6}O₄ cathode, or on both electrodes by a doctor blade process. The resulting thicknesses of the ceramic films were about 4 - 5 µm. As far as we are aware, there is no report involving detailed investigations of the combined use of Al₂O₃-modified LiNi_{0.4}Mn_{1.6}O₄ cathodes and Al₂O₃-modified graphite anodes. The best cycling stability was observed for full cells containing just an Al₂O₃-coated spinel electrode. Microscopic and spectroscopic post-mortem analyses were conducted with full cells including both Al₂O₃-modified electrodes to gain more information on the impact of the ceramic layer on the electrochemical features of high voltage spinel full cells.

To conclude the electrochemical measurements, **rate capability tests** were accomplished at BOL and EOL with C//LiNi_{0.4}Mn_{1.6}O₄ pouch cells. The purpose was to examine the suitability of the selected electrolyte additives and the Al₂O₃ layers for facilitating charge-transfer processes at the electrode surfaces. Generally, all cells showed a strong capacity decay at 5C. This is due to lithium ion migration upon intercalation/deintercalation, which is, however, too slow to realize satisfactory capacities at high C-rates. At BOL, for the subsequent 1C cycle approx. 92 - 98% of the original capacities are retained in LiNi_{0.4}Mn_{1.6}O₄. This means good structural integrity of the spinel composite electrode after high current cycling without structural damage.

At EOL, all cells delivered much lower capacities than at BOL. Consequently, lots of lithium is consumed during cycling due to side reactions and massive surface film formation on the electrodes. Hence, the spinel structure is not completely retained, but exhibits lithium deficiencies. Only 0.5% TMP, 0.5% LiBOB, 0.5% HMDS, and the Al_2O_3 -modified electrodes engender higher specific capacities than the standard electrolyte regarding all C-rates. Cells containing 0.5% TFPi and 0.5% HFiP unveiled, in contrast, similar capacities as the reference. Therefore, these additives develop rather low-impedance layers on the anode/cathode surfaces. Al_2O_3 helps to lower resistances at the electrode surfaces with increasing cycle number. All the other samples hamper the charge-transfer kinetics within the C// $\text{LiNi}_{0.4}\text{Mn}_{1.6}\text{O}_4$ cells, which is verified by a negative impact on their rate capability.

XRD analyses demonstrated considerable changes regarding the fresh and the cycled spinel electrode patterns. Lower and broader reflection intensities of the cycled samples are presumably caused by the formation of thick SPI layers and transition metal dissolution, respectively. Besides, $\text{Li}_x\text{Ni}_{1-x}\text{O}$ impurities ($x \ll 1$) were detected within the XRD spectra of all cycled $\text{LiNi}_{0.4}\text{Mn}_{1.6}\text{O}_4$ cathodes contributing to the structural degradation of the CAM. Ageing of the spinel electrodes is strongly influenced, by the reference electrolyte and the diverse electrolyte additives, which lead to different phase compositions of the cycled $\text{LiNi}_{0.4}\text{Mn}_{1.6}\text{O}_4$ cathodes. In this thesis it is shown, for the first time, that ageing of $\text{LiNi}_{0.4}\text{Mn}_{1.6}\text{O}_4$ cathodes is derived from their phase composition at 0% SOC. The first cubic phase denotes the most intact and the third cubic phase marks the most impaired cathode. An electrolyte additive is only effective when just the second cubic phase is observed for the cycled and completely discharged spinel electrode. In this work, cells comprising 0.5% TMP and 0.5% TFPi reveal the best cycling behavior and the corresponding cycled cathodes exhibit solely the second cubic phase at 0% SOC. For 0.5% LiBOB, 0.5% HMDS, and 0.5% HFiP, the second and the third cubic phases were found, whereas 1.7% TTSP, 1% SEN, 2.5% FEC, 0.5% TEHP, and 2.5% SA resulted in the third cubic phase of $\text{LiNi}_{0.4}\text{Mn}_{1.6}\text{O}_4$ after 250 cycles at 45 °C. Actually, the latter additives accelerate the capacity fading of spinel full cells. The first cubic phase was merely registered for the fresh electrode. Cycled C// $\text{LiNi}_{0.4}\text{Mn}_{1.6}\text{O}_4$ pouch cells with Al_2O_3 -modified electrodes were not investigated by X-ray diffraction owing to problems related to the thickness of the ceramic layer.

Raman spectroscopy of fully discharged spinel cathodes (0% SOC) was used after formatting C// $\text{LiNi}_{0.4}\text{Mn}_{1.6}\text{O}_4$ full cells at 23 °C and after cycling these cells for 250 cycles at 45 °C without and with the utilized electrolyte additives and the Al_2O_3 -coated electrodes. This was done to further confirm the phase compositions of the differently treated positive electrodes and to determine the oxidation states of the nickel and manganese ions within these phases. All in all, the phase compositions and the $\text{Li}_x\text{Ni}_{1-x}\text{O}$ impurities found by XRD spectroscopy could be corroborated. To the best of our knowledge, this is the first time that three cubic phases with

the characteristic A_{1g} , E_g , and T_{2g} symmetries of $\text{LiNi}_{0.4}\text{Mn}_{1.6}\text{O}_4$ cathodes (0% SOC) were attested after formatting and cycling the respective spinel full cells. Furthermore, the lithium contents and the oxidation states of the transition metal cations were documented for the particular cubic phases:

first cubic phase: $\text{Li}_{1.0-0.78}\text{Ni}_{0.4}^{2+}\text{Mn}_{1.6}^{3+/4+}\text{O}_4$

second cubic phase: $\text{Li}_{0.433-0.432}\text{Ni}_{0.4-x}^{3+/4+}\text{Mn}_{1.6-y}^{4+}\text{O}_4$

third cubic phase: $\text{Li}_{0.390-0.207}\text{Ni}_{0.4-x}^{3+/4+}\text{Mn}_{1.6-y}^{4+}\text{O}_4$, but with only a minor Ni^{3+} content

Thus, ageing of a $\text{LiNi}_{0.4}\text{Mn}_{1.6}\text{O}_4$ electrode is given by its phase composition at 0% SOC and can be identified by Raman and XRD spectroscopy. While the first cubic phase represents the most intact, the third cubic phase signifies the most harmed cathode. Nonetheless, the experimentally obtained valences states for the cycled and totally discharged spinel electrodes do not coincide with the calculated values. Transition metal dissolution is a possible reason.

This was verified by **ICP-OES and EDX measurements** of graphite anodes at 0% SOC after cycling C// $\text{LiNi}_{0.4}\text{Mn}_{1.6}\text{O}_4$ pouch cells at 45 °C for 250 cycles in the voltage window of 3.3 - 4.8 V. Thereby, it was observed that Mn ions are more easily washed out the spinel active material than Ni ions. It has to be noted that the actual sum of the dissolved transition metal ions is even higher as presented herein. In general, more than twice as much Ni and Mn ions are registered in the electrolyte solution.^[4,33] The major cause of the metal ion depletion is the acidic component HF in the electrolyte. In terms of electrolyte additives, 0.5% LiBOB, 0.5% TFPI, 0.5% TMP, 0.5% HFIP, and 0.5% HMDS reduce transition metal dissolution, whereas 1.7% TTSP, 1% SEN, 1.5% LiTFSi, 2.5% FEC, 2.5% SA, and 0.5% TEHP lead to higher metal deposits on the anode in comparison to the reference electrolyte. On one hand, the elimination of HF, H_2O , and PF_5 and/or the establishment of a physical protection layer by a thin and stable SPI contribute to the diminution of the transition metal dissolution. LiBOB, TFPI, and HMDS were demonstrated to suppress HF generation by trapping PF_5 and H_2O , respectively. On the other hand, enhanced metal ion depletion is probably based on thick and porous SPI layers. Moreover, Al_2O_3 was proven to be the most effective HF scavenger of all investigated modifications leading to the lowest amounts of Mn and Ni ions accumulated on the anode.

XPS analyses were applied to study the chemical nature and the development of the interfacial layers between the $\text{LiNi}_{0.4}\text{Mn}_{1.6}\text{O}_4$ electrodes and the different electrolyte formulations after formatting C// $\text{LiNi}_{0.4}\text{Mn}_{1.6}\text{O}_4$ pouch cells containing various electrolyte additives at 23 °C and after cycling these cells for 250 cycles at 45 °C. Each additive in the SPI structure is especially examined. It was found that almost none of the additives prevent a thickening of the SPI upon cycling the spinel full cells. In most cases, the SPI has become thicker with increasing cycle number. This implies that some layer components are not stable at elevated temperatures and

readily decompose to create porous surface films. Hence, fresh electrolyte is constantly transported to sections of the cathode surface resulting in continuous degradation reactions. An exception is the addition of 0.5% HMDS to the standard electrolyte. Although the HMDS-based SPI is rather thick after formatting C//LiNi_{0.4}Mn_{1.6}O₄ pouch cells, it is not stable upon cycling. It becomes much thinner than that of the reference. The tendency of HMDS to react with water, which is always present in trace amounts in the cell, is believed to be the origin for the unstable surface layer. Nevertheless, a better CC/CV-cycling behavior is achieved with 0.5% HMDS than with the base electrolyte (see chapter 5.2.2). On one hand, HMDS reduces Mn and Ni dissolution by scavenging HF and H₂O as outlined in chapter 5.4. On the other hand, the SPI is protective in the beginning of the cycling tests and only loses its passivating effect after a few cycles.

In contrast to 0.5% HMDS, 1.7% TTSP generates by far the thickest film of all additives. The ranking of the SPI thicknesses concerning all applied electrolyte additives is depicted in Table 19. The additives are ordered according to their decreasing benefits, whereby those listed above the reference give rise to a higher specific energy over cycle life than the base electrolyte. Interestingly, the thicknesses of the surface layers on the cathode are not directly correlated with the cycling performance of the respective full cells. Instead, the composition of the SPI is more relevant and has a stronger impact on the electrochemical features of the pouch cells.

Each additive modifies the structure of the SPI layer in another way and different film compositions are detected. Generally, it is recognized that phosphates and fluorophosphates included in the SPI improve the cycling performance of spinel full cells. Too many carbonyl and alkoxy groups, in contrast, have a negative effect on the cycling stability. Likewise, salt residues accelerate the capacity decay of the cells. Therefore, most phosphate-based additives are beneficial with regard to the electrochemical characteristics of C//LiNi_{0.4}Mn_{1.6}O₄ pouch cells. Actually, 0.5% TMP and 0.5% TFPi provide the two best cycling results of all additives. Nonetheless, long hydrocarbon side chains should be avoided (cf. 1.7% TTSP or 0.5% TEHP). Furthermore, 2.5% SA, 0.5% TEHP, 2.5% FEC, 1% SEN, and 1.7% TTSP deliver high quantities of carbonates accumulated on the spinel electrode leading to a poor cyclability. An exception is the addition of 0.5% LiBOB. This additive also generates lots of carbonates on the cathode surface but the cells still offer a very good cycling behavior. This is related to the electron-deficient boron atoms, which interact with electron-rich anions (e.g. PF₆⁻) and stabilize the SPI. Another special case is 0.5% HMDS, which is explained above.

By means of the analysis of the TTSP-derived SPI more precise information on the film composition could be gathered. Here, the organic phase of the layer is located at the cathode underneath the inorganic phase, which is positioned towards the electrolyte side. This

coincides with the results reported by Edström and Eriksson et al., who conducted XPS depth profile analyses of manganese spinel electrodes stored or cycled at 60 °C. [465,466]

Moreover, it should be noted that in this thesis TFPI-, HMDS-, SEN-, and TEHP-derived surface layers on high voltage spinel cathodes have been analyzed for the first time. Cycled C//LiNi_{0.4}Mn_{1.6}O₄ pouch cells with Al₂O₃-modified electrodes were not investigated by XPS owing to the thickness of the ceramic layer.

Electrochemical impedance spectroscopy of formatted and cycled C//LiNi_{0.4}Mn_{1.6}O₄ pouch cells enabled a deeper comprehension of the mechanism of each electrolyte additive and the Al₂O₃ coating layers regarding the entire full cell. For all cycled C//LiNi_{0.4}Mn_{1.6}O₄ pouch cells R_i , R_s , and R_{ct} of all cells have markedly increased in comparison to the formatted samples. Nevertheless, the additives, which have improved the cycling behavior of the spinel full cells (0.5% TMP, 0.5% TFPI, 0.5% LiBOB, 0.5% HMDS, and 0.5% HFiP) lead to lower or at least similar resistances than those of the cell with the base electrolyte. In contrast, additives, which have accelerated the capacity decay of C//LiNi_{0.4}Mn_{1.6}O₄ pouch cells (1.7% TTSP, 1% SEN, 2.5% FEC, 0.5% TEHP, and 2.5% SA) cause higher or nearly identical resistances than the base electrolyte. Besides, it is supposed that TFPI, LiBOB, HMDS, HFiP, and FEC also participate in the SEI formation as the corresponding cells reveal higher R_s values than expected from XPS measurements. In general, it is found that the surface film on the cathode has a strong impact on the cycling behavior of the full cells. Thereby, surface films primarily consisting of phosphates and fluorophosphates are more stable under oxidative conditions as those based on carbonyl compounds (mainly carbonates). The latter are more reactive towards PF₅ or POF₃ and are likely to decompose to CO₂ and alkyl fluorides. Moreover, the negative inductive effect of the oxygen atoms is much more pronounced in carbonates than in phosphates owing to the nature of their chemical bonds. While in carbonates only electrons from the second shell are involved in the chemical bonds, phosphorus in phosphates provides electrons from the third shell for bonding with oxygen. Consequently, carbonates are much stronger molecular dipoles than phosphates, provoke stronger polarizations, and establish much thicker electrochemical double layers at the electrolyte-film and film-particle interfaces. Thus, they are the main reason for enhanced charge-transfer resistances of C//LiNi_{0.4}Mn_{1.6}O₄ pouch cells. The carbonate-based additive LiBOB is an exception due to the presence of electron-deficient boron within the structure. It is likely to form Lewis acid-base adducts with electron-rich anions such as PF₆⁻.

Regarding the cells containing Al₂O₃-coated electrodes, surprisingly, lower resistances (R_i , R_s , and R_{ct}) in comparison to the cell with bare electrodes are detected after 250 cycles. Thus, Al₂O₃ coating layers indeed restrain undesired side reactions during cycling (e.g. electrolyte decomposition), inhibit the generation of resistive layers, and suppress the development of

impedances. Besides, the protective effect of Al_2O_3 films does not hinder lithium ion transfer as R_{ct} is also smaller compared to the reference.

Finally the **cycling characteristics of C//LiNi_{0.4}Mn_{1.6}O₄ pouch cells** were further improved based on the findings of the electrochemical, microscopic, and spectroscopic analyses. Thereto, 1C CC/CV-cycling experiments were conducted with spinel full cells comprising various modifications at 45 °C in the voltage region of 3.3 - 4.8 V. It was found that the spinel full cell including a combination of an Al_2O_3 -modified spinel electrode and a base electrolyte modified with 0.5% TMP and 0.1% LiBOB enhances the cycling performance. Actually, the cell delivered the best cycling behavior. It is assumed that TMP and LiBOB establish protective and low-impedance surface films. Both additives reduce Mn and Ni depletion from the composite spinel electrode. Al_2O_3 coating effectively prevents transition metal dissolution and inhibits the production of resistive and thick surface films. Hence, it was shown, for the first time, that the cycling characteristics of C//LiNi_{0.4}Mn_{1.6}O₄ pouch cells are considerably improved by the combination of adding 0.5% TMP and 0.1% LiBOB to the base electrolyte and coating the spinel electrode with an Al_2O_3 -based ceramic layer.

All in all, this thesis provides the first detailed and comprehensive investigation of C//LiNi_{0.4}Mn_{1.6}O₄ full cells including electrochemical, spectroscopic, and microscopic methods. Table 19 gives an overview on the main results gained within in this thesis.

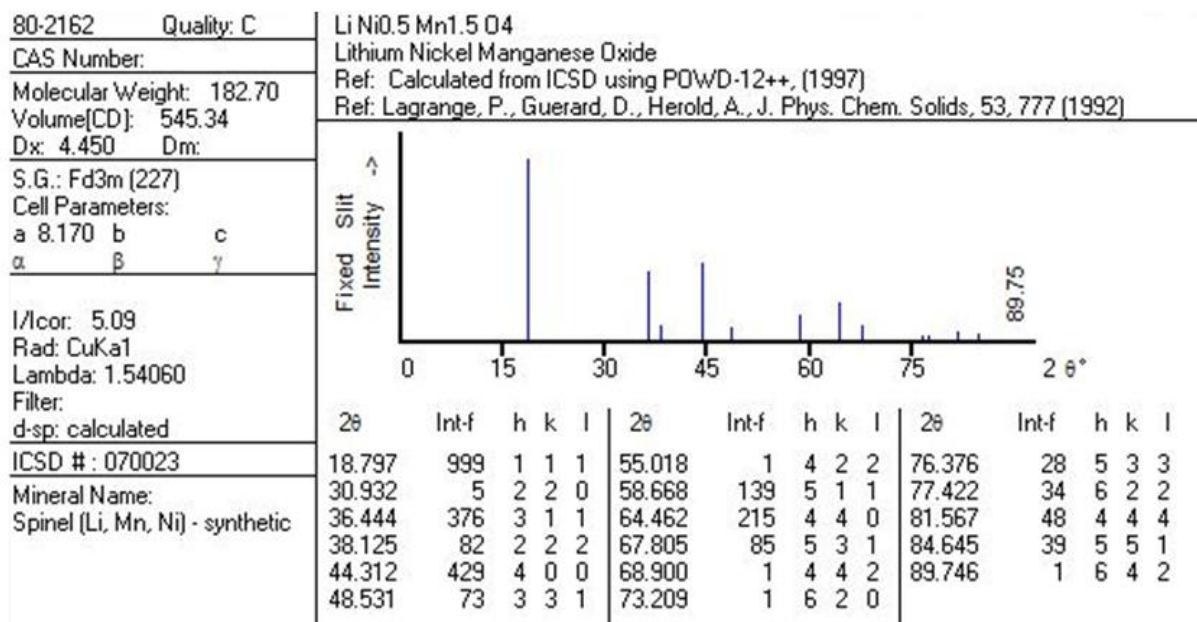
Modification	Ranking of the cycling stability	Influence on the cycling stability	Phase composition of the $\text{LiNi}_{0.4}\text{Mn}_{1.6}\text{O}_4$ cathode	Reduction of the transition metal dissolution	Ranking of the SPI thicknesses	Carbonyl-rich SPI (mainly carbonates)	Phosphate-rich SPI	Reduction of the charge-transfer resistance
0.5% TMP	1	+	2. cubic phase	++	0		✓	+++
0.5% TFPi	2	+	2. cubic phase	++	0		✓	+
0.5% LiBOB	3	+	2. and 3. cubic phase	++	--	✓		++
Al_2O_3 layer on both electrodes	4	+	2. and 3. cubic phase	+++	not examined	not examined	not examined	+
0.5% HMDS	5	+	2. and 3. cubic phase	+	---			++
0.5% HFiP	6	+	2. and 3. cubic phase	+	-		✓	+
reference	7	0	2. and 3. cubic phase	0	0	✓		0
1.7% TTSP	8	-	3. cubic phase	-	+++	✓	✓	-
1% SEN	9	-	3. cubic phase	-	+	✓		--
2.5% FEC	10	-	3. cubic phase	--	-	✓		-
0.5% TEHP	11	-	3. cubic phase	---	+	✓	✓	--
1.5% LiTFSI	12	-	3. cubic phase	--	not examined	not examined	not examined	not examined
2.5% SA	13	-	3. cubic phase	---	+	✓		---

Table 19 Overview on the main results gained within this thesis.

7. Appendix

7.1 X-ray diffraction

A



B

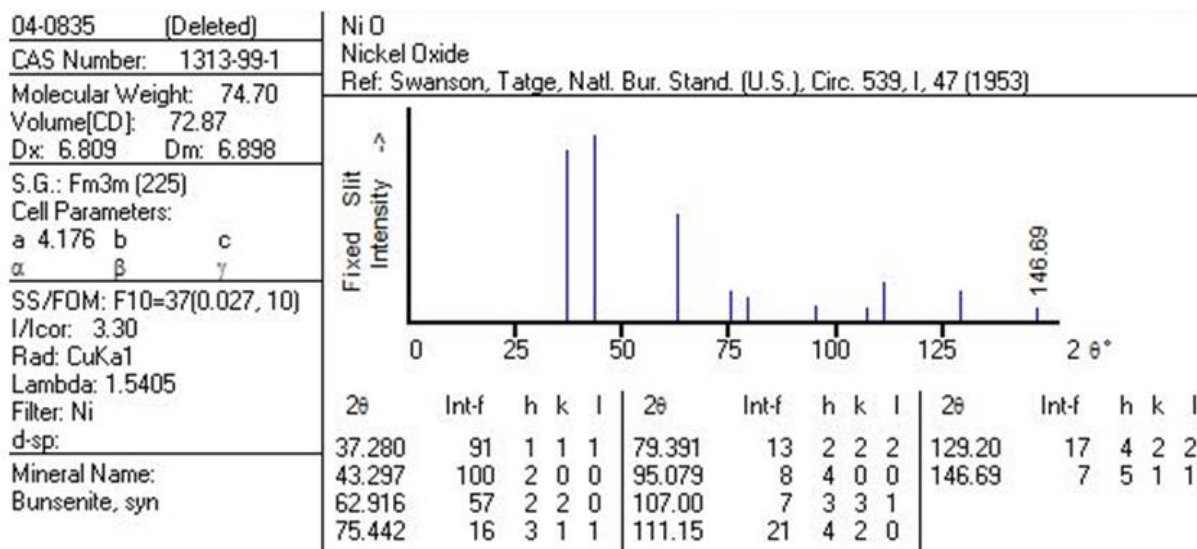


Figure 138 Standard XRD data and patterns for A LiNi_{0.5}Mn_{1.5}O₄ and B NiO.

7.2 Raman spectroscopy

Fitted Raman spectra of formatted $\text{LiNi}_{0.4}\text{Mn}_{1.6}\text{O}_4$ cathodes

First cubic phase

Symmetry species	0.5% TMP	0.5% TFPi	0.5% LiBOB	0.5% HMDS	0.5% HFIP	1.7% TTSP	1% SEN	2.5% FEC	0.5% TEHP	1.5% LiTFSI	2.5% SA
T_{2g}^3	163 220	163 220	161 220	163 220	163 220	163 118	161 118	163 220	163 220	163 118	163 220
E_g	407	409	407	407	409	407	407	407	407	407	407
T_{2g}^2	474	475	474	475	475	475	475	475	474	474	475
T_{2g}^2	500 524	500 525	498 524	500 525	500 525	498 525	498 525	500 525	498 525	498 525	500 525
A_{1g}	594	594	592	594	594	592	592	594	594	592	594
A_{1g}	613	613	613	613	615	613	613	613	613	613	615
A_{1g}	640	640	638	638	640	638	638	640	638	638	640
T_{2g}^1	666	666	664	664	666	664	664	664	664	664	664

Table 20 Assignments and positions of the Raman active modes in cm^{-1} of formatted $\text{LiNi}_{0.4}\text{Mn}_{1.6}\text{O}_4$ cathodes (0% SOC) in cells with various electrolyte additives resulting in the first cubic phase.

Symmetry species	Al_2O_3 coating layer on anode and cathode
T_{2g}^3	163, 220
E_g	407
T_{2g}^2	475
T_{2g}^2	500, 525
A_{1g}	594
A_{1g}	615
A_{1g}	640
T_{2g}^1	666

Table 21 Assignments and positions of the Raman active modes in cm^{-1} of formatted $\text{LiNi}_{0.4}\text{Mn}_{1.6}\text{O}_4$ cathodes (0% SOC) in cells with Al_2O_3 -modified electrodes resulting in the first cubic phase.

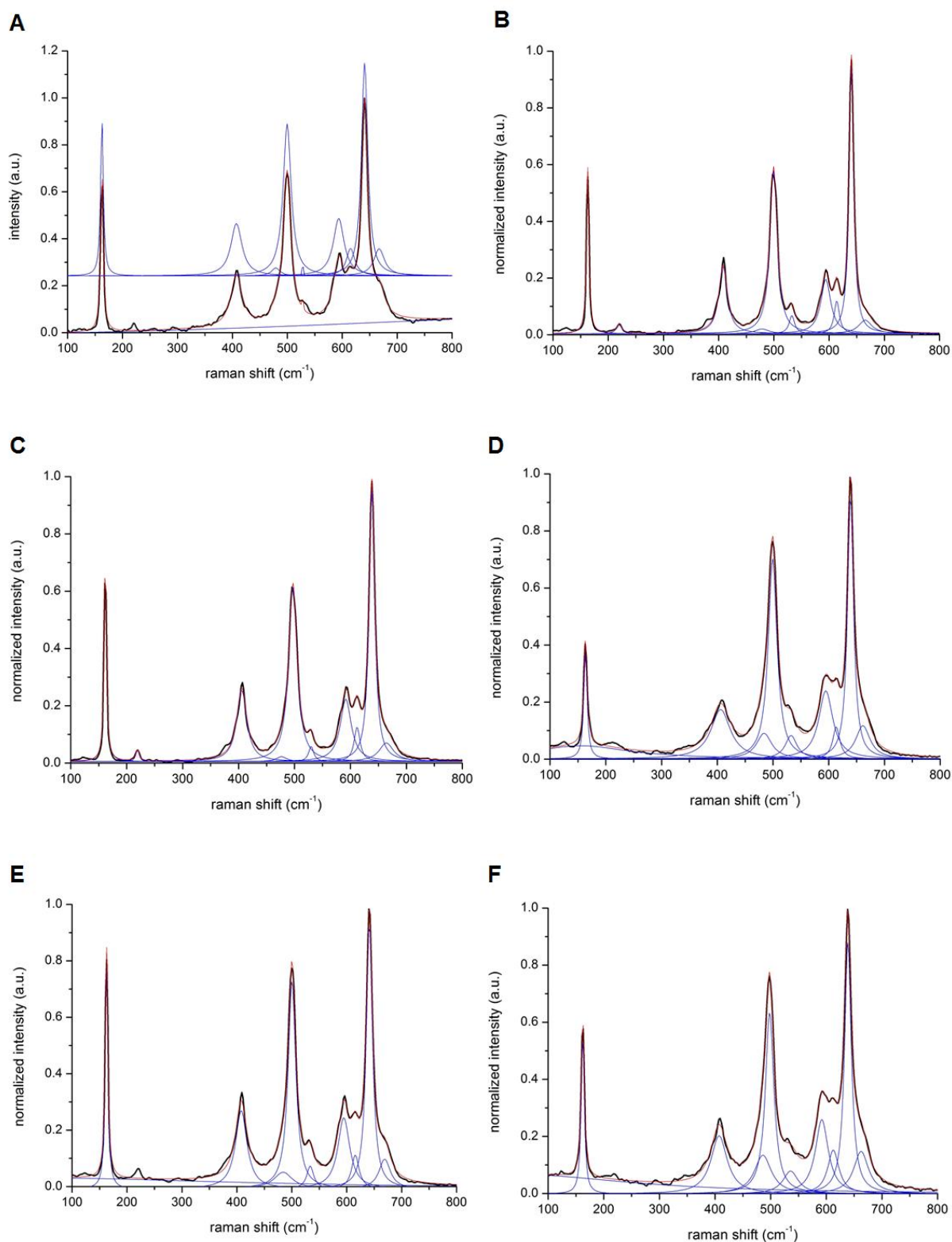


Figure 139 Raman spectra of completely discharged $\text{LiNi}_{0.4}\text{Mn}_{1.6}\text{O}_4$ cathodes after formation at 23 °C with **A** 0.5% TMP, **B** 0.5% TFPI, **C** 0.5% LiBOB, **D** 0.5% HMDS, **E** 0.5% HFIP, and **F** 1.7% TTSP leading to the first cubic phase.

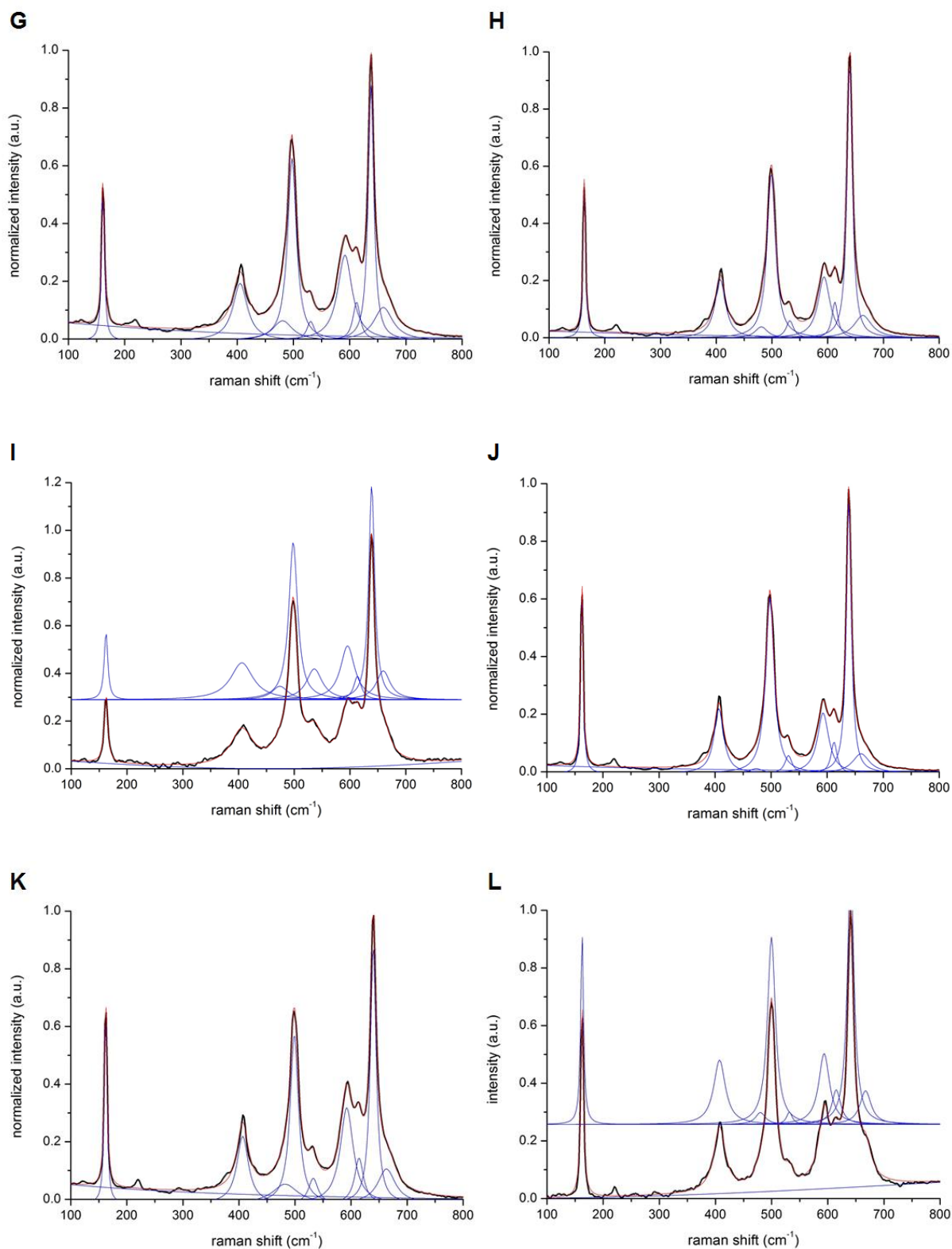


Figure 140 Raman spectra of completely discharged $\text{LiNi}_{0.4}\text{Mn}_{1.6}\text{O}_4$ cathodes after formation at 23 °C with **G** 1% SEN, **H** 2.5% FEC, **I** 0.5% TEHP, **J** 0.5% LiTFSI, **K** 2.5% SA, and **L** Al_2O_3 -modified electrodes leading to the first cubic phase.

Fitted Raman spectra of cycled $\text{LiNi}_{0.4}\text{Mn}_{1.6}\text{O}_4$ cathodes

Second cubic phase

Symmetry species	0.5% TMP	0.5% TFPi	0.5% LiBOB	0.5% HMDS	0.5% HFiP	Al_2O_3 coating layer on anode and cathode
T_{2g}^3	163	163	163	163	163	163
T_{2g}^2	300 - 600	300 - 600	300 - 600	300 - 600	300 - 600	300 - 600
$T_{2g}^2 (\text{Li}_x\text{Ni}_{1-x}\text{O})$	498	498	500	500	500	498
T_{2g}^2	530	532	532	532	530	530
T_{2g}^2	541	541	542	542	542	542
A_{1g}	590	592	592	590	590	592
A_{1g}	638	638	640	640	638	640

Table 22 Assignments and positions of the Raman active modes in cm^{-1} of cycled $\text{LiNi}_{0.4}\text{Mn}_{1.6}\text{O}_4$ cathodes (0% SOC) in cells with various electrolyte additives and Al_2O_3 -modified electrodes resulting in the second cubic phase.

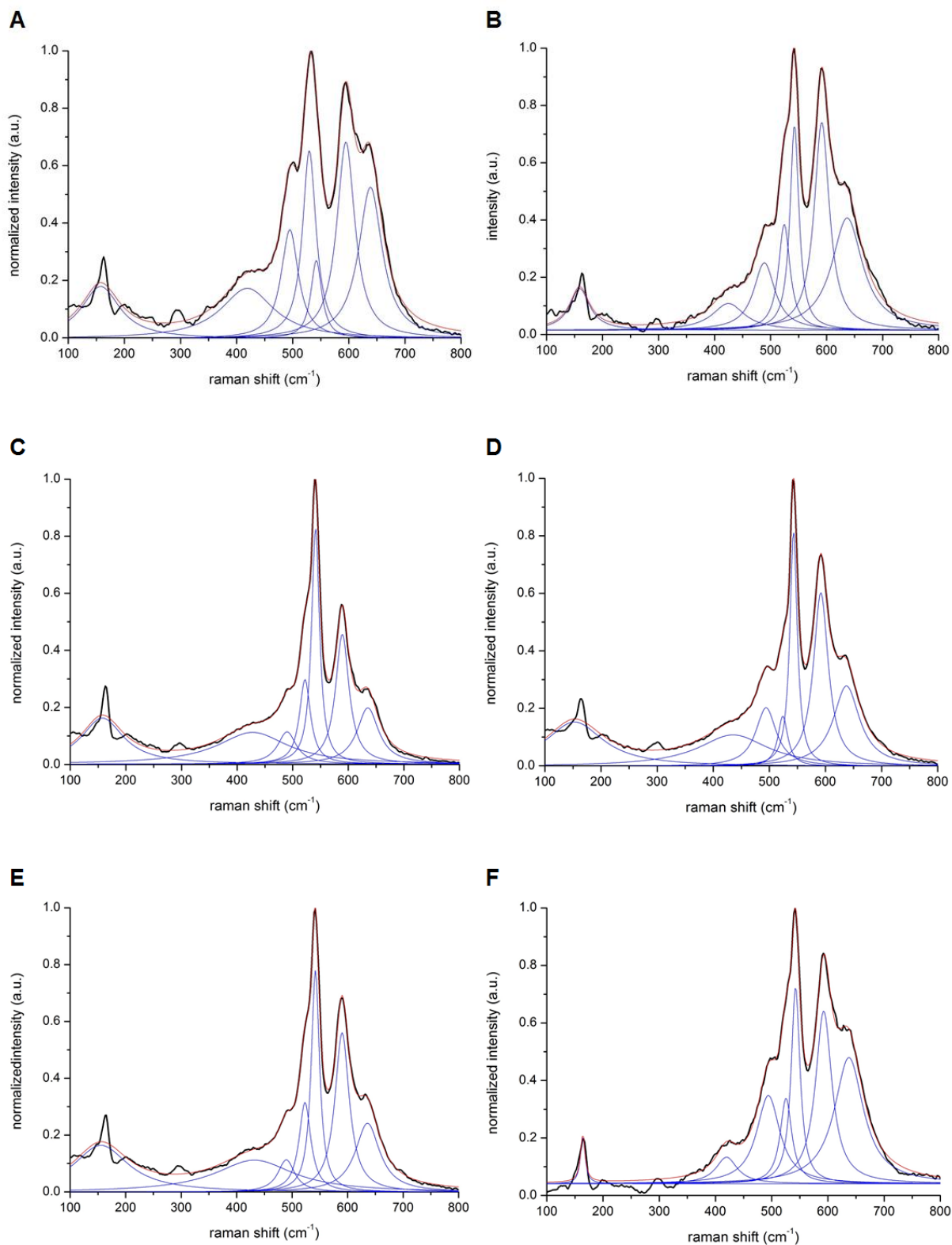


Figure 141 Raman spectra of completely discharged $\text{LiNi}_{0.4}\text{Mn}_{1.6}\text{O}_4$ cathodes after 250 cycles at 45 °C with **A** 0.5% TMP, **B** 0.5% TFPI, **C** 0.5% LiBOB, **D** 0.5% HMDS, **E** 0.5% HFIP, and **F** Al_2O_3 -modified electrodes leading to the second cubic phase.

Third cubic phase

Symmetry species	0.5% LiBOB	0.5% HMDS	0.5% HFIP	1.7% TTSP	1% SEN	2.5% FEC	0.5% TEHP	1.5% LiTFSI	2.5% SA
T_{2g}^3	163	163	163	165	163	163	165	165	163
T_{2g}^2	468	468	470	470	470	468	468	470	468
$T_{2g}^2 (Li_xNi_{1-x}O)$	498	500	500	498	500	500	500	498	500
T_{2g}^2	530	532	530	530	530	530	530	530	530
T_{2g}^2	541	542	542	542	542	542	542	542	542
A_{1g}	590	592	590	590	590	590	590	590	590
A_{1g}	638	640	638	638	638	640	638	638	638

Table 23 Assignments and positions of the Raman active modes in cm^{-1} of cycled $LiNi_{0.4}Mn_{1.6}O_4$ cathodes (0% SOC) in cells with various electrolyte additives resulting in the third cubic phase.

Symmetry species	Al_2O_3 coating layer on anode and cathode
T_{2g}^3	163
T_{2g}^2	468
$T_{2g}^2 (Li_xNi_{1-x}O)$	498
T_{2g}^2	530
T_{2g}^2	542
A_{1g}	590
A_{1g}	638

Table 24 Assignments and positions of the Raman active modes in cm^{-1} of cycled $LiNi_{0.4}Mn_{1.6}O_4$ cathodes (0% SOC) in cells with Al_2O_3 -modified electrodes resulting in the third cubic phase.

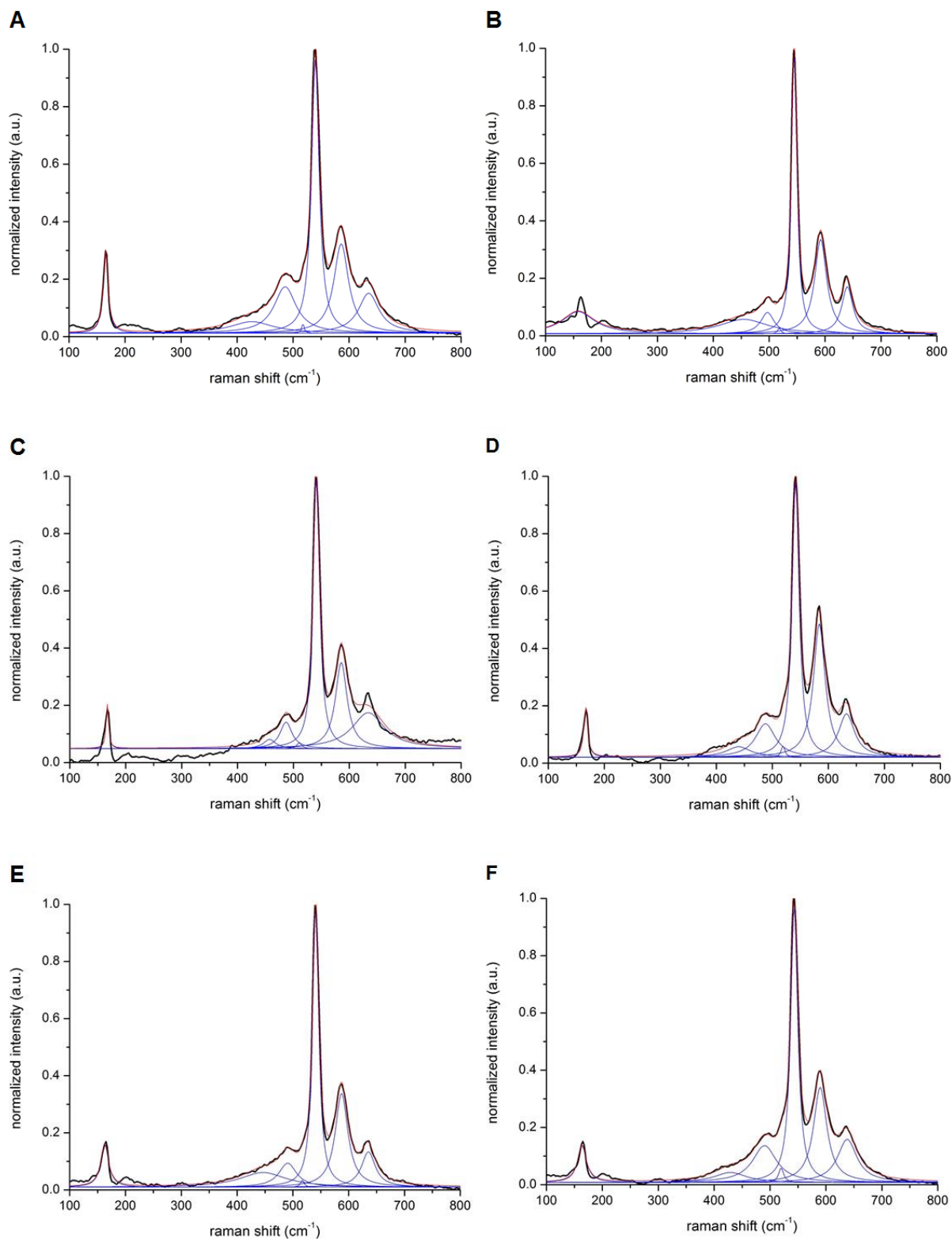


Figure 142 Raman spectra of completely discharged $\text{LiNi}_{0.4}\text{Mn}_{1.6}\text{O}_4$ cathodes after 250 cycles at 45 °C with **A** 0.5% LiBOB, **B** 0.5% HMDS, **C** 0.5% HFIP, **D** 1.7% TTSP, **E** 1% SEN, and **F** 2.5% FEC leading to the third cubic phase.

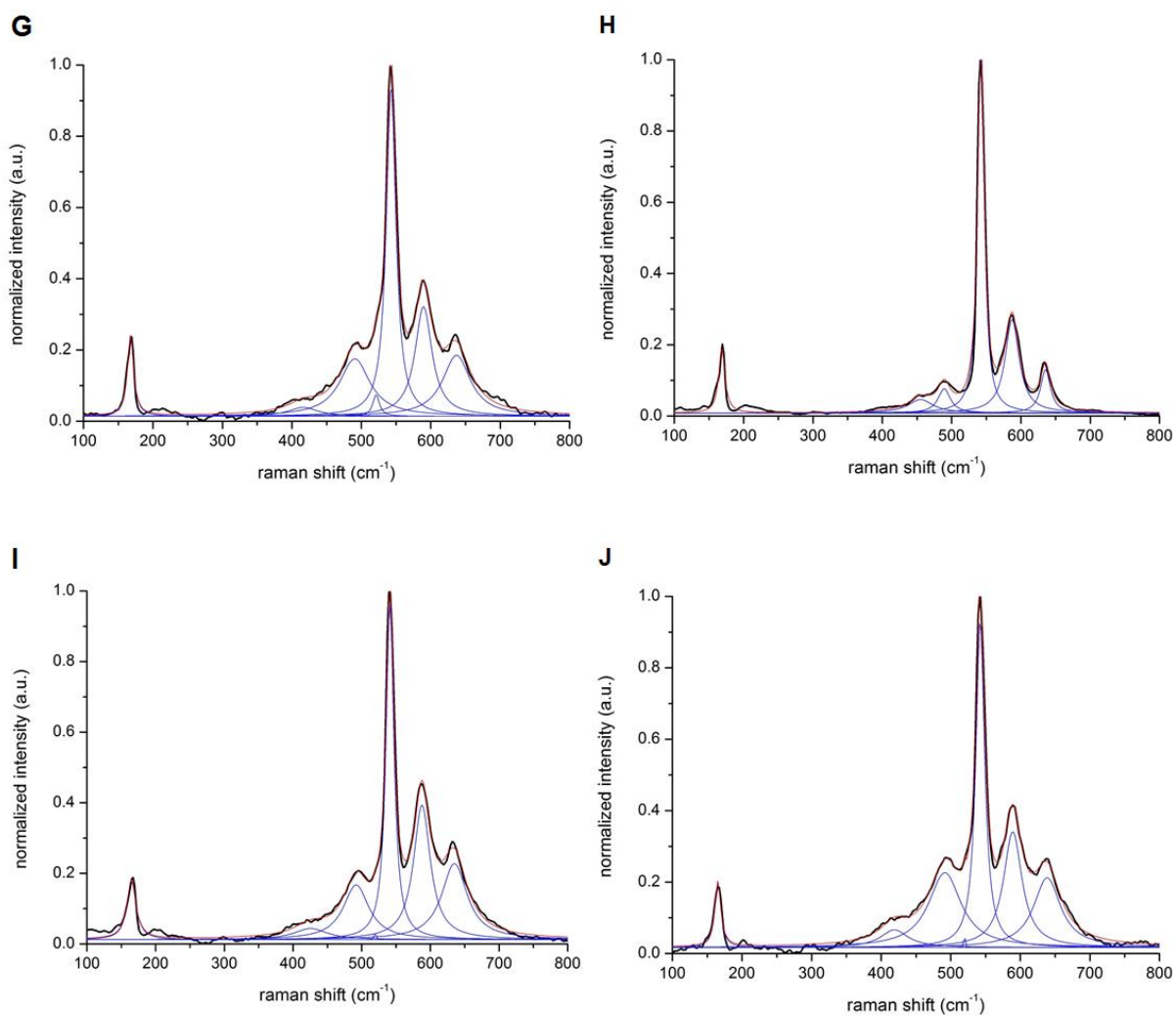


Figure 143 Raman spectra of completely discharged $\text{LiNi}_{0.4}\text{Mn}_{1.6}\text{O}_4$ cathodes after 250 cycles at 45 °C with **G** 0.5% TEHP, **H** 1.5% LiTFSi, **I** 2.5% SA, and **J** Al_2O_3 -modified electrodes leading to the third cubic phase.

7.3 X-ray photoelectron spectroscopy

Reference

C1s

Signal	Binding energy (eV)	FWHM (a.u.)	Area (CPSeV)	Area (%)
C-C				
After formation	284.5	1.2	1999	33.9
After cycling	285.0	1.7	2177	29.7
CH₂				
After formation	285.8	1.4	1863	31.6
After cycling	286.1	1.7	2105	28.8
C-O				
After formation	287.1	1.4	852	14.4
After cycling	287.3	1.7	1417	19.4
C=O				
After formation	288.8	1.4	471	8.0
After cycling	289.1	1.7	911	12.4
CF₂				
After formation	290.3	1.4	716	12.1
After cycling	290.3	1.5	711	9.7

Table 25 Experimental data of the C1s spectra of LiNi_{0.4}Mn_{1.6}O₄ cathodes after formatting C//LiNi_{0.4}Mn_{1.6}O₄ pouch cells containing the base electrolyte at 23 °C and after cycling these cells for 250 cycles at 45 °C.

O1s

Signal	Binding energy (eV)	FWHM (a.u.)	Area (CPSeV)	Area (%)
O²⁻				
After formation	529.5	1.7	1675	29.7
After cycling	529.3	1.8	1584	14.8
C=O				
After formation	532.1	1.9	1982	35.1
After cycling	532.1	2.0	3958	36.9
C-O				
After formation	533.7	1.9	1991	35.2
After cycling	533.8	2.0	5200	48.4

Table 26 Experimental data of the O1s spectra of LiNi_{0.4}Mn_{1.6}O₄ cathodes after formatting C//LiNi_{0.4}Mn_{1.6}O₄ pouch cells containing the base electrolyte at 23 °C and after cycling these cells for 250 cycles at 45 °C.

F1s

Signal	Binding energy (eV)	FWHM (a.u.)	Area (CPS eV)	Area (%)
LiF, NiF₂, MnF₂				
After formation	684.7	2.2	229	3.5
After cycling	684.0	2.3	639	7.2
Li_xPF_y, Li_xPF_yO_z, O=PFOR				
After formation	686.8	2.1	1326	20.0
After cycling	686.9	2.1	4674	52.6
CF₂				
After formation	687.6	2.0	5068	76.5
After cycling	687.6	2.1	3567	40.2

Table 27 Experimental data of the F1s spectra of LiNi_{0.4}Mn_{1.6}O₄ cathodes after formatting C//LiNi_{0.4}Mn_{1.6}O₄ pouch cells containing the base electrolyte at 23 °C and after cycling these cells for 250 cycles at 45 °C.

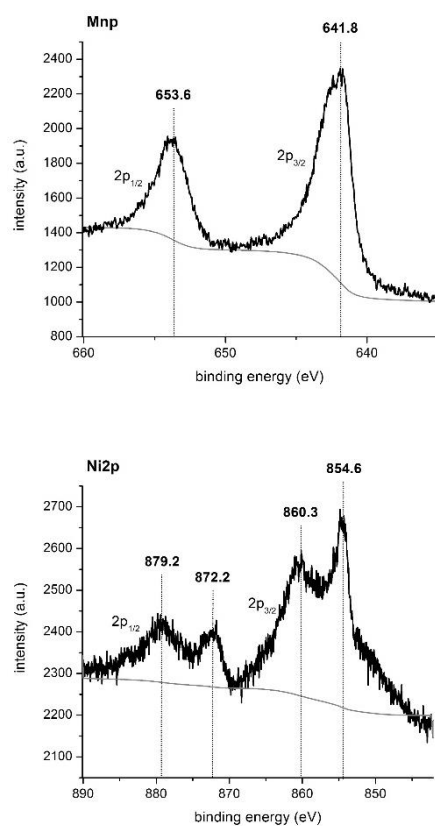
P2p

Signal	Binding energy (eV)	FWHM (a.u.)	Area (CPS eV)	Area (%)
PO₄³⁻				
After formation	133.3	2.1	18	8.1
After cycling	133.6	1.9	40	7.7
Li_xPF_yO_z, O=PFOR				
After formation	134.5	2.0	121	56.0
After cycling	134.7	2.0	196	37.9
Li_xPF_y				
After formation	136.3	2.1	77	35.9
After cycling	136.5	2.0	283	54.5

Table 28 Experimental data of the P2p spectra of LiNi_{0.4}Mn_{1.6}O₄ cathodes after formatting C//LiNi_{0.4}Mn_{1.6}O₄ pouch cells containing the base electrolyte at 23 °C and after cycling these cells for 250 cycles at 45 °C.

Trimethyl phosphate

A



B

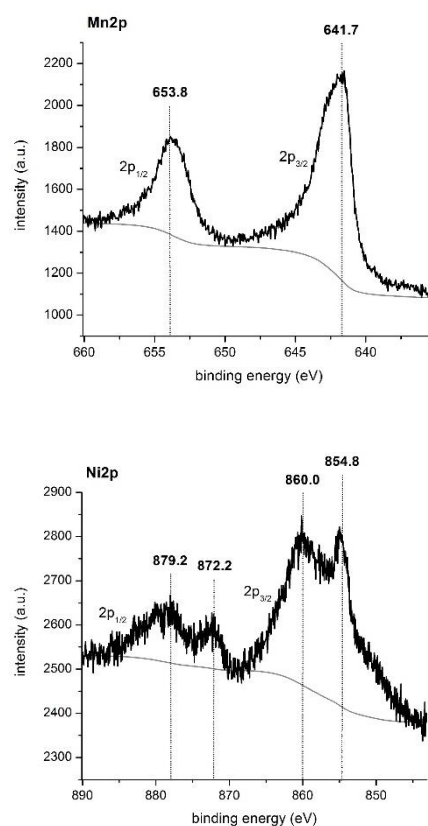


Figure 144 XPS spectra of LiNi_{0.4}Mn_{1.6}O₄ electrodes at 0% SOC after **A** formation C//LiNi_{0.4}Mn_{1.6}O₄ pouch cells with 0.5% TMP at 23 °C and after **B** cycling these cells for 250 cycles at 45 °C.

C1s

Signal	Binding energy (eV)	FWHM (a.u.)	Area (CPS _{SeV})	Area (%)
C-C				
After formation	284.5	1.2	1725	25.9
After cycling	284.7	1.6	1560	21.4
CH₂				
After formation	285.7	1.3	1565	23.5
After cycling	285.9	1.5	2340	32.1
C-O				
After formation	286.8	1.6	1517	22.8
After cycling	287.1	1.7	1527	21.0
C=O				
After formation	288.8	1.9	616	9.2
After cycling	288.9	1.4	604	8.3
CF₂				
After formation	290.3	1.7	1242	18.6
After cycling	290.2	1.7	1254	17.2

Table 29 Experimental data of the C1s spectra of LiNi_{0.4}Mn_{1.6}O₄ cathodes after formatting C//LiNi_{0.4}Mn_{1.6}O₄ pouch cells with 0.5% TMP at 23 °C and after cycling these cells for 250 cycles at 45 °C.

O1s

Signal	Binding energy (eV)	FWHM (a.u.)	Area (CPS _{SeV})	Area (%)
O²⁻				
After formation	529.4	1.3	2314	26.0
After cycling	529.3	1.3	1951	18.2
C=O				
After formation	531.9	2.2	3182	35.7
After cycling	531.9	2.3	3210	30.0
C-O				
After formation	533.6	2.1	3410	38.4
After cycling	533.7	2.3	5532	51.7

Table 30 Experimental data of the O1s spectra of LiNi_{0.4}Mn_{1.6}O₄ cathodes after formatting C//LiNi_{0.4}Mn_{1.6}O₄ pouch cells with 0.5% TMP at 23 °C and after cycling these cells for 250 cycles at 45 °C.

F1s

Signal	Binding energy (eV)	FWHM (a.u.)	Area (CPSeV)	Area (%)
LiF, NiF₂, MnF₂				
After formation	684.3	2.0	310	3.7
After cycling	684.4	1.2	251	2.9
Li_xPF_y, Li_xPF_yO_z, O=PFOR				
After formation	687.0	2.0	2510	29.5
After cycling	686.9	2.1	5275	61.2
CF₂				
After formation	687.6	2.0	5693	66.9
After cycling	687.6	2.1	3091	35.9

Table 31 Experimental data of the F1s spectra of LiNi_{0.4}Mn_{1.6}O₄ cathodes after formatting C//LiNi_{0.4}Mn_{1.6}O₄ pouch cells with 0.5% TMP at 23 °C and after cycling these cells for 250 cycles at 45 °C.

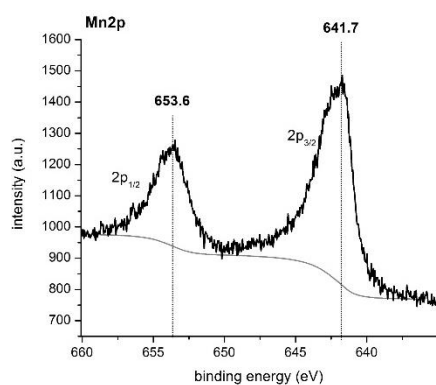
P2p

Signal	Binding energy (eV)	FWHM (a.u.)	Area (CPSeV)	Area (%)
PO₄³⁻				
After formation	133.4	1.5	63	22.1
After cycling	133.7	1.5	95	15.7
Li_xPF_yO_z, O=PFOR				
After formation	134.6	1.7	155	54.0
After cycling	135.1	2.4	343	56.9
Li_xPF_y				
After formation	136.3	1.6	68.9	24.0
After cycling	136.8	1.6	165	27.4

Table 32 Experimental data of the P2p spectra of LiNi_{0.4}Mn_{1.6}O₄ cathodes after formatting C//LiNi_{0.4}Mn_{1.6}O₄ pouch cells with 0.5% TMP at 23 °C and after cycling these cells for 250 cycles at 45 °C.

Tris(2,2,2-trifluoroethyl)phosphite

A



B

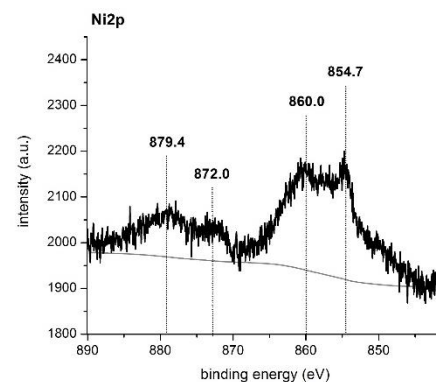
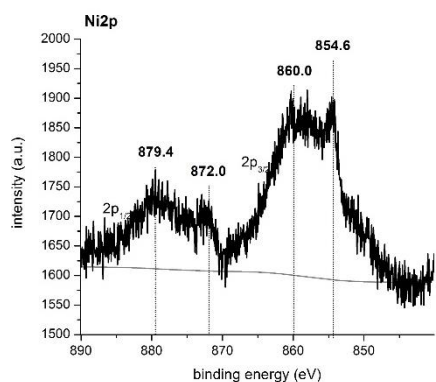
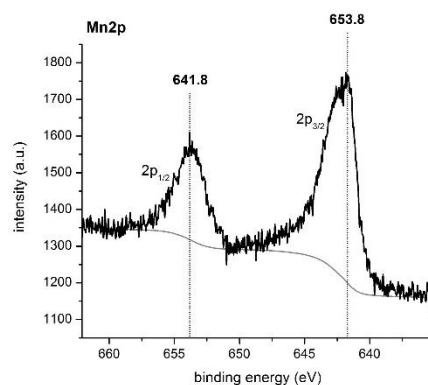


Figure 145 XPS spectra of LiNi_{0.4}Mn_{1.6}O₄ electrodes at 0% SOC after **A** formation C//LiNi_{0.4}Mn_{1.6}O₄ pouch cells with 0.5% TFPi at 23 °C and after **B** cycling these cells for 250 cycles at 45 °C.

C1s

Signal	Binding energy (eV)	FWHM (a.u.)	Area (CPSeV)	Area (%)
C-C				
After formation	284.6	1.2	2419	41.9
After cycling	284.7	1.7	1530	19.6
CH₂				
After formation	285.9	1.3	1469	25.4
After cycling	285.9	1.7	2788	35.6
C-O				
After formation	287.1	1.3	785	13.6
After cycling	287.2	1.7	1858	23.8
C=O				
After formation	288.8	1.4	444	7.7
After cycling	289.0	1.7	698	8.9
CF₂				
After formation	290.3	1.4	658	11.4
After cycling	290.2	1.7	949	12.1

Table 33 Experimental data of the C1s spectra of LiNi_{0.4}Mn_{1.6}O₄ cathodes after formatting C//LiNi_{0.4}Mn_{1.6}O₄ pouch cells with 0.5% TFPi at 23 °C and after cycling these cells for 250 cycles at 45 °C.

O1s

Signal	Binding energy (eV)	FWHM (a.u.)	Area (CPSeV)	Area (%)
O²⁻				
After formation	529.5	1.7	1684	31.5
After cycling	529.4	1.6	1282	11.0
C=O				
After formation	532.0	1.9	1821	34.0
After cycling	532.2	1.9	4554	39.2
C-O				
After formation	533.7	1.9	1847	34.5
After cycling	533.8	1.9	5790	49.5

Table 34 Experimental data of the O1s spectra of LiNi_{0.4}Mn_{1.6}O₄ cathodes after formatting C//LiNi_{0.4}Mn_{1.6}O₄ pouch cells with 0.5% TFPi at 23 °C and after cycling these cells for 250 cycles at 45 °C.

F1s

Signal	Binding energy (eV)	FWHM (a.u.)	Area (CPS _{SeV})	Area (%)
LiF, NiF₂, MnF₂				
After formation	684.2	1.1	266	3.6
After cycling	684.6	1.8	155	2.7
Li_xPF_y, Li_xPF_yO_z, O=PFOR				
After formation	686.9	2.1	1944	26.4
After cycling	687.0	2.0	2046	34.8
CF₂				
After formation	687.7	2.1	5154	70.0
After cycling	687.8	2.2	3678	62.6

Table 35 Experimental data of the F1s spectra of LiNi_{0.4}Mn_{1.6}O₄ cathodes after formatting C//LiNi_{0.4}Mn_{1.6}O₄ pouch cells with 0.5% TFPi at 23 °C and after cycling these cells for 250 cycles at 45 °C.

P2p

Signal	Binding energy (eV)	FWHM (a.u.)	Area (CPS _{SeV})	Area (%)
PO₄³⁻				
After formation	133.6	1.9	61	21.6
After cycling	133.7	2.0	86	18.0
Li_xPF_yO_z, O=PFOR				
After formation	134.6	1.9	147	52.3
After cycling	134.7	2.0	297	62.4
Li_xPF_y				
After formation	136.4	1.8	74	26.2
After cycling	136.2	2.0	94	19.7

Table 36 Experimental data of the P2p spectra of LiNi_{0.4}Mn_{1.6}O₄ cathodes after formatting C//LiNi_{0.4}Mn_{1.6}O₄ pouch cells with 0.5% TFPi at 23 °C and after cycling these cells for 250 cycles at 45 °C.

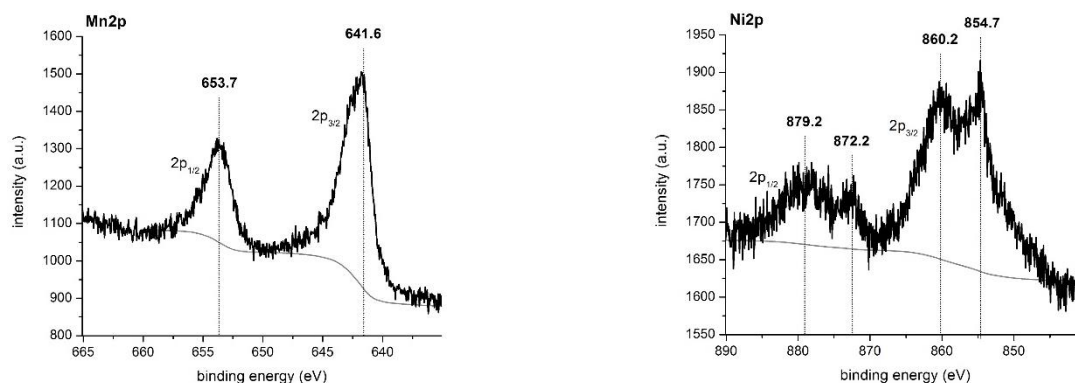
Lithium bis(oxalato)borate

Figure 146 XPS spectra of $\text{LiNi}_{0.4}\text{Mn}_{1.6}\text{O}_4$ electrodes at 0% SOC after cycling C// $\text{LiNi}_{0.4}\text{Mn}_{1.6}\text{O}_4$ pouch cells with 0.5% LiBOB for 250 cycles at 45 °C between 3.3 and 4.8 V.

C1s

Signal	Binding energy (eV)	FWHM (a.u.)	Area (CPSeV)	Area (%)
C-C				
After cycling	284.5	1.2	1033	14.2
CH₂				
After cycling	285.7	1.7	2205	30.3
C-O				
After cycling	287.0	1.9	1873	25.8
C=O				
After cycling	289.0	2.3	1355	18.6
CF₂				
After cycling	290.5	1.6	807	11.1

Table 37 Experimental data of the C1s spectra of $\text{LiNi}_{0.4}\text{Mn}_{1.6}\text{O}_4$ cathodes after cycling C// $\text{LiNi}_{0.4}\text{Mn}_{1.6}\text{O}_4$ pouch cells for 250 cycles with 0.5% LiBOB at 45 °C.

O1s

Signal	Binding energy (eV)	FWHM (a.u.)	Area (CPSeV)	Area (%)
O²⁻				
After cycling	529.5	1.5	1171	13.7
C=O				
After cycling	532.2	2.1	3965	46.4
C-O				
After cycling	533.8	1.8	3414	39.9

Table 38 Experimental data of the O1s spectra of $\text{LiNi}_{0.4}\text{Mn}_{1.6}\text{O}_4$ cathodes after cycling C// $\text{LiNi}_{0.4}\text{Mn}_{1.6}\text{O}_4$ pouch cells for 250 cycles with 0.5% LiBOB at 45 °C.

F1s

Signal	Binding energy (eV)	FWHM (a.u.)	Area (CPS _{SeV})	Area (%)
LiF, NiF₂, MnF₂				
After cycling	684.8	2.1	212	3.2
Li_xPF_y, Li_xPF_yO_z, O=PFOR				
After cycling	687.0	2.0	2184	33.5
CF₂				
After cycling	687.7	1.8	4133	63.3

Table 39 Experimental data of the F1s spectra of LiNi_{0.4}Mn_{1.6}O₄ cathodes after cycling C//LiNi_{0.4}Mn_{1.6}O₄ pouch cells for 250 cycles with 0.5% LiBOB at 45 °C.

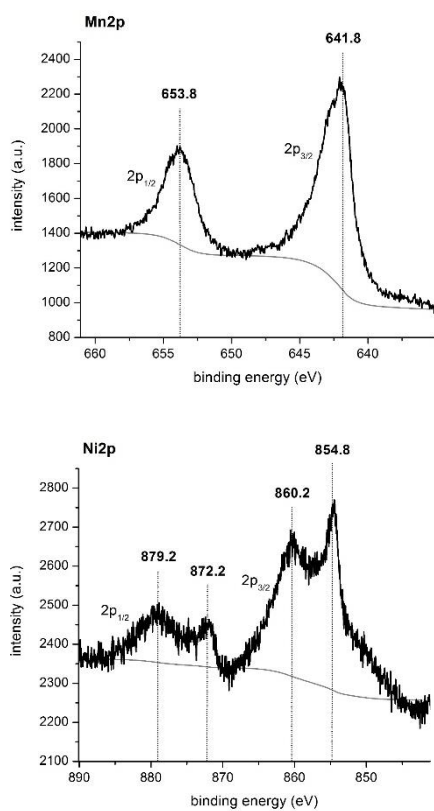
P2p

Signal	Binding energy (eV)	FWHM (a.u.)	Area (CPS _{SeV})	Area (%)
PO₄³⁻				
After cycling	133.3	1.4	10	4.2
Li_xPF_yO_z, O=PFOR				
After cycling	134.5	2.1	161	65.6
Li_xPF_y				
After cycling	136.2	2.3	74	30.2

Table 40 Experimental data of the P2p spectra of LiNi_{0.4}Mn_{1.6}O₄ cathodes after cycling C//LiNi_{0.4}Mn_{1.6}O₄ pouch cells for 250 cycles with 0.5% LiBOB at 45 °C.

Hexamethyldisilazane

A



B

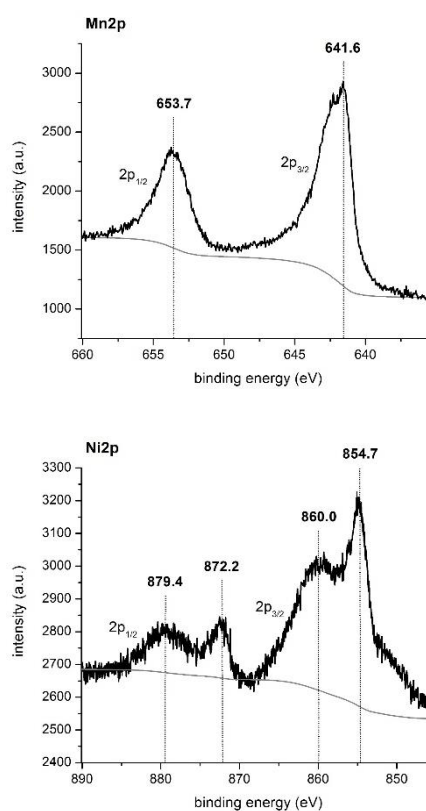


Figure 147 XPS spectra of LiNi_{0.4}Mn_{1.6}O₄ electrodes at 0% SOC after **A** formation C//LiNi_{0.4}Mn_{1.6}O₄ pouch cells with 0.5% HMDS at 23 °C and after **B** cycling these cells for 250 cycles at 45 °C.

C1s

Signal	Binding energy (eV)	FWHM (a.u.)	Area (CPS _{SeV})	Area (%)
C-C				
After formation	284.5	1.0	1447	23.5
After cycling	284.5	1.0	1734	31.9
CH₂				
After formation	285.7	1.6	2131	34.6
After cycling	285.7	1.3	1449	26.7
C-O				
After formation	287.0	2.2	1308	21.3
After cycling	286.9	1.6	1030	19.0
C=O				
After formation	289.1	2.0	659	10.7
After cycling	288.8	1.8	434	8.0
CF₂				
After formation	290.4	1.2	608	9.9
After cycling	290.2	1.3	782	14.4

Table 41 Experimental data of the C1s spectra of LiNi_{0.4}Mn_{1.6}O₄ cathodes after formatting C//LiNi_{0.4}Mn_{1.6}O₄ pouch cells with 0.5% HMDS at 23 °C and after cycling these cells for 250 cycles at 45 °C.

O1s

Signal	Binding energy (eV)	FWHM (a.u.)	Area (CPS _{SeV})	Area (%)
O²⁻				
After formation	529.5	1.2	2146	27.5
After cycling	529.3	1.1	2608	32.4
C=O				
After formation	531.9	2.3	2724	34.9
After cycling	531.4	2.5	2590	32.2
C-O				
After formation	533.6	2.2	2929	37.5
After cycling	533.5	2.4	2850	35.4

Table 42 Experimental data of the O1s spectra of LiNi_{0.4}Mn_{1.6}O₄ cathodes after formatting C//LiNi_{0.4}Mn_{1.6}O₄ pouch cells with 0.5% HMDS at 23 °C and after cycling these cells for 250 cycles at 45 °C.

F1s

Signal	Binding energy (eV)	FWHM (a.u.)	Area (CPSeV)	Area (%)
LiF, NiF₂, MnF₂				
After formation	684.8	2.0	234	2.4
After cycling	684.8	2.0	621	6.4
Li_xPF_y, Li_xPF_yO_z, O=PFOR				
After formation	687.0	1.9	3242	33.7
After cycling	686.9	2.0	4721	48.9
CF₂				
After formation	687.6	1.9	6156	63.9
After cycling	687.6	1.9	4310	44.7

Table 43 Experimental data of the F1s spectra of LiNi_{0.4}Mn_{1.6}O₄ cathodes after formatting C//LiNi_{0.4}Mn_{1.6}O₄ pouch cells with 0.5% HMDS at 23 °C and after cycling these cells for 250 cycles at 45 °C.

P2p

Signal	Binding energy (eV)	FWHM (a.u.)	Area (CPSeV)	Area (%)
PO₄³⁻				
After formation	132.8	1.9	16	5.0
After cycling	133.2	1.2	21	4.9
Li_xPF_yO_z, O=PFOR				
After formation	134.4	2.1	191	58.4
After cycling	134.4	1.9	286	66.4
Li_xPF_y				
After formation	136.4	2.1	119	36.6
After cycling	136.2	2.2	124	28.7

Table 44 Experimental data of the P2p spectra of LiNi_{0.4}Mn_{1.6}O₄ cathodes after formatting C//LiNi_{0.4}Mn_{1.6}O₄ pouch cells with 0.5% HMDS at 23 °C and after cycling these cells for 250 cycles at 45 °C.

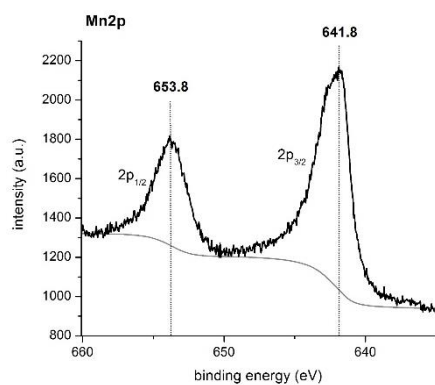
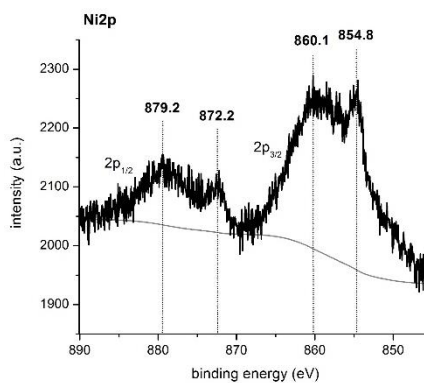
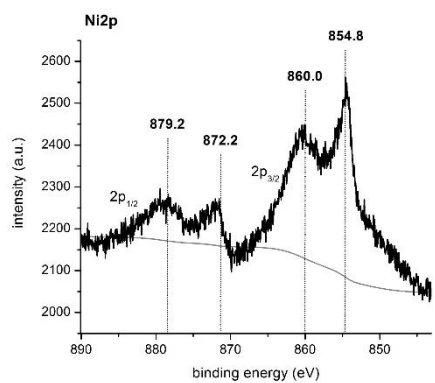
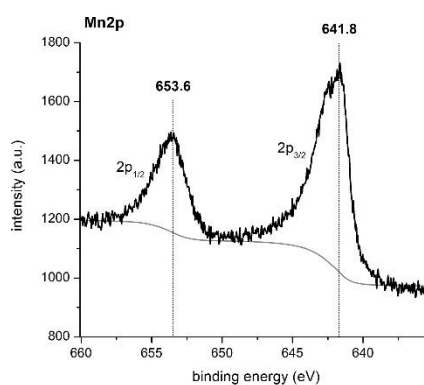
Tris-(1,1,1,3,3,3-hexafluoroisopropyl) phosphate**A****B**

Figure 148 XPS spectra of $\text{LiNi}_{0.4}\text{Mn}_{1.6}\text{O}_4$ electrodes at 0% SOC after **A** formation C// $\text{LiNi}_{0.4}\text{Mn}_{1.6}\text{O}_4$ pouch cells with 0.5% HFIP at 23 °C and after **B** cycling these cells for 250 cycles at 45 °C.

C1s

Signal	Binding energy (eV)	FWHM (a.u.)	Area (CPSeV)	Area (%)
C-C				
After formation	284.5	1.1	1196	21.2
After cycling	284.6	1.4	1092	16.8
CH₂				
After formation	285.7	1.6	1855	33.0
After cycling	285.7	1.5	2005	30.9
C-O				
After formation	286.9	1.6	955	17.0
After cycling	287.0	1.5	1407	21.7
C=O				
After formation	288.8	2.0	698	12.4
After cycling	288.8	1.7	948	14.6
CF₂				
After formation	290.3	1.6	923	16.4
After cycling	290.2	1.7	1039	16.0

Table 45 Experimental data of the C1s spectra of LiNi_{0.4}Mn_{1.6}O₄ cathodes after formatting C//LiNi_{0.4}Mn_{1.6}O₄ pouch cells with 0.5% HFIP at 23 °C and after cycling these cells for 250 cycles at 45 °C.

O1s

Signal	Binding energy (eV)	FWHM (a.u.)	Area (CPSeV)	Area (%)
O²⁻				
After formation	529.4	1.2	1942	25.7
After cycling	529.3	1.3	1303	12.2
C=O				
After formation	531.9	2.3	2791	36.9
After cycling	532.0	2.1	3974	37.1
C-O				
After formation	533.6	2.2	2826	37.4
After cycling	533.6	2.1	5427	50.7

Table 46 Experimental data of the O1s spectra of LiNi_{0.4}Mn_{1.6}O₄ cathodes after formatting C//LiNi_{0.4}Mn_{1.6}O₄ pouch cells with 0.5% HFIP at 23 °C and after cycling these cells for 250 cycles at 45 °C.

F1s

Signal	Binding energy (eV)	FWHM (a.u.)	Area (CPS eV)	Area (%)
LiF, NiF₂, MnF₂				
After formation	684.5	1.7	321	3.8
After cycling	685.2	1.2	199	2.6
Li_xPF_y, Li_xPF_yO_z, O=PFOR				
After formation	687.0	1.8	2275	26.8
After cycling	687.1	1.9	3593	46.1
CF₂				
After formation	687.6	2.2	5895	69.4
After cycling	688.0	2.3	4010	51.4

Table 47 Experimental data of the F1s spectra of LiNi_{0.4}Mn_{1.6}O₄ cathodes after formatting C//LiNi_{0.4}Mn_{1.6}O₄ pouch cells with 0.5% HFiP at 23 °C and after cycling these cells for 250 cycles at 45 °C.

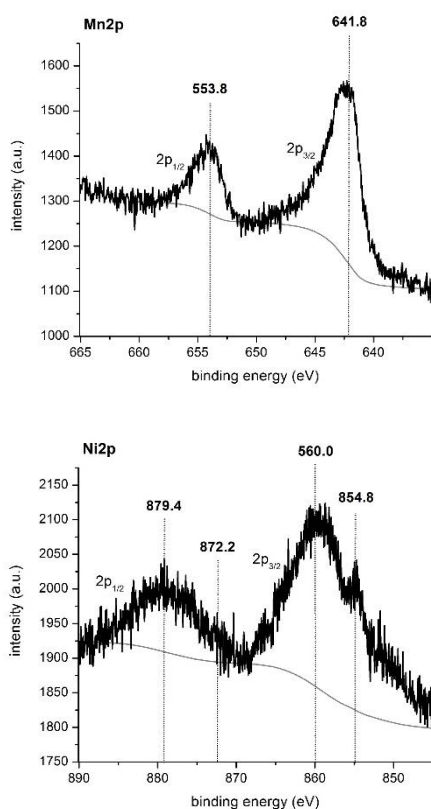
P2p

Signal	Binding energy (eV)	FWHM (a.u.)	Area (CPS eV)	Area (%)
PO₄³⁻				
After formation	133.3	1.5	39	14.4
After cycling	133.7	1.6	66	13.1
Li_xPF_yO_z, O=PFOR				
After formation	134.5	1.9	161	58.5
After cycling	134.7	2.2	277	55.3
Li_xPF_y				
After formation	136.3	2.0	75	27.2
After cycling	136.3	2.1	158	31.6

Table 48 Experimental data of the P2p spectra of LiNi_{0.4}Mn_{1.6}O₄ cathodes after formatting C//LiNi_{0.4}Mn_{1.6}O₄ pouch cells with 0.5% HFiP at 23 °C and after cycling these cells for 250 cycles at 45 °C.

Tris(trimethylsilyl) phosphate

A



B

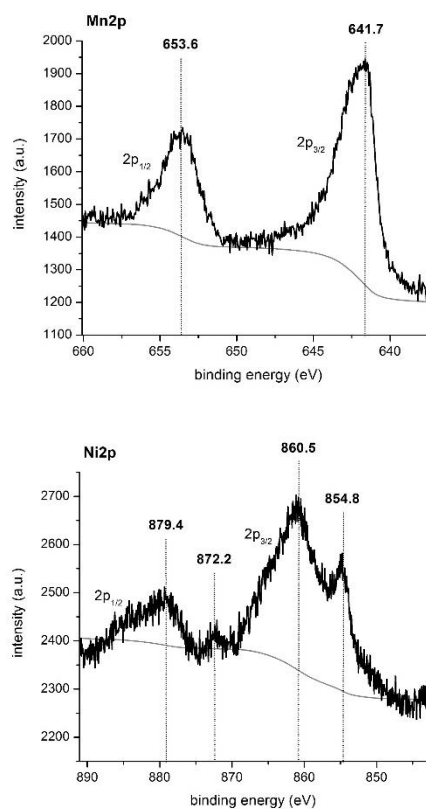


Figure 149 XPS spectra of LiNi_{0.4}Mn_{1.6}O₄ electrodes at 0% SOC after **A** formation C//LiNi_{0.4}Mn_{1.6}O₄ pouch cells with 1.7% TTSP at 23 °C and after **B** cycling these cells for 250 cycles at 45 °C.

Si2p

Signal	Binding energy (eV)	FWHM (a.u.)	Area (CPSeV)	Area (%)
Si2p				
After formation	-	-	-	-
After cycling	95.5	1.0	17.9	100.0

Table 49 Experimental data of the Si2p spectra of LiNi_{0.4}Mn_{1.6}O₄ cathodes after formatting C//LiNi_{0.4}Mn_{1.6}O₄ pouch cells with 1.7% TTSP at 23 °C and after cycling these cells for 250 cycles at 45 °C.

C1s

Signal	Binding energy (eV)	FWHM (a.u.)	Area (CPS _{SeV})	Area (%)
C-C				
After formation	284.7	1.5	1984	31.5
After cycling	284.4	1.2	426	9.6
CH₂				
After formation	285.9	1.6	1684	26.7
After cycling	285.7	1.7	1229	27.7
C-O				
After formation	287.0	1.7	1192	18.9
After cycling	287.3	1.9	1250	28.2
C=O				
After formation	288.8	1.7	747	11.8
After cycling	289.5	2.1	1208	27.2
CF₂				
After formation	290.4	1.7	698	11.1
After cycling	291.4	1.7	325	7.3

Table 50 Experimental data of the C1s spectra of LiNi_{0.4}Mn_{1.6}O₄ cathodes after formatting C//LiNi_{0.4}Mn_{1.6}O₄ pouch cells with 1.7% TTSP at 23 °C and after cycling these cells for 250 cycles at 45 °C.

O1s

Signal	Binding energy (eV)	FWHM (a.u.)	Area (CPS _{SeV})	Area (%)
O²⁻				
After formation	529.5	1.4	755	8.0
After cycling	529.3	1.2	1045	6.3
C=O				
After formation	532.1	2.1	3963	41.8
After cycling	532.6	4.0	6317	38.0
C-O				
After formation	533.8	2.2	4774	50.3
After cycling	536.0	3.7	9246	55.7

Table 51 Experimental data of the O1s spectra of LiNi_{0.4}Mn_{1.6}O₄ cathodes after formatting C//LiNi_{0.4}Mn_{1.6}O₄ pouch cells with 1.7% TTSP at 23 °C and after cycling these cells for 250 cycles at 45 °C.

F1s

Signal	Binding energy (eV)	FWHM (a.u.)	Area (CPSeV)	Area (%)
LiF, NiF₂, MnF₂				
After formation	684.6	2.3	173	3.3
After cycling	685.2	1.9	123	5.1
Li_xPF_y, Li_xPF_yO_z, O=PFOR				
After formation	687.1	2.3	2451	46.5
After cycling	687.0	1.7	5782	73.5
CF₂				
After formation	688.0	2.5	2649	50.2
After cycling	687.8	1.5	521	21.5

Table 52 Experimental data of the F1s spectra of LiNi_{0.4}Mn_{1.6}O₄ cathodes after formatting C//LiNi_{0.4}Mn_{1.6}O₄ pouch cells with 1.7% TTSP at 23 °C and after cycling these cells for 250 cycles at 45 °C.

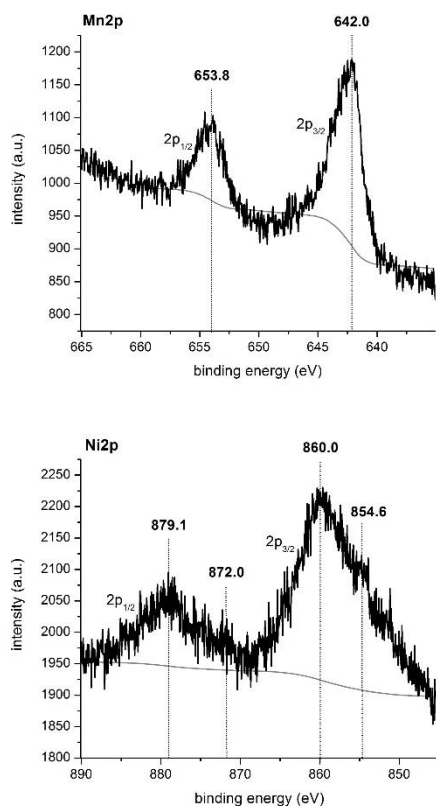
P2p

Signal	Binding energy (eV)	FWHM (a.u.)	Area (CPSeV)	Area (%)
PO₄³⁻				
After formation	133.7	2.4	27	1.9
After cycling	133.6	2.6	331	12.0
Li_xPF_yO_z, O=PFOR				
After formation	135.0	2.5	663	46.5
After cycling	135.8	2.6	1110	40.3
Li_xPF_y				
After formation	136.4	2.5	734	51.6
After cycling	136.7	2.5	1314	47.7

Table 53 Experimental data of the P2p spectra of LiNi_{0.4}Mn_{1.6}O₄ cathodes after formatting C//LiNi_{0.4}Mn_{1.6}O₄ pouch cells with 1.7% TTSP at 23 °C and after cycling these cells for 250 cycles at 45 °C.

Sebaconitrile

A



B

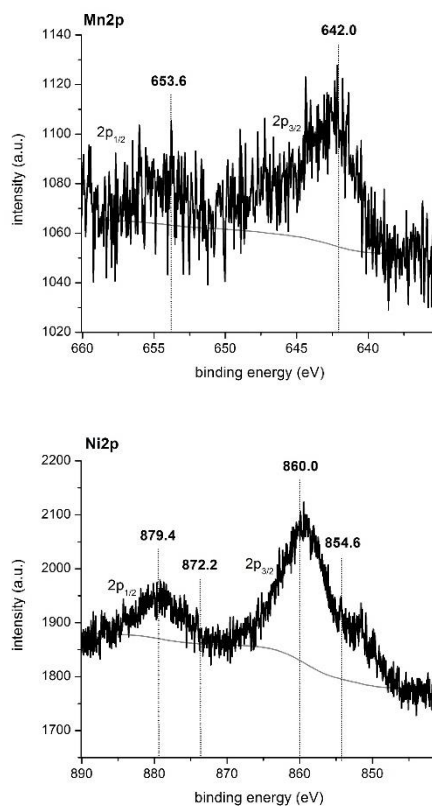


Figure 150 XPS spectra of $\text{LiNi}_{0.4}\text{Mn}_{1.6}\text{O}_4$ electrodes at 0% SOC after **A** formation C// $\text{LiNi}_{0.4}\text{Mn}_{1.6}\text{O}_4$ pouch cells with 1% SEN at 23 °C and after **B** cycling these cells for 250 cycles at 45 °C.

N1s

Signal	Binding energy (eV)	FWHM (a.u.)	Area (CPS _{SeV})	Area (%)
C-N				
After formation	400.3	2.6	762	92.6
After cycling	400.3	2.4	487	69.4
NH₃, NH₂⁺				
After formation	402.2	2.7	61	7.4
After cycling	401.8	2.2	215	30.3

Table 54 Experimental data of the N1s spectra of $\text{LiNi}_{0.4}\text{Mn}_{1.6}\text{O}_4$ cathodes after formatting C// $\text{LiNi}_{0.4}\text{Mn}_{1.6}\text{O}_4$ pouch cells with 1% SEN at 23 °C and after cycling these cells for 250 cycles at 45 °C.

C1s

Signal	Binding energy (eV)	FWHM (a.u.)	Area (CPSeV)	Area (%)
C-C				
After formation	284.7	1.4	2012	29.7
After cycling	284.5	1.9	272	3.2
CH₂				
After formation	285.9	1.4	2081	30.7
After cycling	285.5	1.8	4048	47.4
C-O				
After formation	287.0	1.5	1307	19.3
After cycling	287.0	1.8	2608	30.6
C=O				
After formation	288.7	1.6	621	9.2
After cycling	289.0	1.8	966	11.3
CF₂				
After formation	290.4	1.6	750	11.1
After cycling	290.3	1.8	642	7.5

Table 55 Experimental data of the C1s spectra of LiNi_{0.4}Mn_{1.6}O₄ cathodes after formatting C//LiNi_{0.4}Mn_{1.6}O₄ pouch cells with 1% SEN at 23 °C and after cycling these cells for 250 cycles at 45 °C.

O1s

Signal	Binding energy (eV)	FWHM (a.u.)	Area (CPSeV)	Area (%)
O²⁻				
After formation	529.7	1.8	762	14.0
After cycling	529.6	1.6	109	1.2
C=O				
After formation	532.1	1.9	2280	41.8
After cycling	532.2	1.9	3560	40.3
C-O				
After formation	533.7	1.9	2410	44.2
After cycling	533.8	2.0	5228	58.5

Table 56 Experimental data of the O1s spectra of LiNi_{0.4}Mn_{1.6}O₄ cathodes after formatting C//LiNi_{0.4}Mn_{1.6}O₄ pouch cells with 1% SEN at 23 °C and after cycling these cells for 250 cycles at 45 °C.

F1s

Signal	Binding energy (eV)	FWHM (a.u.)	Area (CPS eV)	Area (%)
LiF, NiF₂, MnF₂				
After formation	684.5	1.9	94	1.0
After cycling	685.2	1.8	112	1.5
Li_xPF_y, Li_xPF_yO_z, O=PFOR				
After formation	686.7	2.1	3468	37.3
After cycling	686.7	1.9	4768	63.9
CF₂				
After formation	687.6	2.0	5732	61.7
After cycling	687.9	1.9	2586	34.6

Table 57 Experimental data of the F1s spectra of LiNi_{0.4}Mn_{1.6}O₄ cathodes after formatting C//LiNi_{0.4}Mn_{1.6}O₄ pouch cells with 1% SEN at 23 °C and after cycling these cells for 250 cycles at 45 °C.

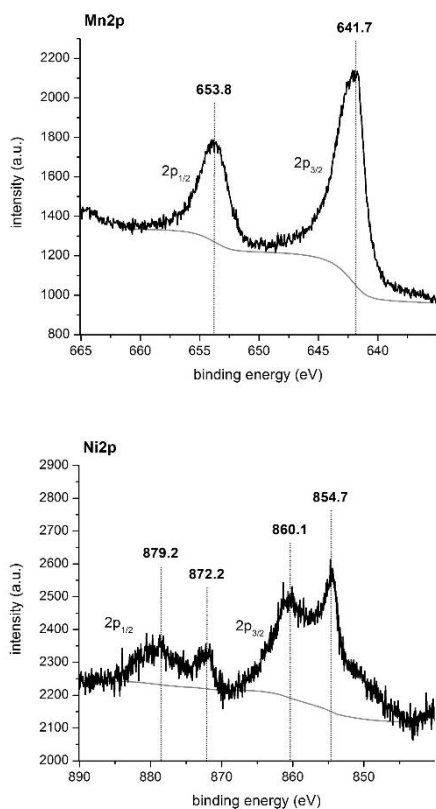
P2p

Signal	Binding energy (eV)	FWHM (a.u.)	Area (CPS eV)	Area (%)
PO₄³⁻				
After formation	133.0	1.8	16	4.1
After cycling	132.8	2.1	21	3.1
Li_xPF_yO_z, O=PFOR				
After formation	135.1	2.2	135	35.9
After cycling	134.7	2.1	222	32.7
Li_xPF_y				
After formation	136.5	1.8	225	60.0
After cycling	136.4	1.9	436	64.2

Table 58 Experimental data of the P2p spectra of LiNi_{0.4}Mn_{1.6}O₄ cathodes after formatting C//LiNi_{0.4}Mn_{1.6}O₄ pouch cells with 1% SEN at 23 °C and after cycling these cells for 250 cycles at 45 °C.

Fluoroethylene carbonate

A



B

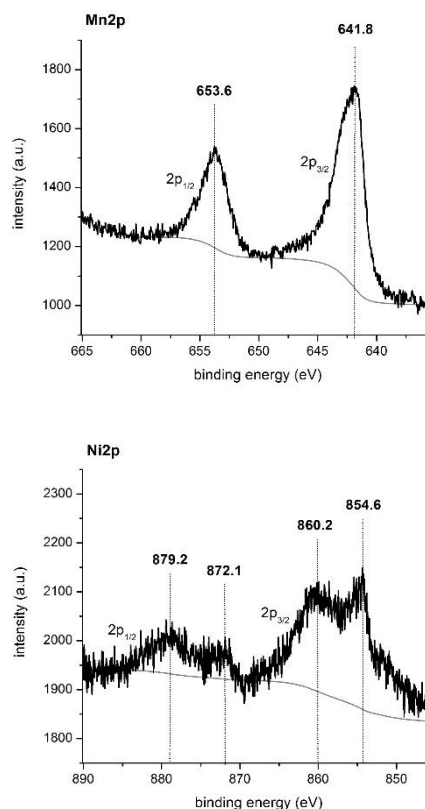


Figure 151 XPS spectra of LiNi_{0.4}Mn_{1.6}O₄ electrodes at 0% SOC after **A** formation C//LiNi_{0.4}Mn_{1.6}O₄ pouch cells with 2.5% FEC at 23 °C and after **B** cycling these cells for 250 cycles at 45 °C.

C1s

Signal	Binding energy (eV)	FWHM (a.u.)	Area (CPS _{SeV})	Area (%)
C-C				
After formation	284.6	1.2	1490	24.7
After cycling	284.6	1.2	983	13.7
CH₂				
After formation	285.7	1.3	1668	27.6
After cycling	285.7	1.4	2110	29.3
C-O				
After formation	286.9	1.6	1148	19.0
After cycling	287.0	1.4	1652	22.9
C=O				
After formation	288.7	1.6	731	12.1
After cycling	288.6	2.0	1197	16.6
CF₂				
After formation	290.3	1.5	1008	16.7
After cycling	290.2	1.9	1257	17.5

Table 59 Experimental data of the C1s spectra of LiNi_{0.4}Mn_{1.6}O₄ cathodes after formatting C//LiNi_{0.4}Mn_{1.6}O₄ pouch cells with 2.5% FEC at 23 °C and after cycling these cells for 250 cycles at 45 °C.

O1s

Signal	Binding energy (eV)	FWHM (a.u.)	Area (CPS _{SeV})	Area (%)
O²⁻				
After formation	529.4	1.3	2110	22.3
After cycling	529.3	1.2	1300	12.1
C=O				
After formation	531.9	2.3	3536	37.4
After cycling	532.1	2.3	4554	42.8
C-O				
After formation	533.6	2.2	3803	40.2
After cycling	533.8	2.0	4780	45.0

Table 60 Experimental data of the O1s spectra of LiNi_{0.4}Mn_{1.6}O₄ cathodes after formatting C//LiNi_{0.4}Mn_{1.6}O₄ pouch cells with 2.5% FEC at 23 °C and after cycling these cells for 250 cycles at 45 °C.

F1s

Signal	Binding energy (eV)	FWHM (a.u.)	Area (CPSeV)	Area (%)
LiF, NiF₂, MnF₂				
After formation	684.8	1.7	261	3.7
After cycling	685.2	1.2	280	3.3
Li_xPF_y, Li_xPF_yO_z, O=PFOR				
After formation	687.0	1.8	1689	23.9
After cycling	686.9	1.6	2669	31.9
CF₂				
After formation	687.6	2.1	5123	72.4
After cycling	687.7	2.0	5429	64.8

Table 61 Experimental data of the F1s spectra of LiNi_{0.4}Mn_{1.6}O₄ cathodes after formatting C//LiNi_{0.4}Mn_{1.6}O₄ pouch cells with 2.5% FEC at 23 °C and after cycling these cells for 250 cycles at 45 °C.

P2p

Signal	Binding energy (eV)	FWHM (a.u.)	Area (CPSeV)	Area (%)
PO₄³⁻				
After formation	132.8	0.5	4	1.5
After cycling	133.6	1.9	43	12.6
Li_xPF_yO_z, O=PFOR				
After formation	134.4	2.0	178	59.6
After cycling	134.6	2.0	181	53.1
Li_xPF_y				
After formation	136.2	2.3	116	38.9
After cycling	136.3	2.0	117	34.2

Table 62 Experimental data of the P2p spectra of LiNi_{0.4}Mn_{1.6}O₄ cathodes after formatting C//LiNi_{0.4}Mn_{1.6}O₄ pouch cells with 2.5% FEC at 23 °C and after cycling these cells for 250 cycles at 45 °C.

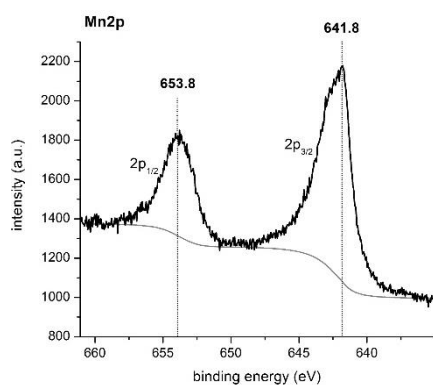
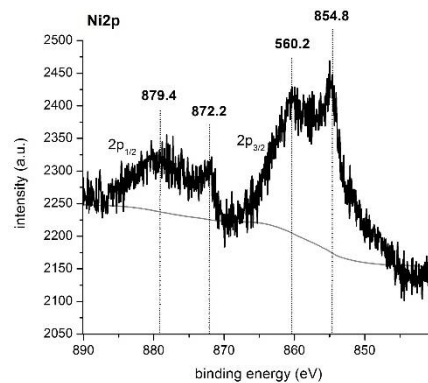
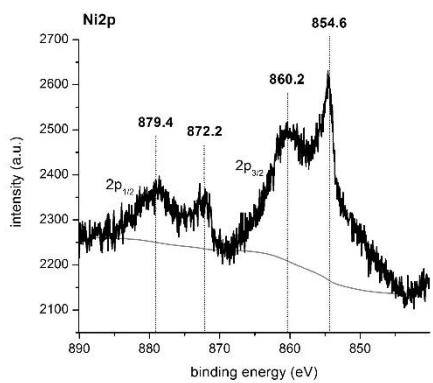
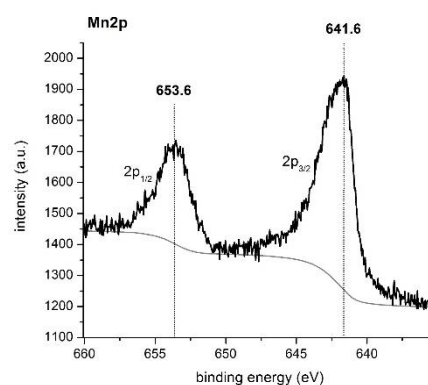
Tris(2-ethylhexyl) phosphate**A****B**

Figure 152 XPS spectra of $\text{LiNi}_{0.4}\text{Mn}_{1.6}\text{O}_4$ electrodes at 0% SOC after **A** formation C// $\text{LiNi}_{0.4}\text{Mn}_{1.6}\text{O}_4$ pouch cells with 0.5% TEHP at 23 °C and after **B** cycling these cells for 250 cycles at 45 °C.

C1s

Signal	Binding energy (eV)	FWHM (a.u.)	Area (CPSeV)	Area (%)
C-C				
After formation	284.5	1.2	1292	21.4
After cycling	284.6	1.1	720	9.0
CH₂				
After formation	285.8	1.7	2331	38.6
After cycling	285.7	1.7	3442	42.9
C-O				
After formation	287.1	1.6	1050	17.4
After cycling	287.1	1.6	1836	22.9
C=O				
After formation	288.8	1.6	655	10.8
After cycling	289.0	1.7	1424	17.7
CF₂				
After formation	290.4	1.5	716	11.9
After cycling	290.4	1.2	612	7.6

Table 63 Experimental data of the C1s spectra of LiNi_{0.4}Mn_{1.6}O₄ cathodes after formatting C//LiNi_{0.4}Mn_{1.6}O₄ pouch cells with 0.5% TEHP at 23 °C and after cycling these cells for 250 cycles at 45 °C.

O1s

Signal	Binding energy (eV)	FWHM (a.u.)	Area (CPSeV)	Area (%)
O²⁻				
After formation	529.5	1.3	1575	20.3
After cycling	529.4	1.3	1218	10.3
C=O				
After formation	531.9	2.2	2910	37.4
After cycling	532.2	2.2	4492	38.1
C-O				
After formation	533.6	2.1	3288	42.3
After cycling	533.7	2.1	6093	51.6

Table 64 Experimental data of the O1s spectra of LiNi_{0.4}Mn_{1.6}O₄ cathodes after formatting C//LiNi_{0.4}Mn_{1.6}O₄ pouch cells with 0.5% TEHP at 23 °C and after cycling these cells for 250 cycles at 45 °C.

F1s

Signal	Binding energy (eV)	FWHM (a.u.)	Area (CPS eV)	Area (%)
LiF, NiF₂, MnF₂				
After formation	685.1	0.1	8	0.1
After cycling	685.0	2.2	367	6.4
Li_xPF_y, Li_xPF_yO_z, O=PFOR				
After formation	686.9	1.8	2752	36.7
After cycling	687.0	1.8	2630	45.8
CF₂				
After formation	687.8	1.8	4748	63.2
After cycling	687.8	2.2	2745	47.8

Table 65 Experimental data of the F1s spectra of LiNi_{0.4}Mn_{1.6}O₄ cathodes after formatting C//LiNi_{0.4}Mn_{1.6}O₄ pouch cells with 0.5% TEHP at 23 °C and after cycling these cells for 250 cycles at 45 °C.

P2p

Signal	Binding energy (eV)	FWHM (a.u.)	Area (CPS eV)	Area (%)
PO₄³⁻				
After formation	133.4	1.5	37	11.1
After cycling	133.6	1.4	56	14.2
Li_xPF_yO_z, O=PFOR				
After formation	134.6	2.0	176	52.3
After cycling	134.6	1.7	195	49.4
Li_xPF_y				
After formation	136.5	2.3	123	36.6
After cycling	136.0	1.9	144	36.4

Table 66 Experimental data of the P2p spectra of LiNi_{0.4}Mn_{1.6}O₄ cathodes after formatting C//LiNi_{0.4}Mn_{1.6}O₄ pouch cells with 0.5% TEHP at 23 °C and after cycling these cells for 250 cycles at 45 °C.

Succinic anhydride

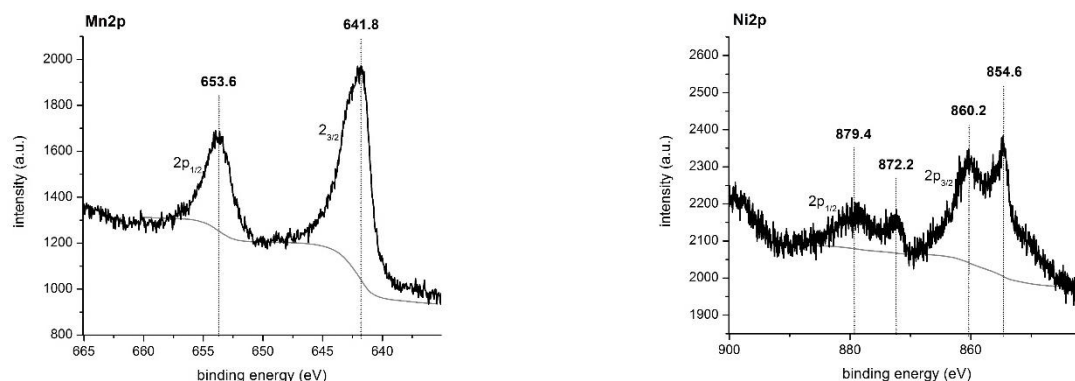


Figure 153 XPS spectra of $\text{LiNi}_{0.4}\text{Mn}_{1.6}\text{O}_4$ electrodes at 0% SOC after cycling C// $\text{LiNi}_{0.4}\text{Mn}_{1.6}\text{O}_4$ pouch cells with 2.5% SA for 250 cycles at 45 °C between 3.3 and 4.8 V.

C1s

Signal	Binding energy (eV)	FWHM (a.u.)	Area (CPSeV)	Area (%)
C-C				
After cycling	284.5	1.2	674	10.2
CH₂				
After cycling	285.7	1.7	2244	33.9
C-O				
After cycling	287.0	2.1	1742	26.3
C=O				
After cycling	289.2	2.1	1583	23.9
CF₂				
After cycling	290.4	1.3	375	5.7

Table 67 Experimental data of the C1s spectra of $\text{LiNi}_{0.4}\text{Mn}_{1.6}\text{O}_4$ cathodes after cycling C// $\text{LiNi}_{0.4}\text{Mn}_{1.6}\text{O}_4$ pouch cells for 250 cycles with 2.5% SA at 45 °C.

O1s

Signal	Binding energy (eV)	FWHM (a.u.)	Area (CPSeV)	Area (%)
O²⁻				
After cycling	529.4	1.3	1684	17.7
C=O				
After cycling	532.1	2.3	4194	44.0
C-O				
After cycling	533.7	2.0	3659	38.4

Table 68 Experimental data of the O1s spectra of $\text{LiNi}_{0.4}\text{Mn}_{1.6}\text{O}_4$ cathodes after cycling C// $\text{LiNi}_{0.4}\text{Mn}_{1.6}\text{O}_4$ pouch cells for 250 cycles with 2.5% SA at 45 °C.

F1s

Signal	Binding energy (eV)	FWHM (a.u.)	Area (CPS _{SeV})	Area (%)
LiF, NiF₂, MnF₂				
After cycling	685.1	2.0	346	4.1
Li_xPF_y, Li_xPF_yO_z, O=PFOR				
After cycling	687.0	1.8	4926	58.1
CF₂				
After cycling	687.8	2.4	3212	37.9

Table 69 Experimental data of the F1s spectra of LiNi_{0.4}Mn_{1.6}O₄ cathodes after cycling C//LiNi_{0.4}Mn_{1.6}O₄ pouch cells for 250 cycles with 2.5% SA at 45 °C.

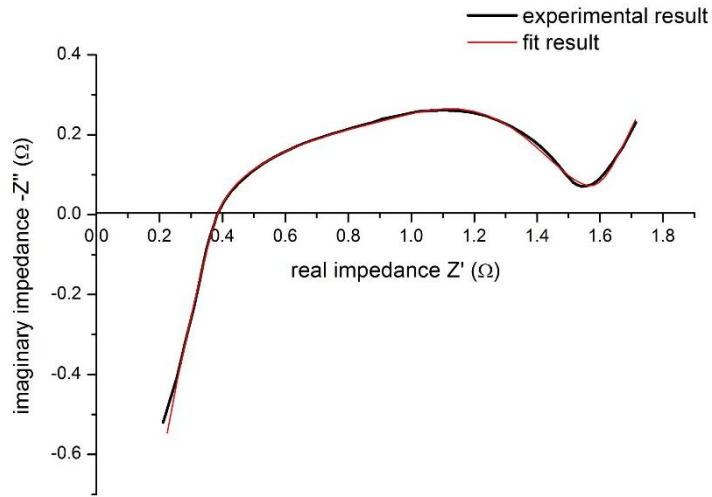
P2p

Signal	Binding energy (eV)	FWHM (a.u.)	Area (CPS _{SeV})	Area (%)
PO₄³⁻				
After cycling	132.8	0.9	17	3.6
Li_xPF_yO_z, O=PFOR				
After cycling	134.3	1.6	203	43.4
Li_xPF_y				
After cycling	135.8	2.3	248	53.0

Table 70 Experimental data of the P2p spectra of LiNi_{0.4}Mn_{1.6}O₄ cathodes after cycling C//LiNi_{0.4}Mn_{1.6}O₄ pouch cells for 250 cycles with 2.5% SA at 45 °C.

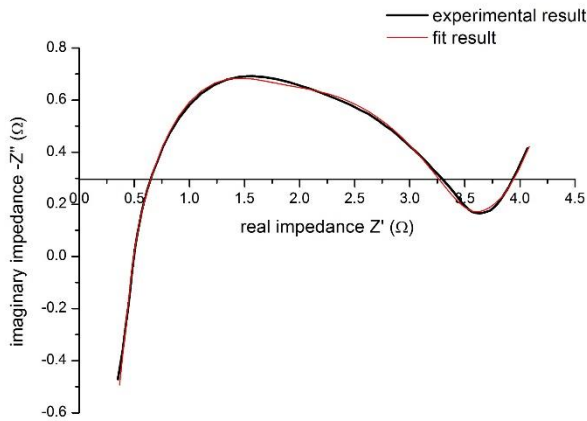
7.4 Electrochemical impedance spectroscopy

Trimethyl phosphate



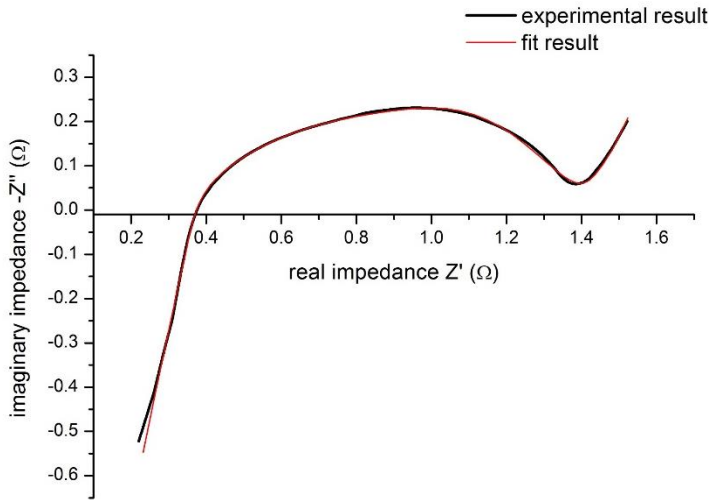
Element	Value	Error %
R_i	0.4	1.2
R_s	0.3	1.0
R_{ct}	1.3	2.0

Figure 154 Nyquist plot and respective EIS data of C//LiNi_{0.4}Mn_{1.6}O₄ cells at 80% SOC after formation C//LiNi_{0.4}Mn_{1.6}O₄ pouch cells with 0.5% TMP at 23 °C.



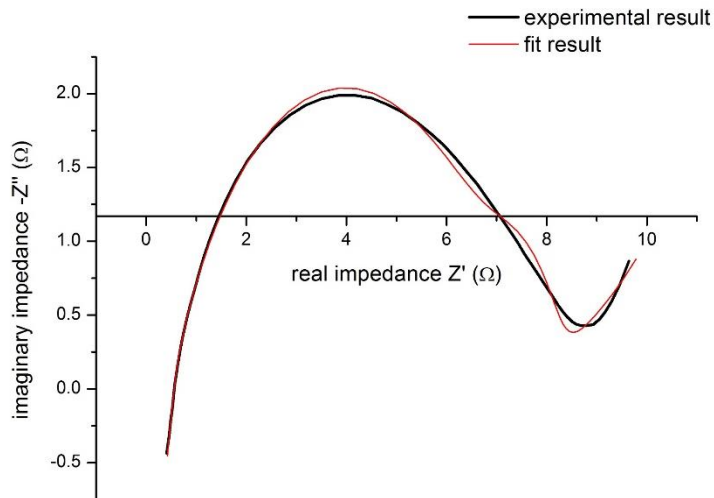
Element	Value	Error %
R_i	0.6	2.9
R_s	0.4	2.9
R_{ct}	2.9	2.9

Figure 155 Nyquist plot and respective EIS data of C//LiNi_{0.4}Mn_{1.6}O₄ cells at 80% SOC after cycling C//LiNi_{0.4}Mn_{1.6}O₄ pouch cells for 250 cycles with 0.5% TMP at 45 °C.

Tris(2,2,2-trifluoroethyl)phosphite

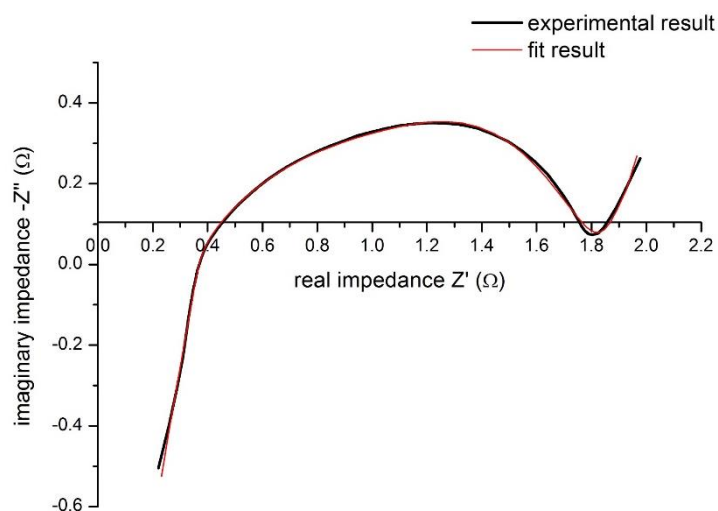
Element	Value	Error %
R_i	0.4	0.9
R_s	0.3	0.6
R_{ct}	1.1	1.7

Figure 156 Nyquist plot and respective EIS data of C//LiNi_{0.4}Mn_{1.6}O₄ cells at 80% SOC after formation C//LiNi_{0.4}Mn_{1.6}O₄ pouch cells with 0.5% TFPI at 23 °C.



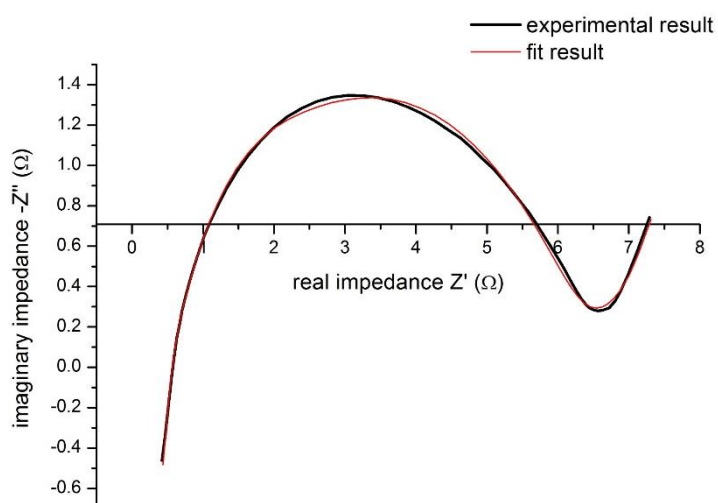
Element	Value	Error %
R_i	0.5	2.0
R_s	0.6	2.5
R_{ct}	7.5	1.6

Figure 157 Nyquist plot and respective EIS data of C//LiNi_{0.4}Mn_{1.6}O₄ cells at 80% SOC after cycling C//LiNi_{0.4}Mn_{1.6}O₄ pouch cells for 250 cycles with 0.5% TFPI at 45 °C.

Lithium bis(oxalato)borate

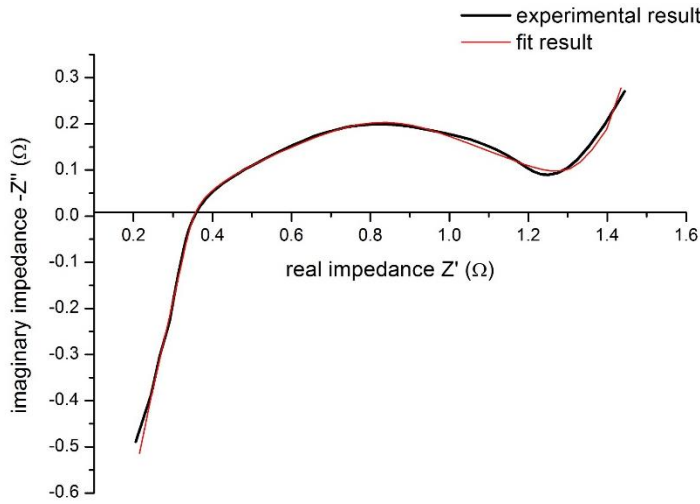
Element	Value	Error %
R_i	0.4	1.0
R_s	0.3	0.5
R_{ct}	1.5	1.6

Figure 158 Nyquist plot and respective EIS data of C//LiNi_{0.4}Mn_{1.6}O₄ cells at 80% SOC after formation C//LiNi_{0.4}Mn_{1.6}O₄ pouch cells with 0.5% LiBOB at 23 °C.



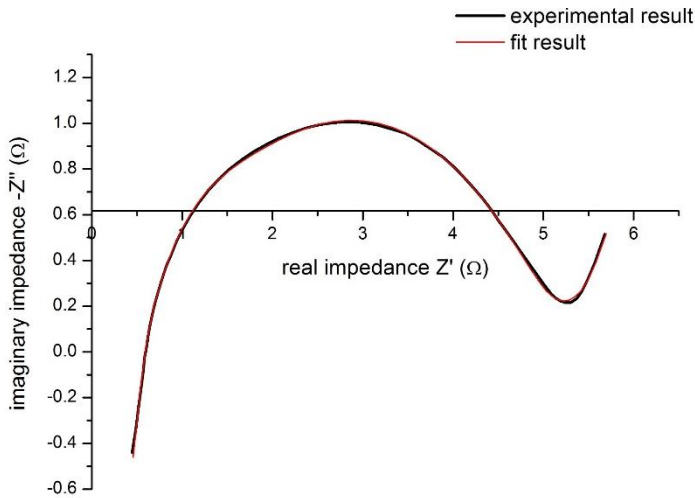
Element	Value	Error %
R_i	0.6	2.9
R_s	0.5	4.9
R_{ct}	5.7	2.2

Figure 159 Nyquist plot and respective EIS data of C//LiNi_{0.4}Mn_{1.6}O₄ cells at 80% SOC after cycling C//LiNi_{0.4}Mn_{1.6}O₄ pouch cells for 250 cycles with 0.5% LiBOB at 45 °C.

Hexamethyldisilazane

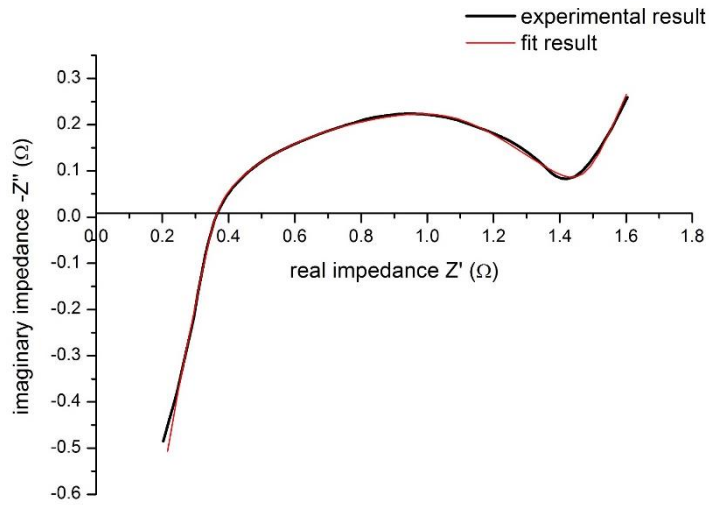
Element	Value	Error %
R_i	0.4	0.7
R_s	0.3	0.9
R_{ct}	1.1	1.4

Figure 160 Nyquist plot and respective EIS data of C//LiNi_{0.4}Mn_{1.6}O₄ cells at 80% SOC after formation C//LiNi_{0.4}Mn_{1.6}O₄ pouch cells with 0.5% HMDS at 23 °C.



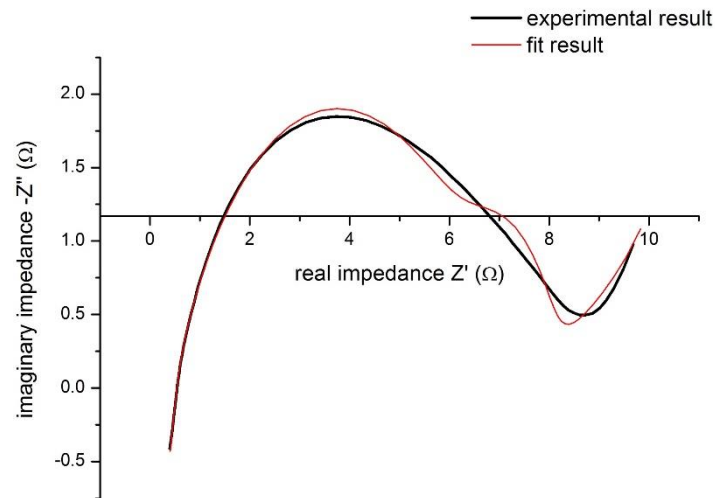
Element	Value	Error %
R_i	0.6	1.7
R_s	0.5	1.0
R_{ct}	4.6	1.5

Figure 161 Nyquist plot and respective EIS data of C//LiNi_{0.4}Mn_{1.6}O₄ cells at 80% SOC after cycling C//LiNi_{0.4}Mn_{1.6}O₄ pouch cells for 250 cycles with 0.5% HMDS at 45 °C.

Tris-(1,1,1,3,3,3-hexafluoroisopropyl) phosphate

Element	Value	Error %
R_i	0.4	1.2
R_s	0.3	1.2
R_{ct}	1.2	1.5

Figure 162 Nyquist plot and respective EIS data of C//LiNi_{0.4}Mn_{1.6}O₄ cells at 80% SOC after formation C//LiNi_{0.4}Mn_{1.6}O₄ pouch cells with 0.5% HFIP at 23 °C.



Element	Value	Error %
R_i	0.6	2.8
R_s	0.4	3.9
R_{ct}	7.3	2.1

Figure 163 Nyquist plot and respective EIS data of C//LiNi_{0.4}Mn_{1.6}O₄ cells at 80% SOC after cycling C//LiNi_{0.4}Mn_{1.6}O₄ pouch cells for 250 cycles with 0.5% HFIP at 45 °C.

Reference

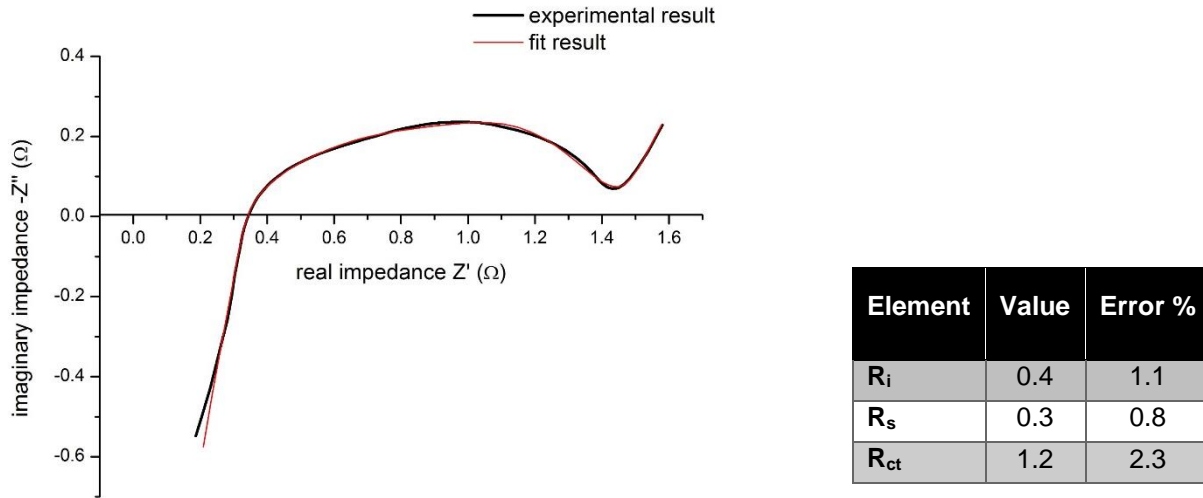


Figure 164 Nyquist plot and respective EIS data of C//LiNi_{0.4}Mn_{1.6}O₄ cells at 80% SOC after formation C//LiNi_{0.4}Mn_{1.6}O₄ pouch cells containing the base electrolyte at 23 °C.

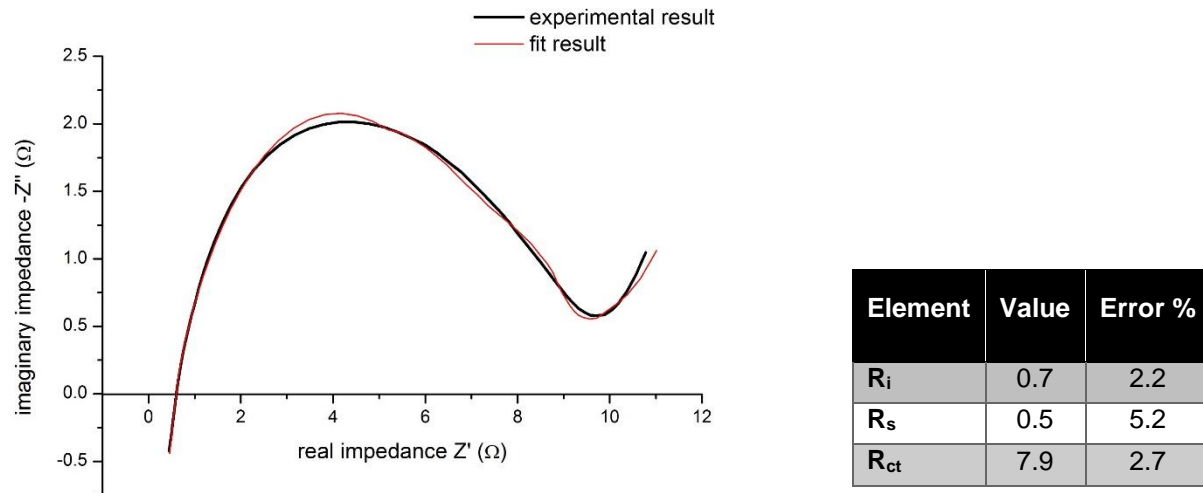
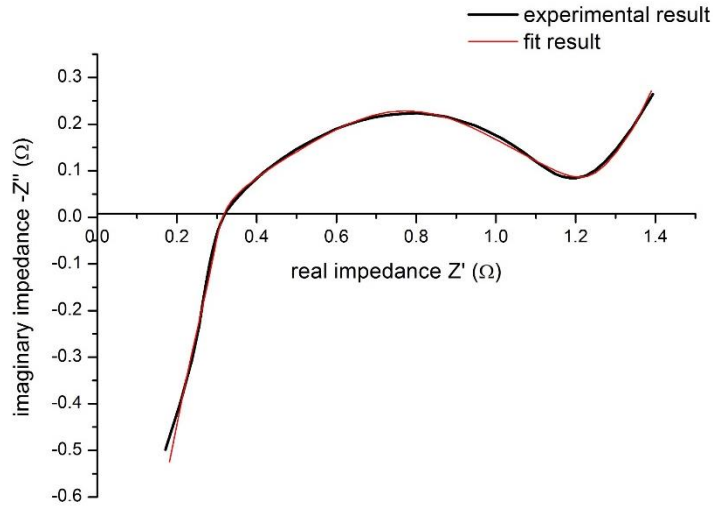
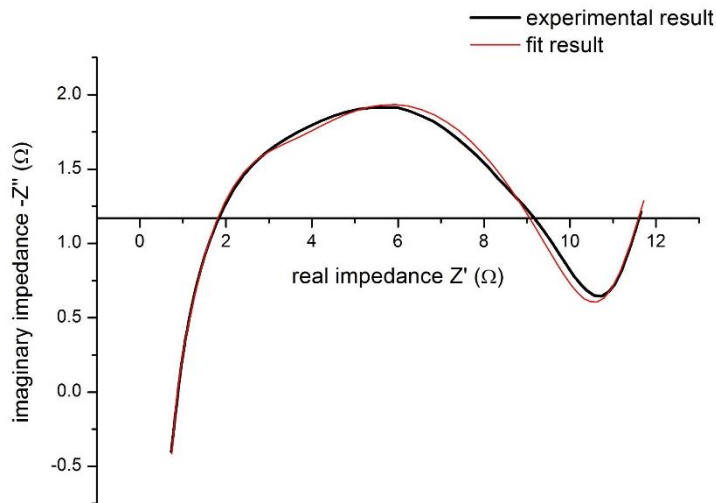


Figure 165 Nyquist plot and respective EIS data of C//LiNi_{0.4}Mn_{1.6}O₄ cells at 80% SOC after cycling C//LiNi_{0.4}Mn_{1.6}O₄ pouch cells for 250 cycles containing the base electrolyte at 45 °C.

Tris(trimethylsilyl) phosphate

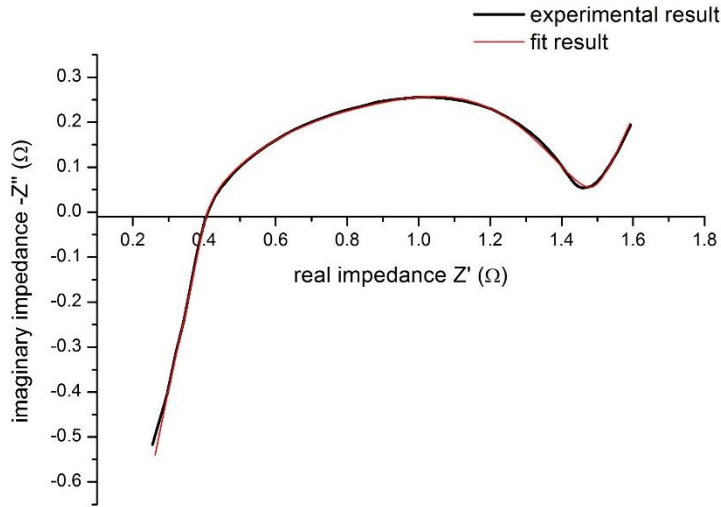
Element	Value	Error %
R_i	0.3	0.8
R_s	0.3	0.9
R_{ct}	1.0	2.0

Figure 166 Nyquist plot and respective EIS data of C//LiNi_{0.4}Mn_{1.6}O₄ cells at 80% SOC after formation C//LiNi_{0.4}Mn_{1.6}O₄ pouch cells with 1.7% TTSP at 23 °C.



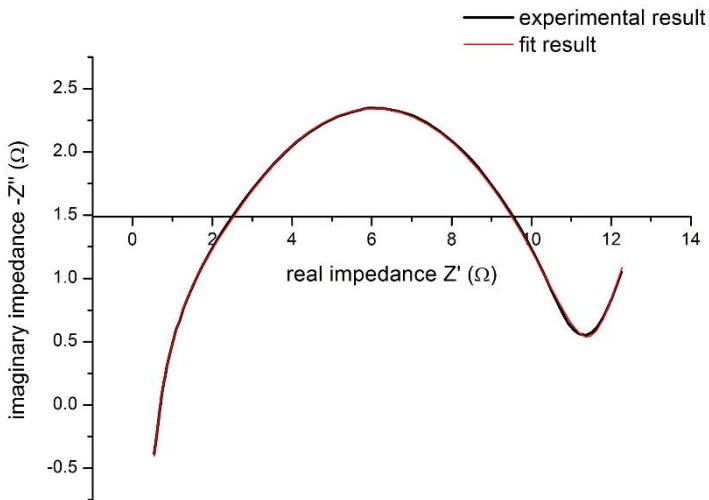
Element	Value	Error %
R_i	1.0	1.4
R_s	1.0	2.5
R_{ct}	9.0	1.9

Figure 167 Nyquist plot and respective EIS data of C//LiNi_{0.4}Mn_{1.6}O₄ cells at 80% SOC after cycling C//LiNi_{0.4}Mn_{1.6}O₄ pouch cells for 250 cycles with 1.7% TTSP at 45 °C.

Sebaconitrile

Element	Value	Error %
R_i	0.4	0.9
R_s	0.4	0.6
R_{ct}	1.1	1.8

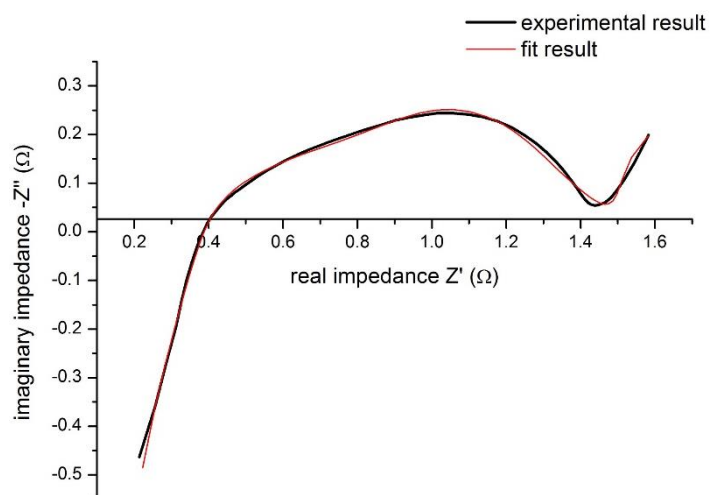
Figure 168 Nyquist plot and respective EIS data of C//LiNi_{0.4}Mn_{1.6}O₄ cells at 80% SOC after formation C//LiNi_{0.4}Mn_{1.6}O₄ pouch cells with 1% SEN at 23 °C.



Element	Value	Error %
R_i	0.8	2.2
R_s	0.5	1.4
R_{ct}	10.5	2.7

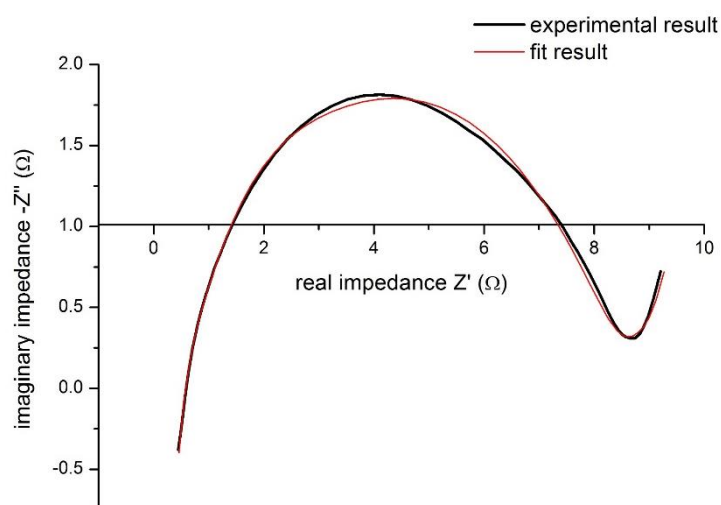
Figure 169 Nyquist plot and respective EIS data of C//LiNi_{0.4}Mn_{1.6}O₄ cells at 80% SOC after cycling C//LiNi_{0.4}Mn_{1.6}O₄ pouch cells for 250 cycles with 1% SEN at 45 °C.

Fluoroethylene carbonate



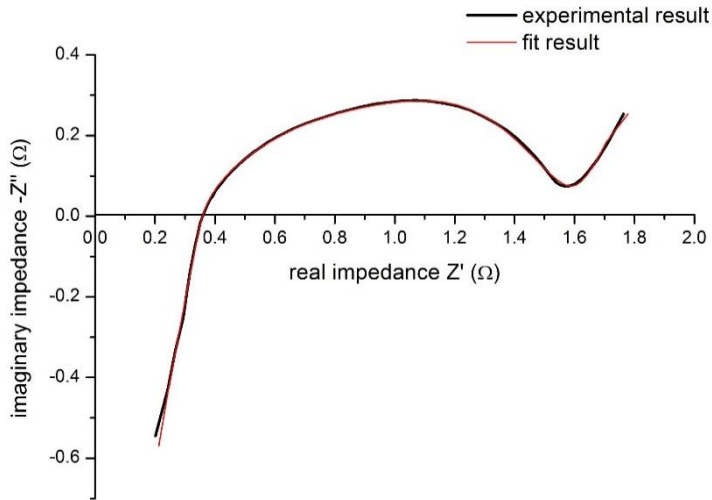
Element	Value	Error %
R_i	0.4	1.3
R_s	0.3	1.6
R_{ct}	1.2	1.4

Figure 170 Nyquist plot and respective EIS data of C//LiNi_{0.4}Mn_{1.6}O₄ cells at 80% SOC after formation C//LiNi_{0.4}Mn_{1.6}O₄ pouch cells with 2.5% FEC at 23 °C.



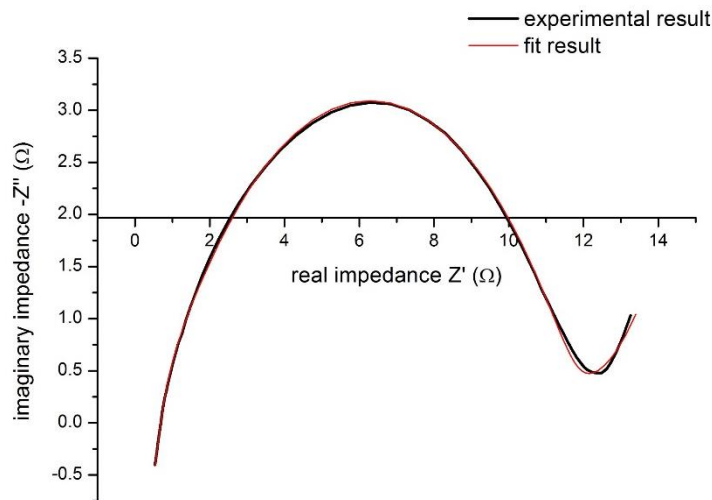
Element	Value	Error %
R_i	0.7	3.3
R_s	0.5	6.8
R_{ct}	9.9	2.5

Figure 171 Nyquist plot and respective EIS data of C//LiNi_{0.4}Mn_{1.6}O₄ cells at 80% SOC after cycling C//LiNi_{0.4}Mn_{1.6}O₄ pouch cells for 250 cycles with 2.5% FEC at 45 °C.

Tris(2-ethylhexyl) phosphate

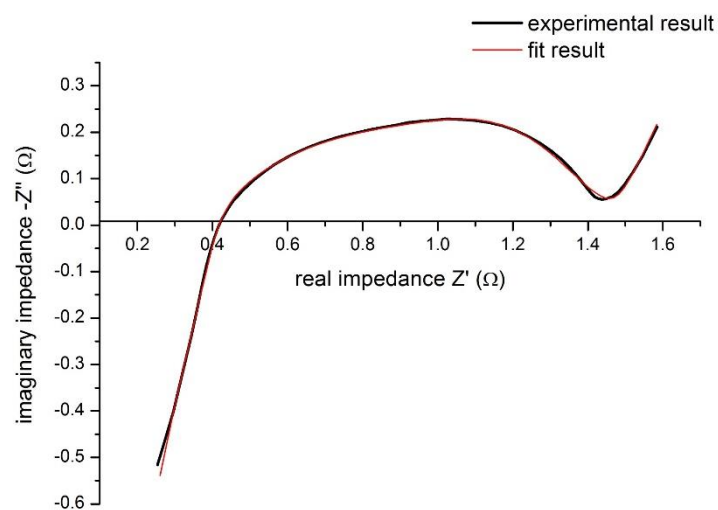
Element	Value	Error %
R_i	0.4	1.1
R_s	0.3	0.6
R_{ct}	1.3	1.8

Figure 172 Nyquist plot and respective EIS data of C//LiNi_{0.4}Mn_{1.6}O₄ cells at 80% SOC after formation C//LiNi_{0.4}Mn_{1.6}O₄ pouch cells with 0.5% TEHP at 23 °C.



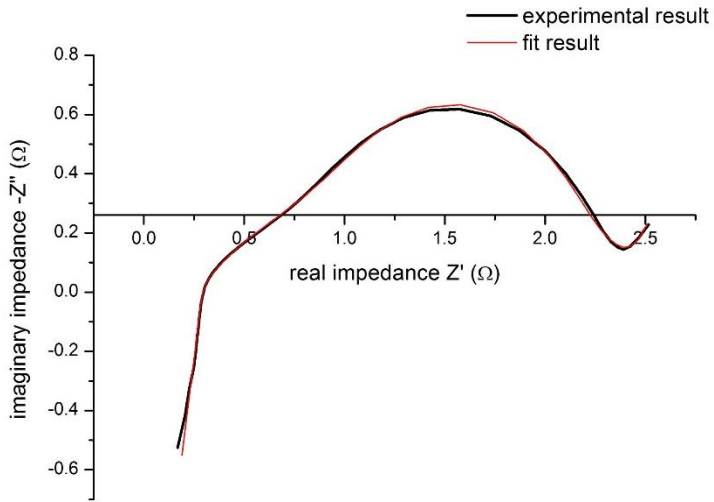
Element	Value	Error %
R_i	0.8	0.6
R_s	0.6	3.7
R_{ct}	11.2	1.8

Figure 173 Nyquist plot and respective EIS data of C//LiNi_{0.4}Mn_{1.6}O₄ cells at 80% SOC after cycling C//LiNi_{0.4}Mn_{1.6}O₄ pouch cells for 250 cycles with 0.5% TEHP at 45 °C.

Lithium bis(trifluoromethanesulfonyl)imide

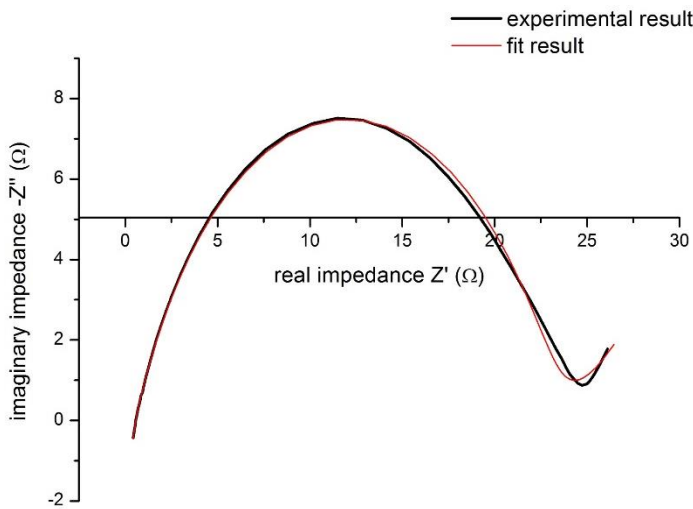
Element	Value	Error %
R_i	0.3	0.8
R_s	0.3	0.7
R_{ct}	1.1	1.8

Figure 174 Nyquist plot and respective EIS data of C//LiNi_{0.4}Mn_{1.6}O₄ cells at 80% SOC after formation C//LiNi_{0.4}Mn_{1.6}O₄ pouch cells with 1.5% LiTFSI at 23 °C.

Succinic anhydride

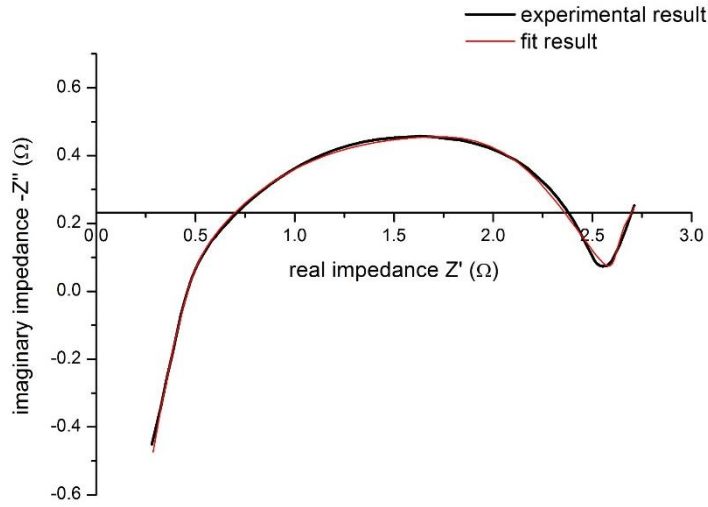
Element	Value	Error %
R_i	0.4	1.1
R_s	0.3	0.7
R_{ct}	2.1	4.7

Figure 175 Nyquist plot and respective EIS data of C//LiNi_{0.4}Mn_{1.6}O₄ cells at 80% SOC after formation C//LiNi_{0.4}Mn_{1.6}O₄ pouch cells with 2.5% SA at 23 °C.



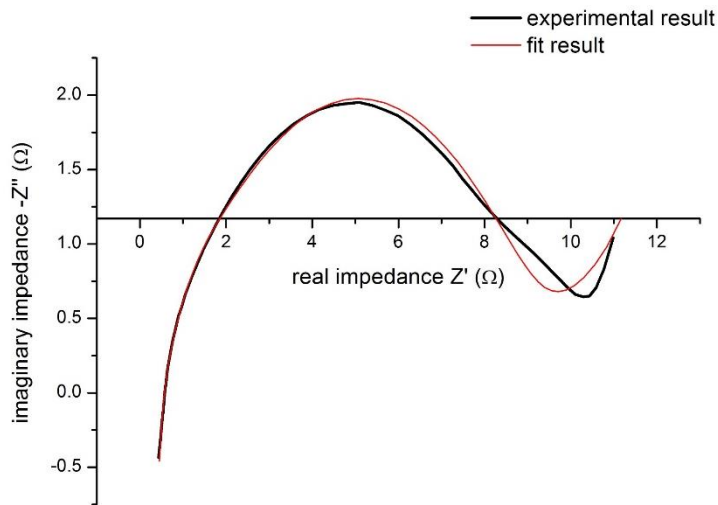
Element	Value	Error %
R_i	0.6	2.4
R_s	0.5	5.3
R_{ct}	23.0	1.7

Figure 176 Nyquist plot and respective EIS data of C//LiNi_{0.4}Mn_{1.6}O₄ cells at 80% SOC after cycling C//LiNi_{0.4}Mn_{1.6}O₄ pouch cells for 250 cycles with 2.5% SA at 45 °C.

Al₂O₃ coating layer on anode and cathode

Element	Value	Error %
R_i	0.5	1.9
R_s	0.4	0.9
R_{ct}	2.3	1.1

Figure 177 Nyquist plot and respective EIS data of C//LiNi_{0.4}Mn_{1.6}O₄ cells at 80% SOC after formation C//LiNi_{0.4}Mn_{1.6}O₄ pouch cells with Al₂O₃ coating layer on anode and cathode at 23 °C.



Element	Value	Error %
R_i	0.6	1.8
R_s	0.4	7.9
R_{ct}	7.7	4.8

Figure 178 Nyquist plot and respective EIS data of C//LiNi_{0.4}Mn_{1.6}O₄ cells at 80% SOC after cycling C//LiNi_{0.4}Mn_{1.6}O₄ pouch cells for 250 cycles with Al₂O₃ coating layer on anode and cathode at 45 °C.

References

- [1] J.-H. Kim, N. P. W. Pieczonka, L. Yang, *ChemPhysChem* **2014**, 15, 1940–1954.
- [2] G. Wang, J. Xie, C. Wu, S. Zhang, G. Cao, X. Zhao, *J. Power Sources* **2014**, 265, 118–124.
- [3] J.-H. Kim, N. P. W. Pieczonka, Z. Li, Y. Wu, S. Harris, B. R. Powell, *Electrochim. Acta*, 90, 556–562.
- [4] N. P. W. Pieczonka, Z. Liu, P. Lu, K. L. Olson, J. Moote, B. R. Powell, J.-H. Kim, *J. Phys. Chem. C* **2013**, 117, 15947–15957.
- [5] X. Yang, J. Xing, X. Liu, T. Wang, W. Peng, J. Xie, *Phys. Chem. Chem. Phys.* **2014**, 16, 24373–24381.
- [6] L. Hu, Z. Zhang, K. Amine, *Electrochem. Commun.* **2013**, 35, 76–79.
- [7] C. Pillot, "Battery Market Development for Consumer Electronics, Automotive, and Industrial: Materials Requirements and Trends", can be found under

[XXI](https://www.google.de/url?sa=t&rct=j&q=&esrc=s&source=web&cd=1&ved=0CDEQFjAA&url=http%3A%2F%2Fwww.rechargebatteries.org%2Fwp-content%2Fuploads%2F2013%2F04%2FBatteries-2012-Roland-Berger-Report1.pdf&ei=BkOKUvGTClrBswa73YCoCw&usg=AFQjCNHHxo788-L-Va0uqV8LDtLEcNMyqA&bvm=bv.56643336,d.Yms&cad=rja.Roland Berger Strategy Consultants GmbH (Ed.), Nice, Frankreich. 2012.

</div>
<div data-bbox=)

- [10] Bundesministerium für Wirtschaft und Technologie (BMWi)Öffentlichkeitsarbeit, "Forschung für eine umweltschonende, zuverlässige und bezahlbare Energieversorgung. Das 6. Energieforschungsprogramm der Bundesregierung", can be found under <http://www.bmwi.de/DE/Mediathek/publikationen,did=427698.html>. Bundesministerium für Wirtschaft und Technologie (BMWi)Öffentlichkeitsarbeit (Ed.), München. **july 2011**.
- [11] Nationale Plattform Elektromobilität (NPE), "Fortschrittsbericht 2014. Bilanz der Marktvorbereitung", can be found under <http://www.bmwi.de/DE/Mediathek/publikationen,did=672614.html>. Gemeinsame Geschäftsstelle Elektromobilität der Bundesregierung (GGEMO) (Ed.). **december 2014**.
- [12] Uwe Spindeldreier, "Energiewende. Verkehr - Wie lässt sich der CO₂-Ausstoß von Autos weiter senken?", can be found under http://www.bundesregierung.de/Webs/Breg/DE/Themen/Energiewende/Fragen-Antworten/7_Verkehr/_node.html#doc605200bodyText3. Presse- und Informationsamt der Bundesregierung (Ed.). **2015**.
- [13] a) T. Kupsh, Dr. Evermor, *A mythic obsession. The world of Dr. Evermor*, Chicago Review Press, Chicago, Ill, **2008**; b) T. Davenport, US132 (A), **1837**.
- [14] a) Miller, T. J. E, *Electronic control of switched reluctance machines*, Newnes, Oxford, Boston, **2001**; b) L. J. Davis, *Fleet fire. Thomas Edison and the pioneers of the electric revolution*, Arcade Publishing, New York, **2003**.
- [15] A. Jossen, W. Weydanz, *Moderne Akkumulatoren richtig einsetzen*, Ubooks, Neusäß, **2006**.
- [16] C. Daniel, J. O. Besenhard, *Handbook of battery materials*, Wiley-VCH Verlag, Weinheim, **2011**.
- [17] L. F. Trueb, P. Rüetschi, *Batterien und Akkumulatoren. Mobile Energiequellen für heute und morgen*, Springer, Berlin, Heidelberg, New York, Barcelona, Budapest, Hongkong, London, Mailand, Paris, Santa Clara, Singapur, Tokio, **1998**.
- [18] a) M. Ehsani, *Modern electric, hybrid electric, and fuel cell vehicles. Fundamentals, theory, and design*, CRC Press, Boca Raton, **2005**; b) A. Linde, *Electric cars - the future is now! Your guide to the cars you can buy now and what the future holds*, Veloce Pub., Dorchester, **2010**.
- [19] a) J. Lowry, J. Larminie, *Electric vehicle technology explained*, Wiley, Hoboken, N.J, **2012**; b) R. Seiffert, *Die Ära Gottlieb Daimlers. Neue Perspektiven zur Frühgeschichte des Automobils und seiner Technik*, Vieweg+Teubner Verlag / Springer Fachmedien Wiesbaden, Wiesbaden, Wiesbaden, **2009**.

- [20] M. W. Robbins, J. Holland, *Whole green catalog. 1,000 best things for you and the earth*, Rodale; Distributed to the trade by Macmillan, [Emmaus, Pa.], [New York], **2009**.
- [21] a) T. Nagaura, *Proceedings of the 5th International Seminar on Lithium Battery Technology and Application*, Deerfield Beach, FL, Florida, **1990**; b) J. R. Dahn, U. v. Sacken, R. Fong, *Primary and Secondary Lithium Batteries Symposium. Abstract No. 42. 178th Meeting of the Electrochemical Society Abstract No. 42 of the 178th*, Seattle, WA, **1990**.
- [22] M. Duvall, *Discussion of the Benefits and Impacts of Plug In Hybrid and Battery Electric Vehicles. Technical Report*, **2010**. MIT Energy Initiative (Ed.).
- [23] R. Korthauer, H.-M. Fischer, C. Funke, K. Demmer, G. Kann, K. Ludwig, "Elektromobilität. Fünf offene Fragen und Antworten. Eine Positionsbestimmung.", can be found under http://www.zvei.org/Publikationen/ZVEI_Elektromobilit%C3%A4t_ES_25.10.12.pdf. ZVEI - Zentralverband Elektrotechnik- und Elektronikindustrie e. V. (Ed.). **october 2012**.
- [24] T. Grünweg, "Hybridtechnik entschlüsselt: Von Seriell bis Parallel. 2. Teil: Mikro-Hybrid", can be found under <http://www.spiegel.de/auto/aktuell/hybridtechnik-entschluesselt-von-seriell-bis-parallel-a-728495-2.html>. SPIEGEL ONLINE GmbH (Ed.). **2010**.
- [25] T. Grünweg, "Hybridtechnik entschlüsselt: Von Seriell bis Parallel. 3. Teil: Mild-Hybrid", can be found under <http://www.spiegel.de/auto/aktuell/hybridtechnik-entschluesselt-von-seriell-bis-parallel-a-728495-3.html>. SPIEGEL ONLINE GmbH (Ed.). **2010**.
- [26] T. Grünweg, "Hybridtechnik entschlüsselt: Von Seriell bis Parallel. 4. Teil: Voll-Hybrid", can be found under <http://www.spiegel.de/auto/aktuell/hybridtechnik-entschluesselt-von-seriell-bis-parallel-a-728495-4.html>. SPIEGEL ONLINE GmbH (Ed.). **2010**.
- [27] T. Grünweg, "Hybridtechnik entschlüsselt: Von Seriell bis Parallel. 6. Teil: Serieller Hybrid", can be found under <http://www.spiegel.de/auto/aktuell/hybridtechnik-entschluesselt-von-seriell-bis-parallel-a-728495-6.html>. SPIEGEL ONLINE GmbH (Ed.). **2010**.
- [28] T. Grünweg, "Hybridtechnik entschlüsselt: Von Seriell bis Parallel. 5. Teil: Parallel-Hybrid", can be found under <http://www.spiegel.de/auto/aktuell/hybridtechnik-entschluesselt-von-seriell-bis-parallel-a-728495-5.html>. SPIEGEL ONLINE GmbH (Ed.). **2010**.

- [29] T. Grünweg, "Hybridtechnik entschlüsselt: Von Seriell bis Parallel. 8. Teil: Plug-In-Hybrid", can be found under <http://www.spiegel.de/auto/aktuell/hybridtechnik-entschluesselt-von-seriell-bis-parallel-a-728495-8.html>. SPIEGEL ONLINE GmbH (Ed.). **2010**.
- [30] M. Beermann, G. Jungmeier, A. Wenzel, J. Spitzer, L. Canella, A. Engel, M. Schmuck, S. Koller, "Quo Vadis Elektroauto? Grundlagen einer Roadmap für die Einführung von Elektro-Fahrzeugen in Österreich", can be found under <https://www.google.de/url?sa=t&rct=j&q=&esrc=s&source=web&cd=1&ved=0CCMQFjAAahUKEwju2JOM3cvIAhVCQBoKHRPRCE0&url=https%3A%2F%2Fwww2.ffg.at%2Fverkehr%2Ffile.php%3Fid%3D308&usg=AFQjCNGm-0a2yyJGcCqVyGO6vFnt9Q98iQ&bvm=bv.105454873,d.bGg&cad=rja>. Bundesministerium für Verkehr, Innovation und Technologie (bmvit) (Ed.), TU Graz; Joanneum Research Forschungsgesellschaft mbH. **april 2010**.
- [31] T. E. Conver, P. L. Corsell, D. W. Crane, K. Czinger, P. A. Darbee, S. Ghasemi, C. Ghosn, R. Lane, R. Lowenthal, A. A. Molinaroli et al., "Electrification Roadmap. Revolutionizing transportation and achieving energy security", can be found under <http://www.electrificationcoalition.org/policy/electrification-roadmap>. Electrification Coalition (Ed.). **november 2009**.
- [32] C. Chanson, J.-P. Wiaux, "Safety of lithium-ion batteries", can be found under https://www.google.de/url?sa=t&rct=j&q=&esrc=s&source=web&cd=1&ved=0CCAQFjAAahUKEwiAk5mJoszIAhUDEiwKHf5BD8s&url=http%3A%2F%2Fwww.rechargebatteries.org%2Fwp-content%2Fuploads%2F2013%2F07%2FLi-ion-safety-July-9-2013-Recharge-.pdf&usg=AFQjCNFiTYZLzdFBcqYNDyqfUFZ_IJzNw&bvm=bv.105454873,d.d24&cad=rja. RECHARGE - The European Association for Advanced Rechargeable Batteries (Ed.). **june 2013**.
- [33] L. Brinkhaus, "Degradation Phenomena of Lithium-rich Lithium-Nickel-Cobalt-Manganese-Oxide in Lithium-Ion-Batteries", can be found under <https://opus4.kobv.de/opus4-fau/frontdoor/index/index/docId/5926>. Friedrich-Alexander-Universität Erlangen-Nürnberg (Ed.), Erlangen. **2015**.

- [34] a) H. Wallentowitz, A. Freialdenhoven, *Strategien zur Elektrifizierung des Antriebsstranges. Technologien, Märkte und Implikationen*, Vieweg+Teubner Verlag / Springer Fachmedien Wiesbaden GmbH, Wiesbaden, Wiesbaden, **2011**;
b) A. Thielmann, A. Sauer, R. Isenmann, M. Wietschel, "Technology Roadmap Energy storage for Electric mobility 2030", can be found under
https://www.google.de/url?sa=t&rct=j&q=&esrc=s&source=web&cd=16&ved=0CEQQFjAFOApqFQoTCPalzMWU28gCFQaILAodnTALTg&url=http%3A%2F%2Fwww.isi.fraunhofer.de%2Fisi-wAssets%2Fdocs%2Ft%2Fen%2FTRM-ESEM-2030_en_web.pdf&usg=AFQjCNGyLQz02zwcnaYYYvx1CQwmUDC7XA&bvm=bv.105841590,d.bGg&cad=rja
a. E&B engelhardt und bauer Druck (Ed.), Fraunhofer Institute for Systems and Innovation Research ISI; German Federal Ministry of Education and Research (BMBF), Karlsruhe. **2012**.
- [35] a) R. Benedix, *Bauchemie. Einführung in die Chemie für Bauingenieure und Architekten*, Springer Vieweg, Wiesbaden, **2015**; b) E. D. Gates, *Introduction to basic electricity and electronics technology*, Delmar/Cengage Learning, Clifton Park, N.Y, **2014**.
- [36] R. Dell, Rand, D. A. J, *Understanding batteries*, Royal Society of Chemistry, Cambridge, **2001**.
- [37] S. C. Mukhopadhyay, *Intelligent sensing, instrumentation and measurements*, Springer, Berlin, New York, **2013**.
- [38] J. Weidner, *Battery and energy technology (general). At the 214th ECS meeting ; October 12 - 17, 2008, Honolulu, Hawai, USA ; [papers .. presented in the Symposium "Battery and Energy Technology Joint General Session", held during the PRiME 2008 joint international meeting of the Electrochemical Society and the Electrochemical Society of Japan]*, Curran, Red Hook, NY, **2009**.
- [39] D. Pavlov, *Leade-Acid Batteries. Science and Technology, a Handbook of LeadeAcid Battery Technology and its Influence on the Product*, Elsevier, Oxford [etc.], **2011**.
- [40] K. Lu, *Materials in energy conversion, harvesting, and storage*, Wiley, Hoboken, N.J, **2014**.
- [41] İ. Dinçer, M. Rosen, *Thermal energy storage. Systems and applications*, Wiley, Hoboken, N.J, **2011**.
- [42] *Automation for productivity. A conference for senior management*;, Institution of Electrical Engineers, London, **1968**.
- [43] T. R. Crompton, *Battery reference book*, Newnes, Oxford, England, Boston, **2000**.

- [44] I. Buchmann, "Memory: Myth or Fact?", can be found under http://batteryuniversity.com/learn/article/memory_myth_or_fact. Battery University (Ed.). **2015**.
- [45] a) H. A. Kiehne, *Battery technology handbook*, Marcel Dekker, New York, **2003**;
b) R.-S. Liu, *Electrochemical technologies for energy storage and conversion*, Wiley-VCH, Weinheim, **2012**.
- [46] O. G. Palanna, *Engineering chemistry*, Tata McGraw-Hill, New Delhi, **2009**.
- [47] R. Dell, Rand, D. A. J, *Clean energy*, Royal Society of Chemistry, Cambridge, **2004**.
- [48] B. Scrosati, W. A. v. Schalkwijk, *Advances in lithium-ion batteries*, Springer, New York [etc.], **2002**.
- [49] K. Ozawa, *Lithium ion rechargeable batteries*, Wiley-VCH, Weinheim, **2009**.
- [50] J. Doelle, "Investigation of Si/C-based anodes for Li-ion batteries", can be found under https://www.google.de/url?sa=t&rct=j&q=&esrc=s&source=web&cd=2&ved=0CCQQFjABahUKEwi-xbra0NrIAhWD1RQKHauYAug&url=https%3A%2F%2Fopus4.kobv.de%2Fopus4-tuberlin%2Ffiles%2F5824%2Fdoelle_janis.pdf&usg=AFQjCNFwFtWeKwKIXP_I no27 WM08fnUxHg&cad=rja. Technischen Universität Berlin (Ed.), Berlin. **2014**.
- [51] M. Rossi, J. Carroll, G. P. Tandon, G. Shaw, F. Barthelat, H. Jin, B. Antoun, J. Kimberley, D. Casem, B. Song, *Proceedings of the 2013 Annual Conference on Experimental and Applied Mechanics*.
- [52] F. H. Cocks, *Energy demand and climate change. Issues and resolutions*, Wiley-VCH, Weinheim, **2009**.
- [53] R. J. Brodd, *Batteries for sustainability. Selected entries from the Encyclopedia of Sustainability Science and Technology*, Springer, New York, **2012**.
- [54] *Transitions to alternative vehicles and fuels*, The National Academies Press, Washington, **2013**
- [55] D. Liu, W. Zhu, J. Trottier, C. Gagnon, F. Barray, A. Guerfi, A. Mauger, H. Groult, C. M. Julien, J. B. Goodenough et al., *RSC Adv* **2014**, 4, 154–167.
- [56] J. B. Goodenough, K.-S. Park, *J. Am. Chem. Soc.* **2013**, 135, 1167–1176.
- [57] A. Kraytsberg, Y. Ein-Eli, *Adv. Energy Mater.* **2012**, 2, 922–939.
- [58] M. S. Whittingham, *Chem. Rev. (Washington, DC, U. S.)* **2004**, 104, 4271–4301.
- [59] M. S. Whittingham, A. J. Jacobson, *Intercalation chemistry*, Academic Press, New York, **1982**.

- [60] J. A. Kilner, *Functional materials for sustainable energy applications*, Woodhead Pub., Oxford, Philadelphia, **2012**.
- [61] C. Menictas, *Advances in batteries for large- and medium-scale energy storage. Applications in power systems and electric vehicles*, Elsevier, Cambridge, Waltham, Kidlington, **2015**.
- [62] L. Campanella, G. Pistoia, *J. Electrochem. Soc.* **1971**, *118*, 1905–8.
- [63] W. Han, M. Hibino, T. Kudo, *Denki Kagaku oyobi Kogyo Butsuri Kagaku* **1998**, *66*, 1230–1233.
- [64] J. O. Besenhard, R. Schoellhorn, *J. Electrochem. Soc.* **1977**, *124*, 968–71.
- [65] a) Whittingham, M. Stanley., *J. Electrochem. Soc.* **1976**, *123*, 315–20; b) C. R. Walk, N. Margalit, *J. Power Sources* **1997**, *68*, 723–725; c) C. Delmas, H. Cognac-Auradou, Cocciantelli, J. M., M. Menetrier, Doumerc, J. P., *Solid State Ionics* **1994**, *69*, 257–64; d) Dickens, P. G., French, S. J., Hight, A. T., Pye, M. F., *Mater. Res. Bull.* **1979**, *14*, 1295–9; e) X. Huang, X. Rui, H. H. Hng, Q. Yan, *Part. Part. Syst. Charact.* **2015**, *32*, 276–294.
- [66] M. Zeng, H. Yin, K. Yu, *Chemical Engineering Journal* **2012**, *188*, 64–70.
- [67] R. Pitchai, V. Thavasi, S. G. Mhaisalkar, S. Ramakrishna, *J. Mater. Chem.* **2011**, *21*, 11040–11051.
- [68] a) C. Delmas, M. Devalette, C. Fouassier, P. Hagenmuller, *Mater. Res. Bull.* **1975**, *10*, 393–8; b) C. Delmas, C. Fouassier, P. Hagenmuller, *J. Solid State Chem.* **1975**, *13*, 165–71; c) C. Delmas, C. Fouassier, J. M. Reau, P. Hagenmuller, *Mater. Res. Bull.* **1976**, *11*, 1081–6; d) C. Delmas, C. Fouassier, *Z. Anorg. Allg. Chem.* **1976**, *420*, 184–92.
- [69] C. Delmas, J. J. Braconnier, C. Fouassier, P. Hagenmuller, *Solid State Ionics* **1981**, *3-4*, 165–9.
- [70] C. M. Julien, A. Mauger, K. Zaghib, H. Groult, *Inorganics* **2014**, *2*, 132–154.
- [71] a) C. Delmas, J. J. Braconnier, P. Hagenmuller, *Mater. Res. Bull.* **1982**, *17*, 117–23; b) C. Delmas, J. J. Braconnier, A. Maazaz, P. Hagenmuller, *Rev. Chim. Miner.* **1982**, *19*, 343–51; c) A. Mendiboure, C. Delmas, P. Hagenmuller, *Mater. Res. Bull.* **1984**, *19*, 1383–92.
- [72] G. Nazri, G. Pistoia, *Lithium batteries. Science and technology*, Kluwer Academic Publishers, Boston, **2004**.
- [73] H. Tukamoto, West, A. R., *J. Electrochem. Soc.* **1997**, *144*, 3164–3168.
- [74] S. Komaba, N. Kumagai, Y. Kataoka, *Electrochimica Acta* **2002**, *47*, 1229–1239.

- [75] a) X. Li, J. Liu, X. Meng, Y. Tang, M. N. Banis, J. Yang, Y. Hu, R. Li, M. Cai, X. Sun, *J. Power Sources* **2014**, *247*, 57–69; b) X. Li, J. Liu, M. N. Banis, A. Lushington, R. Li, M. Cai, X. Sun, *Energy Environ. Sci.* **2014**, *7*, 768–778; c) J. Cho, J.-G. Lee, B. Kim, T.-G. Kim, J. Kim, B. Park, *Electrochim. Acta* **2005**, *50*, 4182–4187; d) G. Li, Z. Yang, W. Yang, *J. Power Sources* **2008**, *183*, 741–748.
- [76] B. Xu, D. Qian, Z. Wang, Y. S. Meng, *Mater. Sci. Eng., R* **2012**, *73*, 51–65.
- [77] a) Thomas, M. G. S. R., David, W. I. F., J. B. Goodenough, P. Groves, *Mater. Res. Bull.* **1985**, *20*, 1137–46; b) J. R. Dahn, U. von Sacken, Michal, C. A., *Solid State Ionics* **1990**, *44*, 87–97; c) M. Broussely, F. Pertion, P. Biensan, Bodet, J. M., J. Labat, A. Lecerf, C. Delmas, A. Rougier, Peres, J. P., *J. Power Sources* **1995**, *54*, 109–14; d) J. R. Dahn, U. von Sacken, Juzkow, M. W., H. Al-Janaby, *J. Electrochem. Soc.* **1991**, *138*, 2207–11; e) W. Ebner, D. Fouchard, L. Xie, *Solid State Ionics* **1994**, *69*, 238–56; f) X.-r. Deng, G.-r. Hu, K. Du, Z.-d. Peng, X.-G. Gao, Y.-N. Yang, *Mater. Chem. Phys.* **2008**, *109*, 469–474.
- [78] P. He, H. Yu, D. Li, H. Zhou, *J. Mater. Chem.* **2012**, *22*, 3680–3695.
- [79] a) G. Dutta, A. Manthiram, J. B. Goodenough, Grenier, J. C., *J. Solid State Chem.* **1992**, *96*, 123–31; b) A. Hirano, R. Kanno, Y. Kawamoto, Y. Takeda, K. Yamaura, M. Takano, K. Ohyama, M. Ohashi, Y. Yamaguchi, *Solid State Ionics* **1995**, *78*, 123–31.
- [80] W. Liu, P. Oh, X. Liu, M.-J. Lee, W. Cho, S. Chae, Y. Kim, J. Cho, *Angew. Chem., Int. Ed.* **2015**, *54*, 4440–4457.
- [81] A. Rougier, P. Gravereau, C. Delmas, *J. Electrochem. Soc.* **1996**, *143*, 1168–75.
- [82] M. Guilmard, L. Croguennec, D. Denux, C. Delmas, *Chem. Mater.* **2003**, *15*, 4476–4483.
- [83] a) T. Ohzuku, T. Yanagawa, M. Kouguchi, A. Ueda, *J. Power Sources* **1997**, *68*, 131–134; b) C. Vogler, B. Loffler, W. Weirather, M. Wohlfahrt-Mehrens, J. Garche, *Ionics* **2002**, *8*, 92–99; c) C. Poullerie, L. Croguennec, P. Biensan, P. Willmann, C. Delmas, *J. Electrochem. Soc.* **2000**, *147*, 2061–2069.
- [84] T. Ohzuku, A. Ueda, M. Kouguchi, *J. Electrochem. Soc.* **1995**, *142*, 4033–9.
- [85] a) I. Saadoune, M. Menetrier, C. Delmas, *J. Mater. Chem.* **1997**, *7*, 2505–2511; b) I. Saadoune, C. Delmas, *J. Mater. Chem.* **1996**, *6*, 193–9; c) C. Delmas, M. Menetrier, L. Croguennec, I. Saadoune, A. Rougier, C. Poullerie, G. Prado, M. Grune, L. Fournes, *Electrochim. Acta* **1999**, *45*, 243–253.
- [86] I. Saadoune, C. Delmas, *J. Solid State Chem.* **1998**, *136*, 8–15.
- [87] A. Rougier, I. Saadoune, P. Gravereau, P. Willmann, C. Delmas, *Solid State Ionics* **1996**, *90*, 83–90.

- [88] C. Delmas, I. Saadoune, A. Rougier, *J. Power Sources* **1993**, *44*, 595–602.
- [89] E. Zhecheva, R. Stoyanova, *Solid State Ionics* **1993**, *66*, 143–9.
- [90] D. Caurant, N. Baffier, B. Garcia, Pereira-Ramos, J. P., *Solid State Ionics* **1996**, *91*, 45–54.
- [91] Z. Liu, A. Yu, J. Y. Lee, *J. Power Sources* **1999**, *81-82*, 416–419.
- [92] a) M. Broussely, P. Biensan, B. Simon, *Electrochim. Acta* **1999**, *45*, 3–22; b) J. Cho, *Chem. Mater.* **2000**, *12*, 3089–3094; c) C.-C. Chang, Kim, J. Y., Kumta, P. N., *J. Power Sources* **2000**, *89*, 56–63; d) Weaving, J. S., F. Coowar, Teagle, D. A., J. Cullen, V. Dass, P. Bindin, R. Green, Macklin, W. J., *J. Power Sources* **2001**, *97-98*, 733–735; e) S. Albrecht, J. Kumpers, M. Kruft, S. Malcus, C. Vogler, M. Wahl, M. Wohlfahrt-Mehrens, *J. Power Sources* **2003**, *119-121*, 178–183; f) C. H. Chen, J. Liu, Stoll, M. E., G. Henriksen, Vissers, D. R., K. Amine, *J. Power Sources* **2004**, *128*, 278–285; g) R. Kosteck, J. Lei, F. McLarnon, J. Shim, K. Striebel, *J. Electrochem. Soc.* **2006**, *153*, A669-A672.
- [93] C. Poullierie, F. Perton, P. Biensan, Peres, J. P., M. Broussely, C. Delmas, *J. Power Sources* **2001**, *96*, 293–302.
- [94] M. Broussely, *Lithium battery discussion [also LiBD], Bordeaux-Arcachon, France, May 27 June 1, 2001: program [and] extended abstracts*, Universite de Science et Technologie, **2001**.
- [95] V. Hennige, "The Tesla Model S Battery. A Battery Pack Analysis Study". AVL List GmbH (Ed.). **2014**.
- [96] D. Ahuja, E. Musk, "ANNUAL REPORT ON FORM 10-K FOR THE YEAR ENDED DECEMBER 31, 2014", can be found under <http://ir.teslamotors.com/secfiling.cfm?filingID=1564590-15-1031&CIK=1318605>. I. Tesla Motors (Ed.). **2015**.
- [97] M. M. Thackeray, S.-H. Kang, C. S. Johnson, J. T. Vaughey, R. Benedek, S. A. Hackney, *J. Mater. Chem.* **2007**, *17*, 3112–3125.
- [98] a) Y. Itou, Y. Ukyo, *Selected papers presented at the 12th International Meeting on Lithium Batteries 12th International Meeting on Lithium Batteries* **2005**, *146*, 39–44; b) I. Bloom, S. A. Jones, V. S. Battaglia, G. L. Henriksen, J. P. Christophersen, R. B. Wright, C. D. Ho, J. R. Belt, C. G. Motloch, *Journal of Power Sources* **2003**, *124*, 538–550.

- [99] a) R. Chen, Whittingham, M. Stanley., *J. Electrochem. Soc.* **1997**, *144*, L64-L67;
b) F. Capitaine, P. Gravereau, C. Delmas, *Solid State Ionics* **1996**, *89*, 197–202;
c) Gummow, R. J., M. M. Thackeray, *J. Electrochem. Soc.* **1994**, *141*, 1178–82;
d) Y. Shao-Horn, S. A. Hackney, Armstrong, A. R., Bruce, P. G., R. Gitzendanner, C. S. Johnson, M. M. Thackeray, *J. Electrochem. Soc.* **1999**, *146*, 2404–2412.
- [100] A. R. Armstrong, P. G. Bruce, *Nature (London)* **1996**, *381*, 499–500.
- [101] P. G. Bruce, A. R. Armstrong, R. L. Gitzendanner, *J. Mater. Chem.* **1999**, *9*, 193–198.
- [102] B. Fuchs, S. Kemmler-Sack, *Solid State Ionics* **1994**, *68*, 279–85.
- [103] Mishra, S. K., G. Ceder, *Phys. Rev. B: Condens. Matter Mater. Phys.* **1999**, *59*, 6120–6130.
- [104] G. Ceder, Mishra, S. K., *Electrochem. Solid-State Lett.* **1999**, *2*, 550–552.
- [105] a) M. Gu, I. Belharouak, J. Zheng, H. Wu, J. Xiao, A. Genc, K. Amine, S. Thevuthasan, D. R. Baer, J.-G. Zhang et al., *ACS Nano* **2013**, *7*, 760–767; b) J. Tu, Zhao, X. B., Cao, G. S., Zhuang, D. G., Zhu, T. J., J. P. Tu, *Electrochim. Acta* **2006**, *51*, 6456–6462.
- [106] Paulsen, J. M., Thomas, C. L., J. R. Dahn, *J. Electrochem. Soc.* **1999**, *146*, 3560–3565.
- [107] a) Y.-I. Jang, B. Huang, Y.-M. Chiang, D. R. Sadoway, *Electrochem. Solid-State Lett.* **1998**, *1*, 13–16; b) Y.-M. Chiang, D. R. Sadoway, Y.-I. Jang, B. Huang, H. Wang, *Electrochem. Solid-State Lett.* **1999**, *2*, 107–110.
- [108] a) Davidson, I. J., McMillan, R. S., Murray, J. J., *J. Power Sources* **1995**, *54*, 205–8;
b) Davidson, I. J., McMillan, R. S., H. Sleg, B. Luan, I. Kargina, Murray, J. J., Swainson, I. P., *J. Power Sources* **1999**, *81-82*, 406–411.
- [109] Y. Koyama, Y. Makimura, I. Tanaka, H. Adachi, T. Ohzuku, *J. Electrochem. Soc.* **2004**, *151*, A1499-A1506.
- [110] a) A. Robert Armstrong, R. Gitzendanner, *Chem. Commun. (Cambridge)* **1998**, 1833–1834; b) A. R. Armstrong, A. J. Paterson, A. D. Robertson, P. G. Bruce, *Chem. Mater.* **2002**, *14*, 710–719; c) Armstrong, A. R., Robertson, A. D., Bruce, P. G., *Electrochim. Acta* **1999**, *45*, 285–294.
- [111] R. Stoyanova, E. Zhecheva, L. Zarkova, *Solid State Ionics* **1994**, *73*, 233–40.
- [112] I. Yanase, T. Ohtaki, M. Watanabe, *Solid State Ionics* **2002**, *151*, 189–196.
- [113] E. Rossen, Jones, C. D. W., J. R. Dahn, *Solid State Ionics* **1992**, *57*, 311–18.
- [114] M. E. Spahr, P. Novak, B. Schnyder, O. Haas, R. Nesper, *J. Electrochem. Soc.* **1998**, *145*, 1113–1121.

- [115] Z. Lu, D. D. MacNeil, J. R. Dahn, *Electrochem. Solid-State Lett.* **2001**, *4*, A191-A194.
- [116] Y.-K. Sun, C. S. Yoon, Y. S. Lee, *Electrochim. Acta* **2003**, *48*, 2589–2592.
- [117] N. Yabuuchi, Y.-T. Kim, H. H. Li, S.-H. Yang, *Chem. Mater.* **2008**, *20*, 4936–4951.
- [118] a) H. Lin, J. Zheng, Y. Yang, *Mater. Chem. Phys.* **2010**, *119*, 519–523; b) Y.-K. Sun, S.-T. Myung, B.-C. Park, H. Yashiro, *J. Electrochem. Soc.* **2008**, *155*, A705-A710; c) N. Yabuuchi, Y.-C. Lu, A. N. Mansour, T. Kawaguchi, Y. Shao-Horn, *Electrochem. Solid-State Lett.* **2010**, *13*, A158-A161.
- [119] F. Zhou, X. Zhao, Smith, A. J., J. R. Dahn, *J. Electrochem. Soc.* **2010**, *157*, A399-A406.
- [120] N. Yabuuchi, T. Ohzuku, *J. Power Sources* **2003**, *119*-121, 171–174.
- [121] J. Choi, A. Manthiram, *J. Electrochem. Soc.* **2005**, *152*, A1714-A1718.
- [122] T. Ohzuku, Y. Makimura, *Chem. Lett.* **2001**, 642–643.
- [123] K. M. Shaju, Subba Rao, G. V., Chowdari, B. V. R., *Electrochim. Acta* **2002**, *48*, 145–151.
- [124] a) Park, S. H., C. S. Yoon, S. G. Kang, H.-S. Kim, S.-I. Moon, Y.-K. Sun, *Electrochim. Acta* **2004**, *49*, 557–563; b) J.-M. Kim, H.-T. Chung, *Electrochim. Acta* **2004**, *49*, 937–944.
- [125] B.-C. Park, H.-B. Kim, S.-T. Myung, K. Amine, I. Belharouak, S.-M. Lee, Y.-K. Sun, *J. Power Sources* **2008**, *178*, 826–831.
- [126] a) M. Yoshio, H. Noguchi, J.-i. Itoh, M. Okada, T. Mouri, *J. Power Sources* **2000**, *90*, 176–181; b) F. Zhou, X. Zhao, C. Goodbrake, J. Jiang, J. R. Dahn, *J. Electrochem. Soc.* **2009**, *156*, A796-A801; c) F. Zhou, X. Zhao, Z. Lu, J. Jiang, J. R. Dahn, *Electrochem. Commun.* **2008**, *10*, 1168–1171; d) J. Wilcox, S. Patoux, M. Doeff, *J. Electrochem. Soc.* **2009**, *156*, A192-A198.
- [127] M.-H. Kim, H.-S. Shin, D. Shin, Y.-K. Sun, *J. Power Sources* **2006**, *159*, 1328–1333.
- [128] K.-S. Lee, S.-T. Myung, K. Amine, H. Yashiro, Y.-K. Sun, *J. Electrochem. Soc.* **2007**, *154*, A971-A977.
- [129] J. DiCarlo, "Roadmap for Cathode Materials for Electric Vehicles", can be found under https://www.google.de/url?sa=t&rct=j&q=&esrc=s&source=web&cd=2&ved=0CCkQFjAB&url=http%3A%2F%2Fwww.cse.anl.gov%2Fus-china-workshop-2012%2Fpdfs%2Fsession4a_testing_safety%2Fdicarlo_4A-3-DiCarlo-BASF-BASFUS-China.pptx&ei=RAWYVZreG8awUY3QgJgD&usg=AFQjCNEWeQKAE5OXe1v7gPVQWqlNI22mzA&bvm=bv.89381419,d.d2s&cad=rja. BASF - The Chemical Company (Ed.). **2012**.

- [130] a) T.-J. Park, J.-B. Lim, J.-T. Son, *Bull. Korean Chem. Soc.* **2014**, *35*, 357–364; b) M. Guilmard, C. Pouillier, L. Croguennec, C. Delmas, *Solid State Ionics* **2003**, *160*, 39–50; c) F. Lin, M. M. Doeff, I. M. Markus, D. Nordlund, T.-C. Weng, M. D. Asta, H. L. Xin, *Nat Commun* **2014**, *5*, 3529.
- [131] Y. Cho, P. Oh, J. Cho, *Nano Lett.* **2013**, *13*, 1145–1152.
- [132] a) Y. Cho, S. Lee, Y. Lee, T. Hong, J. Cho, *Adv. Energy Mater.* **2011**, *1*, 821–828; b) Y.-K. Sun, S.-T. Myung, B.-C. Park, J. Prakash, I. Belharouak, K. Amine, *Nat. Mater.* **2009**, *8*, 320–324.
- [133] A. Boulineau, L. Croguennec, C. Delmas, F. Weill, *Solid State Ionics* **2010**, *180*, 1652–1659.
- [134] M. M. Thackeray, *Prog. Solid State Chem.* **1997**, *25*, 1–71.
- [135] a) K. Numata, C. Sakaki, S. Yamanaka, *Chem. Lett.* **1997**, 725–726; b) K. Numata, C. Sakaki, S. Yamanaka, *Solid State Ionics* **1999**, *117*, 257–263; c) K. Numata, S. Yamanaka, *Solid State Ionics* **1999**, *118*, 117–120.
- [136] P. Kalyani, S. Chitra, T. Mohan, S. Gopukumar, *J. Power Sources* **1999**, *80*, 103–106.
- [137] a) Z. Lu, Beaulieu, L. Y., Donaberger, R. A., Thomas, C. L., J. R. Dahn, *J. Electrochem. Soc.* **2002**, *149*, A778-A791; b) C. Storey, I. Kargina, Y. Grincourt, Davidson, I. J., Yoo, Y. C., Seung, D. Y., *J. Power Sources* **2001**, *97-98*, 541–544; c) C. Pan, Y. J. Lee, B. Ammundsen, C. P. Grey, *Chem. Mater.* **2002**, *14*, 2289–2299; d) E. Shinova, T. Mandzhukova, E. Grigorova, M. Hristov, R. Stoyanova, D. Nihtianova, E. Zhecheva, *Solid State Ionics* **2011**, *187*, 43–49.
- [138] Z. Lu, J. R. Dahn, *J. Electrochem. Soc.* **2002**, *149*, A815-A822.
- [139] S.-H. Kang, P. Kempgens, S. Greenbaum, A. J. Kropf, K. Amine, M. M. Thackeray, *J. Mater. Chem.* **2007**, *17*, 2069–2077.
- [140] C. S. Johnson, N. Li, C. Lefief, J. T. Vaughey, M. M. Thackeray, *Chem. Mater.* **2008**, *20*, 6095–6106.
- [141] F. Amalraj, D. Kovacheva, M. Talianker, L. Zeiri, J. Grinblat, N. Leifer, G. Goobes, B. Markovsky, D. Aurbach, *J. Electrochem. Soc.* **2010**, *157*, A1121-A1130.
- [142] a) B. Song, Z. Liu, M. O. Lai, L. Lu, *Phys. Chem. Chem. Phys.* **2012**, *14*, 12875–12883; b) J. M. Zheng, X. B. Wu, Y. Yang, *Electrochim. Acta* **2011**, *56*, 3071–3078.
- [143] X. Zhang, C. Yu, X. Huang, J. Zheng, X. Guan, D. Luo, L. Li, *Electrochim. Acta* **2012**, *81*, 233–238.

- [144] R. Marom, S. F. Amalraj, N. Leifer, D. Jacob, D. Aurbach, *J. Mater. Chem.* **2011**, *21*, 9938–9954.
- [145] Armstrong, A. R., Robertson, A. D., Bruce, P. G., *J. Power Sources* **2005**, *146*, 275–280.
- [146] a) S. F. Amalraj, L. Burlaka, C. M. Julien, A. Mauger, D. Kovacheva, M. Talianker, B. Markovsky, D. Aurbach, *Electrochim. Acta* **2014**, *123*, 395–404; b) X. Yang, Di Wang, R. Yu, Y. Bai, H. Shu, L. Ge, H. Guo, Q. Wei, L. Liu, X. Wang, *J. Mater. Chem. A* **2014**, *2*, 3899–3911.
- [147] N. Yabuuchi, K. Yoshii, S.-T. Myung, I. Nakai, S. Komaba, *J. Am. Chem. Soc.* **2011**, *133*, 4404–4419.
- [148] a) C. S. Johnson, J.-S. Kim, C. Lefief, N. Li, Vaughey, J. T., M. M. Thackeray, *Electrochem. Commun.* **2004**, *6*, 1085–1091; b) M. M. Thackeray, C. S. Johnson, J. T. Vaughey, N. Li, S. A. Hackney, *J. Mater. Chem.* **2005**, *15*, 2257–2267.
- [149] H. Yu, H. Zhou, *J. Mater. Chem.* **2012**, *22*, 15507–15510.
- [150] a) Y.-K. Sun, M.-J. Lee, C. S. Yoon, J. Hassoun, K. Amine, B. Scrosati, *Adv. Mater. (Weinheim, Ger.)* **2012**, *24*, 1192–1196; b) J. Cho, Y.-W. Kim, B. Kim, J.-G. Lee, B. Park, *Angew. Chem., Int. Ed.* **2003**, *42*, 1618–1621; c) S.-T. Myung, K. Izumi, S. Komaba, Y.-K. Sun, H. Yashiro, N. Kumagai, *Chem. Mater.* **2005**, *17*, 3695–3704.
- [151] a) A. Manthiram, J. B. Goodenough, *J. Power Sources* **1989**, *26*, 403–8; b) A. Manthiram, J. B. Goodenough, *J. Solid State Chem.* **1987**, *71*, 349–60.
- [152] a) A. K. Padhi, K. S. Nanjundaswamy, C. Masquelier, J. B. Goodenough, *J. Electrochem. Soc.* **1997**, *144*, 2581–2586; b) A. K. Padhi, K. S. Nanjundaswamy, J. B. Goodenough, *J. Electrochem. Soc.* **1997**, *144*, 1188–1194.
- [153] A. K. Padhi, K. S. Nanjundaswamy, C. Masquelier, S. Okada, J. B. Goodenough, *J. Electrochem. Soc.* **1997**, *144*, 1609–1613.
- [154] a) K.-S. Park, S. B. Schougaard, J. B. Goodenough, *Adv. Mater. (Weinheim, Ger.)* **2007**, *19*, 848–851; b) J. Chen, Whittingham, M. Stanley., *Electrochem. Commun.* **2006**, *8*, 855–858; c) J. Chen, M. J. Vacchio, S. Wang, N. Chernova, P. Y. Zavalij, Whittingham, M. Stanley., *Solid State Ionics* **2008**, *178*, 1676–1693; d) B. Kang, G. Ceder, *Nature (London, U. K.)* **2009**, *458*, 190–193; e) A. Yamada, Chung, S. C., K. Hinokuma, *J. Electrochem. Soc.* **2001**, *148*, A224–A229; f) S. Yang, Y. Song, K. Ngala, P. Y. Zavalij, M. Stanley Whittingham, *J. Power Sources* **2003**, *119–121*, 239–246.

- [155] a) S.-Y. Chung, J. T. Bloking, Y.-M. Chiang, *Nat. Mater.* **2002**, 1, 123–128; b) Wang, G. X., S. Needham, J. Yao, Wang, J. Z., Liu, R. S., H. K. Liu, *J. Power Sources* **2006**, 159, 282–286; c) Y. Wen, L. Zeng, Z. Tong, L. Nong, W. Wei, *J. Alloys Compd.* **2006**, 416, 206–208; d) M. Zhang, L.-F. Jiao, H.-T. Yuan, Y.-M. Wang, J. Guo, M. Zhao, W. Wang, X.-D. Zhou, *Solid State Ionics* **2006**, 177, 3309–3314.
- [156] a) J. Xu, G. Chen, *Phys. B (Amsterdam, Neth.)* **2010**, 405, 803–807; b) Fisher, Craig A. J., Hart Prieto, Veluz M., Islam, M. Saiful., *Chem. Mater.* **2008**, 20, 5907–5915.
- [157] M. Wagemaker, B. L. Ellis, D. Luetzenkirchen-Hecht, F. M. Mulder, L. F. Nazar, *Chem. Mater.* **2008**, 20, 6313–6315.
- [158] a) S. Yang, Zavalij, P. Y., M. Stanley Whittingham, *Electrochem. Commun.* **2001**, 3, 505–508; b) Y. Wang, J. Wang, J. Yang, Y. Nuli, *Adv. Funct. Mater.* **2006**, 16, 2135–2140; c) R. Dominko, M. Gaberscek, J. Drofenik, M. Bele, S. Pejovnik, J. Jamnik, *J. Power Sources* **2003**, 119–121, 770–773; d) C. Wang, J. Hong, *Electrochem. Solid-State Lett.* **2007**, 10, A65–A69.
- [159] Y. Lin, Gao, M. X., D. Zhu, Liu, Y. F., Pan, H. G., *J. Power Sources* **2008**, 184, 444–448.
- [160] a) X. Kong, R. Chen, WO2014056143A1; b) A. Manthiram, A. V. Murugan, M. Theivanayagam, WO2009061845A1.
- [161] R. Malik, D. Burch, M. Bazant, G. Ceder, *Nano Lett.* **2010**, 10, 4123–4127.
- [162] a) T. Muraliganth, A. V. Murugan, A. Manthiram, *J. Mater. Chem.* **2008**, 18, 5661–5668; b) R. Chen, Y. Wu, X. Y. Kong, *J. Power Sources* **2014**, 258, 246–252; c) J. Huang, Y. Sun, Y. Li, L. Cao, CN102437334A.
- [163] C. R. Sides, F. Croce, V. Y. Young, C. R. Martin, B. Scrosati, *Electrochem. Solid-State Lett.* **2005**, 8, A484–A487.
- [164] J. Chen, *Materials* **2013**, 6, 156–183.
- [165] Gover, R. K. B., P. Burns, A. Bryan, Saidi, M. Y., Swoyer, J. L., J. Barker, *Solid State Ionics* **2006**, 177, 2635–2638.
- [166] A. Nyten, A. Abouimrane, M. Armand, T. Gustafsson, J. O. Thomas, *Electrochem. Commun.* **2005**, 7, 156–160.
- [167] B. L. Ellis, K. Town, L. F. Nazar, *Electrochim. Acta* **2012**, 84, 145–154.
- [168] V. Legagneur, Y. An, A. Mosbah, R. Portal, G. S. A. La Le, A. Verbaere, D. Guyomard, Y. Piffard, *Solid State Ionics* **2001**, 139, 37–46.

- [169] A. Yamada, N. Iwane, Y. Harada, S.-i. Nishimura, Y. Koyama, I. Tanaka, *Adv Mater* **2010**, 22, 3583–7.
- [170] M. M. Thackeray, David, W. I. F., Bruce, P. G., J. B. Goodenough, *Mater. Res. Bull.* **1983**, 18, 461–72.
- [171] M. D. Bhatt, C. O'Dwyer, *Phys. Chem. Chem. Phys.* **2015**, 17, 4799–4844.
- [172] A. F. Holleman, E. Wiberg, N. Wiberg, *Lehrbuch der anorganischen Chemie*, de Gruyter, Berlin, New York, **2007**.
- [173] B. L. Ellis, K. T. Lee, L. F. Nazar, *Chem. Mater.* **2010**, 22, 691–714.
- [174] V. Massarotti, D. Capsoni, M. Bini, *Solid State Commun.* **2002**, 122, 317–322.
- [175] M. Tsunoda, Y. Oshima, M. Yoshinaga, T. Shirasu, *NEC Res. Dev.* **2000**, 41, 13–17.
- [176] a) H. Huang, C. A. Vincent, P. G. Bruce, *J. Electrochem. Soc.* **1999**, 146, 3649–3654; b) Y. Shin, A. Manthiram, *Electrochem. Solid-State Lett.* **2002**, 5, A55-A58; c) Y. Xia, Y. Zhou, M. Yoshio, *J. Electrochem. Soc.* **1997**, 144, 2593–2600; d) Tarascon, J. M., McKinnon, W. R., F. Coowar, Bowmer, T. N., G. Amatucci, D. Guyomard, *J. Electrochem. Soc.* **1994**, 141, 1421–31.
- [177] Kannan, A. M., A. Manthiram, *Electrochem. Solid-State Lett.* **2002**, 5, A167-A169.
- [178] K. Y. Chung, W.-S. Yoon, K.-B. Kim, X.-Q. Yang, S. M. Oh, *J. Electrochem. Soc.* **2004**, 151, A484-A492.
- [179] D. H. Jang, Y. J. Shin, S. M. Oh, *J. Electrochem. Soc.* **1996**, 143, 2204–2211.
- [180] Gummow, R. J., A. de Kock, M. M. Thackeray, *Solid State Ionics* **1994**, 69, 59–67.
- [181] T. Nakajima, H. Groult, *Fluorinated materials for energy conversion*, Elsevier, Amsterdam, San Diego, CA, Oxford, **2005**.
- [182] J. C. Hunter, *J. Solid State Chem.* **1981**, 39, 142–7.
- [183] J. Vetter, P. Novak, M. R. Wagner, C. Veit, K.-C. Moeller, J. O. Besenhard, M. Winter, M. Wohlfahrt-Mehrens, C. Vogler, A. Hammouche, *J. Power Sources* **2005**, 147, 269–281.
- [184] A. Manthiram, *Rechargeable lithium and lithium ion batteries*, Electrochemical Society, Pennington, N.J, **2010**.
- [185] M. Wohlfahrt-Mehrens, C. Vogler, J. Garche, *J. Power Sources* **2004**, 127, 58–64.
- [186] L. Guahua, H. Ikuta, T. Uchida, M. Wakihara, *J. Electrochem. Soc.* **1996**, 143, 178–82.
- [187] K. Amine, H. Tukamoto, H. Yasuda, Y. Fujita, *J. Electrochem. Soc.* **1996**, 143, 1607–1613.

- [188] Y. Gao, K. Myrtle, M. Zhang, J. N. Reimers, J. R. Dahn, *Phys. Rev. B: Condens. Matter* **1996**, *54*, 16670–16675.
- [189] Q. Zhong, A. Banakdarpour, M. Zhang, Y. Gao, J. R. Dahn, *J. Electrochem. Soc.* **1997**, *144*, 205–213.
- [190] H. Kawai, M. Nagata, H. Tukamoto, A. R. West, *J. Mater. Chem.* **1998**, *8*, 837–839.
- [191] C. Sigala, D. Guyomard, A. Verbaere, Y. Piffard, M. Tournoux, *Solid State Ionics* **1995**, *81*, 167–70.
- [192] T. M. Makepeace, G. R. June, DE4328755A1.
- [193] a) T. Ohzuku, S. Takeda, M. Iwanaga, *J. Power Sources* **1999**, *81-82*, 90–94; b) Y. Idemoto, H. Narai, N. Koura, *J. Power Sources* **2003**, *119-121*, 125–129; c) H. Kawai, M. Nagata, H. Kageyama, H. Tukamoto, A. R. West, *Electrochim. Acta* **1999**, *45*, 315–327.
- [194] Y. Wei, K.-B. Kim, G. Chen, *Electrochimica Acta* **2006**, *51*, 3365–3373.
- [195] J. H. Kim, S. T. Myung, C. S. Yoon, S. G. Kang, Y. K. Sun, *Chem. Mater.* **2004**, *16*, 906–914.
- [196] R. Alcantara, M. Jaraba, P. Lavela, J. L. Tirado, *Electrochim. Acta* **2002**, *47*, 1829–1835.
- [197] a) J. Cho, G. B. Kim, H. S. Lim, C.-S. Kim, S.-I. Yoo, *Electrochem. Solid-State Lett.* **1999**, *2*, 607–609; b) M. Lanz, C. Kormann, P. Novak, *J. Solid State Electrochem.* **2003**, *7*, 658–664; c) T. Numata, C. Amemiya, J. Iriyama, T. Miura, M. Shirakata, *NEC Res. Dev.* **2000**, *41*, 8–12; d) T. Numata, C. Amemiya, T. Kumeuchi, M. Shirakata, M. Yonezawa, *J. Power Sources* **2001**, *97-98*, 358–360; e) Ma, Z. F., X. Q. Yang, X. Sun, J. McBreen, *J. New Mater. Electrochem. Syst.* **2001**, *4*, 121–125; f) W. Xu, Angell, C. Austen., *Electrochem. Solid-State Lett.* **2001**, *4*, E1-E4.
- [198] H. Yamane, T. Inoue, M. Fujita, M. Sano, *Journal of Power Sources* **2001**, *99*, 60–65.
- [199] X. Ma, B. Kang, G. Ceder, *J. Electrochem. Soc.* **2010**, *157*, A925-A931.
- [200] K. Saravanan, A. Jarry, R. Kostecki, G. Chen, *Sci. Rep.* **2015**, *5*, 8027.
- [201] J. B. Goodenough, Y. Kim, *Chem. Mater.* **2010**, *22*, 587–603.
- [202] Y. Shin, A. Manthiram, *Electrochim. Acta* **2003**, *48*, 3583–3592.
- [203] C. M. Julien, A. Mauger, *Ionics* **2013**, *19*, 951–988.
- [204] R. Santhanam, B. Rambabu, *Journal of Power Sources* **2010**, *195*, 5442–5451.

- [205] L. Guoqiang, I. Belharouak, *Lithium Ion Batteries - New Developments. LiNi_{0.5}Mn_{1.5}O₄ Spinel and Its Derivatives as Cathodes for Li-Ion Batteries*, InTech, **2012**.
- [206] S. Patoux, L. Daniel, C. Bourbon, H. Lignier, C. Pagano, F. Le Cras, S. Jouanneau, S. Martinet, *Selected Papers presented at the 14th INTERNATIONAL MEETING ON LITHIUM BATTERIES (IMLB-2008)* **2009**, 189, 344–352.
- [207] M. Hu, X. Pang, Z. Zhou, *Journal of Power Sources* **2013**, 237, 229–242.
- [208] T.-F. Yi, Z.-K. Fang, Y. Xie, Y.-R. Zhu, L.-Y. Zang, *Electrochim. Acta* **2014**, 147, 250–256.
- [209] Lazarraga, M. G., L. Pascual, H. Gadjov, D. Kovacheva, K. Petrov, Amarilla, J. M., Rojas, R. M., Martin-Luengo, M. A., Rojo, J. M., *J. Mater. Chem.* **2004**, 14, 1640–1647.
- [210] D. Liu, J. Hamel-Paquet, J. Trottier, F. Barray, V. Gariépy, P. Hovington, A. Guerfi, A. Mauger, C. M. Julien, J. B. Goodenough et al., *Journal of Power Sources* **2012**, 217, 400–406.
- [211] S. Patoux, L. Daniel, C. Bourbon, H. Lignier, C. Pagano, F. Le Cras, S. Jouanneau, S. Martinet, *Selected Papers presented at the 14th INTERNATIONAL MEETING ON LITHIUM BATTERIES (IMLB-2008)* **2009**, 189, 344–352.
- [212] a) X. Y. Feng, C. Shen, X. Fang, C. H. Chen, *Chin. Sci. Bull.* **2012**, 57, 4176–4180; b) J.-H. Kim, S.-T. Myung, Y.-K. Sun, *Electrochim. Acta* **2004**, 49, 219–227; c) T.-F. Yi, X.-G. Hu, *Journal of Power Sources* **2007**, 167, 185–191; d) Y. Xue, Z. Wang, F. Yu, Y. Zhang, G. Yin, *J. Mater. Chem. A* **2014**, 2, 4185–4191; e) M. Zhang, Y. Liu, Y. Xia, B. Qiu, J. Wang, Z. Liu, *J. Alloys Compd.* **2014**, 598, 73–78.
- [213] L. Hernan, J. Morales, L. Sanchez, Castellon, E. Rodriguez, Aranda, M. A. G., *J. Mater. Chem.* **2002**, 12, 734–741.
- [214] H. Luo, P. Nie, L. Shen, H. Li, H. Deng, Y. Zhu, X. Zhang, *ChemElectroChem* **2015**, 2, 127–133.
- [215] J. Song, D. W. Shin, Y. Lu, C. D. Amos, A. Manthiram, J. B. Goodenough, *Chem. Mater.* **2012**, 24, 3101–3109.
- [216] R. Alcantara, M. Jaraba, P. Lavela, J. L. Tirado, P. Biensan, A. de Guibert, C. Jordy, Peres, J. P., *Chem. Mater.* **2003**, 15, 2376–2382.
- [217] a) B. J. Hwang, Wu, Y. W., M. Venkateswarlu, Cheng, M. Y., R. Santhanam, *J. Power Sources* **2009**, 193, 828–833; b) K.-J. Hong, Y.-K. Sun, *J. Power Sources* **2002**, 109, 427–430.

- [218] J. Liu, A. Manthiram, *J. Phys. Chem. C* **2009**, *113*, 15073–15079.
- [219] T. Ohzuku, K. Ariyoshi, S. Yamamoto, *J. Ceram. Soc. Jpn.* **2002**, *110*, 501–505.
- [220] T. Minami, M. Tatsumisago, *Solid state ionics for batteries*, Springer, Tokyo, New York, **2005**.
- [221] a) H. Xia, Meng, Y. S., L. Lu, G. Ceder, *J. Electrochem. Soc.* **2007**, *154*, A737-A743; b) G. Liu, Y. Li, B. Wang, *Int. J. Electrochem. Sci.* **2015**, *10*, 3124–3135.
- [222] Y.-C. Jin, C.-Y. Lin, J.-G. Duh, *Electrochim. Acta* **2012**, *69*, 45–50.
- [223] S. H. Oh, K. Y. Chung, S. H. Jeon, C. S. Kim, W. I. Cho, B. W. Cho, *J. Alloys Compd.* **2009**, *469*, 244–250.
- [224] L. Wang, H. Li, X. Huang, E. Baudrin, *Solid State Ionics* **2011**, *193*, 32–38.
- [225] a) H. Sun, B. Xia, W. Liu, G. Fang, J. Wu, H. Wang, R. Zhang, S. Kaneko, J. Zheng, H. Wang et al., *Applied Surface Science* **2015**, *331*, 309–314; b) Wu, W. W., Chen, J. J., S. Cheng, Xiang, H. F., *Ionics* **2015**, *21*, 1843-1849; c) M. Lin, L. Ben, Y. Sun, H. Wang, Z. Yang, L. Gu, X. Yu, X.-Q. Yang, H. Zhao, R. Yu et al., *Chem. Mater.* **2015**, *27*, 292–303.
- [226] Y. Terada, K. Yasaka, F. Nishikawa, T. Konishi, M. Yoshio, I. Nakai, *Journal of Solid State Chemistry* **2001**, *156*, 286–291.
- [227] S. Mukerjee, X. Q. Yang, X. Sun, S. J. Lee, J. McBreen, Y. Ein-Eli, *Electrochim. Acta* **2004**, *49*, 3373–3382.
- [228] T.-F. Yi, Y. Xie, M.-F. Ye, L.-J. Jiang, R.-S. Zhu, Y.-R. Zhu, *Ionics* **2011**, *17*, 383–389.
- [229] A. Manthiram, K. Chemelewski, E.-S. Lee, *Energy Environ. Sci.* **2014**.
- [230] J. Xiao, X. Yu, J. Zheng, Y. Zhou, F. Gao, X. Chen, J. Bai, X.-Q. Yang, J.-G. Zhang, *Journal of Power Sources* **2013**, *242*, 736–741.
- [231] a) S. W. Oh, S.-T. Myung, H. B. Kang, Y.-K. Sun, *Selected Papers presented at the 14th INTERNATIONAL MEETING ON LITHIUM BATTERIES (IMLB-2008)* **2009**, *189*, 752–756; b) E.-S. Lee, A. Manthiram, *J. Mater. Chem. A* **2013**, *1*, 3118–3126; c) K. R. Chemelewski, A. Manthiram, *J. Phys. Chem. C* **2013**, *117*, 12465–12471; d) G. T.-K. Fey, C.-Z. Lu, T. P. Kumar, *Journal of Power Sources* **2003**, *115*, 332–345.
- [232] Y. Idemoto, H. Sekine, K. Ui, N. Koura, *Solid State Ionics* **2005**, *176*, 299–306.
- [233] H. Arai, K. Sato, Y. Orikasa, H. Murayama, I. Takahashi, Y. Koyama, Y. Uchimoto, Z. Ogumi, *J. Mater. Chem. A* **2013**, *1*, 10442–10449.
- [234] I. Takahashi, H. Murayama, K. Sato, T. Naka, K. Kitada, K. Fukuda, Y. Koyama, H. Arai, E. Matsubara, Y. Uchimoto et al., *J. Mater. Chem. A* **2014**, *2*, 15414-15419.

- [235] a) A. Cao, A. Manthiram, *Phys. Chem. Chem. Phys.* **2012**, *14*, 6724–6728; b) Wu, H. M., J. P. Tu, Yuan, Y. F., Y. Li, Zhao, X. B., Cao, G. S., *Electrochim. Acta* **2005**, *50*, 4104–4108.
- [236] K. Ariyoshi, Y. Iwakoshi, N. Nakayama, T. Ohzuku, *J. Electrochem. Soc.* **2004**, *151*, A296-A303.
- [237] a) X. Wang, J. Wang, J. Wu, B. Cheng, M. Ma, Z. Jiang, *Ionics* **2015**, *21*, 1851-1856; b) Z. Chen, R. Zhao, A. Li, H. Hu, G. Liang, W. Lan, Z. Cao, H. Chen, *J. Power Sources* **2014**, *274*, 265–273.
- [238] H. Rong, M. Xu, B. Xie, X. Liao, W. Huang, L. Xing, W. Li, *Electrochim. Acta* **2014**, *147*, 31–39.
- [239] G. Yan, X. Li, Z. Wang, H. Guo, C. Wang, *Journal of Power Sources* **2014**, *248*, 1306–1311.
- [240] K. Xu, *Chem. Rev. (Washington, DC, U. S.)* **2004**, *104*, 4303–4417.
- [241] K. Xu, Angell, C. Austen., *J. Electrochem. Soc.* **2002**, *149*, A920-A926.
- [242] M. Moshkovich, M. Cojocaru, H. E. Gottlieb, D. Aurbach, *Journal of Electroanalytical Chemistry* **2001**, *497*, 84–96.
- [243] B. Scrosati, Abraham, K. M., W. A. v. Schalkwijk, J. Hassoun, *Lithium batteries. Advanced technologies and applications*.
- [244] G. Yan, X. Li, Z. Wang, H. Guo, X. Xiong, *J. Power Sources* **2014**, *263*, 231–238.
- [245] L. Yang, B. Ravdel, B. L. Lucht, *Electrochem. Solid-State Lett.* **2010**, *13*, A95-A97.
- [246] L. Hu, Z. Zhang, K. Amine, *Journal of Power Sources* **2013**, *236*, 175–180.
- [247] N. P. W. Pieczonka, L. Yang, M. P. Balogh, B. R. Powell, K. Chemelewski, A. Manthiram, S. A. Krachkovskiy, G. R. Goward, M. Liu, J.-H. Kim, *J. Phys. Chem. C* **2013**, *117*, 22603–22612.
- [248] J. Demeaux, M. Caillon-Caravanier, H. Galiano, D. Lemordant, B. Claude-Montigny, *J. Electrochem. Soc.* **2012**, *159*, A1880-A1890.
- [249] W. Xu, X. Chen, F. Ding, J. Xiao, D. Wang, A. Pan, J. Zheng, X. S. Li, A. B. Padmaperuma, J.-G. Zhang, *Journal of Power Sources* **2012**, *213*, 304–316.
- [250] R. Younesi, A. S. Christiansen, R. Scipioni, D.-T. Ngo, S. B. Simonsen, K. Edstroem, J. Hjelm, P. Norby, *J. Electrochem. Soc.* **2015**, *162*, A1289-A1296.
- [251] J. Demeaux, D. Lemordant, M. Caillon-Caravanier, H. Galiano, B. Claude-Montigny, *Electrochim. Acta* **2013**, *89*, 163–172.

- [252] X. Qi, B. Blizanac, A. DuPasquier, A. Lal, P. Niehoff, T. Placke, M. Oljaca, J. Li, M. Winter, *J. Electrochem. Soc.* **2015**, *162*, A339-A343.
- [253] I. Belharouak, *Lithium ion batteries. New developments*, InTech, Rijeka, Croatia, **2012**.
- [254] X. R. Zhang, P. N. Ross, *202nd ECS Meeting Abstracts* **2002**, *UT2002-2*, 201.
- [255] J. Ufheil, A. Würsig, O. D. Schneider, P. Novák, *Electrochemistry Communications* **2005**, *7*, 1380–1384.
- [256] J. Vetter, M. Holzapfel, A. Wuersig, W. Scheifele, J. Ufheil, P. Novák, *Special issue including selected papers from the 3rd International Conference on Materials for Advanced Technologies (ICMAT 2005, Singapore, Malaysia) and the Summer School on Synthesis of Nanostructured Materials for Polymer Batteries (Augustów, Poland) together with regular papers* **2006**, *159*, 277–281.
- [257] K. W. Leitner, H. Wolf, A. Garsuch, F. Chesneau, M. Schulz-Dobrick, *16th International Meeting on Lithium Batteries (IMLB)* **2013**, *244*, 548–551.
- [258] O. Chusid, Ely, Y. Ein, D. Aurbach, M. BAbai, Y. Carmeli, *J. Power Sources* **1993**, *43*, 47–64.
- [259] K. Kanamura, S. Toriyama, S. Shiraishi, Z. Takehara, *Journal of The Electrochemical Society* **1996**, *143*, 2548–2558.
- [260] S. E. Sloop, J. B. Kerr, K. Kinoshita, *J. Power Sources* **2003**, *119-121*, 330–337.
- [261] Andersson, A. M., K. Edström, *Journal of The Electrochemical Society* **2001**, *148*, A1100.
- [262] X. Cui, H. Zhang, S. Li, Y. Zhao, L. Mao, W. Zhao, Y. Li, X. Ye, *Journal of Power Sources* **2013**, *240*, 476–485.
- [263] Z. Zhang, L. Hu, H. Wu, W. Weng, M. Koh, P. C. Redfern, L. A. Curtiss, K. Amine, *Energy Environ. Sci.* **2013**, *6*, 1806–1810.
- [264] C. A. von, K. Xu, *J. Electrochem. Soc.* **2011**, *158*, A337-A342.
- [265] M. Xu, D. Lu, A. Garsuch, B. L. Lucht, *J. Electrochem. Soc.* **2012**, *159*, A2130-A2134.
- [266] L. Xue, K. Ueno, S.-Y. Lee, C. A. Angell, *Journal of Power Sources* **2014**, *262*, 123–128.
- [267] X. Zuo, C. Fan, J. Liu, X. Xiao, J. Wu, J. Nan, *Journal of Power Sources* **2013**, *229*, 308–312.
- [268] K. Matsumoto, M. Martinez, T. Gutel, S. Mailley, E. de Vito, S. Patoux, K. Inoue, K. Utsugi, *J. Power Sources* **2015**, *273*, 1084–1088.
- [269] S. Li, L. Li, J. Liu, J. Jing, X. Li, X. Cui, *Electrochim. Acta* **2015**, *155*, 321–326.

- [270] Y.-M. Song, J.-G. Han, S. Park, K. T. Lee, N.-S. Choi, *J. Mater. Chem. A* **2014**, 2, 9506–9513.
- [271] E. Markevich, G. Salitra, K. Fridman, R. Sharabi, G. Gershinsky, A. Garsuch, G. Semrau, M. A. Schmidt, D. Aurbach, *Langmuir* **2014**, 30, 7414–7424.
- [272] M. Xu, N. Tsiouvaras, A. Garsuch, H. A. Gasteiger, B. L. Lucht, *J. Phys. Chem. C* **2014**, 118, 7363–7368.
- [273] V. Tarnopolskiy, J. Kalhoff, M. Nádherná, D. Bresser, L. Picard, F. Fabre, M. Rey, S. Passerini, *Journal of Power Sources* **2013**, 236, 39–46.
- [274] K. C. Xu, A. V. W. Cresce, US20120225359A1.
- [275] C. J. Dubois, V. A. Petrov, M. G. Roelofs, WO2013180781A1.
- [276] V. V. Bhat, G. Cheng, S. S. Kaye, B. Li, R. Olugbile, J.-H. Yang, US20130059200A1.
- [277] B. Oh, D. Ofer, J. Rempel, S. Sriramulu, B. Barnett, "Novel Li-ion Electrolytes for Extended Temperature and Voltage Conditions", can be found under https://www.google.de/url?sa=t&rct=j&q=&esrc=s&source=web&cd=1&ved=0CCYQFjAA&url=http%3A%2F%2Fma.ecsdl.org%2Fcontent%2FMA2010-02%2F9%2F592.full.pdf&ei=6gpwVb6hC-Ka7gbP44DQCg&usq=AFQjCNH6JMyhQ-mL6SqIVQn6cwS_7tDssw&cad=rja. The Electrochemical Society (Ed.), TIAXX LLC, 218th ECS Meeting. **2010**.
- [278] F. Alloin, O. El Tall, J.-C. Lepretre, L. Cointeaux, L. Boutafa, J. Guindet, J.-F. Martin, *Electrochim. Acta* **2013**, 112, 74–81.
- [279] N. Shao, X.-G. Sun, S. Dai, D.-e. Jiang, *J. Phys. Chem. B* **2011**, 115, 12120–12125.
- [280] K. Xu, Angell, C. A., *Journal of The Electrochemical Society* **1998**, 145, L70.
- [281] Y. Abu-Lebdeh, I. Davidson, *J. Electrochem. Soc.* **2009**, 156, A60-A65.
- [282] D. Orbach, *Nonaqueous electrochemistry*, Marcel Dekker, New York, **1999**.
- [283] T. Achiha, T. Nakajima, Y. Ohzawa, M. Koh, A. Yamauchi, M. Kagawa, H. Aoyama, *Journal of The Electrochemical Society* **2010**, 157, A707.
- [284] D. Nishikawa, T. Nakajima, Y. Ohzawa, M. Koh, A. Yamauchi, M. Kagawa, H. Aoyama, *Journal of Power Sources* **2013**, 243, 573–580.
- [285] X. Wu, X. Li, Z. Wang, H. Guo, P. Yue, *Ionics* **2013**, 19, 379–383.
- [286] Y. Talyosef, B. Markovsky, G. Salitra, D. Aurbach, H.-J. Kim, S. Choi, *Selected papers presented at the 12th International Meeting on Lithium Batteries 12th International Meeting on Lithium Batteries* **2005**, 146, 664–669.

- [287] D. Aurbach, B. Markovsky, Y. Talyossef, G. Salitra, H.-J. Kim, S. Choi, *Special issue including selected papers from the International Power Sources Symposium 2005 together with regular papers* **2006**, 162, 780–789.
- [288] a) Y.-K. Sun, K.-J. Hong, J. Prakash, K. Amine, *Electrochemistry Communications* **2002**, 4, 344–348; b) Y.-K. Sun, C. S. Yoon, I.-H. Oh, *Electrochim. Acta* **2003**, 48, 503–506; c) L. J. Fu, H. Liu, C. Li, Y. P. Wu, E. Rahm, R. Holze, H. Q. Wu, *Solid State Sciences* **2006**, 8, 113–128; d) Y. Kobayashi, H. Miyashiro, K. Takei, H. Shigemura, M. Tabuchi, H. Kageyama, T. Iwahori, *J. Electrochem. Soc.* **2003**, 150, A1577-A1582; e) R. Alcántara, M. Jaraba, P. Lavela, J. L. Tirado, *Journal of Electroanalytical Chemistry* **2004**, 566, 187–192; f) J. Arrebola, A. Caballero, L. Hernan, J. Morales, E. Rodriguez Castellon, Ramos Barrado, J. R., *J. Electrochem. Soc.* **2007**, 154, A178-A184; g) Y. Fan, J. Wang, Z. Tang, W. He, J. Zhang, *Electrochim. Acta* **2007**, 52, 3870–3875; h) Wu, H. M., I. Belharouak, A. Abouimrane, Y.-K. Sun, K. Amine, *J. Power Sources* **2010**, 195, 2909–2913; i) F. Cheng, Y. Xin, Y. Huang, J. Chen, H. Zhou, X. Zhang, *J. Power Sources* **2013**, 239, 181–188; j) Y. Y. Huang, X. L. Zeng, C. Zhou, P. Wu, D. G. Tong, *J Mater Sci* **2013**, 48, 625-635; k) D. Liu, Y. Bai, S. Zhao, W. Zhang, *J. Power Sources* **2012**, 219, 333–338; l) Y.-K. Sun, G.-S. Park, Y.-S. Lee, M. Yoashio, K. S. Nahm, *J. Electrochem. Soc.* **2001**, 148, A994-A998; m) Y. Ein-Eli, Howard, W. F. , Jr., S. H. Lu, S. Mukerjee, J. Mcbreen, J. T. Vaughey, M. M. Thackeray, *J. Electrochem. Soc.* **1998**, 145, 1238–1244; n) D. Liu, J. Trottier, P. Charest, J. Frechette, A. Guerfi, A. Mauger, C. M. Julien, K. Zaghib, *J. Power Sources* **2012**, 204, 127–132.
- [289] Y.-K. Sun, Y.-S. Lee, M. Yoshio, K. Amine, *J. Electrochem. Soc.* **2003**, 150, L11.
- [290] J. Liu, A. Manthiram, *Chem. Mater.* **2009**, 21, 1695–1707.
- [291] J. Liu, A. Manthiram, *J. Electrochem. Soc.* **2009**, 156, A833-A838.
- [292] Z. Chen, Y. Qin, K. Amine, Y.-K. Sun, *J. Mater. Chem.* **2010**, 20, 7606–7612.
- [293] Z. Chen, J. R. Dahn, *Electrochem. Solid-State Lett.* **2003**, 6, A221-A224.
- [294] Y.-K. Sun, Y.-S. Lee, M. Yoshio, K. Amine, *Electrochem. Solid-State Lett.* **2002**, 5, A99-A102.
- [295] G. Xu, Z. Liu, C. Zhang, G. Cui, L. Chen, *J. Mater. Chem. A* **2015**, 3, 4092–4123.
- [296] a) S. S. Zhang, *J. Power Sources* **2006**, 162, 1379–1394; b) W. Li, C. Campion, B. L. Lucht, B. Ravdel, J. DiCarlo, Abraham, K. M., *J. Electrochem. Soc.* **2005**, 152, A1361-A1365; c) W. Li, B. L. Lucht, *J. Power Sources* **2007**, 168, 258–264; d) W. Li, A. Xiao, Lucht, B. L., M. C. Smart, B. V. Ratnakumar, *J. Electrochem. Soc.* **2008**, 155, A648-A657; e) M.-Q. Xu, L.-S. Hao, Y.-L. Liu, W.-S. Li, L.-D. Xing, B. Li, *J. Phys. Chem. C* **2011**, 115, 6085–6094.

- [297] Zhang, S. S., K. Xu, Jow, T. R., *Electrochem. Solid-State Lett.* **2002**, 5, A206-A208.
- [298] Zhang, S. S., K. Xu, Jow, T. R., *J. Power Sources* **2003**, 113, 166–172.
- [299] X. Sun, Lee, H. S., X.-Q. Yang, J. McBreen, *Electrochem. Solid-State Lett.* **2002**, 5, A248-A251.
- [300] X. Chen, W. Xu, J. Xiao, M. H. Engelhard, F. Ding, D. Mei, D. Hu, J. Zhang, J.-G. Zhang, *Journal of Power Sources* **2012**, 213, 160–168.
- [301] N. N. Sinha, J. C. Burns, R. J. Sanderson, J. Dahn, *Journal of The Electrochemical Society* **2011**, 158, A1400.
- [302] a) Seel, J. A., J. R. Dahn, *Journal of The Electrochemical Society* **2000**, 147, 892–898;
b) T. Ishihara, M. Koga, H. Matsumoto, M. Yoshio, *Electrochemical and Solid-State Letters* **2007**, 10, A74.
- [303] J. Syzdek, M. Marcinek, R. Kostecki, *Journal of Power Sources* **2014**, 245, 739–744.
- [304] B. Blizanac, M. Oljaca, A. L. Dupasquier, R. C. Wall, A. Suszko, WO2014205210A1.
- [305] L. Fransson, T. Eriksson, K. Edström, T. Gustafsson, Thomas, J. O., *Journal of Power Sources* **2001**, 101, 1–9.
- [306] T. Yoon, S. Park, J. Mun, J. H. Ryu, W. Choi, Y.-S. Kang, J.-H. Park, S. M. Oh, *Journal of Power Sources* **2012**, 215, 312–316.
- [307] S.-Y. Ha, J.-G. Han, Y.-M. Song, M.-J. Chun, S.-I. Han, W.-C. Shin, N.-S. Choi, *Electrochim. Acta* **2013**, 104, 170–177.
- [308] P. Moss, "Study of Capacity Fade of Lithium-Ion Polymer Battery with Continuous Cycling & Power Performance Modeling of Energy Storage Devices", can be found under http://diginole.lib.fsu.edu/etd/?utm_source=diginole.lib.fsu.edu%2Fetd%2F2227&utm_medium=PDF&utm_campaign=PDFCoverPages, Florida State University, Florida. **2008**.
- [309] M. Wilka, "Untersuchungen von Polarisierungseffekten an Lithium-Ionen-Batterien und deren Einfluss auf Sicherheit, Alterung sowie weiterer anwendungsrelevanter Eigenschaften", can be found under http://vts.uni-ulm.de/query/longview.meta.asp?document_id=8846. Universität Ulm (Ed.), Ulm. **2013**.
- [310] K. E. Aifantis, S. A. Hackney, R. V. Kumar, *High energy density lithium batteries. Materials, engineering, applications*, Wiley-VCH, Weinheim, **2010**.
- [311] T. B. Reddy, *Linden's handbook of batteries. Set 2*, McGraw-Hill Professional; McGraw-Hill [distributor], New York, London, **2010**.

- [312] C. Julien, Z. Stoyanov, *Materials for Lithium-Ion Batteries*, Springer Netherlands; Imprint: Springer, Dordrecht, **2000**.
- [313] E. Quiroga-González, J. Carstensen, H. Föll, *Energies* **2013**, 6, 5145–5156.
- [314] M. Winter, *Rechargeable lithium-ion batteries*, Electrochemical Society, Pennington, **2010**.
- [315] M. C. Smart, B. V. Ratnakumar, *J. Electrochem. Soc.* **2011**, 158, A379-A389.
- [316] C. Dippel, R. Schmitz, R. Mueller, T. Boettcher, M. Kunze, A. Lex-Balducci, G.-V. Roeschenthaler, S. Passerini, M. Winter, *J. Electrochem. Soc.* **2012**, 159, A1587-A1590.
- [317] a) W. Lu, C. M. Lopez, N. Liu, J. T. Vaughey, A. Jansen, D. W. Dees, *J. Electrochem. Soc.* **2012**, 159, A566-A570; b) B. V. Ratnakumar, M. C. Smart, *ECS Trans.* **2010**, 25, 241–252.
- [318] V. Agubra, J. Fergus, *Materials* **2013**, 6, 1310–1325.
- [319] M. Wilka, *Influence of Anode/Cathode Balancing on the Cycling Stability of Lithium Ion Cells*. Haus der Technik e.V. (RWTH Aachen); Cluster EnergieForschung.NRW; Cluster EnergieRegion.NRW; Cluster NanoMikro+Werkstoffe.NRW; MEET Symposium *Advanced Battery Power*, Aachen, **2013**.
- [320] G. Pistoia, *Electric and hybrid vehicles. Power sources, models, sustainability, infrastructure and the market*, Elsevier, Amsterdam, Boston, **2010**.
- [321] R. Fulop, Y.-M. Chiang, K. E. Thomas-Alyea, W. H. Gardner, US20090104510A1.
- [322] M. Wilka, "Influence of anode/cathode balancing on cycling stability of lithium ion cells", can be found under
https://www.google.de/url?sa=t&rct=j&q=&esrc=s&source=web&cd=3&ved=0ahUKEwjVgfnq657JAHWKPRQKHem4AF0QFgg0MAI&url=http%3A%2F%2Fma.ecsdl.org%2Fcontent%2FMA2012-02%2F10%2F844.full.pdf&usg=AFQjCNEv1J_X1XLrNbcdKVZyPBjYAbFhg&cad=rja. The Electrochemical Society (Ed.), Zentrum für Sonnenenergie- und Wasserstoff-Forschung Baden-Württemberg (ZSW), Honolulu. **2012**.
- [323] F. La Mantia, Wessells, C. D., Deshazer, H. D., Y. Cui, *Electrochem. Commun.* **2013**, 31, 141–144.
- [324] J. L. Gomez-Camer, P. Novak, *Electrochem. Commun.* **2013**, 34, 208–210.
- [325] J. R. Belt, D. M. Bernardi, V. Utgikar, *J. Electrochem. Soc.* **2014**, 161, A1116-A1126.
- [326] S. Klink, E. Madej, E. Ventosa, A. Lindner, W. Schuhmann, F. La Mantia, *Electrochem. Commun.* **2012**, 22, 120–123.

- [327] J. S. Newman, K. E. Thomas-Alyea, *Electrochemical systems*, J. Wiley, Hoboken, N.J, **2004**.
- [328] B. Burrows, R. J. Jasinski, *J. Electrochem. Soc.* **1968**, 115, 365–7.
- [329] M. Dolle, F. Orsini, A. S. Gozdz, J.-M. Tarascon, *J. Electrochem. Soc.* **2001**, 148, A851-A857.
- [330] M. Ender, A. Weber, E. Ivers-Tiffée, *J. Electrochem. Soc.* **2012**, 159, A128-A136.
- [331] E. Zolotoyabko, *Basic concepts of X-ray diffraction*.
- [332] C. E. Mortimer, U. Müller, *Chemie. Das Basiswissen der Chemie*, Thieme, Stuttgart, **2007**.
- [333] J. C. Lindon, G. E. Tranter, D. Koppenaal, *ONLINE Encyclopedia of Spectroscopy and Spectrometry, 2nd Edition. 3 volume set*, Elsevier Science, Burlington, **2010**.
- [334] G.-C. Wang, T.-M. Lu, *Rheed transmission mode and pole figures. Thin film and nanostructure texture analysis*.
- [335] G. Wedler, *Lehrbuch der physikalischen Chemie*, Wiley-VCH, Weinheim, **2004**.
- [336] C. Suryanarayana, M. G. Norton, *X-Ray diffraction. A practical approach*, Plenum Press, New York, **1998**.
- [337] L. Spieß, *Moderne Röntgenbeugung. Röntgendiffraktometrie für Materialwissenschaftler, Physiker und Chemiker*, Teubner, Wiesbaden, **2008**.
- [338] U. Pietsch, V. Holý, T. Baumbach, *High-resolution x-ray scattering. From thin films lateral nanostructures*, Springer, New York [etc.], **op. 2004**.
- [339] Y. Waseda, E. Matsubara, K. Shinoda, *X-Ray diffraction crystallography. Introduction, examples and solved problems*, Springer, Berlin, Heidelberg, New York, **2011**.
- [340] J. Stangl, C. Mocuta, V. Chamard, D. Carbone, *Nanobeam X-Ray scattering. Probing matter at the nanoscale*.
- [341] R. Baddour-Hadjean, J.-P. Pereira-Ramos, *Chem. Rev. (Washington, DC, U. S.)* **2010**, 110, 1278–1319.
- [342] R. L. McCreery, *Raman spectroscopy for chemical analysis*, John Wiley & Sons, New York, **2000**.
- [343] J. R. Ferraro, K. Nakamoto, *Introductory Raman spectroscopy*, Academic Press, Boston, **1994**.
- [344] D. L. Wise, *Handbook of pharmaceutical controlled release technology*, Marcel Dekker, New York, **2000**.

- [345] Jag Mohan, *Organic spectroscopy. Principles and applications*, Alpha Science International Ltd., Harrow, U.K, **2004**.
- [346] a) F. A. Cotton, *Chemical applications of group theory*, Wiley, New York, **1990**; b) D. A. Long, *Raman spectroscopy*, McGraw-Hill, New York, **1977**; c) S. Califano, V. Schettino, N. Neto, *Lattice Dynamics of Molecular Crystals*, Springer Berlin Heidelberg, Berlin, Heidelberg, **1981**.
- [347] M. S. Dresselhaus, A. Jorio, R. Saito, *Annu. Rev. Condens. Matter Phys.* **2010**, 1, 89–108.
- [348] W. B. White, B. A. DeAngelis, *Spectrochimica Acta Part A: Molecular Spectroscopy* **1967**, 23, 985–995.
- [349] Y. Dridi, R. Baddour-Hadjean, "Électrochimie et spectroscopie Raman de matériaux d'électrode positive pour batteries Li-ion", can be found under <https://www.google.de/url?sa=t&rct=j&q=&esrc=s&source=web&cd=2&ved=0CCsQFjAB&url=https%3A%2F%2Ftel.archives-ouvertes.fr%2Ftel-00807008%2Fdocument&ei=YAAIVa2ZJ4HOsgHFrYSIDQ&usg=AFQjCNHurXwngEWbXctgKKnnPzQVcZXK0A&bvm=bv.90237346,d.bGg&cad=rja>. Université Paris-Est (Ed.). **2012**.
- [350] C. M. Julien, M. Massot, *Mater. Sci. Eng., B* **2003**, B97, 217–230.
- [351] C. B. Boss, J. Fredeen, "Concepts, Instrumentation and Techniques in Inductively Coupled Plasma Optical Emission Spectrometry", can be found under https://www.google.de/url?sa=t&rct=j&q=&esrc=s&source=web&cd=11&ved=0ahUKEwj50Mb6rKTJAhUJbRQKHTjaDMAQFghkMAo&url=http%3A%2F%2Fwww.perkinelmer.com%2FCMSResources%2FImages%2F44-159043GDE_Concepts-of-ICP-OES-Booklet.pdf&usg=AFQjCNHUmiwLrp0CMPPYI1b-2prxY359jA&cad=rja. I. PerkinElmer (Ed.), PerkinElmer Life and Analytical Sciences, Shelton, CT. **2004**.
- [352] C. R. Brundle, C. A. Evans, S. Wilson, *Encyclopedia of materials characterization. Surfaces, interfaces, thin films*, Butterworth-Heinemann; Manning, Boston, Greenwich, CT, **1992**.
- [353] T. J. Manning, W. R. Grow, *Chem. Educ.* **1997**, 2, No pp. Given.
- [354] N. Tanaka, *Scanning transmission electron microscopy of nanomaterials. Basics of imaging and analysis*.
- [355] T. G. Rochow, P. A. Tucker, *Introduction to Microscopy by Means of Light, Electrons, X Rays, or Acoustics*, Springer US; Imprint: Springer, Boston, MA, **1994**.

- [356] A. Khursheed, *Scanning electron microscope optics and spectrometers*, World Scientific, Singapore, London, **2011**.
- [357] *Scanning electron microscopy and x-ray microanalysis*, Springer, [S.I.], **2013**.
- [358] C. Gong, Y.-J. Bai, Y.-X. Qi, N. Lun, J. Feng, *Electrochim. Acta* **2013**, 90, 119–127.
- [359] H. Leipner, D. Enke, "Elektronenmikroskopische Abbildungsverfahren und Gerätetechnik", can be found under <http://www.cmat.uni-halle.de/~hsl/Nanostructures.htm> I. Martin-Luther-Universität Halle-Wittenberg (Ed.). **2013**.
- [360] C. E. Lyman, *Scanning electron microscopy, X-ray microanalysis, and analytical electron microscopy. A laboratory workbook*, Plenum Press, New York, **1990**.
- [361] Friedrich Reinert and Stefan Hüfner, *New Journal of Physics* **2005**, 7, 97.
- [362] H. Frey, H. R. Khan, *Handbook of thin film technology*, Springer, Berlin, London, **2010**.
- [363] J. F. Moulder, J. Chastain, R. C. King, *Handbook of x-ray photoelectron spectroscopy. A reference book of standard spectra for identification and interpretation of XPS data*, Physical Electronics, Eden Prairie, Minn, **1995**.
- [364] H. Krieger, *Grundlagen der Strahlungsphysik und des Strahlenschutzes*, Vieweg+Teubner Verlag, Wiesbaden, **2012**.
- [365] A. Klein, "Grundlagen der Röntgenphotoelektronenspektroskopie. (X-Ray Photoelectron Spectroscopy "XPS")", can be found under https://www.google.de/url?sa=t&rct=j&q=&esrc=s&source=web&cd=2&ved=0CCMQFjABahUKEwjtpfqZpujIAhUCuBQKHduACjQ&url=http%3A%2F%2Fwww.fkp.uni-hannover.de%2Ffileadmin%2Fpraktikum%2Fanleitung_xps.pdf&usg=AFQjCNERVpBSaUz0xqVGUgusyuntQyccgg&bvm=bv.106130839,d.bGQ&cad=rja. Leibniz Universität Hannover (Ed.), Hannover. **2008**.
- [366] O. Krupin, "Dichroism and Rashba effect at magnetic crystal surfaces of rare-earth metal", can be found under http://www.diss.fu-berlin.de/diss/receive/FUDISS_thesis_000000003802. Freie Universität Berlin (Ed.), Berlin. **2004**.
- [367] W. Schattke, Van Hove, M. A, *Solid-state photoemission and related methods. Theory and experiment*, Wiley-VCH, Weinheim, [Cambridge], **2003**.
- [368] A. Herdt, *Exploring the electronic properties of novel spintronic materials by photoelectron spectroscopy*, Forschungszentrum Jülich, Zentralbibliothek, Jülich, **2012**.

- [369] S. Hüfner, *Photoelectron spectroscopy. Principles and applications ; with 28 tables*, Springer, Berlin [u.a.], **2003**.
- [370] a) B. Feuerbacher, B. Fitton, R. F. Willis, *Photoemission and the electronic properties of surfaces*, Wiley, London, New York, **1978**; b) S. D. Kevan, *Angle-resolved photoemission. Theory and current applications*, Elsevier, Amsterdam, New York, **1992**; c) L. Hedin, S. Lundqvist in *Solid State Physics* (Ed.: Frederick Seitz, David Turnbull and Henry Ehrenreich), Academic Press, **1970**; d) C. O. Almbladh, L. Hedin, Troisième Cycle de la Physique en Suisse Romande, *Beyond the One-electron Model: Many-body Effects in Atoms, Molecules, and Solids*, (Université de Lausanne, Bâtiment des sciences de physique) : Troisième Cycle de la physique en Suisse romande, **1982**.
- [371] N. N., "Basic quantification of XPS spectra", can be found under https://www.google.de/url?sa=t&rct=j&q=&esrc=s&source=web&cd=1&ved=0CClQFjAAahUKEwjwmaHe1u_IAhVEHA8KHbf0Ddo&url=http%3A%2F%2Fwww.casaxps.com%2Fhelp_manual%2Fmanual_updates%2FBasics_Quantification_of_XPS_Spectra.pdf&usg=AFQjCNGUvWQZUSe9svu_0hfh2MNGp65C1Q&bvm=bv.106379543,d.ZWU&cad=rja. CasaXPS (Ed.). **2008**.
- [372] W. Göpel, C. Ziegler, *Struktur der Materie. Grundlagen, Mikroskopie und Spektroskopie*, Teubner, Stuttgart [u.a.], **1994**.
- [373] S. Becker, "Spektroskopische in situ-Untersuchungen der katalytischen CO-Oxidation an oxidmodifizierten Platinmetalloberflächen", can be found under <http://edoc2.bibliothek.uni-halle.de/hs/id/1946>. Universität Magdeburg (Ed.). **2010**.
- [374] D. Ensling, "Photoelektronenspektroskopische Untersuchung der elektronischen Struktur dünner Lithiumkobaltoxidschichten", can be found under <http://tuprints.ulb.tu-darmstadt.de/epda/000818/>. TU Darmstadt (Ed.). **2006**.
- [375] M. Paszkiewicz, F. Allegretti, "Electron spectroscopy of surfaces. Elemental and chemical analysis with X-ray photoelectron spectroscopy", can be found under <https://www.google.de/url?sa=t&rct=j&q=&esrc=s&source=web&cd=1&ved=0CCUQFjAAahUKEwiUzd-NqurlAhXGNhoKHaKEA0w&url=https%3A%2F%2Fwww.ph.tum.de%2Facademics%2Forg%2Fflabs%2Fopra%2Fdocs%2Fuserguide-35.en.pdf&usg=AFQjCNFcWUXfdQD0H96DkICIFB9vGylo7Q&bvm=bv.106379543,d.d2s&cad=rja>. Technische Universität München (Ed.).

- [376] a) S. Tougaard, B. Jørgensen, *Surface and Interface Analysis* **1985**, 7, 17–21; b) D. A. Shirley, *Phys. Rev. B* **1972**, 5, 4709–4714; c) N. N., "Peak fitting in XPS", can be found under
https://www.google.de/url?sa=t&rct=j&q=&esrc=s&source=web&cd=1&ved=0CB0QFjAAahUKEwjkkLnO8fjIAhVJlXoKHTzXDW4&url=http%3A%2F%2Fwww.casaxps.com%2Fhelp_manual%2Fmanual_updates%2Fpeak_fitting_in_xps.pdf&usg=AFQjCNGD7CxXrT6udjnwIC1ezkl44IhmVw&bvm=bv.106923889,d.d2s&cad=rja. **2006**.
- [377] Macdonald, J. R., *Ann Biomed Eng* **1992**, 20, 289–305.
- [378] E. Barsoukov, Macdonald, J. Ross, *Impedance spectroscopy. Theory, experiment, and applications*.
- [379] N. N., "Electrochemical Impedance Spectroscopy (EIS). A Powerful and Cost-Effective Tool for Fuel Cell Diagnostics", can be found under
https://www.google.de/url?sa=t&rct=j&q=&esrc=s&source=web&cd=2&sqi=2&ved=0CCQQFjABahUKEwj7qcqh8o3JAhUFIg8KHbNeDC4&url=http%3A%2F%2Fwww.scribner.com%2Ffiles%2Ftech-papers%2FScribner%2520Associates%2520-%2520Electrochemical%2520Impedance%2520Spectroscopy%2520for%2520Fuel%2520Cell%2520Research.pdf&usg=AFQjCNHwZZw05_1gYcqUmzV4sVHmYmGXSG&bvm=bv.107467506,d.ZWU&cad=rja. I. Scribner Associates (Ed.).
- [380] V. F. Lvovich, *Impedance spectroscopy. Applications to electrochemical and dielectric phenomena*, Wiley, Hoboken, N.J, **2012**.
- [381] M. Albach, *Grundlagen der Elektrotechnik*, Pearson Studium, München, **2011**.
- [382] A. J. Bard, G. Inzelt, F. Scholz, *Electrochemical dictionary*, Springer, Heidelberg, **2012**.
- [383] N. N., "Electrochemical Impedance Spectroscopy (EIS). Part 2 – Experimental Setup", can be found under
https://www.google.de/url?sa=t&rct=j&q=&esrc=s&source=web&cd=3&ved=0CDAQFjACahUKEwjowYGSgZLJAhWKvBoKHbbjAjM&url=http%3A%2F%2Fwww.ecochemie.nl%2Fdownload%2FApplicationnotes%2FAutolab_Application_Note_EIS02.pdf&usg=AFQjCNF2Ykz-vIJHyZ5mN0tVyauJgekQ9Q&bvm=bv.107467506,d.bGQ&cad=rja. Methrom Autolab B. V. (Ed.). **2011**.

- [384] a) N. N., "Electrochemical Impedance Spectroscopy", can be found under https://www.google.de/url?sa=t&rct=j&q=&esrc=s&source=web&cd=3&ved=0CDMQFjACahUKEwjyYeJmpLJAhXEFoKHU_aBVY&url=http%3A%2F%2Fwww.zahner.de%2Fpdf%2FEIS.pdf&usg=AFQjCNEinXAGJgZoa827axkAwJUEZW6EQ&bvm=bv.107467506,d.d24&cad=rja. ZAHNER-elektrik (Ed.). **2015**; b) X.-Z. Yuan, *Electrochemical impedance spectroscopy in PEM fuel cells. Fundamentals and applications*, Springer, London, **2010**.
- [385] P. Marcus, F. Mansfeld, *Analytical methods in corrosion science and engineering*, CRC Press, Boca Raton, **2006**.
- [386] D. Klotz, *Characterization and Modeling of Electrochemical Energy Conversion Systems by Impedance Techniques*, KIT Scientific Publishing, Karlsruhe, **2012**.
- [387] J. R. Macdonald, *Electrochimica Acta* **1990**, 35, 1483–1492.
- [388] C. Beasley, "Basics of Electrochemical Impedance Spectroscopy", can be found under <http://www.gamry.com/application-notes/EIS/basics-of-electrochemical-impedance-spectroscopy/>. Gamry Instruments (Ed.). **2015**.
- [389] W. Strunz, "Einführung in die Impedanzspektroskopie", can be found under <http://docslide.de/documents/strunz-einfuehrung-in-die-impedanzspektroskopie-1-einfuehrung-in-die-impedanzspektroskopie-eis-werner-strunz-zahner-elektrik-kronach.html>. ZAHNER-elektrik (Ed.), Kronach. **2015**.
- [390] N. N., "Electrochemical Impedance Spectroscopy (EIS). Part 3 – Data Analysis", can be found under https://www.google.de/url?sa=t&rct=j&q=&esrc=s&source=web&cd=9&sqi=2&ved=0CEIQFjAlahUKEwis_7L2xJTJAWhDPRoKHx8jA1w&url=http%3A%2F%2Fwww.ecochemie.nl%2Fdownload%2FApplicationnotes%2FAutolab_Application_Note_EIS03.pdf&usg=AFQjCNEoeLdui2qnYx5WXdYW8taZ6doLig&bvm=bv.107467506,d.d2s&cad=rja. Methrom Autolab B. V. (Ed.). **2011**.
- [391] a) E. Barsoukov, D. H. Kim, H.-S. Lee, H. Lee, M. Yakovleva, Y. Gao, J. F. Engel, *Solid State Ionics* **2003**, 161, 19–29; b) E. Barsoukov, J. H. Kim, J. H. Kim, C. O. Yoon, H. Lee, *Solid State Ionics* **1999**, 116, 249–261.
- [392] Pawley, G. S., *J. Appl. Crystallogr.* **1981**, 14, 357–61.

- [393] W. Jaegermann, "DArmstädter Integriertes SYstem für BATterieforschung (DAISY-BAT)", can be found under http://www.mawi.tu-darmstadt.de/of/of/methoden/of_daisybat/index.de.jsp. Technische Universität Darmstadt (Ed.), Darmstadt. **2015**.
- [394] J.-H. Kim, *Getting to the Automotive Advanced Lithium-Ion Battery Frontier*, South Korea, **2012**. General Motors (Ed.).
- [395] W. Zhu, D. Liu, J. Trottier, C. Gagnon, A. Guerfi, C. M. Julien, A. Mauger, K. Zaghib, *J. Power Sources* **2014**, 264, 290–298.
- [396] a) K. R. Chemelewski, E.-S. Lee, W. Li, A. Manthiram, *Chem. Mater.* **2013**, 25, 2890–2897; b) D. W. Shin, C. A. Bridges, A. Huq, M. P. Paranthaman, A. Manthiram, *Chem. Mater.* **2012**, 24, 3720–3731.
- [397] a) J.-S. Kim, C. S. Johnson, J. T. Vaughey, M. M. Thackeray, S. A. Hackney, W. Yoon, C. P. Grey, *Chem. Mater.* **2004**, 16, 1996–2006; b) W. Wen, B. Kumarasamy, S. Mukerjee, M. Auinat, Y. Ein-Eli, *J. Electrochem. Soc.* **2005**, 152, A1902-A1911.
- [398] T. R. Jow, *Electrolytes for lithium and lithium-ion batteries*.
- [399] S. Santhanagopalan, K. Smith, J. Neubauer, G.-H. Kim, M. Keyser, A. A. Pesaran, *Design and analysis of large lithium-ion battery systems*.
- [400] a) Park, S. H., S.-W. Oh, S. H. Kang, I. Belharouak, K. Amine, Y.-K. Sun, *Electrochimica Acta* **2007**, 52, 7226–7230; b) E.-S. Lee, K.-W. Nam, E. Hu, A. Manthiram, *Chem. Mater.* **2012**, 24, 3610–3620; c) Q. L. Wu, Y. Liu, C. S. Johnson, Y. Li, D. W. Dees, W. Lu, *Chem. Mater.* **2014**, 26, 4750–4756; d) J. Rana, S. Glatthaar, H. Gesswein, N. Sharma, J. R. Binder, R. Chernikov, G. Schumacher, J. Banhart, *Journal of Power Sources* **2014**, 255, 439–449.
- [401] a) Abraham, D. P., Knuth, J. L., Dees, D. W., I. Bloom, Christophersen, J. P., *J. Power Sources* **2007**, 170, 465–475; b) M. Broussely, P. Biensan, F. Bonhomme, P. Blanchard, S. Herreyre, K. Nechev, R. J. Staniewicz, *J. Power Sources* **2005**, 146, 90–96; c) H. Yamada, Y. Watanabe, I. Moriguchi, T. Kudo, *Solid State Ionics* **2008**, 179, 1706–1709.
- [402] a) K. Amine, J. Liu, S. Kang, I. Belharouak, Y. Hyung, D. Vissers, G. Henriksen, *Selected papers presented at the conference High Energy Density Electrochemical Power Sources* **2004**, 129, 14–19; b) R. N. Methekar, Northrop, Paul W. C., K.-J. Chen, R. D. Braatz, V. R. Subramanian, *J. Electrochem. Soc.* **2011**, 158, A363-A370; c) D. Aurbach, B. Markovsky, A. Shechter, Y. Ein-Eli, H. Cohen, *J. Electrochem. Soc.* **1996**, 143, 3809–3820; d) P. Ramadass, B. Haran, R. White, B. N. Popov, *J. Power Sources* **2002**, 112, 606–613.

- [403] a) N. Nanbu, M. Takehara, S. Watanabe, M. Ue, Y. Sasaki, *Bull. Chem. Soc. Jpn.* **2007**, *80*, 1302–1306; b) T. Achiha, T. Nakajima, Y. Ohzawa, M. Koh, A. Yamauchi, M. Kagawa, H. Aoyama, *J. Electrochem. Soc.* **2009**, *156*, A483-A488.
- [404] a) R. McMillan, H. Slegre, Shu, Z. X., W. Wang, *J. Power Sources* **1999**, *81-82*, 20–26; b) B. Liu, B. Li, S. Guan, *Electrochem. Solid-State Lett.* **2012**, *15*, A77-A79; c) S.-K. Jeong, M. Inaba, R. Mogi, Y. Iriyama, T. Abe, Z. Ogumi, *Langmuir* **2001**, *17*, 8281–8286; d) I. A. Profatlova, S.-S. Kim, N.-S. Choi, *Electrochim. Acta* **2009**, *54*, 4445–4450; e) S. Tsubouchi, Y. Domi, T. Doi, M. Ochida, H. Nakagawa, T. Yamanaka, T. Abe, Z. Ogumi, *J. Electrochem. Soc.* **2012**, *159*, A1786-A1790; f) L. Liao, P. Zuo, Y. Ma, Y. An, G. Yin, Y. Gao, *Electrochim. Acta* **2012**, *74*, 260–266.
- [405] M.-H. Ryou, G.-B. Han, Y. M. Lee, J.-N. Lee, D. J. Lee, Y. O. Yoon, J.-K. Park, *Electrochim. Acta* **2010**, *55*, 2073–2077.
- [406] a) Y.-M. Lin, K. C. Klavetter, P. R. Abel, N. C. Davy, J. L. Snider, A. Heller, Mullins, C. Buddie., *Chem. Commun. (Cambridge, U. K.)* **2012**, *48*, 7268–7270; b) A. M. Chockla, T. D. Bogart, C. M. Hessel, K. C. Klavetter, Mullins, C. Buddie, B. A. Korgel, *J. Phys. Chem. C* **2012**, *116*, 18079–18086; c) I. A. Profatlova, C. Stock, A. Schmitz, S. Passerini, M. Winter, *J. Power Sources* **2013**, *222*, 140–149; d) D. Mazouzi, N. Delpuech, Y. Oumellal, M. Gauthier, M. Cerbelaud, J. Gaubicher, N. Dupre, P. Moreau, D. Guyomard, L. Roue et al., *J. Power Sources* **2012**, *220*, 180–184; e) H. Nakai, T. Kubota, A. Kita, A. Kawashima, *J. Electrochem. Soc.* **2011**, *158*, A798-A801.
- [407] a) B. Wu, Y. Ren, D. Mu, X. Liu, J. Zhao, F. Wu, *J. Solid State Electrochem.* **2013**, *17*, 811–816; b) L. Liao, X. Cheng, Y. Ma, P. Zuo, W. Fang, G. Yin, Y. Gao, *Electrochim. Acta* **2013**, *87*, 466–472.
- [408] C. Arbizzani, F. de Giorgio, L. Porcarelli, M. Mastragostino, V. Khomenko, V. Barsukov, D. Bresser, S. Passerini, *Journal of Power Sources* **2013**, *238*, 17–20.
- [409] K. Kim, Y. Kim, E.-S. Oh, H.-C. Shin, *Electrochim. Acta* **2013**, *114*, 387–393.
- [410] N. N., "GPS SAFETY REPORT. 1,1,1,3,3,3-hexamethyldisilazane", can be found under https://www.google.de/url?sa=t&rct=j&q=&esrc=s&source=web&cd=1&ved=0CCEQFjAA&url=http%3A%2F%2Fwww.dowcorning.com.cn%2Fzh_CN%2Fcontent%2Fabout%2Faboutehs%2FEHSPortalFiles%2FGPS_Safety_Report_999-97-3.pdf&ei=ruprVcntCqGc7gbV4oCQCA&usg=AFQjCNGHhL8Ui0JajwzM2M-HNlr_pxeX9w&bvm=bv.94455598,d.bGg&cad=rja. Dow Corning Corporation (Ed.). **2015**.
- [411] Y.-k. Li, R.-x. Zhang, J.-s. Liu, *Dianchi* **2009**, *39*, 83–84.
- [412] Y. Marcus, *Ion solvation*, Wiley, Chichester, New York, **1985**.

- [413] Zhang, S. S., Jow, T. R., *Journal of Power Sources* **2002**, 109, 458–464.
- [414] K. Kanamura, *J. Power Sources* **1999**, 81-82, 123–129.
- [415] L. J. Krause, W. Lamanna, J. Summerfield, M. Engle, G. Korba, R. Loch, R. Atanasoski, *J. Power Sources* **1997**, 68, 320–325.
- [416] a) B. Garcia, M. Armand, *J. Power Sources* **2004**, 132, 206–208; b) R.-S. Kuehnel, M. Luebke, M. Winter, S. Passerini, A. Balducci, *J. Power Sources* **2012**, 214, 178–184; c) C. Peng, L. Yang, Z. Zhang, K. Tachibana, Y. Yang, S. Zhao, *Electrochim. Acta* **2008**, 53, 4764–4772.
- [417] a) D. W. McOwen, D. M. Seo, O. Borodin, J. Vatamanu, P. D. Boyle, W. A. Henderson, *Energy Environ. Sci.* **2014**, 7, 416–426; b) K. Matsumoto, K. Inoue, K. Nakahara, R. Yuge, T. Noguchi, K. Utsugi, *Journal of Power Sources* **2013**, 231, 234–238.
- [418] E. Krämer, T. Schedlbauer, B. Hoffmann, L. Terborg, S. Nowak, H. J. Gores, S. Passerini, M. Winter, *Journal of The Electrochemical Society* **2013**, 160, A356.
- [419] B. Qin, Z. Liu, J. Zheng, P. Hu, G. Ding, C. Zhang, J. Zhao, D. Kong, G. Cui, *J. Mater. Chem. A* **2015**, 3, 7773–7779.
- [420] a) Z. Wang, N. Dupré, L. Lajaunie, P. Moreau, J.-F. Martin, L. Boutafa, S. Patoux, D. Guyomard, *Journal of Power Sources* **2012**, 215, 170–178; b) H. Bouayad, Z. Wang, N. Dupre, R. Dedryvere, D. Foix, S. Franger, J.-F. Martin, L. Boutafa, S. Patoux, D. Gonbeau et al., *J. Phys. Chem. C* **2014**, 118, 4634–4648.
- [421] a) P.-J. Alarco, Y. Abu-Lebdeh, A. Abouimrane, M. Armand, *Nat. Mater.* **2004**, 3, 476–481; b) M. Nagahama, N. Hasegawa, S. Okada, *Journal of The Electrochemical Society* **2010**, 157, A748.
- [422] Y. Abu-Lebdeh, I. Davidson, *J. Power Sources* **2009**, 189, 576–579.
- [423] E. Nanini-Maury, J. Światowska, A. Chagnes, S. Zanna, P. Tran-Van, P. Marcus, M. Cassir, *Electrochimica Acta* **2014**, 115, 223–233.
- [424] a) R. Shimizu, T. Yamaguchi, C.-S. Jung, H.-J. Chung, Y.-C. Chang, US20060035144A1; b) K. Abe, T. Hattori, Y. Matsumori, US20040013946A1.

- [425] Y. Abu-Lebdeh, I. Davidson, "New Advanced Lithium-ion battery electrolyte technologies for PHEVs", can be found under https://www.google.de/url?sa=t&rct=j&q=&esrc=s&source=web&cd=4&ved=0CDkQFjAD&url=http%3A%2F%2Fwww.che.ncsu.edu%2FFILEET%2Fphevs%2Fplug-in_2008%2F5A-3_New%2520Advanced%2520Lithium-ion%2520Battery%2520Electrolyte%2520Technologies%2520for%2520PHEVs.pdf&ei=cPpvVbDGG4rvUpT6gLAG&usg=AFQjCNFcWFrKutR3H49v50cIHSEDfm2fEw&cad=rja. National Research Council of Canada, Ottawa, CANADA (Ed.), Institute for Chemical Process and Environmental Technology, San José. **2008**.
- [426] X. Wang, E. Yasukawa, S. Kasuya, *J. Electrochem. Soc.* **2001**, *148*, A1058-A1065.
- [427] H. Ota, A. Kominato, W.-J. Chun, E. Yasukawa, S. Kasuya, *J. Power Sources* **2003**, *119-121*, 393–398.
- [428] X. Wang, C. Yamada, H. Naito, G. Segami, K. Kibe, *Journal of The Electrochemical Society* **2006**, *153*, A135.
- [429] H. Rong, M. Xu, L. Xing, W. Li, *Journal of Power Sources* **2014**, *261*, 148-155.
- [430] J. Liu, A. Manthiram, *J. Electrochem. Soc.* **2009**, *156*, A66-A72.
- [431] B. Huang, X. Li, Z. Wang, H. Guo, X. Xiong, J. Wang, *J. Alloys Compd.* **2014**, *583*, 313–319.
- [432] J. W. Kim, D. H. Kim, D. Y. Oh, H. Lee, J. H. Kim, J. H. Lee, Y. S. Jung, *J. Power Sources* **2014**, *274*, 1254–1262.
- [433] Y. Wang, Q. Peng, G. Yang, Z. Yang, L. Zhang, H. Long, Y. Huang, P. Lu, *Electrochim. Acta* **2014**, *136*, 450–456.
- [434] J. Song, X. Han, K. J. Gaskell, K. Xu, S. B. Lee, L. Hu, *J. Nanopart. Res.* **2014**, *16*, 1–8.
- [435] X. Fang, M. Ge, J. Rong, Y. Che, N. Aroonyadet, X. Wang, Y. Liu, A. Zhang, C. Zhou, *Energy Technol. (Weinheim, Ger.)* **2014**, *2*, 159–165.
- [436] X. Xiao, D. Ahn, Z. Liu, J.-H. Kim, P. Lu, *Electrochemistry Communications* **2013**, *32*, 31–34.
- [437] S.-M. Bak, E. Hu, Y. Zhou, X. Yu, S. D. Senanayake, S.-J. Cho, K.-B. Kim, K. Y. Chung, X.-Q. Yang, K.-W. Nam, *ACS Appl. Mater. Interfaces* **2014**, *6*, 22594–22601.

- [438] a) Ooms, F. G. B., M. Wagemaker, van Well, A. A., Mulder, F. M., E. M. Kelder, J. Schoonman, *Appl. Phys. A: Mater. Sci. Process.* **2002**, *74*, S1089-S1091; b) Potapenko, A. V., Chernukhin, S. I., Romanova, I. V., Rabadanov, K. Sh., Gafurov, M. M., Kirillov, S. A., *Electrochim. Acta* **2014**, *134*, 442–449; c) T. Yang, K. Sun, Z. Lei, N. Zhang, Y. Lang, *Journal of Alloys and Compounds* **2010**, *502*, 215–219.
- [439] J.-H. Kim, C. S. Yoon, S.-T. Myung, J. Prakash, Y.-K. Sun, *Electrochem. Solid-State Lett.* **2004**, *7*, A216-A220.
- [440] D. H. Park, S. T. Lim, S.-J. Hwang, J.-H. Choy, J. H. Choi, J. Choo, *Journal of Power Sources* **2006**, *159*, 1346–1352.
- [441] a) C. Rumble, "Structural and electrochemical Investigation of Li(Ni_{0.4}Co_{0.2}-yAl_yMn_{0.4})O₂ Cathode Material", can be found under http://escholarship.org/uc/item/7p72_79ht. University of California (Ed.), Lawrence Berkeley National Laboratory, Berkeley. **2012**; b) J. E. Post, P. J. Heaney, J. Hanson, *Am. Mineral.* **2003**, *88*, 142–150.
- [442] K. Dokko, M. Mohamedi, N. Anzue, T. Itoh, I. Uchida, *J. Mater. Chem.* **2002**, *12*, 3688–3693.
- [443] C. M. Julien, F. Gendron, A. Amdouni, M. Massot, *Materials Science and Engineering: B* **2006**, *130*, 41–48.
- [444] N. Amdouni, K. Zaghib, F. Gendron, A. Mauger, C. M. Julien, *Ionics* **2006**, *12*, 117–126.
- [445] P. Strobel, A. Ibarra-Palos, M. Anne, C. Poinsignon, A. Crisci, *Solid State Sciences* **2003**, *5*, 1009–1018.
- [446] Y.-P. Zeng, X.-L. Wu, P. Mei, L.-N. Cong, C. Yao, R.-S. Wang, H.-M. Xie, L.-Q. Sun, *Electrochim. Acta* **2014**, *138*, 493–500.
- [447] J. Wang, W. Lin, B. Wu, J. Zhao, *J. Mater. Chem. A* **2014**, *2*, 16434-16442.
- [448] J. H. Lee, K. J. Kim, *Electrochim. Acta* **2014**, *137*, 169–174.
- [449] Ramana, C. V., M. Massot, C. M. Julien, *Surf. Interface Anal.* **2005**, *37*, 412–416.
- [450] a) B. Ammundsen, G. R. Burns, Islam, M. Saiful, H. Kanoh, J. Roziere, *J. Phys. Chem. B* **1999**, *103*, 5175–5180; b) C. Julien, S. Ziolkiewicz, M. Lemal, M. Massot, *J. Mater. Chem.* **2001**, *11*, 1837–1842.
- [451] a) P. Tarte, J. Preudhomme, *Acta Crystallogr.* **1963**, *16*, 227; b) P. Tarte, *Spectrochim. Acta* **1965**, *21*, 313–19.

- [452] T. Aoshima, K. Okahara, C. Kiyohara, K. Shizuka, *Proceedings of the 10th International Meeting on Lithium Batteries* **2001**, 97–98, 377–380.
- [453] a) Q. Zhang, J. Mei, X. Wang, F. Tang, W. Fan, W. Lu, *Electrochim. Acta* **2014**, 143, 265–271; b) W. Huang, L. Xing, Y. Wang, M. Xu, W. Li, F. Xie, S. Xia, *J. Power Sources* **2014**, 267, 560–565.
- [454] M. Yoshio, R. J. Brodd, A. Kozawa, *Lithium-ion batteries. Science and technologies*, Springer, New York, NY, **2009**.
- [455] a) M. S. Ding, Jow, T. Richard., *J. Electrochem. Soc.* **2004**, 151, A2007-A2015; b) J. Li, C. F. Yuan, Z. H. Guo, Z. A. Zhang, Y. Q. Lai, J. Liu, *Electrochim. Acta* **2012**, 59, 69–74.
- [456] A. Webber, *J. Electrochem. Soc.* **1991**, 138, 2586–90.
- [457] Newman, G. H., Francis, R. W., Gaines, L. H., Rao, B. M. L., *J. Electrochem. Soc.* **1980**, 127, 2025–7.
- [458] a) M. S. Ding, K. Xu, Jow, T. Richard., *J. Electrochem. Soc.* **2005**, 152, A132-A140; b) J. Li, K. Xie, Y. Lai, Z. Zhang, F. Li, X. Hao, X. Chen, Y. Liu, *J. Power Sources* **2010**, 195, 5344–5350.
- [459] Ngo, H. L., K. LeCompte, L. Hargens, McEwen, A. B., *Thermochim. Acta* **2000**, 357-358, 97–102.
- [460] P. Hapiot, C. Lagrost, *Chem. Rev. (Washington, DC, U. S.)* **2008**, 108, 2238–2264.
- [461] S. Wenig, G. Topalov, B. Oberschachtsiek, A. Heinzl, I. Mertens, P. Schulz, P. Wasserscheid, "Einsatz ionischer Flüssigkeiten als Elektrolyt in Lithium-Ionen-Zellen", can be found under https://www.google.de/url?sa=t&rct=j&q=&esrc=s&source=web&cd=1&ved=0CCEQFjAAahUKEwieyrvPhdrGAhVC6RQKHfNEADE&url=http%3A%2F%2Fwww.zbt-duisburg.de%2Ffileadmin%2Fuser_upload%2F01-aktuell%2F06-veranstaltungen%2FAiF_BZ-Allianz_2012%2F21_Ionische_Fl%25C3%25BCssigkeiten.pdf&ei=17KkVd6CN8LSU_OJgYgD&usg=AFQjCNEH7fxENFD30trih2rXjciZRn2ECg&cad=rja. Friedrich-Alexander-Universität Erlangen-Nürnberg (Ed.). **2012**.
- [462] D. Aurbach, B. Markovsky, G. Salitra, E. Markevich, Y. Talyossef, M. Koltypin, L. Nazar, B. Ellis, D. Kovacheva, *J. Power Sources* **2007**, 165, 491–499.
- [463] D. Aurbach, *J. Power Sources* **2000**, 89, 206–218.
- [464] L. Yang, B. L. Lucht, *Electrochem. Solid-State Lett.* **2009**, 12, A229-A231.
- [465] K. Edstroem, T. Gustafsson, Thomas, J. O., *Electrochim. Acta* **2004**, 50, 397–403.

- [466] T. Eriksson, Andersson, A. M., C. Gejke, T. Gustafsson, Thomas, J. O., *Langmuir* **2002**, *18*, 3609–3619.
- [467] L. Yang, T. Markmaitree, B. L. Lucht, *J. Power Sources* **2011**, *196*, 2251–2254.
- [468] B. Li, Y. Wang, W. Tu, Z. Wang, M. Xu, L. Xing, W. Li, *Electrochim. Acta* **2014**, *147*, 636–642.
- [469] a) H. Kawaura, D. Takamatsu, S. Mori, Y. Orikasa, H. Sugaya, H. Murayama, K. Nakanishi, H. Tanida, Y. Koyama, H. Arai et al., *Journal of Power Sources* **2014**, *245*, 816–821; b) J. Demeaux, D. Lemordant, H. Galiano, M. Caillon-Caravanier, B. Claude-Montigny, *Electrochimica Acta* **2014**, *116*, 271–277.
- [470] a) D. Aurbach, K. Gamolsky, B. Markovsky, G. Salitra, Y. Gofer, U. Heider, R. Oesten, M. Schmidt, *J. Electrochem. Soc.* **2000**, *147*, 1322–1331; b) N. Liu, H. Li, Z. Wang, X. Huang, L. Chen, *Electrochem. Solid-State Lett.* **2006**, *9*, A328-A331; c) N. Dupre, J.-F. Martin, J. Oliveri, P. Soudan, D. Guyomard, A. Yamada, R. Kanno, *J. Electrochem. Soc.* **2009**, *156*, C180-C185.
- [471] P. Verma, P. Maire, P. Novak, *Electrochim. Acta* **2010**, *55*, 6332–6341.
- [472] C. Drouet, C. Laberty, Fierro, J. L. G, P. Alphonse, A. Rousset, *International Journal of Inorganic Materials* **2000**, *2*, 419–426.
- [473] N. Treuil, C. Labrugere, M. Menetrier, J. Portier, G. Campet, A. Deshayes, J.-C. Frison, S.-J. Hwang, S.-W. Song, J.-H. Choy, *J. Phys. Chem. B* **1999**, *103*, 2100–2106.
- [474] G. Cherkashinin, K. Nikolowski, H. Ehrenberg, S. Jacke, L. Dimesso, W. Jaegermann, *Phys. Chem. Chem. Phys.* **2012**, *14*, 12321–12331.
- [475] a) S. Oswald, K. Nikolowski, H. Ehrenberg, *Anal. Bioanal. Chem.* **2009**, *393*, 1871–1877; b) E. Beyreuther, S. Grafstrom, L. M. Eng, C. Thiele, K. Dorr, *Phys. Rev. B: Condens. Matter Mater. Phys.* **2006**, *73*, 155425/1.
- [476] a) Carver, J. C., Schweitzer, G. K., T. A. Carlson, *J. Chem. Phys.* **1972**, *57*, 973–82; b) G. C. Allen, S. J. Harris, J. A. Jutson, J. M. Dyke, *Applied Surface Science* **1989**, *37*, 111–134.
- [477] S. Ivanova, E. Zhecheva, R. Stoyanova, D. Nihtianova, S. Wegner, P. Tzvetkova, S. Simova, *J. Phys. Chem. C* **2011**, *115*, 25170–25182.
- [478] A. W. Moses, Flores, Harry G. Garcia, J.-G. Kim, M. A. Langell, *Applied Surface Science* **2007**, *253*, 4782–4791.
- [479] S. Verdier, L. El Ouatani, R. Dedryvere, F. Bonhomme, P. Biensan, D. Gonbeau, *J. Electrochem. Soc.* **2007**, *154*, A1088-A1099.

- [480] Y.-C. Lu, A. N. Mansour, N. Yabuuchi, S.-H. Yang, *Chem. Mater.* **2009**, *21*, 4408–4424.
- [481] L. Vogdanis, W. Heitz, *Makromol. Chem., Rapid Commun.* **1986**, *7*, 543–7.
- [482] T. Kawamura, A. Kimura, M. Egashira, S. Okada, J.-i. Yamaki, *Journal of Power Sources* **2002**, *104*, 260–264.
- [483] a) Gnanaraj, J. S., E. Zinigrad, L. Asraf, H. E. Gottlieb, M. Sprecher, M. Schmidt, W. Geissler, D. Aurbach, *J. Electrochem. Soc.* **2003**, *150*, A1533-A1537; b) C. L. Campion, W. Li, B. L. Lucht, *J. Electrochem. Soc.* **2005**, *152*, A2327-A2334; c) B. Ravdel, Abraham, K. M., R. Gitzendanner, J. DiCarlo, B. Lucht, C. Campion, *J. Power Sources* **2003**, *119-121*, 805–810; d) A. Xiao, W. Li, B. L. Lucht, *J. Power Sources* **2006**, *162*, 1282–1288; e) K. Tasaki, K. Kanda, S. Nakamura, M. Ue, *J. Electrochem. Soc.* **2003**, *150*, A1628-A1636; f) L. Terborg, S. Weber, F. Blaske, S. Passerini, M. Winter, U. Karst, S. Nowak, *J. Power Sources* **2013**, *242*, 832–837; g) S. Wilken, M. Treskow, J. Scheers, P. Johansson, P. Jacobsson, *RSC Adv.* **2013**, *3*, 16359–16364.
- [484] S.-Y. Bae, W.-K. Shin, D.-W. Kim, *Electrochimica Acta*.
- [485] H. Deng, I. Belharouak, C. S. Yoon, Y.-K. Sun, K. Amine, *J. Electrochem. Soc.* **2010**, *157*, A1035-A1039.
- [486] M. Xu, Y. Liu, B. Li, W. Li, X. Li, S. Hu, *Electrochem. Commun.* **2012**, *18*, 123–126.
- [487] a) Z. Cai, Y. Liu, J. Zhao, L. Li, Y. Zhang, J. Zhang, *J. Power Sources* **2012**, *202*, 341–346; b) Y. Liu, L. Tan, L. Li, *J. Power Sources* **2013**, *221*, 90–96.
- [488] Vollhardt, Kurt Peter C, H. Butenschön, B. Elvers, N. E. Schore, *Organische Chemie*, Wiley-VCH, Weinheim, **2009**.
- [489] K. M. Shaju, Rao, G. V. Subba, Chowdari, B. V. R., *J. Mater. Chem.* **2003**, *13*, 106–113.
- [490] L. Bergmann, W. Raith, C. Schaefer, *Elektromagnetismus*, de Gruyter, Berlin [u.a.], **2006**.
- [491] T.-F. Yi, C.-Y. Li, Y.-R. Zhu, R.-S. Zhu, J. Shu, *Russ. J. Electrochem.* **2010**, *46*, 227–232.
- [492] Levi, M. D., D. Aurbach, *J. Phys. Chem. B* **1997**, *101*, 4630–4640.
- [493] R. Dedryvere, D. Foix, S. Franger, S. Patoux, L. Daniel, D. Gonbeau, *J. Phys. Chem. C* **2010**, *114*, 10999–11008.